Les brèches associées aux gisements d'uranium de type discordance du bassin Athabasca (Saskatchewan, Canada)

Guillaume Lorilleux

Ecole Doctorale RP2E (Sciences et Ingénierie des Ressources, Produits, Procédés, Environnement)

THESE

Présentée pour l'obtention du titre de

Docteur de l'Institut National Polytechnique de Lorraine
Spécialité : Géosciences

par

Guillaume LORILLEUX

LES BRECHES ASSOCIEES AUX GISEMENTS D'URANIUM DE TYPE DISCORDANCE DU BASSIN ATHABASCA (SASKATCHEWAN, CANADA)

Soutenue publiquement, le 16 Février 2001
devant la Commission d'Examen

JURY

MM. J.-J. ROYER, Ingénieur de Recherche au CNRS, CRPG, Nancy	Président
M. CUNEY, Directeur de Recherche au CNRS, UMR G2R, Nancy	Directeur de Thèse
M. JEBRAK, Professeur, Université du Québec à Montréal, Canada	Co-Directeur de Thèse
K. KYSER, Professeur, Université de Queen, Kingston, Canada	Rapporteur
M. PAGEL, Professeur, Université Paris Sud XI	Rapporteur
J. MONDY, Responsable Régional Exploration, COGEMA, Vélizy	Examinateur
V. MOULIN, Ingénieur, CEA	Examinatrice

UMR G2R 7566 - Géologie et Gestion des Ressources Minérales et Energétiques
Université Henri Poincaré Nancy 1, Faculté des Sciences, BP 239, 54506 Vandoeuvre les Nancy Cedex

Avant-propos

Le sujet de ce travail de doctorat est né en 1997 alors que je participais à la campagne d'exploration de COGEMA Resources Inc (CRI) à Shea Creek dans le Bassin Athabasca (Nord-Saskatchewan, Canada) en tant qu'élève-ingénieur à l'ENSG. Le développement important des brèches associées aux minéralisations uranifères à Shea Creek conduisit Monsieur J. MONDY, alors Vice-Président d'exploration de CRI, à me proposer de réaliser une thèse sur les brèches associées aux gisements d'uranium de type discordance en me basant essentiellement sur l'étude des brèches de Shea Creek.

La première année de thèse de Janvier 1998 à Janvier 1999 s'est déroulée au Canada dans le cadre de la Coopération du Service National en Entreprise (CSNE) à la COGEMA au sein du département d'exploration de CRI. Elle fut consacrée dans sa quasi-totalité au travail d'observation, de mesure et d'échantillonnage à Shea Creek ainsi que dans la Mine à Ciel Ouvert (MCO) de Sue C.

Les études de laboratoire sur les échantillons sélectionnés ont été réalisées en 1999 et 2000 au CREGU et à l'UMR G2R. Deux visites de terrain, au printemps de chaque année, ont permis d'affiner la compréhension des brèches en levant les nouveaux forages d'exploration à Shea Creek et les nouveaux bancs de la MCO de Sue C. La zone de Maw fut visitée en 1999.

Je remercie l'UMR G2R, dirigé par Monsieur P. LANDAIS, le CREGU, dirigé par Monsieur P. SCHUMACHER, le département d'exploration de COGEMA Resources Inc, dirigé par Monsieur J.-C. RIPPERT, le Groupe des Sciences de la Terre (GST) de COGEMA, dirigé par Monsieur P. BRUNETON, ainsi que le Département des Sciences de la Terre de l'UQAM, dirigé par Monsieur M. JEBRAK, pour m'avoir accueilli et donné les moyens humains et techniques de mener à bien cette étude.

Je voudrais également remercier la COGEMA et le CEA qui ont financé les travaux de cette thèse. Ce travail a aussi bénéficié du soutien financier du CNRS pour une partie de la bourse de thèse BDI CNRS/Entreprise.

Je tiens à exprimer mes plus sincères remerciements à tous les membres qui composent le jury et qui ont accepté de juger ce travail :

Monsieur M. CUNEY, Directeur de Recherches au CNRS, a dirigé ma thèse pendant ces 3 années. Il a su me faire partager ses connaissances étendues de la métallogénie de l'uranium et me sensibiliser aux subtilités des bilans de masse géochimiques. J'ai apprécié son

enthousiasme et sa grande disponibilité. Je lui exprime, ici, toute ma gratitude pour sa constante attention aux travaux développés pendant cette thèse.

Monsieur M. JEBRAK, Professeur et Directeur du Département des Sciences de la Terre et de l'Atmosphère de l'Université du Québec à Montréal (UQAM), a co-dirigé ma thèse pendant ces 3 années. Je le remercie pour son accueil chaleureux à l'UQAM pendant 2 semaines en Décembre 1998. Malgré la distance séparant Montréal de Nancy, il m'a beaucoup appris à la fois sur le plan de la connaissance et de la méthode, grâce à la grande richesse de chacune de nos rencontres ainsi qu'aux fréquents échanges de courriers électroniques. Il m'a convaincu de l'importance de comprendre les phénomènes géologiques sur le terrain et m'a fait bénéficier de ses connaissances et de son expérience de la géologie structurale et de l'étude des brèches. Je tiens à lui exprimer toute ma gratitude.

Monsieur K. KYSER, Professeur à l'Université de Queen à Kingston, m'a fait l'honneur de m'inviter à présenter mes travaux de recherche à Geocanada2000, la réunion annuelle des associations géologiques et minéralogiques du Canada (AGC-AMC) qui a eu lieu en Mai 2000. Je lui suis reconnaissant de bien vouloir juger ce travail.

Monsieur M. PAGEL, Professeur à l'Université de Paris Sud XI, a accepté de juger ce mémoire, je l'en remercie sincèrement.

Monsieur J.J. ROYER, Ingénieur de Recherche au CNRS, m'a fait bénéficier de son expérience de la modélisation avec gOcad ainsi que de ses connaissances sur la thermicité des bassins. Il m'a fait l'honneur d'accepter d'examiner ce mémoire et je lui en suis reconnaissant.

Monsieur J. MONDY, Responsable Régional d'Exploration pour l'Australie à la COGEMA, est l'initiateur de ce travail. J'ai pu bénéficier de son expérience de la géologie des gisements d'uranium ainsi que de son point de vue sur mes travaux au cours des réunions d'état d'avancement de la thèse qui ont eu lieu régulièrement pendant ces 3 années. Je le remercie d'avoir accepté la réalisation de cette thèse sous forme de recueil de publications scientifiques et de bien vouloir examiner ce mémoire. Je lui exprime, ici, ma vive reconnaissance.

Madame V. MOULIN, Ingénieur au CEA, a accepté d'examiner ce travail, je l'en remercie.

J'adresse mes sincères remerciements aux personnes qui, par leur contribution, à divers titres, m'ont aidé à accomplir ce travail :

Monsieur P. BRUNETON, Chef du Groupe des Sciences de la Terre (GST) de COGEMA, qui m'a accueilli dans les locaux du GST à Bessines/Gartempe, qui m'a fait bénéficier de ses connaissances sur la géologie des gisements et en particulier sur les altérations associées aux minéralisations et avec lequel j'ai eu plaisir à interagir régulièrement au cours de ces 3 années.

Monsieur J.-C. RIPPERT, Vice-Président d'Exploration de CRI, qui m'a accueilli pendant 15 mois au Département d'Exploration de CRI, qui m'a donné des moyens conséquents sur le terrain pour mener à bien mes travaux et avec lequel j'ai eu plaisir à collaborer.

Monsieur P. PORTELLA, Responsable d'Exploration de l'Est-Athabasca pour CRI, qui m'a appris à lever efficacement les carottes de forage et avec lequel j'ai eu des discussions fructueuses.

Monsieur D. BAUDEMONT, Géologue Structuraliste à CRI, avec lequel j'ai eu plaisir à travailler à l'interprétation de la zone de Anne à Shea Creek.

Monsieur J. REYX, Ingénieur COGEMA au GST, qui m'a apporté des informations précieuses sur la métallographie des minéralisations uranifères.

Monsieur K. WHEATLEY, Géologue d'Exploration à CRI, avec lequel j'ai eu des discussions intéressantes sur la genèse des gisements et qui a amélioré la qualité de l'anglais de certaines parties du mémoire.

Monsieur R. AUMAITRE, Président d'Exploration de COGEMA en 1998 et 1999, et Monsieur E. KONING, Responsable d'Exploration de l'Ouest-Athabasca pour CRI, avec lesquels j'ai eu plaisir à collaborer.

Monsieur C. LE CARLIER DE VESLUD, Ingénieur de Recherches au CNRS, qui, grâce à sa persévérance, a réalisé un travail remarquable et unique de modélisation de corps de brèches avec gOcad, et Monsieur D. BECEL, qui a également largement contribué à la construction du modèle.

Mademoiselle D. BERUBE, qui a réalisé le programme de calcul des cartes de distances euclidiennes et m'a appris la méthode d'analyse fractale des formes de fragments à l'UQAM.

Mademoiselle C. PEIFFERT, qui a réalisé des calculs avec le code EQ3NR/EQ6 avec une grande rapidité.

Madame C. PADFIELD, bibliothécaire de CRI, qui m'a aidé efficacement dans mes recherches bibliographiques pendant mon séjour au Canada.

Messieurs S. WILSON, Géologue d'Exploitation à la MCO de Sue C, et B. KARLSTADT, qui m'ont accueilli et aidé lors de mes visites dans la MCO.

Monsieur D. MACDOUGALL, Géologue du Saskatchewan Energy and Mines, qui m'a aimablement prêté des lames minces de la zone de Maw en 1998.

Madame T. LHOMME, qui a pris beaucoup de soin à la réalisation et l'interprétation des spectres Raman de kaolinite/dickite.

Madame S. BARDA et Messieurs A. KOHLER et F. DIOT du Service Commun d'Analyses par Sondes Electroniques de l'Université Henri Poincaré, qui ont réalisé les analyses et images à la microsonde électronique et au MEB.

Monsieur J. GHANBAJA, du Service Commun de Microscopie Electronique par Transmission, qui a réalisé les analyses et images au MET.

Messieurs A. BOUCHET, F. RASSINEUX et D. MARCHAND qui ont réalisé et interprété une partie des spectres de diffraction aux rayons X.

Monsieur D. FERRAND, litholamelleur à COGEMA, qui a réalisé des lames minces de qualité sur des brèches souvent très friables.

Monsieur P. LAGRANGE, qui a réalisé des photographies d'échantillons de très bonne qualité et qui m'a donné des conseils précieux pour mes présentations.

Les géologues du département d'exploration de CRI avec lesquels j'ai vécu de nombreux mois dans le Nord canadien et qui m'ont permis de travailler dans la bonne humeur, en particulier Messieurs J. ROBBINS, S. ERIKS, G. CHAPMAN, G. LEE, D. MORRISON, C. REVERING et P. MUNHOLLAND.

Je remercie enfin tous les chercheurs et chercheuses de l'UMR G2R avec lesquels j'ai eu beaucoup de plaisir à interagir. Je remercie en particulier les membres de l'équipe de M. CUNEY qui travaillent sur d'autres aspects de la genèse des gisements d'uranium de type discordance et avec lesquels j'ai eu des discussions particulièrement fructueuses: M. BROUAND, D. DEROME, L. HECHT, P. KISTER et C. PEIFFERT.

Je dédie ce mémoire à mes parents.

Résumé : Les gisements d'uranium de type discordance du Bassin Athabasca (Canada) sont fréquemment associés à des corps de brèches qui forment l'encaissant et enveloppent la minéralisation dans des grès quartzeux. Afin de comprendre les mécanismes de formation de ces brèches et leur rôle dans la genèse de ces gisements d'uranium, les brèches associées aux minéralisations en U du prospect de Shea Creek et de la Mine à Ciel Ouvert de Sue C, et à la minéralisation en Y, terres rares et U de la zone de Maw ont été étudiées.

La cartographie structurale et la modélisation 3D mettent en évidence le contrôle de la géométrie des brèches par des failles généralement inverses et graphiteuses dans le socle. L'étude des paragenèses minérales et les calculs d'âges chimiques U-Pb à Shea Creek mettent en évidence 3 phases de bréchification à sudoite-dravite, à Fe-chlorite et à hématite-sidérite. Elles sont respectivement contemporaines de 3 épisodes de réactivations tectoniques et/ou de surrection du bassin entre 1,52 et 1,25 Ga pendant la principale phase de dépôt des minéralisations à haute teneur et vers 900 et 350 Ma au cours de remobilisations des minéralisations uranifères. Les brèches contemporaines de la genèse de la minéralisation primaire se sont formées en 3 stades caractérisées par l'analyse fractale des formes de fragments exprimant leur degré de maturité.

Le premier stade de formation des brèches a été initiée par une réactivation des failles inverses à graphite qui a provoqué une fracturation tectonique localisée dans le cœur des failles et une fracturation hydraulique, plus étendue, dans les zones de silicification massive précoce des grès.

Le deuxième stade correspond à la dissolution du quartz due à la circulation verticale d'un fluide de socle sous-saturé par rapport au quartz dans les grès fracturés. Les rapports fluide/roche minimaux calculés sont très élevés de l'ordre de 3 000 dans la zone de Maw et de 38 000 dans les zones à boules de Sue. Cette variation reflète la diminution de l'intensité de la dissolution avec la distance à la discordance. Le volume minimal de fluide de socle ayant circulé dans les brèches est de l'ordre du kilomètre cube. Les calculs de bilans de masse montrent que les fluides ont apporté les éléments U, V, Mg, B, Al, K, Bi, Ni, Co, Mo, As, S, W, Zn, Y et terres rares, conformément aux néoformations d'illite, de sudoite magnésienne et de dravite et au caractère polymétallique des minéralisations dans les grès.

Le troisième stade s'exprime par des phénomènes d'effondrements gravitaires faisant suite à la formation de cavités de dissolution du quartz. Dans les zones à boules développées dans le cœur des failles, c'est la contraction tectonique qui a progressivement refermé les espaces vides créés par la dissolution. Les pertes de volumes peuvent atteindre 90 % dans les zones de dissolution les plus intenses, proches de la discordance. Dans les zones de faille à très fort pendage, les effondrements se sont propagés jusqu'à plus de 250 m au-dessus de la discordance comme dans la zone de Maw, de la même manière que dans un karst.

La précipitation d'uranium provoquée par le mélange du fluide réducteur de socle sous-saturé par rapport au quartz (> 250°C) avec des fluides diagénétiques oxydants de bassin (< 240°C) a eu lieu pendant un temps de l'ordre de plusieurs millions d'années, en liaison avec la dissolution progressive du quartz libérant l'espace nécessaire au piégeage des minéralisations massives.

Mots-clefs : brèche, uranium, discordance, grès, zone de faille, dissolution, bilans de masse, analyse fractale.

Abstract : Unconformity-type uranium deposits in the Athabasca Basin (Canada) are commonly hosted and surrounded by breccia bodies in quartzose sandstones. In order to understand the mechanisms of breccia formation and their significance for the genesis of uranium deposits, the breccias associated with U mineralizations of the Shea Creek prospect and Sue C open pit, and with the Y-REE-U mineralization of the Maw Zone were studied.

Structural mapping and 3D modeling evidence the control of breccia geometries by reverse faults that are graphite-rich in the basement. The study of mineral paragenesis and calculations of U-Pb chemical ages at Shea Creek reveal 3 breccia phases with sudoite-dravite, Fe-chlorite and hematite-siderite cements. These breccias developed over more than 1 Ga respectively during 3 stages of tectonic reactivations and/or basin uplift mainly between 1.52 and 1.25 Ga during the main event of primary uranium deposition and at about 900 and 350 Ma during phases of uranium remobilization. The breccias coeval with the genesis of the primary mineralization developed in 3 stages characterized by fractal analysis of fragment shapes expressing their degree of maturity.

The first stage of breccia formation has been triggered by a reactivation of graphite-rich reverse faults inducing localized tectonic fracturing in the core of faults and widespread hydraulic fracturing in early silicified zones.

The second stage corresponds to quartz dissolution due to the vertical circulation of a basement fluid undersaturated relative to quartz in fractured sandstones. Calculated minimum fluid/rock ratios are very high with values of 3,000 at the Maw Zone and 38,000 in the Sue « zones à boules » reflecting the decrease of dissolution intensity with the increase of distance to the unconformity. The minimum volume of basement fluids that have circulated through the breccias is about 1 km^3. Mass balance calculations show an input of U, V, Mg, B, Al, K, Bi, Ni, Co, Mo, As, S, W, Zn, Y and REE, in accordance with the new formation of illite, Mg-rich sudoite and dravite and with the polymetallic sandstone-hosted mineralization.

The third stage is expressed by gravity-driven collapse phenomenons resulting from the cavities created by quartz dissolution. In « zones à boules » developed in the core of faults, it is the tectonic contraction that progressively closed the open spaces formed by quartz dissolution. Volume loss values reach 90 % in zones of intense dissolution close to the unconformity. In steeply dipping fault zones, collapse propagated up to more than 250 m above the unconformity as observed at the Maw Zone, like in a karst.

Uranium deposition induced by mixing of the reducing basement fluid undersaturated relative to quartz (> 250°C) with diagenetic oxidizing basin fluids (< 240°C) occurred during about several million years, simultaneously with quartz dissolution providing the space needed to form the massive mineralizations.

Keywords : breccia , uranium, unconformity, sandstone, fault zone, dissolution, mass balance, fractal analysis.

TABLE DES MATIERES

TABLE DES MATIERES

LISTE DES TABLEAUX

LISTE DES TABLEAUX

Liste des tableaux des publications

Liste des tableaux de l'annexe IV

LISTE DES FIGURES

LISTE DES FIGURES

Liste des figures hors publications

Page

Liste des figures des publications

Page

Article 1 : Polyphase hydrothermal breccias associated with unconformity-type uranium mineralization (Canada) : from fractal analysis to structural significance.

Liste des figures des annexes

Page

I. INTRODUCTION GENERALE

I. INTRODUCTION GENERALE

Situation du sujet

La production d'électricité d'origine nucléaire dans le monde est en augmentation et a atteint 2507,9 TWh en 1999. Cette tendance devrait continuer pour différentes raisons. Premièrement, la consommation énergétique mondiale devrait augmenter de près de 50 % d'ici 2015 (source CEA-DSE). Deuxièmement, suite à la réunion de 159 pays à Kyoto en 1997 afin d'adopter un protocole international de lutte contre l'effet de serre, la production d'énergie à partir de combustibles fossiles devrait diminuer dans un certain nombre de pays industrialisés à partir de 2008. Cette diminution devrait s'accompagner d'une croissance de la production d'électricité d'origine nucléaire qui ne génère pas de gaz à effet de serre. Troisièmement, le nucléaire a l'avantage d'être une énergie peu sensible au coût du combustible et qui permet d'assurer l'indépendance énergétique. Ces facteurs favorables au développement de l'énergie nucléaire doivent être pondérés par les problèmes de gestion des déchets radioactifs dont les solutions conditionneront fortement l'avenir de la filière nucléaire.

Les réserves d'uranium dans le monde hors CEI au 1^{ier} Janvier 1999 ont été estimées à 2 274 000 tonnes à un coût inférieur à 80 $/kg U. Au taux annuel de consommation mondiale d'uranium de 59 400 tonnes en 1998 (source CEA/DES), ces réserves représentent 38 années de consommation.

Le marché actuel de l'uranium est instable et incertain du fait de la proportion importante d'uranium provenant de sources secondaires issues de déstockages ou d'excédents militaires. En 1999, 50 % des besoins des réacteurs ont été alimentés par ces sources secondaires et ont entrainé une baisse des prix spots jusqu'à moins de 19.8 $/kg. Dans un tel contexte, les seuls gisements d'uranium économiques sont les gisements de type discordance qui ont les teneurs les plus élevées et des tonnages considérables.

Les gisements d'uranium de type discordance sont situés à proximité de l'interface entre un socle métamorphique et granitique d'âge Archéen à Protérozoïque Inférieur et une couverture sédimentaire gréseuse d'âge Protérozoïque Moyen. Ces gisements ont été découverts en Australie dans le bassin de McArthur et au Canada dans les bassins du Thélon et Athabasca (Fig. I-1). Les gisements du Bassin Athabasca ont les plus fortes teneurs avec 186 000 tonnes à 14 % d'U à McArthur River et 140 000 tonnes à 13,6 % d'U à Cigar Lake. Le premier gisement d'uranium de type discordance du Bassin Athabasca a été découvert en 1968 à Rabbit Lake (Heine, 1986). Les découvertes se sont ensuite multipliées avec les gisements de Cluff Lake entre 1971 et 1974 (Tona et al., 1985), Collins Bay en 1971 et 1972 (Ruzicka, 1986), Key Lake en 1975 (Kirchner et Tan, 1994), Midwest en 1978 (Farstad et Ayers, 1986), Dawn Lake entre 1978 et 1981 (Clarke et Fogwill, 1981), McLean Lake en

1979 et 1980 (Brummer et al., 1981), Eagle Point en 1980, Cigar Lake en 1981 (Fouques et al., 1986), McArthur River en 1988 (McGill et al., 1993) et Sue en 1988 et 1989 (Baudemont et al., 1993) (Fig. I-2). Depuis la fin des années 1980, malgré le maintien de l'effort d'exploration, aucun autre gisement n'a été découvert dans le Bassin Athabasca à l'exception de la zone minéralisée de Shea Creek (Rippert, 2000). Les découvertes de Rabbit Lake et de Cluff Lake ont été réalisées grâce à des levés radiométriques aéroportés qui ont conduit à la découverte d'alignements de blocs glaciaires minéralisés et ensuite des gisements par forages carottés. La découverte de Key Lake a contribué de manière significative à l'établissement d'un modèle d'exploration empirique associant les minéralisations uranifères avec des failles enracinées dans des lithologies riches en graphite et recoupant la discordance et avec des halos d'altération argileuse dans les grès. La plupart des gisements ont ensuite été découverts grâce à ce modèle en testant par sondages les conducteurs graphiteux repérés en géophysique. L'amélioration des techniques géophysiques a permis de détecter des conducteurs électromagnétiques graphiteux à travers des épaisseurs de grès de plus en plus importantes, conduisant ainsi à la découverte de minéralisations à des profondeurs atteignant 450 m à Cigar Lake, 600 m à McArthur River et plus de 700 m sous la surface à Shea Creek (Thomas et al., 2000).

Les gisements d'uranium de type discordance sont généralement localisés à l'intersection d'un ou plusieurs systèmes de failles avec la discordance. Ces failles sont systématiquement graphiteuses dans le socle et ont rejoué, généralement en contraction, après l'induration des grès du Bassin Athabasca (Dahlkamp, 1978 ; Hoeve et Sibbald, 1978 ; Jones, 1980 ; Strnad, 1980 ; Ey et al., 1985). Les gisements sont toujours associés à un halo d'altération argileuse très étendu dans les grès jusqu'à 400 mètres en largeur, 500 mètres en hauteur et plusieurs milliers de mètres en longueur (Thomas et al., 1998). Cependant, dans certains gisements comme McArthur River, le halo d'altération est plus restreint autour de failles du fait d'une forte silicification précoce des grès (McGill et al., 1993). Un halo d'altération à illite et chlorite plus limité en extension est également présent dans le socle (Ruzicka, 1993). Deux grands types de modèles d'altérations dans les grès sont distingués en exploration (Matthews et al., 1997). Le premier type est rencontré dans la partie nord du Bassin Athabasca et est caractérisé par une illitisation et une désilicification des grès. Le gisement correspondant le mieux à ce modèle est Cigar Lake (Bruneton, 1993). Le deuxième type est plutôt rencontré dans la partie sud du Bassin Athabasca et est caractérisé par une silicification, une chloritisation, une dravitisation et une kaolinisation des grès. L'exemple le plus typique de ce modèle est le gisement de McArthur River (McGill et al., 1993). Plusieurs auteurs ont noté la présence de brèches entourant et/ou encaissant la minéralisation uranifère (Hoeve et Sibbald, 1978 ; Wallis et al., 1983 ; Bruneton et Caumartin, 1985 ; Ey et al., 1985 ; Lorilleux, 1999a et b ; 2000).

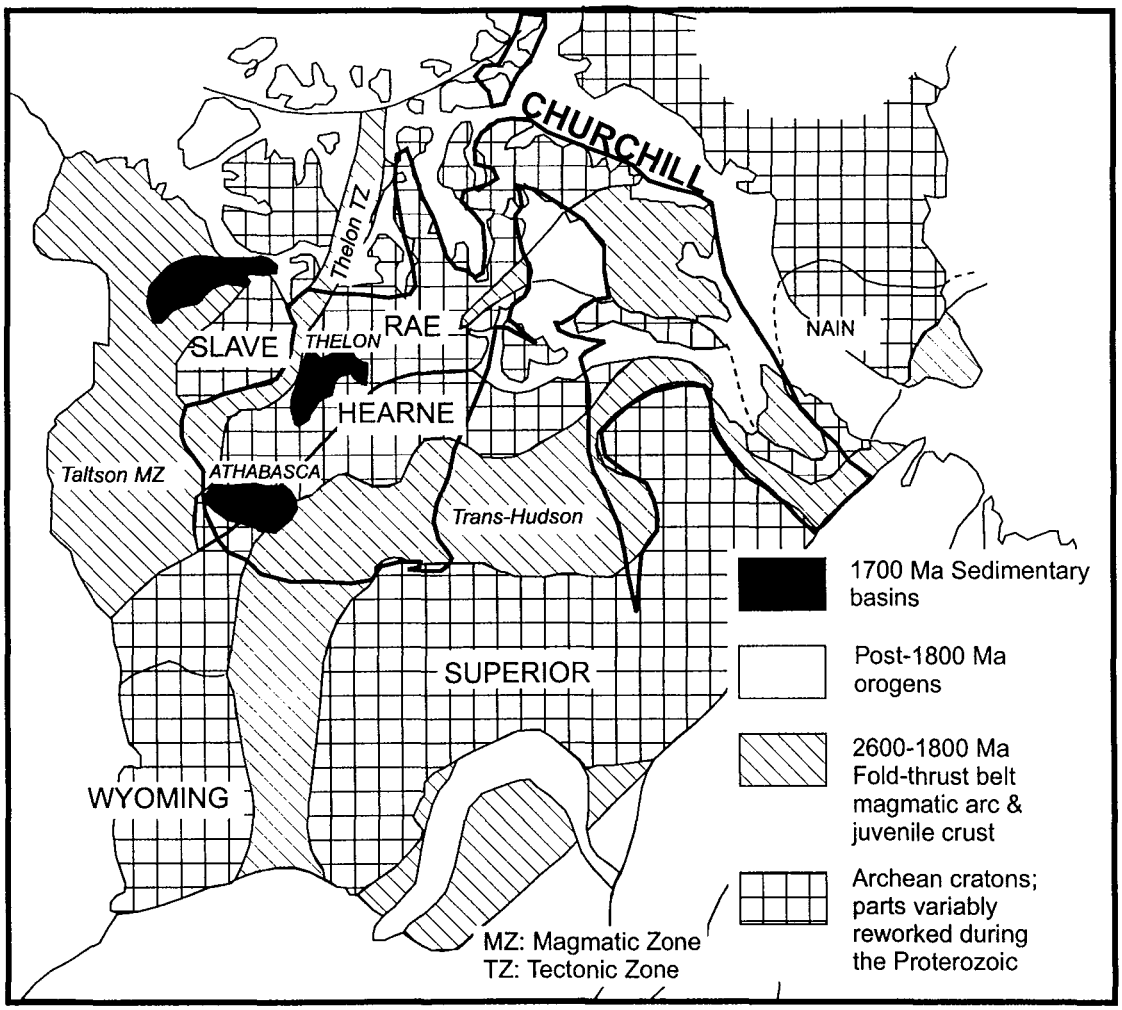

Figure I-1 – Domaines tectoniques du bouclier canadien et position des bassins d'âge Protérozoïque Moyen (modifié de Hoffman, 1989).

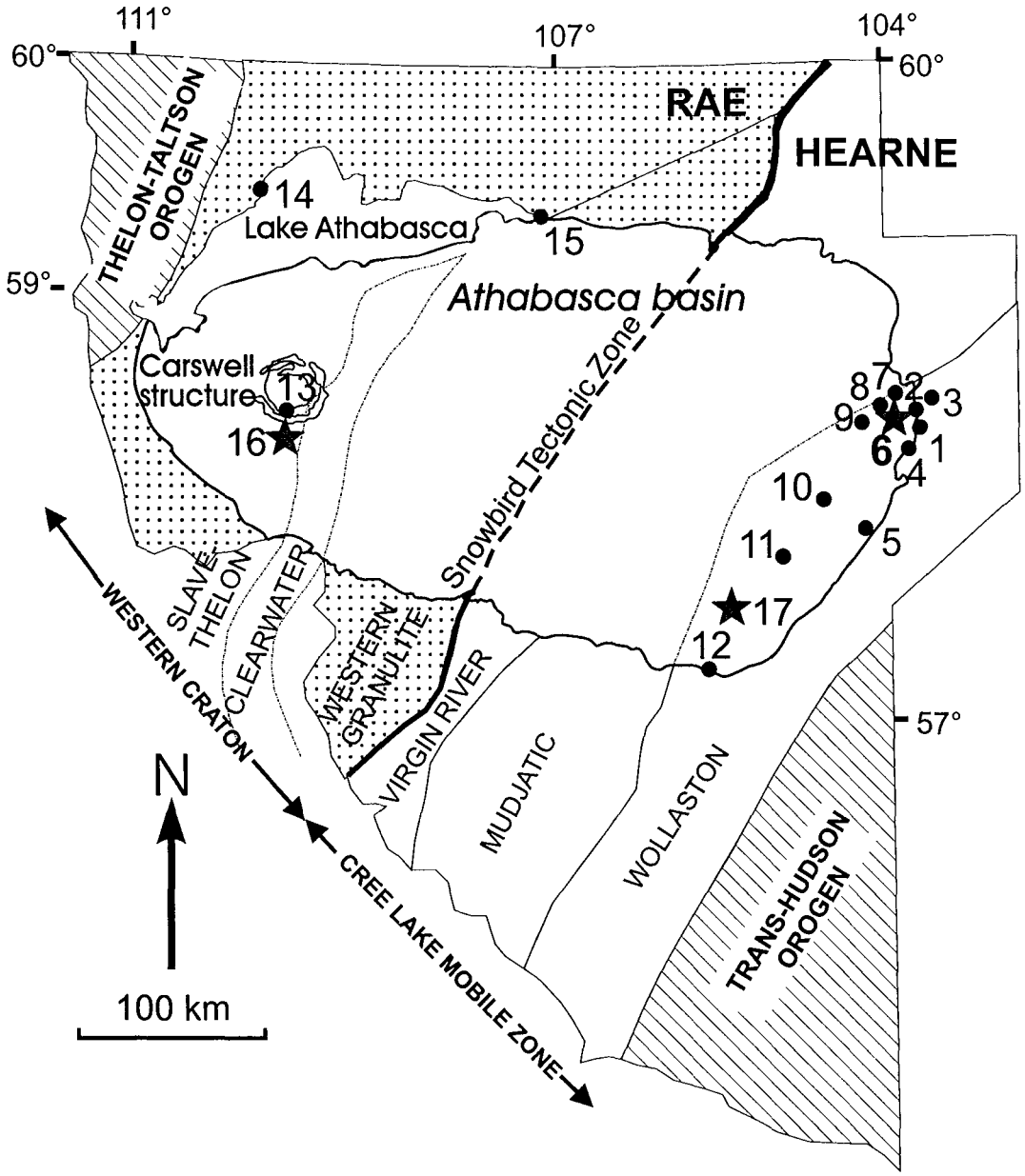

Figure I-2 - Unités crustales et domaines lithostructuraux du socle et principaux gisements d'uranium du Bassin Athabasca (modifié de Ruzicka, 1986). Les 3 étoiles montrent la position des 3 zones d'étude: les gisements de Sue à l'est, le prospect de Shea Creek à l'ouest et la zone de Maw au sud-est. Gisements et minéralisations: 1 = Rabbit Lake, 2 = Collins Bay, 3 = Eagle Point, 4 = Horseshoe and Raven, 5 = West Bear, 6 = McClean and Sue, 7 = JEB, 8 = Dawn Lake, 9 = Midwest, 10 = Cigar Lake, 11 = McArthur River, 12 = Key Lake, 13 = Cluff Lake, 14 = Maurice Bay, 15 = Fond-du-Lac, 16 = Shea Creek, 17 = Maw Zone.

Les brèches sont particulièrement développées dans les halos d'altération des gisements de type sud-Athabasca comme à McArthur River (Matthews et al., 1997). Localement, des affleurements de brèches à dravite ont été découverts plusieurs centaines de mètres au-dessus du gisement de McArthur River (communication personnelle : P. Bruneton). Les minéralisations uranifères peuvent être rencontrées soit dans le socle dans une tranche verticale de 50 mètres sous la discordance et localement jusqu'à 450 mètres sous la discordance (Eagle Point), soit dans les grès jusqu'à 50 mètres au-dessus de la discordance. Localement, des minéralisations perchées peuvent être trouvées jusqu'à plus de 250 mètres au-dessus de la discordance comme à Cigar Lake (Bruneton, 1993). Les minéralisations du socle sont généralement monométalliques avec des oxydes d'uranium et de faibles quantités de sulfures et d'arséniures. Elles correspondent à des gisements de type simple (Fayek et Kyser, 1997). Les minéralisations à la discordance ou dans les grès correspondent au type complexe ou polymétallique. Les oxydes d'uranium y sont associés à des sulfures et arséniures de Ni-Co-As-Fe-Cu-Pb, du V, Au, Zn, Bi, Se et des éléments du groupe du Pt (Hoeve and Sibbald, 1978; Fayek and Kyser, 1997).

Parallèlement à l'établissement d'un modèle d'exploration, 3 principaux modèles de genèse des gisements d'uranium ont été proposés correspondant à des origines différentes pour les fluides minéralisateurs : le modèle supergène, le modèle magmatique hydrothermal et le modèle diagénétique hydrothermal.

Les partisans de l'hypothèse supergène (Knipping, 1974; Langford, 1974; 1977; Robertson et Lattanzi, 1974; Ruzicka, 1975 ; Robertson et al., 1978; Tilsley, 1980) ont fait appel à un lessivage de l'uranium et des autres constituants du minerai dans les roches du socle pendant le développement d'un profil d'altération latéritique avant le dépôt des sédiments du Bassin Athabasca, puis à un transport par des eaux de surface et enfin à une reprécipitation à la rencontre d'un environnement réducteur adapté. Les roches du socle (Knipping, 1974; Langford, 1974; 1977) et les shales riches en matière organique à la base de la formation Athabasca (zone D à Cluff Lake; Robertson et Lattanzi, 1974; Ruzicka, 1975; Pagel et al., 1980) ont été proposés pour former de tels pièges chimiques. Cependant, le développement des halos d'altérations et des brèches dans les grès, les datations des minéralisations uranifères et les études d'inclusions fluides ont montré que les gisements se sont formés postérieurement au dépôt des sédiments Athabasca dans des conditions de diagenèse profonde (Pagel, 1975; 1977 ; Hoeve, 1977 ; Hoeve et Sibbald, 1978; Pagel et al., 1980). De plus, l'école supergène ne fait pas intervenir la tectonique alors que les gisements sont clairement associés à des mouvements tectoniques post-Athabasca (Strnad, 1980).

Une origine magmatique hydrothermale des gisements a été proposée par Little (1974), Morton (1977), Munday (1979) et Binns et al. (1980). Ils ont envisagé des fluides minéralisateurs ascendants chauds d'origine profonde qui se bloqueraient au niveau du piège

de la discordance. Les arguments en faveur d'un tel concept dérivent de l'âge post-Athabasca de la minéralisation et des données d'inclusions fluides indiquant des températures, pressions et salinités élevées pour les solutions minéralisantes. De plus, les éléments Be, Y, Sn, Mo, Bi, B présents dans la minéralisation sont caractéristiques de phénomènes pneumatolytiques-hydrothermaux. Cependant, les âges d'emplacement des granites et des dykes mafiques qui pourraient être à l'origine des fluides ne correspondent pas aux âges de la minéralisation (Le Cheminant et Heaman, 1989 ; Crocker et al., 1993 ; Annesley et al., 1999). De plus, il n'y a pas d'évidences pour dire que l'intrusion de dykes de diabases dans la formation Athabasca fut accompagnée d'une activité hydrothermale significative. Egalement, le magmatisme mafique seul est incompatible avec le large spectre géochimique des gisements. Si Ni, Co, As et Au ont pu être extraits de magmas mafiques, des processus supplémentaires sont nécessaires pour expliquer U et B. La notion que la précipitation de l'uranium a eu lieu en réponse à une ébullition de CO_2 avec l'émergence des solutions ascendantes à la discordance n'a pas pu être confirmée par les études d'inclusions fluides de Pagel (1975a; 1977).

L'hypothèse diagénétique hydrothermale a été proposé pour la première fois par Pagel (1975a) à partir de l'étude d'inclusions fluides mettant en évidence des fluides diagénétiques de bassin (Pagel, 1975b ; 1977 ; Pagel et Jaffrezic, 1977). Le premier modèle complet a été publié par Hoeve et Sibbald (1978). C'est actuellement le modèle qui explique le mieux les caractéristiques des gisements. Hoeve et Sibbald ont proposé que les minéralisations uranifères résultent de l'interaction à la discordance entre des fluides réducteurs riches en méthane circulant le long de failles enracinées dans le socle avec des fluides oxydants de bassin transportant l'uranium. Le méthane aurait été généré par réaction des fluides de bassin avec les lithologies du socle riches en graphite. Les études isotopiques des minéraux d'altérations associés aux gisements ont ensuite confirmé l'importance des fluides diagénétiques ainsi que le mélange de fluides de socle et de bassin (Kotzer et Kyser, 1995). La nature exacte et l'origine des fluides de socle sont encore méconnus. De récentes études d'inclusions fluides, en partie sur les gisements australiens, mettent en évidence un mélange probable entre deux saumures de bassin calciques et sodiques et un fluide de socle plus chaud diluant (Derome et al., 2000a ; 2000b). A partir du calcul des δD de chlorites et d'illites dans des gneiss minéralisés à Key Lake par Wilson et Kyser (1987), Kyser et al. (1989) ont suggéré que les fluides de socle ont une origine profonde et ne sont pas dérivés d'incursions de fluides de bassin. Fayek et Kyser (1997) ont distingué deux variantes du modèle diagénétique-hydrothermal, l'une dans laquelle les fluides de bassin interagissent avec les fluides de socle à la discordance et dans les grès et l'autre dans laquelle les fluides de bassin interagissent directement avec les roches du socle, expliquant ainsi la formation des gisements d'uranium polymétalliques à la discordance et dans les grès, et monométalliques dans le socle, respectivement. D'après Hoeve et Quirt (1984) et Raffensperger et Garven (1995a), les fluides

de bassin ont circulé de manière convective pendant la formation des minéralisations. Le mélange de fluides aurait eu lieu lors d'injections périodiques de fluides de socle dans les grès provoquées par des réactivations tectoniques. Parcontre, Kotzer et Kyser (1995) proposent que les fluides de bassin intervenant dans les processus de minéralisation circulaient latéralement au fond du bassin.

Les brèches associées aux minéralisations n'ont fait l'objet que de très peu d'études détaillées et ont été interprétées de différentes manières. Ey et al. (1985) ont décrit des brèches appelées zones à boules qui encaissent la minéralisation du gisement D à Cluff Lake. Ils les ont interprétées comme résultant de la combinaison d'une déformation et d'une altération hydrothermale intense. Bruneton et Caumartin (1985) ont documenté l'existence de brèches hydrauliques à Cigar Lake. A partir de l'étude du gisement de McClean, Wallis et al. (1983) ont proposé un modèle de formation des gisements associés à des brèches en deux étapes. La première étape correspondrait à l'événement principal de minéralisation associé à de la fracturation en régime extensif et à des zones de précipitation de quartz et de brèches de dissolution dans les grès. La deuxième étape serait une phase d'effondrement et de rebréchification de la minéralisation. Par conséquent, plusieurs hypothèses ont été proposées sur l'origine de la formation des brèches. De plus, les liens génétiques entre les phénomènes de bréchification et les processus de minéralisation sont très mal connus.

Objectifs de l'étude

La forte diminution des découvertes de gisements depuis la fin des années 80 amène les géologues d'exploration à questionner les modèles utilisés. Le fort développement des brèches dans les dernières zones minéralisées découvertes, McArthur River, Shea Creek et dans une moindre mesure Sue, conduit à se demander quelle est leur rôle dans les processus de piégeage des minéralisations uranifères. Comment peuvent-elles permettre d'affiner les modèles génétiques proposés par Fayek et Kyser (1997) ? Comment s'intègrent-elles dans les modèles d'altération des grès proposés par Matthews et al. (1997) ?

Afin de pouvoir répondre à ces questions, trois zones d'étude ont été choisies à différentes distances de la discordance. La première zone sélectionnée est le prospect de Shea Creek situé dans la partie ouest du Bassin Athabasca à quelques kilomètres au sud de Cluff Lake. Les minéralisations à Shea Creek sont situées dans le socle et dans les grès à proximité de la discordance à plus de 700 m de profondeur et sont associées à d'importants corps de brèches dans les grès. La deuxième zone choisie est la Mine à Ciel Ouvert (MCO) du gisement de Sue C, située dans la partie est du Bassin Athabasca. Des brèches et des zones à boules sont développées dans les grès jusqu'à 40 mètres au-dessus de la minéralisation à la discordance (Baudemont et al., 1993). La troisième zone sélectionnée est la zone de Maw, située à 30 km

au NE du gisement d'uranium de Key Lake. Elle a été choisie parce qu'elle montre de spectaculaires affleurements de brèches à dravite à 250 mètres au-dessus de la discordance. De tels affleurements sont très rares dans le Bassin Athabasca qui, dans sa majeure partie, est recouvert d'une couverture glaciaire de plusieurs mètres à plusieurs dizaines de mètres d'épaisseur. Les brèches encaissent une minéralisation à Y et terres rares lourdes et se trouvent à l'aplomb de minéralisations uranifères localisées à la discordance.

La première étape du travail a consisté à étudier les relations spatiales entre les brèches localisées dans les grès et les structures, les altérations, la discordance et les lithologies du socle. A Shea Creek et Douglas River South, les différents objets géologiques ont été levés sur plus d'une centaine de forages, puis cartographiés de l'échelle 1/2000 jusqu'à 1/200 sur certaines coupes. La reconnaissance des différents types de brèches a nécessité l'établissement d'un code de description lié à la forme des fragments et à la nature apparente du ciment. La zone d'exploration la plus active en 1998, 1999 et 2000 a été la zone d'Anne à l'intérieur du prospect de Shea Creek. C'est donc dans cette zone que les brèches ont été étudiées le plus en détail. L'interprétation géologique de la zone d'Anne a beaucoup évolué pendant le déroulement de la thèse du fait de la réalisation pour la première fois de mesures d'orientations de carottes de forages en 1999 ainsi que d'un resserrement de la maille de sondage à 20 m. Le modèle géologique de 1998 est présenté dans la partie II tandis que le modèle de 2000 est présenté dans la partie IV. La cartographie des brèches a été remise à jour chaque année lors de missions de terrain. Dans la MCO de Sue C, les brèches, les structures et les altérations ont été cartographiées sur plusieurs bancs au fur et à mesure de l'approfondissement de la mine de 1998 à l'an 2000. A la Maw Zone, l'orientation des brèches a été mesurée et celles-ci ont été localement cartographiées. Les travaux sur affleurements ont permis d'avoir directement une vision tridimensionnelle des corps de brèches. La compréhension de l'organisation spatiale des brèches à Shea Creek étant beaucoup plus délicate, une modélisation tridimensionnelle avec le logiciel gOcad a été réalisée (voir annexe II).

Ensuite, les textures de brèches ont été décrites en détail dans les différentes zones. Cependant, c'est à Shea Creek que l'étude des textures a été réalisée préférentiellement du fait de la grande variété des types de brèches et de la qualité des observations permise par les carottes de forages. Plus de 200 intervalles de brèches ont été étudiés permettant ainsi d'avoir un bon aperçu statistique des types prédominants et de sélectionner les meilleurs échantillons pour les études de laboratoire (voir échantillons en annexe I et critères de description en annexe IV). A Sue, une étude statistique des formes de fragments des zones à boules a été réalisée.

A Shea Creek et dans la zone de Maw, des échantillons représentatifs des différents types de brèches ont été prélevés. A Sue, des échantillons ont été pris le long d'un profil depuis

l'encaissant jusqu'au cœur d'une zone à boules. Ces échantillons présentés en annexe I ont été sélectionnés afin d'étudier précisément la minéralogie et les textures à l'échelle microscopique et de réaliser des bilans de masse.

Les travaux de terrain ont permis de percevoir les phénomènes impliqués dans la formation des brèches de manière essentiellement qualitative. La deuxième phase d'étude de laboratoire a servi à préciser la nature des phases minérales et à quantifier les processus impliqués dans la formation des brèches.

Les morphologies de fragments de brèches à Shea Creek ont été étudiées par une méthode d'analyse fractale (voir partie II). Dans un premier temps, les photographies de carottes de brèches sciées ont été digitalisées. Ensuite, les images des fragments ont été traitées par un programme développé par Bérubé et Jébrak (1999) dans NIH-Image afin de mesurer leur dimension fractale. Celle-ci donne directement le degré de complexité de la forme des fragments. La distribution statistique des dimensions fractales pour plusieurs types de brèches a permis d'appréhender de manière quantitative les processus dominants dans leur formation.

Les textures des brèches ont été étudiées en lames minces ainsi qu'au MEB sur des surfaces de fragments de brèches de Shea Creek.

Les différentes compositions minéralogiques des ciments des brèches ont été précisées par analyses de diffraction aux rayons X (DRX), par observations de lames minces au microscope pétrographique en lumière transmise et réfléchie, par microscopie électronique à balayage (MEB), par microscopie électronique à transmission (MET), par analyses à la microsonde électronique et par microspectroscopie Raman (voir annexe IV). Des calculs d'âges chimiques avec la méthode de Suzuki et Adachi (1994) ont été réalisés à partir de l'analyses des oxydes d'uranium et de coffinites à la microsonde électronique. Les différents échantillons étudiés ainsi que les analyses sont présentés en annexe. Les paramètres d'analyses ainsi que les standards utilisés pour les analyses à la microsonde électronique sont donnés dans les paragraphes méthodologiques des parties II, III et IV.

Afin de quantifier les processus d'interactions fluides-roche, des calculs de bilans de masse ont été effectués. Dans ce but, les analyses géochimiques de 10 éléments majeurs et de 44 éléments traces des différents types de brèches de Shea Creek, de Sue et de la zone de Maw ont été réalisées par ICP-AES et ICP-MS respectivement (annexe IV). La densité des échantillons a été mesurée en utilisant un picnomètre à eau (voir annexe III). Les calculs de bilans de masse ont été effectués en utilisant la méthode de Grant (1986) qui est une solution graphique simple de la méthode de Gresens (1967) (voir annexe III). L'intérêt de travailler dans les grès quartzeux relativement homogènes du Bassin Athabasca est qu'ils constituent un blanc géochimique, déterminé par la diagenèse régionale, sur lequel se sont superposées des altérations hydrothermales. Cependant, l'homogénéité de la partie quartzeuse majoritaire du grès dissimule une forte hétérogénéité de distribution des minéraux accessoires concentrés en

lits. Or, ce sont ces minéraux accessoires représentés par des oxydes de titane, des zircons et des monazites qui contiennent les éléments les plus stables comme le Ti, Ta, Nb, Th, Zr et Hf. Comme ces éléments stables servent de référence pour déterminer les variations de volume lors des altérations, le choix du protolite a été délicat. Les résultats sont donc présentés avec une marge d'incertitude directement liée à la variabilité de concentration des minéraux accessoires. C'est le Zr qui a été choisi préférentiellement du fait de sa plus forte concentration permettant d'avoir une meilleure précision de sa variation par rapport au protolite. Certains échantillons montrant des évidences texturales d'absence de variations de volume ont servi à déterminer une immobilité de l'aluminium pour certains types d'altération comme l'illitisation dans les zones à boules de Sue. L'aluminium est en effet généralement immobile dans les environnements diagénétiques (Hutcheon, 2000). De plus, la variabilité de proportion des argiles est moindre que celle des minéraux accessoires. L'Al a donc été utilisé pour les altérations à illite à Sue et à carbonates à Shea Creek. Ailleurs, c'est le Zr qui a été utilisé vu que les néoformations de sudoite, de dravite et de Fe-chlorite sont associées à la mobilité très probable de l'aluminium.

Les résultats des analyses géochimiques ont été utilisés pour réaliser des calculs normatifs de composition minéralogique des différents échantillons. Combinés avec les pertes de volume obtenues avec les bilans de masse, ces calculs normatifs ont permis d'estimer la proportion de quartz dissous dans les grès et d'en déduire des rapports volumiques fluides/roche cumulés pour différents types de brèches (voir annexe III).

Ce mémoire est constitué de 5 parties comprenant l'introduction générale et les conclusions générales. Les 3 parties centrales sont présentées sous la forme de quatre publications acceptées, soumises ou soumises prochainement. La deuxième partie (article 1) présente les résultats de l'étude structurale et texturale des brèches de Shea Creek. L'analyse fractale des morphologies de fragments ainsi que l'étude des textures de dissolution au MEB y sont présentées. L'évolution des textures est utilisée pour proposer un modèle de formation des brèches associé à des variations de perméabilité. La troisième partie (article 2) présente les résultats de l'étude structurale, texturale, minéralogique et géochimique des zones à boules de la MCO de Sue C. La combinaison de l'étude structurale et des bilans de masse permet de proposer un modèle quantifié de formation des zones à boules. Des phénomènes d'altération d'une intensité exceptionnelle sont mis en évidence. La quatrième partie (articles 3 et 4) intègre les résultats de l'étude texturale, minéralogique et géochimique des brèches de la zone de Maw, de l'étude minéralogique et géochimique des brèches de Shea Creek ainsi que la synthèse des résultats des trois zones d'études. Les relations des brèches avec les structures, l'évolution des textures et des paragenèses minérales dans l'espace et le temps, les âges chimiques U-Th-Pb et les bilans de masse sont intégrés dans un modèle de formation des brèches associées aux minéralisations uranifères. Les rapports fluide/roche et les temps de

formation des brèches et du dépôt de la minéralisation uranifère sont estimés. L'accent est mis en particulier sur l'organisation géométrique et les relations génétiques possibles entre les trois zones d'études (article 4). Les modèles d'altérations dans les grès sont affinés en tenant compte du développement des brèches.

II. Etude Structurale et Texturale des Breches du Prospect de Shea Creek

II. ETUDE STRUCTURALE ET TEXTURALE DES BRECHES DE SHEA CREEK

Introduction

Le prospect de Shea Creek est situé dans l'ouest du Bassin Athabasca et s'étend de 4 et 30 km au sud de la structure d'impact de Carswell de 39 km de diamètre. La zone de Anne est située au nord du prospect où l'épaisseur des grès est environ de 700 m. Les différentes formations des grès Athabasca sont, du bas vers le haut, Manitou Falls C (MFC), Manitou Falls D (MFD), Lazenby Lake (LZL), Wolverine Point A (WPA), Wolverine Point B (WPB) et Locker Lake (LL). La figure II-1 montre leur représentation dans le modèle gOcad de la zone de Anne à partir des données des différents forages d'exploration. De la même manière, le réseau structural interprété en 1998 a été modélisé sous gOcad (Fig. II-2). Les failles de type II n'apparaissent pas puisqu'elles sont apparues dans l'interprétation en 1999.

Dans les grès de la formation Manitou Falls à Shea Creek, des brèches sont développées de manière extensive généralement dans une tranche inférieure à 30 mètres au-dessus de la discordance et localement au-dessus jusqu'à plus de 50 mètres. Ces brèches forment généralement l'encaissant de la minéralisation uranifère à la discordance. Des zones de brèches sont également développées dans le socle, essentiellement le long de failles. Le but de cette partie est de déterminer les mécanismes qui ont conduit à la formation et à l'évolution des brèches dans les grès de la zone de Anne à Shea Creek. Les brèches ont été étudiées dans les grès parce qu'elles sont plus développées que dans le socle et parce qu'il est plus simple de comprendre leur formation dans les grès qui sont moins complexes minéralogiquement et texturalement que les faciès métamorphiques du socle. Cependant, les types de brèches dans les grès à Shea Creek sont très nombreux et seuls quelques types prédominants ont été étudiés. En particulier, malgré la faible influence de l'impact météorique de Carswell postérieur aux minéralisations, certaines brèches à proximité de la discordance sont interprétées comme étant liées à l'impact. La ressemblance entre les brèches d'impact et certaines brèches à chlorite polymictes est parfois troublante et les choix d'interprétation ont parfois été difficiles.

La première phase du travail a consisté :

(1) à identifier les différents types de brèches sur une centaine de forages,

(2) à étudier leurs relations spatiales avec les failles et la minéralisation.

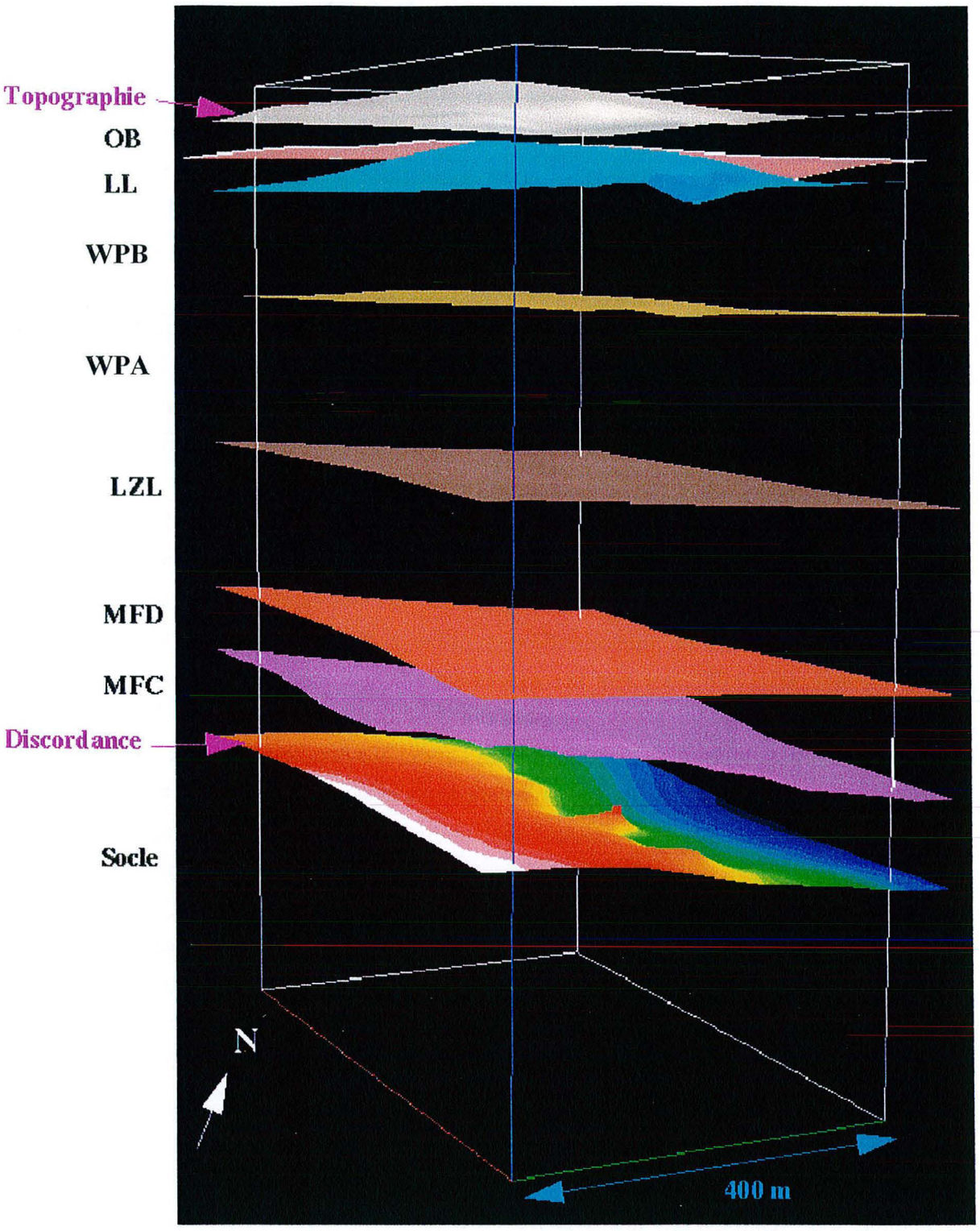

Figure II-1 – Vue du SE du modèle gOcad de la zone de Anne avec la discordance et les formations lithologiques dans les grès. Le dégradé de couleurs sur la discordance correspond aux variations de profondeur.

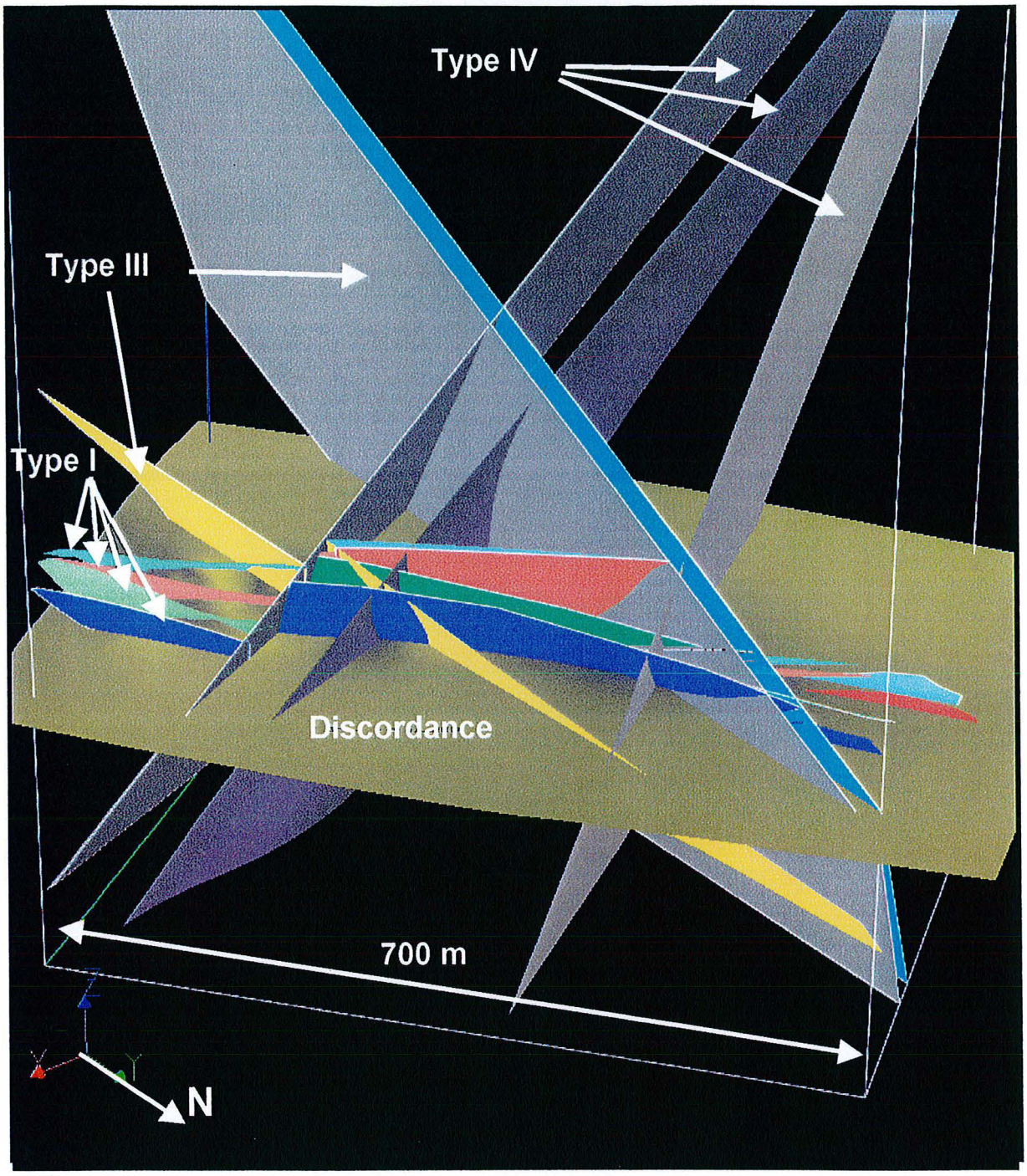

Figure II-2 – Vue du NE du modèle structural complet.

Le polyphasage extrême des altérations plus ou moins pervasives à proximité des minéralisations et de la discordance a rendu le travail de décryptage des différentes phases très difficile et souvent trompeur. On s'est donc attaché à étudier des brèches les plus monogéniques, souvent à l'écart de la minéralisation afin de pouvoir séparer plus facilement les

différentes phases d'altérations. Ainsi, la plupart des échantillons sélectionnés sont peu ou pas minéralisés. Ensuite, les textures de brèches de l'échelle macroscopique à l'échelle du MEB ont été étudiées. Les fragments ont des morphologies parfois complexes qui ont pu être quantifiées par analyse fractale suite au développement d'un programme de calcul de cartes de distances euclidiennes à l'UQAM. L'évolution des textures et des morphologies de fragments dans l'espace et le temps nous a amené à établir un modèle de formation des brèches. L'organisation géométrique des corps de brèches et les relations chronologiques entre les différents types ont permis de situer le développement des corps de brèches dans une histoire tectonique du Bassin Athabasca. Les paragenèses minérales détaillées et les bilans des transferts géochimiques associés au développement des brèches seront abordés dans la partie IV.

ARTICLE 1 :

Polyphase hydrothermal breccias associated with unconformity-type uranium mineralization (Canada): from fractal analysis to structural significance

G. Lorilleux[a], M. Jébrak[b], M. Cuney[a], D. Baudemont[c]

[a] CREGU-UMR G2R 7566, Université Henri Poincaré, BP 23, 54 501 Vandoeuvre-les-Nancy cedex, France

[b] UQAM, DSTA, CP 8888, Centre Ville, Montréal (QUE) H3C 3P8 Canada

[c] COGEMA Resources Inc, Exploration Department, 817-825 45 [th] Street West, P.O. Box 9204, Saskatoon (SK) S7K 3X5 Canada

Accepted in Journal of Structural Geology

Résumé

Les brèches entourant une minéralisation uranifère de type discordance dans les grès du bassin Athabasca, dans le nord de la Saskatchewan, ont été cartographiées et décrites sur carottes de forage. Quatre principaux types de brèches ont été distingués et classifiés chronologiquement en fonction du type de matrice : quartz microcristallin, sudoite-dravite, chlorite ferrifère et polyphasée à carbonate. La cartographie des brèches a montré qu'elles sont contrôlées par différentes familles de failles de socle, incluant une structure graphitique majeure. Les morphologies de fragments de brèches ont été quantifiées en utilisant une méthode d'analyse de dimension fractale. Le pourcentage de matrice et la forme de la courbe de distribution de la morphométrie des fragments permet de déterminer le degré de maturité et la nature des interactions fluide-roche pour chaque type de brèche. Les brèches à quartz microcristallin sont tectoniques et hydrauliques. Les brèches à sudoite-dravite, chlorite ferrifère et polyphasées à carbonate sont formées par dissolution du quartz. Les brèches matures à sudoite-dravite et à chlorite ferrifère présentent des textures d'effondrement liées respectivement à des ouvertures par dissolution et à de la fracturation hydraulique. Les brèches sont l'expression de réactivations de failles de socle postérieures au dépôt des grès (vers 1,7 Ga).

Chaque réactivation sismique créa des conduits structuraux entre des compartiments ayant des pressions différentes, provoquant la circulation de fluides du socle vers les grès. Les fluides furent ralentis dans les grès très fracturés et réagirent avec le quartz pour former des brèches de dissolution. L'interaction de ces fluides dérivés du socle avec des fluides de bassin pourrait être responsable de la formation des minéralisations uranifères de type discordance. Cela expliquerait la corrélation positive entre les corps de brèches et la minéralisation uranifère dans les grès, en particulier pour l'événement à sudoite.

Abstract

Sandstone hosted breccias surrounding unconformity-type uranium ore in the Athabasca Basin, northern Saskatchewan, were mapped and described using drill core. Four main breccia types were distinguished and were classified chronologically based on the type of matrix: microcrystalline quartz, sudoite-dravite, Fe-chlorite and polyphase carbonate. Mapping of the breccias has shown that they are controlled by various sets of basement faults, including a major graphite-rich structure. Breccia fragment morphologies were quantified using a fractal dimension analysis technique. The matrix percentage and the shape of the fragment morphometry distribution curve allow determination of the degree of maturity and the nature of fluid-rock interactions for each breccia.

Microcrystalline quartz breccias are tectonic and fluid-assisted. Sudoite-dravite, Fe-chlorite and polyphase carbonate breccias were formed by dissolution of quartz. Mature sudoite-dravite and Fe-chlorite breccias have collapse textures formed respectively by dissolution opening and fluid-assisted brecciation. Breccias are the expression of basement fault reactivation postdating sandstone deposition (circa 1.7 Ga).

Each seismic event created structural conduits between variably pressured compartments, inducing fluid circulation from the basement to the sandstones. Fluids flowed slower in the strongly fractured sandstones and dissolved quartz to form solution breccias. Interaction of these basement derived fluids with basinal fluids may have led to unconformity-type uranium mineralization deposition. This may explain the good correlation between breccia bodies and sandstone-hosted uranium ore, especially for the sudoite alteration event.

1. Introduction

Breccias are commonly associated with hydrothermal ore deposits. Breccias occurring in mesothermal Au, Cu-Au-U Olympic Dam-type, low temperature F-Ba-Pb-Zn, epithermal Ag-Au and Mississippi Valley-type Zn-Pb deposits are well documented in literature (Jébrak, 1984; Laznicka, 1988; Reeve et al., 1990; Carrier and Jébrak, 1994; Genna et al., 1996; Sass-Gustkiewicz, 1996). Breccia formation has been discussed in particular by Phillips (1986), Sibson (1986), Laznicka (1988; 1989) and Jébrak (1992; 1997).

Numerous breccias have been described associated with the large unconformity-type uranium deposits of the Mesoproterozoic Athabasca basin (Saskatchewan, Canada) containing a resource of over 500 000 tonnes of uranium (Wheatley et al., 1996). These deposits are so-called because they are spatially related to the major unconformity underlying the Athabasca Basin. These breccias surround and locally host the high-grade unconformity-type uranium ores. They have been interpreted as being tectonic (Ey et al., 1985; Baudemont et al., 1993), meteor impact-related (Von Einsiedel, 1981; Harper, 1983; Ey, 1984; Pagel et al., 1985) and of dissolution-collapse origin (Wallis et al., 1983).

The significance of these breccias and their relation to faulting processes remain poorly known. The purpose of this study is to determine the mechanisms that led to the brecciation of the Athabasca sandstones, which host high-grade uranium deposits. A fractal analysis of fragment contours was carried-out in order to quantify their shape complexity. The relationships between fault zones, hydrothermal breccias and uranium ore emplacement was deciphered. Breccia-body geometry and chronological relationships were used to get a better understanding of the organization and functioning of faults in the sandstone basin. Simple textural and mineralogical characteristics of the Athabasca sandstone preclude the breccia features from being controlled by any compositional and structural anisotropy in the parent rocks.

Within the West Athabasca Basin, the Shea Creek exploration zone has been selected for a case study because of the extensive development of breccias, their variety and the dense exploration drilling pattern (20 to 40 m intervals between wells) in the south part, that allows a reconstruction of the 3D geometry of the breccia bodies, and extensive sampling possibilities (Fig. 1). The study area represents a zone of 600 m in length from north to south and 200 m in width.

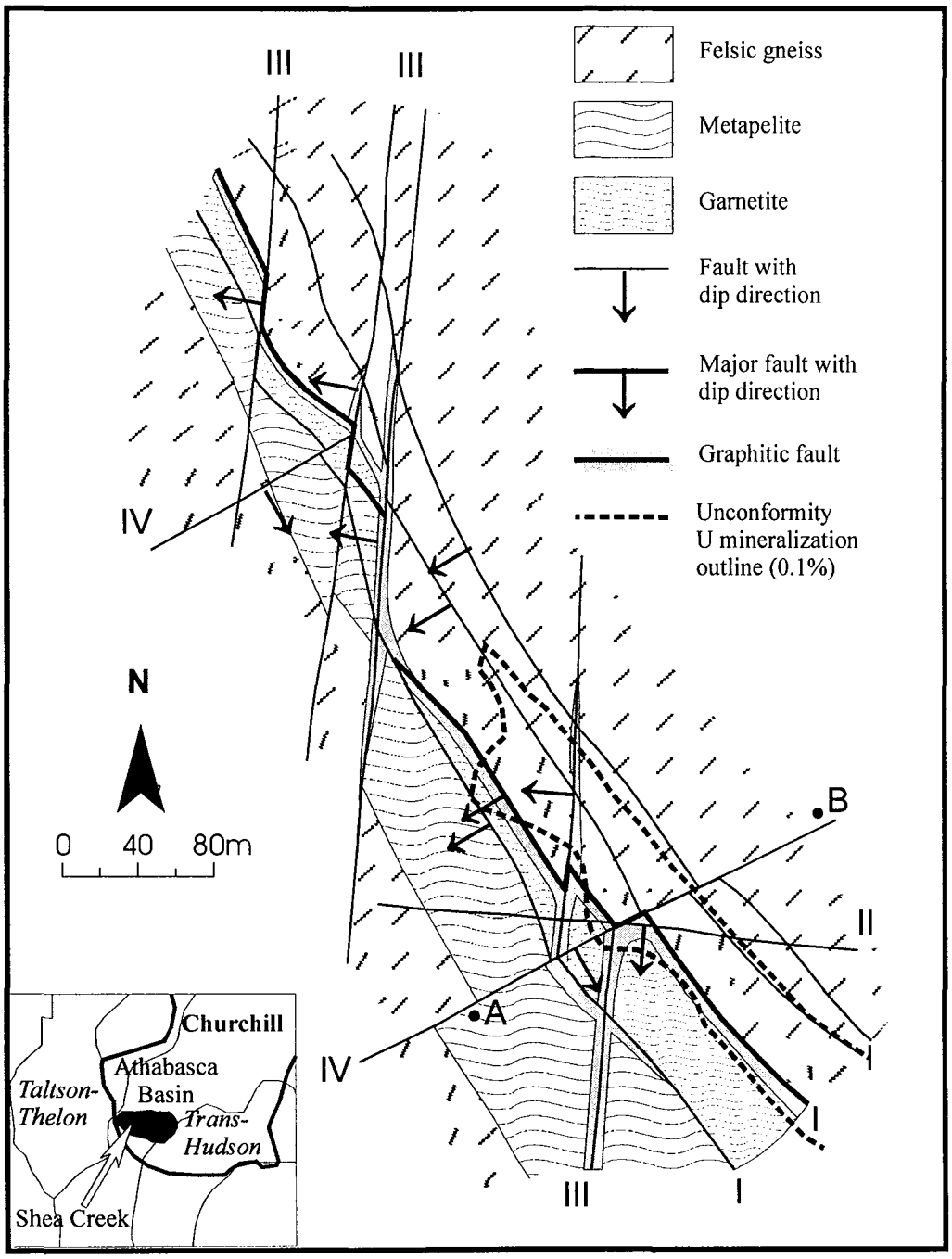

Figure 1 – Geological map of the study area in the south part of the Shea Creek exploration zone at 350 meters below sea level (unconformity level). Felsic orthogneiss is the most widespread lithology and occurs on each side of a partly metasedimentary aluminous gneiss unit divided into metapelites and garnetites. Four types of faults are observed. The main Type I fault separates the metapelites from the felsic gneisses and is the main control of the uranium mineralization. Inset: Location of the Shea Creek area and the Athabasca Basin relative to 2600-1800 Ma fold-thrust belts.

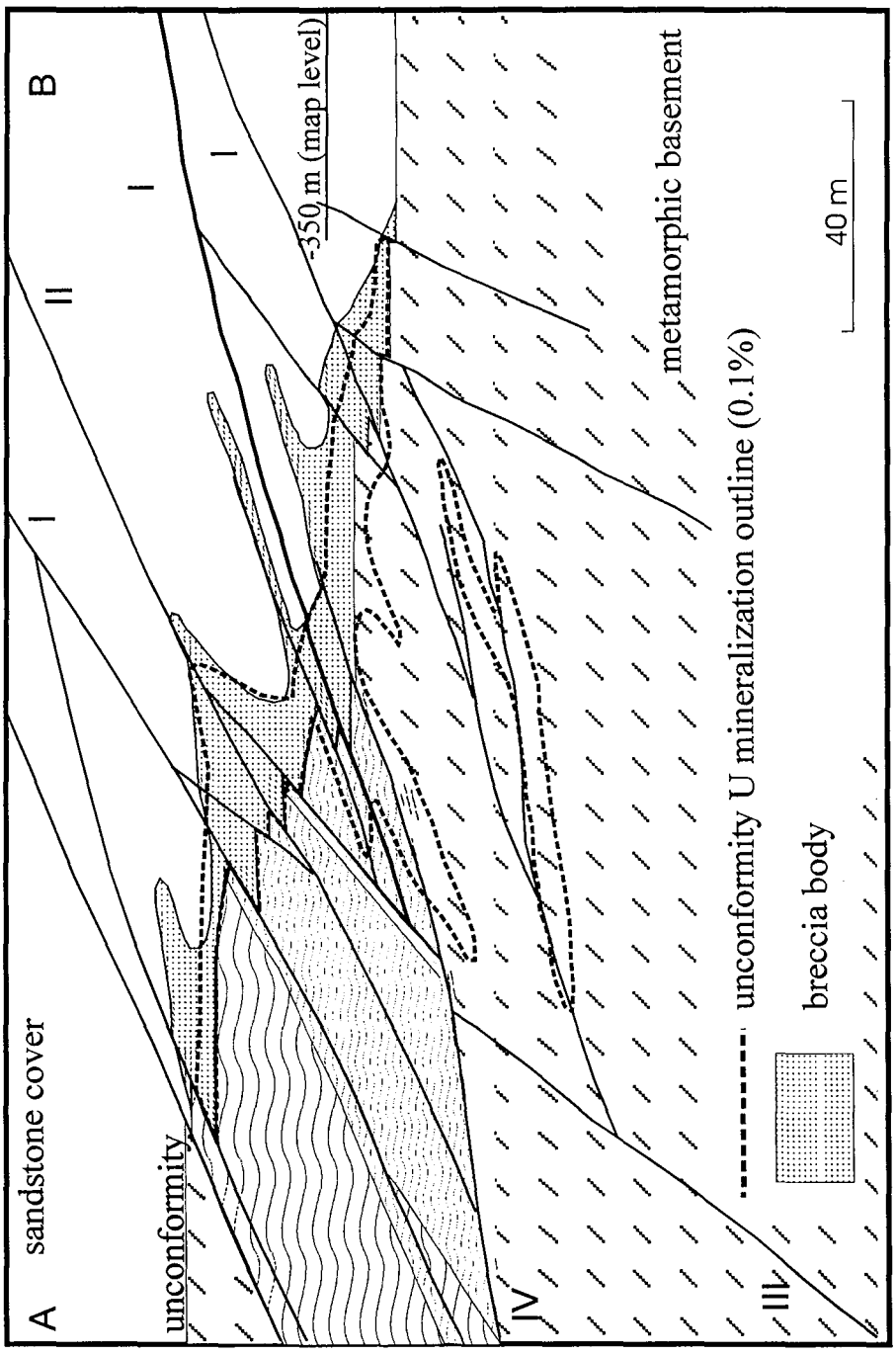

Figure 2 - Cross-section A-B displaying the relationships between the four types of faults, the breccia body, the unconformity and the mineralization. The breccia body includes all the breccia types observed in sandstones. The faults crosscut the unconformity and control the location of ore as well as the breccia body architecture. The lithology legend is the same as for Figure 1.

2. Methodology

Breccias in the sandstones at Shea Creek were observed in core 45 mm in diameter. Detailed descriptions and drawings were made from both whole and sawn core. The closely spaced drilling pattern allowed detailed mapping of structures and breccia bodies (Figs. 1, 2 and 3). The samples were sawn along the core axis and high resolution close-up pictures of the planar sections were taken. The pictures were then scanned at 600 dpi resolution in gray levels. The contrast of the resulting images was then improved using Adobe Photoshop v. 3.0 software in order to easily separate fragments and matrix. In this paper, matrix means interfragmental space that includes both microfragments and cement. Image analysis of the fragments was then performed on a computer using the public domain NIH-Image program developed at the U.S. National Institute of Health. The Euclidian Distance Mapping (EDM) method was used to calculate the fractal dimensions of the fragment morphologies (Fig. 4) (Bérubé and Jébrak, 1999). Stripes of increasing thickness were computed from the particle outline. Then the log of the area of each stripe was plotted against the log of its thickness. The fractal dimension (D) was derived from the slope of the plot (s) using the relationship:

$$D = 2 - s \quad (1)$$

As the EDM method is not accurate for small fragment sizes, only fragment images with areas greater than 10000 pixels were measured. For such fragments, the uncertainty for the EDM method is ±0.01. A minimum of 24 fragments were used to obtain significant Fragment Morphometry Distribution (FMD) curves (Fig. 5). EDM allows high precision fractal analysis and an amplified fractal dimension D^* was used instead of D, with:

$$D^* = (D - 1) \times 100 \quad (2)$$

Petrography of the samples was studied, with emphasis on textural and chronological relationship between fragments and matrix. The fragments from unconsolidated breccias were mechanically removed and cleaned in water by ultrasonic waves. They were then dried and coated with carbon for Scanning Electron Microscope (SEM) studies (Hitachi S-2500 SEM, Henri Poincaré University, Nancy, France). For comparison, non brecciated sandstones, sampled both in the vicinity and far from the U mineralization, were processed using the same methods. We used the terminology of Burley and Kantorowicz (1986) for dissolution textures of fragment surfaces observed under a SEM: pits and notches are typically 1 to 2 μm in size, embayments are about 20 microns and depressions are greater than 20 microns.

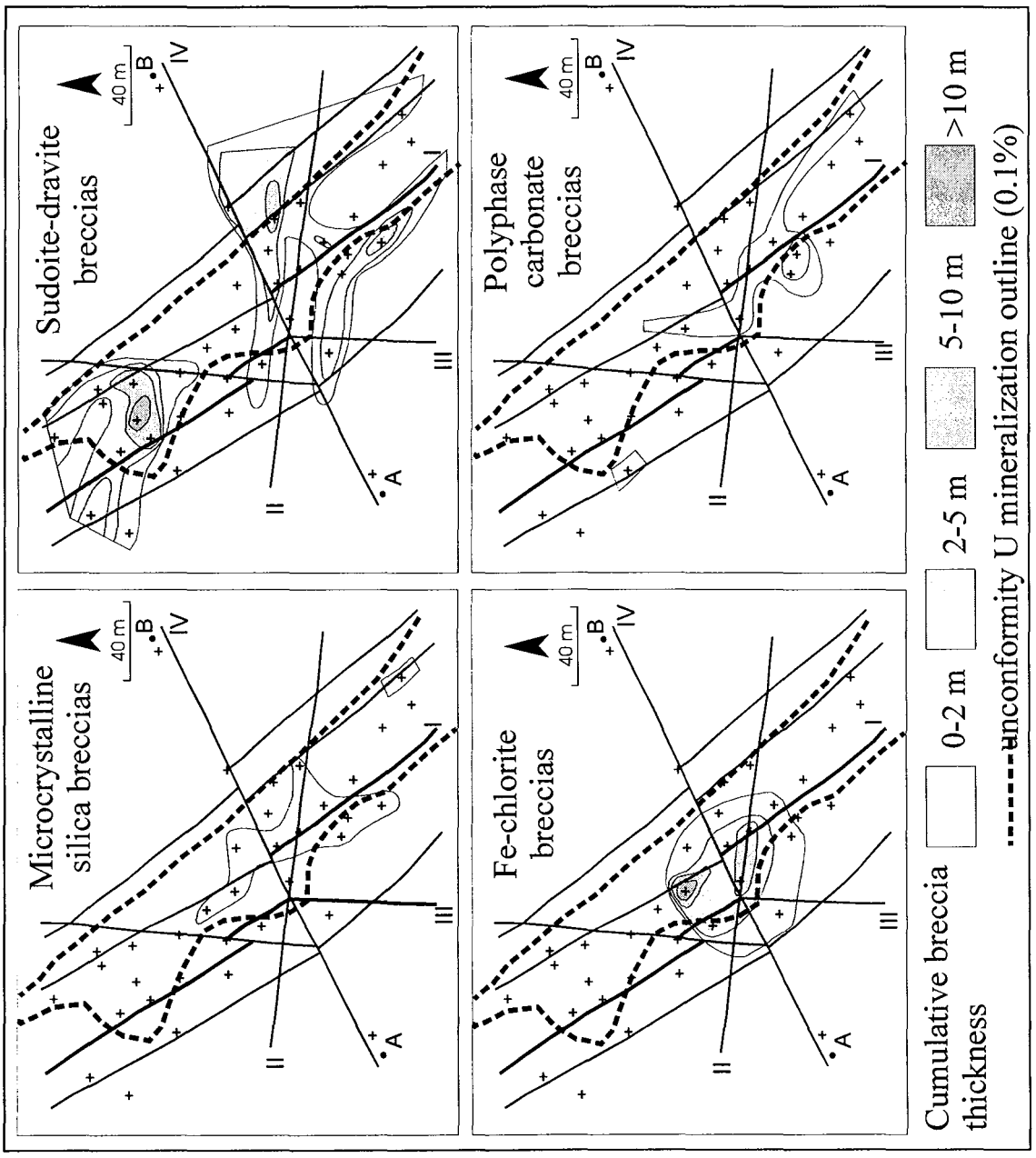

Figure 3 – Cumulative thickness of the different breccia types within 100 meters of sandstones just above the unconformity projected on a structural map of the southern part of the Shea Creek area at 350 meters below sea level (unconformity level, see b). Black crosses represent drill holes intersecting the unconformity.

The breccia cement was analyzed by X-ray diffraction (XRD). On each sample analysed, XRD patterns were determined on the less than 2 micron fractions on oriented aggregates in the range of 35 to 3 Å. On randomly oriented mineral powders, a range of 1.56 to 1.48 Å was used in order to distinguish di- or/and trioctahedral structures of clay minerals. XRD patterns were acquired by ERM (Études Recherches Matériaux) in Poitiers (France) on a Siemens Kristalloflex D501 diffractometer (radiation: Cu Kα), equipped with an X-ray fluorescence detector (Si(Li) diode) cooled by Peltier effect.

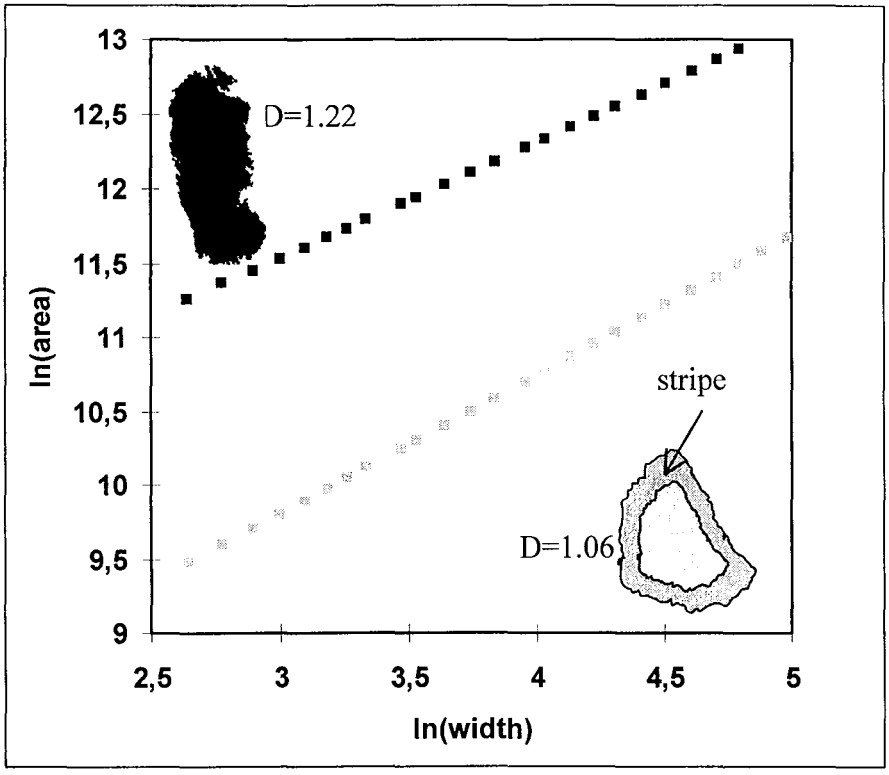

Figure 4 – The fractal dimension D of the particle morphology is computed using the Euclidean distance mapping method (Bérubé and Jébrak 1999). Stripes of increasing thickness are computed from the particle outline. The log of the area of each stripe is then plotted against the log of their thickness. Measurement of two fragments from a polyphase carbonate breccia (black squares) and a sudoite-dravite breccia (gray squares) at Shea Creek.

3. Geological context

The Athabasca Basin lies within the southwest part of the Churchill Structural Province, between the Thelon-Taltson orogenic front (2.0-1.76 Ga; Ross and Eaton, 1997) to the west and the Trans-Hudson Orogen (1.88-1.76 Ga; Chiarenzelli et al., 1998) to the east (Fig. 1). The Thelon-Taltson orogenic front is related to the collision and indentation of the western Rae Province with and by the Archean Slave Province (Hoffman, 1987) and is expressed in the Athabasca Basin by ductile deformation dated between 2.0 and 1.9 Ga. This was followed by a younger, brittle event constrained to 1.84-1.76 Ga (Hoffman, 1987; Villeneuve et al.,

1991). The Shea Creek area is located in the western part of the Basin in the Western Craton which represents a Lower Proterozoic stable cratonic foreland (Hoeve et al., 1980).

The Athabasca Basin formed during the Mesoproterozoic at about 1.7 Ga (Armstrong and Ramaekers, 1985; Kotzer et al., 1992) and is separated from the underlying basement by a major unconformity. It is composed of series of sub-basins oriented NE-SW and controlled by faults rooted in the crystalline basement. The Basin is filled by several lithostratigraphic units, the basal Athabasca Group being the major division (Ramaekers and Dunn, 1977). The Athabasca Group is composed of thick, unmetamorphosed and flat-lying sequences of fluviatile to marine quartzose sandstones deposited in a land-proximal shelf environment (Ramaekers, 1981). A maximum total thickness of 4 to 5 km of sediments in the Basin has been proposed, based on fluid inclusions and diagenetic clay assemblages studies (Pagel, 1975; Hoeve et al., 1981; Halter, 1988).

At Shea Creek, the uneroded sandstone cover is about 700 m thick. Six formations have been distinguished, from bottom to top: Manitou Falls C, Manitou Falls D, Lazenby Lake, Wolverine Point A, Wolverine Point B and Locker Lake. The sandstones hosting the studied breccias mainly belong to the Manitou Falls C Formation. These sandstones directly overlie the basement at Shea Creek and are typically medium to very coarse grained. Rare bedded clay layers are generally one to two cm thick. In non-mineralized zones, clay typically forms 0.5 to 15 percent of the rock and averages around 5 percent (Ramaekers, 1990). Major sandstone cements are quartz syntaxial overgrowths, clay minerals (kaolinite, illite, chlorite) and iron oxides.

Two main Paleoproterozoic basement lithostratigraphic units are found at Shea Creek: a metasedimentary unit in which graphite is mainly concentrated in faults, and a meta-igneous felsic gneiss unit (Fig. 1).

Four types of faults have been recognized, based on their orientation and movement (Table 1). They occur both in the Paleoproterozoic basement and in the Mesoproterozoic cover. Type I reverse faults are regional and oriented N130°-150°. They are described in greater detail below. Type II fault structures are local and oriented N100°-110°. They display late stage normal-sinistral movements with throws up to 10 m. Type III reverse faults are regional and oriented N5°-15°. Like Type I faults, they are graphite-rich and have a ductile pre-Athabasca history. Their post-Athabasca throws may reach 20 m. Type IV fault structures are local and oriented N50°-60°. They display sinistral-reverse to dextral-normal movements with throws of up to 10 m.

FAULT	Type I	Type II	Type III	Type IV
Importance	Regional	Local	Regional	Local
Azimuth	N130-150	N100-110	N5-15	N50-60
Dip	20-40W	50-70N	50-70W	60-80S
Post-Athabasca movements	Reverse	Normal-sinistral	Reverse	Sinistral-reverse to dextral-normal
Post-Athabasca horizontal offset	0 m	15-100 m	0 m	30 m
Post-Athabasca vertical offset	5-10 m (35 m for the fault zone)	2-10 m	10-20 m	10 m
Width in basement	3-5 m	1-10 m	3-5 m	3-5 m
Width in sandstone	10-25 m	1-15 m	20 m	20 m
Characteristics in basement	Graphite-rich and foliation-parallel	No graphite	Graphite-rich and foliation drag folding	No graphite
Style	Ductile-brittle with brittle reactivations	Brittle	Ductile-brittle with brittle reactivations	Brittle

Table 1 – Summary of the main characteristics of the four types of faults.

The N130°-150° Type I structures are the main control for the uranium mineralization. In the basement, the Type I faults are ductile to brittle, 3-5 m wide and represented by graphite- and clay-rich gouges as well as numerous graphite-rich slip planes, parallel to the lithology and foliation. Several nearly parallel Type I faults are grouped into a fault zone up to 80 m wide (Fig. 1 and 2). Type I faults have produced several basement wedges with individual throws of up to 8 m at the unconformity (Fig. 2). A maximum cumulative post-Athabasca throw of 35 m is observed between points A and B at the unconformity (Figs. 1 and 2). In the sandstone, a large Type I fault is represented by a widely fractured zone (10-25 m wide).

These four fault types are associated with breccia bodies and alteration haloes in the sandstones. The alteration haloes are mainly silicification and chloritization and are vertically more extensive than the breccias (up to more than 50 m above the unconformity). Within the alteration haloes, dilational veins have different mineralogical compositions that include quartz, chlorite, dravite, carbonates and pitchblende.

The high-grade uranium ore is found as massive pitchblende veins or impregnations reaching down to 40 m into the basement, and into the sandstone up to 40 m above the unconformity. The main ore pod is located at the unconformity and is partly controlled by Type I faults and parallel low-angle dipping tension gashes (Figs. 1 and 2).

4. Description and mechanisms of formation of the breccias

Breccia fragment morphology and visually determined composition of the cements were used for breccia descriptions in the field. The nature of the cement made it possible to distinguish the different breccia types, whereas the fragment morphology and matrix proportion were used to describe the temporal and spatial breccia evolution within each particular type. Each breccia was characterized in terms of evolutionar maturity (Laznicka, 1988). An immature breccia has a low matrix proportion and weakly corroded and/or abraded and rarely rotated fragments. As the breccia evolved towards a more mature stage, the matrix proportion increases and the fragments become more corroded and/or abraded and rotated. Extreme maturity may be characterized by a decrease of the matrix proportion when collapse occurs.

Four main types of breccias, based on the assemblage of hydrothermal minerals, were recognized in the sandstone at Shea Creek: microcrystalline quartz, sudoite-dravite, Fe-chlorite and polyphase carbonate breccias (Table 2).

4.1. Microcrystalline quartz breccias

Description

Microcrystalline quartz breccias are characterized by white fine-grained quartz-rich matrix. The breccia body is spatially correlated with the main Type I fault (Fig. 3).

On hand specimen, textural variations are related to the maturity of the breccias (Table 2 and Fig. 6a). Immature breccias are represented by an oriented network of white microcrystalline quartz granulation seams or bands. They locally present jigsaw textures. The breccia contacts are typically fracture-controlled with variable dips. Offsets of one mm to several cm are sometimes visible along granulation seams.

The matrix displays either microfragments of detrital quartz (Fig. 7a) or neogenic microcrystalline quartz cement. Quartz microfragments are often angular, locally oriented and sometimes elongated in splinters. They show clean cusps under SEM and are probably of mechanical origin. Consequently, the white fine-grained matrix is either due to the presence of microcrystalline quartz or to the fine granulation of the original detrital quartz grains and overgrowths. Local jigsaw textures are locally recognized at the grain scale.

Breccia body	Microcrystalline quartz	Sudoite-dravite	Fe-chlorite	Polyphase carbonate
Main structural control (order of decreasing importance)	Type I	Type II & I	Intersection of Type I, II and IV	Type I, II & III
Lateral extension	120 m	150 m	80 m	150 m
Vertical extension in sandstones	35 m	35 m	25 m	10 m
Maximum thickness	2 m	Few dm to several m.	Few dm up to 10-15 m.	5 m
Fragments				
Variety	Homolithologic	Homolithologic	Homolithologic to heterolithologic (mature)	Homolithologic to heterolithologic
Alteration	Locally silicified	Locally silicified & rarely chloritized	Silicified & chloritized	Silicified, chloritized & hematized
Orientation	Yes	Rare	Yes when immature	No
Shape	Elongated	Variable and locally ovoïd	Elongated for immature breccias to variable	Complex
Roundness	Angular	Angular to rounded (more rounded when mature)	Angular to rounded	Angular to rounded
Size	1 mm to several cm	1 mm to several cm with tilted blocks	1 mm to several cm with tilted blocks	1 mm to several cm
Rotation	Rare	Common	Yes when mature	Common
Surface SEM textures	Not studied	Etching pits & embayments	Pits and notches mainly & few embayments and depressions	Not studied
Matrix				
Nature	Quartz	Detrital quartz ± sudoite & dravite	Detrital quartz + Fe-chlorite + Fe-kaolinite	Detrital quartz & siderite-chlorite
Quartz Type	Microfragments or newly formed cement	Corroded detrital grains	Corroded detrital grains and angular microfragments	Corroded detrital grains
Microscopic quartz textures	Clean cusps	Dissolution cusps & gulfs	Dissolution cusps & gulfs	Dissolution cusps & gulfs
%matrix	20-60 %	20-60 %	20-70 %	40-90 %
Texture	Jigsaw when immature	Some fragment-supported when mature	Jigsaw when immature; fragment-supported when mature	Jigsaw (rare) when immature
Contacts	Fracture planes	Fracture planes to irregular	Fracture planes to irregular	Fracture planes to irregular

Table 2 – Summary of the main characteristics of the four types of breccias.

Interpretation

Oriented granulation seams in immature microcrystalline quartz breccias express tectonic deformation (Pittman, 1981; Antonellini and Aydin, 1994). The high matrix proportion of mature breccias is related to a strong increase in the spatial density of the deformation bands as well as a probable increase of the displacement. Local jigsaw textures and quartz fillings indicate fluid-assisted fracturing associated with tectonic movements. Angular fragments of sandstone and quartz microfragments (Fig. 7a) show that movements were not sufficient to round them. Therefore, microcrystalline quartz breccias were produced by fluid-assisted tectonic fracturing and microfaulting.

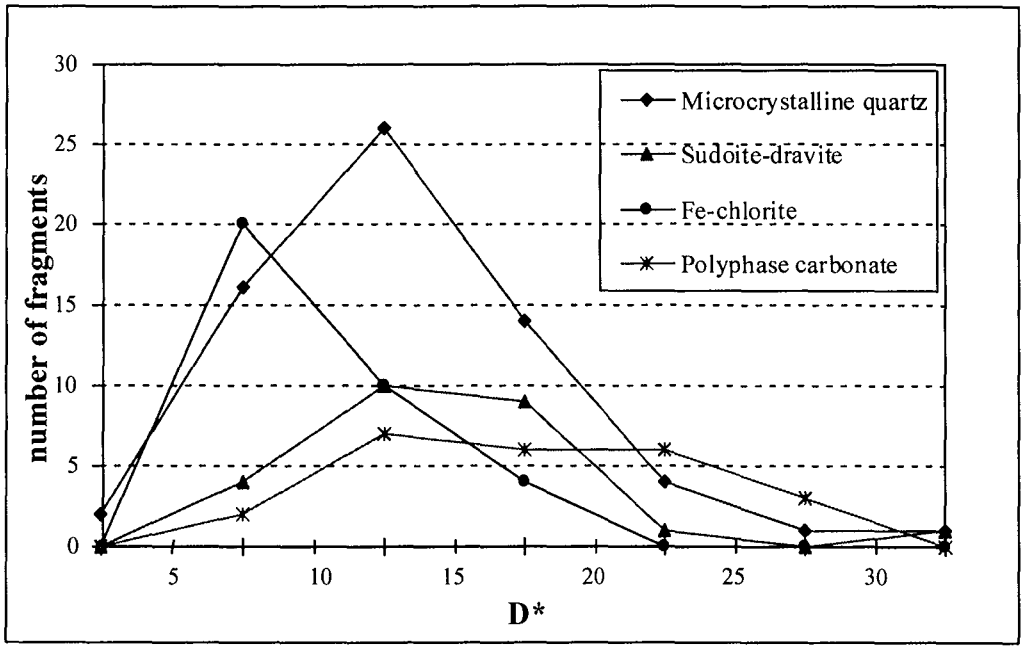

Figure 5 – Fragment morphology (D*) distribution for the four types of breccias studied.

*D** values vary between 2.5 and 32.5 with a median at 12.5; they are globally lower than those for the polyphase carbonate and sudoite-dravite breccia types, whose medians are respectively 17.5 and 13.5. This relatively low value is related to the presence of non-corroded angular fragments. The values between 25 and 35 are related to a late corrosion event observed on numerous samples. As they are found in fragments of other breccia types, microcrystalline quartz breccias are considered to be the product of the earliest breccia event (Fig. 8).

4.2. Sudoite-dravite breccias

Description

Sudoite-dravite breccias are characterized by a matrix containing mainly detrital quartz grains and a very low proportion of white to light green cement.

Sudoite-dravite breccias compose the external zone of a coeval sudoite-rich breccia body centered on the unconformity-type U mineralization. The sudoite breccias form a compact body that extends vertically and laterally into sudoite-dravite breccias along faults. Sudoite-dravite breccias are mainly controlled by Type II and I faults (Fig. 3).

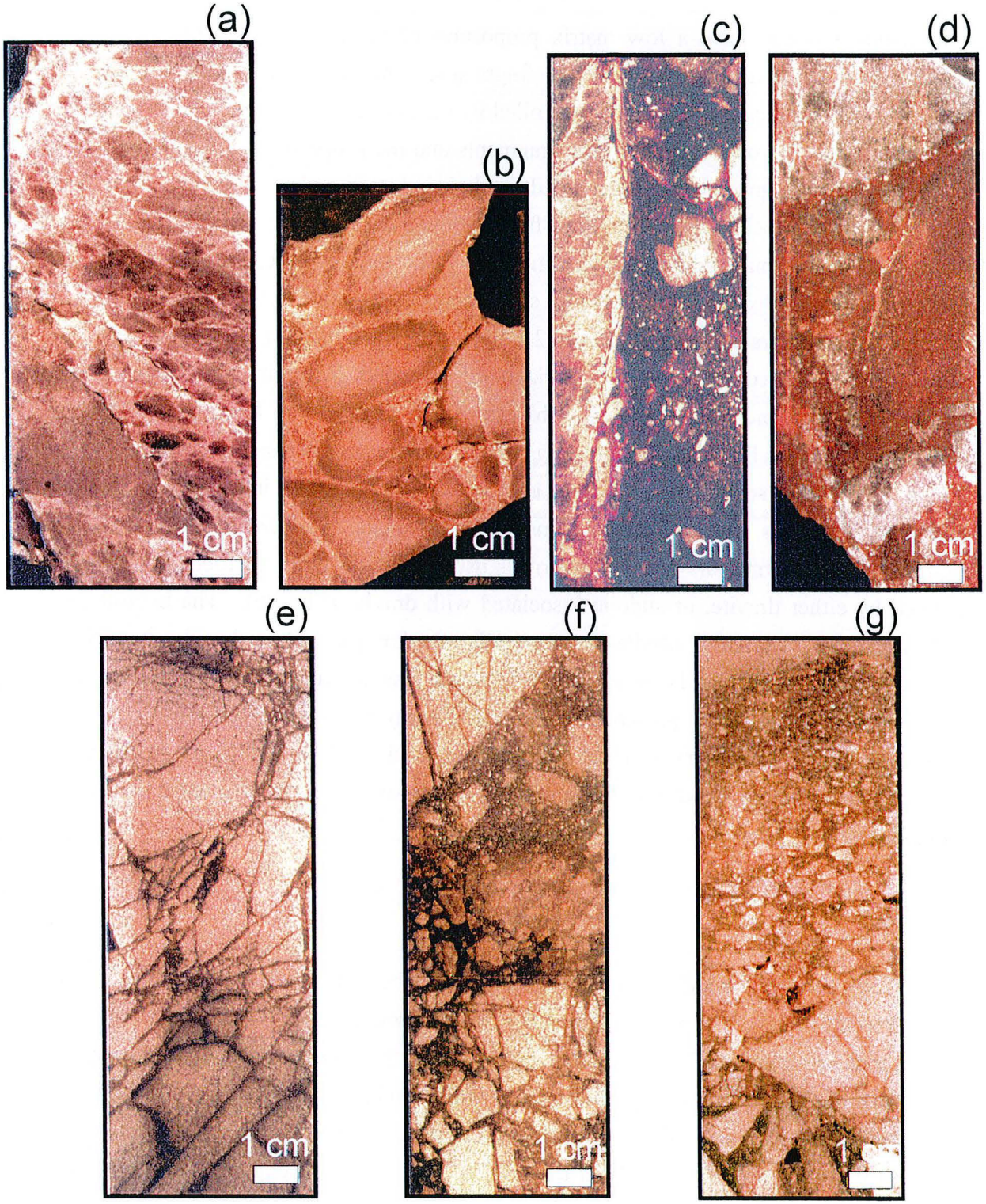

Figure 6 – Photographs illustrating the different types of fragment morphologies and the different textures. (a) orientation of the fragments and anastomosing deformation bands and quartz-filled fractures in a microcrystalline quartz breccia. (b) Well rounded fragments with reaction rims in a sudoite-dravite breccia. (c) Fragment (on the left) of a microcrystalline quartz breccia in a Fe-chlorite breccia (d) Complex fragment shapes in a polyphase carbonate breccia. The dark zone on the right is a sandstone ghost-fragment replaced by carbonate and hematite. Sequence (e) to (g) shows evolution from an immature to a mature Fe-chlorite breccia. Note the strong fracturing in the immature stage and the increase of matrix proportion, the corrosion of fragments and their reorganization into a graded bedding in the mature stage.

Immature breccias have a low matrix proportion of about 20 to 30 vol. % and have oriented, non-rotated and weakly corroded fragments. Fragment borders are controlled by fractures which are themselves locally controlled by sandstone bedding. Mature breccias have non-oriented, locally rotated and rounded fragments and the proportion of matrix is up to 60 vol. %. Locally, fragments may be rimmed by dark indented stylolitic seams. These occur either between interlocked fragments or at fragment-matrix limits and tend to be horizontal. Rounded fragments may show reaction rims (Fig. 6b). Quartz liesegang rings could also locally produce rounded fragments because of the contrasting degree of silicification Most of the D^* values of the fragments are between 2.5 and 22.5, with a median of 13.5 (Fig. 5).

Fragment-supported textures with horizontally oriented fragments have been locally observed in mature breccias. Some tilted blocks, a few dm to more than one m wide, are locally found between breccias. Rotation angle tends to increase when size decreases (Fig. 9).

At a microscopic scale, fragment edges are rarely sharp and often irregular and corroded. Within the fragments, detrital quartz grains with diagenetic overgrowths are corroded by sudoite and hydrothermal dravite. The matrix is usually composed of corroded quartz grains cemented by either dravite, or sudoite associated with dravite (Fig. 7b). The hydrothermal dravite is present as oriented needle-shape crystals of a few μm to less than 1 μm, different from dravite crystallized as large spherulites several tens of μm in size situated between quartz grains. Illite is locally present as revealed by X-ray diffraction (XRD) patterns. The global proportion of quartz grains in the matrix is greater than 85%. Grains are commonly in contact, frequently interlocked (pressure solution), but dissolution is more intense than within the fragments.

Interpretation

As breccias evolve towards a mature stage, fragments become rounded. D* value are low, with a median value of 13.5. The existence of well-rounded and non-rotated fragments indicates that the rounding is of chemical origin rather than mechanical. The presence of reaction rims on the borders of fragments and the corrosion textures of the quartz grains in the matrix confirm the chemical origin of these breccias (Fig. 6b and 7b). This evolution shows that quartz dissolution propagated from the original fractures. Consequently, they are called solution breccias.

There are two possible interpretations to explain the local presence of stylolites at fragment edges. Their presence at the fragment-matrix boundary suggests that they could be pre-existing stylolites acting as micro-permeability barriers during solution breccia formation. However, the presence of interlocked fragments and detrital quartz grains within the matrix

indicates that dissolution may be coeval with a deformation of the breccia medium under pressure. As stylolites tend to be horizontal, they could be due to compaction phenomena.

Local fragment-supported textures and horizontally oriented fragments in mature breccias probably indicate a collapse phenomenon. This is confirmed by the relationship between the rotation angle and size of the tilted blocks (Fig. 9). A temporary loss of cohesion of the breccia may occur when the amount of dissolved material becomes very large, inducing gravity control of the fragment organization (Knipe, 1993). This would explain the rotation of fragments commonly observed in mature breccias.

4.3. Fe-chlorite breccias

Description

In hand specimen, Fe-chlorite breccias are characterized by a dark green to olive green clay-rich matrix (Figs. 6c, 6e, 6f and 6g). They may be slightly U mineralized. Fe-chlorite breccias form an 80 m-wide body controlled by the intersection of the main Type I fault with a Type II fault (Fig. 3). They are rooted at the unconformity where they are at their maximum. In upper sections they appear to follow the geometry of the Type I and Type II faults.

These breccia bodies usually correspond to alternating breccia units and tilted blocks of sandstone. In the core, tilted blocks may exceed one m in height and are considered to be breccia megafragments. The rotation angle of fragments generally increases as size decreases (Fig. 9).

Immature Fe-chlorite breccias have rather angular, slightly corroded and elongated fragments. They are often oriented and rarely rotated (Fig. 6e). Matrix percentage is low, about 20 to 30 vol. %. Jigsaw textures are common with local dilation ratios (matrix/fragment volume ratios) greater than 1.

Mature breccias are locally heterolithic. Fragments in heterolithic breccias show different types or degree of silicification and chloritization. The scarcity of heterolithic breccias is partly due to the homogeneous nature of the Manitou Falls sandstones. Fragments in mature breccias have complex and variable shapes. Both angular and corroded fragments may coexist (Fig. 6g). D^* values vary between 2.5 and 22.5, with a median at 9, indicative of angular and weakly corroded fragments (Fig. 5).

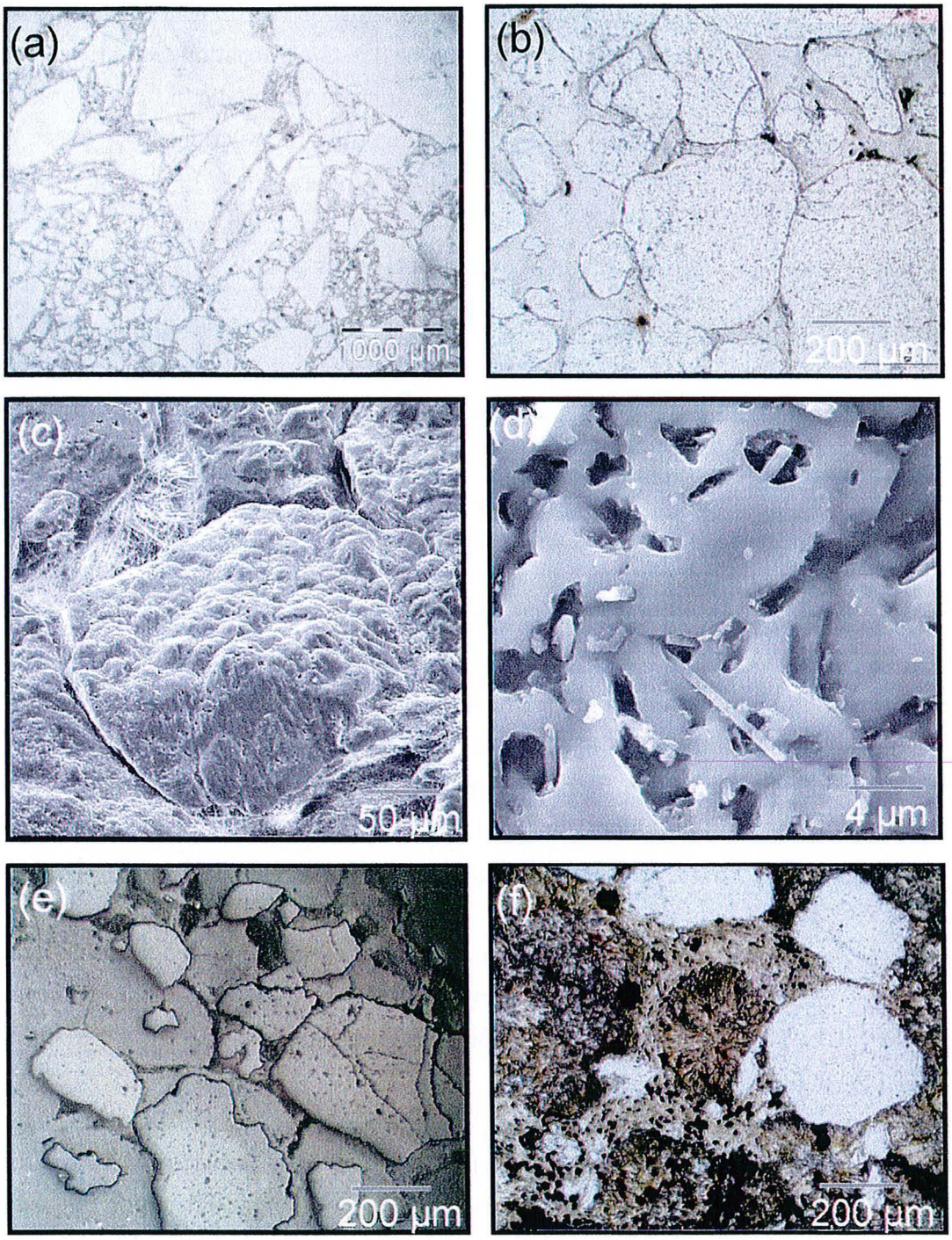

Figure 7 – Photographs illustrating different microscopic textures of the breccias. (a) Non-oriented quartz clasts in the matrix of a microcrystalline quartz breccia (transmitted light). (b) Corroded detrital quartz grains in a sudoite- and dravite-rich cement within the matrix of a sudoite-dravite breccia (transmitted light). (c) Secondary electron SEM image of a corroded detrital quartz grain at the surface of a Fe-chlorite breccia fragment. Note the numerous dissolution pits and embayments. The white needle-shaped minerals between quartz grains are dravite. (d) Secondary electron SEM image of dissolution textures on a quartz grain. Note the corrosion pits and the dravite needles which are also corroded. (e) Corrosion textures of detrital quartz grains in the matrix of a Fe-chlorite breccia (reflected light). Note the hematite rims showing the location of the grain borders prior to the dissolution. (f) Corroded detrital quartz grains in a cement of chlorite and siderite nodules of a polyphase carbonate breccia.

Fragments in the heterolithic breccias are rarely oriented and commonly rotated. However, fragment rotations are difficult to recognize because of the disappearance of the bedding due to intense alteration. The matrix varies between 30 and 70 vol. % and textures are matrix to fragment-supported. In the case of fragment-supported breccias, the fragments are rotated and there is a high proportion of angular fragments. Graded bedding is locally observed in the upper part of fragment-supported breccia units (Fig. 6g).

At a microscopic scale, the outline of angular and weakly corroded fragments described above is sharp and cross-cuts indistinct detrital grains and authigenic quartz. In corroded fragments, clay minerals have developed within corrosion cusps of detrital quartz grains, quartz overgrowths and quartz idiomorphic crystals. The transition between the fragments and the matrix is more progressive than for angular fragments. Typical quartz dissolution textures were observed with SEM on fragment surfaces (Table 2 and Fig. 7c and 7d).

The matrix is usually composed of quartz grains in a cement. Quartz grains are both corroded detrital grains, displaying complex shapes (Fig. 7e) and angular microfragments. The proportion of the latter locally varies from 0 to about 50%. The global proportion of quartz grains in the matrix varies from close to zero to more than 60%. Corroded euhedral quartz grains are also locally present. The cement is composed of Fe-chlorite mixed with Fe-rich kaolinite, smectite and variable proportions of dravite according to microscopic observations and XRD. Locally, fragments of sudoite mixed with dravite are also observed. Some late siderite crystals are present in shrinkage cracks formed in smectite.

Uranium mineralization is present as pitchblende and coffinite replacing and corroding idiomorphic pyrite disseminated within the clay-matrix.

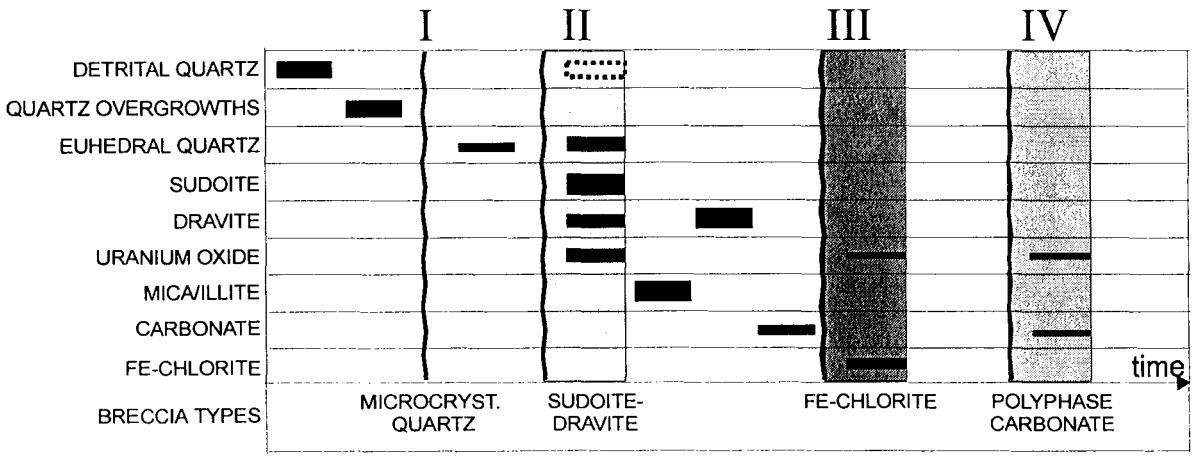

Figure 8 - Simplified paragenetic diagram showing chronological relationships between the four breccia varieties. Wavy lines = tectonic reactivations initiating fluid circulation, shaded areas = subsequent solution breccias, black rectangles = precipitation, empty dashed rectangle = dissolution.

Interpretation

The existence of typical jigsaw textures in weakly corroded fragments is representative of hydraulic brecciation. However, the presence of corroded fragments and ubiquitous microscopic quartz dissolution textures indicate a chemical control of the breccia formation.

The evolution of a Fe-chlorite breccia from an immature to a mature stage is characterized by a displacement and mixing of angular and corroded fragments. Fragment-supported textures and graded bedding, and the relationship between rotation angle and size of tilted blocks in mature breccia zones indicate collapse phenomenon (Fig. 9). Such collapse events could explain the mixing of differently altered fragments.

4.4. Polyphase carbonate breccias

Description

Polyphase carbonate breccias typically display a red clay- and carbonate-rich matrix (Fig. 6d). They are locally associated with uranium mineralization. The body geometry of these breccias is controlled by the main Type I fault and Type II and III faults (Tab. 2 and Fig. 3). Their bodies are narrower than the other types of breccias and are located close to the unconformity.

Rare immature breccias have sub-angular fragments with a low matrix proportion and jigsaw textures. Mature breccias are commonly heterolithic and contain fragments of variably silicified, chloritized, hematized and carbonate-rich sandstone and of hematized and argillized basement fragments. They are matrix-supported and contain mostly rounded and corroded fragments. D* values vary largely from 2.5 to 32.5 with a median at 17.5 (Fig. 5). These values are globally higher than for the other types of breccias and reflect more complex fragment morphologies. Matrix proportion varies between 40 and 90 vol. %. In the matrix, a greater percentage of quartz grains is sometimes found close to the edges of the fragments over distance of a few mm, indicative of a corroded fragment rim. Locally, quartz grain distribution in the matrix is oriented within a fragment outline. Such distribution may then represent the bedding of an original sandstone fragment, replaced by hematite and carbonates (Fig. 6d).

At microscopic scale, sandstone fragments display corrosion of detrital quartz grains and their overgrowths by carbonates. The matrix is usually composed of corroded quartz grains in a cement of chlorite, illite and siderite (Fig. 7f). Siderite crystallized as spherulites and its proportion is highly variable. Very fine hematite disseminations give the rock a red colour. The global proportion of quartz grains within the matrix varies from 5% to 40 vol. %.

Jigsaw textures are locally observed between fractured quartz grains within the matrix. Some corroded euhedral quartz grains are also present.

Interpretation

Jigsaw textures in immature polyphase carbonate breccias and their remnants in more mature breccias indicate the existence of a possible early hydraulic fracturing event. This event is strongly overprinted by quartz corrosion as evidenced by the complex shapes of corroded fragments and microscopic dissolution textures.

The presence of basement fragments in some of the mature breccias could be related to the proximity of the unconformity, and to reverse Type I faults creating basement wedges in sandstones.

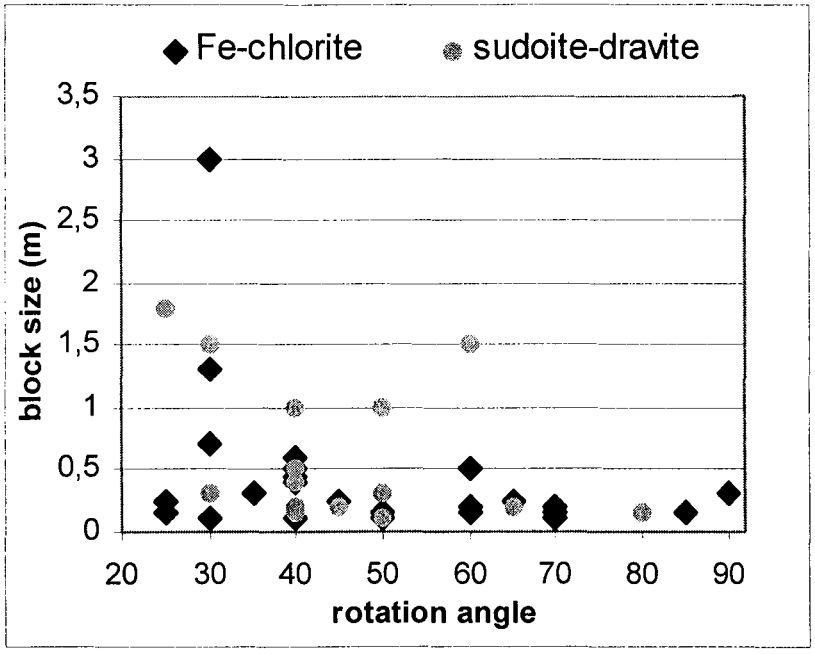

Figure 9 – Diagram showing the relationship between rotation angle and size of tilted blocks in sudoite-dravite and Fe-chlorite breccias. Rotation angle tends to increase as the size decreases.

5. Discussion

5.1. Chronological relationships

Crosscutting relationships between breccias and replacement minerals within their cements are the main criteria used to establish chronological relationships. A simplified chronological diagram is presented in Figure 8.

Fragments of microcrystalline quartz are locally isolated and corroded within a sudoite-dravite matrix. Contacts between microcrystalline quartz and sudoite-dravite breccias indicate

the progression of a sudoite-dravite corrosion front that has altered the microcrystalline quartz texture. In addition, microcrystalline quartz breccias never contain fragments of other types of breccias. Therefore, they are considered to be the product of the earliest breccia event. In most of the unconformity-type uranium deposits of the Athabasca Basin, the primary uraninite mineralization event occurred between 1.55 and 1.0 Ga (Lainé, 1985; Fayek and Kyser, 1997). At Cigar Lake, this event is dated at 1341 ± 12 Ma (U-Pb) and is contemporaneous with sudoite breccias (Pacquet and Weber, 1993). Consequently, the microcrystalline quartz breccias formed between approximately 1.7 and 1.3 Ga, after the induration of the basal sediments of the Athabasca Basin.

Fragments of sudoite-dravite breccias are observed within Fe-chlorite breccias. Consequently, sudoite-dravite breccias formed before Fe-chlorite breccias. The relationship between sudoite and associated dravite is not clear. They might be contemporaneous as documented by Pacquet and Weber (1993) at Cigar Lake, but dravite might also be related to a later event. One of the several dravite events observed at Shea Creek is clearly later than the sudoite phase. Pacquet and Weber (1993) indicate a K-Ar age of 925 ± 25 Ma for the ferrikaolinite in perched bodies at Cigar Lake. The slightly mineralized Fe-chlorite breccias, that contain Fe-rich kaolinite, might therefore be coeval with this phase.

Polyphase carbonate breccias contain chloritized fragments that are interpreted to be coeval with the sudoite-dravite breccias. Siderite crystals were observed in cracks formed in the matrix of Fe-chlorite breccias. These crystals are assumed to be contemporaneous with the siderite present in the matrix of polyphase carbonate breccias that, consequently, would be younger than the other types of breccias. These breccias could have formed between 300 and 200 Ma as indicated by dating of a pitchblende-carbonate association in the Dominique-Peter unconformity-type U deposit located in the western part of the Athabasca Basin (Bell, 1985). Fe-chlorite and polyphase carbonate breccias are commonly U mineralized and are therefore probably related to secondary U mineralization and remobilization events.

Consequently, the four types of breccias described in Shea Creek might be representative of a discontinuous geological evolution which began at about 1.7 Ga and possibly lasted to about 200 Ma.

5.2. Breccia maturation

The textural characteristics and the morphometric measurements of the four types of breccias allow interpretation of each of them in terms of maturity (Fig. 10).

Immature breccias

Immature microcrystalline quartz breccia fragments are controlled by granulation seams and fluid-assisted quartz-filled fractures. The fracture intensity may vary in space according to the distance to the faults.

Immature sudoite-dravite breccias have fracture-controlled, weakly corroded and oriented fragments. They are coeval with the primary uraninite mineralization event that probably coincided with a period of peak diagenesis under a 4 to 5 km thick sedimentary pile (Pagel, 1975; Fayek and Kyser, 1997). Fractures may therefore be fluid-assisted, as fluid pressures in sedimentary basins below 3 km depths are commonly lithostatic (Hedenquist et al., 1992; Egeberg, 1992). Fluid-assisted fracturing would also have been favored by the previous silicification event that created impermeable zones above the unconformity. Such a fracturing regime is indicated by the jigsaw textures observed in immature Fe-chlorite and polyphase carbonate breccias.

Therefore, the first stage of breccia formation is controlled by tectonic and fluid-assisted fractures as indicated by fragment shapes and low values of D^* in immature breccias (Fig. 10).

Mature breccias

Fractal analysis of the fragment shapes allows recognition of both the intensity and type of corrosion processes, and also its kinetic component.

D^* median values for the four breccia types vary from 9 to 17.5 corresponding to different complexity levels of the fragment shapes (Fig. 5). For each breccia type, increasing D^* values indicate the evolution from an immature to a mature stage. This evolution is also characterized by an increase of the matrix proportion and by a loss of the fragments original orientation. In the case of microcrystalline quartz breccias, the maturation corresponds to a strong increase of fracturing intensity. Sudoite-dravite, Fe-chlorite and polyphase carbonate breccia maturation is mainly associated with quartz dissolution.

Fragment morphologies of solution breccias are controlled by the quartz consumption reaction. Two different regimes of the dissolution reaction may be distinguished (Hurst and Bjørkum, 1986; Jébrak, 1997). In the diffusion-limited regime, only the most exposed part of the solid is reached and consumed as a reactant; corners will become smooth and fragments may ultimately take a spherical morphology, decreasing the fractal dimension. Such a process will occur if there is a strong chemical disequilibrium between the rock and the fluid. In the kinetic regime, the alteration-dissolution rate is limited only by the chemical reaction rate. The fluid has a relatively low chemical reactivity and the reaction will enhance the contrasting compositions of the fragments and create more complex shape contours. Increasing D^* values

are therefore significant of an evolution from diffusion-limited to kinetic processes in quartz dissolution that indicates a decrease in hydrothermal solution undersaturation.

However, detailed analysis reveal a more complex history: in Fe-chlorite breccias, the observation of some complex shapes and pervasively altered fragments as well as the predominance of pits on fragment surfaces (Tab. 2 and Fig. 7d) would indicate local kinetic regimes (Burley and Kantorowicz, 1986). In sudoite-dravite breccias, the presence of rounded fragments is probably indicative of a diffusion-limited dissolution regime.

The FMD is indicative of the evolution of the corrosion process. Microcrystalline quartz breccias, sudoite-dravite and polyphase carbonate breccias display normal FMD that demonstrate homogeneous fragment shapes and a stationary process: the same D^* value for the different fragments within a type of breccia indicate that the same corrosion process reach an equilibrium within the sandstone.

The Fe-chlorite breccias FMD curve is not unimodal. This reflects the superimposition of the quartz dissolution process on another phenomenon. Low values represent non-corroded fragments fallen from the breccia hanging wall during the collapse event. Higher values would be representative of the fragments corroded by the dissolution event prior to the collapse.

The last stage of evolution of Fe-chlorite breccias is a collapse event. There are two possible origins for this collapse. The first hypothesis is a chemical origin. If more quartz is dissolved than new clay minerals are formed, cavities will appear and may enhance fluid flow and a positive feedback loop, resulting in further dissolution leading to cavity enlargement. If large enough, collapse could occur and produce graded-bedded and fragment-supported textures as well as a mixture of corroded and angular fragments. Similar textures were observed by Dzulyński and Sass-Gustkiewicz (1989) in solution-collapse breccias hosting Mississippi Valley type deposits.

The second hypothesis is a fluid-assisted origin. The local presence of angular and very weakly corroded fragments organized in jigsaw textures suggest fluid-assisted brecciation. The matrix of such jigsaw breccias contains corroded detrital quartz grains within a clay cement. This means that the fluid has probably dissolved and corroded quartz grains by percolation along fractures before the hydraulic event causing detrital quartz grains to fall into the matrix during the brecciation. This interpretation is the most probable as it explains all the features of the Fe-chlorite breccias. As the dissolution phase occurred before the collapse event, it caused an inverse evolution of the breccia maturity (Fig. 10) because of the incorporation of non-corroded fragments coming from the breccia fractured walls.

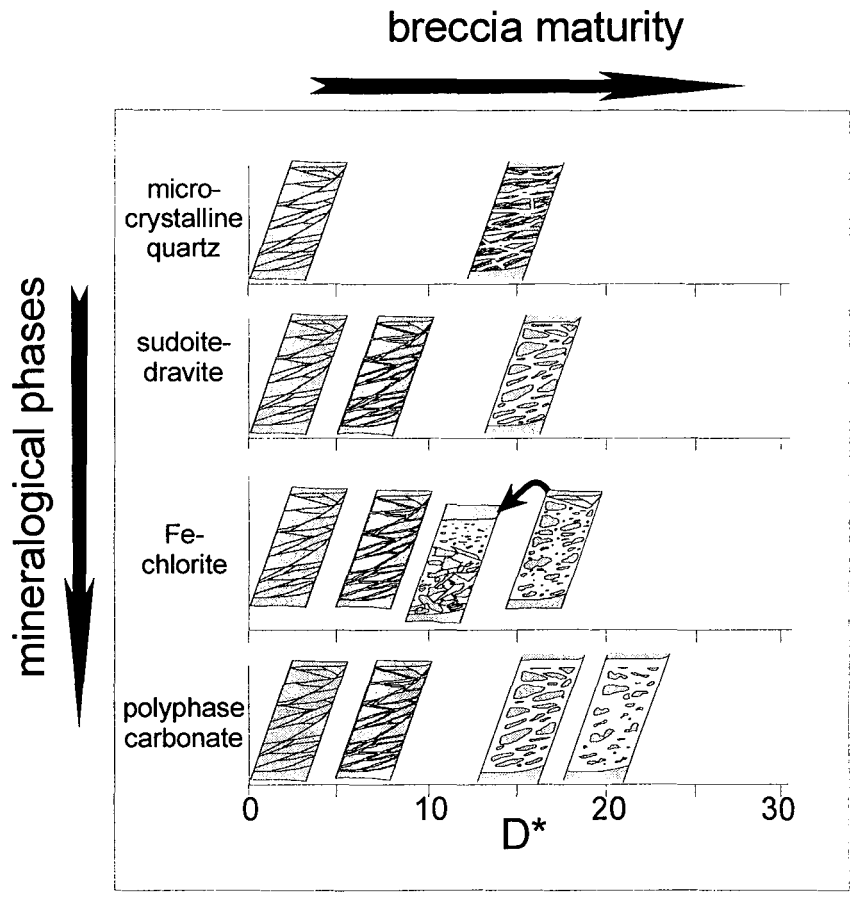

Figure 10 – Synthetic diagram showing the temporal evolution of each breccia type according to their main descriptive features and fragment morphometry measurements. Note the reverse evolution for the last stage of Fe-chlorite collapse breccias.

Fluid-assisted brecciation may have been triggered by two different processes. The first process is permeability sealing by cementation contemporaneous with the quartz dissolution. This could have led to the formation of abnormally pressured compartments (Doligez et al., 1988) and subsequent hydraulic brecciation and collapse following the expansion phase. Even small amounts of secondary mineral precipitation can dramatically affect the permeability in a granular media (Tenthorey et al., 1998). The second process is a tectonic movement which could have interrupted the dissolution process and created openings and associated critical breccias (Jébrak, 1997). In both cases, the location of the breccia body at the intersection of Type I, II and IV faults (Fig. 3) indicates that the collapse has probably been favored by a strongly fractured zone.

Some collapse textures were also observed in the sudoite-dravite breccias. The absence of corroded and non-corroded fragment mixtures indicates rather minor collapse. The absence of jigsaw textures suggests a dissolution origin rather than a fluid-assisted origin.

Mature breccia fragment morphologies therefore reflect two types of breccia formation: solution and fluid-assisted. They represent, respectively, the chemical and physical aspects of

fluid-rock interactions. Both solution and fluid-assisted types may occur as part of the evolution of the same breccia system as demonstrated by the Fe-chlorite breccias.
Consequently, maturity corresponds to the temporal evolution of breccias. Furthermore, spatial variations of fracture intensity at the immature stage also control the maturity as they induce permeability variations. Breccia maturity varies therefore both in space and time.

5.3. Fluid circulation and ore genesis

The spatial organization of breccia bodies suggests a strong control by faults. At the 400 m scale of the study area, the major Type I fault seems to be the principal control, but extended breccia bodies occur mostly at or close to fault intersections. In addition, the formation of immature breccias is triggered by tectonic and fluid-assisted fractures. As the fluids were undersaturated relative to quartz, it is improbable that they came from the sandstones. They were probably derived from the basement along permeability channels such as the main graphite-rich Type I shear zone, or the cross-cutting high angle faults such as the Type II structures, or intersections of both (Kyser et al., 1989) that are commonly quartz-free. Shear zones are proposed as conduits for focused flow of overpressured fluids (Kerrich and Allison, 1978; Robert et al., 1983; Ridley, 1993). The graphite enrichment in the basement of the major Type I fault could be responsible for reactivation during almost every seismic event due to the lubricating properties of graphite. At each seismic event, transient fluids would have moved rapidly along the basement channels (high pressure regime) and then would have slowed down in the strongly fractured sandstones (low pressure regime) above the unconformity.

Analysis of mature breccias indicates that breccia development is controlled by fluid-rock interactions. Therefore, breccia-forming events in sandstone coincide with basement fault reactivation and subsequent onsets of fluid circulation. This circulation have been favored by a high fracture permeability, especially at fault intersections, relative to early silicified sandstones (Fig. 8).

Analysis of mature breccias indicates that breccia development is controlled by fluid-rock interactions. Therefore, breccia-forming events in sandstone coincide with basement fault reactivation and subsequent onsets of fluid circulation. This circulation have been favored by a high fracture permeability, especially at fault intersections, relative to early silicified sandstones (Fig. 8). Fluids, widely dispersed in the fractured zone, reacted with the local lithologies leading to breccia development. Consequently, the expression of the type I and II faults in the sandstones would be an "island" in the sense of Newman (1993): a wide zone where fluids may infiltrate the surrounding rocks. According to the genetic models of Hoeve

et al. (1980) and Fayek and Kyser (1997), the fluids interacted with basinal fluids, leading to uranium ore deposition.

The weak spatial correlation of sudoite-dravite breccias with uranium mineralization is due to their zoning relationship with coeval and extremely mature sudoite breccias that are closer to the unconformity and show good correlation with the U ore. Fe-chlorite and polyphase carbonate breccias also display a good correlation with U mineralization but are more local than the sudoite breccias.

5.4. Tectonic history

The reverse Type I fault movements that are contemporaneous with the microcrystalline quartz breccias could be the expression of a post-Thelon-Taltson orogenic readjustment event between 1.7 and 1.5 Ga. The weak development of these breccias in sandstones as well as their tectonic nature indicates rather limited fluid circulation.

The second event of sudoite-dravite and sudoite breccia formation is associated with the reactivation of Type I and Type II faults. It is contemporaneous with the main primary U-mineralization event and the peak diagenesis period. The presence of shallow dipping pitchblende-filled tension gashes indicates a reverse movement along the Type I faults. The wide development of sudoite-rich breccias as well as the extent and high-grade of the U-mineralization suggest a major fluid circulation phase. The contemporaneous formation of other unconformity-type uranium deposits in the western and eastern parts of the Athabasca Basin indicates that this is a regional compressional phase. The presence of almost undeformed Mackenzie diabase dikes dated 1.27 Ga (Le Cheminant and Heaman, 1989) suggests that this phase occurred between 1.5 and 1.3 Ga. Sudoite and sudoite-dravite breccias are partly superimposed on the earlier microcrystalline quartz breccias which could have formed fluid conduits, especially in silicified sandstones (Fig. 8).

Fe-chlorite breccia formation corresponds to a probable reactivation of Type II and/or IV faults with a composite strike- and dip-slip movement. It indicates a strong rotation of the regional stress field as the major Type I faults are not reactivated. Their possible 925 ± 25 Ma age could correspond to a regional uranium mineralization event or a remobilization phase dated at 918 and 860 Ma, at the Key Lake and Rabbit Lake unconformity-type deposits respectively (Lainé, 1985). Fe-chlorite breccias are partly superimposed on the two previous breccia types. The reactivation event triggered local fluid circulation at the intersection of Type I, II and IV faults.

The polyphase carbonate breccia-forming event corresponds to the reactivation of the reverse Type I and Type II and III faults, probably during a late tectonic phase between 300 and 200 Ma. The existence of remobilized uranium mineralization dated at 290, 215 and 200

Ma respectively at Maurice Bay, Key Lake and Rabbit Lake deposits (Lainé, 1985), located in the east part of the Athabasca Basin, suggests that the event is regional. The limited extension of the breccia bodies suggests a small reactivation event with minor fluid flow compared to the major sudoite-dravite breccia phase.

The four breccia bodies studied, therefore, may be related to regional tectonic events between 1.7 Ga and 200 Ma. However, more systematic age determinations would be necessary to ascertain the general validity of these ages. Different breccia body controls indicate variations of the regional stress field between each seismic event.

6. Conclusion

Four breccia types have been distinguished in the sandstones surrounding unconformity-type uranium mineralization in the southern part of the Shea Creek area: microcrystalline quartz, sudoite-dravite, Fe-chlorite and polyphase carbonate breccias.

Their fragment morphologies have been quantified using fractal dimension analysis. The matrix percentage and the shape of the fragment morphometry distribution (FMD) curves have been used to determine the degree of maturity and the nature of fluid-rock interactions for each breccia. The fractal dimension increases with the degree of maturity.

Microcrystalline quartz breccias are tectonic and fluid-assisted. Their maturation corresponds to an increase of fracturing density. Sudoite-dravite, Fe-chlorite and polyphase carbonate breccias are solution breccias. Solution breccia maturation may be described in three phases. In the first phase, fault reactivation and fluid overpressure induced fracturing and fluid circulation. The second phase is characterized by quartz dissolution resulting from the chemical interaction of a basement-derived fluid with the overlying sandstones. Collapse may occur in a third phase due to fluid-assisted brecciation or dissolution opening and is exemplified by Fe-chlorite and sudoite-dravite breccias, respectively. Consequently, breccia development is the result of alternating physical and chemical fluid-rock interactions, with respectively high and low rates. In the former case, breccia maturity evolution would represent spatial variations whereas in the latter it would correspond to temporal variations.

The four breccia bodies are mainly controlled by reverse Type I faults and intersections with other types of faults. They are the expression of basement fault reactivations occurring between 1.7 Ga and 200 Ma. The first seismic reactivation could be the expression of minor readjustment movements following the Thelon-Taltson orogeny. The second deformational event between 1.5 and 1.3 Ga was a regional compressional phase leading to the main primary uranium mineralization. The third and forth events could also have been regional as they are possibly contemporaneous with mineralization phases dated circa 900 Ma and between 300

and 200 Ma, respectively in several deposits. Different breccia body controls indicate major changes of the regional stress field with time.

Each seismic event created structural connections between variably pressured compartments, inducing fluid circulation from the basement to the sandstones. Fluids were slowed down in the widely fractured sandstones, giving them time to react with the quartz to form solution breccias. Interaction of these fluids with basin fluids may have led to unconformity-type uranium mineralization deposition. This may explain the good correlation of breccia bodies with the mineralization, especially for the sudoite event.

Acknowledgements

We are grateful to COGEMA and Cogema Resources Inc for their financial and technical support. More specifically, we would like to thank Patrice Bruneton and Ken Wheatley for helpful review, Philippe Portella for stimulating discussions, and Roland Aumaître, Claude Caillat, Jean-Claude Carisey, Jean Mondy and Jean-Claude Rippert for permission to publish the geological data collected in the field in June of 1999. The manuscript was improved by Peter Laznicka and Charlie Sammis.

References

Antonellini, M., Aydin, A., 1994. Effect of faulting on fluid flow in porous sandstones: petrophysical properties. AAPG Bulletin 78, 355-377.

Armstrong, R.L., Ramaekers, P., 1985. Sr isotopic study of Helikian sediment and diabase dikes in the Athabasca Basin, northern Saskatchewan. Canadian Journal of Earth Sciences 22, 399-407.

Baudemont, D., Piquard, J.P., Ey, F., Zimmerman, J., 1993. The Sue Uranium Deposits, Saskatchewan, Canada. Exploration Mining Geology 2, 179-202.

Bell, K., 1985. Geochronology of the Carswell area, Northern Saskatchewan. In: Lainé, R., Alonso, D., Svab, M. (Eds.), The Carswell structure uranium deposits, Saskatchewan. Geological Association of Canada Special Paper 29, pp. 33-46.

Bérubé, D., Jébrak, M., 1999. High precision boundary fractal analysis for shape characterization. Computers & Geosciences 25, 1059-1071.

Burley, S.D., Kantorowicz, J.D., 1986. Thin section and S.E.M. textural criteria for the recognition of cement-dissolution porosity in sandstones. Sedimentology 33, 587-604.

Carrier, A., Jébrak, M., 1994. Structural evolution and metallogeny of the Silidor mesothermal gold-quartz deposit, southern Abitibi greenstone belt, Quebec. Geological Association of Canada - Mineralogical Association of Canada, Annual meeting abstracts, Waterloo. No. 19, A-18.

Chiarenzelli, J., Aspler, L., Villeneuve, M., Lewry, J., 1998. Early Proterozoic Evolution of the Saskatchewan Craton and its Allochthonous Cover, Trans-Hudson Orogen. Journal of Geology 106, 247-267.

Doligez, B., Burrus, J., Ungerer, P., 1988. Hydraulic fracturing during basin scale fluid migration: an integrated approach. In: Hitchon, B., Bachu, S. (Eds.), Fluid flow, heat transfer and mass transport in fractured rocks. 4th Canadian/American Conference on Hydrogeology, pp. 251-259.

Dzuslynski, S., Sass-Gustkiewicz, M., 1989. Pb-Zn ores. In: Bosak, P., Ford, D.C., Glazek, J., Horacek, I. (Eds.), Paleokarst. A Systematic and Regional Review. Elsevier and Academia, Amsterdam and Praka, pp. 377-396.

von Einsiedel, C.A., 1981. Petrography and geochemistry of the Cluff Lake breccias, Carswell structure, Northern Saskatchewan. Bachelor thesis, Carleton University, Ottawa, Ontario.

Egeberg, P.K., 1992. Brines in sedimentary environments. Academic Press, London.

Ey, F., 1984. Un exemple de gisement d'uranium sous discordance: les minéralisations protérozoïques de Cluff Lake, Saskatchewan, Canada. Thèse d'Etat, Université Louis Pasteur.

Ey, F., Gauthier-Lafaye, F., Lillié, F., Weber, F., 1985. A uranium unconformity deposit: the geological setting of the D orebody (Saskatchewan-Canada). In: Lainé, R., Alonso, D., Svab, M. (Eds.), The Carswell structure uranium deposits, Saskatchewan. Geological Association of Canada Special Paper 29, pp. 121-138.

Fayek, M., Kyser, T.K., 1997. Characterization of multiple fluid-flow events and Rare-Earth-Element mobility associated with formation of unconformity-type uranium deposits in the Athabasca Basin, Saskatchewan. The Canadian Mineralogist 35, 627-658.

Genna, A., Jébrak, M., Marcoux, E., Milési, J.P., 1996. Genesis of cockade breccias in the tectonic evolution of the Cirotan epithermal gold system, West Java. Canadian Journal of Earth Sciences 33, 93-102.

Gindy, A.R., Al-Shakiry, A.J., Sa'ad, N.A., 1985. Spheroidal weathering in marls and chalks of Gebel Gurnah near Luxor, Southern Egypt. Journal of Sedimentary Petrology. V. 55, p. 762-768.

Halter, G., 1988. Zonalités des altérations dans l'environnement des gisements d'uranium associés à la discordance du Protérozoïque Moyen (Saskatchewan, Canada). Thèse de doctorat, Université Louis Pasteur, Strasbourg.

Harper, C.T., 1983. The geology and uranium deposits of the central part of the Carswell Structure, Northern Saskatchewan, Canada. Unpublished Ph.D. Thesis, Colorado School of Mines, Golden, Colorado.

Hedenquist, J.W., Reyes, A.G., Simmons, S.F., Taguchi, S., 1992. The thermal and geochemical structure of geothermal and epithermal systems: a framework for interpreting fluid inclusion data. European Journal of Mineralogy 4, 989-1015.

Hoeve, J., Sibbald, T.I.I., Ramaekers, P., Lewry, J.F., 1980. Athabasca Basin unconformity-type uranium deposits: a special class of sandstone-type deposits? In: Ferguson, S., Goleby, A. (Eds.), Uranium in the Pine Creek Geosyncline. IAEA, Vienna, pp. 575-594.

Hoeve, J., Rawsthorn, K., Quirt, D., 1981. Uranium Metallogenetic Studies: Clay Mineral Stratigraphy and Diagenesis in the Athabasca Group. Saskatchewan Research Council Publication 22, pp. 76-89.

Hoffman, P.F., 1987. Continental transform tectonics: Great Slave Lake shear zone (ca. 1.9 Ga), northwest Canada. Geology 15, 785-788.

Hurst, A.R., BjØrkum, P.E., 1986. Discussion: Thin section and S.E.M. textural criteria for the recognition of cement-dissolution porosity in sandstones. Sedimentology 33, 605-614.

Jébrak, M., 1984. Contribution à l'histoire naturelle des filons F-Ba des Hercynides françaises et marocaines. Thèse ès Sciences, Document BRGM 99.

Jébrak, M., 1992. Les textures intra-filoniennes, marqueurs des conditions hydrauliques et tectoniques. Chronique de la Recherche Minière 506, 25-35.

Jébrak, M., 1997. Hydrothermal breccias in vein-type ore deposits: A review of mechanisms, morphology and size distribution. Ore Geology Reviews 306, 1-24.

Kerrich, R., Allison, I., 1978. Vein geometry and hydrostatics during Yellowknife mineralization. Canadian Journal of Earth Sciences 15, 1653-1660.

Knipe, R.J., 1993. The influence of Fault Zone Processes and Diagenesis on Fluid Flow. In: Horbury, A.D., Robinson, A.G. (Eds.), Diagenesis and Basin Development. AAPG, Studies in Geology 36, pp. 135-148.

Kotzer, T.G., Kyser, T.K., Irving, E., 1992. Paleomagnetism and the evolution of fluids in the Proterozoic Athabasca Basin, northern Saskatchewan, Canada. Canadian Journal of Earth Sciences 29, 1474-1491.

Kyser, T.K., Wilson, M.R., Ruhrmann, G., 1989. Stable isotope constraints on the role of graphite in the genesis of unconformity-type uranium deposits. Canadian Journal of Earth Sciences 26, 490-498.

Lainé, R., 1985. The Carswell uranium deposits - An example of not so unique unconformity-related uranium mineralization. In: Lainé, R., Alonso, D., Svab, M. (Eds.), The Carswell structure uranium deposits, Saskatchewan. Geological Association of Canada Special Paper 29, pp. 225-230.

Laznicka, P., 1988. Breccias and coarse fragmentites. Developments in Economic Geology, 25. Elsevier, Amsterdam.

Laznicka, P., 1989. Breccias and ores. Part 1: history, organization and petrography of breccias. Ore Geology Reviews 4, 315-344.

Le Cheminant, A.N., Heaman, L.M., 1989. Mackenzie igneous events, Canada: Middle Proterozoic hotspot magmatism associated with ocean opening. Earth Planetary Sciences Letters 96, 38-48.

Newman, J., Mitra, G., 1993. Lateral variations in mylonite zone thickness as influenced by fluid-rock interactions, Linville Falls fault, North Carolina. Journal of Structural Geology 15, 849-863.

Pacquet, A., Weber, F., 1993. Pétrographie et minéralogie des halos d'altération autour du gisement de Cigar Lake et leurs relations avec les minéralisations. Canadian Journal of Earth Sciences 30, 674-688.

Pagel, M., 1975. Détermination des conditions physico-chimiques de la silicification diagénétique des grès Athabasca (Canada) au moyen des inclusions fluides. Compte-rendu de l'Académie des Sciences 280, série D, 2301-2304.

Pagel, M., Weatley, K., Ey, F., 1985. The origin of the Carswell circular structure. In: Lainé, R., Alonso, D., Svab, M. (Eds.), The Carswell structure uranium deposits, Saskatchewan. Geological Association of Canada Special Paper 29, pp. 213-223.

Phillips, W.J., 1986. Hydraulic fracturing effects in the formation of mineral deposits. Institution of Mining and Metallurgy Transactions, section B: Applied Earth Science 95, B17-B24.

Pittman, E.D., 1981. Effect of fault-related granulation on porosity and permeability of quartz sandstones, Simpson Group (Ordovician), Oklahoma. AAPG Bulletin 65, 2381-2387.

Ramaekers, P., Dunn, C.D., 1977. Geology and geochemistry of the eastern margin of the Athabasca Basin. Saskatchewan Geological Society Special Publication 3, pp. 297-322.

Ramaeker, P., 1981. Hudsonian and Helikian basins of the Athabasca region, Northern Saskatchewan. Geological Survey of Canada Paper 81, pp. 219-233.

Ramaekers, P., 1990. Geology of the Athabasca Group (Helikian) in Northern Saskatchewan. Saskatchewan Energy and Mines, Saskatchewan Geological Survey, report 195.

Reeve, J.S., Cross, K.C., Smith, R.N., Oreskes, N., 1990. Olympic Dam. Copper-Uranium-Gold-Silver deposit. In: Hughes E.E. (Ed.), Geology of the mineral deposits of Australia and Papua New Guinea. The Australasian Institute of Mining and Metallurgy, Melbourne, pp. 1009-1035.

Ridley, J., 1993. The relations between mean rock stress and fluid flow in the crust: with reference to vein- and lode-style gold deposits. Ore Geology Reviews 8, 23-37.

Robert, F., Brown, A.C., Audet, A.J., 1983. Structural control of gold mineralization at the Sigma Mine, Val d'Or, Québec. Canadian Institute of Mining, Metallurgy and Petroleum Bulletin 76, 72-80.

Ross, G.M., Eaton, D.W., 1997. Winagami reflection sequence: Seismic evidence for postcollisional magmatism in the Proterozoic of western Canada. Geology 25, 199-202.

Sammis, C.G., Biegel, R.L., 1986. A self-similar model for the kinematics of gouge deformation. AGU fall meeting. Eos Transactions 67, 1187.

Sass-Gustkiewicz, M., 1996. Internal sediments as a key to understanding the hydrothermal karst origin of the upper silesian Zn-Pb ore deposits. Society of Economic Geologists, Special Publication 4, pp. 171-181.

Sibson, R.H., 1986. Brecciation processes in fault zones: inferences from Earthquake rupturing. Pure and Applied Geophysics 124, 161-175.

Spoljaric, N., 1971. Origin of colors and ironstone bands in the Columbia Formation, Middletown-Odessa Area, Delaware. Southeastern Geology, Durham, North Carolina 12, 253-266.

Tenthorey, E., Scholz, C.H., Aharonov E., Léger, A., 1998. Precipitation sealing and diagenesis. 1. Experimental results. Journal of Geophysical Research 103, 23951-23967.

Villeneuve, M.E., Thériault, R.J., 1991. U-Pb ages and Sm-Nd signature of two granites from the Fort Simpson magnetic high, northwest Canada. Canadian Journal of Earth Sciences 28, 1003-1008.

Wallis, R.H., Saracoglu, N., Brummer, J.J., Golightly, J.P., 1983. Geology of the McLean uranium deposits. In: Cameron, E.M. (Ed.), Uranium exploration in Athabasca Basin, Saskatchewan, Canada. Saskatchewan Energy and Mines, Geological Survey of Canada, pp. 71-110.

Wheatley, K., Murphy, J., Leppin, M., Cutts, C., Climie, J.A., 1996. Advances in the genetic model and exploration techniques for unconformity type uranium deposits in the Athabasca basin. Canadian Institute of Mining, Metallurgy and Petroleum (CIM) conference, May 1996.

III. Etude Structurale, Mineralogique et Geochimique des Breches de la Mine a Ciel Ouvert de Sue C

III. Etude Structurale, Mineralogique et Geochimique des Breches de la Mine a Ciel Ouvert de Sue C

Introduction

L'étude des brèches hydrothermales dans la zone de Anne à Shea Creek a montré que le développement des brèches associées aux minéralisations uranifères a été initié par des réactivations tectoniques. Les fractures et brèches tectoniques et hydrauliques ainsi créées ont provoqué une forte augmentation de perméabilité générant la circulation de fluides dans les fractures. Les interactions fluides-roche le long des fractures se sont accompagnées d'une évolution des brèches par des phénomènes chimiques de dissolution du quartz et de précipitation de phases minérales variées telles la sudoite, la dravite, la chlorite ferrifère, la sidérite et l'hématite. Pour certaines de ces brèches, la dernière phase de l'évolution est un effondrement du système.

Figure III-1 – Vue panoramique vers le nord de la MCO de Sue C en Juin 2000.

Les zones à boules représentent un cas particulier de brèches hydrothermales dans le Bassin Athabasca. Elles contiennent des fragments de grès argilisés avec des formes d'ellipsoïdes

pouvant atteindre 1 m de large, emballés dans une matrice argileuse. Elles ont été décrites et étudiées pour la première fois dans le gisement de D à Cluff Lake où elles encaissent la minéralisation uranifère (Ey et al., 1985). Elles sont interprétées comme résultant de mouvements tectoniques et d'une altération hydrothermale intense. Elles semblent donc pouvoir se former de la même manière que les brèches étudiées à Shea Creek dans la partie II. Cependant, il existe des différences importantes dans la formation des deux types de brèches.

Le but de cette partie est de préciser les mécanismes structuraux, minéralogiques et géochimiques de formation des zones à boules et de quantifier les phénomènes d'interactions fluides-roche. Leur importance pour l'exploration est également traitée.

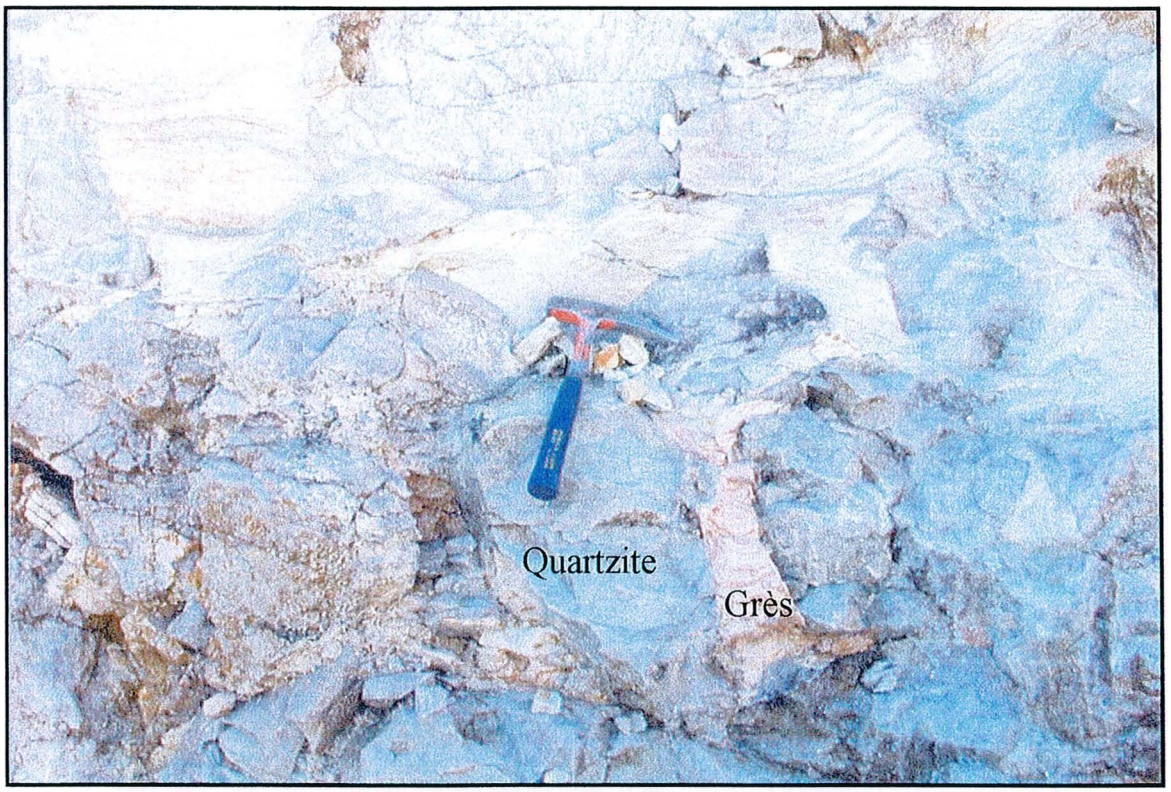

Figure III-2 – Brèche de pente à la discordance montrant des blocs de quartzite cimentés par de l'argile et du grès

La zone d'étude est la MCO de Sue C qui montre des affleurements de bonne qualité (Fig. III-1). Par rapport à l'étude de carottes de forage, l'intérêt principal de travailler dans une MCO est de pouvoir appréhender l'organisation des objets géologiques en 3 dimensions, ce qui est très rare dans le Bassin Athabasca. Le creusement de la mine a débuté en 1997 et les premières observations ont été effectuées en Janvier 1998. L'été 1998, une cartographie structurale complète a été réalisée et deux visites en 1999 et 2000 ont permis de suivre l'évolution des structures et des brèches au fur et à mesure de l'approfondissement de la mine.

De superbes affleurements de brèches de pente ou « pseudo-fanglomérats » correspondant à des glissements de terrain au niveau de la paléo-topographie formée par la discordance ont été observés (Fig. III-2). Ils sont les témoins d'une activité tectonique syn-sédimentaire précoce. Les zones à boules étudiées dans cette partie illustrent une activité tectonique postérieure au dépôt des sédiments Athabasca.

Les relations spatiales entre les zones à boules et les structures, leur orientation ainsi que la forme des boules ont d'abord été étudiées afin de comprendre les contrôles structuraux des zones à boules. L'étude minéralogique et les calculs de bilan de masse de l'encaissant des zones à boules, des boules et de la matrice ont permis de comprendre la nature des processus de précipitation, de dissolution et de transformation des phases minérales et de quantifier leur intensité. Le rapport fluides/roche et le temps de formation des brèches sont estimés. Les conditions thermiques de genèse des zones à boules ont été précisées en utilisant le géothermomètre illite de Cathelineau et Izquierdo (1988). Les différents processus impliqués dans la genèse des zones à boules sont intégrés dans un modèle synthétique étroitement lié à la formation des minéralisations uranifères.

ARTICLE 2 :

Chemical brecciation processes in the Sue unconformity-type uranium deposits, Eastern Athabasca Basin (Canada)

G. Lorilleux[a,*], M. Cuney[a], M. Jébrak[b], J.C. Rippert[c], P. Portella[c]

[a] CREGU-UMR G2R 7566, Université Henri Poincaré, BP 23, 54 501 Vandoeuvre-les-Nancy, France

[b] UQAM, DSTA, CP 8888, Montréal (QUE) H3C 3P8 Canada

[c] COGEMA Resources Inc, Exploration Department, 817-825 45 [th] Street West, P.O. Box 9204, Saskatoon (SK) S7K 3X5 Canada

Submitted to Journal of Geochemical Exploration

* *Corresponding author.*

E-mail addresses and fax numbers: *guillaume.lorilleux@g2r.uhp-nancy.fr, (33) 3 83 91 38 01 (G. Lorilleux), michel.cuney@g2r.uhp-nancy.fr, (33) 3 83 91 38 01 (M. Cuney), jebrak.michel@uqam.ca, 1 514 987 7749 (M. Jébrak), jcrippert@cri.ca, 1 306, 343 4632 (J.C. Rippert).*

Résumé

La bréchification chimique dans les grès est associée à plusieurs gisements d'uranium de type discordance dans le Bassin Athabasca, nord Saskatchewan (Canada). Elle s'exprime à travers la formation de brèches appelées zones à boules. Les zones à boules correspondent à des fragments de grès argilisés ayant des formes de boules avec des tailles variant de quelques centimètres à 1 m emballés par une matrice argileuse. Elles furent cartographiées et décrites en détail dans la mine à ciel ouvert du gisement de type discordance de Sue C. Dans cette mine, les zones à boules ont jusqu'à 5 m de large et s'étendent verticalement sur 20 à 30 m. Elles sont localisées le long d'une faille inverse riche en graphite contrôlant les gisements de Sue A et B, et sont plus développées dans des zones d'intersection avec des structures dextres orientées NE. Leur maturité, définie par le pourcentage de matrice, augmente près de la discordance et aux intersections de failles. La distribution statistique des formes de boules est typiquement log-normale.

Des échantillons de boules, de matrice et de grès ont été pris le long d'un profil traversant une zone à boule pour des études pétrographiques et géochimiques. Le développement des zones à boules est caractérisé par la dissolution massive du quartz, par le lessivage de l'hématite primaire, la précipitation de minéraux du groupe des crandallite-florencite-goyazite et par le remplacement de la dickite par de l'illite. La composition chimique des illites déterminée par microsonde électronique indique une température de formation entre 240 et 280°C, légèrement supérieure à la température du maximum de diagenèse dans le bassin. Les calculs de bilan de masse montrent que les fluides hydrothermaux ont apporté les éléments V, K, Rb, B, W, Zn, terres rares légères, Mg, Cr, Sr, U et Y et ont lessivé Si et Fe. La dissolution massive du quartz fut accompagnée d'une perte de volume de près de 85 %.

La formation des zones à boules fut déclenchée par fracturation tectonique dans les grès pendant une phase de réactivation de faille. L'augmentation de perméabilité conséquente à la fracturation induit la circulation de fluides de socle dans les grès. Ces fluides étaient sous-saturés en silice et provoquèrent la dissolution du quartz autour des fractures conduisant ainsi à la formation de fragments arrondis. Les morphologies rondes sont probablement dues à une dissolution en régime limité par la diffusion. L'argilisation massive associée fut responsable de l'auto-colmatage du système hydrothermal. La forte perméabilité fut probablement régénérée périodiquement par des réactivations sismiques, expliquant ainsi un rapport fluide/roche minimum de 38 000 calculé avec une saturation en silice du fluide de 90 %. Les espaces vides créés par la dissolution du quartz furent accommodés par un fluage sub-continu de la matrice argileuse pendant les phases de contraction tectonique intersismique, créant ainsi une perméabilité à l'échelle du grain. Le fluage de la matrice fut accompagné par la rotation des boules, augmentant le processus d'arrondissement. Ces phénomènes furent contemporains

de la formation des minéralisations uranifères haute-teneur de type discordance. Les enrichissements en terres rares légères de la matrice par rapport aux boules et en terres rares lourdes des boules par rapport à la matrice montrent qu'un fractionnement chimique s'est couplé à la déformation différentielle entre les boules et la matrice. Le temps nécessaire pour la formation des zones à boules fut probablement supérieur à 1 million d'années, indiquant un processus relativement lent.

Mots-clefs: brèche, uranium, perméabilité, dissolution, zone de cisaillement, fractionnement.

Abstract

Chemical brecciation in sandstones is associated with several unconformity-type uranium deposits in the Athabasca Basin, northern Saskatchewan (Canada), and is expressed through "zones à boules" breccia formation. "Zones à boules" are represented by ball shape argillized sandstone fragments, typically varying in size from several centimeters to 1 m, wrapped in a clay matrix. These were mapped and described in detail at the Sue C open pit unconformity-type uranium deposit. Here, the "zones à boules" are up to 5 m wide and have a vertical extension of 20 to 30 m. They are located along an eastern graphitic reverse fault controlling the Sue A and B deposits, and are well developed at intersections with dextral NE-trending structures. Their maturity, characterized by the matrix percentage, increases with proximity to the unconformity and at fault intersections. Ball shape distribution is typically log-normal.

Ball, matrix and wall rock samples were taken along a profile crossing a "zone à boules" for petrographic and geochemical studies. The "zones à boules" development is characterized by massive quartz dissolution, leaching of hematite, crandallite-florencite-goyazite minerals precipitation and replacement of dickite by illite. Illite chemical composition determined by electron microprobe indicates formation temperatures between 240 and 280°C similar to slightly higher than peak diagenesis temperature in the basin. Mass balance calculations show that the hydrothermal fluids added V, K, Rb, B, W, Zn, LREE, Mg, Cr, Sr, U and Y and leached out Si and Fe. Massive quartz dissolution was accompanied by about 85% volume loss.

"Zones à boules" were initiated by tectonic fracturing in sandstones during fault reactivation. The subsequent permeability increase induced the circulation of basement fluids in the sandstone. These fluids were undersaturated relative to silica and provoked quartz dissolution around fractures leading to rounded fragments formation. The rounded morphologies are probably due to a diffusion-limited regime of dissolution. Associated massive argillization was responsible for self sealing of the hydrothermal system. The high permeability was probably periodically rejuvenated by seismic reactivations, causing a

minimum fluid/rock ratio of 38,000 calculated with a silica saturation of the fluid of 90%. Sub-continuous ductile creep of the clay matrix by reaction weakening during interseismic tectonic contraction accommodated the open spaces created by quartz dissolution resulting in grain-scale permeability. The matrix creep was accompanied by ball rotation, enhancing the shape rounding process. These processes were coeval with the formation of structurally controlled high-grade unconformity-type uranium mineralization. Enrichments of LREE in the matrix relative to the balls and of HREE in the balls relative to the matrix indicate that a chemical partitioning was coupled with the strain partitioning between balls and matrix. The length of time involved in the formation of the "zones à boules" was probably greater than 1 million years indicating a rather slow process.

Keywords: breccia, uranium, permeability, dissolution, shear zone, partitioning.

1. Introduction

Hydrothermal breccias containing spheroidal fragments are commonly found associated with epigenetic hydrothermal deposits (Laznicka, 1988; Clark, 1990; Reeve et al., 1990). They generally form by corrosive wear, wear-abrasion (Jébrak, 1997), hypogene exfoliation (Sillitoe, 1985) and/or by the development of curviplanar fractures resulting from the propagation of a shock wave (Clark, 1990). Fragments are typically a few centimeters in size. Breccias containing decimeter- to meter-size rounded fragments may form in surficial environment by spheroidal weathering (Augustithis and Ottemann, 1966; Augustithis et al., 1980; Shahabpour, 1998) but are poorly documented in hydrothermal environments.

In the Athabasca Basin, "zones à boules" represent an unusual case of hydrothermal breccias containing 10 cm to 1 m diameter ball-shaped fragments developed in sandstones. Fragments are partly to totally clay-altered, striated and wrapped in clay. They were for the first time documented by Ey et al. (1985) in the Cluff D unconformity-type uranium deposit located in the West Athabasca Basin. They represent one of the most important tectonic feature associated with the Cluff D deposit and are strongly affected by the Carswell meteorite impact event. "Zones à boules" were also observed by Baudemont et al. (1993) in the Sue C deposit, the object of this paper, and are also present in the Rabbit Lake deposit, in the Cluff Claude deposit and in the Shea Creek exploration zone, just south of Cluff Lake. Their close association with unconformity-type uranium mineralization makes the understanding of their development of major importance for exploration.

Breccia formation has been discussed particularly by Phillips (1986), Sibson (1986), Laznicka (1988 ; 1989), Jébrak (1992; 1997) and Lorilleux et al. (2000) but « zones à boules » formation was not considered. "Zones à boules" were interpreted by Ey et al. (1985) as resulting from tectonic movements combined with hydrothermal alteration. However, no quantitative data were provided concerning the alteration geochemistry and the formation of the balls. The purpose of this study is to examine the geochemical and structural mechanisms of formation of the "zones à boules" and to determine their significance for uranium exploration. The area of study was confined to the Sue C open pit (Fig. 1b and 2). The main structural control in the area is a series of N10-15° faults, along which are located five uranium deposits defining the Sue trend (Baudemont et al., 1993). The open pit provided good quality exposures of "zones à boules". Detailed field and microscopic descriptions have been combined with mass balance calculations in order to understand quantitatively the coupling relationship between tectonic movements and hydrothermal alteration.

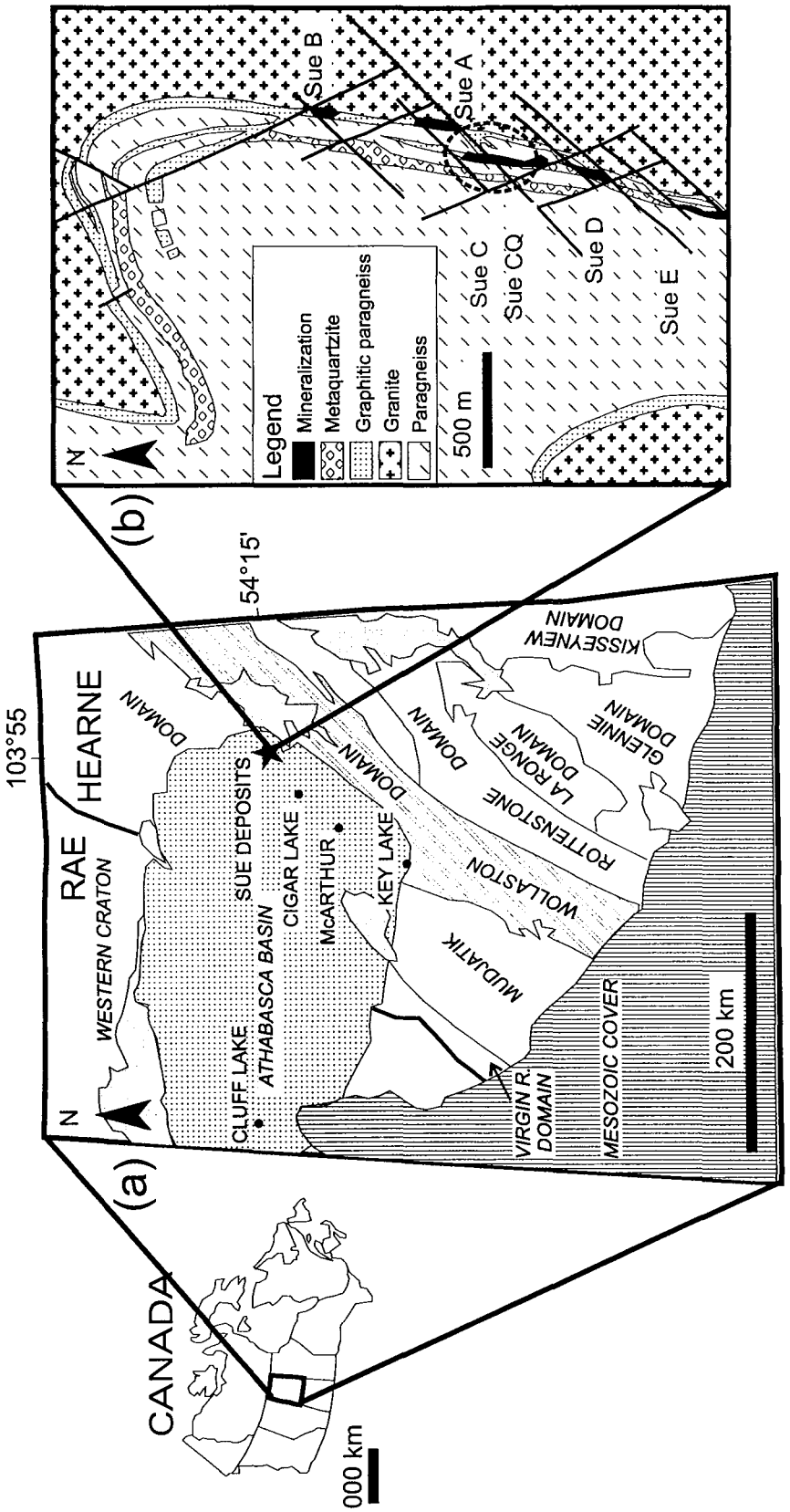

Figure 1 – (a) Location of the Athabasca basin in Canada and of the Sue deposits at the eastern edge of the basin in the Wollaston Domain. (b) Basement lithologies and structural controls of the Sue deposits located on the western flank of the Collins Bay granitic dome (modified from Baudemont et al., 1993). The dashed oval indicates the position of the Sue C open pit.

2. Methodology

"Zones à boules" were described on bench exposures of the Sue C open pit. Their structural-controlled factors were determined by their orientations in the wall and/or ball orientation measurements. Ball shapes were systematically measured. The ball size distribution curve has been plotted using Statistica software.

Five samples, 1 to 5, were taken along a 6 m profile crossing a "zone à boule". Two other samples, 6 and 7, were taken in an other breccia outcrop and in a non-altered sandstone respectively (see annexe I). Petrographic characteristics of these non-mineralized samples have been studied by optical microscopy. Their mineralogy was determined by X-ray diffraction (XRD) on whole-rock samples at the UQAM (Montréal, Canada) and by transmission electron microscope (TEM), coupled with X-ray analysis at the Université Henri Poincaré (Nancy, France) after agate mortar crushing. Illite chemical composition was analysed by electron microprobe at 10 nA and at 15 kV with an average counting time of 9 seconds for the peak and 5 seconds for the background. The standards used for the analysis of Na, Mg, Al, Si, Cl, K, Ca, Ti, V, Cr, Mn, Fe and Ni in illites were respectively albite, olivine, albite, orthose, scapolite, orthose, wollastonite, $MnTiO_3$, pure vanadium, Cr_2O_3, $MnTiO_3$, hematite and NiO. Relative proportions of quartz, dickite and kaolinite have been calculated by norm analysis.

Mass balance calculations were determined using geochemical analysis of 10 major and 44 trace elements on whole rock samples 1, 2, 3, 4, 5 and 7 - by ICP-AES and ICP-MS at the CRPG (Nancy) following a procedure described by Govindaraju and Mevelle (1987) (Table 1). Density of dry samples have been determined using a picnometer with water (Vigneresse and Cannat, 1987) (Table 1). The geochemical composition of samples 1 and 7 have been used in the calculation of an average protolith composition. Mass balance calculations were resolved using the Grant method (Grant, 1986) which consists in a simple graphical solution of Gresens' equation (Gresens, 1967) (see annexe III).

3. Geological setting

3.1. Regional geology

The unconformity-type Sue deposits (A, B, C, CQ, D, E) are located at the eastern edge of the Athabasca Basin in northern Saskatchewan (Fig. 1a). They lie within the Precambrian Wollaston Domain, a lithostructural unit of the Hearne Sub-province in the Churchill Structural Province (Fig. 1a). The Wollaston Domain forms a fold belt along the northwestern margin of the Trans-Hudson orogen (Ghandi, 1995) and is characterized by gneiss domes,

consisting of Archean granitoid cores wrapped in Lower Proterozoic supracrustal rocks (Hoeve et al., 1980). The Sue deposits are clustered on the western flank of the Archean Collins Bay granitic dome at the western edge of the Wollaston Domain, along a N12° trend (Baudemont et al., 1993) (Fig. 1b).

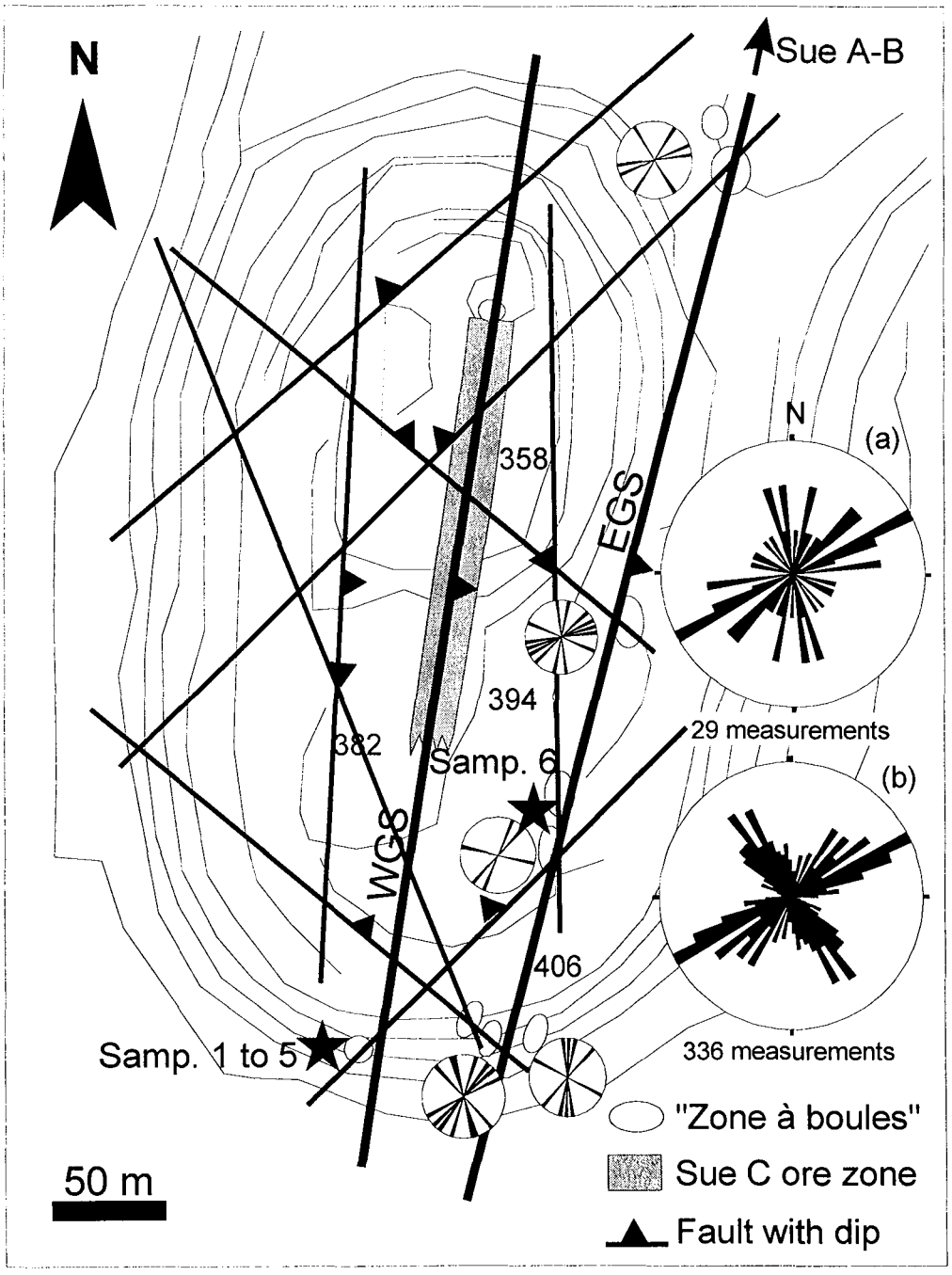

Figure 2 – Simplified structural map of the Sue C open pit with the location of samples 1 to 6 (black stars). Small stereograms represent "zones à boules" wall strikes at different locations. Note the alignment of breccias along the Eastern Graphitic Structure (EGS). (a) Stereogram of "zones à boules" wall strikes. (b) Stereogram of fracture strikes in the Sue C open pit.

The Athabasca Basin formed during the Middle Proterozoic at about 1.7 Ga (Armstrong and Ramaekers, 1985; Kotzer et al., 1992). It is separated from the underlying Archean and Lower Proterozoic basement by a major unconformity. The basin is composed of sub-basins oriented NE-SW and controlled by faults rooted in the basement. The main faults are oriented N20° and N70°. The basin is interpreted as having been filled by several stratigraphic units, the Athabasca Group being the lower and thickest unit (Ramaekers and Dunn, 1977). The Athabasca Group is composed of thick, unmetamorphosed and flat-lying sequences of fluviatile to marine quartzose sandstones deposited in a proximal shelf environment (Ramaekers, 1981). A maximum total thickness of 4 to 5 km of sediments in the basin has been proposed based on fluid inclusions and diagenetic clay assemblages studies (Pagel, 1975; Hoeve et al., 1981; Halter, 1988).

3.2. Local Geology

Lower Proterozoic metasediments along the Sue trend are oriented parallel to the western edge of the Collins Bay dome and dip steeply to the east (Fig. 1b). Two main graphitic paragneiss units approximately 80 m apart occur within the felsic and cordierite-sillimanite-garnet paragneisses (Fig. 1b). A metaquartzite unit is present within tens of meters to the west of the western graphitic unit (Fig. 1b) (Baudemont and Pacquet, 1996).

In the Sue area, the remaining Middle Proterozoic sandstone cover is between 50 and 70 m thick. Two formations have been distinguished from bottom to top: Manitou Falls b and Manitou Falls c, both which are medium to very coarse grained. The MFb member is characterized by the presence of at least 2 % of clast-supported conglomeratic beds 2 cm thick or more, interbedded with sandstones. The MFc is more homogeneous with less than 2 cm thick conglomerate beds. Rare siltite layers are generally 1 to 2 cm thick. Heavy minerals layers, generally less than 1 mm thick, are common at the base of the MFc and in the MFb. Their distribution shows great variability at the millimeter to decimeter scale. In non-mineralized zones, clay typically forms 0.5 to 15 % of the rock and averages around 5 % (Ramaekers, 1990). Major cements are quartz displaying syntaxial overgrowths, clay minerals (kaolinite, illite, chlorite) and iron oxides.

Three main fault systems exist in the Sue area: N10-15° steeply dipping to the east, N50-60° dipping to the northwest and N140-160° dipping to the northeast (Fig. 1b and 2). They crosscut the unconformity and show respectively reverse, dextral-reverse and normal-sinistral post-Athabasca movements. The first set is represented by two graphite-rich reverse faults parallel to the foliation trending N12°E and is hosted in the basement by the two graphitic units. This set produced a cumulated down-drop of 5 to 30 m of the western block after sandstone deposition (Baudemont and Pacquet, 1996). The western graphitic structure (WGS)

and the eastern graphitic structure (EGS) respectively control the Sue C, D and E, and the Sue A and B deposits. The northeast-trending set is also graphite-bearing and locally associated with Ni-As and U mineralization (Baudemont et al., 1993; Baudemont and Pacquet, 1996). The northwest-trending set is less evident than the other sets and does not exhibit direct control of the uranium mineralization. The three fault systems resulted from a major EW contraction event (Baudemont et al., 1993) using the definition of contraction proposed by Marrett and Peacock (1999). The reverse faults created intense fracturing and tilted the bedding planes in the sandstone.

Baudemont et al. (1993) described strong hydrothermal alterations associated with the Sue deposits both in basement and sandstone. Clay alteration is strongly developed and is composed of illite in the sandstone, and illite and sudoite in the basement. In the basement lithologies beneath the Sue A and B deposits, intense quartz dissolution occurred. Aluminum phosphates and dravite are ubiquitous. In the basement of the Sue C deposit, the WGS separates an eastern argillized block from a western locally feldspathic metaquartzite unit. In the sandstone, primary hematite has been leached out and the illite content was increased towards both the mineralization and strongly fractured zones. Micro-"zone à boules", as well as massive clay zones up to several meters thick, contain concentrations of heavy minerals beds. An earthy red-brown hematitic clay zone, up to 20 m thick, wraps the mineralization at Sue A and B.

The Sue A and B deposits are sandstone-hosted and relatively low grade, 1.26 % and 0.73 % U respectively. They are very rich in Ni and As, 3.57 % Ni and 4.46 % As for Sue A, and 1.67 % Ni and 1.86 % As for Sue B. The Sue C, D and E deposits consist of basement-hosted vein-type mineralization that may occur down to more than 100 m below the unconformity. The Sue C deposit is high-grade with an average of 4.5 % U, and poor in Ni and As. The Sue D mineralized zone is divided into an upper, low-grade (0.3 % U) lens and a lower high-grade (1.7 % U) lens. The Sue E deposit averages 1.76 % U with 0.7 % Ni and 1.1 % As (Baudemont et al., 1993).

4. "Zone à boules" characteristics

4.1. Structural controls

Mapping of "zones à boules" exposures in the sandstone of the Sue C pit (Fig. 2) indicated that they are aligned along the EGS and typically occur at fault intersections with NE structures, as determined by strike measurements. Two exposures are located outside of this fault: a small "zone à boules" occurs above the Sue C mineralization along the WGS on the northern wall of the pit, and another located along a NE fault on the southern wall of the pit

close to the WGS. "Zones à boules" were found up to more than 50 m above the unconformity. They form breccia units of 1 to 5 m wide and extend vertically from a few meters to at least 20 m. Their borders are generally fracture-controlled and irregular. They may display dome-shapes vertically limited by a stratigraphic layer or by a gently dipping joint. Controlling fractures are commonly curved. Breccia bodies occur either in the core of strongly fractured and argillized zones or as pockets within low to moderately fractured zones. Fracture density around "zones à boules" may reach 20 vertical fractures per meter with fracture openings of 0.1 to 0.5 mm. A stereogram plot of the strikes of 29 "zones à boules" (Fig. 2a) indicates a predominance of NE to NNE trending fractures; however, NS and NNW strikes are also common. Less common are NW and EW orientations (Fig. 2). The stereogram plot of 336 fractures measured systematically all around the pit (Fig. 2b) indicates a predominance of second-order NE to ENE trending fractures and a lesser amount of NW to NNW azimuths. First-order WGS and EGS are very weakly expressed outside of "zones à boules".

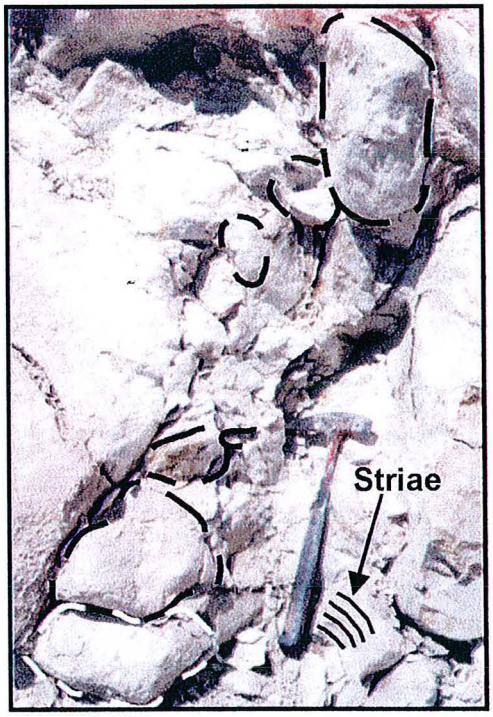

Figure 3 – Photograph of a 1 meter-wide "zone à boules" outcrop located in the eastern part of the Sue pit on the EGS. The low matrix percentage indicates a low maturity degree. Flattened balls in the bottom left and corner of the picture show a local stratigraphic control. Note the curved striae in clay just below the hammer.

4.2. Macroscopic textural and petrographic characteristics

"Zones à boules" are composed of altered sandstone balls wrapped in red, green, yellow and/or white massive clay locally displaying a flow texture (Fig. 3). The surrounding fractured wall rock shows leaching of primary hematite, evidenced by the disappearance of its purple

color, and the development of a white to yellow clay alteration. "Zone à boules" maturity can be defined by their matrix percentage and the ball roundness. Figure 4 displays the evolution from an immature breccia with a low matrix percentage and fracture-controlled weakly rounded fragments to a mature breccia with a high matrix proportion and well rounded balls. More mature breccias are found proximal to the unconformity than immature breccias. Sandstone fragments have been progressively replaced by clay as the maturity increased. A clay envelope has been developed within the external rim of sandstone fragments and generally extends slightly in the long direction (Fig. 4). A yellowish limonitic zone containing centimeter-size black iron hydroxide concretions is usually observed inside the fragments surrounded by the clay envelope (Fig. 4). The presence of a silicified core in the center of the ball limits the extension of the limonitic rim. Fragments usually possess one or two fractures perpendicular to their length that contain euhedral quartz that is earlier than the illite clay. In mature "zones à boules", sandstone fragments may be totally replaced by clay.

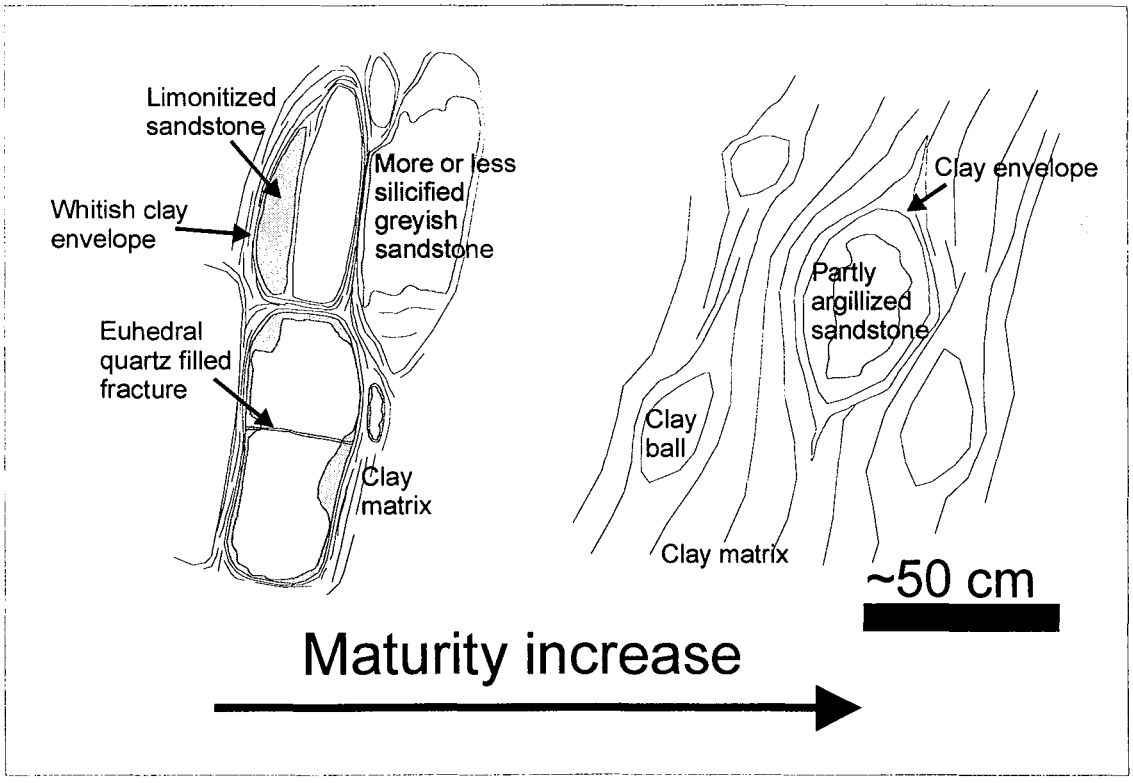

Figure 4 – Drawing showing the maturity evolution of a "zone à boules". Note the increase of matrix percentage and ball roundness with maturity.

The figure 5a shows a clay ball with heavy mineral layers indicating the original beds. These layers appear to be deformed on each side of a sandstone remnant due to volume loss during clay alteration. Their orientation commonly indicates rotation. Some clay balls display

a well developed zoned hematite distribution increasing towards the center (Fig. 5b). Such zones correspond to Liesegang rings formed by a diffusion process.

The most common fragment shape is an ellipsoid like a rugby ball (Fig. 5c). Average length, width and height of 82 balls from separate breccia exposures are 25 ± 22 cm, 16 ± 11 cm and 12 ± 11 cm respectively. The distribution of the ball width is log-normal (Fig. 6a). The linear relationship between the length and the width and height (Fig. 6b) shows that the shape ratios R1 = width / length and R2 = height / length are constant indicating a more or less flattened ellipsoid shape. Some of the ball widths or heights are parallel to the sandstone beds indicating a lithological control of their shape (Fig. 3). Consequently, some balls may form within compartments bounded by stratigraphic surfaces and joints developed within beds around faults (Narr and Suppe, 1991; Gross et al., 1997). This may explain the occurrence of "zones à boules" that are vertically limited by a bed.

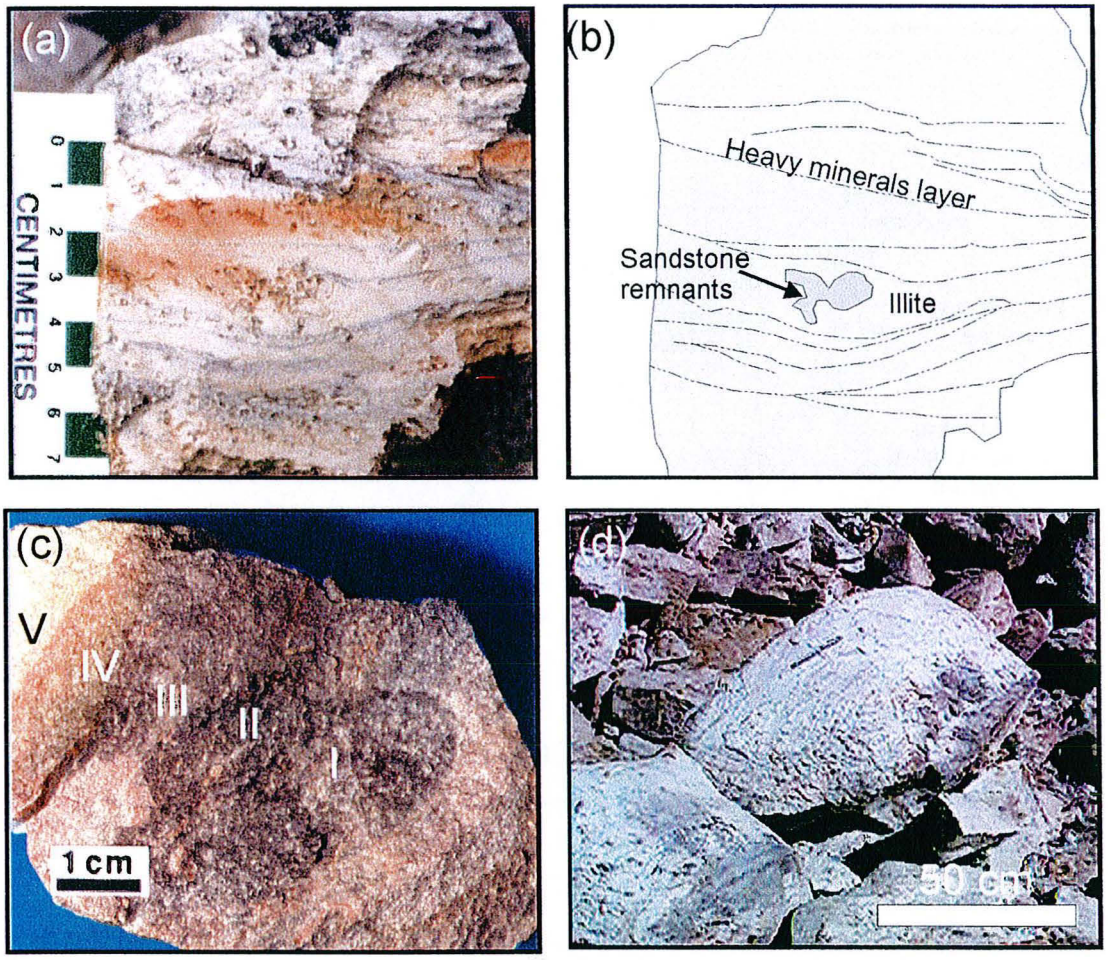

Figure 5 –Photograph (a) and schematic drawing (b) of an illitized sandstone fragment. The high concentration of heavy minerals layers and their local deformation around a sandstone remnant indicate volume loss during alteration. (c) Illitized ball showing a concentric zonation from red in the center to light yellow along the borders (I to V). This is due to a decreasing content of hematite away from the center. (d) Large ball with slickensides.

Most of the balls display striations on their surface and even more so within their clay envelope (Fig. 2 and 5c). Striations are typically parallel to the maximum length or to the width of the balls, and occasionally are oblique. This indicates that ball shapes are, at least partly, controlled by tectonic movements. Striations are typically slightly curved, indicating ball rotation. More than 50 % of the balls have two or locally three striae orientations superimposed, or existing on different sides of the ball. Superimposed striae indicate fault reactivation. Observed vertical and horizontal striae are due to reverse and strike-slip faulting respectively. The occurrence of different striae orientations on a ball could be due to the influence of other nearby rotating fragments.

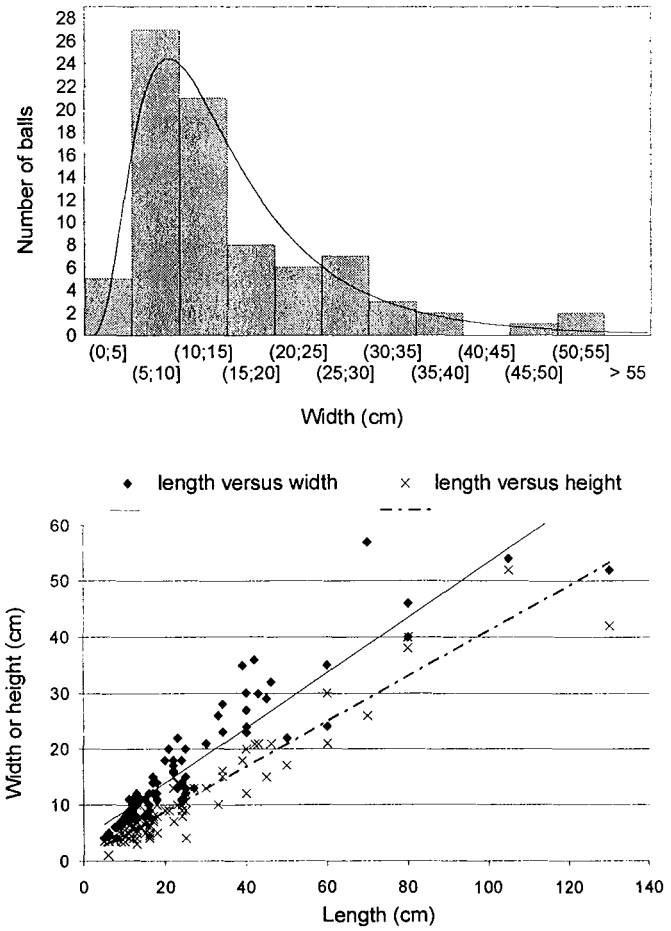

Figure 6 – (a) Distribution of the width of 82 balls. The curve indicates a log-normal distribution. (b) Linear relation between the length and the width and height. (c) Bivariate histogram of the shape ratios R1 = width / length and R2 = height / length.

4.3. Mineralogy

Five samples have been taken along a 6 m profile crossing a "zone à boule" (Fig. 2). Samples 1, 2 and 3 are fine to very coarse-grained sandstones at 4, 2 and 1 m respectively

from the breccia contact. Samples 4 and 5 come from the "zone à boule", with sample 4 from a clay ball and sample 5 from the clay matrix. Sample 6 is a clay ball taken from another breccia exposure (Fig. 2) and sample 7 is a typically non-altered purple, fine- to very coarse-grained sandstone.

Sandstone samples typically display compaction-related pressure-solution contacts between detrital quartz grains. Samples 1 to 3, located close to a "zone à boule", have well developed microscopic corrosion textures of detrital quartz and their overgrowths (Fig. 7a). In the non-altered sample 7, taken far from any "zone à boule", the corrosion of detrital quartz grains is less developed but quartz overgrowths have been selectively dissolved. Quartz proportions do not vary significantly outside of the "zone à boule". However, it decreases dramatically within the breccia matrix or in clay-rich fragments (Fig. 8).

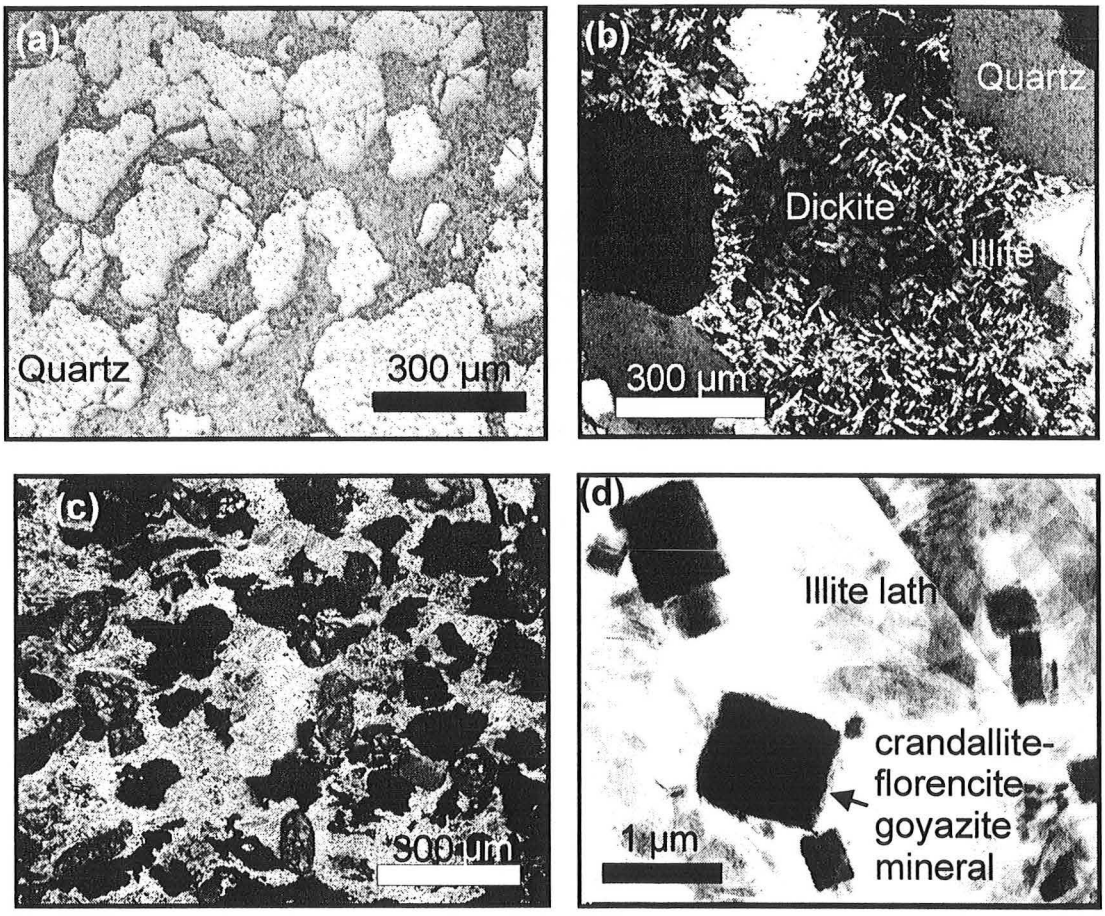

Figure 7 – Microscopic photographs illustrating different microscopic textures. (a) Corrosion textures of detrital quartz grains. Cement between grains is illite (polarized reflected light). (b) Remplacement of dickite by illite (plane polarized transmitted light). (c) High concentration of zircons and Ti- and Fe-oxides in a totally illitized sandstone ball (polarized transmitted light). (d) TEM image of crandallite-goyazite-florencite minerals (black squares).

Dickite, identified by Raman microspectroscopy, and illite constitute the main cement between quartz grains in all sandstone samples. XRD and norm analysis indicates that the

proportion of dickite decreases from the non-altered zone towards the breccia whereas the illite percentage increases (Fig. 8). The replacement of dickite by illite observed in thin section with plane polarized transmitted light confirms XRD analysis (Fig. 7b). However, the presence of dickite in quartz corrosion cusps indicates that the quartz has been partly dissolved prior to illite crystallization. Therefore, the regional dickite diagenesis was accompanied by a first phase of quartz dissolution. Samples 4, 5 and 6 are composed mostly of massive illite. Electron microprobe analysis indicates that illites are locally chloritized or that illite is locally mixed with chlorite. They might be a mixture of 2M1 and 2M2 illites as documented in the Cluff D "zones à boules" by Halter (1988). Illite crystals have lath shapes with sizes of 2 μm to 10 μm in sample 4, and up to 40 μm in sample 5, indicating higher crystallization temperatures than what would be expected in a diagenetic environment.

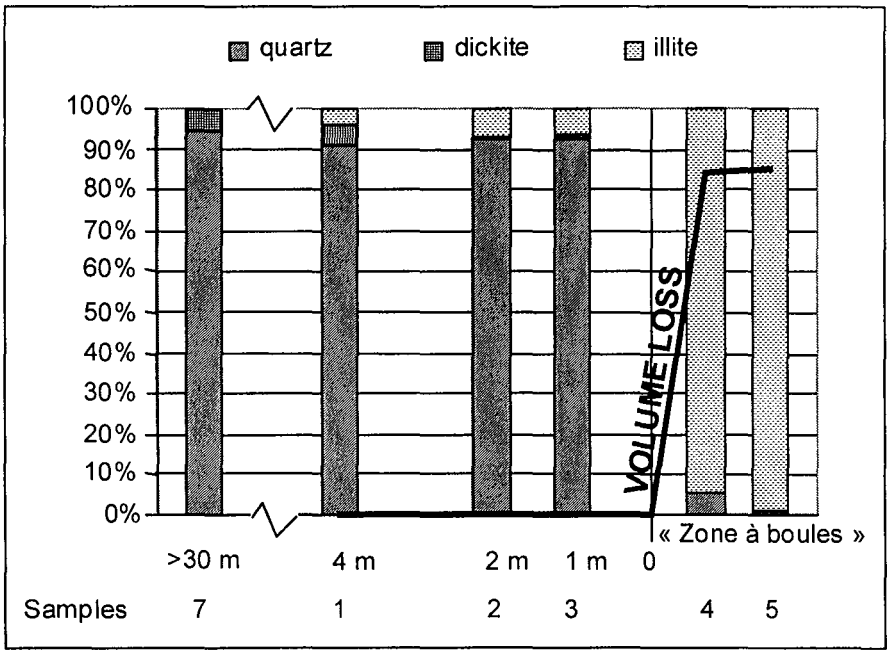

Figure 8 – Proportion of quartz, dickite and illite in samples 1, 2, 3, 4, 5 and 7 showing the progressive replacement of dickite by illite toward the breccia and the massive dissolution of quartz within the "zone à boules".

Detrital accessory minerals are mainly zircon with xenotime overgrowths, Ti-oxides (anatase, rutile) and tourmaline (schorl), with hematite and magnetite present in lesser amounts. In sandstone samples, accessory minerals are found mostly as heavy mineral layers. Clay balls and the matrix display high concentrations of zircons, anatase and schorl (Fig. 7c). Schorls are commonly surrounded by secondary dravite overgrowths in strongly argillized samples. The clay ball corresponding to sample 6 contains a high proportion of hematite (Fig. 5b) which is probably not detrital in origin because of its elevated content compared to unaltered sandstones. Heavy mineral layering is commonly preserved in clay balls (Fig. 5a). LREE-Sr-Ca-Fe aluminous hydroxy-phosphates of the crandallite-goyazite-florencite group

occur in all samples with sizes varying from less than 0.1 µm to 2 µm (Fig. 7d). Their concentration is especially high in clay samples 4 and 5. TEM-coupled X-ray analysis show that they contain up to 7.4 wt% SO_4 due to a probable solid solution with woodhousite (Ca Al_3 (PO_4 SO_4) $(OH)_6$ with P/S > 1) and/or svanbergite (Sr Al_3 (PO_4 SO_4) $(OH)_6$ with P/S > 1), up to 2.7 wt% ThO_2 and up to 0.9 wt% As_2O_3. They are associated with illite and their euhedral shapes indicate that they are newly formed minerals.

Anastomosing microscopic illite bands are present within massive clay. The bands are 20 to 60 µm wide and locally clearly crosscut already crystallized illite. They might be indicative of previously existing microfractures.

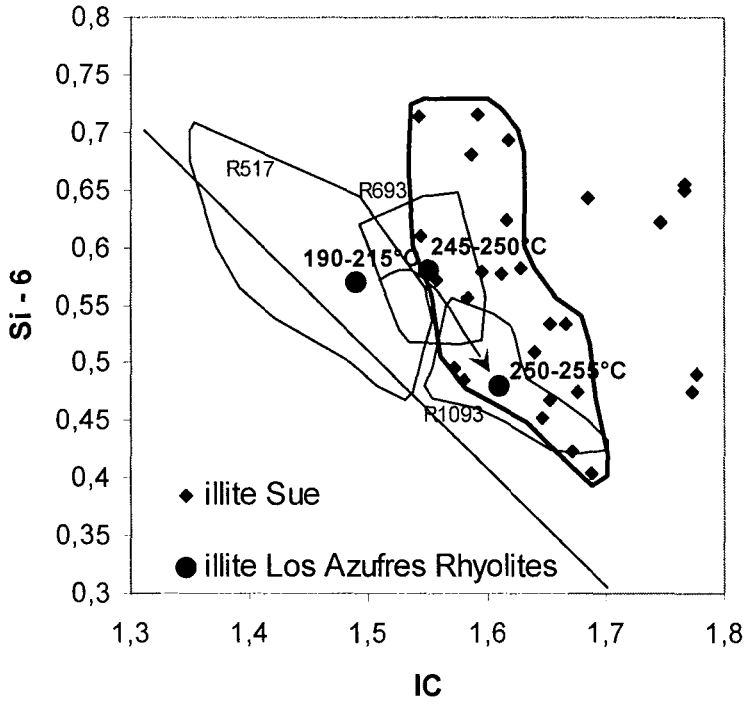

Figure 9 – (Si – 6) versus IC (interlayer charge) plot of illites from samples 1, 3, 4, 5 and 6 and of 3 average illites from Los Azufres rhyolites (Cathelineau and Izquierdo 1988). Envelopes R517, R693 and R1093 indicate their chemical variations. The line gives the theoretical trend corresponding to the I_{-1} $(Si_{+1}$ $Al_{-1})_{IV}$ substitution (muscovite-pyrophyllite) for R^{2+} = 0 (no muscovite – celadonite substitution). The arrow indicates the temperature increase with the CI parameter.

5. Temperature-composition relationships of illite minerals

Illites have been analysed by electron microprobe and their structural formula have been calculated on the basis of 22 oxygen atoms (complete formula). All of the Fe has been assumed to be trivalent. The average structural formulae of 27 hydrothermal illites is presented in table 2 together with structural formulas of hydrothermal illites from rhyolites

and andesites of the Los Azufres geothermal system (Cathelineau and Izquierdo, 1988). The Sue C illites have a chemical composition close to the muscovite end-member with a minor Mg-celadonitic substitution. They are similar to the illites from the Los Azufres rhyolites except for Mg and Fe values. Cathelineau and Izquierdo (1988) have established that illite interlayer charge (IC) increases with crystallization temperature in a hydrothermal environment. In a Si - 6 versus IC diagram (Fig. 9), the Sue illite composition field is shifted to the right with respect to the Los Azufres illite field indicating slightly higher temperatures of crystallization (between 240 and 280°C). The illites having the highest interlayer charge are not included in the Sue illite field as they may be derived from residual detrital muscovites (petrographic observations). This temperature range is similar to slightly higher than the temperature of basin fluids characterizing peak diagenesis estimated by illite cristallinity index and fluid inclusions studies (240 ± 40°C, Halter, 1988; 170-240°C, Kotzer and Kyser, 1995).

6. Mass balance calculations

The use of the Grant method to perform mass balance calculations is justified by the pervasive character of the alteration observed around and within the "zone à boules". The most stable elements used for mass balance calculations are Ta, Ti, Nb, Hf, Zr and Th, all hosted by heavy minerals, and Al. For example, the constant ratio Hf/Zr for samples 1 to 5 indicates that Hf is mostly present in zircons and does not move significantly during alteration. It is confirmed by the chemical composition of zircons in sample 4, determined by electron microprobe analysis, indicating weak to no alterations. However, the Manitou Falls sandstones containing the "zones à boules" show a great variability of the heavy mineral layers abundance at the centimeter to decimeter scale. Considering the fact that volume loss has occurred, it is therefore impossible to find the exact proportion of heavy minerals for each altered sample. Al solubility at 300°C in uncomplexing media is very low, about 10^{-6} mol / kg at pH = 4.5 after Salvi et al. (1998). Furthermore, as the Al content in sandstones depends on the clay mineral proportion, its variability is less important than for the heavy minerals. Therefore, Al has been considered to be the best immobile element and has been used for mass balance calculations. An uncertainty domain of 50 % enrichment and 50 % depletion has been considered in order to take into account the variability of initial Al content.

An average protolith composition has been calculated using the non-altered sample 7 and the slightly altered sample 1. The proximal sample 1 has been considered in order to get a protolith composition as close as possible as the one for samples 2 to 5.

Sample Nature	7 sst	1 sst	Av. 7 & 1 Sst (protolith)	2 sst	3 sst	Av. 2 & 3 Sst (wall rock)	4 Clay ball	5 Clay matrix
Distance (m)	> 30	4	-	2	1	-	0	0
Density	2.44	2.48	2.46	2.42	2.44	2.43	1.37	1.32
SiO2 (%)	96.9	95.6	96.2	95.4	95.7	95.5	52.5	48.1
TiO2	0.03	0.09	0.06	0.1	0.12	0.11	0.93	0.5
Al2O3	2.3	3.3	2.8	2.7	2.6	2.6	30.6	34.0
Fe2O3	0.2	0.1	0.16	0	0.18	0.09	0.45	0.45
MgO	0.07	0.07	0.07	0.07	0.07	0.07	1.3	1.0
CaO	0.07	0.07	0.07	0.07	0.07	0.07	0.18	0.15
K2O	0.03	0.4	0.22	0.68	0.63	0.66	8.9	9.6
P2O5	0.05	0.05	0.05	0.03	0.03	0.03	0.24	0.46
PF	0.81	0.88	0.845	0.46	0.51	0.49	5.02	5.95
As (ppm)	4.7	2.1	3.4	2.4	3.2	2.8	35.2	53.2
B	3	37	20	58	63	61	650	775
Ba	16	12	14	12	12	12	158	190
Be	0.6	0.6	0.6	0.6	0.6	0.6	3.1	5.0
Bi	0.03	0.2	0.1	0.1	0.2	0.2	4.2	19.8
Cd	0.20	0.20	0.20	0.20	0.20	0.20	0.51	0.00
Ce	36.2	24.2	30.2	21.5	26.4	23.9	325.8	530.6
Co	0.6	0.2	0.4	0.2	0.2	0.2	0.9	1.5
Cr	3	6	4	3	6	5	68	86
Cs	0.1	0.1	0.1	0.1	0.1	0.1	0.6	0.4
Cu	3	3	3	3	5	4	14	15
Dy	0.79	0.88	0.84	0.82	1.04	0.93	20.08	10.29
Er	0.35	0.50	0.42	0.50	0.54	0.52	9.24	3.67
Eu	0.30	0.24	0.27	0.24	0.25	0.25	3.57	4.70
Ga	2.8	5.6	4.2	6.8	7.7	7.2	100.3	141.1
Gd	1.22	1.20	1.21	1.07	1.22	1.15	19.37	24.70
Ge	0.8	0.9	0.8	0.8	0.9	0.9	1.1	1.3
Hf	1.51	4.60	3.06	4.66	5.39	5.02	55.32	17.61
Ho	0.14	0.17	0.15	0.16	0.20	0.18	3.50	1.35
La	15.58	11.15	13.37	10.07	12.10	11.08	163.56	271.45
Lu	0.05	0.08	0.07	0.09	0.11	0.10	1.39	0.43
Mo	0.2	0.2	0.2	0.3	0.2	0.2	1.3	1.5
Nb	1.0	2.5	1.7	2.4	2.8	2.6	27.7	19.1
Nd	11.7	8.4	10.1	7.2	8.8	8.0	126.0	205.6
Pb	9.6	9.8	9.7	9.0	11.7	10.4	122.6	133.6
Pr	3.35	2.33	2.84	2.10	2.65	2.37	35.30	58.33
Rb	1	5	3	7	7	7	96	90
Sb	0.07	0.07	0.07	0.07	0.1	0.1	1.1	0.9
Sm	2.04	1.42	1.73	1.31	1.59	1.45	22.20	34.23
Sn	0.30	0.30	0.30	0.30	0.30	0.30	3.7	2.0
Sr	209	56	133	49	58	54	985	2610
Ta	0.11	0.31	0.21	0.26	0.30	0.28	3.26	1.70
Tb	0.19	0.16	0.17	0.14	0.18	0.16	3.43	2.71
Th	5.2	5.8	5.5	5.3	8.1	6.7	71.8	108.7
Tm	0.04	0.08	0.06	0.09	0.09	0.09	1.32	0.42
U	1.6	2.8	2.2	2.1	3.1	2.6	36.3	29.9
V	3	16	9	18	34	26	1007	1519
W	0.2	1.2	0.7	1.3	1.5	1.4	20.7	20.8
Y	3.61	4.97	4.29	5.29	6.03	5.66	107.18	37.73
Yb	0.32	0.52	0.42	0.58	0.63	0.61	9.00	3.04
Zn	3.00	3.00	3.00	3.00	3.00	3.00	39	77
Zr	61.8	198.5	130.1	208.8	225.3	217.1	2121.0	725.1

Table 1 - Results of the density measurements and of the geochemical analysis of major and trace elements for samples 7, 1, 2, 3, 4, 5. The calculated average chemical composition (av.) of the protolith and wall rock samples is also presented. When values were less than the detection limit, the 2/3 value of the detection limit was systematically attributed. Sst = sandstone, distance = distance from the "zone à boules".

Petrographic observations and quartz percentages of sandstone samples 2 and 3 (Fig. 8) show that the volume loss during the alteration process is negligible in these samples. Consequently, mass balance calculations have been performed at constant volume for these samples. Figure 10a shows the changes of element concentration in the wall rock relative to

the average protolith using a calculated average sample between 2 and 3 (Table 1). The large variation in Ti, Zr, Hf, Nb, Ta and Th abundance shows the highly variable proportion of accessory minerals in the original sandstone. Also, the slight Al depletion confirms that Al is the best immobile element. Hydrothermal fluids have brought K, B, Rb and W to the "zone à boule" wall rock whereas Sr has been leached out. K and Rb enrichments are due to illite crystallization, and B enrichment to dravite overgrowths on detrital tourmaline. Depletion in Sr may be due to dissolution of crandallite-florencite-goyazite minerals. Fe depletion results from hematite leaching.

	Los Azufres							Sue
Sample	R517	R693	R109 3	A451	A847	A114 0	A1150	1, 3 & 6
n	18	12	12	8	9	5	8	27
K	1.45	1.48	1.56	1.46	1.48	1.68	1.73	1.60
Na	0.02	0.01	0.03	0.03	0.09	0.02	0.02	0.00
Ca	0.01	0.03	0.01	0.07	0.03	0.00	0.00	0.00
IC	1.49	1.55	1.61	1.63	1.63	1.70	1.75	1.61
Si (IV)	6.57	6.58	6.48	6.65	6.67	6.81	6.88	6.60
Al (IV)	1.43	1.42	1.52	1.35	1.33	1.19	1.12	1.40
Al (VI)	3.84	3.80	3.82	3.63	3.40	3.22	3.06	3.74
Fe^{2+}	0.10	0.13	0.18	0.25	0.35	0.36	0.49	0.05 (Fe^{3+})
Mg	0.09	0.08	0.03	0.20	0.38	0.51	0.52	0.21
Mn	0.01	0.01	0.00	0.00	0.00	0.00	0.00	0.00
Ti	0.00	0.00	0.00	0.00	0.00	0.00	0.00	0.00
Fe + Mg + Mn	0.21	0.22	0.22	0.45	0.73	0.87	1.01	0.26
OC	0.07	0.16	0.12	0.21	0.33	0.60	0.79	0.21

Table 2 - Average structural formulae and parameters (IC interlayer charge; OC octahedral charge) of Sue illites and of illites from rhyolites (R) and andesites (A) of Los Azufres for comparison (Cathelineau and Izquierdo 1988). All the iron present in the Sue illites is assumed to be Fe^{3+}.

Petrographic observations indicate that all the quartz has been leached out in sample 5, (about 94 %) estimated from normative calculations on the non-altered sample 7. Assuming constant Al content, dickite alteration to illite would correspond to a negligible volume variation. As illite proportions in the clay sample 5 is about 99 % in average , the volume loss during the hydrothermal alteration would be about 94 %, subtracting the 5 % initial dickite proportion from the final illite content and neglecting the small density difference between quartz, dickite and illite. A similar volume loss of 94 % has been calculated by Percival (1990) in the massive clay alteration cap of the large Cigar Lake unconformity-type uranium deposit. A calculation, assuming Al was immobile, using the Grant method gives a volume loss of 84 % for the clay ball (sample 4) and of 85 % for the clay matrix (sample 5), (Fig. 8).

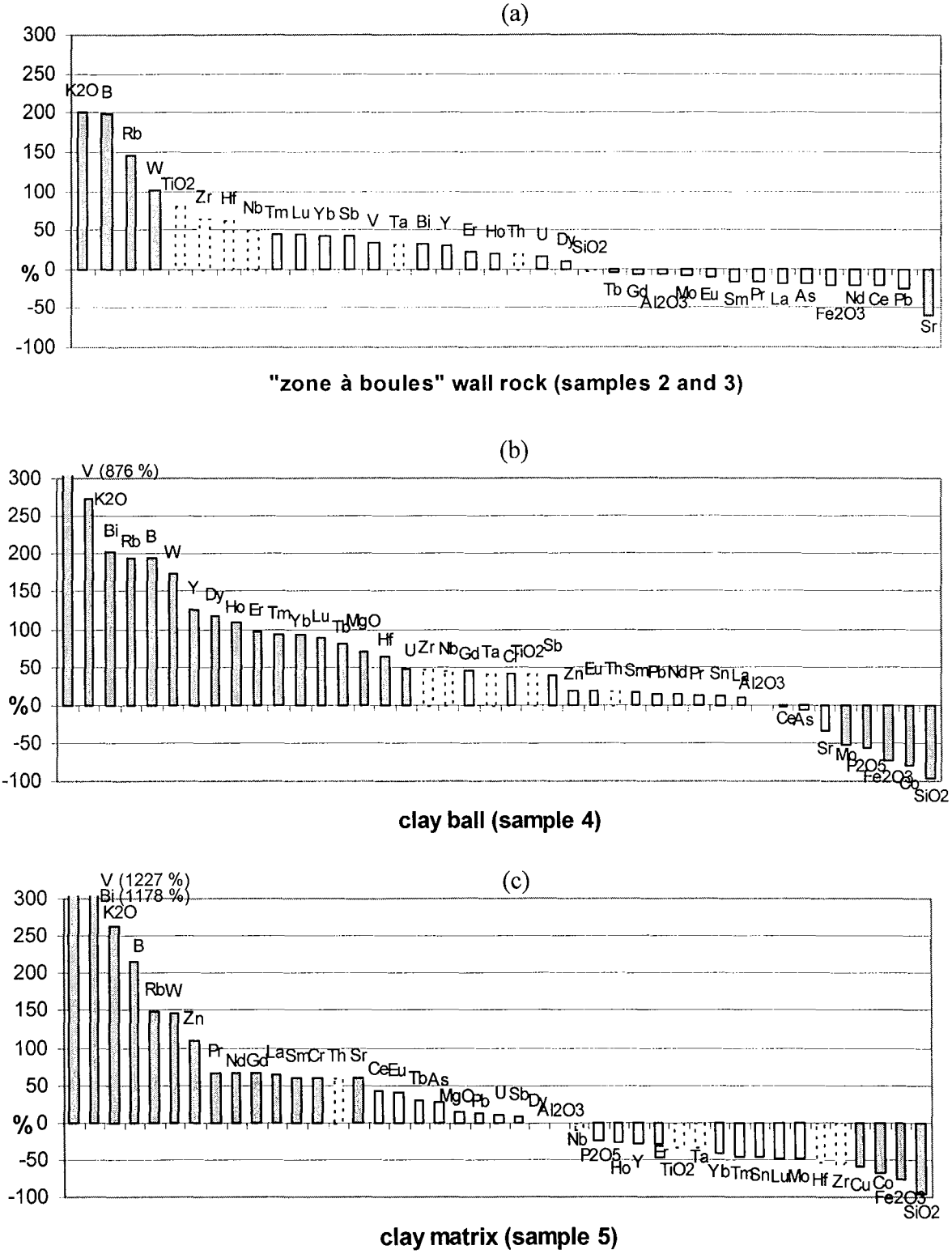

Figure 10 - Elemental depletion-enrichment factor relative to the average protolith for the "zone à boules" wall rock (a) and the clay ball (b) and matrix (c). Constant volume has been assumed for the "zone à boules" wall rock whereas Al immobility has been considered for the "zone à boules". Dashed white bars correspond to changes of concentration of stable elements due to different initial concentration in the sample and the average protolith. White bars indicate uncertain enrichments or depletions due to concentrations variations below 50 % that partially reflect the variability of the protolith. Grey bars correspond to reliable chemical variations.

The density of sample 5, about 1.32, is very low compared to the theoretical density of muscovite, about 2.8. Consequently, the 9 % difference between the 2 methods is explained by a high microporosity of sample 5. Therefore, the best volume loss value is given by the Grant method.

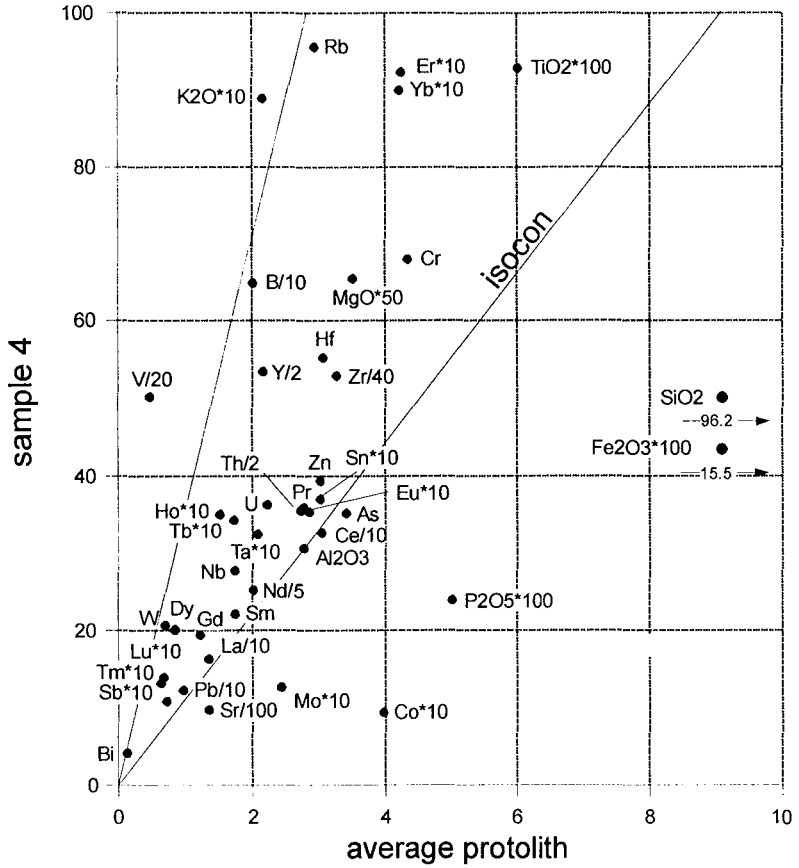

Figure 11 – Isocon diagram for sample 4 relative to the average protolith. The isocon is determined by considering Al as an immobile element. The angle between the isocon and the bissector corresponds to the amount of volume loss (84 %). The location of elements above or below the isocon indicates enrichment or depletion respectively, taking into account the effect of volume loss. Note the strong depletion in Si.

The isocon diagram for the clay ball (sample 4), (Fig. 11) shows strong enrichments in most of the elements due to the volume loss. Strong Si depletion is directly associated with quartz dissolution. The isocon determined using Al as an immobile element indicates which elements were brought or remobilized by the fluids and which ones have the same chemical behavior. V, K, Bi, Rb, B, W, Y, HREE, Mg and U are enriched whereas Si, Co, Fe, P and Mo are depleted (Fig. 10b and 11). Strong K, Rb and Mg enrichments are due to major illite crystallization. Mg is also associated with B in newly formed dravite overgrowths and with Cr in minor amounts of newly formed chlorite precipitation. V enrichment is the most spectacular and seems to correlate with Bi (Fig. 11). It can be related to the high vanadium values surrounding the uranium mineralization (Baudemont et al., 1993) and is probably due to V-rich illite and adsorption on Ti-oxides. HREE and Y enrichments are probably due to

xenotime new formation on detrital zircons and to zircon alteration as described in the Athabasca sandstone by Quirt et al. (1991) and Hecht and Cuney (2000 a, b). Microprobe analysis of xenotime overgrowths in sample4 give uranium contents up to 0.94 %. Therefore, xenotime new formation could explain the U enrichment of the clay balls. Depletion in Sr indicates dissolution of crandallite-florencite-goyazite minerals. Fe depletion results from hematite leaching. The clay matrix (sample 5) displays the same chemical variations as sample 4, with the exception of REE, Y, Sr and Zn (Fig. 10c). In this sample, LREE, Sr and Zn are enriched whereas HREE and Y have been leached out. LREE and Sr are probably associated in newly formed minerals of the crandallite-florencite-goyazite group. Calculations on REE changes of concentration in the whole "zone à boule", using an estimation of 65 % for the matrix percentage, show no significant variations for HREE whereas LREE are enriched. The differential enrichments in HREE and LREE in the balls and matrix are illustrated in figure 12.

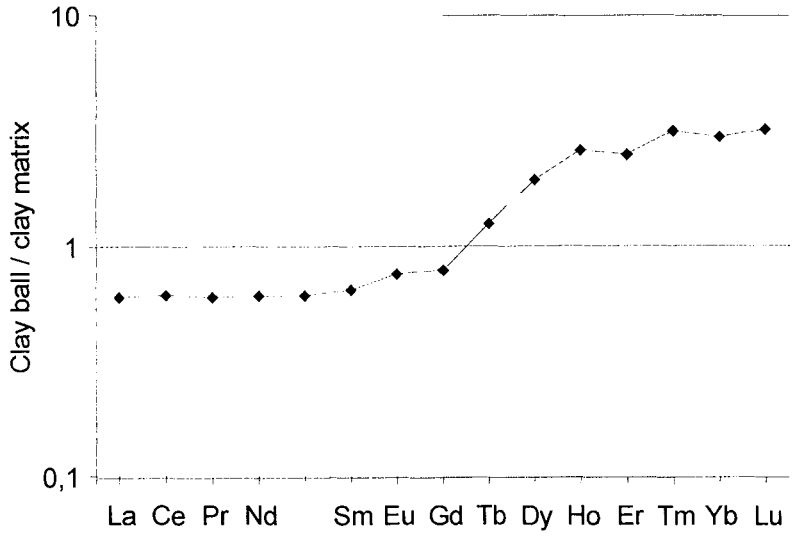

Figure 12 – REE pattern for the clay ball sample 4 normalized to the clay matrix sample 5 illustrating the differential chemical behavior of LREE and HREE in the clay balls and matrix. Clay balls have been HREE enriched and LREE depleted relative to the clay matrix.

Enriched and depleted elements are globally similar in the "zone à boules" and its wall rock. They indicate mainly illite and dravite crystallization and hematite dissolution. However, the intensity of the alteration is considerably more important in the "zone à boules" due to massive quartz dissolution and subsequent volume loss. This volume loss combined with a partitioning model and desilicification has also been proposed along a shear zone by O'Hara and Blackburn (1989). The "zone à boules" formation is accompanied by a chemical partitioning of REE with enrichments in LREE and Sr and depletion in HREE in the matrix relative to the balls.

7. Discussion

7.1. Tectonic controls

"Zones à boules" are clearly controlled by the eastern graphitic structure (EGS) and seem to be more developed at intersections with NE-trending structures. Their widths up to 5 m, suggest possible vertical movements of about the same amplitude along the EGS fault during formation of the "zone à boules" (Scholz, 1990). This is consistent with the 5 to 30 m down-drop of the western block. As most of the Sue primary uranium mineralization formed during a contractional tectonic event (Baudemont et al., 1993), the syn-tectonic development of "zones à boules" was probably contemporaneous with primary uranium mineralization.

The log-normal distribution statistics of the size of the ball indicates that they were initiated by tectonic fracturing (Rouleau and Gale, 1985; Rives et al., 1992). The ball shape is primarily controlled by the fracture network along the EGS, or locally by the sandstone beds. This shows that prismatic fracturing, with at least 3 fracture orientations, or with 2 orientations combined with bedding planes, is needed to create the balls. Anastomosing fracture zones may also be favorable to ball development and could explain the presence of curved fractures at the breccia contact. The increase of matrix percentage toward the unconformity could be caused by an increase of the fracture spatial density. The presence of early euhedral quartz filling length-perpendicular fractures within sandstone balls may represent tension gashes formed together with a fracture network during an initial tectonic contraction phase (Fig. 13). This fracture network would have bounded sandstone blocks that eventually evolved into balls.

The presence of striae on clay ball surfaces preferentially oriented parallel to the ball length and/or width confirms that tectonic movements were coeval with the ball formation. The presence of pervasive striae within clay envelopes around balls suggests a possible sub-continuous deformation process. The illite-rich matrix probably favored ductile creep by reaction weakening (Cox et al., 2000) whereas the balls probably behaved in a brittle manner. An analogous mechanical behavior has been described in mylonitic environment (Laznicka, 1988; Passchier and Trouw, 1996; Kisters et al., 2000). As for the separatrix surface of mantled porphyroclasts at the microscopic scale (Passchier and Trouw, 1996), the striae were probably formed by the differential movement between the creeping matrix and the rotating fragments. Laznicka (1988) described ball breccias as a special case of porphyroclastic mylonite, in which rolled hard, brittle fragments are enclosed in a ductile mylonitic matrix. Some of the fractures perpendicular to the ball length observed within sandstone balls could be the expression of their brittle behavior. They may also express a boudinage of the balls in a

pure shear deformation. However, simple shear has to occur to explain the 5 to 30 m post-Athabasca offset along the EGS. Therefore, pure shear deformation possibly occurred but were not coeval with reverse movements along the EGS.

7.2. Hydrothermal fluids

Massive illite crystallization, quartz dissolution and considerable volume loss indicate major fluid-rock interactions within "zones à boules". Illite replaced diagenetic dickite found in non-altered zones of the Sue C pit. Estimated temperatures from illite chemistry are comprised between 240 and 280 °C, probably slightly higher than those of diagenetic fluids. Therefore, the fluids responsible for the formation of illite may correspond to a specific hydrothermal event localized along the EGS and locally along NE-trending structures. Tectonic fracturing of sandstones by reactivation of the EGS created permeability paths allowing fluids to circulate in the overlying sandstone. Fluid focusing has occurred in zones of low fluid pressure at fault intersections. This, together with the prismatic fracturing needed to form the balls, explains the preferential occurrence of "zones à boules" at structural intersections. The maturity evolution of "zones à boules" indicates that quartz corrosion occurred along fractures and propagated towards the fragment center. Preservation of silicified sandstone cores within balls results from the low permeability of silicified sandstone. Fragments totally replaced by clay were probably less silificied and therefore more permeable.

Using the average mineral chemical compositions determined from microprobe analysis, the following chemical reaction (1) is proposed to explain the alteration of dickite to illite:

$$1.13\ SiO_2 + Al_4Si_4O_{10}(OH)_8 + 0.04\ Fe^{3+} + 0.15\ Mg^{2+} + 1.24\ K^+ \leftrightarrow$$
$$1.55\ [K_{0.8}Si_{3.3}Al_{0.7}(Al,Fe)_{1.9}Mg_{0.1}O_{10}(OH)_2] + 1.62\ H_2O + 1.65\ H^+ \quad (1)$$

The reaction (1) shows that K^+ and Mg^{2+} brought in by the fluids as K and Mg are present in very small amount in the protolith. Fe was probably provided by hematite dissolution as mass balance calculations indicate Fe leaching. The ratio $[K^+]$ / $[H^+]$ was close to 100 according to the Log ($[K^+]/[H^+]$) versus Log$[H_4SiO_4]$ diagram in the Si-Al-K system at 200°C (Fritz, 1981). The reaction (1) demonstrates that quartz dissolution is needed to crystallize the illite from dickite. However, the quantity of consumed quartz is limited by the initial amount of dickite. Considering 5 wt. % of dickite and 94 wt. % of quartz in a non-altered sandstone, 88.4 wt. % of quartz would be dissolved after completion of reaction (1) to explain the massive quartz depletion observed in "zone à boules". Fluids were therefore silica-undersaturated. Quartz dissolution (reaction (2)) should have taken place in addition to reaction (1):

$$SiO_2 + 2\ H_2O \leftrightarrow H_4SiO_{4(aq)} \quad (2)$$

Silica undersaturated fluids probably came from the graphite-rich basement faults where quartz may be absent (see part II). This explains why dissolution is more developed proximal to the unconformity, for fluid undersaturation in silica would decrease with the amount of time the fluid circulated in the sandstone.

At the time of mineralization, the sediment pile was probably about 5 km thick (Pagel, 1975) giving a lithostatic pressure of about 130 MPa. The quartz solubility at 250°C and 100 MPa is about 10^{-2} mol / kg using the solubility of quartz in pure water given by Tester et al. (1994). Assuming a silica saturation of 90% and 60% and considering samples 7 and 4 as being representative of the rock composition before and after alteration, the fluid/rock ratio is greater than 38,000 and 10,000 respectively. This shows that a considerable amount of fluids has to have circulated within the shear zone-hosted "zone à boules". The fluid/rock ratio may even be higher because quartz solubility at 250°C in NaCl bearing solutions tends to be lower than in pure water (Fournier, 1983). Similar fluid/rock ratios, up to 10,000, have also been documented by Fyfe and Kerrich (1985), Sinha et al. (1986) and Goddard and Evans (1995) in shear zones. Such high fluid/rock ratios are probably necessary to explain the formation of the high-grade Sue A and B unconformity-type uranium mineralization.

Mass balance calculations show that hydrothermal fluids brought into the "zone à boules" the following elements, presented in order of decreasing abundance - V, K, Rb, B, U, W, Bi, Zn, Mg, Sr, LREE, Cr, and Y. Si, together with small amounts of Co, Fe, P and Mo were leached out of the zone. Such enrichments and depletions reflect newly formed illite, chlorite, dravite and crandallite-florencite-goyazite group minerals crystallization and quartz and hematite dissolution. Enrichments in elements such as Mg, Bi, Cr, W and Zn probably indicate basement-derived fluids.

Illite alteration in sandstones has been commonly described as being associated with unconformity-type uranium mineralization at Sue and in other deposits of the Athabasca Basin (Halter et al., 1988; Baudemont et al., 1993; Iida, 1993; Percival et al., 1993). The age of this hydrothermal event may correspond to the 1293 ± 36 Ma K-Ar age determined by Clauer et al. (1985) on illites from the Cluff D deposit "zone à boules". Therefore, it is contemporaneous with the main uranium unconformity-type mineralization event in the Athabasca Basin (Hoeve et al., 1980; Lainé, 1985; Fayek and Kyser, 1997). As U has been slightly enriched in the "zones à boules", hydrothermal fluids implicated in their formation were probably similar to the mineralizing fluids. The absence of uranium mineralization within the "zones à boules" might indicate that reducing basement fluids did not mix diagenetic oxidizing fluids at that location. This confirms that illite alteration results from a pH front rather than from a redox front (Hoeve and Quirt, 1984).

7.3. "Zones à boules" evolution and permeability control of deformation

During the first phase of "zone à boules" development, a tectonic reactivation of the EGS induced the formation of fractures and tension gashes in sandstones (Fig. 13). The subsequent permeability increase was accompanied by fluid circulation and euhedral quartz precipitation in the tension gashes. A second tectonic reactivation is responsible for the development of more fractures and for circulation of basement fluids in the sandstone. These fluids were undersaturated relative to silica, leading to quartz dissolution, and they also leached the primary hematite. The basement fluids were K, B, Mg, V, Cr, LREE and U rich and induced alteration of dickite to illite. They also allowed minor formation of dravite, chlorite and crandallite-florencite-goyazite minerals (Fig. 13). Such fluid flow could have been driven by fluid buoyancy or fluid pressure (Cox et al., 2000). The fluid buoyancy is evidenced by temperature gradients indicated by the anomalous temperature formation of illites within the "zones à boules". Basement fluid flow in the sandstone has also been evidenced in the Shea Creek exploration zone (see part II). Clay mineral precipitation and quartz dissolution along fractures were responsible for the formation of sandstone fragments in a clay matrix. In zones of moderate fracturing and limited fluid circulation, the matrix percentage remained low, leading to immature "zones à boules". In such immature breccias, rounded fragments may indicate quartz dissolution in a diffusion-limited regime (Jébrak, 1997; see part II) rather than ball rotation. In strongly fractured sandstone, generally in the core of the EGS and close to the unconformity, sandstone fragments have been totally dissolved leading to a high matrix percentage typical of mature "zones à boules".

The intensity of alteration in mature "zones à boules" and the calculated high fluid/rock ratio imply strong fluid focusing and sustainable permeability in order to allow fluid circulation. The permeability evolution results from the competition between chemical and deformation processes (Rice, 1992; Cox, 1995) (Fig. 13). Permeability increases with quartz dissolution and decreases with illite precipitation. However, the 85 % calculated volume loss in the most mature zones indicates that the porosity and permeability created by massive quartz dissolution has been accommodated. The absence of collapse phenomenons and the syn-tectonic evidence of "zones à boules" hydrothermal alteration suggest that volume loss has been balanced by tectonic contraction during reverse movements of the EGS, resulting in massive clay alteration (Fig. 13). This alteration event acted as a negative feedback for fluid circulation by self-sealing of the system (Knipe, 1993; Cox, 1995; Tenthorey et al., 1998; Etheridge, 2000). This probably occurred between seismic phases by sub-continuous ductile creep of the matrix. Consequently, the main mechanism to renew permeability would be periodic EGS seismic reactivations as documented elsewhere by Sibson et al. (1988), Knipe

(1993), Hickman et al. (1995) and Cox (1995). Reactivations are evidenced by several superimposed striaes on balls and would be favored by the lubricant properties of the graphite present in the extension of the fault in the basement. Tectonic reactivation may have reopened or created new microfractures acting as discrete fluid channelways. Fracture openings would have been favored by high fluid pressures, possibly close to lithostatic, due to the low permeability of the sealed system. That would explain the illite cross-cutting anastomosing bands observed in thin section.

The formation of balls in a clay matrix corresponds to strain partitioning, such as between lithons and wrapping mylonites at the Renco mine in Zimbabwe (Kisters et al., 2000), due to the competency contrast between clay and sandstone. The differential enrichment in LREE and HREE between the balls and matrix indicates that this strain partitioning was coupled with a chemical partitioning.

By estimating the fluid velocity of the fractured sandstone, it is possible to constrain the minimum time of formation of the "zone à boules". The 5 m wide, 20 m long and 20 m high totally argillized "zone à boules" located along the EGS has been used for this determination. The initial width of the zone was 33 m before the 85 % volume loss. An initial fracture frequency of 20 vertical fractures per meter with fracture openings of 0.1 mm has been estimated, taking into account the strongly fractured rock immediately adjacent to the "zone à boules". Using the cubic law, calculated fracture permeabilities are 2×10^{-12} m^2 (Fig. 13). This permeability is higher than the Darcy type sandstone permeability which was probably below 10^{-15} m^2, considering its low porosity, possibly below the percolation treshold, due to compaction and cementation by quartz and dickite (Cox et al., 2000). Using the hydraulic conductivity formulae for a family of fractures (Snow, 1969; Ababou, 1991), and neglecting sandstone permeability, the calculated hydraulic conductivity is 260 $m.year^{-1}$. This value represents a maximal order of magnitude for the fluid velocity as rugosity and irregularity of fractures were not taken into account. Considering a minimum fluid/rock ratio of 38,000, the possible time of formation of the "zone à boules" is about 1,460,000 years, with fracture openings of 0.1 mm and a fluid velocity of 260 $m.year^{-1}$. As the quartz dissolution kinetics are assumed to be very fast and as all the fluid flowing through the system did not react with the rock, the calculated time is minimal. Furthermore, this calculation assumes a constant fracture permeability. In reality, such permeability values correspond to seismic events. The low grain-scale permeability during interseismic ductile creep (Cox and Etheridge, 1989; Cox et al., 2000) would control the overall time of formation of the "zones à boules" which is therefore in the order of a few million years.

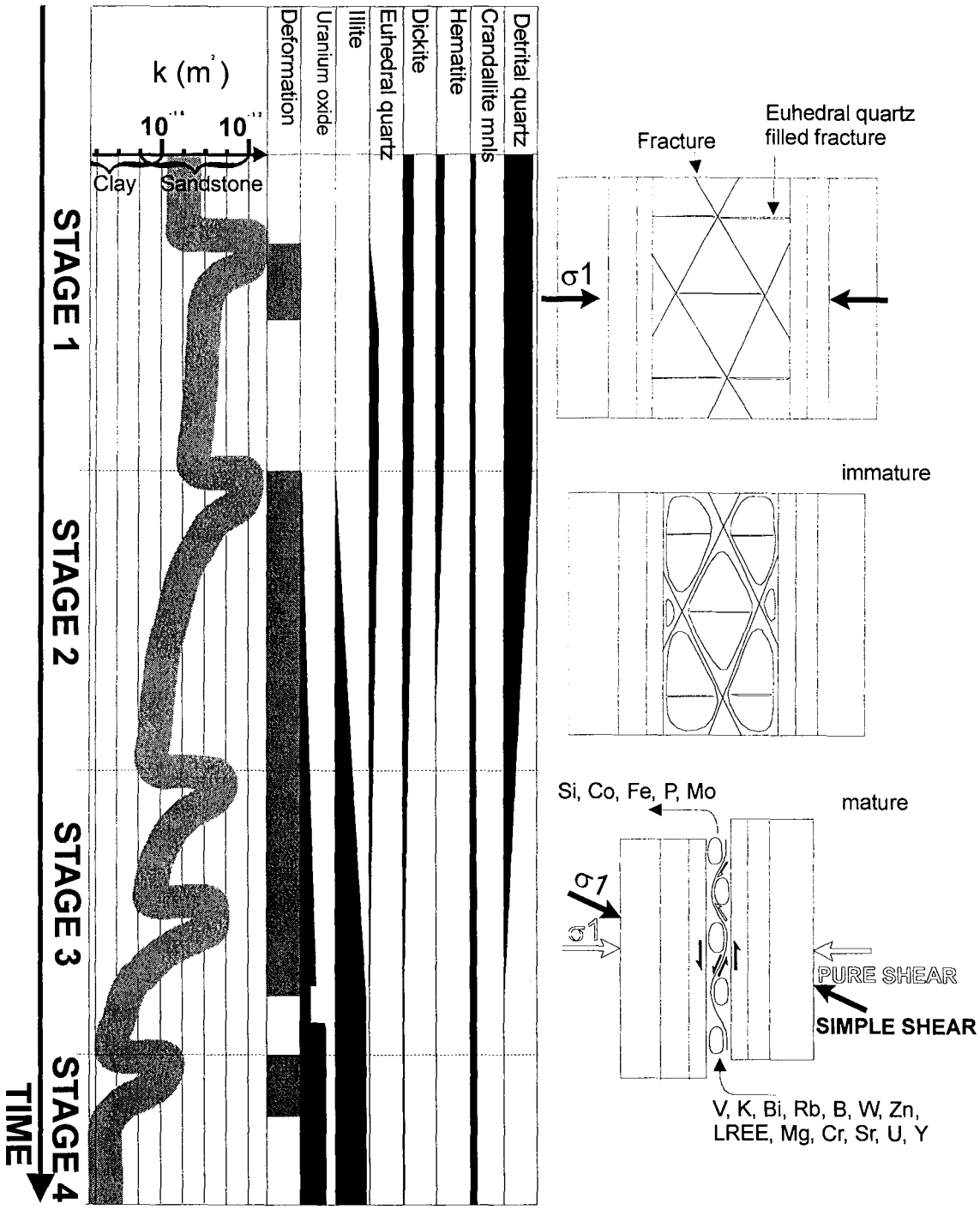

Figure 13 – Synthetic drawing showing the "zone à boules" and permeability evolution in 4 stages. The relative scale between drawings is respected. The initial permeability is assumed to be about 10^{-15} m^2 and 2×10^{-12} m^2 for the unfractured and fractured sandstone respectively, using 0.1 mm fracture openings. The first stage corresponds to the development of fractures and quartz-filled tension gashes in the sandstone during contraction. The second stage is characterized by tectonically induced fluid circulation in the fractures accompanied by quartz dissolution, hematite leaching and dickite replacement by illite. This is responsible for the formation of immature "zones à boules". The third stage is characterized by extreme quartz dissolution and major volume loss during a tectonic contraction phase. It leads to the formation of mature "zones à boules". The fourth stage corresponds to late tectonic reactivation accompanied by ball rotation. Each deformation phase is accompanied by sharp permeability increases but the overall trend is a decrease of the fault permeability due to self-sealing by clay.

8. Conclusion

"Zones à boules" are hydrothermal shear zone-hosted breccias developed in sandstones around unconformity-type uranium mineralization. They formed during peak diagenesis at similar to slightly higher temperatures, between 240 and 280°C. Their evolution was controlled by intense chemical processes combined with minor fault movements.

"Zones à boules" were initiated by fracturing having a log-normal distribution and occurred mainly at fault intersections. Fracturing was followed by strongly focused basement fluid circulation in sandstones. Reverse and dextral tectonic movements occurred after this fracturing event along the EGS and the NE-trending faults respectively. Faults were reactivated several times with cumulated offsets limited to a few meters. Pure shear may have occurred in addition to simple shear. Reaction weakening due to clay alteration induced matrix ductile creep and ball rotation during aseismic phases resulting in a strain partitioning.

The extreme hydrothermal alteration in "zones à boules" results from the chemical interaction of basement fluids with the sandstone. It is a chemical brecciation process characterized by major quartz dissolution and minor hematite dissolution, alteration of dickite to illite and precipitation of dravite and crandallite-florencite-goyazite minerals. The meaning of chemical brecciation used here is different from the one used by Sawkins (1969) to describe a type of crackle breccias. Quartz dissolution is accompanied by about 85 % volume loss and implies a minimum fluid/rock ratio of about 38,000 assuming 90% silica saturation of the fluid. Mass balance calculations indicate Si and Fe leaching and enrichments in V, K, Rb, B, W, Zn, LREE, Mg, Cr, Sr, U and Y. The alteration resulted in a chemical partitioning between clay balls, enriched in HREE, and the clay matrix, enriched in LREE. It has to be noticed that quartz dissolution preceding dickite precipitation indicates a regional diagenetic event and is not related to hydrothermal alteration.

The permeability increase by quartz dissolution is balanced by tectonic contraction during interseismic ductile creep of the matrix. The resulting self-sealing of the system induced a progressive decrease of the permeability controlled by grain-scale dilatancy that was renewed several times by seismic fault reactivations.

Ball exfoliations were created by rotation during tectonic movements and by quartz dissolution in a diffusion-limited regime over a period of time, probably more than several million years, indicating rather slow processes such as spheroidal alteration at the surface.

"Zones à boules" are probably coeval with high-grade primary uranium mineralization which occurred at about 1.3 Ga. They are the expression of the hydrothermal alteration and tectonic movements both genetically associated with the ore formation. From an exploration standpoint, three criteria may be used to identify potential mineralized zones. The first one is the presence of massive illitic argillization indicating the circulation of important quantities of

basement fluids in the sandstone. The second one is the illitic nature of the clay indicating hydrothermal fluids with $[K^+]$ / $[H^+]$ ratios of about 100. The last one is the presence of balls showing that the fluids circulated in an active reverse fault zone. When these three criteria are satisfied and if the reverse structure is graphite-rich in the basement, uranium mineralized zones may be found along the reverse fault, preferably at intersections with other structures. Such fault intersections are favorable targets because they would have focused fluid circulation with possible fluid mixing. Reducing fluids coming from the basement along the reverse graphitic fault could have been mixed with uranium-bearing oxidizing basin fluids focused along the crosscutting structures, inducing uranium precipitation.

Acknowledgements

COGEMA and COGEMA Resources Inc are greatly acknowledged for their financial and technical support. M. Cathelineau provided valuable discussion about illite geothermometry. T. Lhomme is thanked for her assistance with Raman spectroscopy. We also thank S. Barda, F. Diot and J. Ghanbaja for technical assistance with electron microprobe determination and TEM. The manuscript benefited from discussions with L. Hecht and J. Sausse, and from reviews by P. Bruneton and J. Mondy. K. Weathley is gratefully thanked for improving the quality of the English.

References

Ababou, R., 1991. Approaches to large scale unsaturated flow in heterogeneous stratified and fractured geologic media. Section 4.2: Hydraulic properties of saturated fractured media. - Report NUREG/CR-5743, U.S. Nuclear Regulatory Commission, Washington D.C.

Armstrong, R.L., Ramaekers, P., 1985. Sr isotopic study of Helikian sediment and diabase dikes in the Athabasca Basin, northern Saskatchewan. Canadian Journal of Earth Sciences, 22, 399-407.

Augustithis, S.S., Ottemann, J., 1966. On diffusion rings and sphaeroidal weathering. Chemical Geology, 1, 201-209.

Augustithis, S.S., Mposkos, E., Vgenopoulos, A., 1980. Leaching of bauxites. "Traveaux" ICSOBA. Zagreb, 11, 334-345.

Baudemont, D., Pacquet, A., 1996. The Sue D and E uranium deposits, Northern Saskatchewan: evidence for structurally controlled fluid circulation in the Athabasca Basin. MinExpo'96 Symposium, Advances in Saskatchewan Geology and Mineral Exploration, pp. 85-94.

Baudemont, D., Piquard, J.P., Ey, F., Zimmerman, J. 1993. The Sue Uranium Deposits, Saskatchewan, Canada. Exploration and Mining Geology, 2, 179-202.

Cathelineau, M., Izquierdo, G., 1988. Temperature – composition relationships of authigenic micaceous minerals in the Los Azufres geothermal system. Contributions to Mineralogy and Petrology, 100, 418-428.

Clark, A.H., 1990. The slump breccias of the Toquepala porphyry Cu-(Mo) deposit, Peru: Implications for fragment rounding in hydrothermal breccias. Economic Geology, 85, 1677-1685.

Clauer, N., Ey, F., Gauthier-Lafaye, F.,1985. K-Ar dating of different rock types from the Cluff Lake uranium ore deposits (Saskatchewan-Canada). In: R. Lainé, D. Alonso and M. Svab (Editors), The Carswell structure uranium deposits, Saskatchewan. Geological Association of Canada Special Paper 29, pp. 47-54.

Cox, S.F., 1995. Faulting processes at high fluid pressures: an example of fault valve behavior from the Wattle Gully Fault, Victoria, Australia. Journal of Geophysical Research, 100, 12841-12859.

Cox, S.F., Etheridge, M.A., 1989. Coupled grain-scale dilatancy and mass transfer during deformation at high fluid pressures: examples from Mount Lyell, Tasmania. Journal of Structural Geology, 11, 147-162.

Cox, S.F., Knackstedt, M.A., Braun, J., 2000. Principles of structural control on permeability and fluid flow in hydrothermal systems. Reviews in Economic Geology. In press.

Etheridge, M.A., 2000. Regional to local structural controls on hydrothermal mineralisation – Practical tools for finding, delineating and mining ore deposits. GeoCanada2000, The Millennium Geoscience Summit, GAC-MAC joint annual meeting: Calgary, abstract 1260 (Conference CD).

Ey, F., Gauthier-Lafaye, F., Lillié, F., Weber, F., 1985. An uranium unconformity deposit: the geological setting of the D orebody (Saskatchewan-Canada). In: R. Lainé, D. Alonso and M. Svab (Editors), The Carswell structure uranium deposits, Saskatchewan. Geological Association of Canada Special Paper 29, pp. 121-138.

Fayek, M., Kyser, T.K., 1997. Characterization of multiple fluid-flow events and Rare-Earth-Element mobility associated with formation of unconformity-type uranium deposits in the Athabasca Basin, Saskatchewan. The Canadian Mineralogist, 35, 627-658.

Fournier, R.O., 1983. A method of calculating quartz solubilities in aqueous sodium chloride solutions. Geochimica et Cosmochimica Acta., 47, 579-586.

Fritz, B., 1981. Etude thermodynamique et modélisation des réactions hydrothermales et diagénétiques. Ph.D. Thesis, Université Louis Pasteur, Strasbourg.

Fyfe, W.S., Kerrich, R., 1985. Fluids and thrusting. Chemical Geology, 49, 353-362.

Gandhi, S.S., 1995. An overview of the exploration history and genesis of Proterozoic uranium deposits in the Canadian Shield. Exploration and Research for Atomic Minerals, Special issue: first-order uranium exploration target selection in the Proterozoic of India, 8, 1-47.

Goddard, J.V., Evans, J.P., 1995. Chemical changes and fluid-rock interactions in faults of crystalline thrust sheets, northwestern Wyoming, U.S.A. Journal of Structural Geology, 17, 533-547.

Govindaraju, K., Mevelle, G., 1987. Fully automated dissolution and separation methods for inductively coupled plasma emission spectrometry rock analysis. Journal of Analytic and Atomic Spectroscopy, 2, 615-621.

Grant, J.A., 1986. The isocon diagram, a simple solution to Gresens' equation for metasomatic alteration. Economic Geology, 81, 1976-1982.

Gresens, R.L., 1967. Composition-volume relationships of metasomatism. Chemical Geology, 2, 47-65.

Gross, M.R., Bahat, D., Becker, A., 1997. Relations between jointing and faulting based on fracture-spacing ratios and fault-slip profiles: a new method to estimate strain in layered rocks. Geology, 25, 887-890.

Halter, G., 1988. Zonalités des altérations dans l'environnement des gisements d'uranium associés à la discordance du Protérozoïque Moyen (Saskatchewan, Canada). Ph.D. Thesis, Université Louis Pasteur, Strasbourg.

Halter, G., Pagel, M., Sheppard, S.M.F., Weber, F., Clauer, N., 1988. Rétromorphose, paléoaltération, diagenèse et hydrothermalisme de l'encaissant des gisements uranifères dans la structure de Carswell (Saskatchewan-Canada). In: Gisements Métallifères dans leur Contexte Géologique, Document du BRGM, 158, 1, pp. 365-388.

Hecht, L., Cuney, M., 2000a. Mechanism of uranium mobilization in the Athabasca basin and basement by hydrothermal and/or diagenetic fluids. GeoCanada2000, The Millennium Geoscience Summit, GAC-MAC joint annual meeting: Calgary, abstract 191 (Conference CD).

Hecht, L., Cuney, M., 2000b. Hydrothermal alteration of monazite in the Precambrian crystalline basement of the Athabasca Basin (Saskatchewan, Canada): implications for the formation of unconformity-related uranium deposits. Mineralium Deposita, 35, 791-795.

Hickman, S., Sibson, R., Bruhn, R., 1995. Introduction to special section: mechanical involvement of fluids in faulting. Journal of Geophysical Research, 100, 12831-12840.

Hoeve, J., Quirt, D., 1984. Mineralization and host rock alteration in relation to clay mineral diagenesis and evolution of the middle-Proterozoic Athabasca Basin, northern Saskatchewan, Canada. Saskatchewan Research Council Technical Report no. 187.

Hoeve, J., Sibbald, T.I.I., Ramaekers, P., Lewry, J.F., 1980. Athabasca Basin unconformity-type uranium deposits: a special class of sandstone-type deposits? In: S. Ferguson and A. Goleby (Editors), Uranium in the Pine Creek Geosyncline. IAEA, Vienna, pp. 575-594.

Hoeve, J., Rawsthorn, K., Quirt, D., 1981. Uranium Metallogenetic Studies: Clay Mineral Stratigraphy and Diagenesis in the Athabasca Group. Saskatchewan Research Council Publication 22, pp. 76-89.

Iida, Y., 1993. Alteration and ore-forming processes of unconformity-related uranium deposits. Resource Geology Special Issue, 15, 299-308.

Jébrak, M., 1992. Les textures intra-filoniennes, marqueurs des conditions hydrauliques et tectoniques. Chroniques de la Recherche Minière, 506, 25-35.

Jébrak, M., 1997. Hydrothermal breccias in vein-type ore deposits: A review of mechanisms, morphology and size distribution. Ore Geology Reviews, 306, 1-24.

Kisters, A.F.M., Kolb, J., Meyer, F.M., Hoernes, S., 2000. Hydrologic segmentation of high-temperature shear zones: structural, geochemical and isotopic evidence from auriferous mylonites of the Renco mine, Zimbabwe. Journal of Structural Geology, 22, 811-829.

Knipe, R.J., 1993. The influence of Fault Zone Processes and Diagenesis on Fluid Flow. In: A.D. Horbury and A.G. Robinson (Editors), Diagenesis and Basin Development. AAPG, Studies in Geology, 36, pp. 135-148.

Kotzer, T.G., Kyser, T.K., 1995. Petrogenesis of the Proterozoic Athabasca Basin, northern Saskatchewan, Canada, and its relation to diagenesis, hydrothermal uranium mineralization and paleohydrogeology. Chemical Geology, 120, 45-89.

Kotzer, T.G., Kyser, T.K., Irving, E., 1992. Paleomagnetism and the evolution of fluids in the Proterozoic Athabasca Basin, northern Saskatchewan, Canada. Canadian Journal of Earth Sciences, 29, 1474-1491.

Lainé, R., 1985. The Carswell uranium deposits - An example of not so unique unconformity-related uranium mineralization. In: R. Lainé, D. Alonso and M. Svab (Editors), The Carswell structure uranium deposits, Saskatchewan, Geological Association of Canada Special Paper 29. pp. 225-230.

Laznicka, P., 1988. Breccias and coarse fragmentites. Developments in Economic Geology, 25. Elsevier, Amsterdam.

Laznicka, P., 1989. Breccias and ores. Part 1: history, organization and petrography of breccias. Ore Geology Reviews, 4, 315-344.

Lorilleux, G., Cuney, M., Jébrak, M., Mondy, J., 2000. A new approach of unconformity-type uranium metallogenesis from a structural breccia study (Northern Saskatchewan, Canada). GeoCanada2000, The Millennium Geoscience Summit, GAC-MAC joint annual meeting: Calgary, abstract 232 (Conference CD).

Marrett, R., Peacock, D.C.P., 1999. Strain and stress. Journal of Structural Geology, 21, 1057-1063.

Narr, W., Suppe, J., 1991. Joint spacing in sedimentary rocks. Journal of Structural Geology, 13, 1037-1048.

O'Hara, K., Blackburn, W.H., 1989. Volume-loss model for trace-element enrichments in mylonites. Geology, 17, 524-527.

Pagel, M., 1975. Détermination des conditions physico-chimiques de la silicification diagénétique des grès Athabasca (Canada) au moyen des inclusions fluides. Compte-rendu de l'Académie des Sciences 280, série D, 2301-2304.

Passchier, C.W., Trouw, R.A.J., 1996. Microtectonics. Springer-Verlag, Berlin, Heidelberg.

Percival, J.B., 1990. Clay mineralogy, geochemistry and partitioning of uranium within the alteration halo of the Cigar Lake uranium deposit, Saskatchewan, Canada. PhD Thesis, Carleton University.

Percival, J.B., Bell, K., Torrance, J.K., 1993. Clay mineralogy and isotope geochemistry of the alteration halo at the Cigar Lake uranium deposit. Canadian Journal of Earth Sciences, 30, 689-704.

Phillips, W.J., 1986. Hydraulic fracturing effects in the formation of mineral deposits. Institution of Mining and Metallurgy Transactions, section B: Applied Earth Science 95, B17-B24.

Quirt, D., Kotzer, T., Kyser, T.K., 1991. Tourmaline, phosphate minerals, zircon, and pitchblende in the Athabasca Group: Maw Zone and McArthur River areas, Saskatchewan. In: Summary of Investigations 1991, Saskatchewan Geological Survey, Saskatchewan Energy and Mines, Miscellaneous Report 91-4.

Ramaekers, P., 1981. Hudsonian and Helikian basins of the Athabasca region, Northern Saskatchewan. Geological Survey of Canada Paper 81, pp. 219-233.

Ramaekers, P., 1990. Geology of the Athabasca Group (Helikian) in Northern Saskatchewan. Saskatchewan Energy and Mines, Saskatchewan Geological Survey, report 195.

Ramaekers, P., Dunn, C.D., 1977. Geology and geochemistry of the eastern margin of the Athabasca Basin. Saskatchewan Geological Society Special Publication 3, pp. 297-322.

Reeve, J.S., Cross, K.C., Smith, R.N., Oreskes, N., 1990. Olympic Dam. Copper-Uranium-Gold-Silver deposit. In: E.E. Hughes (Editor), Geology of the mineral deposits of Australia and Papua New Guinea. The Australasian Institute of Mining and Metallurgy, Melbourne, pp. 1009-1035.

Rice, J.R., 1992. Fault Stress States, Pore Pressure Distributions, and the Weakness of the San Andreas Fault. In: B. Evans and T.-F. Wong (Editors), Fault Mechanics and Transport Properties in rocks, Academic Press, pp. 475-503.

Rives, T., Razack, M., Petit, J.-P., Rawnsley, K.D., 1992. Joint spacing: analogue and numerical simulations. Journal of Structural Geology, 14, 925-937.

Rouleau, A., Gale, J.E., 1985. Statistical characterization of the fracture system in the Stripa Granite, Sweden. International Journal of Rock Mechanics and Mining Sciences, 22, 353-367.

Salvi, S., Pokrovski, G.S., Schott, J., 1998. Experimental investigation of aluminum-silica aqueous complexing at 300°C. Chemical Geology, 151, 51-67.

Sawkins, F.J., 1969. Chemical brecciation, an unrecognized mechanism for breccia formation? Economic Geology, 64, 613-617.

Scholz, C.H., 1990. The Mechanics of Earthquakes and Faulting. Cambridge University Press, New York.

Shahabpour, J., 1998. Liesegang blocks from sandstone beds of the Hodjedk Formation, Kerman, Iran. Geomorphology, 22, 93-106.

Sibson, R.H., 1986. Brecciation processes in fault zones: inferences from Earthquake rupturing. Pure and Applied Geophysics, 124, 161-175.

Sibson, R.H., Robert, F., Poulsen, K.H., 1988. High-angle reverse faults, fluid-pressure cycling, and mesothermal gold-quartz deposits. Geology, 16, 551-555.

Sillitoe, R.H., 1985. Ore-related breccias in volcanoplutonic arcs. Economic Geology, 80, 1467-1514.

Sinha, A.K., Hewitt, D.A., Rimstidt, J.D., 1986. Fluid interaction and element mobility in the development of ultramyonites. Geology, 14, 883-886.

Snow, D.T., 1969. Anisotropic permeability of fractured media. Water Resources Research, 5, 1273-1289.

Tenthorey, E., Scholz, C.H., Aharonov, E., Léger, A., 1998. Precipitation sealing and diagenesis. 1. Experimental results. Journal of Geophysical Research, 103, 23951-23967.

Tester, J.W., Worley, W.G., Robinson, B.A., Grigsby, C.O., Feerer, J.L., 1994. Correlating quartz dissolution kinetics in pure water from 25 to 625°C. Geochimica et Cosmochimica Acta, 58, 2407-2420.

Vigneresse, J.L., Cannat, M., 1987. Mesures de paramètres physiques dans le sondage d'Echassières (vitesse sismique, porosité, densité). Mémoire Géologie profonde de la France , tome 1. Géologie de la France, no. 2-3, pp. 145-148.

IV. Etude Structurale, Texturale, Mineralogique et Geochimique Comparee des Breches de la Maw Zone, de Shea Creek et de Sue : Implications pour la Genese des Mineralisation Uranifere

IV. Etude Structurale, Texturale, Mineralogique et Geochimique Comparee des Breches de la Maw Zone, de Shea Creek et de Sue : Implications Pour la Genese des Mineralisations Uraniferes

(a)

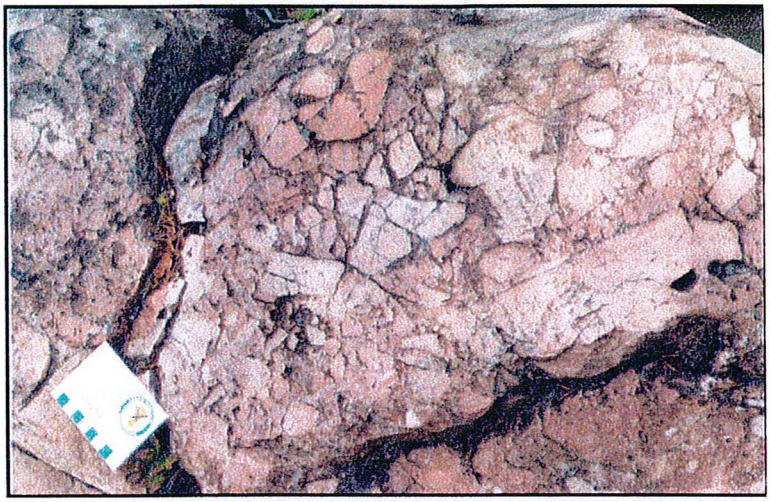

(b)

(c)

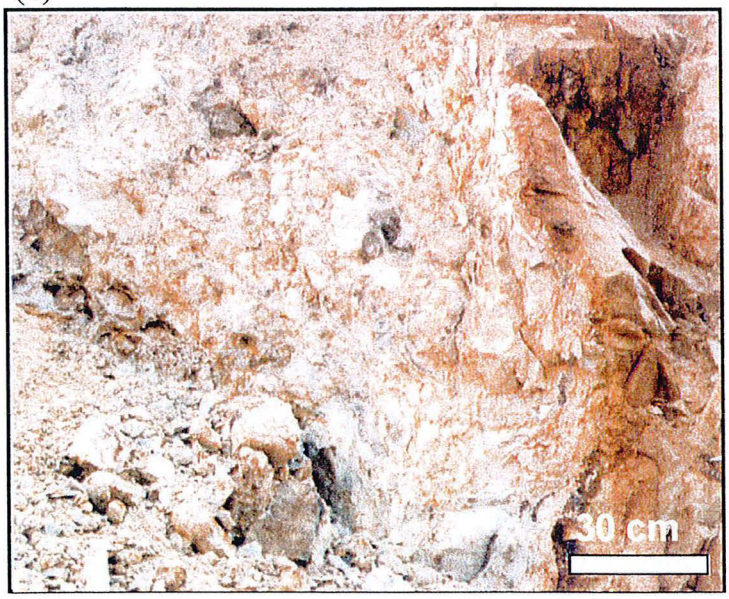

Figure IV-1 – (a) Affleurement de brèche d'effondrement dans la zone de Maw. (b) Brèche de dissolution-effondrement dans une carotte de forage à Shea Creek.(c)Affleurement de zone à boules dans la MCO de Sue C.

Introduction

La formation des zones à boules, étudiée dans la MCO de Sue C, a été initiée par une fracturation des grès liée à une réactivation tectonique régionale. La circulation d'énormes quantité de fluides sous-saturés en silice dans les fractures ainsi créées a provoqué la dissolution massive du quartz et le remplacement de la dickite diagénétique par de l'illite hydrothermale (Fig. IV-1). La phase de fracturation initiale ainsi que le développement des brèches par dissolution sont des processus de même nature que ceux observés à Shea Creek (Fig. IV-1). Par contre, l'action simultanée de la déformation tectonique en contraction et de la dissolution du quartz est caractéristique des zones à boules.

L'étude de la zone de Maw vient en complément des travaux réalisés à Shea Creek et dans la MCO de Sue C. En effet, la zone de Maw montre de spectaculaires affleurements de brèches encaissant une minéralisation à Y et terres rares lourdes à 250 mètres au-dessus d'une minéralisation uranifère à la discordance (Fig. IV-1).

Comment ces différents corps de brèches peuvent-ils être réunis dans un modèle synthétique de formation des brèches ? Le but de cette partie est de montrer, d'une part comment les brèches de Shea Creek, de Sue et de la zone de Maw peuvent s'intégrer dans un modèle synthétique de genèse associées aux gisements d'uranium, et d'autre part quel est le rôle des brèches dans le piégeage des minéralisations uranifères.

Les relations entre les différents types de brèches et les structures tectoniques, les textures de brèches, les successions paragénétiques minérales et les bilans de masse sont présentés pour les trois zones d'étude. A Shea Creek, la succession paragénétique a fait l'objet d'un calage relatif dans le temps grâce aux calculs d'âges chimiques. La température de formation des brèches à Fe-chlorite a été estimée par le géothermomètre de Cathelineau et Nieva (1985). Les rapports fluide/roche cumulés ont été évalués. La modélisation tridimensionnelle des corps de brèches à Shea Creek avec le logiciel gOcad (voir annexe II) a permis d'obtenir précisément leur volume et ainsi de pouvoir calculer le volume minimum de fluide nécessaire pour former les brèches. Les temps de formation des brèches et de dépôt des minéralisations uranifères ont également été estimés. La géométrie des corps de brèches modélisée en 3 dimensions et celle des brèches de Sue et de la zone de Maw ont été associées dans un schéma synthétique d'organisation des brèches par rapport aux failles et à la minéralisation. Parallèlement à ce modèle géométrique, un modèle génétique de formation des brèches et de la minéralisation uranifère est proposé. Les brèches de la zone de Maw et de Sue permettent de préciser le modèle établi à Shea Creek qui constitue le cœur de l'étude du fait de leur position différente par rapport aux failles et à la discordance et de leur différent degré de maturité.

Les modèles existant dans la littérature sont essentiellement déduits d'études isotopiques, d'inclusions fluides ou de modélisation numérique. L'originalité de cette approche réside dans la quantification des processus physico-chimiques de dissolution du quartz, de piégeage de la minéralisation uranifère et d'effondrement gravitaire.

Le premier article de synthèse est une version longue intégrant tous les éléments de réflexion destinée à Economic Geology. Le deuxième article de synthèse soumis à Geology est également dans une version longue.

ARTICLE 3 :

Hydrothermal breccias associated with unconformity-type uranium mineralizations in the Athabasca Basin: implications for fluid flow and mineralization (Canada)

G. Lorilleux[a,*], M. Cuney[a], M. Jébrak[b], J. Mondy[c], P. Bruneton[d]

[a] CREGU-UMR G2R 7566, Université Henri Poincaré, BP 23, 54 501 Vandoeuvre-les-Nancy, France

[b] UQAM-DSTA , CP 8888, Montréal (QUE) H3C 3P8 Canada

[c] COGEMA, 2-4 rue Paul Dautier, BP 4, 78 141 Vélizy-Villacoublay cedex, France

[d] COGEMA GST, 1 avenue du Brugeaud, 87 250 Bessines-sur-Gartempe, France

Destiné à Economic Geology
(version longue)

* *Corresponding author.*
E-mail address: guillaume.lorilleux@g2r.uhp-nancy.fr

Résumé

Les gisements d'uranium du Bassin Athabasca sont fréquemment encaissés par des corps de brèches dans les grès. Les brèches associées à la minéralisation en Y et terres rares de la zone de Maw à 250 m au-dessus de la discordance et aux minéralisations uranifères situées juste au-dessus de la discordance à Shea Creek et à Sue ont été étudiées. L'étude structurale, texturale, minéralogique et géochimique des brèches des 3 zones permet de proposer un modèle de formation des brèches associé à la genèse des gisements.

La géométrie des corps de brèches est contrôlée par des failles généralement inverses, riches en graphite dans le socle et recoupant la discordance. Les brèches se sont développées sur plus de 1 Ga au cours de plusieurs phases d'activité tectonique et de dépôt et/ou remobilisation d'uranium entre 1,52 et 1,25 Ga et vers 900 et 350 Ma. Le principal épisode de formation des brèches est contemporain de la phase majeure de minéralisation primaire à haute teneur et peut être décrit en 3 étapes.

La première étape correspond à la formation de brèches immatures provoquée par des réactivations de failles. Elle est caractérisée par de la fracturation hydraulique étendue dans les zones de silicification précoce de la zone de terminaison des failles (dans la zone de Maw) ou de la zone d'endommagement des failles (à Shea Creek) et par de la fracturation tectonique dans le cœur des failles dans les grès peu ou pas silicifiés (à Sue).

La deuxième étape correspond au développement de la dissolution du quartz par migration verticale d'un fluide de socle sous-saturé en silice dans les grès fracturés. Cette phase de dissolution s'accompagne d'une augmentation de maturité exprimée par une augmentation du pourcentage volumique de matrice et de la complexité de morphologies de fragments quantifiée par analyse fractale. Le fluide circulant vers le haut se rééquilibra progressivement avec le quartz générant ainsi une décroissance de l'intensité de dissolution du quartz depuis la discordance à Sue et à Shea Creek à la zone de Maw. Les rapports fluide/roche minimaux sont de l'ordre de 3 000 dans la zone de Maw et atteignent 38 000 dans le cœur des failles près de la discordance représenté par les zones à boules de Sue. Les volumes minimaux de fluide de socle ayant circulés dans les brèches sont de l'ordre de 1 km^3. La dravite dans la zone de Maw, l'illite, la sudoite et la dravite à Shea Creek et l'illite à Sue ont précipité en même temps comme ciment des brèches pendant la dissolution du quartz. Les brèches sont enrichies en U, V, Mg, B, Al, K, Bi, Ni, Co, Mo, As, S, W, Zn, Y et terres rares conformément aux altérations à sudoite, dravite et illite et avec les minéralisations polymétalliques des grès.

La troisième étape correspond à des effondrements gravitaires des systèmes de brèche induits par les cavités créées par la dissolution du quartz. Les pertes de volume atteignant 90 % à la discordance expriment des effondrements majeurs qui se sont propagés localement jusqu'à plus de 250 m au-dessus de la discordance comme dans la zone de Maw conduisant ainsi au

développement de karsts dans les grès. Dans les zones à boules au cœur des failles, les pertes de volume résultent de la contraction tectonique contemporaine de la dissolution.

La dissolution du quartz dans les grès pourrait être une conséquence du développement d'une réaction d'illitisation hydrothermale des feldspaths dans le socle accompagnée de consommation de quartz avec log $[K^+]/[H^+] \sim 4$. Au début de l'illitisation, le fluide de socle, à une température supérieure à 250°C, était encore en équilibre avec le quartz et précipitait le quartz par refroidissement dans les grès à une température inférieure à 240°C, expliquant la silicification pervasive précoce. La dissolution totale du quartz aurait ensuite provoqué la sous-saturation du fluide de socle.

Le mélange du fluide réducteur de socle avec les fluides oxydants de bassin a provoqué la précipitation d'uranium par diminution de la fugacité en oxygène. La porosité élevée et les cavités créées par la dissolution intense du quartz à la discordance ont joué le rôle de piège pour le dépôt de l'uranium. La dissolution du quartz et la précipitation de l'uranium se développèrent en même temps sur plusieurs millions d'années. La perméabilité élevée et constante nécessaire au maintien d'un front d'oxydo-réduction stationnaire afin de permettre le dépôt de la minéralisation à haute teneur fut fournie par la dissolution du quartz dont le taux était supérieur à celui de précipitation d'argiles. Cependant, la reprécipitation de quartz au-dessus des brèches et les effondrements ou la contraction tectonique eurent tendance à faire décroître la perméabilité. Occasionnellement, des cycles de diminution de perméabilité, d'accroissement de pression de fluides et de réouvertures de failles inverses en valve sismique permirent de renouveler la perméabilité du système hydrothermal.

Les gisements d'uranium de type discordance dans les grès peuvent être classés en fonction du développement des brèches. Les gisements associés des corps de brèches étendus dans les grès sont associés à des silicifications précoces massives, a des altérations à chlorite sudoïtique magnésienne et à dravite et à de la dissolution de quartz limitée dans l'espace autour de fractures. Les gisements sans brèches dans les grès sont associés à une très faible silicification précoce, à des zones d'illite massive dues à la dissolution pervasive du grès et à des halos d'altérations à illite très étendus latéralement.

Abstract

Unconformity-type uranium deposits in the Athabasca Basin are commonly hosted and surrounded by breccia bodies in sandstones. The breccias associated with the Maw Zone Y-REE mineralization located at 250 m above the unconformity and with the Shea Creek and Sue U mineralizations located just above the unconformity were studied. Structural, textural, mineralogical and geochemical studies of the breccias in the 3 zones allow to propose a model of breccia formation associated with uranium deposition.

The geometry of the breccia bodies is controlled by faults cross-cutting the unconformity and generally reverse and graphite-rich in the basement. Breccia formation occurred over more than 1 Ga during several phases of tectonic activity and uranium mineralization deposition and/or remobilization between 1.52 and 1.25 Ga and at about 900 and 350 Ma. The main stage of breccia formation is coeval with the main primary uranium mineralization event and can be described in 3 steps of maturity evolution.

The first step of immature breccia formation was triggered by fault reactivation and is characterized by widespread hydraulic fracturing in the early silicified damage zone of faults (at Shea Creek) or in fault termination zones (at the Maw Zone) and by spatially limited tectonic fracturing in the core of faults in non- to weakly silicified sandstones (at Sue).

The second step corresponds to the development of quartz dissolution by vertical migration of silica undersaturated basement fluids in the fractured sandstones. It is accompanied with maturity increase expressed by an increase of matrix volumic percentage and of the complexity of fragment shapes quantified by fractal analysis. Quartz dissolution intensity decreased upward from the unconformity at Sue and Shea Creek to the Maw Zone as fluids flowing upward progressively re-equilibrated with quartz. Calculated fluid/rock ratios are about 3,000 at the Maw Zone and increase up to 38,000 in the core of faults at the unconformity represented by the Sue "zones à boules". The minimum volume of fluids that have circulated in the breccias is about 1 km^3. Dravite at the Maw Zone, illite, sudoitic chlorite and dravite at Shea Creek and illite at Sue precipitated simultaneously as breccia cement during the quartz dissolution process. The fluids brought U, V, Mg, B, Al, K, Bi, Ni, Co, Mo, As, S, W, Zn, Y and REE to the breccias, in accordance with the sudoite, dravite and illite alterations and with the polymetallic sandstone-hosted mineralizations.

The third step corresponds to collapse of the breccia system due to creation of important cavities by quartz removal. Volume losses up to 90 % at the unconformity indicate major collapse phenomenons that propagated locally up to more than 250 m above the unconformity like at the Maw Zone leading to the development of karsts in sandstones. In the core of faults like in the Sue "zones à boules", volume loss resulted from tectonic contraction rather than collapse.

Quartz dissolution in sandstones might be due to the development of hydrothermal illitization in the basement that was accompanied with quartz consumption with log $[K^+]/[H^+] \sim 4$. At the onset of the illitization, the basement fluids, at a temperature above 250°C, were still in equilibrium with quartz and precipitated quartz by cooling in the sandstone at a temperature less than 240°C, explaining the early pervasive silicification. When the quartz in the basement was totally consumed by illitization, the basement fluids became undersaturated and began to dissolve quartz in sandstones.

Reducing basement fluids mixed with oxidizing and uranium-bearing basin fluids as they penetrated into the sandstones inducing uranium precipitation. The high porosity created by the intense quartz dissolution at the unconformity formed the trap for uranium deposition. Quartz dissolution and uranium deposition occurred simultaneously over several millions years. The sustainable permeability required to maintain a stationary redox front to allow the deposition of high grade uranium mineralization was provided by quartz dissolution that acted as a positive feedback loop. However, quartz reprecipitation above the breccias and collapse or tectonic contraction tended to decrease the permeability. Periodically, cycles of permeability decrease, fluid pressure increase and subsequent fault re-opening probably occurred by fault-valve behavior in order to renew the permeability of the system.

Sandstone-hosted unconformity-type deposits can be classified based on the occurrence of breccias. Deposits associated with extended breccia bodies in sandstones are associated with early massive silicification, sudoite and dravite alterations and spatially limited quartz dissolution. Deposits without breccias in sandstones are associated with only minor silicification, with massive illite alteration due to pervasive quartz dissolution and also with extensive lateral illite alteration haloes.

1. Introduction

Unconformity-type uranium deposits are located close to the unconformity between an Archean to Lower Proterozoic metamorphic and granitic basement and a Middle Proterozoic sandstone cover. They have been found in Canada in the Athabasca and Thelon Basins and in Australia in the McArthur Basin. With large tonnages and very high grades - 219,000 tons at 14% U_3O_8 at McArthur River (Canada) - they are the most economic uranium deposits in the world. The Athabasca Basin located in northern Saskatchewan (Fig. 1) is the premier host for unconformity-type deposits and has an estimated resource in excess of 373,000 tons of U at a cost less than 40 $ / kg U (Thomas et al., 1998).

The most accepted metallogenetic model of unconformity-type uranium mineralizations is diagenetic-hydrothermal. The first complete diagenetic-hydrothermal model has been presented by Hoeve and Sibbald (1976, 1978). They proposed that the unconformity-type uranium mineralizations resulted from the interaction at the unconformity of methane-bearing reducing solutions circulating upward along basement-rooted faults with 200°C uranium-bearing oxidizing basin fluids. The methane would have been generated by reaction of the basin fluids with faulted graphite-rich basement rocks with which the deposits are commonly associated (Hoeve and Sibbald, 1978; Thomas et al., 1998). The participation of diagenetic basin fluids in the mineralization process is widely accepted as it is demonstrated by both isotopic and fluid inclusions studies (Pagel, 1975b; 1977; Pagel and Jaffrezic, 1977; Kotzer and Kyser, 1995). However, the origin of basement fluids is still controversed. Kyser et al. (1989), using δD values of chlorites and illites of mineralized gneisses at Key Lake (Wilson and Kyser, 1987), proposed that the basement fluids were not derived from the basin fluids but were rather deeply sourced in the basement. Fayek and Kyser (1997) have proposed two variants of the diagenetic-hydrothermal model, one in which basin fluids interact with basement fluids at the unconformity and another in which basin fluids interact directly with basement rocks, explaining respectively the formation of uranium deposits at the unconformity or in the sandstone, and in the basement. The bulk of the uranium mineralization is hosted by faults within breccias, veins and impregnations (Hoeve and Sibbald, 1978; Lorilleux et al., 2000).

Basement-hosted mineralizations are generally monometallic with uranium oxides and trace amounts of sulfides and arsenides. They are referred to as simple-type deposits (Fayek and Kyser, 1997) and typically occur within 50 m and locally up to 400 m below the unconformity (Thomas et al., 1998). Mineralizations located at the unconformity or in the sandstone, referred as complex-type, are polymetallic because Ni-Co-As-Fe-Cu-Pb sulfides and arsenides, V, Zn, Au, Pt-group elements, Bi and Se are associated with uranium oxides (Hoeve and Sibbald, 1978; Fayek and Kyser, 1997). They are typically located within 25-50 m

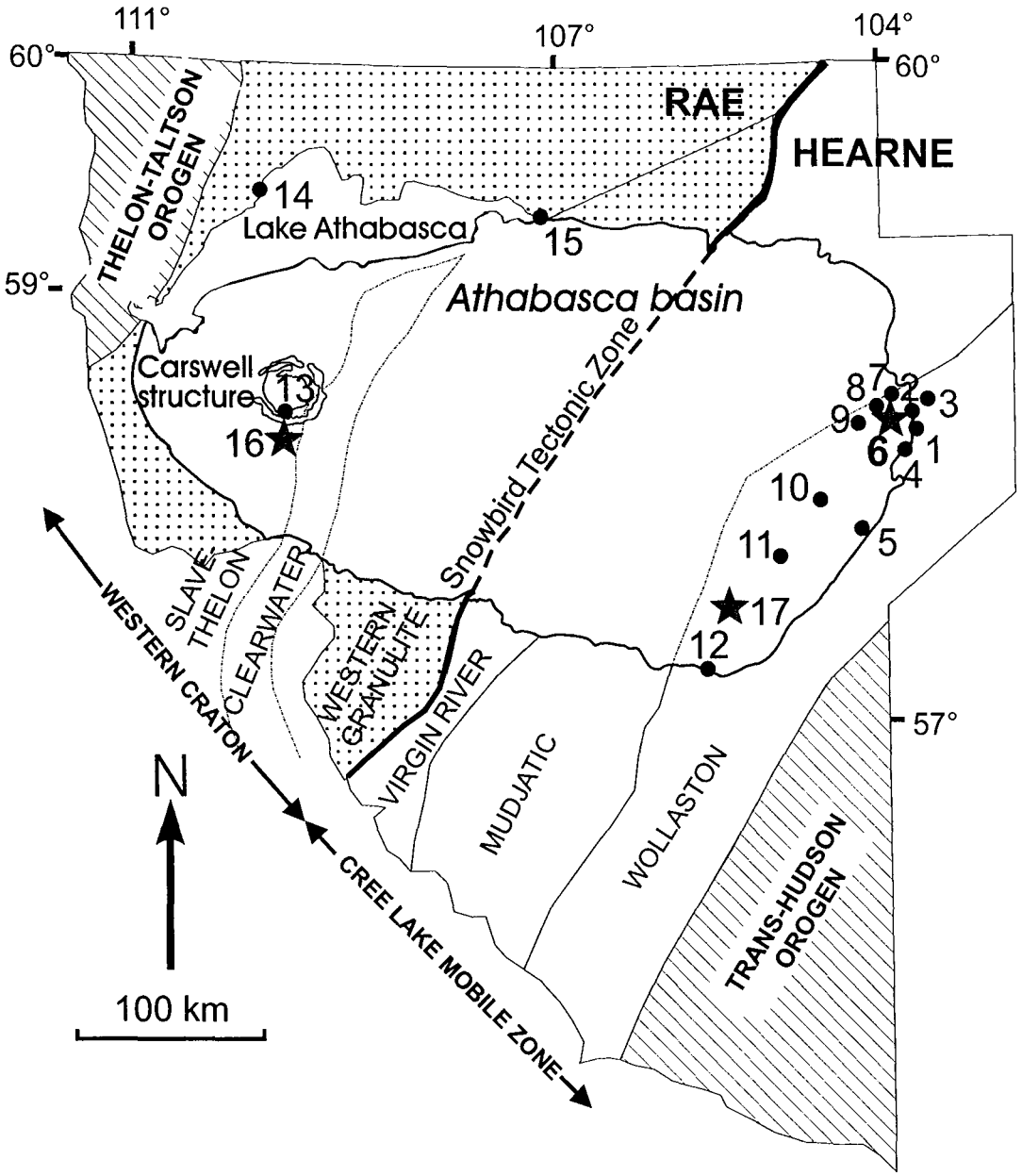

Figure 1 – Crustal units and lithostructural domains of the sub-Athabasca basement and main uranium deposits in the Athabasca Basin (modified from Ruzicka, 1986). The three stars indicate the location of the Maw Zone in the southeast, of the Sue deposits in the east and of the Shea Creek exploration zone in the west. Deposits and mineralizations: 1 = Rabbit Lake, 2 = Collins Bay, 3 = Eagle Point, 4 = Horseshoe and Raven, 5 = West Bear, 6 = McClean and Sue, 7 = JEB, 8 = Dawn Lake, 9 = Midwest, 10 = Cigar Lake, 11 = McArthur River, 12 = Key Lake, 13 = Cluff Lake, 14 = Maurice Bay, 15 = Fond-du-Lac, 16 = Shea Creek, 17 = Maw Zone.

of the basement-sandstone unconformity. Perched mineralization may be found up to 250 m (Cigar Lake) above the unconformity in the sandstone (Fouques et al., 1986).

The main primary unconformity-type uranium mineralization event in the Athabasca Basin is comprised between 1.52 and 1.25 Ga after K/Ar and U/Pb datations mainly (Hoeve et al., 1980; Hoeve and Quirt, 1984; Lainé, 1985; McGill et al., 1993). A second uranium mineralization stage has been documented around 1.1 Ga (Lainé, 1985). Two further mineralization-remobilization events between 0.9 and 0.8 Ga and between 0.5 and 0.2 Ga are given by Hoeve and Quirt (1984) and Lainé (1985).

Several authors have emphasized the major influence of the hydrodynamic controls on the deposit formation. Hoeve and Quirt (1984) and Raffensperger and Garven (1995a) have proposed a convective mechanism of fluid circulation in the sandstone. Fluid mixing would have occurred during periodic basement fluid injections in sandstones due to reactivation of graphite-rich basement rooted faults. Kotzer and Kyser (1995) proposed the existence of extensive lateral movements of the basinal fluids involved in the mineralization.

Unconformity-type uranium mineralizations have been described as being associated with extensive alteration haloes in the sandstone up to 400 m wide at the base of the sandstone, up to 500 m thick and up to more than several thousand meters along strike (Thomas et al., 1998). Such extended alteration haloes are consistent with convective cells. However, the alteration haloe in the sandstone at McArthur River, which is the largest deposit of the Athabasca basin, is more restricted around faults due to a strong silicification of the sandstone (McGill et al., 1993). Two types of sandstone-hosted alteration haloes have been distinguished around unconformity-type uranium deposits. The first type has been encountered in the northern part of the Athabasca basin and is characterized by desilicification and illitization. The second type is dominantly represented in the southern part of the basin and corresponds to dravitization, chloritization and kaolinization (Matthews et al., 1997).

Unconformity-type uranium mineralizations are commonly hosted and surrounded by breccias in the sandstone within a few tens of meters. Such breccias have been observed around the recently discovered Shea Creek mineralization (Lorilleux et al., 2000; Rippert, 2000; see part II), at Cluff D and Claude deposits (Ey et al., 1985) (not taking into account impact-related breccias), at Sue (see part III), at Rabbit Lake and at McArthur River. They show a great variety of geometries, textures and mineralogy, depending of the type of mineralization. They are present in the two types of alteration haloes but are more developed in the southern type. Uranium-bearing breccias in the Athabasca Basin have been interpreted as being tectonic (Ey et al., 1985), hydraulic (Bruneton and Caumartin, 1985) and dissolution-collapse (Wallis et al., 1983 ; Lorilleux et al., 2000; see part III). However, their genetic relationship with the mineralization was not evaluated.

Three zones of study have been chosen in the Athabasca Basin (Fig. 1). The Maw Zone, located 30 km northeast of the Key Lake uranium deposits in the southeastern Athabasca Basin, is a breccia-hosted Y-REE mineralization located in the sandstone 200 m above an uranium enrichment zone located at the unconformity. It is one of the very rare natural breccia outcrop of the Basin. The Shea Creek uranium mineralizations, recently discovered (Rippert et al., 2000) and located in the west Athabasca Basin, south of the Cluff Lake mine site, show spectacular breccia development surrounding and hosting high-grade mineralization. The Sue C uranium deposit open pit is located in the eastern Athabasca Basin and displays good quality exposures of breccias associated with structures controlling the Sue A and B deposits.

The purpose of this paper is to understand the processes of formation of the trap for the uranium ore bodies and to constrain and quantify the evolution of the physical and chemical parameters controlling fluid circulation and uranium mineralization. The textural, mineralogical and geochemical evolution of the breccias is studied in this goal.

2. Methodology

The study of exposures in the Sue C open pit, core rocks in the Shea Creek exploration area and outcrops at the Maw Zone has allowed to describe and map the structures, the alterations and the breccias associated with the mineralizations. Sandstone-hosted breccias were studied because of their extensive development, and because of the simple textural and mineralogical characteristics of the Athabasca sandstone making the understanding of the breccia genesis easier than in the metamorphosed basement rocks.

At Shea Creek, the closely spaced drilling pattern allowed detailed mapping of structures and breccia bodies. The geometry of breccias of the south part of the Shea Creek exploration prospect has been represented using the three-dimensional modeling software gOcad (see annexe II). The model was constructed using the location of breccia zones in drill holes and the interpreted outline of breccia bodies in cross-sections. As the structural control of the breccias is well established (see part II), the surface of the breccia bodies between cross-sections was interpolated using fault direction as a guideline. The volume of the breccia bodies was calculated by an implemented gOcad function.

The breccia textures have been observed on macroscopic samples, in thin sections and with Scanning Electron Microscope (SEM Hitachi S-2500) in the three zones of study. Textural and chronological relationships between fragments and matrix were particularly characterized. Breccias have been classified using their degree of maturity that increases with matrix percentage. Most of the samples were taken close to, but outside of mineralized zones in order to get rid of complex, polyphase and strongly mature breccias. The study, when possible, of

weakly to moderatly mature monophased breccias allowed to understand the processes of fragmentation and the nature of the cement for each single breccia event.

At Shea Creek, detailed descriptions and drawings of sandstone breccias were realized both on whole and saw-split core rocks 45 mm in diameter. The variety of breccia types and their extensive development permitted to apply a statistical method of classification based on fractal analysis of fragment morphologies. This method allowed to quantify the intensity and type of corrosion processes (see part II).

SEM observations of fragments of unconsolidated breccias of the Shea Creek area were realized (see part II).

The ball-shaped breccia fragments found in the Sue C open pit were systematically measured. The distribution curve of the ball sizes has been plotted using Statistica software (see part III).

On Shea Creek samples, X-ray diffraction patterns were determined on the less than 2 micron fractions on oriented aggregates in the range of 35 to 3 angströms (see annexe IV). On randomly oriented powders, a range of 1.56 to 1.48 angströms was used in order to distinguish di- or/and trioctahedral structures of clay minerals. Acquisition of X-ray diffraction patterns for Shea Creek samples was performed by ERM (Etudes Recherches Matériaux) in Poitiers (France) on a Siemens Kristalloflex D501 diffractometer (radiation: Cu Kα) equipped with an X-ray fluorescence detector (Si(Li) diode) cooled by Peltier effect. The mineralogy of breccia samples at Sue was determined by X-ray diffraction (XRD) on whole-rock samples at the UQAM (Montréal, Canada) and by transmission electron microscope (TEM), coupled with X-ray analysis at the Université Henri Poincaré (Nancy, France) after agate mortar crushing (see annexe IV).

Raman microspectroscopy was used at the UMR G2R 7566 (Nancy, France) to determine the polytype of the kaolinite minerals in breccias of Sue and Shea Creek (see annexe IV).

Illite, chlorite and kaolinite chemical compositions of Sue and Shea Creek breccias were analyzed by electron microprobe (Cameca SX50, Université Henri Poincaré, Nancy, France) at 10 nA and at 15 kV with an average counting time of 9 seconds for the peak and 5 seconds for the background (see annexe IV). The standards used for the analysis of Na, Mg, Al, Si, Cl, K, Ca, Ti, V, Cr, Mn, Fe and Ni in clay minerals were respectively albite, olivine, albite, orthose, scapolite, orthose, wollastonite, $MnTiO_3$, pure vanadium, Cr_2O_3, $MnTiO_3$, hematite and NiO.

Uranium oxides and silicates were analyzed by electron microprobe at 10 nA and at 15 kV (see annexe IV). The standards used for the analysis of Si, S, Ca, Ti, Fe, As, Y, Ce, Gd, Yb, Pb, Th, U in uranium minerals were respectively orthose, FeAsS, wollastonite, $MnTiO_3$, hematite, AsGa, $Y_3Fe_5O_{12}$(Grenat), $CePO_4$, GdTiGe, $YbCo_2Si_2$, $PbCrO_4$, ThO_2 and UO_2. Chemical Th-U-total Pb isochron ages were determined using a formulae proposed by Suzuki and Adachi (1994).

Geochemical analysis of 10 major and 44 trace elements on 23 whole rock breccia samples were performed in the three study areas - by ICP-AES and ICP-MS at the CRPG (Nancy) following a procedure described by Govindaraju and Mevelle (1987). Density of dry samples have been determined using a picnometer with water (Vigneresse and Cannat, 1987). Mass balance calculations were resolved using the Grant method (Grant, 1986) which consists in a simple graphical solution of Gresens' equation (Gresens, 1967) (see annexe III). Al and Nb have been considered as immobile respectively in the Sue and Shea Creek zones whereas constant volume has been considered at the Maw Zone. Relative proportions of the main minerals constituting the breccias have been calculated by norm analysis in the three zones of study.

3. Geological setting

3.1. Geology of the basement

The Athabasca Basin lies within the southwest part of the Churchill Structural Province, between the Thelon-Taltson orogenic front to the west and the Trans-Hudson orogen to the east (Fig. 1). The Thelon-Taltson orogenic front is related to the collision and indentation of the western Rae Province by the Archean Slave province in an east-dipping subduction zone from 2.0 to 1.76 Ga (Hoffman, 1987; Ross and Eaton, 1997). It is expressed in the Athabasca Basin by ductile deformation between 2.0 and 1.9 Ga, followed by a younger, brittle event constrained to 1.84-1.76 Ga (Hoffman, 1987; Villeneuve et al., 1991). The Trans-Hudson orogen evolved from a west-dipping subduction zone with collision of the Superior province into the Hearne Province from 1.88 to 1.76 Ga (Chiarenzelli et al., 1998). This two coeval orogens were contemporaneous with a major crustal imbrication located southwest of the Athabasca Basin in the Alberta basement and referred to as the east Alberta orogen (1.85-1.78 Ga; Ross et al., 1995).

On the basis of lithologic, structural and metamorphic criteria, the sub-Athabasca basement has been divided in several crustal units, each of them being composed of several lithostructural domains (Lewry and Sibbald, 1980) (Fig. 1).

3.2. The Athabasca Basin

The Athabasca Basin formed during the Middle Proterozoic at about 1.7 Ga (Armstrong and Ramaekers, 1985; Kotzer et al., 1992) and is separated from the underlying basement by a major unconformity. It is composed of sub-basins oriented NE-SW and controlled by faults rooted in the basement. The basin is interpreted as having been filled by several stratigraphic

units, the Athabasca Group being the major unit located at the base (Ramaekers and Dunn, 1977). The Athabasca Group is composed of thick, unmetamorphosed and flat-lying sequences of fluviatile to marine quartzose sandstones deposited in a proximal shelf environment (Ramaekers, 1981). A maximum total thickness of 4 to 5 km of sediments in the basin has been proposed based on fluid inclusions and diagenetic clay assemblages studies (Pagel, 1975b; Hoeve et al., 1981; Halter, 1988).

The present thickness of the basin is about 70 m at Sue, 700 m at Shea Creek and 250 m at the Maw Zone. The sandstones hosting these three zones of study are all part of the Manitou Falls formation of the Athabasca Group. The Manitou Falls formation is subdivided into 4 members called MFa, MFb, MFc and MFd from bottom to top (Ramaekers, 1990). The MFb member which hosts the Sue A and B mineralizations consists of sandstones containing at least 2 % of clast-supported conglomerates found in beds 2 cm thick. The MFc member hosts the Shea Creek mineralization and breccias. It consists of sandstones containing conglomerates beds less than 2 cm thick and less than 1 % clay intraclast-rich layers. The MFd member hosts the Maw Zone Y and REE mineralization and breccias. It comprises relatively well-sorted quartz arenites containing greater than 1 % clay intraclast-rich layers. The MFb and MFc members are both medium- to very coarse-grained sandstone whereas the MFd member is fine- to coarse-grained sandstone. Heavy minerals layers, generally less than 1 mm thick, are common at the base of these two members. Their distribution shows great variability at the millimeter to decimeter scale. In non-mineralized zones, clay typically forms 0.5 to 15 % of the rock and averages around 5 % (Ramaekers, 1990).

Early syn-depositional tectonic movements have been evidenced by the presence of a fanglomerate unit, better called debris flow by Quirt (2000), at the base of the Athabasca sandstone. This debris flow unit has been observed at McArthur River and in the Sue C open pit.

The Athabasca sandstones have undergone a deep to anchizonal diagenesis characterized by quartz overgrowths, hematite, crandallite group minerals, anatase and dickite. Diagenetic 2M illite is developed in zones of peak diagenesis (Halter et al., 1988). Apatite and sudoite crystallizations are locally present. Temperatures of early diagenetic fluids were estimated by fluid inclusions studies in quartz overgrowths at about 180°C in the Rumple Lake area and 220°C in the Carswell area (Pagel, 1975a; 1975b), and at about 160°C in the McArthur area (Kotzer and Kyser, 1995). Peak diagenesis was characterized by temperatures estimated between 200 and 240°C after illite crystallinity index, fluid inclusions and isotope equilibration temperature studies (Hoeve et al., 1981; Halter, 1988 ; Kotzer and Kyser, 1995).

3.3. The Maw Zone

The Maw Zone is a rather unique REE and Y mineralized occurrence located in the southeastern part of the Athabasca Basin, 30 km northeast of the Key Lake uranium deposit. It lies in the upper part of the MFc and in the MFd (SMDC report, 1992), between 200 and 250 m above the unconformity where small uranium enrichment occurs (MacDougall, 1990; Quirt et al., 1991; SMDC report, 1992) (Fig. 2).

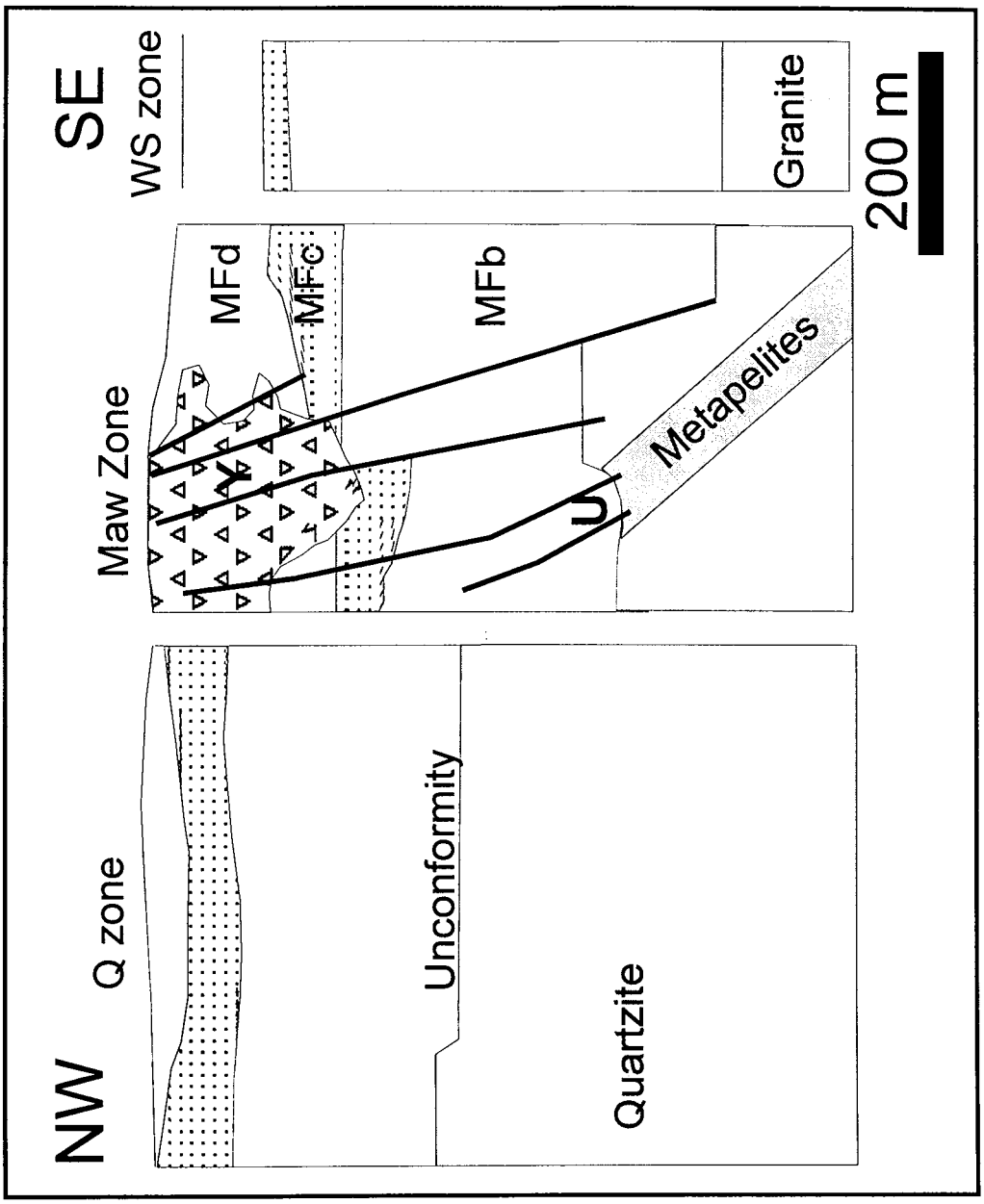

Figure 2 – Composite cross-section of the Maw Zone. From the west to the east, the sections represented are 32S, 1215S (Maw Zone) and 0 (modified from a SMDC report on the Wheeler River Project, 1992).

The Maw Zone is on the eastern side of a southeast-dipping northeast-trending reverse fault. The fault is believed to occur at the contact between an Archean granitic gneiss dome

and Wollaston Group pelitic graphitic gneiss. It is on the northwest side of a basement topographic high, formed by metaquartzite and pelitic gneiss, that underlies the Maw Zone (Quirt et al., 1991).

Alteration at the Maw Zone is characterized by pervasive silicification and extended dravite-rich breccia development. Drusy quartz- and dravite-filled fractures are also common.

The REE mineralization is contained within the sandstone breccia and consists in microcrystalline xenotime, surrounded by acicular dravite (Quirt et al., 1991). The zone is described as containing 336,000 tonnes at 0.25 % of yttrium oxide (Agip Canada Ltd, 1985; Energy Mines and Resources, 1989).

3.4. The Shea Creek area

At Shea Creek, six formations have been distinguished in the sandstone, and from bottom to top are named: MFc, MFd, Lazenby Lake (LzL), Wolverine Point A (WPa), Wolverine Point B (WPb) and Locker Lake (LL) (see part II). The mineralization is hosted by the MFc formation.

Two main Lower Proterozoic basement lithostratigraphic groups are found at Shea Creek: a metasedimentary unit containing mostly shear-related graphite located between two orthoderived felsic gneiss units (Fig. 3a and 3b). The metasedimentary unit is divided into metapelites and garnetites.

Three types of faults have been recognized, based on their orientation and kinematic (Fig. 3a and 3b). They occur both in the Lower Proterozoic basement and in the sandstone cover. Type I reverse faults are developed at the regional scale and oriented N130-150° with a dip of 20 to 40° toward the west. They may display post-Athabasca vertical offsets of 5 to 10 m. In the basement, the type I faults are ductile and brittle, 3-5 m wide and represented by graphite- and clay-rich gouges as well as numerous graphite-rich slip planes, parallel to the lithology and foliation. Type II structures are local and oriented N100-110 with a dip of 50 to 70° toward the northeast. They display late normal-sinistral movements with vertical offsets up to 10 m. Type III are regional reverse faults, oriented N5-15 with a dip of 50 to 70° toward the west. Like type I faults, they have a ductile ante-Athabasca history and are locally graphite-rich. Their post-Athabasca vertical offsets may reach 20 m.

A maximal cumulated post-Athabasca vertical offset of 35 m is observed between points A and B at the unconformity due to the combinaison of offsets of the 3 fault types (Fig. 3a and 3b). The type I and type II faults are the main controls of the uranium mineralization in the sandstone. In the basement, the mineralization seems more controlled by type III faults.

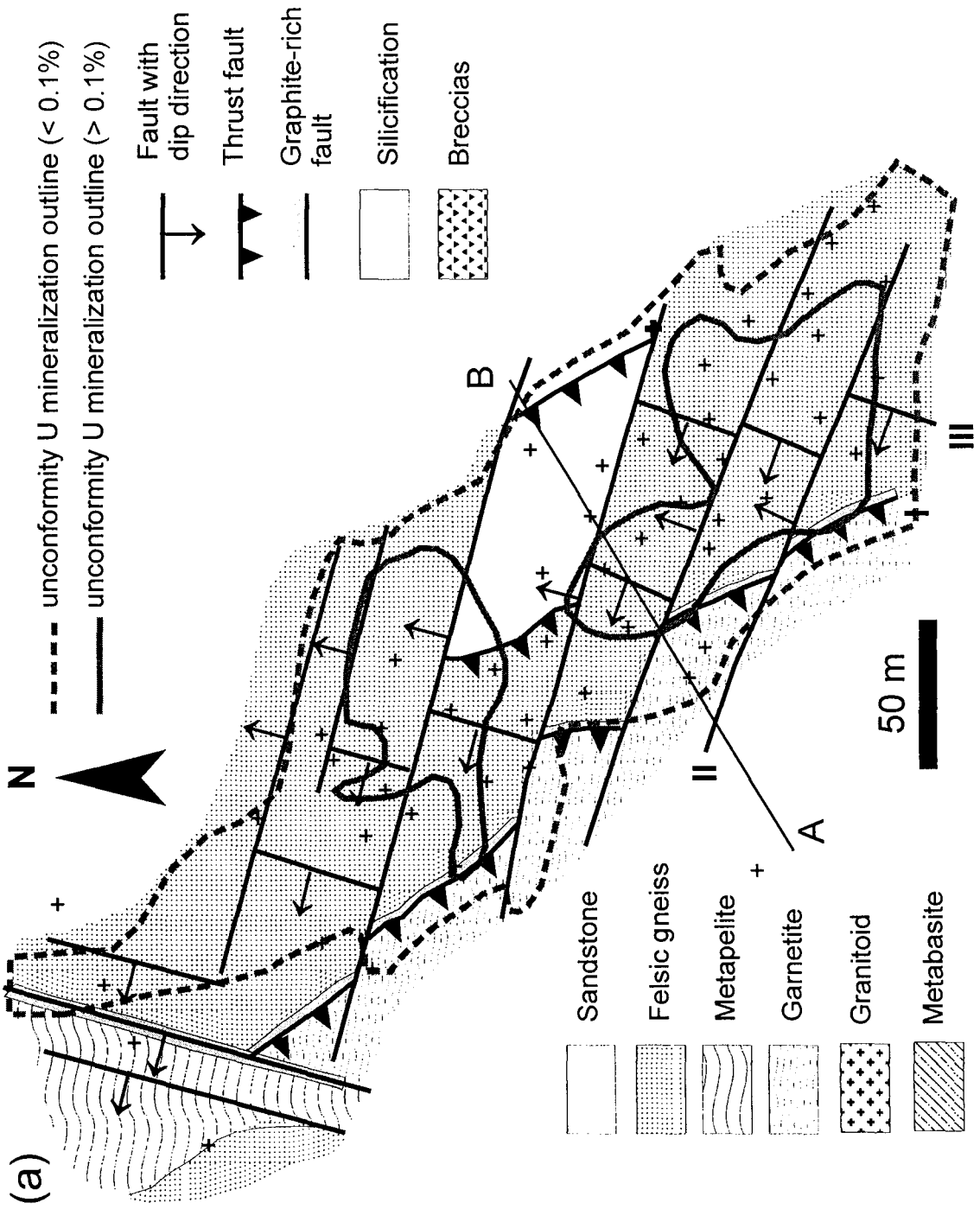

Figure 3 – (a) Geological map of the Anne area in the south part of the Shea Creek exploration zone at 360 meters below sea level (unconformity level). Orthoderived felsic gneiss is the most ubiquitous lithology and occurs each side of a partly metasedimentary aluminous gneiss unit divided into metapelites and garnetites. Three types of faults are observed. The main type I fault separates the metasediment rocks from the felsic gneisses. The type I and type II faults are the main controls of the mineralization. The line A-B indicates the location of the cross-section.

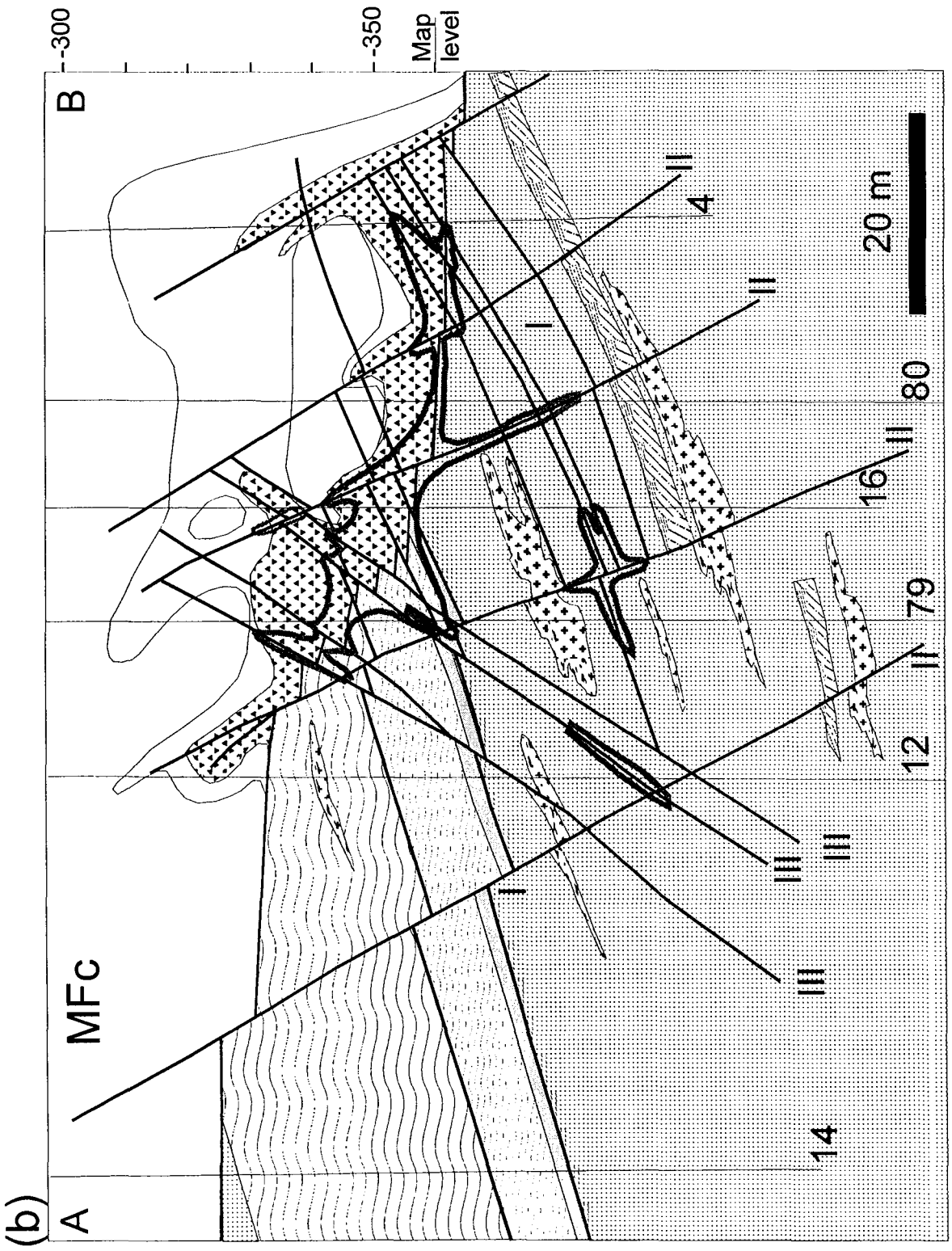

Figure 3 - (b) Cross-section A-B displaying the relationships between the three types of faults, the dissolution breccia body, the unconformity, the mineralization and the silicification. The faults crosscut the unconformity and control the mineralization location as well as the breccia body organization. More specifically, the breccias have finger shapes along faults and enlarge at the unconformity. Note the silicification halo around breccias.

These 3 fault types are associated with breccia bodies and alteration haloes in the sandstone (see part II). The alteration halos mainly correspond to silicification and chloritization and are vertically more extensive than the breccias (up to more than 50 m above the unconformity) (Fig. 3b). Within the alteration haloes, veins display different mineralogical fillings including quartz, chlorite, dravite, carbonates and pitchblende.
High-grade uranium mineralization is found as massive pitchblende veins or impregnations down to 40 m in the basement and in the sandstones up to 40 m above the unconformity. The main mineralized pod is located at the unconformity and is partly controlled by type I faults, parallel shallow dipping tension gashes and type II faults (Fig. 3b).

3.5. The Sue deposits

The unconformity-type Sue deposits (A, B, C, CQ, D, E) are located at the eastern edge of the Athabasca Basin in northern Saskatchewan (Fig. 1). They are clustered on the western flank of the Archean Collins Bay granitic dome at the western edge of the Precambrian Wollaston Domain, along a N12° trend (Baudemont et al., 1993) (Fig. 4).

Lower Proterozoic metasediments along the Sue trend are oriented parallel to the edge of the Collins Bay dome and dip steeply to the east (Fig. 4). Two main graphitic paragneiss units approximately 80 m apart occur within the felsic and cordierite-sillimanite-garnet paragneisses (Fig. 4). A metaquartzite unit is present tens of meters to the west of the western graphitic unit (Fig. 4) (Baudemont and Pacquet, 1996).

Three main fault systems exist in the Sue area: N10-15 steeply dipping to the east, N50-60 dipping to the northwest and N140-160 dipping to the northeast (Fig. 4). They crosscut the unconformity and show respectively reverse, dextral-reverse and normal-sinistral post-Athabasca movements. The first set is represented by two graphite-rich reverse faults parallel to the foliation trending N12E and hosted in the basement by the two graphitic units. This set produced a cumulated down-drop of 5 to 30 m of the western block after sandstone deposition (Baudemont and Pacquet, 1996). The western graphitic structure (WGS) and the eastern graphitic structure (EGS) respectively control the Sue C, D and E, and the Sue A and B deposits. The northeast-trending set is also graphite-bearing and locally associated with Ni-As and U mineralization (Baudemont et al., 1993; Baudemont and Pacquet, 1996). The three fault systems resulted from a major EW contraction event (Baudemont et al., 1993). The reverse faults created intense fracturing and tilted the bedding planes in the sandstone.

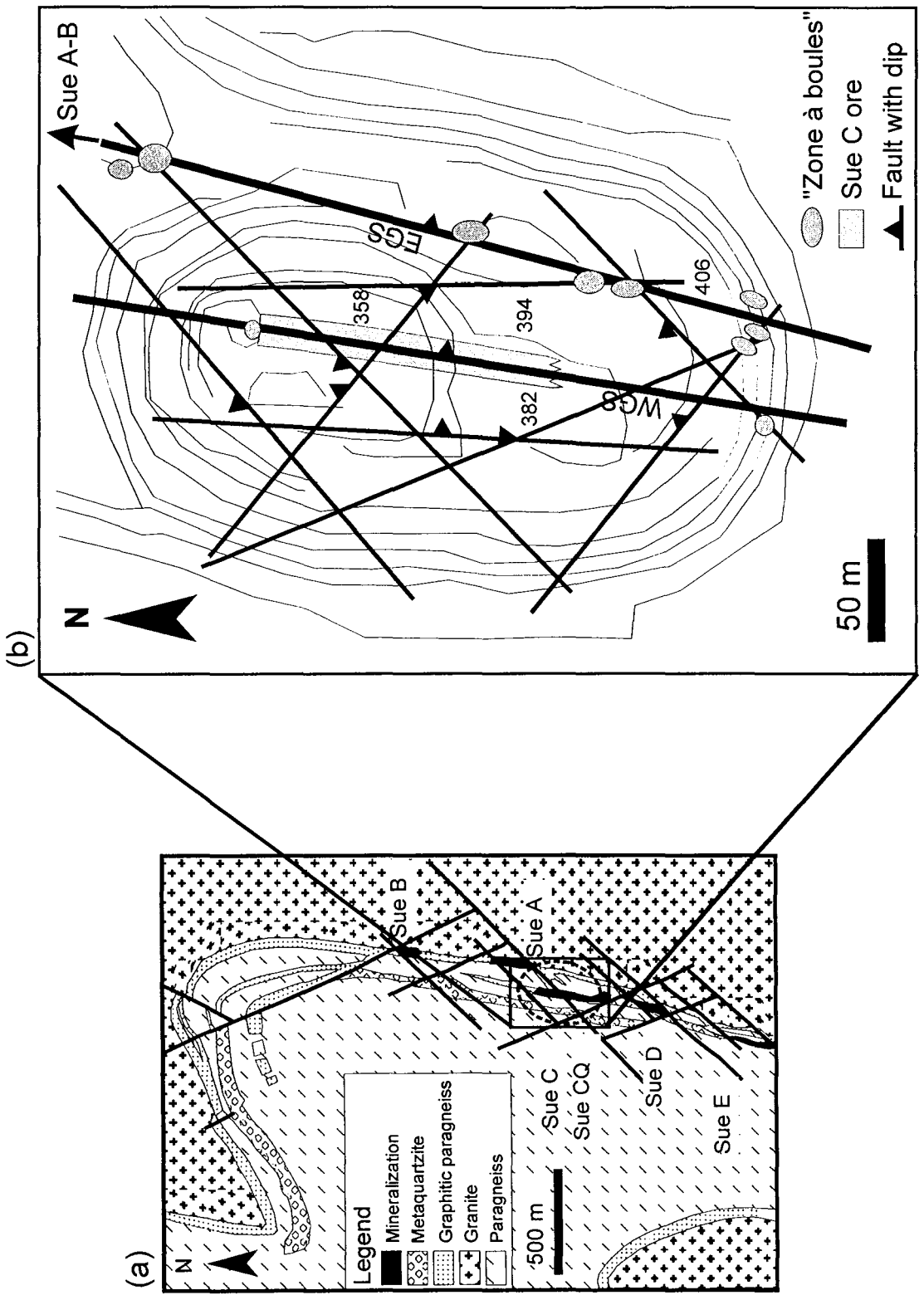

Figure 4 – (a) Basement lithologies and structural controls of the Sue deposits located on the western flank of the Collins Bay granitic dome (modified from Baudemont et al., 1993). The dashed oval indicates the position of the Sue C open pit. (b) Simplified structural map of the Sue C open pit. Note the alignment of breccias along the EGS.

Baudemont et al. (1993) described strong hydrothermal alterations associated with the Sue deposits both in basement and sandstone. Clay alteration is composed of illite in the sandstone, and illite and sudoite in the basement. In the sandstone, primary hematite has been leached out and the illite content increased towards strongly fractured mineralized zones. An earthy red-brown hematitic clay zone, up to 20 m thick, wraps the mineralization at Sue A and B. Newly formed aluminum phosphates and dravite are ubiquitous. Intense quartz dissolution occurred both in the basement lithologies beneath the Sue A and B deposits and in sandstones. In the sandstone of the Sue C open pit, quartz dissolution is mainly developed along the EGS. It is expressed by "zones à boules" that consist in illitized and striated sandstone balls wrapped in massive illite (see part III).

The Sue A and B deposits are relatively low grade, 1.26 % and 0.73 % U respectively. They are very rich in Ni and As, 3.57 % Ni and 4.46 % As for Sue A, and 1.67 % Ni and 1.86 % As for Sue B. The Sue C, D and E deposits consist of basement-hosted vein-type mineralization that may occur down to more than 100 m below the unconformity.

4. Breccia geometry and structural controls

4.1. The Maw Zone

At the Maw Zone, breccia units of at least 20 m long and 6 m wide are well exposed on outcrops (Fig. 5a). The overall breccia body, located between 200 and 250 m above the unconformity, crosscuts the sandstone stratigraphy. The mapping of the tilting of breccia fragments indicates N70 and N110 structural trends (Fig 6). The N70 direction corresponds locally to regional structural orientations whereas N110 structures are not well known in the area. A schematic cross-section realized by SMDC geologists shows that breccias have an overall funnel shape controlled by a northeast-trending reverse fault zone rooted in graphite-rich lithologies (Figs. 2 and 5a). Their volume has been estimated at 40,000 m^3 from outcrop and drill hole data.

4.2. The Shea Creek area

At Shea Creek, sudoite-dravite and Fe-chlorite solution breccias were mapped in sandstones. Cross-section mapping and three-dimensional modeling with the gOcad software show that sudoite-dravite breccias tend to have finger shapes, enlarged at the unconformity (see annexe II) (Fig. 3b). Fe-chlorite breccia bodies display a dome shape at the intersection of several faults (see annexe II).

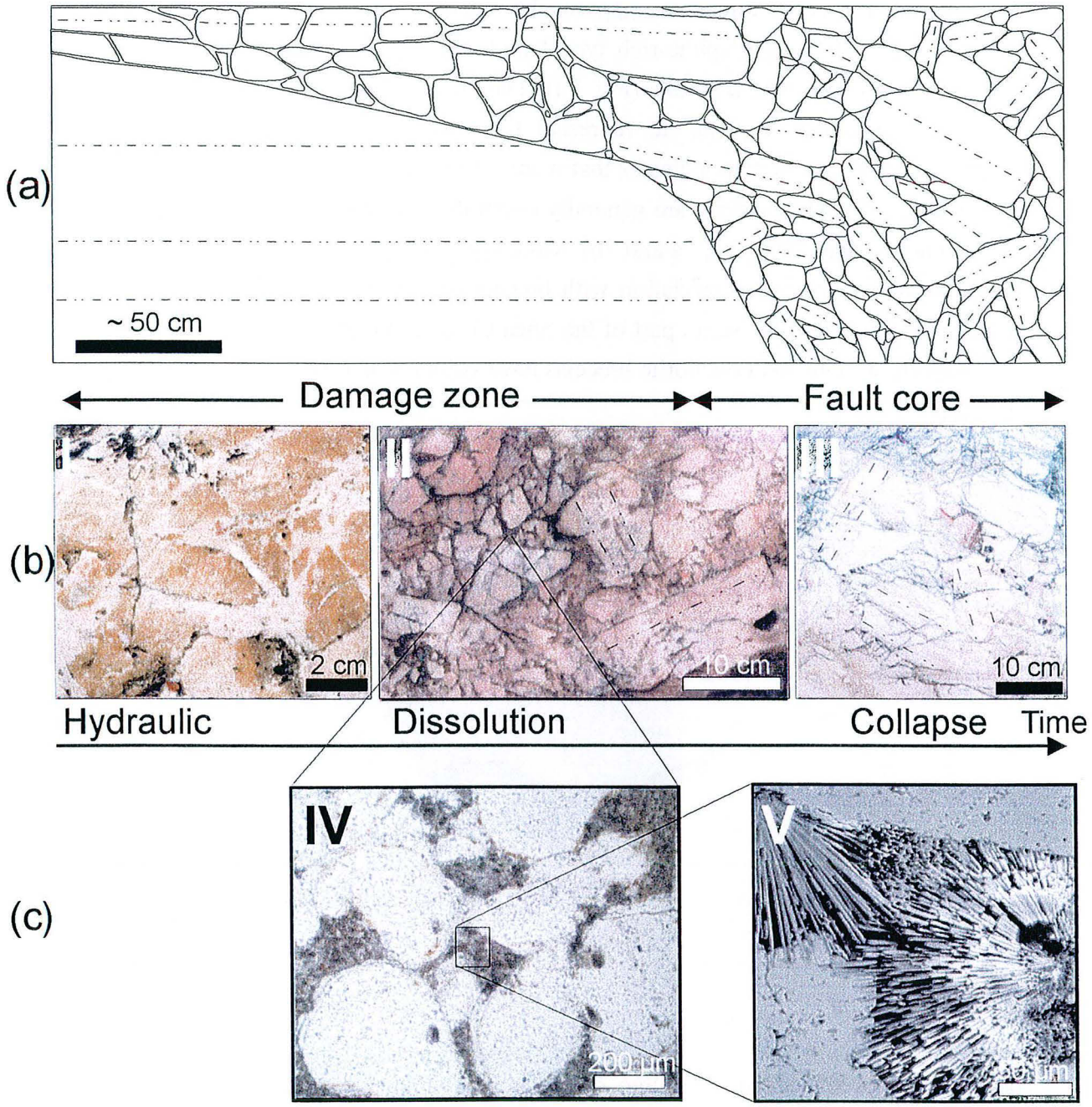

Figure 5 – (a) Schematic breccia body geometry at the Maw Zone. The center (on the right) of the breccia body is the fault core and is characterized by collapse. The border (on the left) represents the damage zone of the fault and is characterized by hydraulic breccias with weak dissolution of quartz. (b) Photographs illustrating the spatial zonation of the breccia textures from the border to the center of the body. Picture I represents a breccia with weak dissolution and jigsaw textures indicating initial hydraulic fracturing. Picture II shows the passage from the left to the right of solution breccia to collapse breccia. Picture III represents a typical collapse breccia. Note the tilted fragments with the highlighted bedding (dash-dotted lines). The evolution from hydraulic to solution and collapse breccias is both spatial and temporal. (c) Picture IV: microscopic photograph of the matrix of a solution breccia at the Maw Zone showing a high proportion of corroded detrital quartz grains in a dravite cement (polarized transmitted light). Picture V: secondary electrons SEM image showing a detail of the matrix of a solution breccia. Note the radiating dravite grown in the cavities created by quartz dissolution.

The cumulated breccia thickness map at the unconformity shows that breccias are preferentially oriented along graphite-rich type I faults and type II faults, and locally show negative correlation with type III faults (Fig. 7a). The breccia thickness was weighted by the breccia matrix percentage in order to represent the most mature breccias. The weighted cumulated breccia thickness map indicates that mature breccias are controlled by graphite-rich type I faults (Fig. 7b). The breccias are generally controlled by structures that are mineralized close to the unconformity (Fig. 3b, 7a and 7b). More specifically, the mineralization outline in sandstones shows a very good correlation with breccia bodies (Fig. 7a and 7b). The breccia volumes were estimated in the south part of the Shea Creek exploration zone using the gOcad software. Sudoite-dravite and Fe-chlorite breccias have volumes of 166,000 m^3 and 30,000 m^3, respectively.

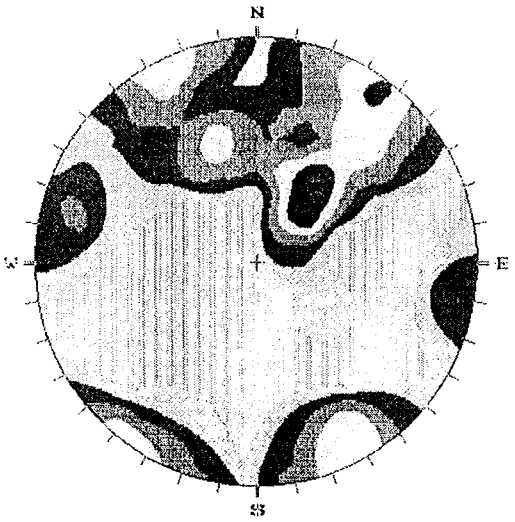

Figure 6 – Stereonet of the poles of the sandstone stratigraphy in the breccia fragments at the Maw Zone. Two main azimuths of tilting appear : N70 and N110.

4.3. The Sue C open pit

The breccias associated with the Sue deposits have elongated finger shapes. They are located just above the unconformity and are typically 10 to 20 m high and 5 m wide. They occur either in the core of strongly fractured and argillized zones or as pockets within low to moderately fractured zones. Mapping of "zones à boules" exposures in the sandstone of the Sue C pit (Fig. 4) indicated that they are aligned along the EGS and typically occur at fault intersections with NE structures, as determined by strike measurements (see part III). The breccia volume in the Sue C open pit was estimated at 10,000 m^3.

Conclusions

Consequently, the breccia bodies at the Maw Zone, at Sue and at Shea Creek all show strong structural controls by steeply to gently dipping reverse faults which are graphite-rich in the basement. They are the same faults controlling the uranium unconformity-type mineralizations and the REE mineralization at the Maw Zone.

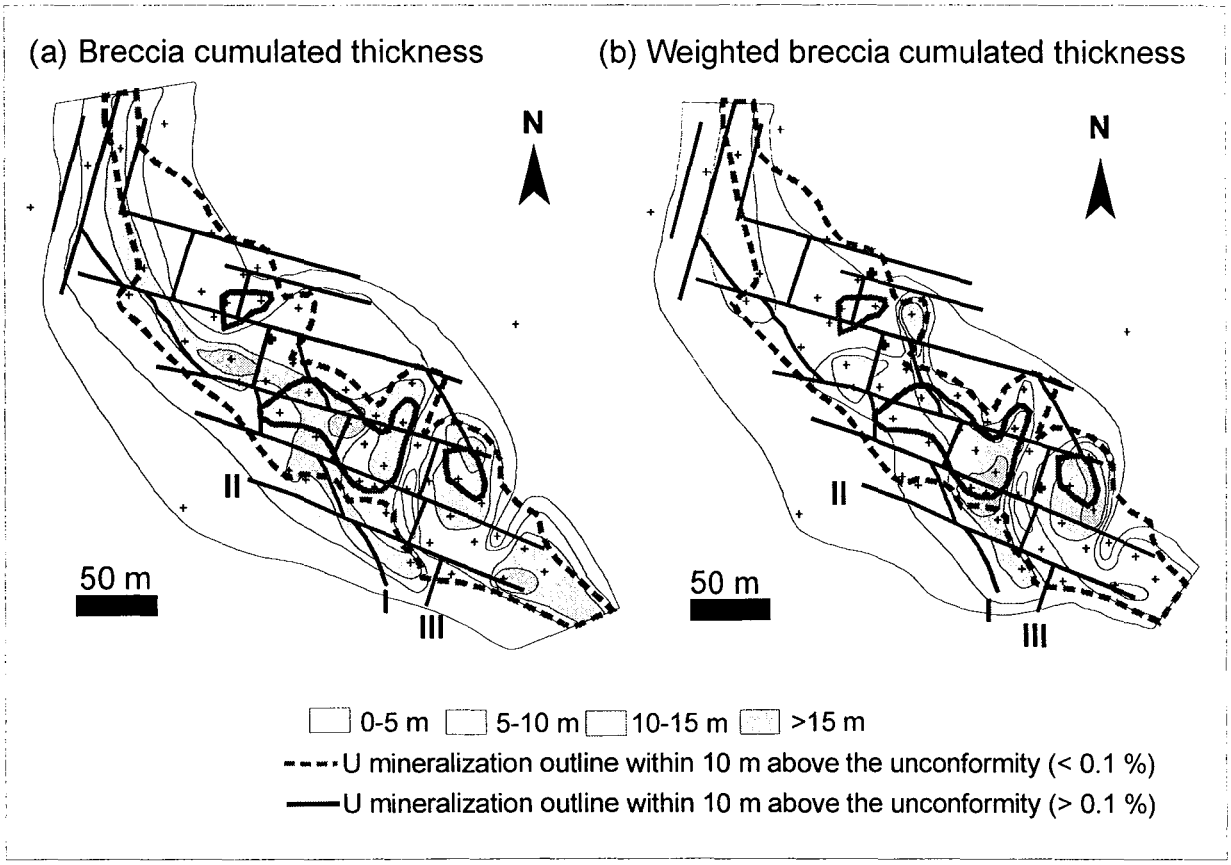

Figure 7 – (a) Cumulated thickness of the different breccia types within 100 meters of sandstones just above the unconformity projected on a structural map of the southern part of the Shea Creek area at 360 meters below sea level (unconformity level, see fig. 3). Black crosses represent drill holes impacts at the unconformity. (b) Weighted cumulated breccia thickness unconformity map corresponding to the thickness of the most mature breccias.

5. Breccia textures and maturity evolution

5.1. The Maw Zone

The breccias at the Maw Zone have typically a low matrix percentage, about 15 vol. % in average, and consist of slightly rounded silicified sandstone fragments in a matrix mostly composed of 85 to 90 wt. % of corroded detrital quartz grains and dravite (Fig. 5b and 5c). The low matrix percentage expresses the low maturity degree of these breccias. The most immature breccias have jigsaw textures and are found on the borders of the funnel-shaped body (Fig. 5a and 5b). The fractures are commonly controlled by the stratigraphy. The rounded fragment

shapes and the presence of corroded detrital quartz grains in the matrix indicate quartz dissolution in the matrix and on the fragments borders (Fig. 5b and 5c). The dravite crystallized as radiated bunches within interstitial spaces between corroded quartz and within dissolution cusps (Fig. 5c). In the center of the funnel, breccias are heterolithic with tilted fragments and fragment-supported textures (Fig. 5a and 5b).

The development of jigsaw textures and the local stratigraphic control of fractures are the expression of hydraulic brecciation possibly related to a fault termination zone as it has been documented by Cox et al. (2000). The formation of rounded fragment corners rather than cusps producing complex shapes indicates a probable diffusion-limited regime of dissolution. The heterolithic breccias with fragment-supported textures and the tilting of fragments indicate the occurrence of collapse. The mapping of fragment tilting indicates that this collapse occurred along structural trends. The low dissolution rate in these breccias suggests that the collapse is not a consequence of the dissolution occurring within the breccias but is rather due to dissolution occurring at the unconformity below and associated with unconformity-type uranium enrichment.

5.2. The Shea Creek area

In the Shea Creek area, several breccia types have been distinguished in the sandstones surrounding unconformity-type uranium mineralization: microcrystalline quartz, sudoite, dravite, calcite, Fe-chlorite and polyphase carbonate breccias. Immature breccias show typical jigsaw patterns indicating fluid-assisted fracturing (see part II) (Fig. 8a and 8e). In mature breccias, except microcrystalline quartz ones, the presence of numerous corroded detrital quartz grains in the matrix and the ubiquitous presence of quartz dissolution textures at the macroscopic, thin section and SEM scales clearly demonstrate the major role of dissolution in the breccia formation (see part II) (Fig. 8b, 8c, 8f, 8g, 8h, 8i, 8j and 8k).

Some of these solution breccias may be called pseudo-breccias as quartz dissolution is pervasive and not developed enough to destroy the sandstone cohesion (Fig. 8c).

Dravite breccias commonly display shallow dipping contacts. Their matrix show pseudo-flow banding textures parallel to the contacts and formed by orientation of acicular dravite and alignment of numerous accessory minerals along layers parallel to the dravite orientation (Fig. 8h). The high concentration of accessory minerals suggests volume loss after dissolution. Therefore, the shallow dipping pseudo-flow bandings might result from vertical contraction due to pure shear induced by gravity after quartz dissolution. Sudoite breccias are commonly fragment-supported and contain horizontally oriented elongated fragments in mature zones. They display a negative correlation between rotation angle and size of the tilted blocks indicating collapse phenomenons (see part II). Fe-chlorite breccias are commonly heterolithic,

fragment-supported and present the same relation between rotation angle and size of the tilted blocks as in sudoite breccias. Graded-bedding textures are locally observed in the upper part of fragment-supported breccia units. Consequently, Fe-chlorite breccias also present major evidences of collapse. That would explain their dome shape typical of collapse breccia bodies like in Mississippi Valley type deposits (Sass-Gustkiewicz, 1996; Dzuslynski and Sass-Gustkiewicz, 1989).

The variety of breccia types at Shea Creek is not only expressed by the nature of the cement, but also by the fragment shapes. Fractal analysis of the fragment morphologies has allowed recognition of the intensity and type of corrosion processes, and also its kinetic processes (see part II) (Fig. 8l). In microcrystalline quartz breccias, the low fractal dimensions represent angular fragments formed during the first step of hydraulic brecciation. In sudoite breccias, medium fractal dimensions characterize the predominance of rounded fragments. They are the expression of the second step of sandstone dissolution in a slow diffusion-limited regime (Jébrak, 1997). That is confirmed by the occurrence of dissolution embayments in these breccias (Burley and Kantorowicz, 1986) (Fig. 8j). In Fe-chlorite breccias, the bimodal fragment shape distribution curve indicates a mixing of non-corroded angular fragments with corroded fragments due to a third step of collapse (see part II). The observation of some complex shapes and pervasively altered fragments as well as the abundance of pits observed with a SEM on fragment surfaces would indicate a fast kinetic regime of dissolution (Fig. 8c and 8k) (Burley and Kantorowicz, 1986). In polyphase carbonate breccias, the globally high fractal dimension values reflect more complex fragment morphologies, suggesting a possible kinetic regime of dissolution (Jébrak, 1997).

5.3. The Sue C open pit

The breccias observed in the Sue C open pit are "zones à boules" (see part III) (Fig. 9a). The statistical distribution of the ball shapes is log-normal. As the balls formed initially by fracturing, this log-normal distribution indicates tectonic fracturing (see part III). That is consistent with the narrow finger shapes of the breccia bodies restricted to the core of the EGS. The development of ball shapes is due to quartz dissolution in diffusion-limited regime combined with rotation during reverse fault movements. The presence of superimposed striaes indicates the occurrence of several tectonic reactivation phases. The sandstone samples located close to a "zone à boule" have well developed microscopic corrosion textures of detrital quartz and of their overgrowths (Fig. 9b).

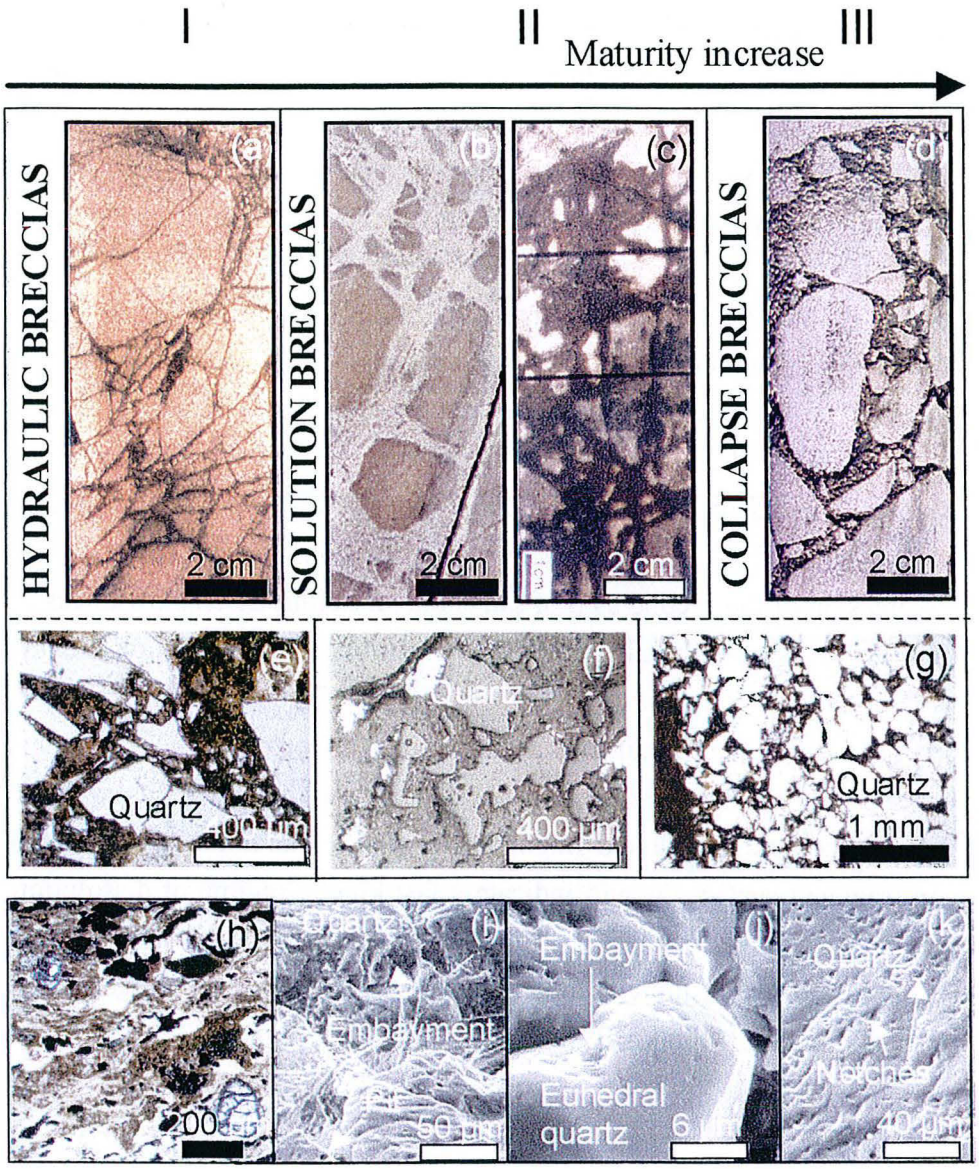

Figure 8 – (a) to (l): figures presenting the various breccia textures encountered in the sandstone at Shea Creek. Numbers I, II and III represent the typical evolution of a breccia. (a) to (j): typical breccia textures at different scales. (a) to (d): macroscopic photographs. (a) Strongly silicified fractured sandstone. Note the jigsaw textures significant of hydraulic fracturing. (b) Sudoite solution breccia. The original jigsaw pattern is partly disappeared due to quartz dissolution. (c) Fe-chlorite solution breccia. Note the complex shapes of the fragments due to propagation of a corrosion front from a fracture network. (d) Solution-collapse breccia. Note the fragment-supported texture and the rotated fragments. (e) to (h): microscopic photographs. (e) Hydraulically fractured detrital quartz grains in the matrix of a breccia. Note the quartz splinters indicating no significant movement. (f) Strongly corroded detrital quartz grains. Note the spectacular dissolution cusps. (g) Breccia showing a fragment on the right and the matrix on the left. The detrital quartz grains within the fragment and the matrix are corroded. The sharp fragment edge is interpreted to result from fracturing during collapse subsequent to dissolution. (h) Pseudo-flow banding texture in the matrix of a dravite breccia. Note the abundance of accessory minerals (zircons, schorls, Ti-oxides). (i) to (k): secondary electrons SEM images of surfaces of fragments of solution breccias. (i) Corroded detrital quartz grains. Note the dissolution pits and embayments. The needles are dravite crystals. (j) Dissolution embayment in a euhedral quartz typical of dissolution in diffusion-limited regime. (k) Dissolution notches on quartz typical of dissolution in kinetic regime.

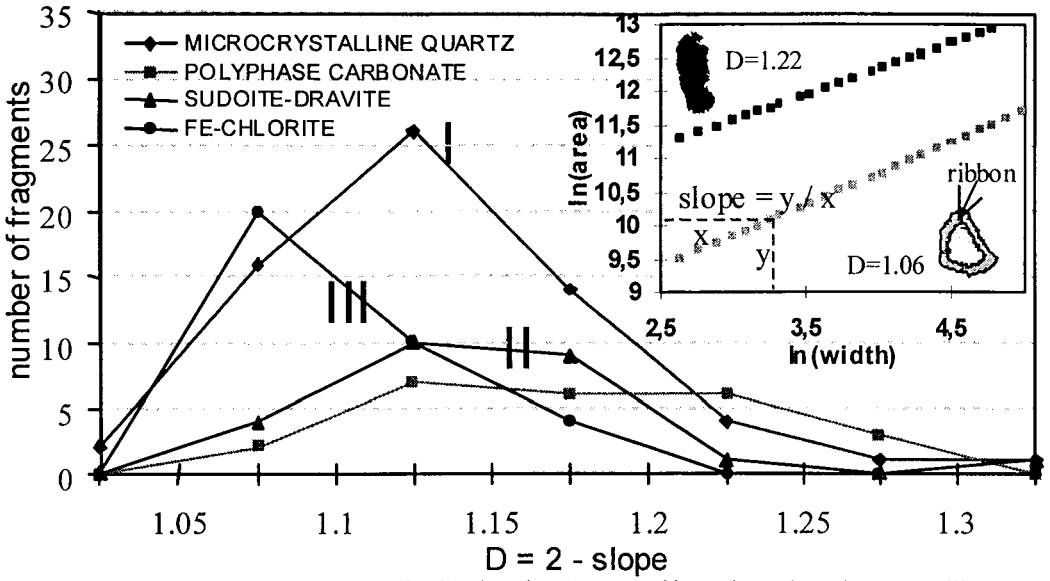

Figure 8 - (I) Fragment morphometry (D) distribution for 4 types of breccias. The microcrystalline quartz breccia fragment shapes have low fractal dimensions typical of hydraulic fracturing (step I). The sudoite-dravite and polyphase carbonate breccia fragment morphologies have rather high fractal dimensions indicating quartz dissolution (step II). The Fe-chlorite breccia fragment shape distribution curve is bimodal indicating mixing of corroded and non-corroded fragments due to collapse (step III). The inset in the right hand corner is an example of Richardson plot used to calculate the fractal dimension of fragment morphology. Two breccia fragments are presented with their fractal dimensions.

At the unconformity, the matrix percentage may be greater than 50 % and sandstone balls are totally argillized, indicating a high maturity degree.

Conclusions

Consequently, breccias at Sue, at Shea Creek and at the Maw Zone are mainly solution breccias. Their maturation may be described in three steps : (I) tectonic and hydraulic fracturing, (II) sandstone dissolution and (III) collapse. The maturity increases in space from the Maw Zone solution breccias to the Shea Creek solution breccias and to the « zones à boules » just above the unconformity at Sue defining a vertical maturity gradient.

6. Mineralogy and chemical ages

In the three zones of study, quartzose sandstone deposition was followed by early diagenesis characterized by primary hematite crystallization and quartz overgrowths. Dickite, a kaolinite polytype identified by Raman microspectroscopy, crystallized after partial dissolution of quartz overgrowths during intense diagenesis. Illite, probably formed during peak diagenesis, was identified in the sandstone surrounding Shea Creek. However, as the clay proportion is very small, the K content of the reference samples is close to the detection limit (Table 1). In other areas of the basin, a small proportion of diagenetic chlorite may also occur

in the sandstone (Hoeve et al., 1981). At the Maw Zone, clay minerals have been dissolved before or during a strong silicification event.

Detrital accessory minerals are mainly Fe-Ti oxides, fresh to metamict zircons with xenotime overgrowths, and tourmaline (schorl). Exsolution lamellae of rutile following rhombohedral directions indicate pseudomorphosis after ilmenite. These accessory minerals are found mostly as heavy mineral layers. Detrital monazite crystals have been altered to crandallite-group minerals, mainly goyazite and florencite, during diagenesis.

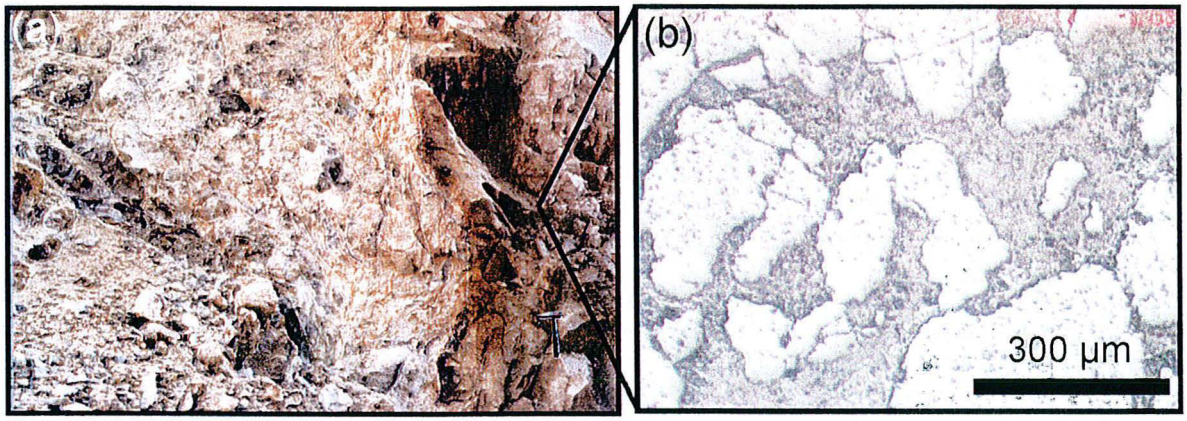

Figure 9 – (a) "Zone à boules" exposure in the Sue C open pit mine showing illitized balls wrapped in massive illite. (b) Microscopic photograph of corroded detrital quartz grains in the sandstone close to the wall of a "zone à boules" (polarized reflected light).

6.1. The Maw Zone

At the Maw Zone, the mineral paragenesis of the sandstone was established using field observations and the study of 12 samples (Fig. 10a) (see annexe I). Where the sandstone is not brecciated, it is systematically strongly silicified. Detrital quartz grains are recrystallized with formation of new crystals crosscutting and removing former detrital grain borders. No diagenetic assemblage was observed, suggesting that diagenetic minerals like dickite or illite have been dissolved prior to or during the pervasive silicification. Locally, the silica deposition is expressed by euhedral quartz crystallization within small open fractures. Strongly silicified sandstone may display an emerald green color due to Cr-rich radiated needles of dravite originating from surface defects on detrital quartz grains (Quirt et al., 1991) (Fig. 10b). This dravite is probably coeval with the silicification event. An other event of dravite precipitation is indicated by aggregates of spherulitic dravite crystallized within the space created by quartz dissolution. The presence of dravite surrounding corroded former euhedral quartz suggests that this dravite is later than euhedral quartz (Fig. 10c). The dravite associated with corroded detrital quartz grains forms the matrix of the collapse-dominated solution breccias at the Maw Zone and is intergrown with xenotime (Quirt et al., 1991). This dravite is alkali-free and less

chromiferous than the first dravite. Xenotime, together with altered zircon, form the Y and REE mineralization at the Maw Zone. This mineralization is assumed to have been formed by the same hydrothermal processes that led to uranium enrichment at the unconformity below (Quirt et al., 1991). Euhedral quartz were also observed crystallized on dravite coatings in fractures or cementing dravitized sandstone fragments (Fig. 10d). Consequently, these observations evidence a late phase of euhedral quartz crystallization.

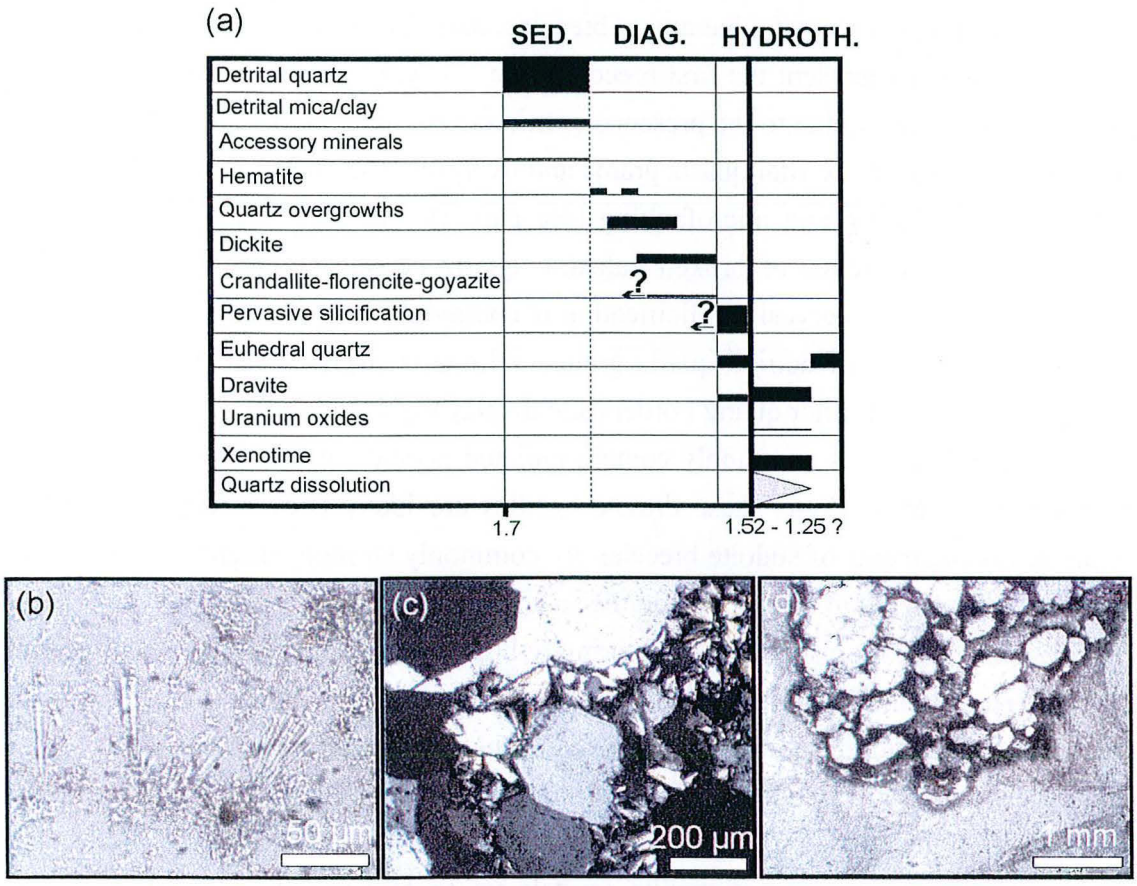

Figure 10 – (a) Mineral paragenesis established in the sandstone of the Maw Zone. The diagram represents successively sandstone deposition, diagenesis and a hydrothermal event of yttrium mineralization and uranium enrichment. Vertical lines represent fracturing and hydraulic brecciation events. The thickness of the black rectangles is representative of the abundance of the corresponding phase. (b), (c) and (d) Microscopic photographs. (b) Radiated needles of probably Cr-rich dravite originating from surface defects on a detrital quartz grain (polarized transmitted light). (c) Spherulitic aggregates of dravite surrounding corroded former euhedral quartz (plane polarized transmitted light). (d) Fragment of dravitized sandstone surrounded by euhedral quartz (polarized transmitted light).

6.2. The Shea Creek area

The mineralogy of about 50 samples representing the different hydrothermal breccia types observed in the sandstone at Shea Creek was studied. The various breccia types represent several stages, each characterized by a specific mineralogical assemblage, generally observed in the matrix of the breccias. The mineral paragenesis is divided into 4 main stages (Fig. 11).

Stage 1: The earliest hydrothermal event in the sandstone is characterized by silicification. Silicification may be pervasive forming a halo around the mineralization (Fig. 3b), or occurs as euhedral quartz crystallization and microcrystalline quartz breccia formation (Fig. 12a and 11b). Euhedral quartz crystals are found in slightly curved commonly vertical tension fractures, in local jogs and were seen once as breccia cement. They commonly show a zonation with milky quartz in the internal zones and clear quartz in the external zones. Locally, they appear to be skeletal. Microcrystalline quartz breccias, only found individually or in fragments of other breccia types, represent the first breccia event. They are characterized by white fine-grained quartz-rich matrix, due to the presence of microcrystalline quartz cement or to the fine granulation of the original detrital quartz grains and overgrowths. They are produced by fluid-assisted tectonic fracturing and microfaulting (see part II). The early formation of euhedral quartz is evidenced by relics of broken euhedral quartz crystals within a microcrystalline quartz cement (Fig. 12b). Pervasive silicification is commonly intense and characterized by a complete recristallization of detrital quartz grains and quartz overgrowths (Fig. 12a). Newly formed crystals crosscut former quartz borders and display triple junctions.

Strongly silicified zones commonly contain radiated needles of dravite within interstitial quartz. Like at the Maw Zone, these dravite needles are likely coeval with the pervasive silicification. As fragments of sudoite breccias are commonly strongly silicified, the pervasive silicification is considered to be earlier than the sudoite breccias.

Stage 2: This stage represents the main primary high grade uranium mineralization event. It is characterized by the formation of sudoite-dravite breccias (see annexe I). It begins with massive quartz dissolution creating open spaces. The presence of corroded quartz grains wrapped by dickite, dravite, sudoite and illite cement indicates filling of open spaces during and/or closely after the quartz removal.

Large worm-like aggregates of dickite crystals up to 500 μm in size within dravite-, sudoite- and/or illite-rich breccias show that dickite is the earliest clay cement (Fig. 12c). Raman microspectroscopy indicates that alternations of kaolinite and dickite layers may occur.

Sudoite-dravite breccia bodies present a zonation around the unconformity mineralization with predominant dravite over sudoite in the external zone, predominant sudoite over dravite in the inner part and illite intermixed with sudoite within the mineralization. Massive dravite may also be found occasionnally close to the unconformity.

Dickite, sudoite and illite are found as fragments within dravite suggesting that they may be earlier (Fig. 12f and 12g). However, the sudoite-dravite zonation indicates that dravite may be coeval with sudoite. The presence of dravite cross-cutting sudoite in the center of the breccia body suggests that the mineralogical zonation moved back toward the unconformity at the end of the hydrothermal system activity, due to a decreasing intensity of basement fluid input. Therefore, we propose that dravite, sudoite and illite cements are coeval.

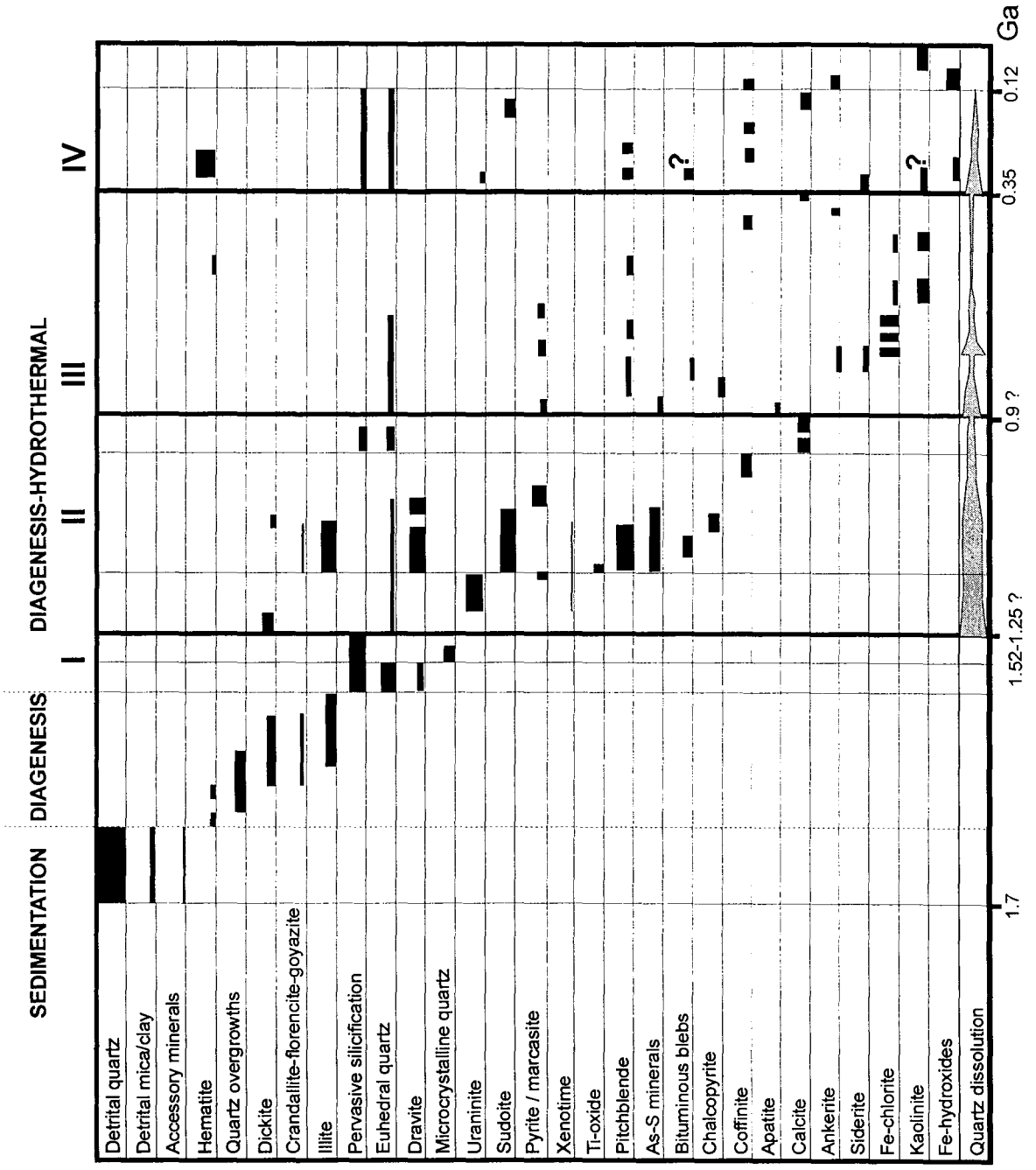

Figure 11 – Mineral paragenesis established in the sandstone of the Shea Creek exploration zone. The diagram represents successively sandstone deposition, diagenesis and several hydrothermal stages of uranium mineralization and brecciation. Stages: I = silicification, II= main U mineralization associated with illite, sudoite and dravite breccias, III = U mineralization and/or remobilization associated with Fe-chlorite breccias, IV = U remobilization associated with hematite and siderite breccias. Coeval dissolution and precipitation of quartz is related to re-deposition of quartz above zones of quartz dissolution. Vertical lines represent fracturing and hydraulic brecciation events. The thickness of the black rectangles is representative of the abundance of the corresponding phase.

Sudoite-dravite breccias have a matrix composed of a high proportion of corroded detrital quartz grains, up to 85%, and of dravite and sudoite cement. Dravite is acicular and commonly display spherulitic textures. In massive dravite zones, pseudo-flow banding textures are common (Fig. 12f). The dravite breccias are polyphase as dravite aggregates are crosscut by others. The dravite cement contains a very high proportion of accessory minerals like zircons, anatase and schorls and very few corroded quartz remnants indicating intense dissolution (Fig. 12f). Accessory minerals are commonly organized parallel to the pseudo-flow banding together with early aggregates of more or less illitized dickite (Fig. 12f).

In sudoite breccias, XRD analysis does not show systematically the predominance of peaks at 4.73 Å over peaks at 7.00 Å, suggesting the presence of a mixture of sudoite (di-trioctahedral chlorite) with trioctahedral chlorite or the existence of mixed-layers. However, the chemical composition of these chlorites suggests that they mostly correspond to sudoites (Fig. 13). Their average formulae is $(K_{0.07}, Na_{0.01}, Ca_{0.01})$ $(Si_{3.33}$ $Al_{0.67})$ $Al_{2.84}$ $(Fe_{0.2}, Mg_{1.77}, Ni_{0.05})$ O_{10} $(OH)_8$ (Table 2). The presence of K is either due to mixing with, or pollution by, illite. They have AlIV, AlVI, Mg and Fe values similar to the sudoites of the Cigar Lake and Cluff D uranium deposits alteration haloes (Halter, 1988) (Fig. 13 and 14). Therefore, the spatially associated sudoite breccias and uraninite and pitchblende unconformity mineralization suggests that they are contemporaneous.

The structural formula of clay minerals at the contact with uranium oxides suggest that they are mixed layer illite-chlorite minerals (Table 2). Locally, mixed layer illite-chlorite minerals are also found in the alteration halo. The presence of mixed layer illite-chlorite minerals associated with dravite in the vicinity of perched mineralizations suggests that unconformity and perched mineralizations are coeval.

Minerals of the crandallite-florencite-goyazite group are closely associated with illite cement (Fig. 12c). Idiomorphic xenotime overgrowths were observed on zircons within the sudoite-dravite matrix suggesting that xenotime new formation may be coeval with uranium mineralization (Fig. 12d). The local presence of bituminous blebs trapped between 2 growth zones of euhedral quartz shows that quartz deposition occurred after the stage 1. Therefore, some of the euhedral quartz present within the silicification halo surrounding breccias and mineralization may have formed by redeposition of the silica dissolved below after vertical transport. The presence of multiple euhedral quartz growth zones in some fractures indicates several fluid pulses.

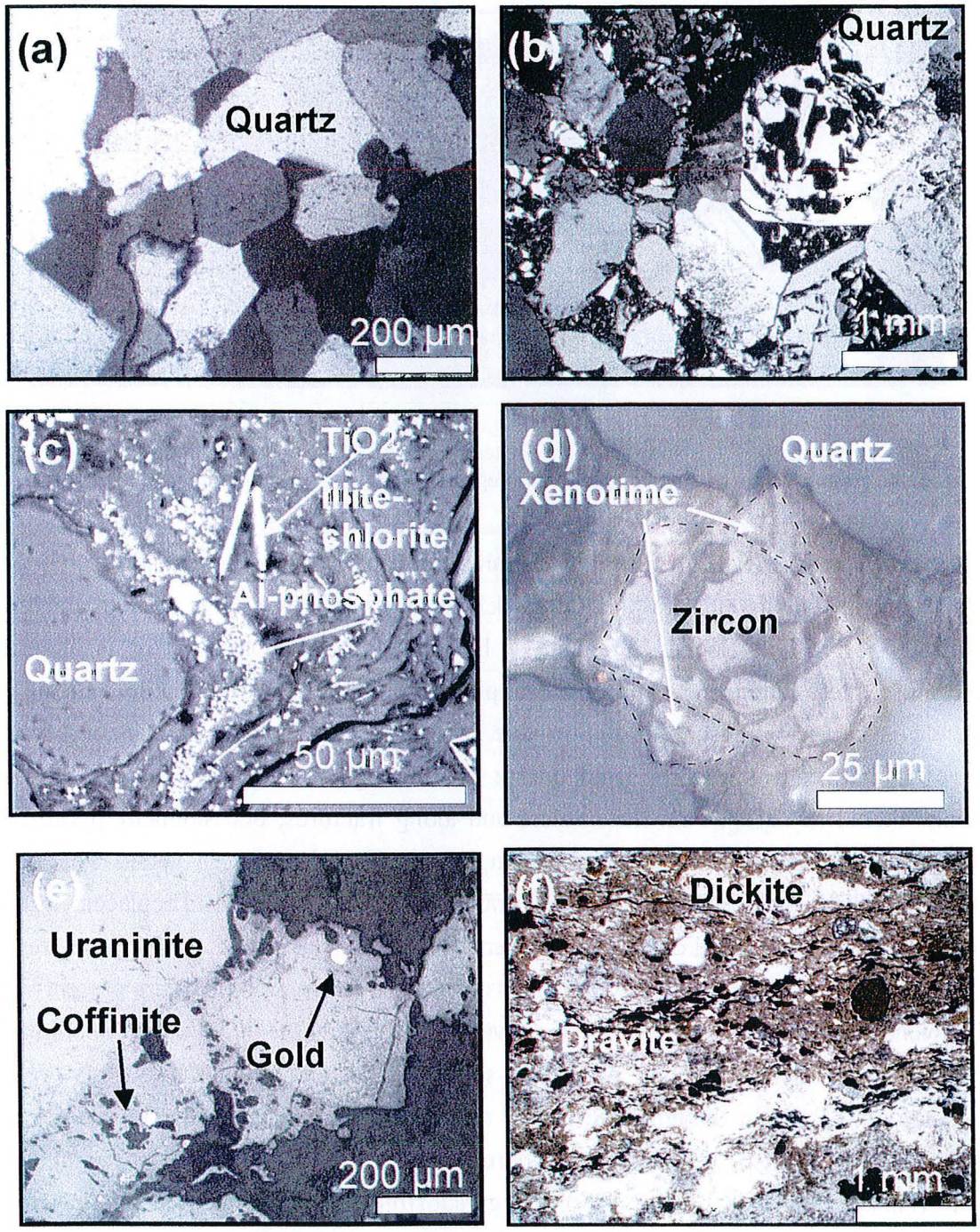

Figure 12 – Microscopic photographs of Shea Creek samples. (a) Totally recrystallized sandstone. Note the euhedral quartz crystals and the triple junctions (plane polarized transmitted light). (b) Euhedral quartz brecciated by microcrystalline quartz (plane polarized transmitted light). (c) Ti-oxide and euhedral minerals of the crandallite-florencite-goyazite group within illite surrounding corroded quartz grains (SEM back-scattered electron image). (d) Zoned zircon with sub-idiomorphic xenotime overgrowths in the matrix of a sudoite-dravite breccia (sample Shea16) (polarized reflected light). (e) Uraninite fragments (1.2 Ga) brecciated by coffinite and altered to coffinite. Note the gold bleb within pitchblende (polarized reflected light). (f) Dravite containing zircons, schorls, Fe-Ti oxides and dickite fragments all aligned along the pseudo-flow texture orientation (polarized transmitted light).

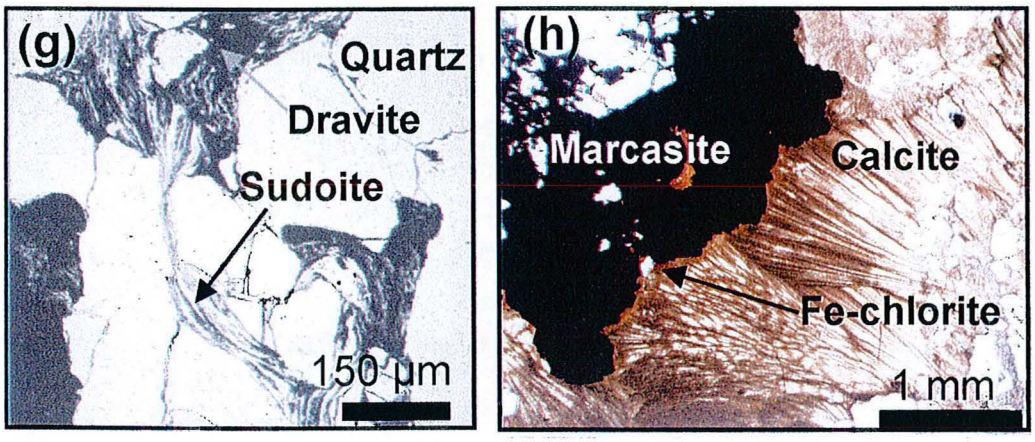

Figure 12 - (g) Detrital quartz grains and sudoite brecciated by dravite (SEM back-scattered electron image). (h) Eudral marcasite crystals within calcite. Fe-chlorite impregnates the calcite (polarized transmitted light).

Ore metallic minerals: High reflectance uraninite occurs as euhedral cubic crystals or as radiated elements within chlorite- and illite-rich breccias within a few meters above the unconformity (Fig. 12e). Locally, uraninite is brecciated by pitchblende, that is altered to coffinite (Fig. 12e). Pitchblende and pyrite impregnation of worm-like dickite indicate that pitchblende is coeval with sudoite and/or illite crystallization. Pyrite was also observed as cement of hydraulically microbrecciated quartz grains. High reflectance uraninite cubes are commonly altered to coffinite on the borders and along fractures, occasionnally pyrite-filled, showing that coffinite is later than uraninite and pyrite (Fig. 12e). A Si versus Pb diagram expressed in millications shows two trends of uraninite alteration: a trend of replacement of Pb by Si due to slow diffusion and coffinitization trend (Fig. 15).

Subidiomorphic U-Ti-Si and Ti-oxide crystals as well as native gold blebs are present within the pitchblende indicating that they may be coeval with it (Fig. 12e). Native gold is commonly associated with Bi seleno-tellurides. Arsenides, sulfoarsenides and sulfides frequently crosscut or rim uraninite, or appear disseminated in low reflectance pitchblende or in the sudoite, illite and dravite matrix. Ni, Co, Fe sulfoarsenides are common and locally rimmed by pitchblende. Niccolite (NiAs), rammelsbergite ($NiAs_2$) and gersdorffite (NiAsS) appear commonly in this chronological order. Gersdorffite may form overgrowths on Ti-oxide minerals. Bravoite [(Ni, Fe)S_2] and skutterudite [(Ni, Co)As_3] are locally developed and occur later than gersdorffite. Lollingite (FeAsS) is also part of the metallic mineral assemblage and is altered to native As. Late molybdenite may also occur very locally. Bituminous blebs, locally found as fragments within dravite, are locally rimmed by chalcopyrite and then by pyrite indicating that this pyrite generation is later than chalcopyrite which is later than the carbonaceous material.

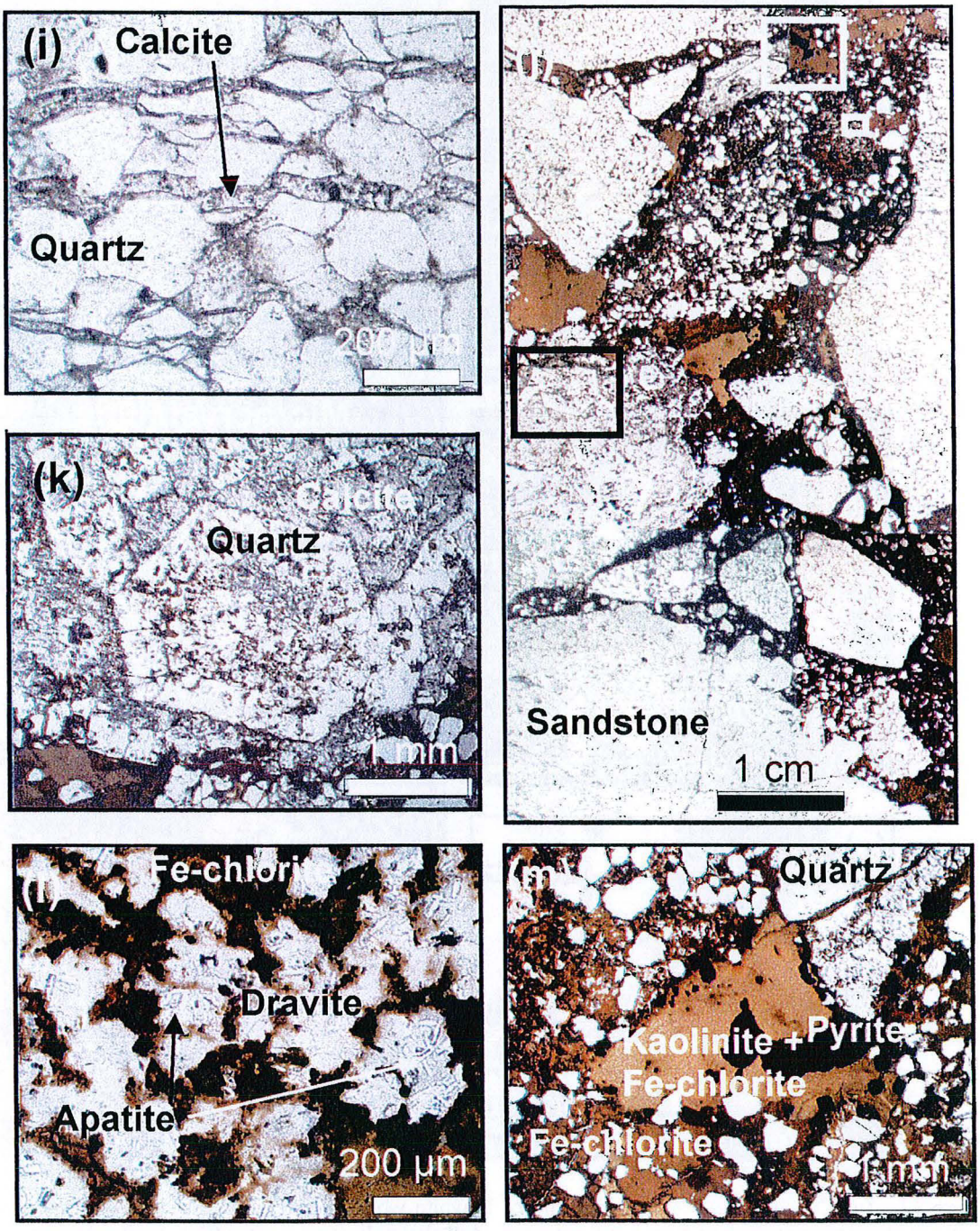

Figure 12 - (i) Calcite veins in sandstone (polarized transmitted light). (j) Thin section of a heterolithic collapse breccia. Fragments are sandstone bounded by corroded former euhedral quartz, clusters of euhedral quartz replaced and brecciated by carbonates (k) and dravite impregnated by Fe-chlorite (l). Vugs left after Fe-chlorite crystallization are filled with pyrite and a mixing of kaolinite and Fe-chlorite (m) (polarized transmitted light).

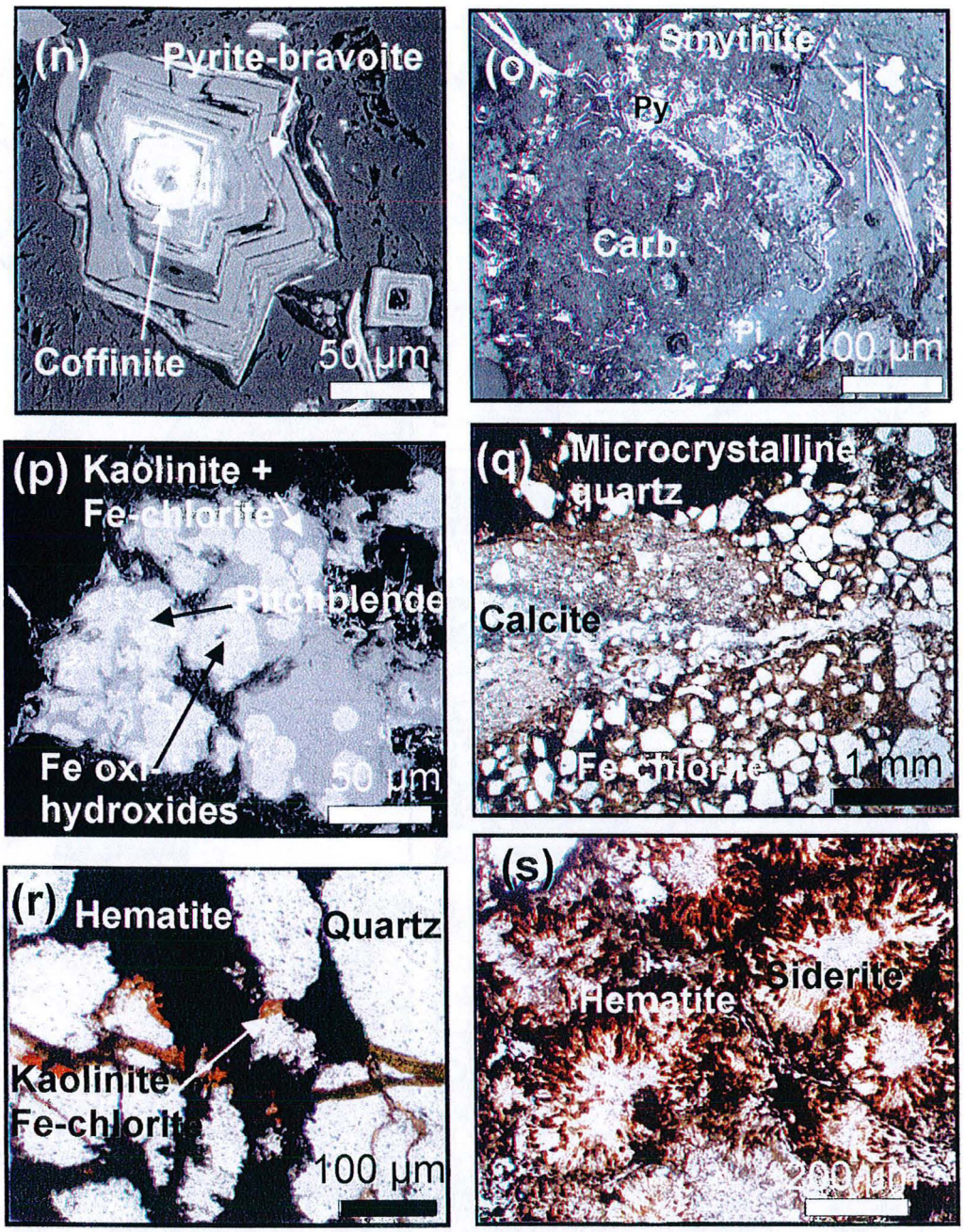

Figure 12 - (n) Euhedral skeletal zoned pyrite or bravoite whose center is replaced by coffinite (SEM back-scattered electron image). (o) Cluster of former euhedral skeletal zoned pyrites (Py). Pyrites have been replaced by pitchblende (Pi) and carbonaceous matter (Carb.). Euhedral chalcopyrite crystals are disseminated within the pitchblende surrounding the cluster. Note the smythite elongated crystals within pitchblende (polarized reflected light). (p) Fe oxi-hydroxides nodules containing dots of uranium oxides impregnating a mixing of kaolinite and Fe-chlorite within perched mineralization. The nodules and the mixing of kaolinite and Fe-chlorite are crosscut by a later mixing of kaolinite and Fe-chlorite (SEM back-scattered electron image). (q) Microcrystalline quartz breccia crosscut by a Fe-chlorite breccia. A calcite vein crosscuts both breccias (polarized transmitted light). (r) Radiated aggregates of hematite along fractures crosscutting veins of kaolinite mixed with Fe-chlorite (polarized transmitted light). (s) Siderite spherulites intergrown with hematite in their external zones (polarized transmitted light).

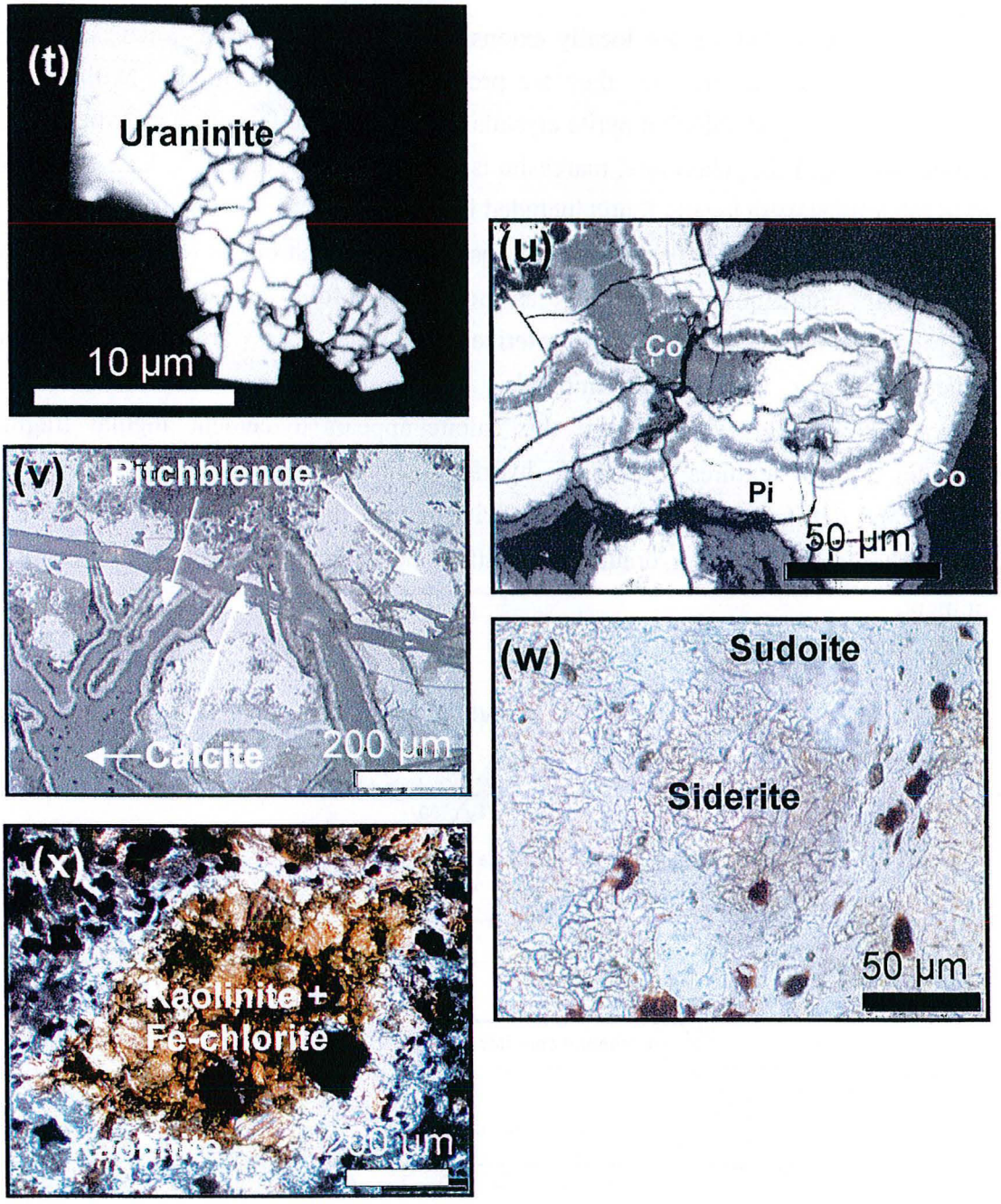

Figure 12 - (t) Euhedral uraninite newly formed at about 350 Ma and included within a hematite breccia matrix (perched mineralization) (SEM back-scattered electron image). (u) Colloform bands of pitchblende (Pi) and coffinite (Co) surrounding pitchblende recrystallized at 350 Ma at the unconformity (SEM back-scattered electron image). (v) Late calcite crosscutting pitchblende and colloform bands of pitchblende and coffinite (polarized reflected light). (w) Fragments of corroded siderite surrounded by a sudoitic chlorite (polarized transmitted light). (x) Dickite cluster mixed with Fe-chlorite and replaced on the borders by late kaolinite (plane polarized transmitted light).

Locally, kaolinite or dickite rims bituminous blebs or fills the space between broken fragments of a deformed plumboferrite ($PbFe_4O_7$) within dravite showing that a kaolinite polytype crystallized after the bituminous blebs and before dravite.

Acicular marcasite crystals are locally extensively developed within dravite and display pseudo-sagenite twins showing that they are probably coeval with dravite. Millimeter-size idiomorphic marcasite and euhedral pyrite crystals occur in calcite forming the cement of local calcite breccias (Fig. 12h). Therefore, marcasite is prior to calcite. Calcite is later than dravite as dravite spherulites were locally found included in calcite.

Two phases of calcite crystallization were observed. The first one is represented by veins up to 50 µm in width, possibly hydraulic as they tend to follow the detrital quartz grains borders (Fig. 12i). The second one is characterized by a more or less brownish calcite, finely impregnated by later Fe-rich clay minerals, and crystallized as radiated fans several millimeters in size (Fig. 12h). Locally, this calcite appears to cement angular fragments organized in jigsaw textures indicating hydraulic brecciation. However, most of the idiomorphic and detrital quartz included in calcite display dissolution textures evidencing a dissolution phase prior to the hydraulic brecciation, possibly during sudoite-dravite breccia development.

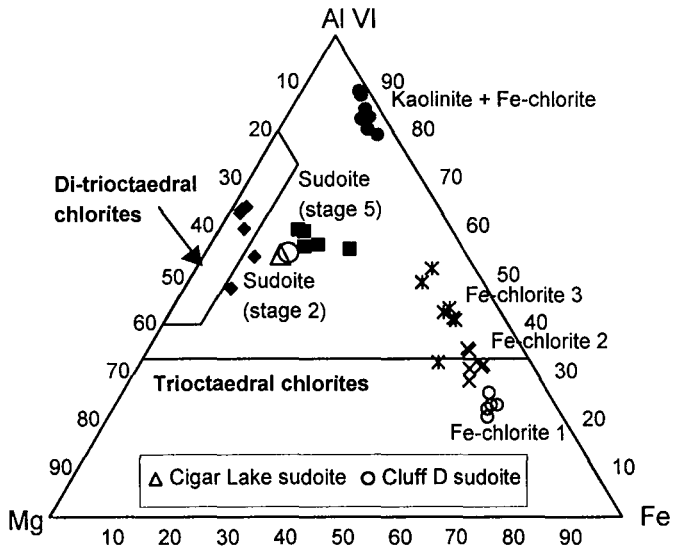

Figure 13 – Classification of Shea Creek chlorites in a AlVI-Mg-Fe ternary diagram. Fe-rich chlorite are trioctahedral whereas Mg-rich chlorites are close to the sudoite field (after Halter, 1988).

Chemical ages: 140 microprobe analysis were realized in the center of a euhedral uraninite several millimeters in size and located at 5 m above the unconformity. The average chemical age obtained with the formulae of Suzuki and Adachi (1994) is 1.21 ± 0.4 Ga, consistent with the range of ages of primary uranium mineralization given in the literature (Hoeve and Quirt, 1984; Lainé, 1985; Fayek and Kyser, 1997). The age of pitchblende mineralization was not determined because of highly variable Pb contents.

Stage 3: This stage corresponds to a second mineralization event associated with the formation of olive green to brownish Fe-chlorite breccias (Fig. 12j) (see annexe I). This event occurred up to 40 m above the unconformity forming perched mineralization, generally of lower grade than the primary unconformity mineralization.

The presence of fragments of skeletal euhedral quartz crystals replaced and brecciated by calcite in Fe-chlorite breccias show that Fe-chlorite is later than stage 2 calcite (Fig. 12k). Fe-chlorite was observed as a cryptocristalline groundmass or as crystals a hundred microns in size associated with corroded detrital and euhedral quartz grains in the matrix.

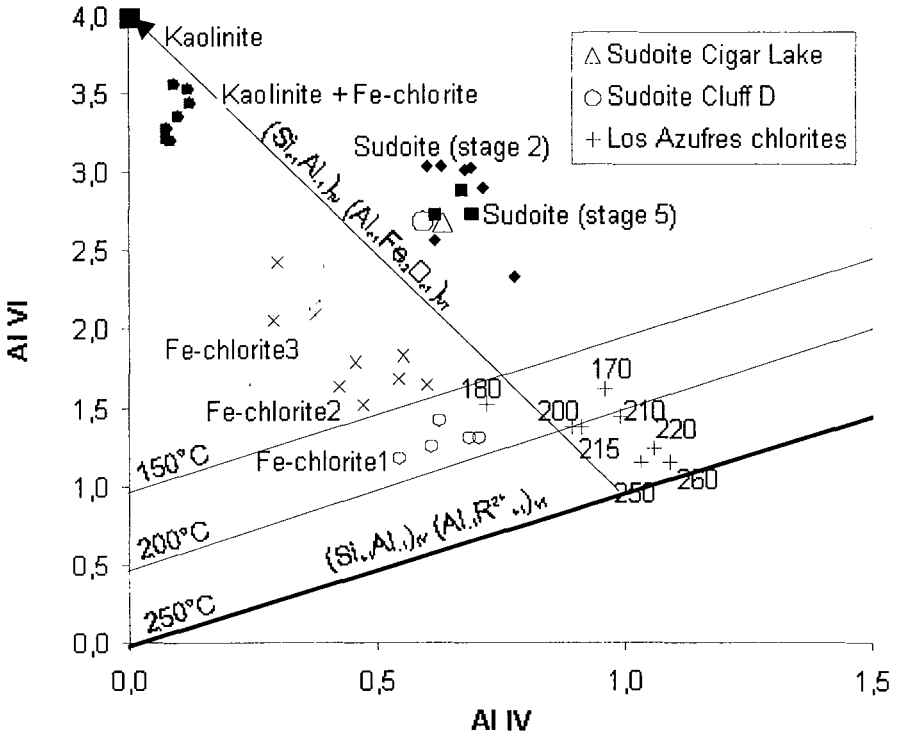

Figure 14 – Representation of chlorites in a AlIV versus AlVI diagram. AlIV and AlVI values of Shea Creek sudoites are very similar to the values of sudoites in the alteration haloes of Cigar Lake and Cluff Lake D unconformity-type uranium deposits. Note the evolution of Fe-chlorites toward the kaolinite pole with time. The temperatures defined by Cathelineau and Nieva (1985) on Los Azufres chlorites are used to determine the approximate temperature of Fe-chlorite 1.

Three different Fe-chlorites have been distinguished based on their chronological relationships and on their location in AlIV versus AlVI and AlVI-Mg-Fe diagrams (Fig. 13 and 14). Fe-chlorites 1, 2 and 3, in chronological order, have the following formula: $(K_{0.01}, Ca_{0.02})$ $(Si_{3.37}\ Al_{0.63})\ Al_{1.3}\ (Mg_{0.65}, Fe_{3.68}, Ni_{0.01})\ O_{10}\ (OH)_8$, $(K_{0.02}, Ca_{0.04})\ (Si_{3.49}\ Al_{0.51})\ Al_{1.69}\ (Mg_{0.54}, Fe_{3.11}, Ni_{0.02})\ O_{10}\ (OH)_8$ and $(K_{0.06}, Na_{0.03}, Ca_{0.03})\ (Si_{3.66}\ Al_{0.34})\ Al_{2.13}\ (Mg_{0.51}, Fe_{2.38}, Ni_{0.01})$ $O_{10}\ (OH)_8$ (Table 2). The presence of K either indicates that they are not pure chlorites or that they are polluted by illite. The AlVI-Mg-Fe ternary diagram (Fig. 13) shows that Fe-chlorite1

and Fe-chlorite2 are trioctahedral. However, trioctahedral chlorites were not detected by XRD analysis. Locally, XRD analysis indicates the possible presence of smectite.

Leaf-shaped siderites and ankerites disseminated in the matrix also formed shortly before or during Fe-chlorite crystallization. Fragments of dravite aggregates impregnated by Fe-chlorite were observed in the matrix (Fig. 12l). They contain disseminated prismatic apatite crystals that probably formed at the beginning of stage 3 as they are not found in pure dravite breccias and as they also occur within Fe-chlorite. Apatite was also observed as tabular prismatic crystals at the surface of a fracture. The association of apatite with dravite may account for a mass transfer of F. Partly corroded early euhedral quartz, probably formed during stage 1, are present on the edge of some collapsed fragments (Fig. 12j). The vugs left after Fe-chlorite crystallization were filled by pyrite growing on the walls of the vugs and then by Fe-rich kaolinite or a cryptocristalline mixing of kaolinite and Fe-chlorite (Fig. 12m).

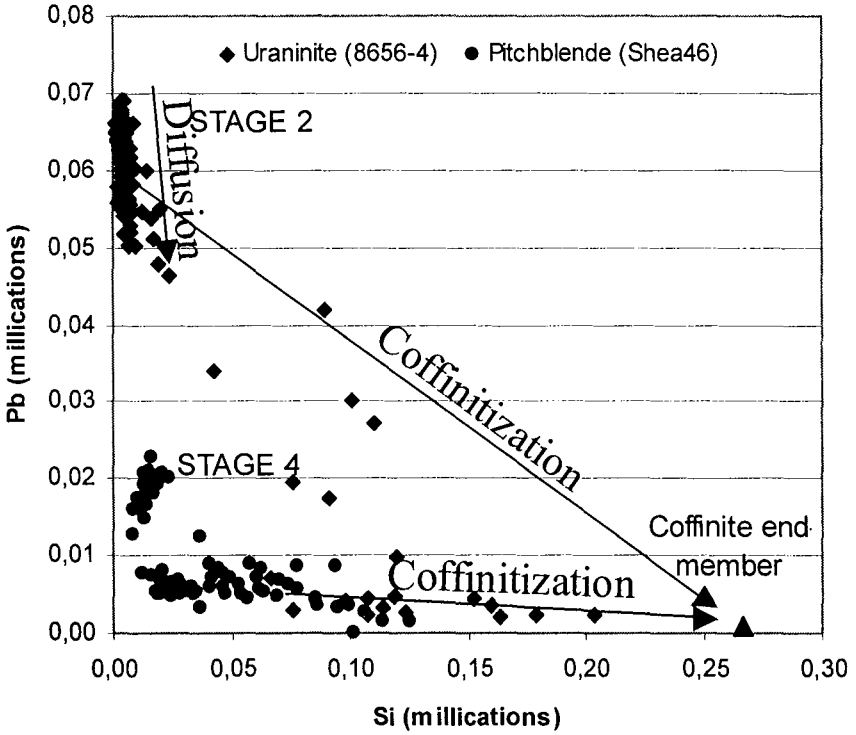

Figure 15 – Si (millications) versus Pb (millications) diagram of stage 2 primary uraninites (1.2 Ga) and of pitchblende. Replacement of Pb by Si in pitchblende by diffusion may have occurred during stage 4 remobilization (350 Ma). A coffinitization trend of uraninite also appears.

Fe-rich kaolinite or kaolinite mixed with Fe-chlorite is very difficult to distinguish from Fe-chlorite, even at microscopic scale. Fe-chlorite also occurred mixed with dickite in previously described breccias. The average formulae of Fe-rich kaolinite or kaolinite mixed with Fe-chlorite is $(K_{0.07}, Na_{0.01}, Ca_{0.01})$ $(Si_{3.9}\ Al_{0.1})$ $(Al_{3.37}\ Fe_{0.55}\ Mg_{0.12})$ (Table 2). The high Fe content (8 % Fe_2O_3 in average, see annexeIV-tableau AIV-20) could correspond to Fe-rich kaolinite minerals as up to 7 % Fe_2O_3 was determined in Fe-rich kaolinite particles by Petit and Decarreau (1990). However, the excess octahedral charge (Al^{3+} + Fe^{3+}) relative to the

tetrahedral charge (Si^{4+}) indicate abundance of Fe oxides external to the kaolinite structure. In addition, the Fe/(Fe+Mg) ratio of these kaolinite is about 0.82 and is similar to the Fe/(Fe+Mg) ratio of Fe-chlorite minerals (between 0.82 and 0.85). Therefore, the formulae is more probably representative of a mixing of kaolinite with Fe-chlorite than a Fe-rich kaolinite.

Idiomorphic zoned skeletal pyrite crystals are disseminated within the Fe-chlorite cement or are grouped in clusters, showing that they are prior to Fe-chlorite (Fig. 12n). Locally, Ni was detected in pyrite by X-ray analysis coupled with SEM indicating the probable existence of bravoite. Pyrite crystals are commonly replaced by pitchblende in their center or along zones. Locally, pyrites are partly replaced to totally pseudomorphosed by carbonaceous matter (Fig. 12o). Carbonaceous matter is occasionally surrounded by pitchblende associated with disseminated euhedral chalcopyrite crystals.

Corroded pitchblende fragments and clusters of pyrite replaced by pitchblende and/or carbonaceous matter are surrounded by a rim of radiated aggregates of more or less corroded elongated prismatic crystals having a composition between pyrite and pyrrhotite, possibly greigite (Fe_3S_4). Pyrrhotite may have formed around pyrite clusters by reduction due to action of C as proposed by Hall (1986). Acicular smythite crystals several hundreds of microns in length occur within the clay matrix generally close to mineralized fragments. A vug occurring within pitchblende contains elongated crystals of pyrite and small pyrite cubes replacing former tabular unidentified crystals. These tabular crystals are surrounded by a thin rim of pitchblende and by coffinite. This shows that phases of pitchblende crystallization alternate with phases of Fe-sulfide deposition.

One phase of pitchblende deposition corresponds to tiny U-oxide inclusions within hematite and Fe-hydroxides nodules impregnating kaolinite mixed with Fe-chlorite (Fig. 12p). A later kaolinite mixed with Fe-chlorite crosscut the uraniferous nodules. Uranium silicates, possibly coffinite, rim corroded pyrites or pitchblende.

A late phase of ankerite and calcite crystallization occurred within vugs or as veins crosscutting Fe-chlorites and sulfides (Fig. 12q). Ankerite crystals formed on the borders of vugs whereas calcite crystallized in the middle. Therefore, calcite is later than ankerite.

Important lead loss in pitchblende precludes from giving any significant chemical age. An approximate age of 900 Ma can be proposed for the Fe-chlorite breccias by comparison with a possibly similar paragenetic sequence (Fe-rich kaolinite or kaolinite mixed with Fe-chlorite) dated 900 ± 50 Ma using a K-Ar method in the Cigar Lake deposit (Philippe et al., 1993).

Chlorite geothermometer: The location of Fe-chlorites 1, 2 and 3 and of later kaolinite mixed with Fe-chlorite in a AlIV versus AlVI diagram (Fig. 14) shows an evolution towards the kaolinite pole possibly due to an increasing abundance of mixed layer kaolinite-chlorite minerals. Cathelineau and Nieva (1985) have established that in a hydrothermal environment, the temperature of crystallization of chlorite decreases linearly parallel to the substitution

vector $(Si_{+1}Al_{-1})_{IV}$ $(Al_{+1}Fe_{-2}\square_{+1})_{VI}$, where □ is the vacancy (Fig. 14). The chlorites of the Los Azufres geothermal field used by Cathelineau and Nieva (1985) were plotted in the AlIV versus AlVI diagram with their estimated temperatures. The isotherms defined by the data at Los Azufres were used to estimate a temperature of crystallization of Fe-chlorites 1 of about 180°C. As the other chlorite types are probably mixed layer minerals, they cannot be compared with Los Azufres chlorites.

Stage 4: This stage is characterized by a weakly mineralized event, located between 30 and 40 m above the unconformity. It is associated with hematite and siderite (see annexe I). Hematite-filled fractures crosscut fractures filled with kaolinite mixed with Fe-chlorite, indicating that hematite is later than these clay minerals (Fig. 12r). Hematite is also present between corroded detrital quartz grains and occasionally as replacement of former euhedral pyrites disseminated in kaolinite mixed with Fe-chlorite. It is frequently found crystallized in radiated aggregates. Hematite-goethite nodules display intergrowths with siderite spherulites in the matrix of polyphase carbonate breccias, showing that siderite, hematite and goethite are coeval (Fig. 12s). Part of the hematite continued to be deposited later as it also surrounds siderite.

The perched mineralization consists of pitchblende enclosing hematite crystals, followed by botryoidal concretions of coffinite in vugs. Very locally, uraninites less than 10 μm in size are included in hematite, showing that it is earlier (Fig. 12t). At the unconformity, primary pitchblende is corroded and contains banded pitchblende and coffinite with colloform textures within vugs or syneresis cracks (Fig. 12u). Calcite veins, usually shallow dipping, crosscut the various uranium mineral phases suggesting late crystallization (Fig. 12v).

A late chlorite generation locally occurs around corroded siderite crystals. (Fig. 12w). XRD analysis indicates a mixture of trioctahedral with some di-trioctahedral chlorite. The average chlorite formulae is $(K_{0.08}, Ca_{0.02})$ $(Si_{3.33}$ $Al_{0.67})$ $Al_{2.79}$ $(Fe_{0.87}$ $Mg_{1.22})$ O_{10} $(OH)_8$. Their location close to the di-trioctahedral chlorite field in a AlVI-Mg-Fe ternary diagram (Fig. 13) shows that they can be assimilated to sudoites. They have similar AlIV, AlVI, Mg and Fe values to the sudoites of the Cigar Lake and Cluff D uranium deposits alteration haloes (Halter, 1988) (Fig. 13 and 14).

Late urchin-like aggregates of goethite crystallized in vugs on hematite or replaced hematite. Kaolinite appears to replace Fe-chlorite in some breccias, however its chronological relationship with Fe-oxi-hydroxides is not clearly established (Fig. 12x). Kaolinite is the latest phase which seems to be still crystallizing in relation with present meteoric fluids circulation (Kotzer and Kyser, 1995).

The observation at macroscopic scale of silicification of solution breccia matrix suggests the occurrence of pervasive silicification posterior to stage 2. Late euhedral quartz crystals, possibly related to this silicification event, occur within vugs of these resilicified solution

breccias. These may have formed by silica reprecipitation after dissolution in zones of solution breccia development during stages 3, 4 or 5.

Chemical ages: A sample taken within a 2 m-thick massive pitchblende mineralization gives a chemical age of 356 ± 23 Ma indicating a probably totally remobilized uranium (Fig. 15). The pitchblende analysed was corroded and surrounded by colloform pitchblende and coffinite. A small unaltered euhedral uraninite of the perched mineralization gives an age of 348 ± 24 Ma. These results suggest that uranium may have been remobilized and/or redeposited at the unconformity during primary pitchblende alteration and recrystallization at about 350 Ma. Part of this remobilized uranium might have moved upward to form the perched mineralization. The chemical age obtained on perched botryoidal concretions of coffinite is 128 ± 9 Ma using the formulae of Montel et al. (1996). The late coffinite bands crystallized around pitchblende at the unconformity have a chemical age of 113 ± 13 Ma. Therefore, the latest event of uranium mineralization or remobilization seems to have occurred at about 120 Ma.

6.3. The Sue C open pit

The mineralogy of two clay balls and of a clay matrix taken within "zones à boules" and of several samples taken at different distances from their walls was studied (see annexe I). XRD analysis and norm calculation indicate that the proportion of dickite decreases from the non-altered zone towards the breccia whereas the illite percentage increases (Fig. 16a, 16b, 16c and 16d). The two clay balls and the clay matrix are mostly composed of massive illite (Fig. 16d). Electron microprobe analysis indicates that illites are locally chloritized or that illite-chlorite mixed layers may exist. They might be 3T illites as documented in the Cluff D "zones à boules" by Halter (1988). Illite crystals have lath shapes with sizes of 2 μm up to 40 μm, indicating higher crystallization temperatures than expected in a diagenetic environment. Clay balls and the matrix display high concentrations of zircons, anatase and schorl (Fig. 16d). Schorls are commonly surrounded by secondary dravite needles overgrowths in strongly argilized samples. Heavy mineral layering is commonly preserved in clay balls. Euhedral LREE-Sr-Ca-Fe aluminous hydroxy-phosphates of the crandallite-goyazite-florencite group occur in all samples with sizes varying from less than 0.1 μm to 2 μm. Their concentration is especially high in the core of the structure.

The mineral paragenesis corresponds to the major hydrothermal stage of uranium mineralization (Fig. 17) (see part III). Euhedral quartz filled fractures were formed during and/or after the diagenetic dickite crystallization. Then, the hydrothermal stage was initiated by tectonic fracturing and developed by quartz dissolution, replacement of dickite by illite and hematite dissolution during "zones à boules" formation (Fig. 16c) (see part III). It is

contemporaneous with the main uranium mineralization. Minor chlorite crystallization and dravite overgrowths on schorl are probably coeval with illitization.

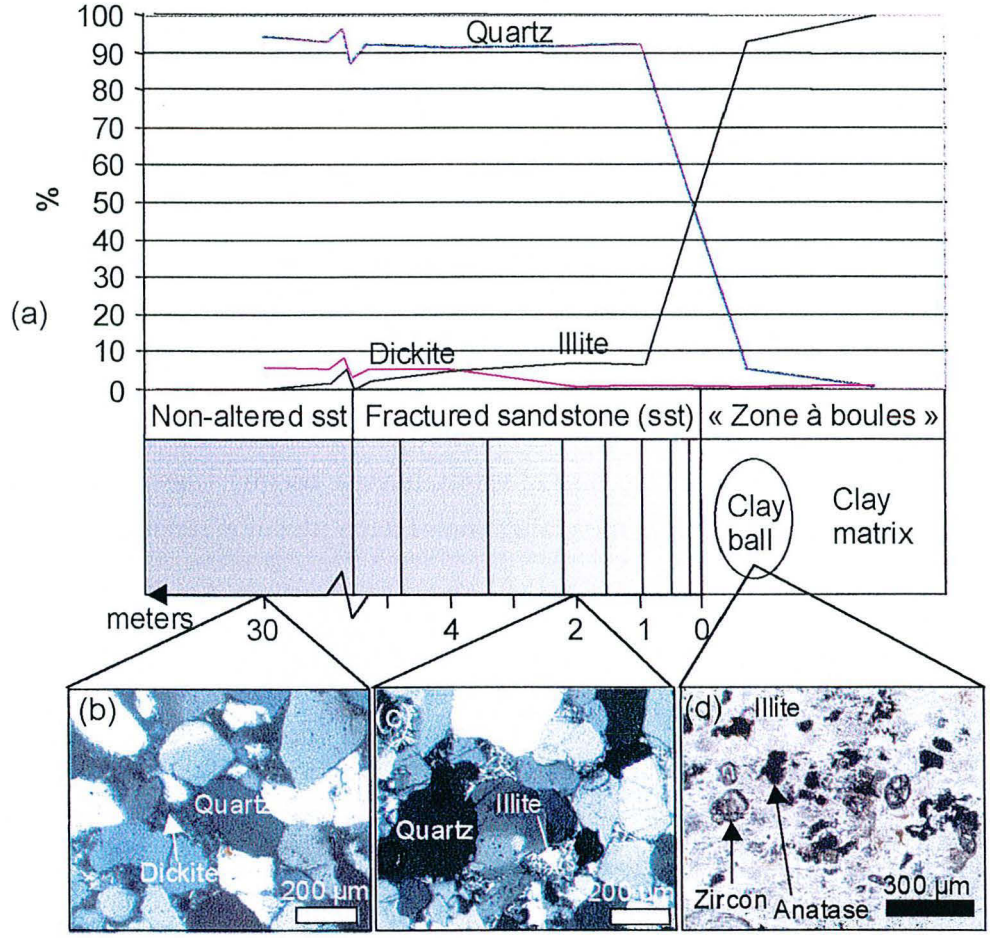

Figure 16 – (a) Schematic « zone à boules » profile showing increase of illite proportion and decrease of quartz and dickite proportion toward the « zone à boules ». (b) Microscopic photograph of non-altered sandstone far from any « zone à boules » showing corroded detrital quartz grains and dickite (plane polarized transmitted light). (c) Microscopic photograph of sandstone located at 2 meters from a « zone à boules ». The dickite is replaced by illite (plane polarized transmitted light). (d) Microscopic photograph of a clay ball. It is composed of massive illite. Note the high concentration of accessory minerals, zircons and anatase mainly (polarized transmitted light).

The Sue C illites (Table 2) have a chemical composition close to the muscovite end-member with a minor celadonitic substitution. The average theoretical illite formulae is $K_{0.8}Si_{3.3}Al_{0.7}(Al,Fe)_{1.9}Mg_{0.1}O_{10}(OH)_2$. The Sue illites have similar chemical composition as illites from the rhyolites of the geothermal Los Azufres area (Cathelineau and Izquierdo, 1988). The average illite interlayer charge (IC) is higher at Sue than at Los Azufres indicating slightly higher temperatures of crystallization (between 240 and 280°C) (see part III). This temperature range is close to the temperature of diagenetic fluids estimated by fluid inclusions, illite cristallinity index and isotope equilibration temperature studies between 200 and 240°C.

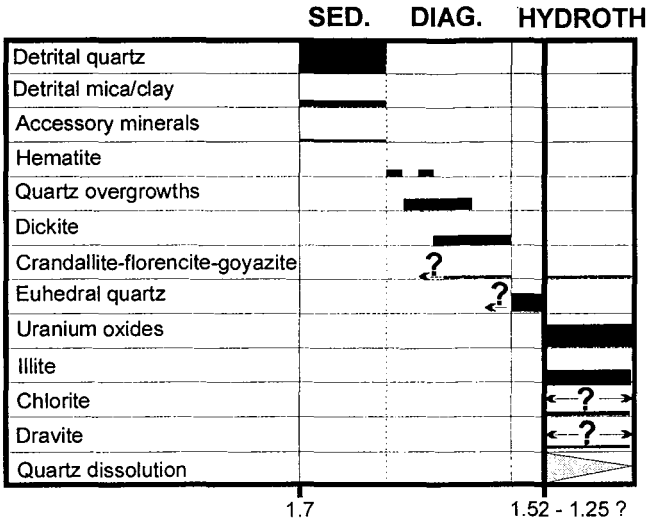

Figure 17 – Mineral paragenesis in the Sue C open pit mine. The diagram represents successively sandstone deposition, diagenesis and the uranium mineralization event. Vertical lines represent fracturing and hydraulic brecciation events. The thickness of the black rectangles is representative of the abundance of the corresponding phase.

7. Mass balance calculations

Mass balance calculations are strongly dependant of the choice of the protolith. An ideal protolith is a non-altered sample having the same mineralogical and chemical composition than the altered rock before the alteration. The apparent homogeneity of quartzose Athabasca sandstones suggests that the selection of a protolith should be easy. However, the immobile elements Ta, Ti, Nb, Hf and Zr used for mass balance calculations are present within detrital heavy minerals whose concentrations are highly variable. Therefore, the choice of a protolith in the Athabasca sandstone is particularly difficult, especially in the coarse-grained to conglomeratic basal Manitou Falls formation which globally contains a higher proportion of detrital heavy minerals than the overlying formations.

Al is also generally immobile in diagenetic sedimentary environments as it participates in mass transfer rather than mass transport processes (Hutcheon, 2000). Al solubility at 300°C in uncomplexing media is very low, about 10^{-6} mol / kg at pH = 4.5 after Salvi et al. (1998). As it is concentrated within interstitial clay minerals of the sandstone, Al content is variable but less than Ta, Ti, Nb, Hf and Zr. Therefore, Al was considered to be the best immobile element and was used for mass balance calculations at Sue and some of the Shea Creek samples. However, at the Maw Zone, the presence of newly formed dravite in strongly silicified sandstone where little Al was available and where no volume loss occurred suggests that Al was mobile. Consequently, Al was also probably mobile during the formation of sudoite-dravite breccias at Shea Creek. Some samples of Fe-chlorite breccias at Shea Creek display jigsaw textures with non-corroded fragments separated by a Fe-chlorite and kaolinite cement.

Sample	8956-3 Protolith 1	8956-5 Protolith 2	MC98-3 Protolith 3	Average protolith (Shea Creek)	SHEA2	SHEA7	SHEA28	SHEA16	SHEA 11
Drill hole	Erc1	Erc1	Erc1	-	Dgs11	She62	She62	She16	Dgs9
Depth (meters)	162.6	303.2	793	-	611.8	716	718.9	711	704.1
Unc. depth	796.3	796.3	796.3	-	707.2	724	724	723.15	706.2
U ore depth (grade)	-	-	-	-	-	-	-	718.6 (high)	-
Breccia type or lithology	sandstone	sandstone	sandstone	sandstone	Microcryst. quartz	Sudoite-dravite	Sudoite-dravite	Sudoite-dravite	Sudoite-dravite
Stage	-	-	-	-	1	2	2	2	2
Density	2.54	2.54	2.41	2.50	2.44	-	2.29	2.35	2.52
SiO2 (%)	98.7	96.7	97.0	97.4	99.0	89.4	88.6	97.4	93.6
TiO2	0.03	0.03	0.22	0.09	0.03	1.30	0.95	0.05	1.46
Al2O3	0.4	0.4	0.4	0.4	0.4	5.4	4.6	1.0	1.0
Fe2O3 (total)	0.2	1.9	1.9	1.3	0.1	0.4	0.9	0.3	0.2
MgO	0.07	0.07	0.07	0.07	0.1	1.0	1.5	0.4	0.5
MnO	0.02	0.02	0.02	0.02	0.02	0.02	0.02	0.02	0.02
CaO	0.07	0.07	0.07	0.07	0.1	0.1	0.1	0.1	0.1
Na2O	0.03	0.03	0.03	0.03	0.03	0.03	0.03	0.03	0.03
K2O	0.09	0.03	0.03	0.05	0.03	0.13	0.05	0.03	0.03
P2O5	0.06	0.07	0.03	0.05	0.03	0.16	0.11	0.03	0.10
CO2	0.06	0.39	0.04	0.16	0.8	0.17	0.07	0.07	6.63
S	0.007	0.007	0.007	0.007	0.007	0.06	0.12	0.046	0.015
FeO	0.01	0.56	0.05	0.21	0.03	0.06	0.31	0.14	0.15
PF	0.21	0.53	0.38	0.37	0.68	2.04	2.06	0.68	3.32
As (ppm)	1.0	0.8	0.3	0.7	0.3	4.3	17.2	11.1	1.2
B	14	9	28	17	87	295	255	285	64
Ba	17	12	7	12	2	21	11	2	9
Be	0.6	0.6	0.6	0.6	0.6	1.3	1.7	0.6	0.6
Bi	0.03	0.03	0.03	0.03	0.24	0.85	0.36	4.33	0.07
Cd	0.2	0.2	0.2	0.2	0.2	0.2	0.4	0.5	0.2
Co	0.2	0.2	0.2	0.2	0.2	1.0	3.4	70.5	0.7
Cr	3	8	9	7	3	31	25	11	22
Cu	3	3	3	3	3	18	26	147	11
Ga	0.6	0.9	1.1	0.9	0.8	8.4	7.3	2.9	2.0
Ge	0.66	0.65	0.63	0.65	0.71	1.11	1.05	1.02	0.84
Hf	0.89	1.89	4.13	2.30	1.18	25.23	21.37	3.23	24.21
In	0.1	0.1	0.1	0.1	0.07	0.07	0.07	0.07	0.07
Mo	0.1	0.2	0.2	0.1	0.1	0.3	0.8	0.8	0.2
Nb	0.6	0.6	3.1	1.4	0.3	18.1	13.0	1.0	18.7
Ni	3	3	3	3	3	37	93	585	10
Pb	3.0	4.0	1.5	2.9	4	19	18	9	8
Rb	1.5	0.7	1.6	1.3	0.7	2.3	1.2	0.7	0.7
Sb	0.7	0.1	0.7	0.5	0.07	0.3	0.9	1.3	0.2
Sn	0.3	0.3	0.4	0.3	0.3	2.0	1.6	0.3	0.6
Sr	84	133	48	88	17	335	197	17	157
Ta	0.06	0.07	0.39	0.17	0.04	2.40	1.73	0.11	2.28
Th	1.88	2.80	10.4	5.0	1.62	75.03	47.91	2.55	80.69
U	0.5	0.7	1.0	0.7	2.8	28.6	31.3	9.7	18.7
V	2	4	12	6	1	53	49	72	19
W	0.1	0.2	0.2	0.2	0.1	6.2	4.1	0.4	2.1
Y	2.17	3.13	5.58	3.63	1.43	39.19	19.96	17.50	6.54
Zn	3	3	3	3	3	29	27	88	14
Zr	32.5	70.8	174.6	92.6	43.0	987.0	868.0	112.0	998.0
La	8.63	12.65	9.5	10.3	10.56	129.75	73.16	6.16	66.83
Ce	18.17	27.94	21.80	22.64	21.82	247.36	141.30	11.39	124.70
Pr	1.98	2.84	2.20	2.34	2.46	27.38	14.87	1.19	13.29
Nd	7.3	9.4	9.0	8.5	8.8	90.7	53.0	4.1	43.5
Sm	1.25	1.59	1.53	1.46	0.96	12.53	7.56	0.81	4.51
Eu	0.20	0.27	0.16	0.21	0.09	1.60	0.91	0.18	0.51
Gd	0.88	1.36	1.07	1.10	0.33	6.96	3.89	1.68	1.94
Tb	0.12	0.16	0.15	0.15	0.05	1.25	0.59	0.39	0.26
Dy	0.52	0.74	0.94	0.73	0.30	6.95	3.32	2.77	1.41
Ho	0.08	0.12	0.18	0.13	0.05	1.24	0.60	0.57	0.22
Er	0.26	0.34	0.39	0.33	0.15	3.30	1.70	1.34	0.75
Tm	0.03	0.05	0.07	0.05	0.03	0.42	0.23	0.19	0.12
Yb	0.26	0.33	0.56	0.38	0.19	2.75	1.58	1.06	0.85
Lu	0.04	0.05	0.08	0.06	0.03	0.40	0.27	0.16	0.16

Table 1

Sample	SHEA21	SHEA 13	SHEA 10	SHEA22	SHEA24	SHEA 12	SHEA1
Drill hole	Dgs11	She80	She66	She12	She12	She16	She79
Depth (m.)	690.6	697.6	675.5	702.3	701.3	702.5	709.1
Unconformity depth	707.2	717	701.9	709.5	709.5	723.15	717.4
U ore depth	-	716.5 (moder.)	668 (moder.)	709 (low)	709 (low)	718.6 (high)	716 (high)
Breccia type	Sudoite-dravite	Dravite	Dravite	Calcite	Calcite	Fe-chlorite	Fe-chlorite
Stage	2	2	2	2	2	3	3
Density	2.45	2.37	2.42	2.65	2.65	2.32	2.41
SiO2 (%)	95.5	97.1	92.5	77.7	78.2	84.3	87.7
TiO2	0.22	0.05	0.19	0.09	0.07	0.22	0.09
Al2O3	1.4	0.9	3.9	0.8	0.7	4.0	1.2
Fe2O3 (total)	0.3	0.1	0.6	1.0	1.5	7.1	6.3
MgO	0.9	0.2	1.1	0.3	0.3	1.0	0.7
MnO	0.02	0.02	0.02	0.29	0.30	0.02	0.15
CaO	0.1	0.1	0.1	10.6	10.2	0.2	0.1
Na2O	0.03	0.03	0.05	0.03	0.03	0.05	0.03
K2O	0.03	0.03	0.03	0.03	0.03	0.03	0.03
P2O5	0.03	0.03	0.05	0.14	0.12	0.10	0.06
CO2	0.05	0.17	0.1	7.99	7.55	0.44	3.05
S	0.007	0.007	0.015	0.29	0.62	0.18	0.18
FeO	0.19	0.1	0.18	0.36	0.43	2.01	4.01
PF	0.70	0.47	1.40	8.35	8.05	3.26	3.53
As (ppm)	0.3	4.1	0.7	90.5	76.6	35.0	96.4
B	130	450	1495	280	215	1320	160
Ba	2	2	6	11	10	16	9
Be	0.6	0.6	1.3	0.6	0.6	2.1	0.6
Bi	0.03	0.18	0.08	48.39	16.88	63.79	38.27
Cd	0.2	0.2	0.2	0.2	0.2	0.2	0.2
Co	2.5	0.6	1.6	0.9	0.3	137.8	38.6
Cr	12	9	19	18	16	47	13
Cu	8	25	7	24	19	138	68
Ga	2.7	2.0	8.1	2.2	1.8	8.0	2.5
Ge	0.81	0.85	1.71	0.70	0.68	1.59	0.89
Hf	11.74	2.84	8.88	3.21	2.74	8.85	3.74
In	0.07	0.07	0.07	0.07	0.07	0.8	0.3
Mo	0.4	0.3	0.5	11.0	6.9	1.6	0.8
Nb	3.5	0.9	3.3	1.6	1.2	3.6	1.8
Ni	17	6	20	9	3	224	139
Pb	8	4	8	72	63	109	39
Rb	0.7	0.7	0.7	0.7	0.7	0.7	0.7
Sb	0.2	0.07	0.7	1.3	1.0	1.2	4.4
Sn	0.7	0.3	1.1	0.3	0.3	0.3	0.8
Sr	17	17	57	468	378	306	104
Ta	0.37	0.10	0.44	0.17	0.14	0.32	0.19
Th	5.38	2.54	15.91	4.93	4.02	8.07	6.13
U	16.3	16.5	47.5	27.0	25.6	175.0	987.0
V	22	41	31	39	26	222	82
W	2.1	0.2	0.5	0.9	0.7	3.6	1.2
Y	7.16	6.49	21.83	38.79	39.27	30.09	11.46
Zn	15	5	6	8	8	6	7
Zr	469.0	110.8	348.3	126.4	99.1	328.4	138.4
La	7.11	5.18	22.42	31.97	25.69	38.23	21.95
Ce	13.71	9.98	46.82	71.33	55.78	75.01	49.98
Pr	1.49	1.05	5.17	7.78	6.15	7.82	6.20
Nd	4.9	4.2	17.8	29.0	22.7	27.0	24.7
Sm	0.88	0.64	2.72	4.50	3.21	4.70	3.65
Eu	0.12	0.10	0.42	0.76	0.58	1.04	0.63
Gd	0.71	0.66	2.38	4.04	4.10	4.86	2.52
Tb	0.16	0.14	0.51	0.97	1.06	0.92	0.41
Dy	1.15	0.87	3.57	6.59	6.95	5.68	2.27
Ho	0.24	0.19	0.74	1.23	1.24	1.05	0.40
Er	0.61	0.47	1.68	2.72	2.75	2.58	1.01
Tm	0.11	0.07	0.24	0.32	0.32	0.38	0.15
Yb	0.84	0.42	1.47	1.72	1.66	1.99	0.85
Lu	0.15	0.06	0.22	0.23	0.22	0.28	0.11

Table 1

Sample	SHEA3	SHEA15	SHEA20	SHEA19	MAW1 (protolith)	MAW5	MAW7	MAW9
Drill hole	She16	She12	She12	She93	outcrop	outcrop	84-4	84-4
Depth	696.8	698.8	706	719.9	0	0	8	44.2
Unconformity	723.15	709.5	709.5	737	~270	~270	~270	~270
U ore depth	718.6 (high)	709 (low)	709 (low)	725-735 (low)	~270	~270	~270	~270
Breccia type	Fe-chlorite	Fe-chlorite	Fe-chlorite	Polyphase carbonate	Sandstone (with dravite)	dravite	dravite	Dravite+ quartz
Stage	3	3	3	4	-	-	-	-
Density	2.56	2.54	2.55	3.03	2.62	2.62	2.59	2.61
SiO2 (%)	76.5	85.4	88.5	57.9	98.9	98.2	96.1	94.5
TiO2	0.05	0.23	0.40	0.38	0.03	0.03	0.03	0.03
Al2O3	1.2	2.8	3.6	1.9	0.5	1.0	1.9	3.1
Fe2O3 (total)	11.9	6.1	4.5	27.5	0.07	0.07	0.07	0.07
MgO	1.3	0.8	0.7	0.4	0.07	0.2	0.4	0.6
MnO	0.48	0.18	0.02	0.07	0.02	0.02	0.02	0.02
CaO	0.9	0.4	0.1	0.1	0.07	0.07	0.07	0.07
Na2O	0.03	0.03	0.06	0.03	0.03	0.03	0.03	0.03
K2O	0.03	0.07	0.03	0.03	0.03	0.03	0.03	0.03
P2O5	0.24	0.05	0.09	0.03	0.03	0.03	0.03	0.05
CO2	7.72	2.61	0.19	11.92	0.05	0.04	0.05	0.06
S	0.37	0.033	0.37	0.011	0.007	0.007	0.007	0.007
FeO	8.59	3.91	1.82	20.96	0.03	0.03	0.03	0.03
PF	7.42	3.70	2.17	11.56	0.21	0.29	0.48	0.77
As (ppm)	603.8	24.4	46.1	1.3	0.6	0.7	0.7	0.7
B	155	600	1435	150	220	545	1030	2130
Ba	26	7	25	8	7	6	8	7
Be	1.1	0.6	2.7	1.2	0.6	0.6	0.6	0.6
Bi	164.24	5.08	3.35	3.58	0.03	0.03	0.12	0.06
Cd	0.2	0.2	0.2	0.2	0.2	0.2	0.2	0.2
Co	236.4	0.4	5.5	0.4	0.2	0.2	0.2	0.2
Cr	22	19	23	17	25	326	34	43
Cu	377	8	57	8	3	3	6	8
Ga	4.1	4.6	6.6	3.5	1.4	3.1	5.1	7.3
Ge	0.78	1.01	1.51	0.86	0.80	0.94	1.45	1.51
Hf	3.34	6.18	7.99	11.94	3.51	0.92	2.73	1.35
In	1.9	0.07	0.07	0.07	0.07	0.07	0.07	0.07
Mo	2.0	0.9	1.3	1.6	0.1	0.1	0.1	0.1
Nb	1.1	3.9	6.0	5.6	0.8	0.4	0.8	0.4
Ni	208	5	46	11	3	3	3	3
Pb	161	28	52	10	1.7	1.2	1.8	1.8
Rb	0.7	0.7	0.7	0.7	0.7	0.7	0.7	0.7
Sb	2.6	0.3	3.0	0.5	0.07	0.07	0.07	0.07
Sn	0.3	0.3	0.3	0.8	0.3	0.3	0.3	0.3
Sr	966	118	153	78	21	28	22	20
Ta	0.11	0.44	0.71	0.58	0.08	0.04	0.07	0.04
Th	3.96	11.19	15.25	14.92	2.29	1.59	3.20	1.83
U	226.0	25.4	383.0	31.0	1.7	0.6	1.9	2.9
V	45	58	93	48	10	20	33	54
W	0.8	1.7	3.4	2.0	0.6	0.1	0.1	0.2
Y	7.07	35.78	15.04	27.96	3.62	2.54	4.89	48.10
Zn	11	7	9	9	3	3	3	3
Zr	130.5	238.3	282.6	456.1	135.2	34.1	113.0	53.2
La	90.95	30.81	19.34	22.81	7.16	8.67	6.51	5.06
Ce	191.50	62.73	54.98	44.80	14.30	17.48	13.73	10.02
Pr	20.05	7.24	8.15	4.93	1.41	1.67	1.33	1.08
Nd	68.3	27.0	31.0	17.2	5.0	5.5	4.1	3.7
Sm	8.18	3.95	7.06	3.14	0.68	0.74	0.67	0.67
Eu	1.30	0.66	1.45	0.48	0.13	0.12	0.11	0.25
Gd	3.89	3.91	3.71	3.31	0.54	0.55	0.54	2.47
Tb	0.55	0.94	0.68	0.68	0.11	0.08	0.13	1.00
Dy	1.97	5.96	3.43	4.49	0.63	0.42	0.80	7.32
Ho	0.27	1.11	0.55	0.85	0.13	0.08	0.15	1.42
Er	0.81	2.74	1.41	2.13	0.32	0.22	0.37	3.19
Tm	0.09	0.41	0.20	0.31	0.05	0.04	0.06	0.39
Yb	0.53	2.08	1.36	1.93	0.35	0.25	0.38	2.33
Lu	0.08	0.29	0.17	0.31	0.06	0.04	0.07	0.30

Table 1 - Major and trace elements geochemical and density data for the Shea Creek and Maw Zone samples used for mass balance calculations. When values were less than the detection limit, the 2/3 value of the detection limit was systematically attributed.

Area	Sue	Shea	Shea	Shea	Shea	Shea	Shea	Shea
Type of clay	Illite	Illite + sudoite? (II)	Sudoite (II)	Sudoite (IV)	Fe-chlo (III-1)	Fe-chlo (III-2)	Fe-chlo (III-3)	Kaol + Fe-chlo (III)
n	27	7	7	5	5	6	7	7
Si (IV)	3.30	3.13	3.33	3.33	3.37	3.49	3.66	3.90
Al (IV)	0.70	0.87	0.67	0.67	0.63	0.51	0.34	0.10
Al (VI)	1.87	1.22	2.84	2.79	1.30	1.69	2.13	3.37
Fe^{2+}	0.03 (Fe^{3+})	0.53 (Fe^{3+})	0.20	0.87	3.68	3.11	2.38	0.55 (Fe^{3+})
Mg	0.10	0.5	1.77	1.22	0.65	0.54	0.51	0.12
Mn	0.00	0.01	0.00	0.00	0.00	0.00	0.00	0.00
K	0.80	0.47	0.07	0.08	0.01	0.02	0.06	0.07
Na	0.00	0.02	0.01	0.00	0.00	0.00	0.03	0.01
Ca	0.00	0.02	0.01	0.02	0.02	0.04	0.03	0.01
Ni	0.00	0	0.05	0.00	0.01	0.02	0.01	0.00
IC	0.80	0.54	0.10	0.12	0.06	0.10	0.16	0.10
Fe+Mg+Mn+Ni	0.13	1.04	2.02	2.09	4.34	3.67	2.90	0.67
6-(AlVI+Fe+Mg+Mn+Ni)	4	3.74	1.14	1.12	0.36	0.64	0.97	1.96
Fe/(Fe+Mg+Mn+Ni)	0.23	0.51	0.01	0.42	0.85	0.85	0.82	0.82

Table 2 - Average half structural formula and IC parameter (interlayer charge) of Sue illites, Shea Creek chlorites and kaolinites. All the Fe present in the Sue illites and Shea Creek kaolinites mixed with Fe-chlorite is assumed to be trivalent whereas Fe in chlorites is assumed to be divalent.

Consequently, sudoite, dravite, Fe-chlorite and kaolinite crystallizations do not result from mass transfer but rather from mass transport of Al. Instead of Al, Zr has been chosen as immobile element in these samples because its content is generally higher than Th and Ta and because recent studies have demonstrated that Zr is only very slightly removed during alteration (Hecht and Cuney, 2000). In order to take into account the variability of initial immobile elements budget, an uncertainty domain of 50 % enrichments and 50 % depletions was defined.

Mass balance calculations were performed by the use of the Grant method in the three zones of study (Table 1) (see annexe III). This method is originally dedicated to be used for pervasive and homogeneous alterations. In the case of breccia samples, the results of the method are dependent on the proportion of matrix. The main phenomena that occurred in the studied breccias is quartz dissolution accompanied with volume loss. Estimation of this volume loss is necessary to quantify the amount of dissolved quartz and the element enrichment/depletion factors due to fluid/rock interactions.

The fluid/rock ratios associated with the different hydrothermal alteration phases in the three zones of study were calculated using the quartz solubility and the amount of dissolved quartz during each phase. The quartz solubility value of 10^{-2} mol / kg in pure water at 250°C and 100 MPa (Tester et al., 1994) was chosen in order to represent the peak diagenetic conditions during the hydrothermal events. The vertical maturity gradient defined between the

low mature Maw Zone breccias and the mature Shea Creek and Sue breccias (§ 5.3) shows a decrease of the dissolution intensity from the unconformity upward. Therefore, the fluid undersaturation in silica was higher at the unconformity and lower above. As the fluid undersaturation decreased with time due to re-equilibration with quartz, the fluid was migrating upward along the reverse structure in the sandstone. A silica saturation of 90 % just above the unconformity for Sue and Shea Creek and of 99 % 200 m above the unconformity at the Maw Zone were considered in fluid/rock ratio calculations to reflect the increase in silica saturation of the basement fluids migrating upward. However, these values are hypothetical because they cannot be constrained precisely yet. For a silica saturation of 90 % and 99 %, the quartz solubility is 10^{-3} and 10^{-4} mol / kg, respectively.

7.1. The Maw Zone

At the Maw Zone, 3 strongly silicified breccia samples were studied, namely Maw5, Maw7 and Maw9 (see annexe I). The protolith Maw1 is a brecciated sandstone sample with a low matrix percentage about 10 % and with a higher detrital quartz proportion than the other samples (Table 3). It was selected in spite of its slight alteration because of its proximity to the other samples. This proximity allows to compare samples with a similar initial sandstone composition. Maw5 has a slightly green color. Its matrix percentage is difficult to measure due to the very progressive transition between the matrix and the sandstone but is estimated at about 15 %. Maw7 has 35 % matrix. Euhedral quartz in a vug indicate late silicification after quartz dissolution and dravite precipitation. Maw9 is a polyphase hydraulic breccia with a matrix mainly composed of newly formed quartz. Newly formed quartz crystals grew on earlier dravite coatings on sandstone fragments.

The pervasive character of the dravitization and the low matrix percentage in sample Maw5 suggest no to very little volume loss. Therefore, constant volume was considered in mass balance calculations for this sample (Fig. 18). The isocon diagram for sample Maw7 indicates a slight volume increase if Zr is taken as an immobile element (Fig. 18). However, the slight Zr depletion in sample Maw7 relative to the protolith is more probably related to the variability of Zr content in the sandstone. As Zr is located close to the constant volume isocon, constant volume was also assumed in this sample. The strong depletion in Zr relative to the protolith in sample Maw9 suggests volume increase (Fig. 18) consistent with the hydraulic breccia texture of the sample. The calculated volume increase is about 61 % considering Zr immobile. The volume increase due to hydraulic brecciation only is probably higher than 61 % but this value also includes volume loss due to the quartz dissolution phase.

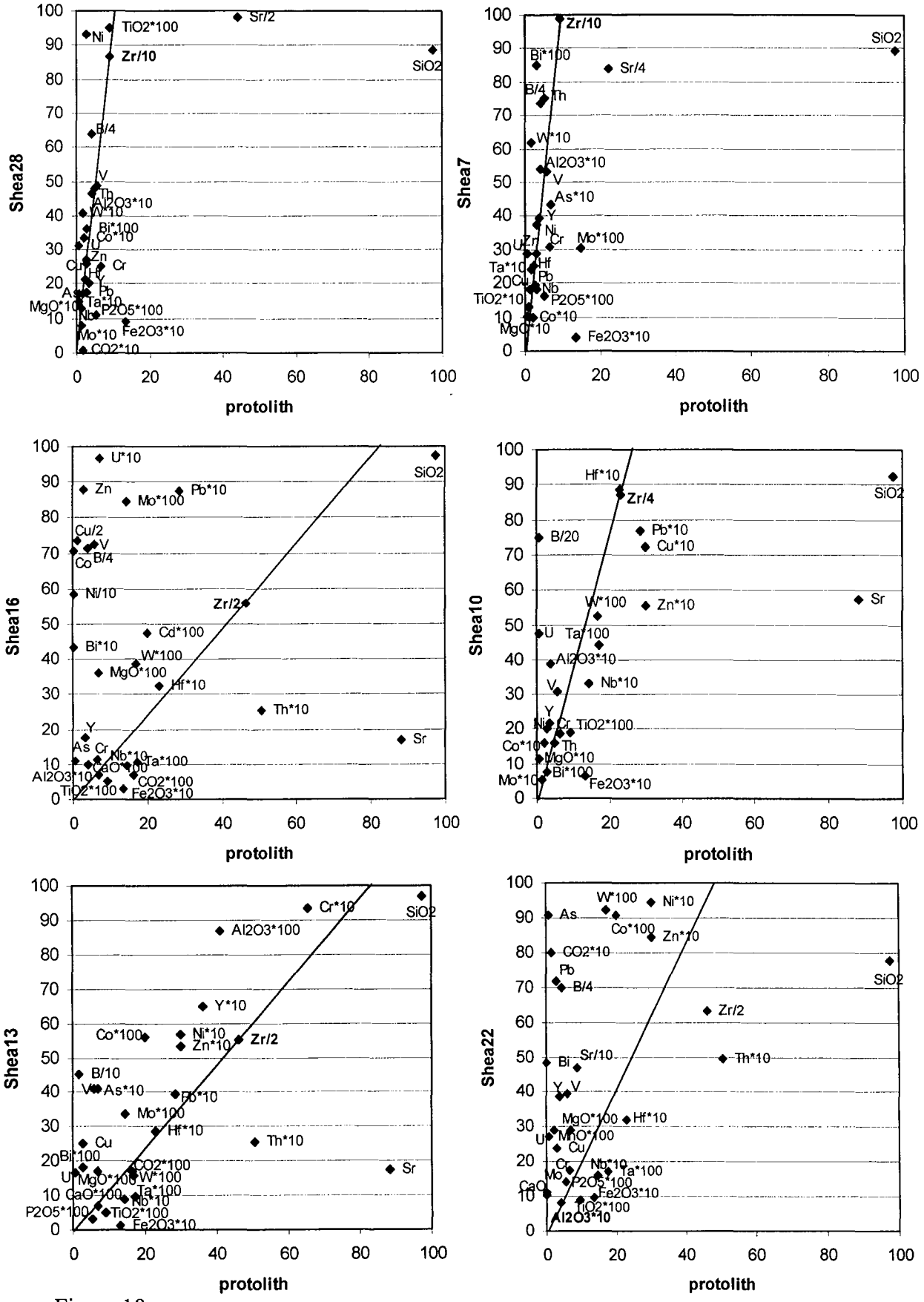
Shea28
protolith
Sr/2
TiO2*100
Ni
Zr/10
SiO2
B/4
V
Th
Al2O3*10
W*10
Bi*100
Co*10
U
Zn
Cr
Cu
Hf
Pb
As
MgO*10
Ta*10
Nb
P2O5*100
Mo*10
Fe2O3*10
CO2*10
Shea7
protolith
Zr/10
SiO2
Bi*100
Sr/4
B/4
Th
W*10
Al2O3*10
V
As*10
Y
Ni
Cr
Mo*100
U
Zn
Ta*10
Hf
Pb
20Cu
Nb
TiO2*10
P2O5*100
Co*10
MgO*10
Fe2O3*10
Shea16
protolith
U*10
SiO2
Zn
Pb*10
Mo*100
Cu/2
V
Co
B/4
Ni/10
Zr/2
Cd*100
Bi*10
W*100
MgO*100
Hf*10
Th*10
Y
Sr
As
Cr
Nb*10
Ta*100
CaO*100
Al2O3*10
CO2*100
TiO2*100
Fe2O3*10
Shea10
protolith
Hf*10
Zr/4
SiO2
B/20
Pb*10
Cu*10
Sr
W*100
Zn*10
U
Ta*100
Al2O3*10
Nb*10
V
Y
Ni
Cr
TiO2*100
Co*10
Th
MgO*10
Mo*10
Bi*100
Fe2O3*10
Shea13
protolith
Cr*10
SiO2
Al2O3*100
Y*10
Co*100
Ni*10
Zn*10
Zr/2
B/10
V
As*10
Pb*10
Mo*100
Hf*10
Th*10
Cu
Bi*100
Sr
CO2*100
U
MgO*100
W*100
CaO*100
Ta*100
Nb*10
P2O5*100
TiO2*100
Fe2O3*10
Shea22
protolith
W*100
Ni*10
As
Co*100
Zn*10
CO2*10
Pb
SiO2
B/4
Zr/2
Bi
Sr/10
Th*10
Y
V
MgO*100
Hf*10
U
MnO*100
Cu
Cr
Nb*10
Mo
Ta*100
CaO
P2O5*100
Fe2O3*10
TiO2*100
Al2O3*10

Figure 18

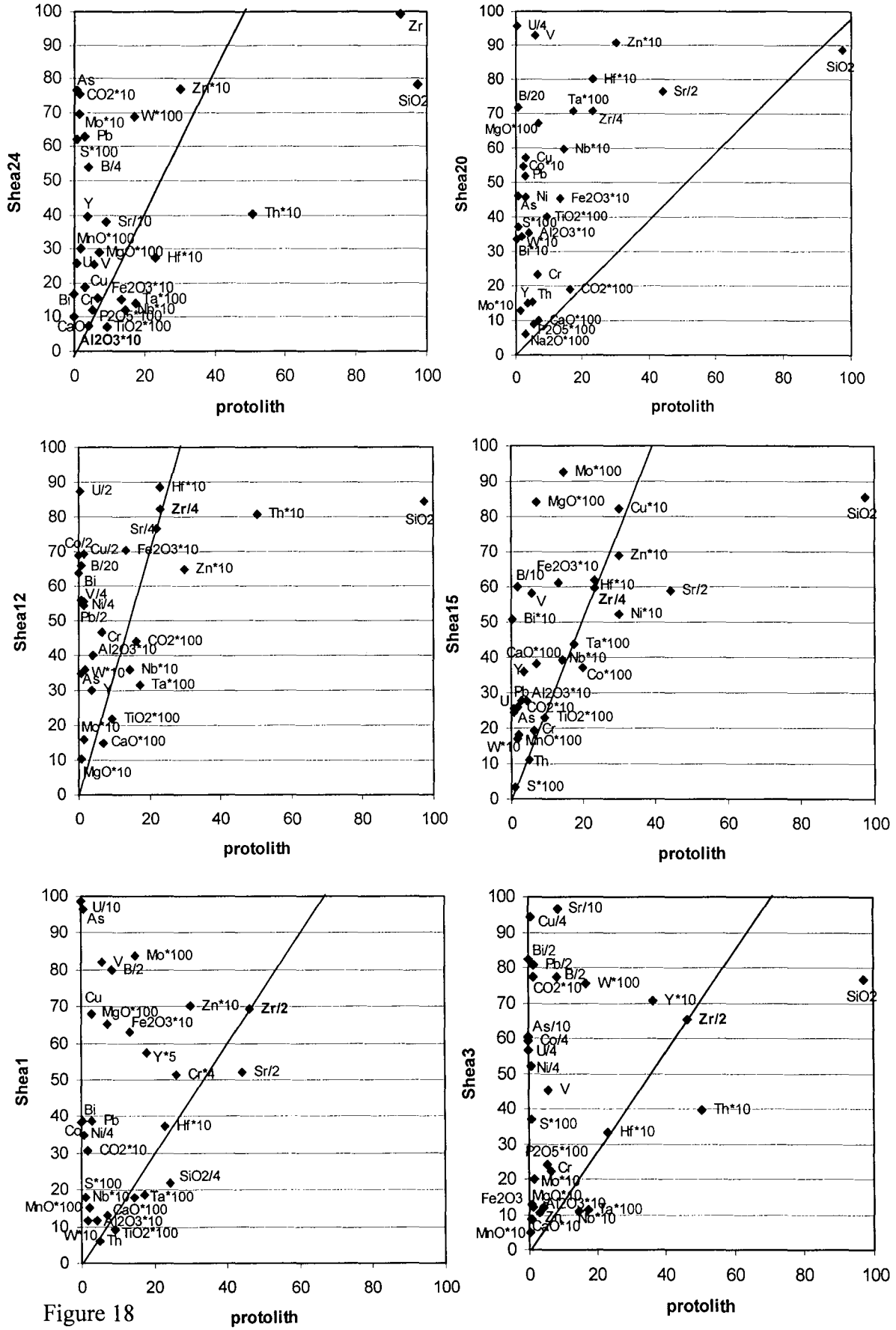
Shea24
protolith
Zr
SiO2
As
CO2*10
Zn*10
W*100
Mo*10
Pb
S*100
B/4
Y
Th*10
Sr/10
MnO*100
MgO*100
Hf*10
U
V
Cu
Fe2O3*10
Bi
Cr
Ta*100
Nb*10
P2O5*100
CaO
TiO2*100
Al2O3*10
Shea20
protolith
U/4
V
Zn*10
SiO2
Hf*10
Sr/2
B/20
Ta*100
MgO*100
Zr/4
Nb*10
Cu
Co*10
Pb
Ni
As
Fe2O3*10
S*100
TiO2*100
Al2O3*10
W*10
Bi*10
Cr
Y
Th
CO2*100
Mo*10
CaO*100
P2O5*100
Na2O*100
Shea12
protolith
U/2
Hf*10
Zr/4
Th*10
SiO2
Sr/4
Co/2
Cu/2
Fe2O3*10
B/20
Zn*10
Bi
V/4
Ni/4
Pb/2
Cr
CO2*100
Al2O3*10
W*10
Nb*10
As
Ta*100
TiO2*100
Mo*10
CaO*100
MgO*10
Shea15
protolith
Mo*100
MgO*100
Cu*10
SiO2
Zn*10
B/10
Fe2O3*10
Hf*10
Sr/2
V
Zr/4
Ni*10
Bi*10
Ta*100
CaO*100
Nb*10
Y
Co*100
Pb
Al2O3*10
U
CO2*10
As
TiO2*100
Cr
MnO*100
W*10
Th
S*100
Shea1
protolith
U/10
As
V
Mo*100
B/2
Cu
MgO*100
Zn*10
Zr/2
Fe2O3*10
Y*5
Cr*4
Sr/2
Bi
Pb
Co
Hf*10
Ni/4
CO2*10
SiO2/4
S*100
Nb*10
Ta*100
MnO*100
CaO*100
Al2O3*10
W*10
TiO2*100
Th
Shea3
protolith
Sr/10
Cu/4
Bi/2
Pb/2
B/2
CO2*10
W*100
Y*10
SiO2
Zr/2
As/10
Co/4
U/4
Ni/4
V
Th*10
S*100
Hf*10
P2O5*100
Cr
Mo*10
Fe2O3
MgO*10
Al2O3*10
Ta*100
Zn
Nb*10
MnO*10
CaO*10

Figure 18

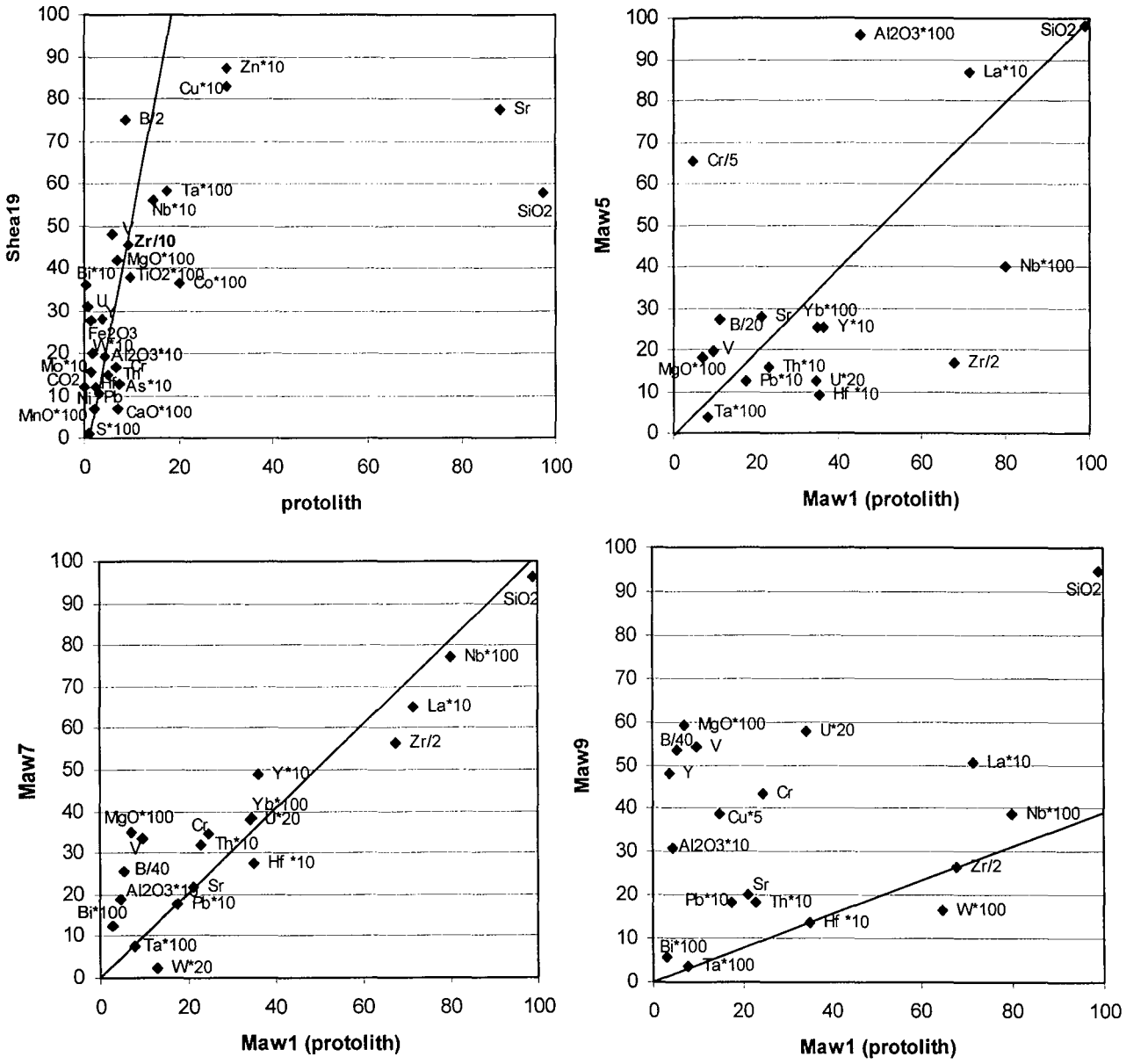

Figure 18 – Isocon diagrams for the Maw Zone and Shea Creek samples. The immobile element (Al or Zr) used to trace the isocon in each diagram is in bold character. The angle between the isocon and the bissector corresponds to the amount of volume loss. The location of elements above or below the isocon indicates enrichment or depletion respectively, taking into account the effect of volume loss. Constant volume was used to trace the isocon for samples Maw5, Maw7 and Shea20. Note the volume increase in sample Maw9 due to late hydraulic brecciation. Note the common depletion in Si due to quartz dissolution and responsible for important volume loss.

Elemental enrichment/depletion diagrams for samples Maw5 and Maw7 indicate enrichments in Mg, B, Al and V, in order of decreasing importance (Fig. 19). Mg, B and Al enrichments are related to dravite crystallization. Cr and Bi are strongly enriched in sample Maw5 and Maw7, respectively. Cr enrichment is related to Cr-rich dravite as documented by Quirt et al. (1991). In sample Maw5, the abundance of Cr, and therefore of Cr-rich dravite, would explain the slightly green color of the sample (Table 1). The maximal enrichment/depletion factors increase from sample Maw5 to sample Maw9 together with the

increase of the matrix percentage, indicating increasing hydrothermal alteration. Almost all the elements are enriched in sample Maw9 except W (Fig. 19). The depletion in W reflects enrichment of the slightly altered protolith due to the high mobility of W.

Enrichments in Y, V, Cu, Bi, U, As and Pb, together with the dravite alteration, suggest that the hydrothermal fluids were the same than those responsible for unconformity-type uranium mineralization. The REE patterns normalized to the protolith and corrected by the volume variations are presented in figure 20 for the 3 samples. The sample Maw5 appears to be depleted in HREE. Variations for the sample Maw7 are limited. The sample Maw9 shows a spectacular enrichment in HREE, simultaneous with Y and P enrichment indicating xenotime mineralization.

As the fluids circulated on 250 m from the unconformity to the Maw Zone, they had time to partially equilibrate with quartz. Therefore, a high silica saturation of 99 % was chosen. A fluid/rock ratio of about 3,000 was calculated for samples Maw5 and Maw7 assuming 10 % of matrix (Table 3).

7.2. The Shea Creek area

The average chemical composition of 3 non-altered samples with different heavy mineral layers abundance was chosen in order to get an average of the quantity of accessory and clay minerals and therefore of Al and Zr contents. The 3 samples were taken in a non-altered and non-mineralized drill hole located 5 km west of the Shea Creek exploration zone. The samples studied are presented in chronological order.

Sudoite-dravite breccias have been studied on 5 samples, namely Shea28, Shea7, Shea16, Shea10 and Shea13 (see annexe I). Shea28 and Shea7 are pure matrix samples. They have a low dravite proportion and are located at several tens of meters laterally of the unconformity mineralization. The isocon diagrams of these samples indicate a strong volume loss estimated at 88 % assuming immobile Zr for Shea28 (Figure 18 and table 3). The high friability of Shea7 did not allow the measure its density and therefore to estimate any volume loss for this sample. Shea16 is a sudoite breccia with 30 % of matrix and has a low proportion of dravite (table 3). It is located 7 m above a strongly mineralized zone. The isocon diagram shows a volume loss of 12 %. Shea10 is a sudoite-dravite breccia with 50 % matrix and about 8.2 % of sudoite and 4.4 % of dravite (table 3). The isocon diagram of Shea10 indicates significant volume loss calculated at 73 % assuming Zr immobility (Fig. 18). Shea13, with 10 % of matrix and about the same proportion of sudoite as dravite, has a volume loss of 12 %. These results show that volume loss increases with volumic matrix percentage. As the matrix percentage is difficult to estimate, it is not possible to establish a precise relationship between the 2 parameters.

	quartz	dravite	sudoite	Fe-chlorite	Kaolinite + Fe-chlorite	Kaolinite /dickite	illite	calcite	ankerite	siderite	pyrite	hematite	TiO2	total	Matrix %	Volume loss %	Fluid /rock ratio
Shea28	83.3	0.8	10	0	0	2.4	0.5	0	0	0	0	0	0.95	97.95	100	88	36712
Shea7	83	0.9	8.3	0	0	5	1.3	0	0	0	0	0	1.3	99.8	100	~80-90	37171
Shea16	96	0.8	3	0	0	0	0	0	0	0	0	0	0	99.8	30	12	7328
Shea10	87.9	4.4	8.2	0	0	0	0	0	0	0	0	0	0	100.5	50	73	30676
Shea13	96.1	1.3	1.4	0	0	0	0	0	0	0	0	0	0	98.8	10	12	6939
Shea22	76.4	0	0	2.5	1.1	0	0	18.9	0	0	0	0	0	98.9	35	53	24500
Shea24	77	0	0	2	1.1	0	0	18.1	0	0	0	0	0	98.2	40	48	22641
Shea20	83.1	4.2	0	9.3	1.6	0	0	0	0	0	0.7	0	0	98.9	50 (pseudo)	0	6471
Shea12	75.8	3.9	0	21.1	0	0	0	0.3	0	0	0.3	0	0	101.4	75	70	31506
Shea15	81.4	1.8	0	4.7	3.4	0	0.7	0	1.5	5.3	0	0	0	98.8	60	62	27229
Shea1	84.4	0.5	0	9.3	0	0	0	0	0.5	7.5	0.3	0	0	102.5	35	31	16877
Shea3	75	0.5	0	4.7	0.6	0	0	0.8	1.7	13.5	0.7	0	0	97.5	20	31	18229
Shea19	55.7	0	3.6	0	0	1.9	0	0	0	31.4	0	5.6	0	98.2	50	83	35512
8956-3	98.2	0	0	0	0	0.3	0.8	0	0	0	0	0	0	99.3	0	0	-
8956-5	96.2	0	0	0	0	1	0	0	0	0	0	0	0	97.2	0	0	-
MC98-3	96.5	0	0	0	0	1	0	0	0	0	0	0	0	97.5	0	0	-
Maw5	97.6	1.6	0	0	0	0	0	0	0	0	0	0	0	99.2	15	0	4803
Maw7	95	3.1	0	0	0	0	0	0	0	0	0	0	0	98.1	35	0	11352
Maw9	92	6.3	0	0	0	0	0	0	0	0	0	0	0	98.3	50	-61 (gain)	?
Maw1	98.7	0.65	0	0	0	0	0	0	0	0	0	0	0	99.35	10	0	-

Table 3 – Results of the norm calculations for the Shea Creek and Maw Zone samples. The matrix and volume loss percentages as well as the fluid/rock ratios are also given. The fluid/rock ratios have been calculated assuming a silica saturation of 90 % and 99 % at Shea Creek and at the Maw Zone, respectively.

Enrichments in B, Mg and Al reflect sudoite and dravite new formation in the 5 samples (Fig. 19). Enrichments in U, Ni, Co, As, S, Bi, Cu, Zn, V and Mo are typical of complex-type deposits and are directly associated with the mineralizing fluids. In Shea16, the maximal elemental enrichment factors are one to two orders of magnitude greater than those of the other samples, probably due to its close proximity to high grade U mineralization. Fe, Si, Sr and P have been leached out, in order of decreasing importance. The leaching of quartz, expressed by Si depletion, is the main factor controlling volume loss. Fe depletion is due to the leaching of primary hematite. Depletions in Sr and P correspond to leaching of diagenetic goyazite.

Taking into account volume loss, Shea28 appears to be depleted in HREE relative to the protolith (Fig. 21). REE content variations for Shea7 are within the uncertainty domain. The samples Shea16, Shea10 and Shea13, located close to mineralization, show depletions in LREE and enrichments in intermediate to heavy REE. LREE depletion, together with P, is probably due to diagenetic florencite leaching. Enrichments in intermediate to heavy REE, together with Y, are related to xenotime replacement of zircon or new formation (Fig. 12d) (Quirt et al., 1991). Part of the phosphorus of xenotime may come from crandallite-group mineral leaching. Xenotime may be U-rich explaining the enrichments in U of the samples. Such enrichments in intermediate to HREE are also typical of uranium oxides (Pagel et al., 1987; Quirt et al., 1991; Fayek and Kyser, 1997) and suggest that uranium mineralization may have been present in these samples and leached out.

Hydraulic calcite breccias occurring at the end of stage 2 are represented by samples Shea22 and Shea24 (see annexe I). With matrix percentages of 40 and 35 %, they show volume losses of 53 and 48 %, respectively (Fig. 18 and table 3). This volume loss represents the quartz dissolution phase that occurred during sudoite-dravite breccia formation, partially compensated by volume increase due to hydraulic brecciation.

Ca, C and Mn enrichments are due to calcite crystallization. The calcite cement results from mass transport of Ca and C (Fig. 19). Enrichments in Mg and B correspond to local dravite crystallization prior to the calcite. Mg is also incorporated in late Fe-chlorite impregnating the calcite. Like in sudoite-dravite breccias, Fe and Si have been leached out due to hematite and quartz dissolution, respectively. Significant enrichments in Bi, As, S, Mo, U and Pb are due to the close vicinity of uranium mineralization 8 m below the 2 samples. As in sudoite-dravite breccias, intermediate and heavy REE have been enriched together with Y (Fig. 21). That suggests xenotime new formation and/or the existence of a previous mineralization leached out and partly replaced by calcite. Sr enrichment indicates probable goyazite new formation (Fig. 19).

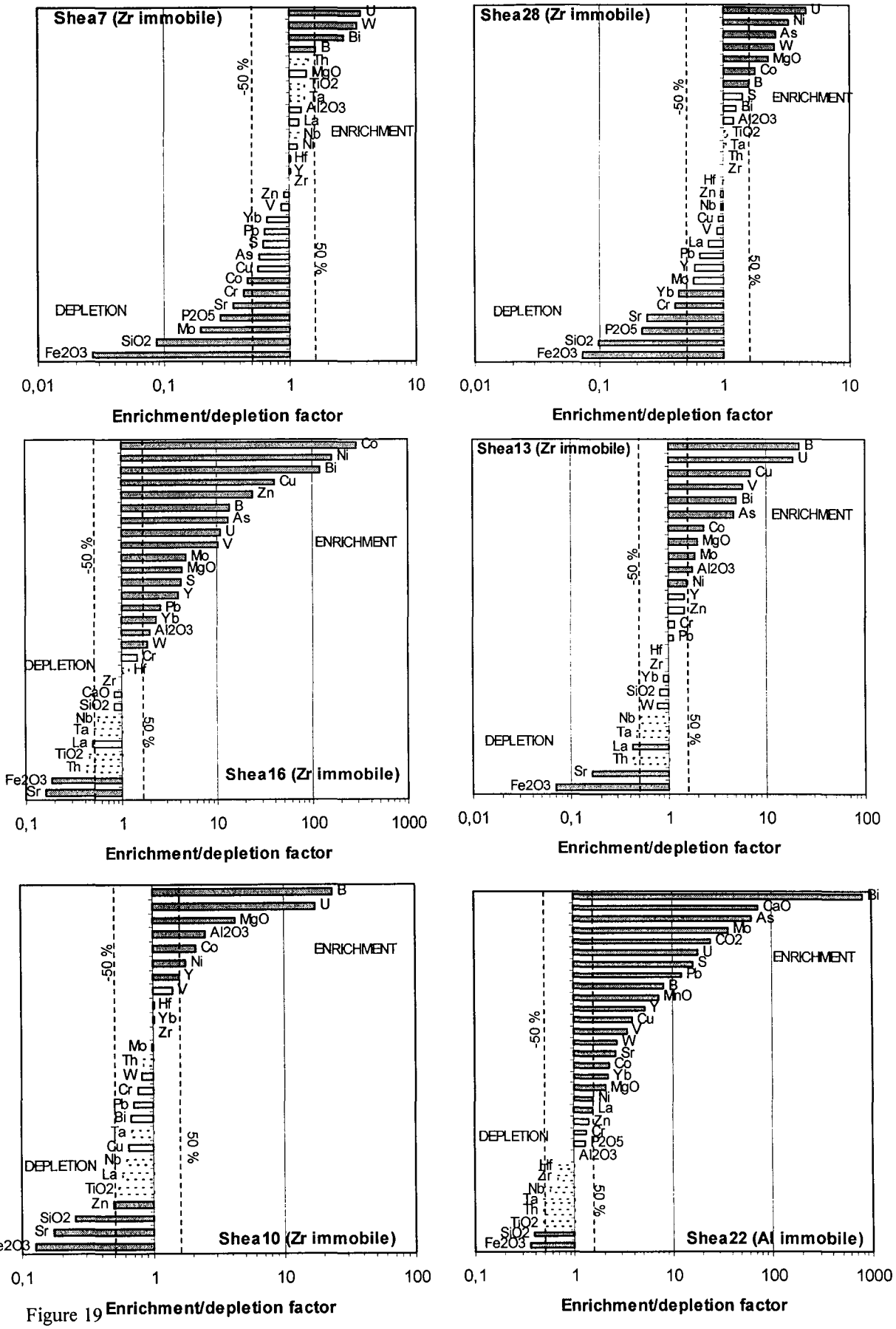
Shea7 (Zr immobile)
Shea28 (Zr immobile)
Shea16 (Zr immobile)
Shea13 (Zr immobile)
Shea10 (Zr immobile)
Shea22 (Al immobile)
ENRICHMENT
DEPLETION
-50 %
50 %
Enrichment/depletion factor

Figure 19

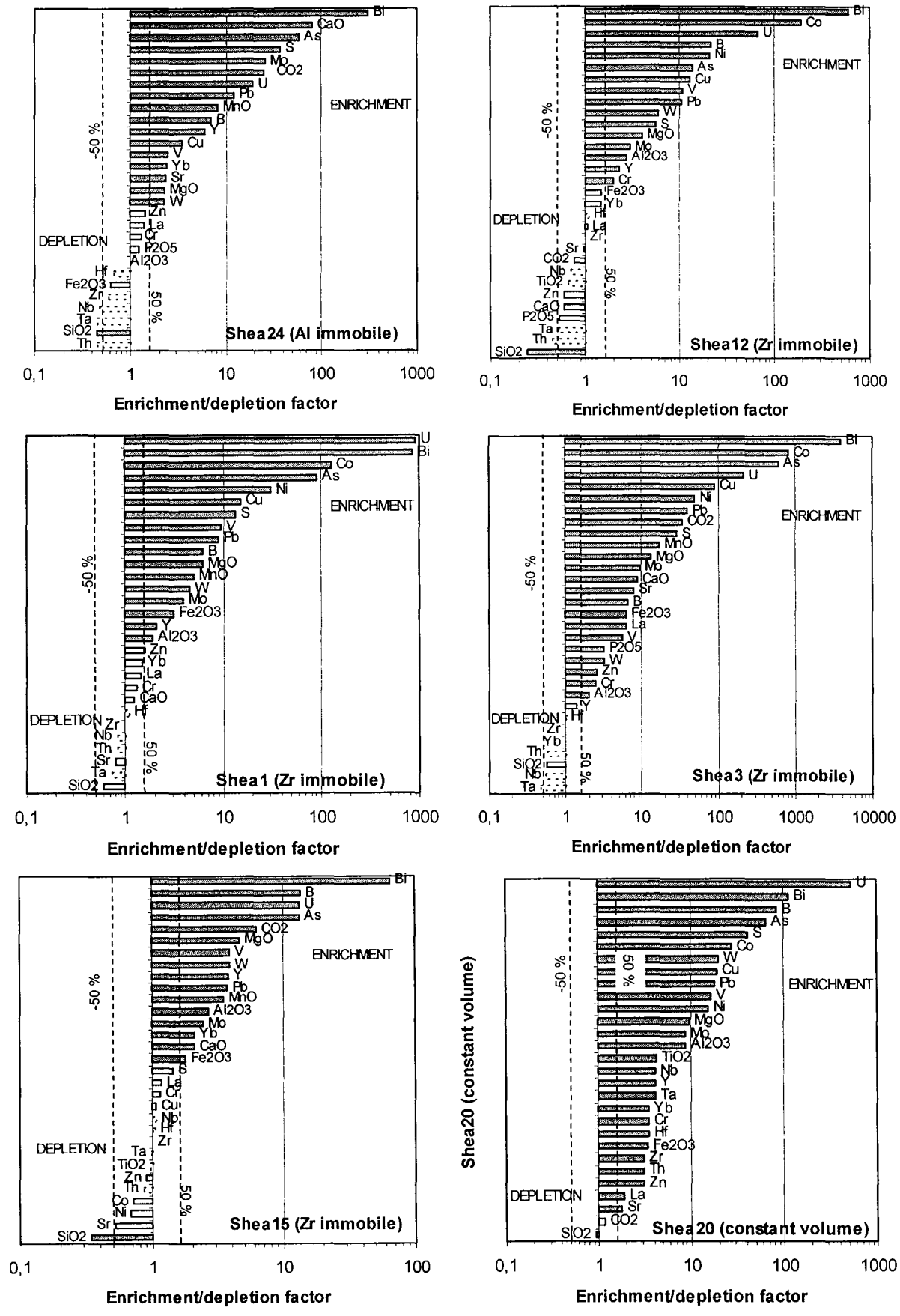
Shea24 (Al immobile)
Shea12 (Zr immobile)
Shea1 (Zr immobile)
Shea3 (Zr immobile)
Shea15 (Zr immobile)
Shea20 (constant volume)
ENRICHMENT
DEPLETION
-50 %
50 %
Enrichment/depletion factor
Shea20 (constant volume)

Figure 19

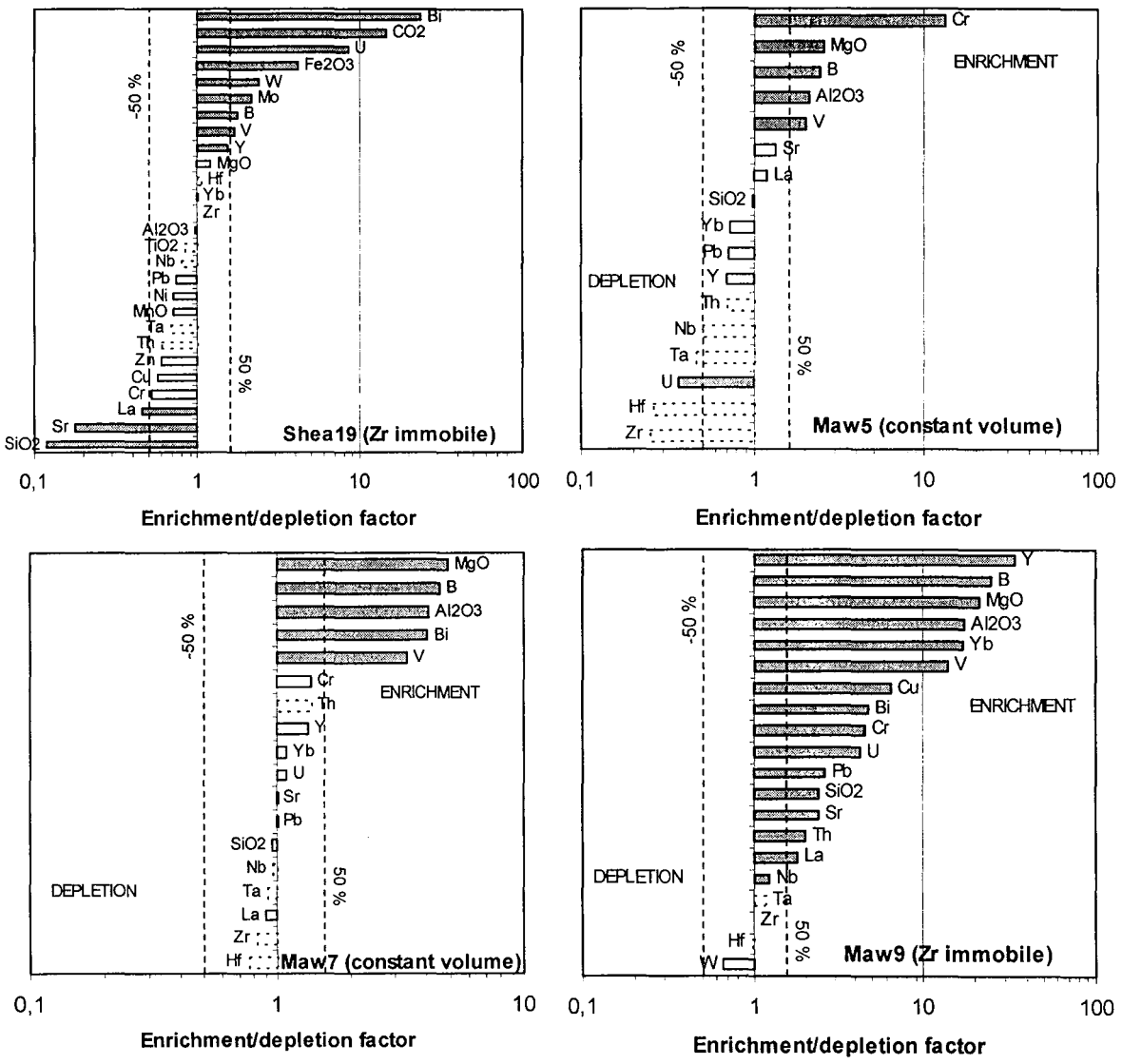

Figure 19 - Elemental enrichment/depletion factors diagrams for the Maw Zone and Shea Creek samples. Dashed white bars correspond to changes of concentration of stable elements due to different initial concentration in the sample and the protolith. White bars indicate a high uncertainty due to weak concentrations variations, below 50 % enrichment and 50 % depletion. Grey bars correspond to reliable chemical variations. Note the enrichments in Mg, B and Al related to dravite crystallization.

The stage 3 of Fe-chlorite brecciation is represented by samples Shea20, Shea12, Shea15, Shea1 and Shea3 (see annexe I). These 5 samples are all located within 25 m above unconformity uranium mineralization. Shea1 is slightly mineralized. The Shea20 sample is a pseudo-breccia showing a Fe-chlorite corrosion front propagating from a fracture network in the sandstone (Fig. 8c). Consequently, no volume loss or gain occurred. If constant volume is assumed, the slope of the isocon is the ratio of the protolith density over the sample density. Most elements including Al are strongly enriched (Fig. 18). As Al was clearly mobile, Zr was used instead of Al for mass balance calculations for samples Shea12, Shea15, Shea1 and

Shea3. Calculated volume losses for Shea12, Shea15, Shea1 and Shea3 are 70, 62, 31 and 31 % with matrix percentages of 75, 60, 35 and 20, respectively (Fig. 18 and table 3). Like in sudoite-dravite breccias, there is a good positive correlation between the matrix percentage and the amount of volume loss.

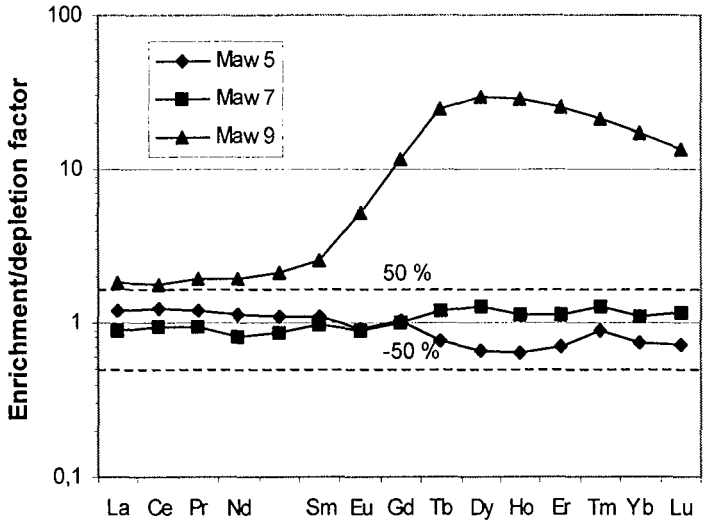

Figure 20 - REE pattern normalized to the protolith Maw1 and corrected from the volume variations for the Maw Zone samples. The 2 dashed lines indicate the interval of uncertainty. Note the strong enrichment in HREE in sample Maw9, associated with Y enrichment.

Bi, U, Co, B, As, S, Ni, Cu, V, W, Pb, Mg, Mo, Mn, C, Al, Fe and Y are enriched in order of decreasing importance (Fig. 19). Bi, Co, As, S, Ni, Cu, Pb and Mo enrichments are related to sulfides and arsenides forming the polymetallic mineralization. V is commonly present within the clay minerals associated with the mineralization. Enrichments in B indicate that Fe-chlorite breccias occurred in already dravitized zones. Enrichments in Mg and Al are partially due to stage 2 dravite but also to Fe-chlorite new formation. Fe enrichment is explained by Fe-rich clays, sulfides and carbonates crystallization. C, Ca, Mn and Fe enrichments correspond to ankerite and siderite new formation. Si depletion is due to quartz dissolution.

REE patterns normalized to the protolith of Shea12 and Shea15 are similar to those of the calcite breccias with strong intermediate to heavy REE enrichments compatible with the significant enrichment in Y of these samples (Fig. 21). They might indicate xenotime new formation, either during stage 3 or during stage 2, or the existence of a previous uranium oxides mineralization. The sample Shea20, located below Shea15 and closer from U mineralization, shows a high intermediate and heavy REE enrichment and an almost equivalent enrichment of LREE. The Shea1 REE pattern is almost flat with a slight enrichment in intermediate and heavy REE due to uranium oxides mineralization. The sample Shea3,

closer from high grade U mineralization than Shea12, is strongly enriched in LREE. Such enrichment can be correlated with the high Sr and P enrichments in this sample, suggesting new formation of goyazite-florencite minerals. A positive Eu enrichment anomaly is present in each of the 5 samples, suggesting a very low fO_2 that stabilized Eu^{2+} by sorption on surface of Ca-rich minerals (Bau and Möller, 1991). Such a reducing environment is consistent with the presence of Fe-sufides and Fe-chlorites.

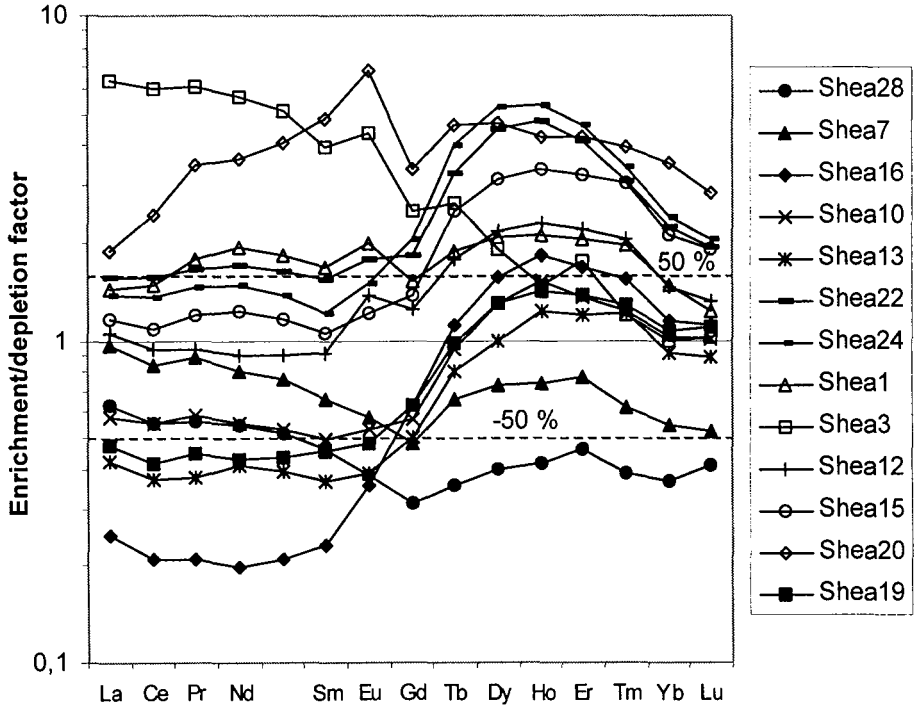

Figure 21 – REE pattern normalized to the protolith and corrected from the volume variations for the Shea Creek samples. The 2 dashed lines indicate the interval of uncertainty. Most of the samples are enriched in HREE and tend to be depleted in LREE.

The stage 4 of hematite and siderite breccias is represented by sample Shea19 (see annexe I). Late sudoite with a similar composition as stage 2 sudoite occurs in this sample. This suggests that Al may have been mobile like in stage 2. Therefore, Zr was used instead of Al for mass balance calculations. The calculated volume loss is 83 %. Bi, C, U, Fe, W, Mo, B, V and Y are enriched, in order of decreasing importance (Fig. 19). Si, Sr and LREE are the main elements depleted, in order of decreasing importance. C and Fe are related to siderite crystallization. Si depletion is related to quartz dissolution. B enrichment reflects stage 2 dravite crystallization.

LREE are strongly depleted and intermediate to heavy REE slightly enriched (Fig. 21). LREE and Sr depletions are related to goyazite-florencite minerals leaching. Intermediate to

heavy REE and Y enrichments are probably due to xenotime new formation or to uranium oxides that have been leached out.

Fluid/rock ratios

Fluid/rock ratios were calculated for each sample assuming a silica saturation of the fluid of 90 % (table 3) (see annexe III). This silica saturation value is lower than the value used at the Maw Zone in order to account for the fact that fluids were just emerging from the basement and did not have time to equilibrate with quartz. The average fluid/rock ratios integrated at the breccia bodies scale are approximately 5,000, 7,000, 6,000, 6,000 and 7,000 for sudoite, dravite, calcite, Fe-chlorite and polyphase carbonate breccias, respectively, considering 10 % of matrix.

7.3. The Sue C open pit

The Sue "zones à boules" are characterized by strong Si depletion and K and Rb enrichments due to massive quartz dissolution and illite replacement of diagenetic dickite (see part III). Quartz dissolution was accompanied by about 85 % volume loss, assuming immobile Al. Like at the Maw Zone and at Shea Creek, hydrothermal fluids brought V, B, U, Bi, Mg and Y, in order of decreasing importance, into the Sue "zone à boules" whereas Fe has been leached out. W, Zn, Sr, LREE and Cr are also enriched like in some Shea Creek breccias like Shea3. In addition to quartz dissolution and illite crystallization, enrichments and depletions reflect newly formed sudoite, dravite and crandallite-florencite-goyazite group minerals crystallization and hematite dissolution. The clay matrix displays the same chemical variations as the clay balls, with the exception of REE, Y, Sr and Zn. In the matrix, LREE, Sr and Zn are enriched whereas HREE and Y have been leached out. LREE and Sr are probably associated in newly formed minerals of the crandallite-florencite-goyazite group. Calculations on REE changes of concentration in the whole "zone à boule", using an estimation of 65 % for the matrix percentage, show no significant variations for HREE whereas LREE are enriched. Therefore, the alteration resulted in a chemical partitioning between clay balls, enriched in HREE, and the clay matrix, enriched in LREE.

Assuming a silica saturation of 90 %, the calculated fluid/rock ratio is greater than 38,000 for a totally illitized zone (see part III).

Conclusions

Breccias at the Maw Zone, at Shea Creek and at Sue are characterized by Si depletion and volume loss due to quartz dissolution. The volume loss increases with matrix percentage (Fig. 22). Fe is depleted due to primary hematite leaching. V, Bi and U are enriched indicating that the same mineralizing fluids have circulated in the 3 areas. Systematic Mg enrichment is related to a basement fluid involved in the crystallization of dravite at the Maw Zone, Mg-rich sudoite and dravite at Shea Creek and Mg-rich illite at Sue. As enrichment at the Maw Zone and As, S and Ni enrichments at Shea Creek also evidence local specific signature of the basement fluid. Intermediate and heavy REE and Y are strongly enriched at the Maw Zone, and to a lesser extend close to uranium mineralization at Shea Creek and in balls of "zones à boules" due to xenotime and/or REE- and Y-rich uranium oxide crystallization. LREE are generally depleted in samples enriched in intermediate and heavy REE. REE enrichment/depletion patterns in Fe-chlorite breccias are variable and difficult to interpret. Strong LREE enrichments are observed in some Fe-chlorite breccia samples. Only a slight enrichment in Y is noted in the Sue "zones à boules" and LREE are enriched instead of intermediate and heavy REE. Correlation of LREE and Sr enrichment/depletion patterns reflects goyazite-florencite minerals precipitation or leaching.

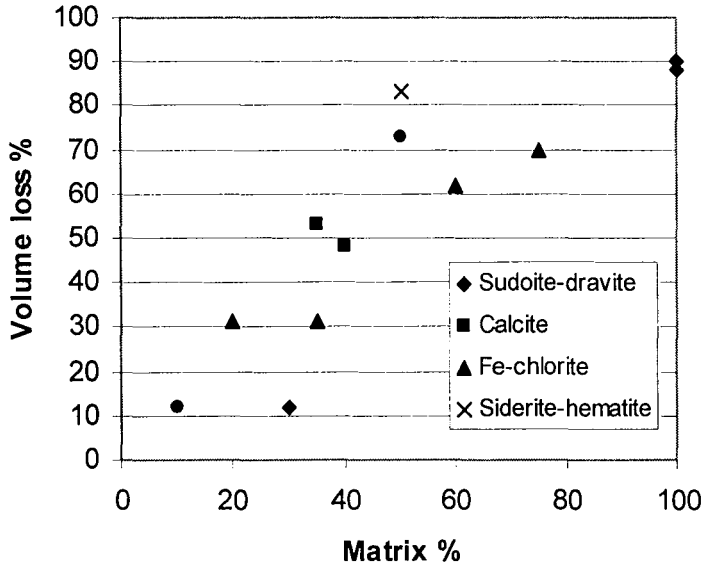

Figure 22 – Volume loss percentage versus matrix percentage diagram displaying a positive correlation.

8. Discussion

8.1. Evidence of repeated seismic activity over 1 Ga

The sandstone-hosted breccias associated with high-grade unconformity-type uranium deposits and Y and REE mineralizations in the Athabasca Basin are controlled by basement-rooted and graphite-rich reverse structures. The several stages of brecciation observed at Shea

Creek and at the Maw Zone and the superimposed striaes on fragments of « zones à boules » indicate that the basement-rooted faults were reactivated several times. These reactivations were probably favored by the presence of graphite along faults in the basement that acted as a lubricant. Most of the reactivations occurred in a contraction tectonic regime. However, type II faults at Shea Creek also evidence post-Athabasca sinistral-normal movements. The determination of the succession of tectonic events was based on the Shea Creek area because it appears to have recorded more phases than the Sue or Maw zones.

Several ages of uranium mineralization have been obtained by U-Pb and K-Ar mainly between 1.52 and 1.25 Ga, around 1.1 Ga, between 0.9 and 0.8 Ga and between 0.5 and 0.2 Ga (Hoeve and Quirt, 1984 ; Lainé, 1985 ; McGill et al., 1993; Fayek and Kyser, 1997).

Sudoite, dravite and illite breccias at Shea Creek are coeval with the main mineralizing stage between 1.52 and 1.25 Ga. The illite-rich « zones à boules » and the massive illite associated with the Sue A and B deposits are also coeval with the primary uranium mineralization. The dravite breccias at the Maw Zone are possibly related to the unconformity uranium mineralization below and are therefore very likely contemporaneous with the dravite breccias associated with the mineralization at Shea Creek.

Fe-chlorite breccias at Shea Creek, showing local mixing with kaolinite, might be coeval with a second mineralization and/or remobilization event at about 900 Ma, by comparison with a possibly similar Fe-rich kaolinite or kaolinite mixed with Fe-chlorite paragenetic sequence dated 900 ± 50 Ma in the Cigar Lake deposit (Philippe et al., 1993). Consequently, the Fe-chlorite breccia episode might also be regional. The geometry of Fe-chlorite breccia bodies at Shea Creek shows that the stress regime differed from the one prevailing during the first mineralization event (see part II)

The hematite- and siderite-rich breccias are contemporaneous with a third event of mineralization and/or remobilization at about 350 Ma. It is also a regional event related to a rapid uplift of the basin associated with incursion of meteoric fluids in the ore zones (Hoeve and Quirt, 1984; Kotzer and Kyser, 1995).

The last phase of uranium remobilization at Shea Creek occurred at about 120 Ma. The samples studied are located at about 5 km south from the 39 km in diameter Carswell meteoric impact crater. The impact event was dated at 115 ± 10 Ma by Bottomley et al. (1990) using a ^{40}Ar-^{39}Ar method. That suggests that this last phase of uranium remobilization could have been triggered by the very close Carswell meteoric impact. Therefore, the polyphase breccia system associated with unconformity-type uranium mineralizations developed during at least 3 regional tectonic reactivations that occurred over 1 Ga. Each breccia event has been accompanied by uranium mineralization and/or remobilization.

8.2. Porosity, permeability, fluid pressure evolution and basement fluid circulation

Early strong pervasive silicification of sandstones around basement-rooted faults was observed in the three zones of study but is mostly developed at Shea Creek and at the Maw Zone. It probably occurred during conditions of deep diagenesis at the onset of the hydrothermal activity (Fig. 10, 11 and 17). It dramatically decreased the sandstone porosity and permeability and increased its competency. Therefore, the silicified sandstone acted as an impermeable cap for the basement fluids that were probably circulating upward along graphite-rich fault zones which were more permeable than the surrounding gneisses. This cap induced fluid pressure increase of the basement fluids, decreasing the effective stress and favoring fault reactivation (Sibson, 2000) (Fig. 23 and 24).

Fault reactivation was expressed by seismic slip along the fault in the basement and by fault propagation in the sandstone (step I). In zones of strong early silicification, this fault propagation was characterized by the predominance of extended hydraulic fracturing in the damage zone of the fault over localized fault slip in the core of the fault (Fig. 24). Widespread fracturing occurred in zones of strong silicification just above the unconformity due to the strong competency of the sandstone. Hydraulic fracturing also occurred higher in the sandstone in the termination zone of the fault, explaining the occurrence of hydraulic breccias at the Maw Zone (Cox et al., 2000) (Fig. 24 and 25). Hydraulic breccias could also have been critical (Jébrak, 1997) or implosion breccias (Sibson, 1994) because the mechanical contrast between basement rocks and sandstone would have created fault refraction at the unconformity leading to potential dilational jog formation during fault movement. In zones of less intense early silicification, fracturing was tectonic and more localized around the core of the fault, represented by "zones à boules" at Sue.

The newly formed fracture permeability permitted basement fluids to percolate in the sandstone (step II). As the basement fluids penetrated through the sandstone, they probably mixed with basin fluids. The vertical quartz dissolution intensity gradient evidenced in the three zones of study indicates that the mixed basement and basin fluids were undersaturated in silica and were circulating upward in the fractured sandstone (see part 7). Upward circulation of basement fluids in sandstones is also supported by the mineralogical zonation of the alteration halo at Shea Creek with illite-chlorite, sudoite, dravite and quartz from the inner part to the outer part of the halo (Fig. 25). This zonation is also chemical with predominance of K-Mg-Al, Mg-Al, Mg-Al-B and Si over the other elements, respectively from the inner part to the outer part of the halo. Dravite would result from basin-basement fluid mixing with B and Mg provided respectively by basin and basement fluids (Kotzer and Kyser, 1995). Another evidence of silica undersaturation is the absence of amorphous silica along the fault path in the basement that would have precipitated if the fluids were saturated as they were moving upward

in a cooler environment. The very good spatial correlation between the graphite-type I fault and breccias at Shea Creek (Fig. 7) clearly indicates that graphite-rich faults were the main channels for upward migration of basement silica undersaturated fluids.

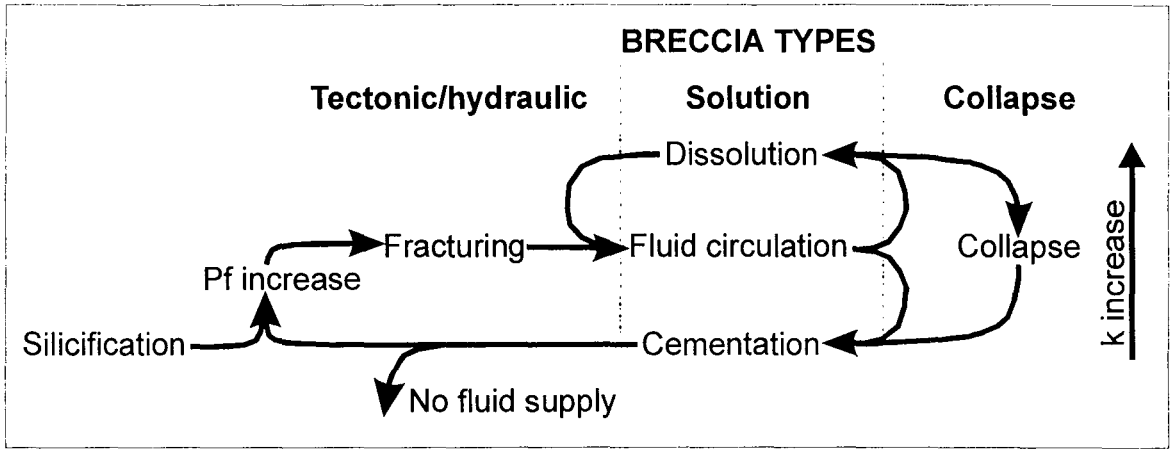

Figure 23 – Fluid pressure and permeability cycle associated with breccia development in sandstones.

This basement fluid circulation could have been driven by two different processes : buoyancy and/or pressure gradient. Buoyancy-driven flow is probable as basement fluids were hotter (see part III) and likely less saline and less dense than the diagenetic brines as proposed in Australian unconformity-type uranium deposits by Derome et al. (2000a). The low interconnectivity of pores in the basement rocks at a depth greater than 5 km indicates that fluid pressure was probably close to lithostatic. It is therefore possible that permeable faults provided transient pathways for rapid upward migration of fluids under high driving pressure gradients by tapping suprahydrostatically pressured deep level fluid reservoirs (Cox et al., 2000). This hypothesis is consistent with the several thousand meters extension of some faults cross-cutting the unconformity, evidenced by seismic signals (Hajnal et al., 1997).

The newly formed dilational jogs and Riedel shears at the unconformity and the termination zones of the shear faults at the unconformity or above like at the Maw Zone were zones of low mean stress. Low mean stress was also particularly developed at fault intersections. In case of lithostatic fluid pressures, variations in mean stress at any depth were reflected by variations in fluid pressure. Therefore, fluid flow would have been focused toward these zones of low mean stress (Ridley, 1993). Not only the basement fluids should have been focused toward these zones, but also basin fluids circulating laterally in the coarse-grained to conglomeratic basal sandstone of the basin. That would explain the preferential development of solution breccias at fault intersections, along shear faults at the unconformity or at fault

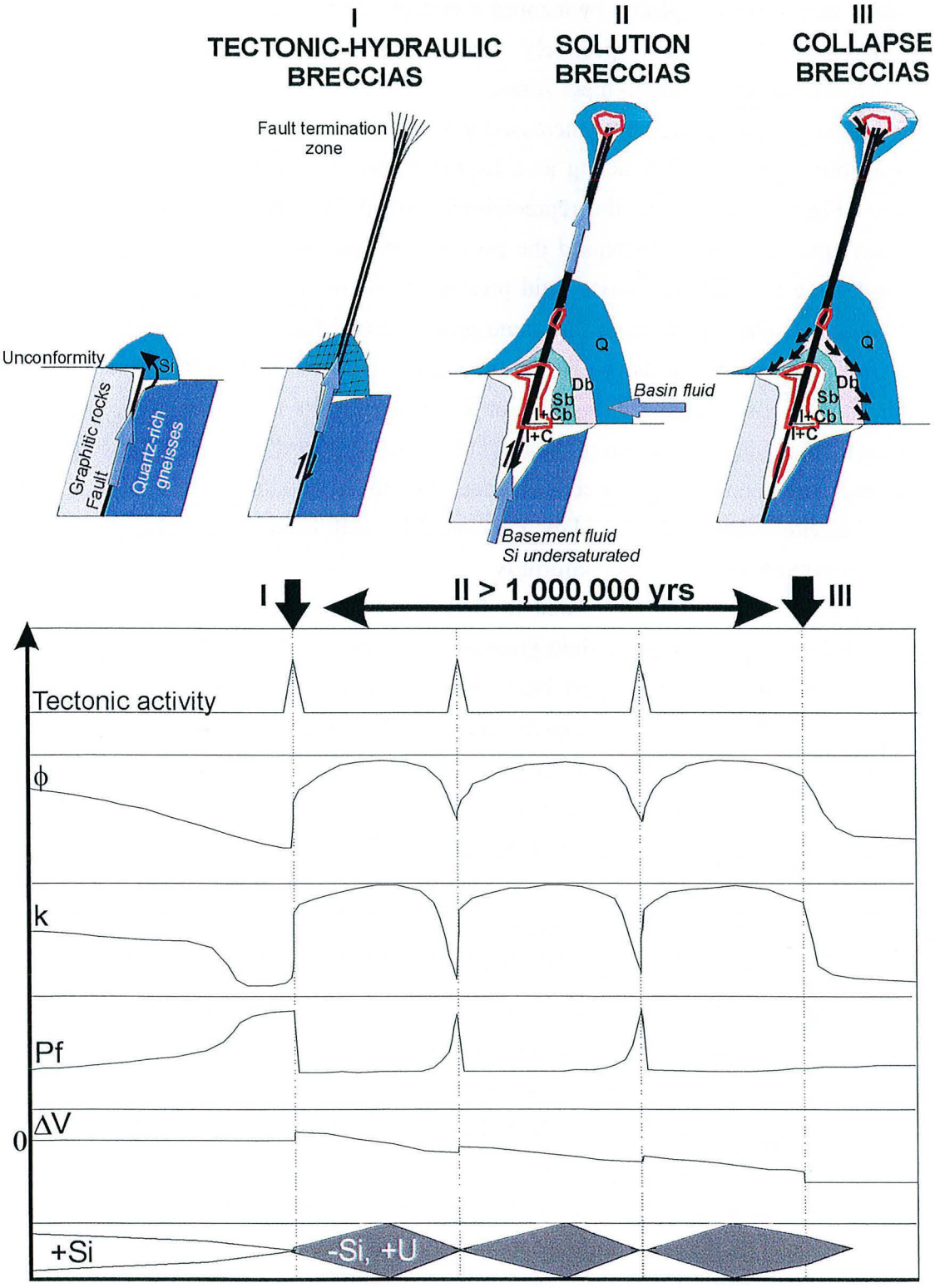

Figure 24 – Schematic drawing showing the formation of uranium mineralization and associated breccias in 3 steps. Unc: unconformity, Q: quartz, Db: dravite breccias, Sb: sudoite breccias, I+Cb: Illite+chlorite breccias. Evolution of porosity, permeability and volume of breccias as well as the fluid pressure of the basement fluids at the unconformity are qualitatively shown.

termination zones as exemplified by « zones à boules » at Sue, and solution breccias at Shea Creek and at the Maw Zone, respectively. That would also explain that basin/basement fluid mixing occurred preferentially in these zones.

The quartz dissolution strongly increased the porosity of the sandstone further increasing the permeability and therefore acting as a feedback loop maintaining fluid circulation for a long time (Fig. 23). However, the reprecipitation of quartz in an external zone above the dissolution area could have decreased the porosity and permeability, leading to self-sealing. This self-sealing would have induce fluid pressure increase and further hydraulic brecciation (Fig. 23 and 24). The repetition of this same process could have lead to the propagation of a breccia front upward with massive silica at the head of the front and quartz dissolution below. Therefore, the maximal quartz dissolution at the unconformity can be explained not only by the maximal silica undersaturation of the fluid circulating upward but also by the longuest time of fluid-rock interactions. As a consequence, the massive silicification surrounding the immature dravite breccias at the Maw Zone could result from the quartz dissolution that probably occurred below at the unconformity.

Such a fluid cycle could be related to fault-valve or load-strengthening fault behavior (Sibson, 1994 ; Cox, 1995). Each fluid pressure increase would have decreased the effective stress triggering fault re-opening and basement fluid injection in sandstone. Such behavior would have been favored by the impossibility for the basement fluids to escape laterally because of the low permeability of the surrounding rocks and because of the impervious graphite-rich slikensided planes parallel to the fault. That would explain the occurrence of multiple euhedral quartz growth zones in fractures above the dissolution zone due to several fluid pulses.

Clay minerals and dravite cementation occurred in zones of quartz dissolution and could have also contributed to self-sealing below the silica front. That would have also induced fluid pressure increase and subsequent re-opening of the system below the silica cap leading to another phase of quartz dissolution and mineral cementation. That would explain the occurrence of several phases of the same mineral precipitation within one main stage like in Fe-chlorite breccias at Shea Creek. These fluid cycles would also explain the alternation between oxidizing and reducing conditions observed at Shea Creek and in several deposits in response to the predominance of one or the other type of fluid (Hoeve and Sibbald, 1978). High-angle reverse faults, that are commonly associated with unconformity-type uranium deposits (Thomas et al., 1998), are particularly favorable to fault-valve behavior (Sibson, 1994).

When a sufficient quantity of quartz was dissolved, collapse occurred (step III), creating volume loss and closing porosity. This could have also led to fluid pressure increase and fault reopening (Fig. 23). Most of the collapse probably occurred progressively during the

dissolution (step II) of sandstone, explaining the very high volume loss percentages. Collapse would have propagated to higher levels like at the Maw Zone due to massive dissolution below (Fig. 24). The breccia maturation would have been stopped by an interruption of the fluid supply, possibly due to chemical sealing of the fault below or to a change in the stress regime (Fig. 23 and 24). At the end of the hydrothermal activity, the alteration front would move back toward the unconformity inducing locally oxidation of previously deposited reduced paragenesis, silica precipitation in corroded zones and dravite precipitation in already chloritized areas.

In the core of the faults, represented by "zones à boules", the porosity created by quartz dissolution has been accomodated by tectonic contraction, possibly leading also to fluid pressure increase and subsequent fault re-opening.

Consequently, the breccia system could have propagated upward along faults by a succession of basement fluid injections. However, the period of time between each permeability decrease and subsequent fault re-opening would have been rather long as stationary hydrodynamic and redox conditions seem to be required for the deposition of high grade uranium mineralization (Hoeve et al., 1980 ; Hoeve et Quirt, 1985). The different stages of illite-sudoite-dravite, calcite and Fe-chlorite suggest that several basement fluid pulses may have been repeated through the basin history between 1.52 and 0.9 Ga.

Hematite-siderite breccias of stage 4 at Shea Creek formed during a period of rapid uplift and erosion of the basin due to the incursion of meteoric fluids (Hoeve and Quirt, 1984). Therefore, the fluids in the sediment pore spaces probably contracted due to the cooling effect, causing significant reduction in pore-fluid pressure (Magara, 1986). The resulting fluid pressure gradient could have been responsible for further fracturing and fluid input in the breccia zone. The fluids involved in the formation of these hematite breccias were probably meteoric as indicated by $\delta^{18}O$- and δD-values of coeval kaolinites (Kotzer and Kyser, 1995).

8.3. Origin of fluid undersaturation in silica

Quartz dissolution in the sandstone surrounding unconformity-type uranium deposits of the Athabasca Basin was documented by Pagel (1975a), Pagel et al. (1980), Hoeve and Quirt (1984; 1985), Iida (1993) and Ruzicka (1996). However, the origin of fluid undersaturation in silica remains unknown. The fluid responsible for quartz dissolution seems to result from mixing of a basement fluid with a basin fluid in equilibrium with quartz.

One hypothesis to explain quartz dissolution is that the basement fluids were equilibrated with totally quartz-depleted zones, leading to their silica undersaturation. Petrographic studies of some altered graphite-rich metamorphic rocks along the graphite-rich type I fault at Shea Creek show the absence of quartz (Lorilleux, 1997). However, it is not reasonable to consider

that the fluids were not locally in contact with quartz as quartz veins and fragments are occasionnally present within graphite-rich faults. Furthermore, enrichments of elements like W in breccias show that the basement fluids have probably circulated through granitic rocks containing quartz.

A second hypothesis to explain quartz dissolution would be a chemical reaction occurring in the basement that would undersaturate the fluid in silica. Hydrothermal illite and chlorite alterations are intensively developed in the basement rocks below unconformity-type uranium mineralizations, together with massive quartz dissolution (Hoeve et al., 1980 ; Halter, 1988 ; Baudemont et al., 1993 ; Iida, 1993 ; McGill et al., 1993; Kotzer and Kyser, 1995). In conditions of $[K^+]/[H^+]$ ratio greater than 10^4, a fluid undersaturated in silica in contact with illite may be stable (Fritz, 1981). Therefore, the hydrothermal alterations observed in the basement are compatible with the circulation of a silica undersaturated fluid but it is not clear how they may product such a fluid. In the sandstone, as the mixed fluid circulated upward along faults, it progressively become equilibrated with quartz leading to only minor dissolution like at the Maw Zone.

8.4. Fluid temperatures

Illite geothermometry shows that the fluids responsible for quartz dissolution and illite crystallization in the Sue « zones à boules » had a temperature about 260 ± 20°C, representing the mineralizing fluid temperature during the first uranium deposition event, between 1.52 and 1.25 Ga.

The occurrence of uraninite crystals is also consistent with a temperature greater than 250 to 300°C (Albarède et al., 1985). The presence of dickite prior to the main mineralization event indicates conditions of peak diagenesis during uranium deposition. The estimated temperature of basin fluids during peak diagenesis is between 200 and 240°C (Hoeve et al., 1981; Halter, 1988 ; Kotzer and Kyser, 1995). Therefore, the temperature of the mineralizing fluids was higher than the one of the diagenetic fluids during peak diagenesis. That probably reflects mixing of basin fluids with hotter basement fluids.

Chlorite geothermometry in Fe-chlorite breccias (stage 3) at Shea Creek gives fluid temperatures of about 180°C at 900 Ma, indicating a significant cooling of basement and/or basin fluids. Kaolinite mixed with Fe-chlorite, later than Fe-chlorite, would have formed in a still cooler environment.

Siderite-hematite breccias (stage 4) probably formed at about 350 Ma and would correspond to the incursion of meteoric waters less than 50°C (Kotzer and Kyser, 1995). However, very local uraninite new formation suggests a possible injection of hot basement fluids at that time.

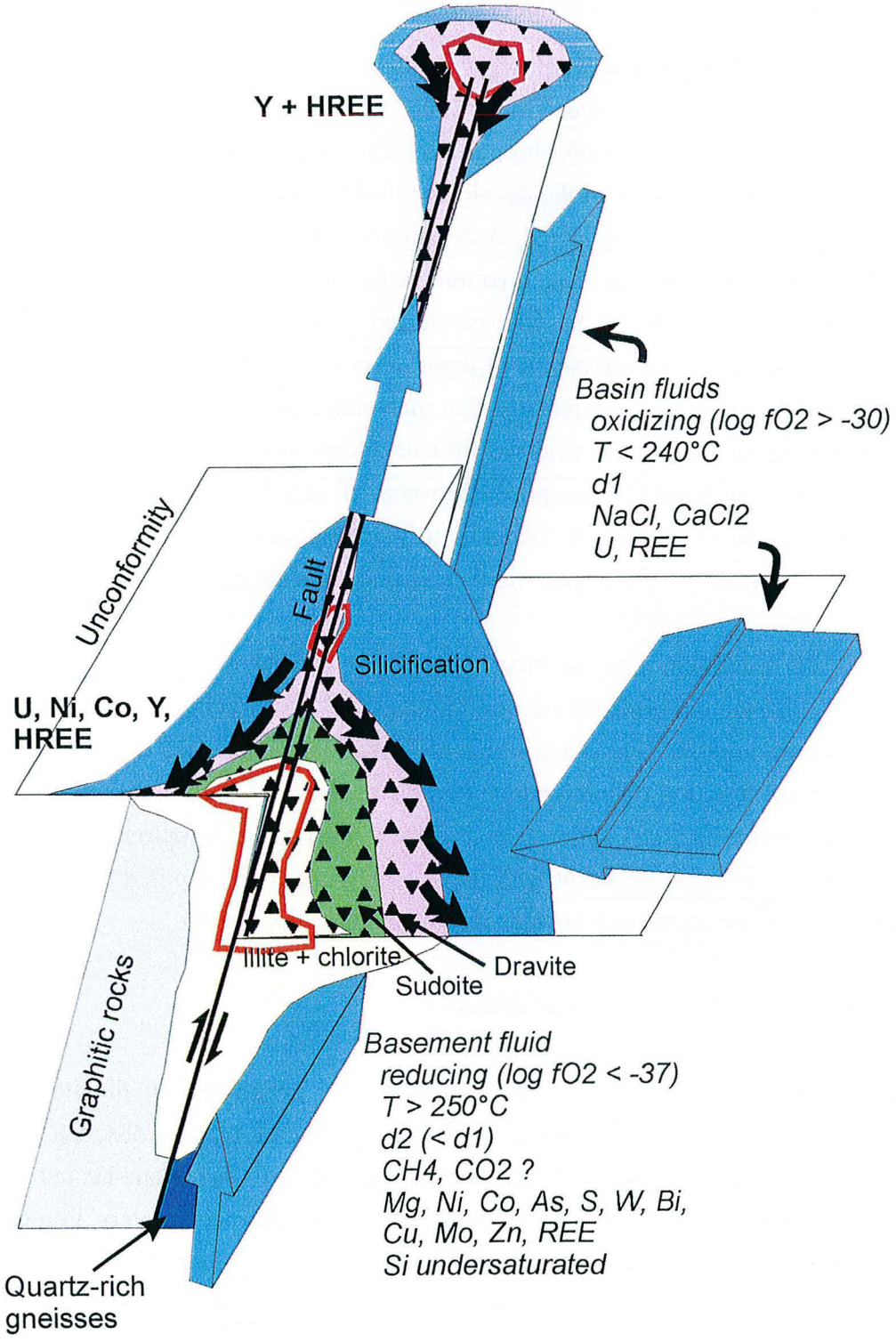

Figure 25 – Schematic model of formation of an unconformity-type uranium deposit associated with the development of breccias up to several hundreds of meters above the unconformity and the formation of Y and HREE mineralizations (not to scale). Note the mineralogical zonation in the alteration halo in sandstones. The black arrows indicate collapse.

8.5. Hydrothermal fluid volume and time of breccia formation

The very high calculated fluid/rock ratios indicate that huge volumes of hydrothermal fluids have circulated within the breccias. In order to estimate the time of formation of the breccias, a fluid circulating vertically through a breccia volume of 10^4 m^3 with a horizontal surface of 10^3 m^2, corresponding to the development of breccias along the unconformity over an average height of 10 m, is considered. A dissolution efficiency of 100 % is assumed. The fluid volume required to form this breccia volume is 10^8 m^3, assuming a fluid/rock ratio of 10^4 with silica saturation close to 90 %. The connected porosity and subsequent permeability varies with time due to the development of dissolution cavities that may have enhanced the porosity but also to mineral precipitation that may have sealed the system. But average connected porosities of 1 % were considered for calculation. The time of breccia formation for a fluid/rock ratio of 10^4 would be comprised between 10^6 and 10^8 years for a porosity of 1 % and for a fluid circulation velocity of 100 and 1 m/year respectively (Fig. 26). Fluid velocities in the order of magnitude of 100 m/year were estimated for a strongly fractured zone (see part III).

Therefore, the minimum time of breccia formation is probably about 1 million years. However, as the dissolution probably occurred in slow diffusion-limited regime (part 5.2), the calculated times are minimal. The overall time of formation of one stage of breccia formation also depends on the duration of interseismic periods of fluid pressure build-up to reopen the connectivity of the breccia system after their sealing by mineral precipitation. The long time of formation of the breccias is consistent with the probably long time required to form the large high-grade uranium mineralizations (Raffensperger and Garven, 1995b).

8.6. Uranium deposition and basin fluid volume

Evidences of basement fluid flow in sandstones and occurrence of dravite as breccia cement strongly indicate basin-basement fluid mixing. Therefore, our observations are in accordance with the diagenetic hydrothermal model of sandstone-hosted uranium mineralization proposed by Fayek and Kyser (1997). The absence or very limited quartz dissolution in the sandstone above the basement-hosted Sue C deposit (Fig. 4) would be consistent with the absence of basement fluids in the basement-hosted uranium mineralization model proposed by Fayek and Kyser (1997).

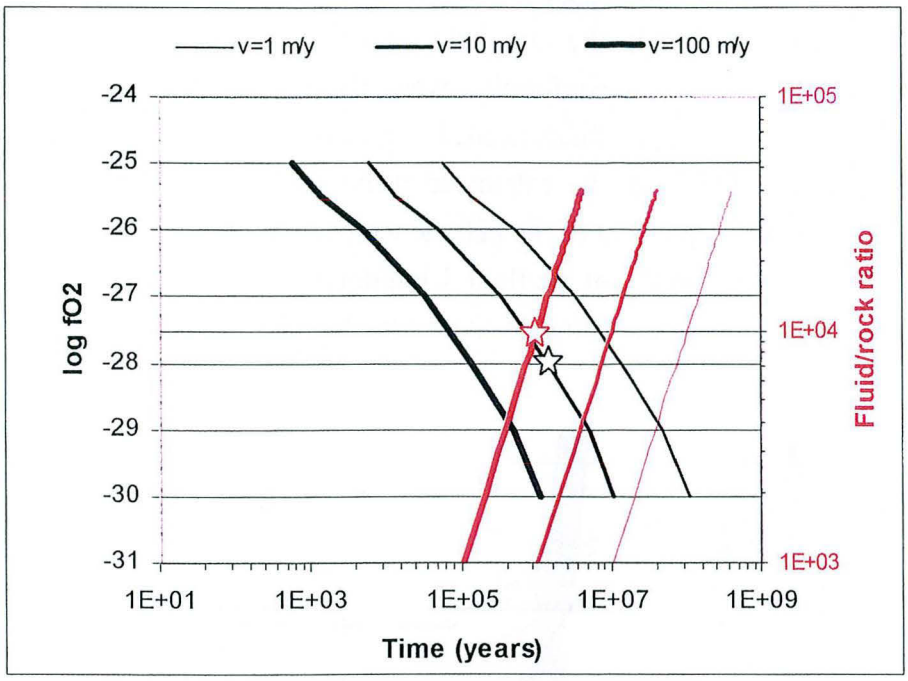

Figure 26 – Diagram displaying the hydrothermal fluid/rock ratio versus time of quartz dissolution (red lines) and the basin fluid fO2 versus time of uranium deposition (black lines). The different line thickness represent different fluid velocities (1, 10 and 100 m/year). Connected porosity is 1 %. The time of quartz dissolution was calculated considering the formation of 10^4 m^3 of breccias and a fluid with a silica saturation of 90 %. The time of uranium deposition was calculated for the deposition of 10^4 tons of U from basin fluids at pH=4.45, T=200°C and with a chemical composition proposed by Komninou and Sverjensky (1996). The two stars indicate that the time required for the formation of 10^4 m^3 of solution breccias is about the same as the time needed to precipitated an uranium deposit of 10^4 tons considering a fluid/rock ratio of 10^4 and basin fluid fO2 of 10^{-28}.

The cavities created by quartz dissolution were the site of fluid mixing between a reducing silica undersaturated basement fluid flowing upward through the breccias and uranium-bearing oxidizing basin fluids. Basin fluids circulated either in convection cells (Hoeve and Quirt, 1984; Raffensperger and Garven, 1995a) or laterally along the unconformity at the bottom of the basin (Kotzer and Kyser, 1995). The latter hypothesis is more likely as basal sandstone formations are typically coarse-grained to conglomeratic and therefore more permeable than the overlying formations. Furthermore, the study of clay mineral assemblages in the Athabasca formations indicates that they are controlled by lithological factors (Hoeve et al., 1981). That suggests that convection-related cross-formational flow of pore waters between units with contrasting clay mineral assemblages was probably very limited. Basin fluids circulating along the unconformity may have been conducted by fault-unconformity intersections due to the several tens of meters high preferential pathways formed by the faulted unconformity. In case of lithostatic to sub-lithostatic fluid pressure regime, both basement and basin fluids were probably focused in zones of low mean stress at intersections of one or several faults with the unconformity.

The sudden drop of fO_2 of the basin fluids due to mixing with reducing fluids induced uranium oxide precipitation within the dissolution cavities of the sandstone. The maximal dissolution zones close to the unconformity were therefore the best trap for uranium mineralization. The volume of basin fluids needed to precipitate the uranium mineralization of an average 10^4 tons U deposit can be calculated using calculated uranium solubility. The solubility of UO_2 is mainly dependant of the pH, the temperature, the nature and concentration of the complexing agent and the fO_2 of the fluid. Uranium is assumed to have been transported by oxidizing diagenetic fluids circulating in the basin (Kotzer and Kyser, 1995 ; Fayek and Kyser, 1997).

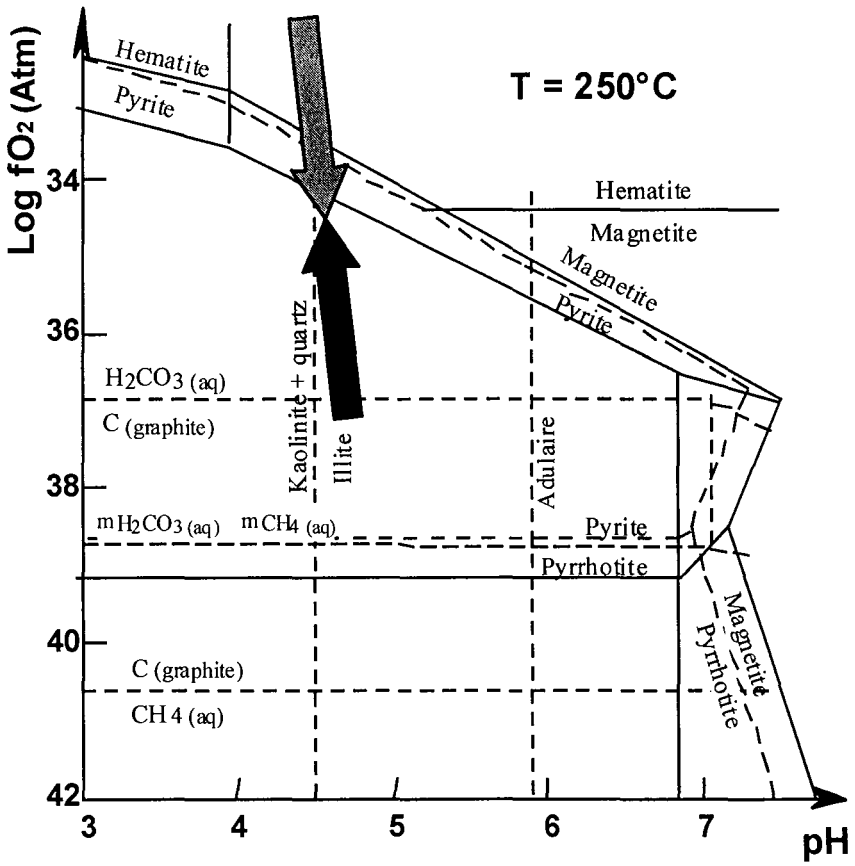

Figure 27 – fO2 versus pH diagram for Fe species at 250°C (modified from Arnold and Guha, 1980). The grey and black arrows represent respectively the possible basin and basement fluid paths during fluid mixing at the unconformity. Basin fluids were in equilibrium with hematite, quartz and dickite before mixing, excepted in zones of the basin where diagenetic illite is predominant over dickite. Basement fluids were in equilibrium with illite and graphite before mixing. As illite is Si-rich, the illitization of dickite is accompanied with quartz consumption. The precipitation of pyrite during the U mineralization indicates that the fO_2 of the mixed fluid is below the hematite-pyrite boundary.

The pH of the basin fluid was buffered by the coexistence of illite and kaolinite and was therefore most probably comprised between 4 and 5 (Hoeve and Quirt, 1984) (Fig. 27). The temperature of the uranium-bearing fluids was probably comprised between 200 and 240°C. The basin fluids were in equilibrium with hematite. Therefore, the oxygen fugacity of the fluid

may have been above the pyrite/hematite boundary (fig. 27). Fluid inclusion studies indicate that the basin fluids contained up to 30 wt. % NaCl (Pagel et al. 1980; Derome et al., 2000b) and up to 40 wt. % $CaCl_2$ + $MgCl_2$ (Derome et al., 2000b). Several authors have suggested that, at such pH, temperature and high content of Cl^-, the uranyl-chloride complex UO_2Cl^+ was probably predominant over other complexes like carbonate, phosphate, sulfate, hydroxide and fluoride (Nguyen-Trung, 1985; Wilde and Wall, 1987; Pagel et al., 1988; Raffensperger and Garven, 1995b; Komninou and Sverjensky, 1996). Furthermore, gold, that is occasionnally associated with primary mineralization (Shea Creek, Cluff D deposit), may also be transported as chloride complexes (Jaireth, 1992). However, Fayek and Kyser (1997) propose that U was mostly transported as fluoride complexes in the diagenetic basin fluids because detrital fluor-apatite was altered to F-poor crandallite group minerals releasing F, P, and HREEs into solution. Calculations using the computer code EQ3NR/EQ6 (Wolery and Daveler, 1992) indicate that at 250°C, pH = 5.5, 177 g/l Cl^- and 10 mg/l F^-, uranyl-fluoride complexes (62.7 %) are largely predominant over uranyl-chloride complexes (1.9 %). The calculations also show abundant uranyl-hydroxide complexes (35 %). So, in spite of the high concentration of Cl^-, the predominant complexes transporting uranium in the basin fluids might have been fluorides and hydroxides and in lesser amounts chlorides. In order to constrain the validity of this assertion, it would be necessary to estimate the initial quantity of fluor-apatite and to be able to measure the quantity of F^- in fluid inclusions of the basin.

At the magnetite/hematite boundary, 200°C, pH = 4 and fO_2 = -40 the solubility of U is only about 24 ppb with transport as uranyl-hydroxyde complexes (Nguyen-Trung, 1985). Komninou and Sverjensky (1996) proposed a significantly higher oxygen fugacity for the Athabasca Basin fluids with log fO_2 = -25 at 200°C. They calculated an U solubility of 17 ppm with transport as uranyl-chloride complexes at pH=4.45 and 200°C with a low concentration in F^- of 10^{-6} mg/l and a concentration in Cl^- of 177.265 g/l. In the physico-chemical conditions proposed by Komninou and Sverjensky, the basin fluid volume needed to precipitate 10^4 tons of U with a deposition efficiency of 100% is given in figure 28 as a function of fO_2. The basin fluid volume would be in the same order of magnitude as the fluid volume calculated to form 10^4 m^3 of breccias as observed at Shea Creek with a silica undersaturation of 90 % for a fO_2 between 10^{-28} and 10^{-29}.

The variations of fO_2, pH and mineralogy in the sandstones just above the unconformity during basin-basement fluid mixing are illustrated in figure 27. Before fluid mixing, the basement fluid was in equilibrium with illite, graphite and pyrite whereas basin fluids were in equilibrium with hematite, quartz and dickite. However, in some parts of the basin where diagenetic illite predominates over dickite, basin fluids would have been in equilibrium with illite. Fluid mixing resulted in dickite alteration to illite and quartz dissolution at a pH buffered around 4.5. Quartz dissolution is mainly due to silica undersaturation of the basement fluid but

also to the new formation of Si-rich illites. The drop in fO_2 of basin fluids induced uranium oxide precipitation in the same time as quartz dissolution. At Shea Creek, the precipitation of pyrite during the main mineralization event indicates that the fO_2 of the mixed fluid was below the hematite-pyrite boundary.

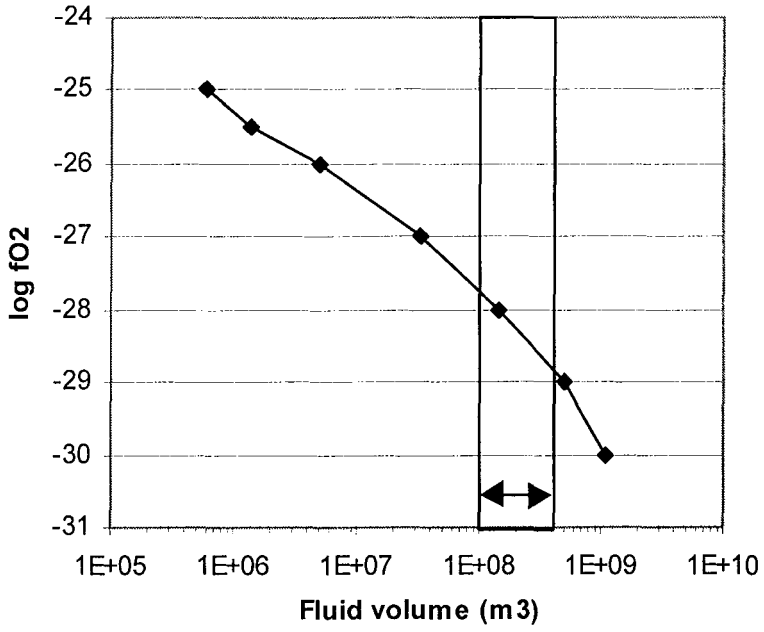

Figure 28 – Diagram representing the volume of basin fluids required to precipitate 10^4 tons of U in function of fO2 at pH=4.45 and T=200°C using the chemical composition of mineralizing fluids proposed by Komninou and Sverjensky (1996). The vertical lines give the range of hydrothermal fluid volume needed to form 10^4 m^3 of breccias with a silica saturation of 90 % and a fluid/rock ratio of 10^4.

The diagenetic basin fluids were circulating within the relatively permeable coarse-grained to conglomeratic basal formations and were probably slower than the basement-derived hydrothermal fluids circulating upward in faults. Therefore, fluid velocities of 10 and 100 m/year were taken for the diagenetic and hydrothermal fluids, respectively. Assuming a connected porosity of 1 % in the breccia zone and a fO2 of 10^{-28} for the basin fluids, the time necessary to precipitate the uranium oxides is at least about 1.4×10^6 years (Fig. 26). The time necessary to form a breccia volume of 10^4 m^3 with the same permeability and a fluid velocity of 100 m/year is at least 10^6 years. Therefore, the time of formation of the uranium deposits and associated solution breccias is probably greater than several million years because a maximal efficiency of uranium deposition and quartz dissolution have been assumed in the preceding calculations. These results have to be taken with care as numerous parameters like silica undersaturation, rock permeability and oxygen fugacity are not very well constrained.

8.7. Uranium mineralization-related chemical variations

Enrichments in Bi, Ni, Co, Cu, Mo, As, and S at Shea Creek are typical of complex-type uranium deposits. The polymetallic signature is less expressed in the Sue "zones à boules" with Bi, W and Zn enrichments and at the Maw Zone with only Bi and As enrichments. The similar REE enrichment/depletion signature in sudoite, dravite, calcite and polyphase carbonate breccias at Shea Creek suggests that REE mobility mainly occurred during the primary uranium mineralization event. Accordingly, Fayek and Kyser (1997) indicate that REE are not substantially remobilized or fractionated during alteration of uraninite by late meteoric waters. Y and intermediate and heavy REE enrichments related to xenotime crystallization are typically associated with the mineralization. In addition, significant HREE and Y enrichments in uraninites and pitchblendes from most unconformity-type uranium deposits were observed (Quirt et al., 1991; Fayek and Kyser, 1997). Therefore, the mineralizing fluids were rich in Y and intermediate and heavy REE. Chemical partitioning is commonly observed between LREE and HREE due to their different chemical behavior. The REE mobility is not dependant of fO2, except for Eu and Ce, but rather of temperature, pH and type of complexing agent. Therefore, REE deposition or leaching is not dependant of the unconformity-controlled redox front as uranium and may occur higher above the unconformity or laterally away from uranium mineralization. The cooling of hydrothermal fluids circulating upward might have been the cause of Y and HREE deposition at the Maw Zone.

8.8. Sandstone alteration models

Two types of alteration haloes in sandstones have been distinguished respectively in the north and south part of the Athabasca Basin (Matthews et al., 1997). The north Athabasca type is characterized by widespread illitization, the absence of early silicification and is typically represented by the Cigar Lake deposit. The south Athabasca type corresponds to strong early silicification, chloritization and dravitization and is probably best represented by the McArthur River deposit.

The silicification and the sudoite and dravite alterations observed in the Shea Creek sandstones are typical of the south type (Fig. 25). The early massive silicification has permitted the development of extended breccia bodies. The strong competency of the silicified sandstone favored widespread fracturing and its very low permeability limited quartz dissolution to fracture borders only, making possible the preservation of fragments. Broad zones of brecciation associated with the strong silicification, chloritization and dravitization are also documented at McArthur River (Matthews et al., 1997).

The illitic alteration at Sue corresponds to the north Athabasca type. Zones of massive argilization were mostly formed by volume loss due to pervasive quartz dissolution. Such pervasive dissolution was made possible by the significant Darcy-type permeability of the non-silicified sandstones that precluded from fragment preservation and breccia formation. At Cigar Lake also, only little breccias of the type observed at Shea Creek were documented (Bruneton and Caumartin, 1985). However, early pervasive silicification locally occurred at Sue and favored the development of "zones à boules" breccias.

Therefore, a new classification of unconformity-type uranium deposits can be proposed with 2 end-members: one characterized by intense early silicification and breccia development due to quartz dissolution limited in space and the other characterized by massive clay alteration and widespread quartz dissolution.

If the hypothesis that the quartz dissolution in the sandstone is due to illite alteration in the basement (see § 8.3), the amount of silicification in the sandstone would be proportional to the amount of quartz to be consumed in the development of illitization in the basement in order to get silica undersaturated fluids. That seems to be confirmed by the mineralogical composition of basement rocks below different deposits. The Cigar Lake basement rocks are typical graphite-rich metasediments relatively poor in quartz that would explain the very limited silicification in sandstones. The basement rocks below the Sue A and B deposits are graphite-rich metasediments and granites of the Collins Bay dome. The higher proportion of quartz in granites than in metasediments would account for the local silicification that favored "zones à boules" developement in sandstones. At Shea Creek, the predominance of felsic gneisses over graphite-rich quartz depleted rocks would explain the massive silicification in sandstones. At McArthur River, the basement contains significant zones of quartzites that would account for the massive early silicification in sandstones. Matthews et al. (1997) documented that silicification of sandstone is particularly prominent above or in the vicinity of basement quartzite ridges. Therefore, there seems to be a correlation between the amount of quartz in the basement rocks and the development of silicification and therefore of breccias in sandstones.

9. Conclusions

Unconformity-type uranium mineralization depositions and/or remobilizations in the Athabasca Basin have been initiated by at least 3 main regional tectonic events between 1.52 and 1.25 Ga, at about 900 Ma and around 350 Ma.

The first uranium deposition stage occurred during peak diagenesis at a temperature greater than 250°C. It is associated with the development of dravite breccias and Y+HREE mineralization at the Maw Zone, the formation of sudoite and dravite breccias at Shea Creek and the development of illite-rich "zones à boules" at Sue. The breccias associated with

uranium mineralizations developed in 3 steps: hydraulic, dissolution and collapse. This evolution reflects increasing fluid-rock interactions expressed by increasing matrix proportion mainly resulting from quartz dissolution and also from clay and dravite new formation.

During the regional tectonic events, graphite-rich basement rooted reverse faults have been preferentially reactivated. Fault propagation in sandstones was expressed by localized tectonic fracturing to widespread hydraulic fracturing in areas silicified at an early stage (step 1). The newly formed fracture permeability caused probably both buoyancy- and fluid pressure gradient-driven basement fluid circulation upward in sandstones.

Early silicification occurred by mixing between hot basement fluids flowing upward and cooler basin fluids circulating laterally along the unconformity. During the development of silicification in the sandstone, illitization accompanied with quartz consumption probably occurred in the basement rocks below. When quartz was totally leached out in the alteration zones below the unconformity, the basement fluids became silica undersaturated and began to dissolve quartz when they reached the sandstone at the unconformity (step 2).

Intense quartz dissolution was associated with important volume losses up to 80-90 % at Shea Creek and in "zones à boules" at Sue. At the Maw Zone, located 250 m above the unconformity, the fluids had time to partially re-equilibrate with quartz and induced therefore only minor quartz dissolution. The collapse at the Maw Zone was induced by the volume loss and collapse that probably occurred at the unconformity below, like at Shea Creek or at Sue (step 3), leading to the development of karst systems in sandstones. At Shea Creek where early silicification was intense, quartz dissolution is widespread but limited around fractures excepted at the unconformity. At Sue, quartz dissolution was expressed by massive illitization in "zones à boules" due to a weaker early silicification.

The fluid/rock ratios calculated using silica saturation of 90 % at the unconformity and of 99 % at the Maw Zone are between 38,000 and 3,000, respectively in the Sue "zones à boules" and at the Maw Zone. The time of formation of the breccias is estimated to be in the order of magnitude of a few million years assuming a fluid velocity of 100 m/year and a connected porosity of 1%. Such a long time of formation is consistent with the slow diffusion-limited regime of dissolution evidenced in sudoite-dravite breccias and the time probably required to form high grade uranium deposits.

The porosity created by quartz dissolution was the site of mixing between the reducing silica undersaturated basement fluids and the uranium-bearing oxidizing basin fluids and formed the trap for uranium mineralization. Quartz dissolution was very likely coeval with uranium oxides deposition. Considering a fO_2 of 10^{-28} for basin fluids transporting uranium as uranyl-chloride complexes, the time necessary to form a deposit of 10^4 tons of U would be about a few million years for a fluid velocity of 10 m/year and a connected porosity of 1%, that is a similar time than what is necessary to form 10^4 m^3 of breccias.

Sustainable fracture permeability and fluid circulation from the basement to the sandstone was necessary in order to produce a stationary redox front at the unconformity. The permeability would have been maintained by an equilibrium between quartz dissolution acting as a positive feedback loop and collapse, tectonic contraction and alteration mineral precipitation that tended to decrease permeability. Occasionnally or periodically, sealing of the hydrothermal system induced fluid pressure increase and subsequent reopening possibly by a fault-valve seismic mechanism.

A new approach of the classification of Matthews et al. (1997) of sandstone alteration types is proposed based on the occurrence of breccias. Deposits that belong to the south Athabasca models are associated with extended breccia bodies in silicified sandstones and spatially limited quartz dissolution. Deposits of the north Athabasca model show very weak breccia development, massive clay alteration due to pervasive quartz dissolution and extended lateral clay alteration haloes.

The genetic model of uranium deposition and breccia formation proposed in this paper is consistent with the model proposed by Fayek and Kyser (1997). Basement fluids are necessary to explain the formation of quartz dissolution in sandstone-hosted mineralizations that would result from basin-basement fluid mixing. The absence or very limited quartz dissolution above the basement-hosted Sue C mineralization suggests that basement fluids might not be involved in the formation of basement-hosted mineralizations as proposed by Fayek and Kyser (1997). Therefore, the classification of deposits based on breccia occurrences would be valid only for mineralizations occurring in the sandstone or just at the unconformity.

Acknowledgements

COGEMA and COGEMA Resources Inc are gratefully acknowledged for their financial, logistical, technical and geological support. COGEMA and CAMECO are thanked for permission to publish the geological data collected in the field from 1998 to 2000. We would also like to thank C. Peiffert for realizing calculations with the computer code EQ3NR/EQ6. The manuscript benefited from discussions with M. Cathelineau, D. Derome and M. Brouand.

References

Agip Canada Ltd., 1985, Saskatchewan Energy and Mines, Assessment File 74H06-NW-0080.

Albarède, F., Michard, A., and Cuney, M., 1985, Les chronomètres uranium-thorium-plomb, in Roth, E., and Poty, B., eds., Méthodes de datation par les phénomènes nucléaires naturels. Applications: Paris, Masson, Série Scientifique, Collection CEA, p. 123-173.

Armstrong, R.L., and Ramaekers, P., 1985, Sr isotopic study of Helikian sediment and diabase dikes in the Athabasca Basin, northern Saskatchewan: Canadian Journal of Earth Sciences, v. 22, p. 399-407.

Bau, M., and Möller, P., 1991, REE systematics as source of information on minerogenesis, in Pagel, M., and Leroy, J., eds., Source, Transport and Deposition of Metals, Proceedings of the 25 years SGA anniversary meeting, Nancy: Balkema, Rotterdam, p. 17-20.

Baudemont, D., Piquard, J.P., Ey, F., and Zimmerman, J., 1993, The Sue Uranium Deposits, Saskatchewan, Canada: Exploration and Mining Geology, v. 2, p. 179-202.

Baudemont, D., and Pacquet, A., 1996, The Sue D and E uranium deposits, Northern Saskatchewan: evidence for structurally controlled fluid circulation in the Athabasca Basin, in MinExpo'96 Symposium, Advances in Saskatchewan Geology and Mineral Exploration: p. 85-94.

Bottomley, R.J., York, D., and Grieve, R.A.F., 1990, ^{40}Argon-^{39}Argon dating of impact craters, in Proceedings of the 20th Lunar and Planetary Science Conference: p. 421-431.

Bruneton, P., and Caumartin, P., 1985, Le gisement d'uranium de Cigar Lake (Saskatchewan, Canada) – Contribution à la compréhension des mécanismes de formation des gisements de l'Athabasca, in Program and extended abstracts, Concentration mechanisms of uranium in geological environments: Nancy, France, p. 211-214.

Burley, S.D., and Kantorowicz, J.D., 1986, Thin section and S.E.M. textural criteria for the recognition of cement-dissolution porosity in sandstones: Sedimentology, v. 33, p. 587-604.

Cathelineau, M., and Nieva, D., 1985, A chlorite solid solution geothermometer. The Los Azufres (Mexico) geothermal system : Contributions to Mineralogy and Petrology, v. 91, p. 235-244.

Cathelineau, M., and Izquierdo, G., 1988, Temperature – composition relationships of authigenic micaceous minerals in the Los Azufres geothermal system: Contributions to Mineralogy and Petrology, v. 100, p. 418-428.

Chiarenzelli, J., Aspler, L., Villeneuve, M., and Lewry, J., 1998, Early Proterozoic Evolution of the Saskatchewan Craton and its Allochthonous Cover, Trans-Hudson Orogen: The Journal of Geology, v. 106, p. 247-267.

Cox, S.F., 1995, Faulting processes at high fluid pressures: an example of fault valve behavior from the Wattle Gully Fault, Victoria, Australia : Journal of Geophysical Research, v. 100, p. 12841-12859.

Cox, S.F., Knackstedt, M.A., and Braun, J., 2000, Principles of structural control on permeability and fluid flow in hydrothermal systems: Reviews in Economic Geology, (in press).

Derome, D., Cuney, M., Cathelineau, M., Fabre, C., Brisset, F., 2000a, Fluid regime in the Kombolgie sandstones in the vicinity of unconformity-type uranium deposits (Northern Territory, Australia), in Proceedings, GeoCanada2000, The Millennium Geoscience Summit, Calgary: GAC-MAC joint annual meeting, abstract 178 (Conference CD).

Derome, D., Cathelineau, M., Cuney, M., Fabre, C., Dubessy, J., Lhomme, T., 2000b, Reconstitution of the composition of individual fluid inclusion using microthermometry, Raman microspectroscopy and Laser Induced Breakdown Spectroscopy. Application to the genesis of Australian and Canadian world-class unconformity-type uranium deposits, in Proceedings Symposium Metallogeny2000, December 2000, Nancy, France

Dzuslynski, S., and Sass-Gustkiewicz, M., 1989, Pb-Zn ores, in Bosak, P., Ford, D.C., Glazek, J., and Horacek, I., eds., Paleokarst. A Systematic and Regional Review: Amsterdam and Praka, Elsevier and Academia, p. 377-396.

Energy Mines and Resources, 1989, Canadian mineral deposits not being mined in 1989: National Mineral Inventory, Mineral Policy Sector, Mineral Bulletin MR 223, Sask. 47.

Ey, F., Gauthier-Lafaye, F., Lillié, F., and Weber, F., 1985, A uranium unconformity deposit: The geological setting of the D orebody (Saskatchewan-Canada), in Lainé, R., Alonso, D., and Svab, M., eds., The Carswell structure uranium deposits, Saskatchewan: Geological Association of Canada Special Paper 29, p. 121-138.

Fayek, M., and Kyser, T.K., 1997, Characterization of multiple fluid-flow events and Rare-Earth-Element mobility associated with formation of unconformity-type uranium deposits in the Athabasca Basin, Saskatchewan: The Canadian Mineralogist, v. 35, p. 627-658.

Fouques, J.P., Fowler, M., Knipping, H.D., and Schimann, K., 1986, The Cigar Lake uranium deposit: discovery and general characteristics, in Evans, E.L., ed., Uranium Deposits of

Canada: Canadian Institute of Mining Metallurgy and Petroleum (CIM), special volume 33.

Fritz, B., 1981, Etude thermodynamique et modélisation des réactions hydrothermales et diagénétiques [Ph.D. thesis]: Strasbourg, Louis Pasteur University, Sciences Géologiques, mémoire 65, 197 p.

Govindaraju, K., and Mevelle, G., 1987, Fully automated dissolution and separation methods for inductively coupled plasma emission spectrometry rock analysis: Journal of Analytic and Atomic Spectroscopy, v. 2, p. 615-621.

Grant, J.A., 1986, The isocon diagram, a simple solution to Gresens' equation for metasomatic alteration: Economic Geology, v. 81, p. 1976-1982.

Gresens, R.L., 1967, Composition-volume relationships of metasomatism: Chemical Geology, v. 2, p. 47-65.

Hajnal, Z., Annesley, I.R., White, D., Matthews, R.B., Sopuck, V., Koch, R., Leppin, M., and Ahuja, S., 1997, Sedimentary-hosted mineral deposits: a high-resolution seismic survey in the Athabasca Basin, in Gubins, A.G., ed., Proceedings of Exploration 97: Fourth Decennial International Conference on Mineral Exploration, p. 421-432.

Hall, A.J., 1986, Pyrite-pyrrhotine redox reactions in nature: Mineralogical Magazine, v. 50, p. 223-229.

Halter, G., 1988, Zonalités des altérations dans l'environnement des gisements d'uranium associés à la discordance du Protérozoïque Moyen (Saskatchewan, Canada) [Ph.D. thesis]: Strasbourg, Louis Pasteur University, 252 p.

Halter, G., Pagel, M., Sheppard, S.M.F., Weber, F., and Clauer, N., 1988, Rétromorphose, paléoaltération, diagenèse et hydrothermalisme de l'encaissant des gisements uranifères dans la structure de Carswell (Saskatchewan-Canada), in Gisements Métallifères dans leur Contexte Géologique: Document du BRGM no. 158, v.1, p. 365-388.

Hecht, L., and Cuney, M., 2000, Mechanism of uranium mobilization in the Athabasca basin and basement by hydrothermal and/or diagenetic fluids, in Proceedings, GeoCanada2000, The Millennium Geoscience Summit, Calgary: GAC-MAC joint annual meeting, abstract 191 (Conference CD).

Hoeve, J., and Sibbald, T.I.I., 1976, Rabbit Lake uranium deposit, in Dunn, C.E., ed., Uranium in Saskatchewan: Geological Society of Saskatchewan Special Publication no. 3, p. 331-354.

Hoeve, J., and Sibbald, T.I.I., 1978, On the genesis of Rabbit Lake and other unconformity-type uranium deposits in northern Saskatchewan, Canada: Economic Geology, v. 73, p. 1450-1473.

Hoeve, J., Sibbald, T.I.I., Ramaekers, P., and Lewry, J.F., 1980, Athabasca Basin unconformity-type uranium deposits: a special class of sandstone-type deposits?, in Ferguson, S., and Goleby, A., eds., Uranium in the Pine Creek Geosyncline: International Atomic Energy Agency, Vienna, p. 575-594.

Hoeve, J., Rawsthorn, K., and Quirt, D., 1981, Uranium Metallogenetic Studies: Clay Mineral Stratigraphy and Diagenesis in the Athabasca Group: Saskatchewan Research Council Technical Report no. 22, p. 76-89.

Hoeve, J., and Quirt, D., 1984, Mineralization and host rock alteration in relation to clay mineral diagenesis and evolution of the middle-Proterozoic Athabasca Basin, northern Saskatchewan, Canada: Saskatchewan Research Council Technical Report 187, 187 p.

Hoeve, J., and Quirt, D., 1985, A stationary redox front as a critical factor in the formation of high-grade, unconformity-type uranium ores in the Athabasca Basin, Saskatchewan, in Program and extended abstracts, Concentration mechanisms of uranium in geological environments: Nancy, France, p. 219-224.

Hoffman, P.F., 1987, Continental transform tectonics: Great Slave Lake shear zone (ca. 1.9 Ga), northwest Canada: Geology, v. 15, p. 785-788.

Hoffman, P.F., 1989, Precambrian geology and tectonic history of North America, in Bally, A.W., and Palmer, A.R., eds., The Geology of North America - An Overview: Boulder, Colorado, Geological Society of America, The Geology of North America, v. A, p. 447-512.

Hutcheon, I., 2000, Principles of diagenesis and what drives mineral change, in Kyser, K., ed., Fluids and Basin Evolution: Mineralogical Association of Canada, Short Course Series, v. 28, p. 93-114.

Iida, Y., 1993, Alteration and ore-forming processes of unconformity-related uranium deposits: Resource Geology Special Issue, no. 15, p. 299-308.

Jaireth, S., 1992, The calculated solubility of platinum and gold in oxygen-saturated fluids and the genesis of platinum-palladium and gold mineralization in the unconformity-related uranium deposits : Mineralium Deposita, v. 27, p. 42-54.

Jébrak, M., 1997, Hydrothermal breccias in vein-type ore deposits: A review of mechanisms, morphology and size distribution: Ore Geology Reviews, v. 306, p. 1-24.

Komninou, A., and Sverjensky, D.A., 1996, Geochemical modeling of the formation of an unconformity-type uranium deposit : Economic Geology, v. 91, p. 590-606.

Kotzer, T.G., Kyser, T.K., and Irving, E., 1992, Paleomagnetism and the evolution of fluids in the Proterozoic Athabasca Basin, northern Saskatchewan, Canada : Canadian Journal of Earth Sciences, v. 29, p. 1474-1491.

Kotzer, T.G., and Kyser, T.K., 1995, Petrogenesis of the Proterozoic Athabasca Basin, northern Saskatchewan, Canada, and its relation to diagenesis, hydrothermal uranium mineralization and paleohydrogeology: Chemical Geology, v. 120, p. 45-89.

Kyser, T.K., Wilson, M.R., and Ruhrmann, G., 1989, Stable isotope constraints on the role of graphite in the genesis of unconformity-type uranium deposits : Canadian Journal of Earth Sciences, v. 26, p. 490-498.

Lainé, R., 1985, The Carswell uranium deposits-An example of not so unique unconformity-related uranium mineralization, in Lainé, R., Alonso, D., and Svab, M., eds., The Carswell structure uranium deposits, Saskatchewan: Geological Association of Canada Special Paper 29, p. 225-230.

Lewry, J.F., and Sibbald, T.I.I., 1980, Thermotectonic evolution of the Churchill Province in Northern Saskatchewan: Tectonophysics, v. 68, p. 45-82.

Lorilleux, G., 1997, Lithogéochimie des formations métamorphiques et plutoniques encaissant les gisements d'uranium de type discordance [M.Sc. thesis] : Nancy, Institut National Polytechnique de Lorraine, 39 p.

Lorilleux, G., Cuney, M., Jébrak, M., and Mondy, J., 2000, A new approach of unconformity-type uranium metallogenesis from a structural breccia study (Northern Saskatchewan, Canada), in Proceedings, GeoCanada2000, The Millennium Geoscience Summit, Calgary: GAC-MAC joint annual meeting, abstract 232 (Conference CD).

MacDougall, D.G., 1990, Rare Earth Element mineralization in the Athabasca Group-Maw Zone, in Summary of Investigations 1990: Saskatchewan Geological Survey, Saskatchewan Energy and Mines, Miscellaneous Report 90-4, p. 103-105.

Magara, K., 1986, Geological models of petroleum entrapment : London, Elsevier Applied Science Publishers, 328 p.

Matthews, R., Koch, R., and Leppin, M., 1997, Advances in integrated exploration for unconformity uranium deposits in Western Canada, in Gubins, A.G., ed., Proceedings of Exploration 97: Fourth Decennial International Conference on Mineral Exploration, p. 993-1024.

McGill, B.D., Marlatt, J.L., Matthews, R.B., Sopuck, V.J., Homeniuk, L.A., and Hubregtse, J.J., 1993, The P2 North uranium deposit, Saskatchewan, Canada : Exploration and Mining Geology, v. 2, p. 321-331.

Montel, J.-M., Foret, S., Veschambre, M., Nicollet, C, and Provost, A., 1996, Electron microprobe dating of monazite : Chemical Geology, v. 131, p. 37-53.

Nguyen Trung, C., 1985, Géochimie théorique et expérimentale des oxydes d'uranium dans des solutions aqueuses de 25 à 700°C, sous une pression de 1 à 6000 bars. Synthèse hydrothermale de certains minéraux d'uranium (VI) et (IV) [Ph.D. thesis]: Nancy, Institut National Polytechnique de Lorraine, tome I, 479 p.

Pagel, M., 1975a, Cadre géologique des gisements d'uranium dans la structure Carswell (Saskatchewan-Canada). Etude des phases fluides [Ph.D. thesis]: Nancy, Henri Poincaré University (Nancy I), 157 p.

Pagel, M., 1975b, Détermination des conditions physico-chimiques de la silicification diagénétique des grès Athabasca (Canada) au moyen des inclusions fluides: Comptes Rendus de l'Académie des Sciences, v. 280, D, p. 2301-2304.

Pagel, M., 1977, Microthermometry and chemical analysis of fluid inclusions from the Rabbit Lake uranium deposit, Saskatchewan, Canada : Institution of Mining and Metallurgy Transactions, section B, v. 86, p. B157-B158.

Pagel, M., and Jaffrezic, H., 1977, Analyses chimiques des saumures des inclusions du quartz et de la dolomite du gisement d'uranium de Rabbit Lake (Canada). Aspect méthodologique et importance génétique : Comptes Rendus de l'Académie des Sciences, v. 284, série D-113.

Pagel, M., Poty, B., and Sheppard, S.M.F., 1980, Contribution to some Saskatchewan uranium deposits mainly from fluid inclusion and isotopic data, in Ferguson, S., and Goleby, A., eds., Uranium in the Pine Creek Geosyncline : International Atomic Energy Agency, Vienna, p. 639-654.

Pagel, M., Pinte, G., and Rotach-Toulhoat, N., 1987, The rare earth elements in natural uranium oxides, in Monograph Series on Mineral Deposits : Gebrüder Borntraeger, Berlin, v. 27, p. 81-85.

Pagel, M., Halter, G., Ruhlmann, F., and Tona, F., 1988, Evolution polycyclique de la province uranifère Athabasca (Saskatchewan - Canada) et genèse des gisements liés spatialement à la discordance du Protérozoïque Moyen dans la structure de Carswell, in Gisements Métallifères dans leur Contexte Géologique : Document du BRGM no. 158, v.1, p. 389-413.

Petit, S., and Decarreau, A., 1990, Hydrothermal (200°C) synthesis and crystal chemistry of iron-rich kaolinites: Clay Minerals, v. 25, p. 181-196.

Philippe, S., Lancelot, J.R., Clauer, N., and Pacquet, A., 1993, Formation and evolution of the Cigar Lake uranium deposit based on U-Pb and K-Ar systematics: Canadian Journal of Earth Sciences, v. 30, p. 720-730.

Quirt, D., Kotzer, T., and Kyser, T.K., 1991, Tourmaline, phosphate minerals, zircon, and pitchblende in the Athabasca Group: Maw Zone and McArthur River areas, Saskatchewan, in Summary of Investigations 1991: Saskatchewan Geological Survey, Saskatchewan Energy and Mines, Miscellaneous Report 91-4, p. 181-191.

Quirt, D., 2000, Sub-Athabasca Group fanglomerate in the McArthur River-Read Lake area, Saskatchewan, in Proceedings, GeoCanada2000, The Millennium Geoscience Summit, Calgary: GAC-MAC joint annual meeting, abstract 251 (Conference CD).

Raffensperger, J.P., and Garven, G., 1995a, The formation of unconformity-type uranium ore deposits; 1. Coupled groundwater flow and heat transport modeling: American Journal of Science, v. 295, p. 581-636.

Raffensperger, J.P., and Garven, G., 1995b, The formation of unconformity-type uranium ore deposits; 2. Coupled hydrochemical modeling: American Journal of Science, v. 295, p. 639-696.

Ramaekers, P., 1981, Hudsonian and Helikian basins of the Athabasca region, Northern Saskatchewan: Geological Survey of Canada Paper 81-10, p. 219-233.

Ramaekers, P., 1990, Geology of the Athabasca Group (Helikian) in Northern Saskatchewan: Saskatchewan Energy and Mines, Saskatchewan Geological Survey, report 195, 49 p.

Ramaekers, P., and Dunn, C.D., 1977, Geology and geochemistry of the eastern margin of the Athabasca Basin: Saskatchewan Geological Society Special Publication no. 3, p. 297-322.

Ridley, J., 1993, The relations between mean rock stress and fluid flow in the crust: with reference to vein- and lode-style gold deposits : Ore Geology Reviews, v. 8, p. 23-37.

Rippert, J.C., Koning, E., Robbins, J., Koch, R., and Baudemont, D., 2000, The Shea Creek Uranium Project, West Athabasca Basin, Saskatchewan, Canada, in Proceedings, GeoCanada2000, The Millennium Geoscience Summit, Calgary: GAC-MAC joint annual meeting, abstract 570 (Conference CD).

Ross, G.M., Milkereit, B., Eaton, D., White, D., Kanasewitch, E.R., and Burianyk, M.J.A., 1995, Paleoproterozoic collisional orogen beneath the western Canada sedimentary basin imaged by Lithoprobe crustal seismic-reflection data: Geology, v. 23, p. 195-199.

Ross, G.M., and Eaton, D.W., 1997, Winagami reflection sequence: Seismic evidence for postcollisional magmatism in the Proterozoic of western Canada: Geology, v. 25, p. 199-202.

Ruzicka, V., 1986, Uranium deposits in the Rabbit Lake-Collins Bay area, Saskatchewan, in Evans, E.L., ed., Uranium Deposits of Canada: Canadian Institute of Mining Metallurgy and Petroleum Special Volume 33, p. 144-154.

Ruzicka, V., 1996, Unconformity-associated uranium, in Eckstrand, O.R., Sinclair, W.D., and Thorpe, R.I., eds., Geology of Canadian Mineral Deposit Types : Geological Survey of Canada, Geology of Canada, no. 8, p. 197-210.

Salvi, S., Pokrovski, G.S., and Schott, J., 1998, Experimental investigation of aluminum-silica aqueous complexing at 300°C : Chemical Geology, v. 151, p. 51-67.

Sass-Gustkiewicz, M., 1996, Internal sediments as a key to understanding the hydrothermal karst origin of the upper silesian Zn-Pb ore deposits: Society of Economic Geologists, Special Publication no. 4, p. 171-181.

Sibson, R.H., 1994, Crustal stress, faulting and fluid flow, in Parnell, J., ed., Geofluids: Origin, Migration and Evolution of fluids in Sedimentary Basins : Geological Society Special Publication no. 78, p. 69-84.

Sibson, R.H., 2000, Tectonic controls on maximum sustainable overpressure: fluid redistribution from stress transitions : Journal of Geochemical Exploration, v. 69, p. 471-475.

SMDC, 1992, Wheeler River Project. Inedited document.

Suzuki, K., and Adachi, M., 1994, Middle Precambrian detrital monazite and zircon from the Hida gneiss on Oki-Dogo Island, Japan: their origin and implications for the correlation of basement gneiss of Southwest Japan and Korea: Tectonophysics, v. 235, p. 277-292.

Tester, J.W., Worley, W.G., Robinson, B.A., Grigsby, C.O., and Feerer, J.L., 1994, Correlating quartz dissolution kinetics in pure water from 25 to 625°C: Geochimica et Cosmochimica Acta, v. 58, p. 2407-2420.

Thomas, D.J., Matthews, R.B., and Sopuck, V., 1998, Athabasca Basin Unconformity-Type Uranium Deposits: A Synopsis of the Empirical Model and Review of Exploration and Production Trends, in Proceedings, Canadian Institute of Mining, Metallurgy and Petroleum meeting, Montréal.

Vigneresse, J.L., and Cannat, M., 1987, Mesures de paramètres physiques dans le sondage d'Echassières (vitesse sismique, porosité, densité), in Mémoire Géologie profonde de la France , tome 1: Géologie de la France, no. 2-3, p. 145-148.

Villeneuve, M.E., and Thériault, R.J., 1991, U-Pb ages and Sm-Nd signature of two granites from the Fort Simpson magnetic high, northwest Canada: Canadian Journal of Earth Sciences, v. 28, p. 1003-1008.

Wallis, R.H., Saracoglu, N., Brummer, J.J., and Golightly, J.P., 1983, Geology of the McLean uranium deposits, in Cameron, E.M., ed., Uranium exploration in Athabasca Basin, Saskatchewan, Canada: Saskatchewan Energy and Mines, Geological Survey of Canada, p. 71-110.

Wilde, A.R., and Wall, V.J., 1987, Geology of the Nabarlek uranium deposit, Northern Territory, Australia : Economic Geology, v. 82, p. 1152-1168.

Wilson, M.R., and Kyser, T.K., 1987, Stable isotope geochemistry of alteration associated with the Key Lake uranium deposit : Economic Geology, v. 82, p. 1450-1557.

Wolery, T.J., and Daveler, S.A., 1992, EQ3/6, a software package for geochemical modeling of aqueous systems. UCRL-MA-110772 PT I-IV : Berkeley, University of California, Lawrence Livermore National Laboratory.

ARTICLE 4 :

Uranium-bearing breccias in the Athabasca Basin, Saskatchewan (Canada)
Hydrothermal karsts in Proterozoic sandstones

Guillaume Lorilleux CREGU-UMR G2R 7566, U. H. P., BP 23, F-54501 Vandoeuvre, France
Michel Jébrak UQAM-DSTA, CP 8888, Montréal (QUE) H3C 3P8 Canada
Michel Cuney CREGU-UMR G2R 7566, U. H. P., BP 23, F-54501 Vandoeuvre, France
Christian Le Carlier de Veslud CRPG, BP 20, F-54501 Vandoeuvre, France
Jean-Jacques Royer CRPG, BP 20, F-54501 Vandoeuvre, France

Destiné à GEOLOGY
(version longue)

Résumé

La modélisation tridimensionnelle de la géométrie des brèches, l'analyse fractale des morphologies de fragments et les calculs de bilans de masse montrent que les brèches associées aux minéralisations uranifères encaissées par les grès Protérozoïque Moyen du Bassin Athabasca sont l'expression d'une karstification hydrothermale. La formation des karsts a été déclenchée par un événement tectonique entre 1,52 et 1,25 Ga provoquant une fracturation tectonique et hydraulique et initiant la circulation verticale ascendante de fluides de socle sous-saturés en silice dans les grès fracturés. Les systèmes de karsts se sont ensuite développés par dissolution du quartz et effondrements gravitaires mis en évidence par des pertes de volume spectaculaires pouvant atteindre 90 %. Les zonations de perméabilité latérales et verticales des principales failles inverses contrôlant la minéralisation uranifère dans les grès ont constitué un paramètre majeur de l'évolution des karsts. L'intensité de dissolution était maximale à la discordance jouant le rôle de piège pour la minéralisation uranifère. Les très forts rapports fluide/roche jusqu'à 38 000 dans le cœur de la faille contrôlant les gisements de Sue A et B mettent en évidence la percolation d'énormes quantités de fluides et une longue période d'activité du système karstique hydrothermal. Ces facteurs apparaissent indispensables pour expliquer les forts tonnages et les très hautes teneurs des gisements d'uranium de type discordance.

Mots-clefs : karst, dissolution, grès, brèche, uranium.

Abstract

3D modeling of the geometry of breccias, fractal analysis of the morphology of the breccia fragments and mass balance calculations indicate that breccias associated with uranium mineralizations hosted by the Proterozoic Athabasca sandstone are the expression of hydrothermal karstification. Karst formation has been triggered by a tectonic event between 1.52 and 1.25 Ga inducing tectonic and hydraulic fracturing and initiating circulation of silica undersaturated basement fluids upward in the fractured sandstone. The karst systems developed by quartz dissolution and subsequent collapse, evidenced by spectacular volume losses up to 90 %. The lateral and vertical permeability zonation in the sandstone of the main reverse structures controlling the uranium mineralization was a major parameter of the karst evolution. The intensity of dissolution was maximal at the unconformity acting as a trap for the uranium mineralization. The very high fluid/rock ratios up to 38,000 in the core of the fault controlling the Sue A and B uranium deposits indicate percolation of huge amounts of fluids

and a long time of activity of the hydrothermal karst systems. That appear to be one of the major parameters explaining the large tonnages and very high grades of the unconformity-type uranium deposits.

Keywords : karst, dissolution, sandstone, breccia, uranium.

1. Introduction

The unconformity-type uranium deposits of the Athabasca Basin (Canada) (Fig. 1) contain the largest high-grade uranium concentrations in the world (219 000 tons at 14% U_3O_8 in the McArthur River deposit). With average enrichment factors up to 60 000, they are today the most economic deposits and make Canada the world's largest producer of uranium.

Unconformity-type uranium deposits of the Athabasca Basin are commonly surrounded and hosted by hydrothermal breccias in the Proterozoic Athabasca sandstone (Wallis et al., 1983; Ey et al., 1985). The aim of this study is to determine the main factors linking the genesis of such high-grade uranium mineralizations with extended breccia development in sandstones. Breccias occurring in the Athabasca Basin have been interpreted as being tectonic (Ey et al., 1985; Baudemont et al., 1993) and dissolution-collapse (Wallis et al., 1983).

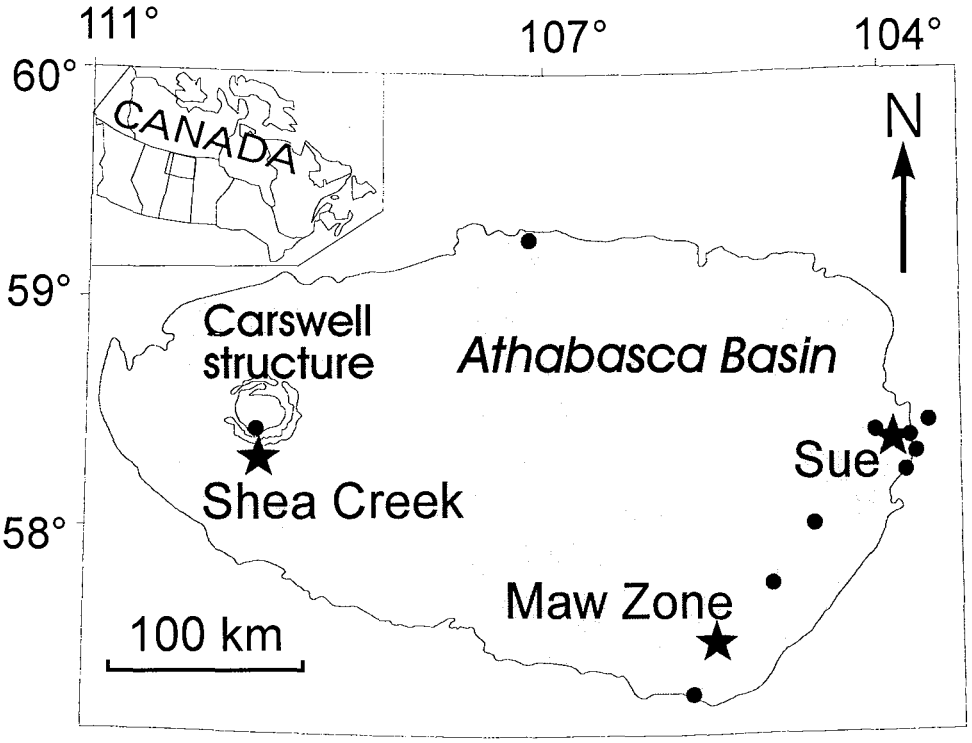

Figure 1. Location of the Athabasca Basin (Canada) with the main unconformity-type uranium deposits (black dots). Black stars indicate the areas of study.

Three study areas have been selected in the Athabasca Basin according to their location relative to the unconformity and to the mineralized faults: the Sue C deposit (open pit mine), the Shea Creek prospect and the Maw Zone (yttrium mineralization and uranium enrichment) (Fig. 1). A 3D model of Shea Creek breccia body geometries has been built using the Gocad software and the logging of breccias in about 50 drill holes (see annexe II). Fractal analysis of fragment morphologies and mass balance calculations have permitted to quantify the intensity of brecciation and the amount of fluids involved in the quartz dissolution process. We

demonstrate that the uranium and yttrium mineralizations are associated with the development of hydrothermal karsts in Proterozoic sandstones due to intensive quartz dissolution and associated collapse events along reverse fault zones.

2. Methodology

Sandstone-hosted breccias have been studied on the walls of the Sue C open pit, on core in the Shea Creek exploration zone and on outcrops at the Maw Zone. Fragment morphologies of the Shea Creek breccias have been quantified using the Euclidian Distance Mapping (EDM) method (Bérubé and Jébrak, 1999). Stripes of increasing thickness were computed from the particle outline. Then the log of the area of each stripe was plotted against the log of their thickness in a Richardson plot (Fig. 2). The fractal dimension (D) was derived from the slope of the plot (s) using the relationship D = 2 – s. Fragment morphometry distribution curves have been plotted for each breccia type.

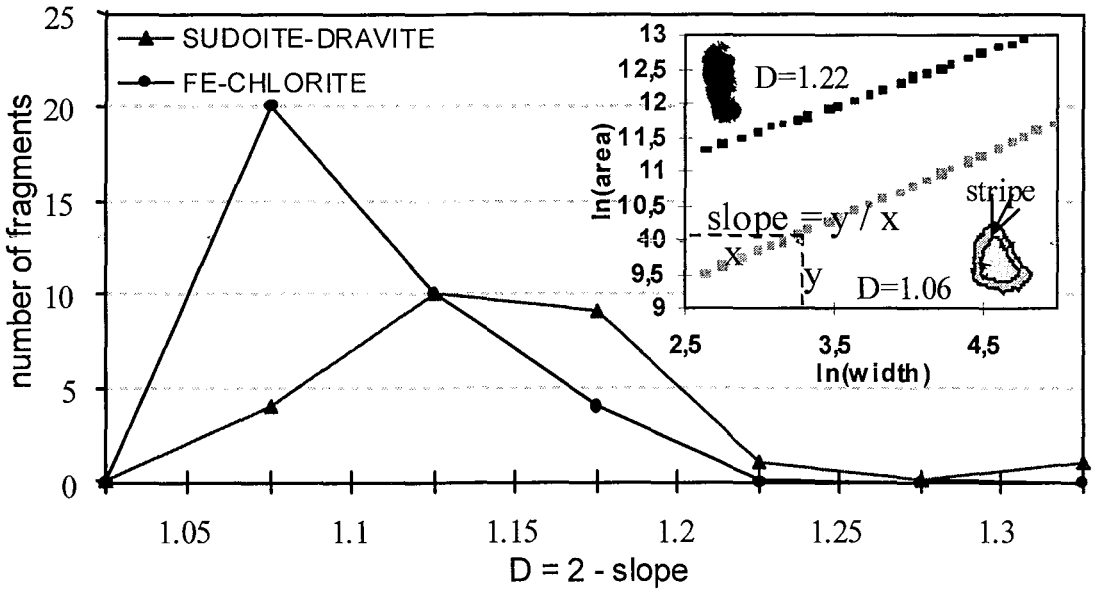

Figure 2. Fragment morphologies D distribution for the two types of breccias studied at Shea Creek. The inset in the right hand corner is an example of Richardson plot used to calculate the fractal dimension of fragment morphology. Two breccia fragments are presented with their fractal dimensions.

The breccia dissolution textures have been observed on macroscopic samples, in thin sections and with Scanning Electron Microscopy (SEM) (see part II). Breccias have been classified using their maturity degree. The maturity increases with matrix percentage and intensity of brecciation.

Mass balance calculations were based on geochemical whole rock analysis by ICP-AES and ICP-MS (10 major and 44 trace elements) and density measurements of breccia samples (see part III and IV-paper 3). Density of dry samples has been determined using a picnometer with water. Mass balance calculations have been realized using the Grant method that consists

in a simple graphical solution of Gresens' equation. Al appears to be immobile at Sue whereas it is enriched in some of the Shea Creek samples. At Shea Creek, Zr is one of the most stable elements. As a consequence, Al and Zr have been considered as immobile elements in the Sue and Shea Creek breccias. At the Maw Zone, no volume variation has been assumed in the mass balance calculations because of petrographic and geochemical evidences of very weak quartz dissolution.

3. Geological setting

The Athabasca Basin formed during the Middle Proterozoic at about 1.7 Ga (Kotzer et al., 1992). The basin is separated from the underlying basement by a major unconformity. It is composed of sub-basins oriented NE-SW and controlled by faults rooted in the basement. The Athabasca Group filling the basin consists of thick, unmetamorphosed and flat-lying sequences of fluviatile to marine quartzose sandstones deposited in a proximal shelf environment (Ramaekers, 1981). A maximum total thickness of 4 to 5 kilometers of sediments has been proposed from fluid inclusions and diagenetic clay assemblages studies (Pagel, 1975; Halter, 1988). The present thickness of the basin is about 70 meters at Sue, 700 meters at Shea Creek and 250 meters at the Maw Zone.

The Sue (A and B), Shea Creek and Maw Zone mineralizations are located in the basal Manitou Falls lithologies which are typically medium-grained to conglomeratic. Heavy minerals layers, generally less than 1 millimeter thick, are common in the basal members of the Manitou Falls formation. Their distribution shows great variability at the millimeter to decimeter scale. Major sandstone cements are quartz displaying syntaxial overgrowths, clay minerals (kaolinite, illite, chlorite) and iron oxides. The three mineralized areas are hosted by reverse shear zones crosscutting the unconformity and containing graphite in the basement. The mineralizing event is coeval with reverse movements along graphite-rich faults during contraction tectonics (Baudemont et al., 1993). The sandstone-hosted mineralizations are associated with breccia bodies and alteration haloes. The alteration haloes are composed of illite at Sue, of quartz, sudoitic chlorite, dravite and Fe-chlorite at Shea Creek and of quartz and dravite at the Maw Zone. The Sue, Shea Creek and Maw Zone breccias have been chosen because they are respectively located at an increasing distance from the unconformity.

4. Results

4.1. Sue C open pit

The Sue C open pit presents local but intense brecciation phenomenons within 50 meters above the unconformity. The main structural control of the Sue deposits is a serie of N12 graphite-rich reverse faults. The Sue A and B uranium mineralization is sandstone-hosted up to 50 meters above the unconformity whereas the Sue C, D and E uranium deposits consist of basement-hosted vein-type mineralizations occurring down to more than 100 meters below the unconformity (Baudemont et al., 1993).

The breccias have elongated finger shapes narrowly controlled by the graphite-rich reverse basement-rooted structure controlling also the Sue A and B deposits. They are more developed at fault intersections, are located just above the unconformity and are typically 10 to 20 meters high, 5 meters wide and 10 meters long.

They are composed of illitized striated sandstone balls wrapped in massive illite and are called "zones à boules", that were described for the first time in the Cluff D uranium deposit (Ey et al., 1985). The ball shapes are due to quartz dissolution in a diffusion-limited regime (Jébrak, 1997) combined with ball rotation during reverse fault movements. At the unconformity, the illitic matrix percentage may be greater than 50 vol. % and sandstone balls are totally illitized, indicating an extreme degree of maturity. Microscopic observations indicate that illite replaces diagenetic dickite showing Al transfer rather than transport. Therefore, Al was considered as immobile in mass balance calculations. Extreme volume loss has been calculated due to intense quartz dissolution (Table 1). As only limited collapse has been observed, the volume loss was probably accommodated by tectonic contraction because of the reverse movements and ball rotations observed along the fault.

4.2. Shea Creek

The Shea Creek area was selected because of the widespread breccia development in the sandstone surrounding the high-grade uranium mineralization. The Shea Creek ore is found down to 40 meters in the basement and, in the sandstone up to 40 meters above the unconformity (Rippert et al., 2000).

Sudoite-dravite and Fe-chlorite breccias, defined by the nature of their cement, are the main breccia types in sandstones. Three-dimensional modeling using systematic breccia logging along about 50 drill holes shows that sudoite-dravite breccias have finger shapes. The breccia fingers enlarge at the unconformity, and are controlled by mineralized reverse structures which are graphite-rich in the basement (Fig. 3). The development of Fe-chlorite breccias is later than the sudoite-dravite breccias. The Fe-chlorite breccia bodies display a dome shape developed at the intersection of several faults (Fig. 3).

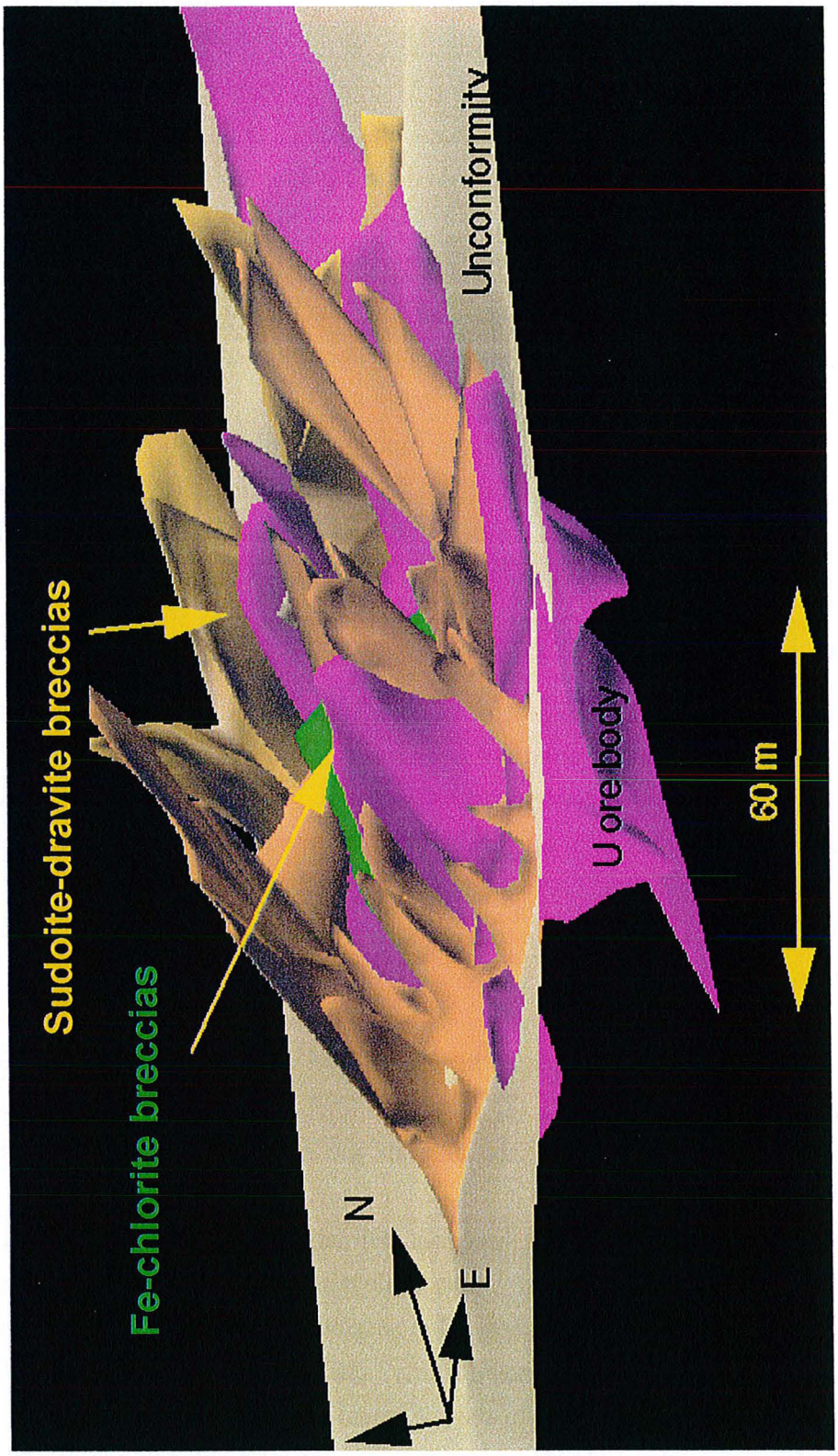

Figure 3. Three-dimensional model of the mineralization and associated breccias in the south of the Shea Creek exploration zone. Note the structurally controlled finger shape of the sudoite-dravite dissolution breccias and the dome shape of the Fe-chlorite dissolution-collapse breccias.

Immature sudoite-dravite and Fe-chlorite breccias display typical jigsaw patterns indicating fluid-assisted fracturing (see part II). The predominance of rounded fragments characterized by medium fractal dimensions (Table 1) in sudoite-dravite breccias is the expression of sandstone dissolution in a slow diffusion-limited regime. Low median fractal dimension in Fe-chlorite breccias indicates a mixing of non-corroded angular fragments with corroded fragments. The observation of some complex shapes and pervasively altered fragments as well as the abundance of pits observed with a SEM on fragment surfaces would indicate a kinetic regime of dissolution (Burley and Kantorowicz, 1986). The typical presence of numerous corroded detrital quartz grains in the matrix and the ubiquitous presence of quartz dissolution textures at the macroscopic, thin section and SEM scales, clearly demonstrate the role of dissolution in the breccia formation.

Breccia type		Ball breccias (Sue)	Sudoite-dravite (Shea Creek)	Fe-chlorite (Shea Creek)	Dravite (Maw Zone)
Geometry	Volume (m^3)	~ 10 000	166 000*	30 000*	~ 40 000
	Shape	Finger	Finger	Dome	Funnel
	Structural control	High	High	Medium	Medium
	Distance from the unconformity (m)	0 → 30	0 → 30	0 → 30	0 → 200
Textures	Fragment shape	Ball	Corroded	Angular and corroded	Slightly rounded
	Fractal dimension	Low	Medium (1.17†)	Low (1.12†)	Low
	Fragment composition	Illitized sandstone	Silicified sandstone	Variably silicified sandstone	Silicified sandstone
	Matrix composition	Illite	Sudoite-dravite	Fe-chlorite, kaolinite, sulfides	Dravite
	Fragment/matrix relationships	Matrix-supported	Matrix-supported	Fragment-supported	Fragment-supported
Dissolution intensity	Water/rock ratio§	> 38 000	> 5 000	> 6 000	> 3 000
	Volume loss (%)#	85	Up to 90	Up to 70	Negligible
	Breccia maturity	High	Medium to high	Low to high	Low
	Dissolution regime	Diffusion-limited	Diffusion-limited	Kinetic	Diffusion-limited
	Economic substances	U	U, Ni, Co	U, Ni, Co	Y, HREE

* Volume calculated with Gocad.
† Average fractal dimension calculated using the EDM method developed by Bérubé and Jébrak (1999) with NIH image.
§ Water/rock ratio calculated with 90% silica saturation for the Sue C and the Shea Creek breccias and with 99% for the Maw Zone breccias. The values given for Shea Creek and the Maw Zone are for 10 vol. % matrix in average.
# Volume loss calculated using immobile Al for the « zones à boules » and immobile Zr for sudoite-dravite breccias and Fe-chlorite breccias.

Table 1 – Solution-collapse breccia characteristics in the Athabasca Basin.

Fe-chlorite breccias are commonly fragment-supported and display graded-bedding textures in the upper part of fragment-supported breccia units (Fig. 4). They present a negative correlation between rotation angle and size of the tilted blocks. Consequently, they display major evidences of collapse due to quartz dissolution. That would explain their dome shape (Fig. 3) typical of collapse breccia bodies like in Mississippi Valley type deposits (Dzuslynski and Sass-Gustkiewicz, 1989). Collapse phenomenons have also occurred in sudoite-dravite breccias but are less developed than in Fe-chlorite breccias as evidenced by local fragment-supported textures and horizontally oriented elongated fragments in mature zones. Mass

balance calculations using immobile Zr indicate volume loss up to 90 % in sudoite-dravite mature zones with an average of 8 % in the overall breccia body (Table 1). The calculated volume loss in Fe-chlorite breccias is highly variable. It is negligible in low matrix collapse zones in the upper part of the body and about 65 % in average in zones with 60 to 70 vol. % of matrix. Weak volume loss zones may therefore occur in the upper part of the body where collapsed sandstone fragments dominate over residual minerals after dissolution.

Figure 4. Photograph of a Fe-chlorite solution-collapse breccia at Shea Creek with fragment-supported texture and graded-bedding in the upper part of the breccia.

4.3. Maw Zone

The Maw Zone was chosen because of the large development of breccias between 200 and 250 meters above the unconformity. The breccias, located below and within intraclast-rich sandstone lithologies, host yttrium and REE mineralization. Small uranium enrichment occurs at the unconformity below the breccia body (MacDougall, 1990; Quirt et al., 1991).

The breccias display an overall funnel shape controlled by a reverse structure rooted in graphite-rich lithologies. Their volume has been estimated at 40,000 m^3 from outcrop and drill hole data (Table 1). They have typically a low matrix percentage, about 15 vol. % in average

and rarely up to 30 vol. %. They consist of slightly rounded silicified sandstone fragments in a matrix mostly composed of 85 to 90 wt. % of corroded detrital quartz grains and dravite. The low matrix percentage and the high proportion of detrital quartz grains in the matrix express the low maturity degree of these breccias. The most immature breccias have jigsaw textures and are found on the margins of the funnel. Jigsaw textures are the expression of hydraulic brecciation that could be related to the termination zone of the basement-rooted reverse fault (Cox et al., 2000). The rounded fragment shapes and the presence of corroded detrital quartz grains in the matrix indicate quartz dissolution in the matrix and on the fragments borders. The formation of rounded shapes rather than cusps producing complex shapes suggests a probable diffusion-limited regime of dissolution (Jébrak, 1997) (Table 1). In the center of the funnel, breccias are heterolithic with tilted fragments and fragment-supported textures, indicating the occurrence of collapse. The systematic measurements of the azimuth of tilted blocks demonstrate that this collapse occurred along structural trends. Mass balance calculations show negligible volume loss due to poorly developed dissolution (Table 1). Therefore, the collapse could not be attributed to the dissolution at the Maw Zone.

4.4. Genesis of breccias

The spatial correlation between breccias and uranium mineralizations at Shea Creek and Sue and the presence of typical unconformity-type hydrothermal alteration minerals such as sudoitic chlorite, illite and dravite in the breccia cement of the three zones of study suggests that breccias and unconformity-type uranium mineralizations are coeval.

Sandstone-hosted immature breccias show that they were initiated by hydraulic or tectonic fracturing along reverse faults which are graphite-rich in the basement. The similar ages of uranium mineralizations in various deposits (Cumming and Krstic, 1992) indicate that breccia formation was triggered by a regional tectonic reactivation of reverse faults between 1.52 and 1.25 Ga. The maturity evolution of the breccias mainly results from progressive quartz dissolution in response to circulation of a fluid undersaturated in silica. Such fluid flow occurred in the fractures and permeable matrix of the tectonic and hydraulic breccias. The maturity of the breccias decreases with the distance to the unconformity as indicated by extremely mature "zones à boules" just above the unconformity at Sue, mature breccias at Shea Creek and immature breccias at the Maw Zone, creating a vertical maturity gradient. Where dissolution created enough space, collapse occurred except in "zones à boules" where volume loss has been accommodated by tectonic contraction.

5. Discussion

5.1. Vertical fluid flow and uranium entrapment

Fayek and Kyser (1997) have proposed that uranium mineralization at the unconformity results from the mixing of reducing basement fluids flowing upward in the basement with oxidizing basin fluids circulating laterally in the sandstone. The evidence of a vertical maturity gradient in sandstones shows that the dissolution intensity decreased upward. Therefore, as the fluid undersaturation in silica would have decreased with time, our results indicate that fluids were migrating upward along the reverse structure in the sandstone. Consequently, the fluid probably derives from the quartz-depleted basement below, along graphite-rich reverse structures.

A silica saturation of 90 % just above the unconformity for Sue and Shea Creek and of 99 % 200 meters above the unconformity at the Maw Zone were considered in fluid/rock ratio calculations to reflect the increase in silica saturation of the basement fluids migrating upward. However, these values are hypothetical because they cannot be constrained precisely yet. The very high calculated fluid/rock ratios (Table 1) indicate a long time of formation consistent with the slow diffusion-limited regime of dissolution. Assuming an hydraulic conductivity of 100 m/year and a connected porosity of 1 %, the time of formation of breccias of the Sue C open pit mine is about 800 000 years. The minimal fluid volumes which have circulated in the faulted sandstones have been estimated between 0.16 and 2.5 km^3 using the breccia volumes, the volume loss values and the fluid/rock ratios.

The massive quartz dissolution in sandstones near the unconformity has created the empty space needed for the deposition of uranium mineralization. The basement fluids dissolving quartz also interacted with basin fluids leading to uranium oxide precipitation. Therefore, the mineralization was coeval with the development of hydrothermal breccias in sandstones.

5.2. Hydrothermal karsts

"Zones à boules" were initiated by tectonic fracturing in the core of the faults whereas solution-collapse breccias at Shea Creek and at the Maw Zone were initiated by hydraulic fracturing in the damage zone of the faults (Caine et al., 1996). Then, circulation of silica undersaturated fluids induced massive quartz dissolution and subsequent collapse. The collapse-dominated solution breccias at the Maw Zone and in the upper part of Fe-chlorite breccia bodies at Shea Creek are due to collapse propagation after intense quartz dissolution below.

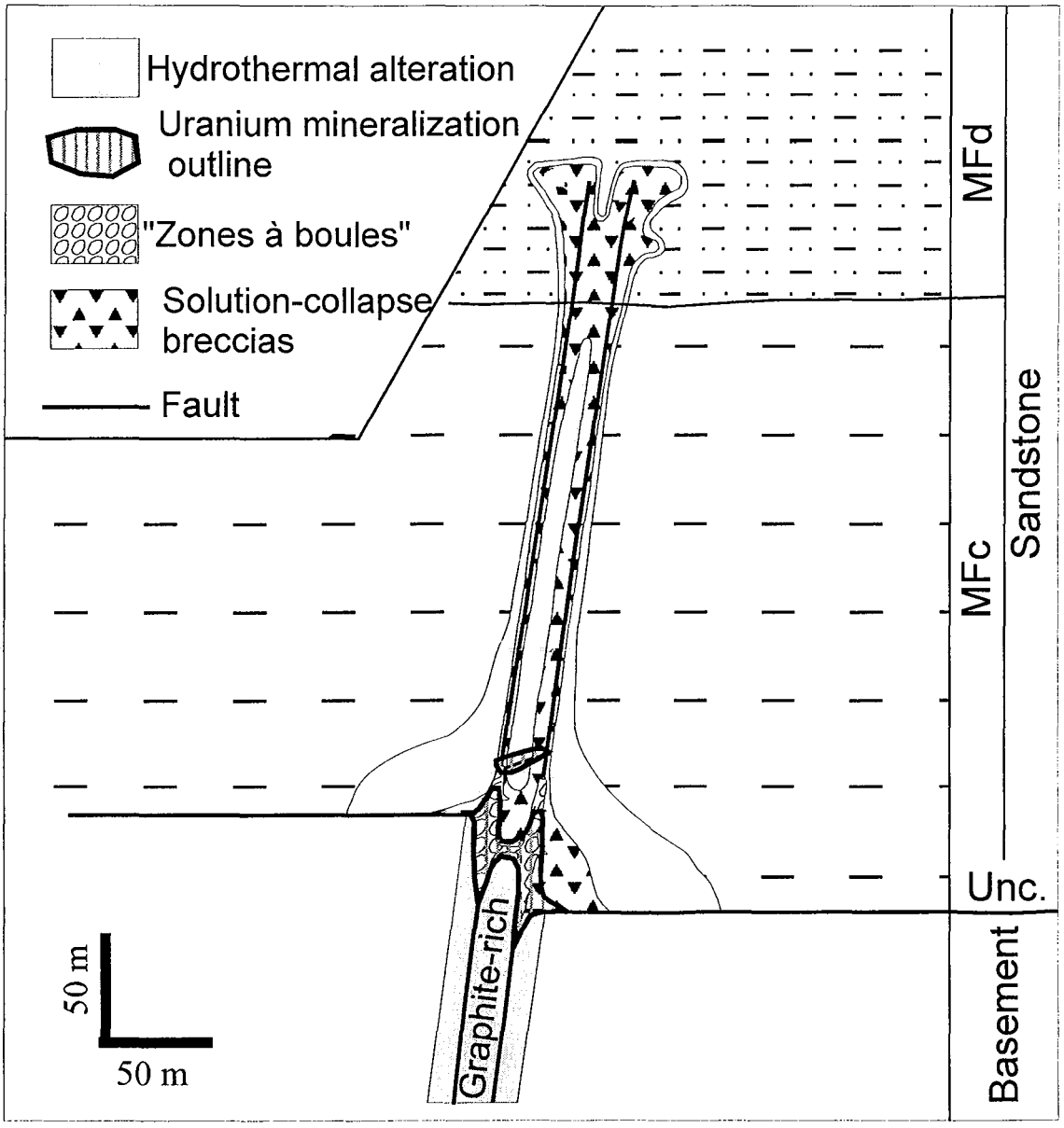

Figure 5. Schematic model of structurally controlled hydrothermal karst development in the sandstone surrounding an unconformity-type uranium deposit. The ball breccias are located in the center of the system in the fault core close to the unconformity whereas solution-collapse breccias are developed in the damage zone around and higher above the unconformity (Unc.).

Consequently, the importance of dissolution observed at the base of the Athabasca sandstones and the collapse structures associated with U and REE-Y mineralization can be compared to hydrothermal karsts developed in limestones (Fig. 5). Such hydrothermal karstification is found in Pb-Zn Mississippi Valley type deposits (Dzuslynski and Sass-Gustkiewicz, 1989; Clendenin and Duane, 1990), in basement-hosted unconformity-type uranium mineralizations (Ferguson et al., 1980) and in breccia pipe uranium deposits in Colorado (U.S.A.) (Finch, 1992).

5.3. Permeability evolution

The higher fluid/rock ratio in "zones à boules" than in the surrounding solution-collapse breccias indicate that the permeability was higher in the fault core than in the damage zone. Therefore, basement fluids circulated rapidly upwards along the fault core and slowed down laterally and above in the hydraulically formed damage zone. As a consequence, the permeability of the hydrothermal system was dependant on the fault zonation. Quartz dissolution would have operated as a fluid feedback mechanism allowing the sustainable permeability required for the circulation of the huge quantity of fluids needed for quartz dissolution and massive uranium precipitation. Dissolution and collapse due to fluid focusing in fault zones were also described by Knipe (1993). Breccias evolved from tectonic fracture zones to "zones à boules" in the core of the faults close to the unconformity and from hydraulic breccias to solution-collapse breccias in an extended damage zone (Fig. 5).

6. Conclusion

The genesis of unconformity-type uranium deposits has been triggered by a regional tectonic reactivation between 1.52 and 1.25 Ga initiating circulation of a silica undersaturated basement fluid upward in the sandstone. This fluid flow induced the formation of a hydrothermal karst system by intense quartz dissolution and subsequent collapse propagation. The fluid mixing between basement and uranium-bearing basin fluids occurred within the spaces created by quartz dissolution inducing uranium oxides precipitation. The intensity of dissolution was maximal at the unconformity creating the best trap for the world class unconformity-type uranium mineralizations. The very high calculated fluid/rock ratios indicate that huge volumes of fluids have circulated within the reverse faults. That would be one of the parameters explaining the large tonnages and very high grades of the unconformity-type uranium deposits. The long time of formation of the uranium mineralization, requiring a stationary redox front, is evidenced by the very high fluid/rock ratios and by a diffusion-limited regime of quartz dissolution.

Acknowledgments

We would like to acknowledge COGEMA and COGEMA Resources Inc for their financial and technical support. COGEMA and CAMECO are thanked for permission to publish the geological data collected in the field and in laboratory. D. Becel is thanked for his help in the construction of the Gocad model. The manuscript benefited from reviews by Patrice Bruneton, Jean Mondy and Jean-Claude Rippert.

References cited

Baudemont, D., Piquard, J.P., Ey, F., and Zimmerman, J., 1993, The Sue Uranium Deposits, Saskatchewan, Canada: Exploration and Mining Geology, v. 2, p. 179-202.

Bérubé, D., and Jébrak, M., 1999, High precision boundary fractal analysis for shape characterization: Computers & Geosciences, v. 25, p. 1059-1071.

Burley, S.D., and Kantorowicz, J.D., 1986, Thin section and S.E.M. textural criteria for the recognition of cement-dissolution porosity in sandstones: Sedimentology, v. 33, p. 587-604.

Caine, J.S., Evans, J.P., and Forster, C.B., 1996, Fault zone architecture and permeability structure: Geology, v. 24, p. 1025-1028.

Clendenin, C.W., and Duane, M.J., 1990, Focused fluid flow and Ozark Mississippi Valley-type deposits: Geology, v. 18, p. 116-119.

Cox, S.F., Knackstedt, M.A., and Braun, J., 2000, Principles of structural control on permeability and fluid flow in hydrothermal systems: Reviews in Economic Geology, (in press).

Cumming, G.L., and Krstic, D., 1992, The age of unconformity-related uranium mineralization in the Athabasca Basin, northern Saskatchewan: Canadian Journal of Earth Sciences, v. 29, p. 1623-1639.

Dzuslynski, S., and Sass-Gustkiewicz, M., 1989, Pb-Zn ores, in Bosak, P., Ford, D.C., Glazek, J., and Horacek, I., eds., Paleokarst. A Systematic and Regional Review: Amsterdam and Praka, Elsevier and Academia, p. 377-396.

Ey, F., Gauthier-Lafaye, F., Lillié, F., and Weber, F., 1985, A uranium unconformity deposit: The geological setting of the D orebody (Saskatchewan-Canada), in Lainé, R., Alonso, D., and Svab, M., eds., The Carswell structure uranium deposits, Saskatchewan: Geological Association of Canada Special Paper 29, p. 121-138.

Fayek, M., and Kyser, T.K., 1997, Characterization of multiple fluid-flow events and Rare-Earth-Element mobility associated with formation of unconformity-type uranium deposits in the Athabasca Basin, Saskatchewan: The Canadian Mineralogist, v. 35, p. 627-658.

Ferguson, J., Ewers, G.R., and Donnelly, T.H., 1980, Model for the development of economic uranium mineralization in the Alligators Rivers uranium field: N.T., in Ferguson, S.

and Goleby, A., eds., Uranium in the Pine Creek Geosyncline: Vienna, International Atomic Energy Agency, p. 563-574.

Finch, W.I., 1992, Descriptive model of solution-collapse breccia pipe uranium deposits, in Bliss, J.D., ed., Developments in mineral deposit modeling: U.S. Geological Survey Bulletin 2004, p. 33-35.

Halter, G., 1988, Zonalités des altérations dans l'environnement des gisements d'uranium associés à la discordance du Protérozoïque Moyen (Saskatchewan, Canada) [Ph.D. thesis]: Strasbourg, Louis Pasteur University, 252 p.

Jébrak, M., 1997, Hydrothermal breccias in vein-type ore deposits: A review of mechanisms, morphology and size distribution: Ore Geology Reviews, v. 306, p. 1-24.

Knipe, R.J., 1993, The influence of Fault Zone Processes and Diagenesis on Fluid Flow, in Horbury, A.D., and Robinson, A.G., eds., Diagenesis and Basin Development: The American Association of Petroleum Geologists, Studies in Geology, v. 36, p. 135-148.

Kotzer, T.G., Kyser, T.K., and Irving, E., 1992, Paleomagnetism and the evolution of fluids in the Proterozoic Athabasca Basin, northern Saskatchewan, Canada: Canadian Journal of Earth Sciences, v. 29, p. 1474-1491.

MacDougall, D.G., 1990, Rare Earth Element mineralization in the Athabasca Group-Maw Zone, in Summary of Investigations 1990: Saskatchewan Geological Survey, Saskatchewan Energy and Mines, Miscellaneous Report 90-4, p. 103-105.

Pagel, M., 1975, Détermination des conditions physico-chimiques de la silicification diagénétique des grès Athabasca (Canada) au moyen des inclusions fluides: Comptes Rendus de l'Académie des Sciences, v. 280, D, p. 2301-2304.

Quirt, D., Kotzer, T., and Kyser, T.K., 1991, Tourmaline, phosphate minerals, zircon, and pitchblende in the Athabasca Group: Maw Zone and McArthur River areas, Saskatchewan, in Summary of Investigations 1991: Saskatchewan Geological Survey, Saskatchewan Energy and Mines, Miscellaneous Report 91-4, p. 181-191.

Ramaekers, P., 1981, Hudsonian and Helikian basins of the Athabasca region, Northern Saskatchewan: Geological Survey of Canada Paper 81-10, p. 219-233.

Rippert, J.C., Koning, E., Robbins, J., Koch, R., and Baudemont, D., 2000, The Shea Creek Uranium Project, West Athabasca Basin, Saskatchewan, Canada, in Proceedings, GeoCanada2000, The Millennium Geoscience Summit, Calgary: GAC-MAC joint annual meeting, abstract 570 (Conference CD).

Thomas, D.J., Matthews, R.B., and Sopuck, V., 1998, Athabasca Basin Unconformity-Type Uranium Deposits: A Synopsis of the Empirical Model and Review of Exploration and

Production Trends, in Proceedings, Canadian Institute of Mining, Metallurgy and Petroleum meeting, Montréal.

Wallis, R.H., Saracoglu, N., Brummer, J.J., and Golightly, J.P., 1983, Geology of the McLean uranium deposits, in Cameron, E.M., ed., Uranium exploration in Athabasca Basin, Saskatchewan, Canada: Saskatchewan Energy and Mines, Geological Survey of Canada, p. 71-110.

V. Conclusions Generales

CONCLUSIONS GENERALES

L'étude structurale, texturale, minéralogique et géochimique des brèches associées aux minéralisations de Shea Creek, de Sue et de la zone de Maw permet de proposer une histoire de développement des systèmes brèchiques dans le Bassin Athabasca. Les 3 zones d'étude ont permis d'approcher les brèches à différentes positions par rapport à la discordance, aux failles et à la minéralisation uranifère ainsi qu'à différents niveaux d'intensité de développement, permettant ainsi de comprendre leur évolution dans l'espace et dans le temps et leur rôle dans la formation des gisements d'uranium.

Les brèches associées aux gisements d'uranium de type discordance du Bassin Athabasca : reflets d'une histoire tectonique polyphasée

Les brèches intra-grès associées aux gisements d'uranium de type discordance du Bassin Athabasca se sont développées au cours de plusieurs événements régionaux de réactivations tectoniques de failles de socle sur une période supérieure à 1 Ga. La plupart de ces événements de bréchification des grès sont contemporains de phases de minéralisation et/ou de remobilisation d'uranium. Dans les exemples étudiés, le polyphasage des brèches est essentiellement exprimé à Shea Creek.

La toute première phase de bréchification apparaît au début du dépôt des sédiments Athabasca avec la formation de glissements de terrain interprétés comme étant liés à des mouvements tectoniques et souvent appelés fanglomérats. Ces glissements de terrain apparaissent souvent à proximité du contact entre des quartzites et des schistes graphiteux préférentiellement réactivés à cause du contraste de compétence (MCO de Sue C, McArthur River).

Le premier événement de bréchification post-Athabasca eu lieu avant le dépôt de la minéralisation primaire entre 1.7 Ga, âge du dépôt des sédiments Athabasca, et 1.52-1.25 Ga. Il s'agit de brèches tectoniques et/ou hydrauliques à quartz microcristallin dont le développement dans les grès est limité. Elles se sont développées au cours ou légèrement après un événement de silicification pervasive précoce.

Le deuxième événement de bréchification post-Athabasca est le plus important en extension et a eu lieu entre 1.52 et 1.25 Ga. Il est représenté par des brèches à chlorite sudoïtique ± illite à Shea Creek et est responsable de la formation des brèches à illite de type zones à boules dans la MCO de Sue C et des brèches à dravite dans la zone de Maw. Il est contemporain de la principale phase de dépôt d'uraninite et de pechblende. Il est l'expression d'une phase de réactivation tectonique faisant rejouer des failles riches en graphite en régime

de compression. La contrainte maximale $\sigma 1$ serait globalement EW mais avec des variations importantes jusqu'à 60° d'écart entre les trois zones d'étude.

Le troisième événement de bréchification post-Athabasca a probablement eu lieu vers 900 Ma et est représenté par des brèches à Fe-chlorite. Il correspond à une minéralisation et/ou remobilisation d'uranium avec dépôt de pechblende et de coffinite parfois perché plusieurs dizaines de mètres au-dessus de la discordance. C'est l'événement le moins bien contraint du point du vue de l'âge puisque seuls une comparaison avec des argiles de mêmes caractéristiques datées par K-Ar à Cigar Lake et sa chronologie relative avec les autres phases permet de proposer cette âge.

Le quatrième événement de bréchification post-Athabasca a eu lieu vers 350 Ma et est exprimé par des brèches à sidérite-hématite. Il correspond à une minéralisation et/ou remobilisation d'uranium avec précipitation de pechblende, de coffinite et très accessoirement d'uraninite souvent en minéralisations perchées jusqu'à plus de 40 m au-dessus de la discordance à Shea Creek. Cet événement est très développé à Shea Creek comme le montre la présence de minéralisations métriques à pechblende massive complètement remobilisées.

A Shea Creek, il existe aussi un événement de coffinitisation vers 120 Ma probablement provoqué par de la fracturation et des changements physico-chimiques importants liés à l'impact météorique de Carswell dont le bord de l'anneau est à quelques kilomètres seulement des échantillons étudiés. L'événement de Carswell a en effet été daté à 115 ± 10 Ma par la méthode ^{40}Ar-^{39}Ar.

La complexité et le polyphasage des altérations à Shea Creek est probablement à corréler avec la complexité structurale du site puisque au moins trois familles de failles majeures ont été mises en évidence. Les différents types de failles ont pu jouer le rôle de conduits pour des fluides de nature différente au cours des phases de réactivations. Les différentes orientations des structures ont créé un potentiel de réactivation important pour une large gamme de régimes de contraintes permettant ainsi de faire rejouer la zone à chaque période d'activité sismique régionale. La précipitation de chlorite et de sulfures au cours des phases à 1,52-1,25 et 0,9 Ga suggère la prédominance de fluides réducteurs même si des alternances de conditions oxydantes et réduites apparaissent localement pendant chaque phase indiquant un envahissement total du système par les saumures de bassin oxydantes. La néoformation d'hématite vers 350 Ma indique plutôt des conditions oxydantes dues à l'incursion de fluides météoriques.

Relations spatiales entre les brèches, les failles et la discordance

La géométrie des brèches associées aux gisements d'uranium de type discordance du Bassin Athabasca est contrôlée par l'orientation des failles enracinées dans le socle qui ont été

réactivées pendant et après le dépôt et l'induration des sédiments Athabasca. Les brèches se développent dans les grès préférentiellement le long de failles inverses graphiteuses dans le socle du fait du caractère lubrifiant du graphite qui a favorisé les réactivations en régime compressif. Ces failles ont des pendages variables allant de 30 à 40° pour des failles de type I à Shea Creek à près de 90° pour les failles contrôlant les minéralisations à Sue. Si on considère une faille inverse avec un jeu post-Athabasca, les différents types de brèches rencontrés s'organisent spatialement en fonction de la zonation à la fois horizontale et verticale de la faille. Les zones à boules se forment dans le cœur de la faille au niveau de la discordance où les mouvements et la contraction sont les plus importants. Elles ont des formes en doigts étroits allongés parallèlement à la faille qui peuvent atteindre plus de 20 m de haut, plusieurs dizaines de mètres de long et 5 m de large. Les brèches hydrauliques et de dissolution se développent latéralement dans la zone d'endommagement autour du cœur de la faille au niveau de la discordance et verticalement dans la zone de terminaison de faille. Le caractère hydraulique des brèches est le plus marqué dans la zone de terminaison de faille et est progressivement effacé par la dissolution en approchant de la discordance. Les brèches de terminaison de faille, représentées par la zone de Maw à 250 m au-dessus de la discordance, se développent sur au moins 20 m de long et 6 m de large. Verticalement, elles peuvent s'étendre sur plus de 200 m et rejoindre très probablement les corps de brèches développés à la discordance. Ce dernier type de brèche ne se développe que pour des failles à fort pendage. Quand le pendage est plus faible comme pour les failles de type I à Shea Creek, les failles deviennent rapidement horizontales et la zone de terminaison de faille peut se trouver à moins de 50 m de la discordance. Les brèches de dissolution à sudoite-dravite ont des formes de doigts allongés parallèles aux failles mais plus larges et étalées à la discordance que les zones à boules (voir annexe II). Elles ont un volume de 166 000 m^3 dans la zone de Anne à Shea Creek et atteignent 30 m de haut, près de 100 m de large le long de la discordance et plusieurs centaines de mètres de long. Les brèches de dissolution à Fe-chlorite se développent dans des zones de percolation maximale à l'intersection de plusieurs failles d'orientations différentes et ont une forme de dôme avec un contrôle plus faible par l'orientation des failles que les brèches à sudoite-dravite (voir annexe II). Le corps à Fe-chlorite a un volume de l'ordre de 30 000 m^3 et une hauteur de plus de 30 m, ainsi qu'une largeur et une longueur de près de 70 m.

Evolution de la maturité des brèches : développement d'un système karstique

La maturité d'une brèche augmente avec le pourcentage de matrice et la dimension fractale des fragments qui exprime leur complexité morphologique. L'évolution de la maturité

des brèches reflète directement les processus impliqués dans leur genèse. Trois étapes de développement ont pu être distinguées dans les gisements d'uranium de type discordance.

La première étape est représentée par des brèches immatures qui sont des brèches tectoniques caractérisées par la prédominance de la fracturation sur l'attrition ou des brèches hydrauliques avec un faible rapport de dilatation (volume de matrice) / (volume de fragments). Ces brèches se sont formées lors des réactivations tectoniques des failles de socle. Les zones à boules, situées dans le cœur des failles comme à Sue, ont été initiées par une fracturation tectonique tandis que les brèches de dissolution dans la zone de Maw et à Shea Creek ont été initiées par une fracturation hydraulique dans la zone d'endommagement ou dans la zone de terminaison de faille. Cette fracturation hydraulique a été provoquée par une surpression de fluides ascendants sous des zones imperméables de silicification précoce dans les grès.

La deuxième étape de maturation des brèches correspond au développement de la dissolution du quartz. La dissolution du quartz s'accompagne d'une augmentation du pourcentage de matrice ainsi que d'un accroissement de la complexité des fragments lié à la formation de figures de corrosion. Les brèches matures sont développées essentiellement près de la discordance à Shea Creek et à Sue, tandis que dans la zone de Maw les brèches sont restées immatures du fait de la saturation progressive en silice du fluide ascendant. La dissolution maximale se développe au cœur des failles dans les zones à boules. La maturité et donc l'intensité de la dissolution décroît ainsi avec la distance à la discordance et aux failles.

La troisième étape de maturation correspond à des phénomènes d'effondrements gravitaires provoqués par la formation de cavités de dissolution. Ces effondrements s'accompagnent d'une inversion de maturité due à l'augmentation de la quantité de fragments et au mélange de fragments anguleux et corrodés. Dans les zones à boules, la dissolution du quartz est compensée non pas par des effondrements mais par la contraction tectonique qui est maximum dans le cœur des failles.

Le pourcentage de matrice est un meilleur paramètre que la forme des fragments pour connaître le degré de maturité d'une brèche. En effet, la forme des fragments dépend non seulement du degré de corrosion mais également du régime de dissolution. En régime de dissolution limité par la diffusion, les fragments vont avoir tendance à s'arrondir tandis qu'en régime cinétique, les formes de fragments sont plus complexes et mettent en évidence les hétérogénéités de texture et de composition initiales. Les brèches de dissolution contemporaines de l'événement de minéralisation principal (stade 2) se sont formées en régime lent, limité par la diffusion. Les brèches de dissolution à Fe-chlorite plus tardives (stade 3) se sont plutôt formées en régime de dissolution rapide, limité par la cinétique.

Une corrélation entre le type d'effondrement et le type de dissolution peut être ici proposée. Les effondrements dans les brèches à sudoite-dravite conduisent moins souvent à des mélanges polymictes et à des brèches supportées par les fragments que les brèches de

dissolution à Fe-chlorite. Cela suggère que la dissolution lente dans les brèches du stade 2 s'accompagnerait d'effondrements progressifs avec maintien d'une grande quantité de grains de quartz corrodés entre les fragments limitant ainsi les contacts fragments-fragments. Au contraire, la dissolution plus rapide des brèches du stade 3 permettrait de maintenir l'existence de cavités plus longtemps et de provoquer ainsi des effondrements plus rapides et plus spectaculaires.

La maturité des brèches étant liée à la quantité de quartz dissous, le pourcentage de matrice peut être utilisé pour estimer la perte de volume liée à la dissolution du quartz, aux néoformations près. Ceci n'est cependant pas valable dans les zones à boules où le quartz est dissous à la fois dans la matrice et dans les boules, ni dans certaines zones d'effondrements où les fragments sont concentrés à la base du système. Les pertes de volume calculées dans les zones à boules et localement dans les brèches de dissolution à sudoite-dravite les plus matures à Shea Creek peuvent atteindre 80 à 90 % indiquant des phénomènes de dissolution extrêmes. En revanche, dans la zone de Maw où la dissolution du quartz est très faible, les pertes de volume sont négligeables. Les effondrements observés dans la zone de Maw sont probablement liés à des pertes de volume en-dessous à la discordance. Les brèches associées aux gisements d'uranium de type discordance peuvent donc conduire au développement de systèmes karstiques verticaux de plus de 250 m de haut dans les grès avec une dissolution importante à la discordance et des effondrements dans les parties supérieures.

Zonation minéralogique

Les brèches contemporaines de l'événement de minéralisation principal entre 1.52 et 1.25 Ga à Shea Creek montrent une zonation minéralogique verticale et en partie latérale du fait du faible pendage des failles de type I. Au niveau de la discordance et au contact de la minéralisation uranifère, le ciment des brèches est constitué de minéraux interstratifiés chlorite-illite. Au-dessus, c'est la chlorite sudoïtique qui prédomine mélangée avec un peu de dravite. Encore au-dessus, c'est la dravite qui prédomine sur la sudoite. Localement, un peu d'illite est mélangé à la sudoite et à la dravite. La dickite apparaît également dans le halo d'altération et est parfois massive associée à de la dravite à la discordance. Une partie de cette dickite est probablement héritée de la dickite diagénétique mais la taille très importante de certains cristaux et certaines zones de cristallisation massive indiquent qu'elle pourrait être également en partie hydrothermale. Ces brèches sont entourées d'une silicification pervasive formée par reprécipitation du quartz dissous dans les brèches.

Une telle zonation illustre un front géochimique probablement lié à l'interaction d'un fluide de socle circulant dans les failles recoupant la discordance avec un fluide de bassin circulant latéralement au fond du bassin. Elle pourrait résulter d'un gradient de proportion de

fluides de socle par rapport aux fluides de bassin contrôlant la précipitation des phases minérales en fonction de leur produit de solubilité. La dravite résulte selon Kotzer et Kyser (1995) d'un mélange de fluides de socle et de bassin et serait à l'extérieur du halo parce qu'elle nécessite du B fourni par le fluide de bassin tandis que la sudoïte magnésienne contient du Mg et de l'Al fournis par le fluide de socle et précipite donc plus près de la discordance.

Si la dissolution du quartz dans le socle est bien à l'origine de la silicification précoce dans les grès, le développement du halo d'altération et des brèches correspond à une migration vers le haut d'un front de dissolution précédé d'un front de silicification. Cette migration exprime un envahissement progressif des grès du bassin par le fluide de socle.

Circulation des fluides au cours du développement des brèches

Au minimum deux fluides peuvent être distingués : une saumure diagénétique de bassin oxydante et un fluide de socle réducteur ascendant le long de failles. Le fluide minéralisateur serait un mélange des fluides de bassin et de socle d'après le modèle diagénétique hydrothermal. Le fluide de bassin circulait soit par des mouvements convectifs, soit latéralement le long de la discordance. L'hypothèse de circulation le long de la discordance semble plus probable puisque les forts contrastes entre les assemblages argileux dans les différentes formations indiquent que la circulation verticale des fluides était probablement réduite. De plus, les niveaux grossiers à conglomératiques de la base des grès de la formation Manitou Falls sont plus perméables que les grès sus-jacents. Les travaux de Derome (2000b) ont montré qu'il existe en fait davantage de types de fluides et en particulier plusieurs types de saumures. Le fluide de socle est soit dérivé d'un fluide de bassin percolant dans le socle, soit un fluide profond sans lien avec les fluides de bassin.

La silicification pervasive précoce des grès en halos centrés autour de failles inverses à graphite est très développée dans certaines zones minéralisées comme Shea Creek ou McArthur River. Elle est probablement postérieure à une réactivation de faille qui a induit la circulation d'un fluide de socle chaud ascendant qui, en se refroidissant dans les grès, a provoqué la précipitation de quartz. Cette phase pourrait être contemporaine du début de l'illitisation dans le socle. La fermeture de porosité liée à cette silicification a provoqué une diminution de perméabilité induisant une surpression de fluide de socle sous-jacent. L'augmentation de pression de fluides s'est accompagnée d'une diminution de la contrainte effective provoquant un rejeu inverse de la faille et sa propagation dans les grès.

La propagation de la faille dans la couverture gréseuse est caractérisée par de la fracturation hydraulique dans la zone d'endommagement silicifiée et par des mouvements tectoniques inverses le long de plans de glissement dans le cœur de la faille. La forte

compétence des grès silicifiés aurait été responsable de la formation de larges zones de fractures permettant la percolation des fluides jusqu'à plusieurs dizaines de mètres autour des failles dans les grès. La fracturation hydraulique s'est également développée dans la zone de terminaison de faille représentée par la zone de Maw. Une partie des brèches hydrauliques est probablement de type critique développée dans des ouvertures créées à la discordance par la réfraction de la faille dans les grès.

La perméabilité des grès ainsi renouvelée a permis la circulation ascendante des fluides de socle induisant une nouvelle silicification et une autre phase de rejeu de la faille. Un tel cycle pourrait correspondre à un fonctionnement en valve sismique de la faille. Les brèches précoces à quartz microcristallin pourraient être l'expression de ces réactivations au cours de l'événement de silicification. Au bout de plusieurs cycles, les fluides sont devenus sous-saturés probablement du fait de la dissolution totale du quartz dans les zones illitisées de socle sous-jacent.

Le gradient vertical de maturité de la zone de Maw perchée dans les grès aux brèches de Shea Creek, puis celles de Sue au niveau de la discordance montre que le fluide sous-saturé en silice a dû circuler verticalement dans les grès le long de failles. La décroissance de l'intensité de la dissolution en s'éloignant de la discordance est due au rééquilibrage progressif du fluide avec le quartz du grès. Les pertes de volume considérables à la discordance montrent que le taux de dissolution était supérieur au taux de néoformations minérales. Ceci indique un fort accroissement de la perméabilité qui a permis la circulation d'une grande quantité de fluides nécessaires à la dissolution du quartz et à la précipitation d'oxydes d'uranium.

Il est probable que la précipitation de minéraux argileux et de dravite combinée avec les effondrements ou la contraction tectonique aient fait diminuer la perméabilité provoquant occasionnellement ou périodiquement des surpressions de fluides à l'origine d'un fonctionnement des failles inverses en valve sismique avec réouverture du système et nouvelle injection de fluide de socle dans le bassin. Il est également possible que la cimentation des grès au-dessus des brèches par du quartz provenant de la dissolution sous-jacente ait provoqué des surpressions de fluide et des réouvertures des failles inverses accompagnées de fracturation de la zone silicifiée. Les fluides injectés lors de ces phases sismiques auraient alors pu circuler plus haut dans les grès dans les fractures nouvellement créées et ainsi propager le front de dissolution vers le haut.

Les rapports fluides/roche cumulés ont été calculés avec un pourcentage de sous-saturation en silice de 10 % juste au-dessus de la discordance et de 1 % seulement au niveau des brèches de la zone de Maw afin de rendre compte du gradient de sous-saturation des fluides. Les rapports fluides/roche ont des valeurs très élevées de quelques milliers dans les corps de brèches de dissolution à Shea Creek et dans la zone de Maw et atteignent près de 40 000 dans les zones à boules. De plus, ce sont des valeurs minimum puisqu'on a considéré que tout le

fluide a réagi avec la roche avec une cinétique maximale. Les volumes de fluides nécessaires pour dissoudre le quartz sont de l'ordre du kilomètre cube pour 200 000 m^3 de brèches à 10 % de matrice ou pour 5 000 m^3 de brèches complètement argilisées avec 80 % de perte de volume.

Caractéristiques des fluides

Les fluides de la diagenèse précoce dans le Bassin Athabasca ont des températures croissantes de l'est vers l'ouest du bassin avec 160°C dans la zone de McArthur River, 180°C dans la zone de Rumple Lake au centre du bassin et 220°C dans les grès autour de la structure de Carswell. Les fluides de la diagenèse profonde ont des températures estimées entre 200 et 240°C. Le géothermomètre à illite appliqué dans les zones à boules de Sue contemporaines de la phase principale de minéralisation donne une température de 260 ± 20°C supérieure à la celle des fluides de la diagenèse profonde. Les cristallisations d'uraninites automorphes contemporaines de l'illite hydrothermale indiquent des températures supérieures à 250°C. En accord avec le modèle diagénétique hydrothermal, ces températures résultent probablement du mélange de fluides diagénétiques de bassin et d'un fluide de socle plus chaud de température supérieure à 250°C. Le géothermomètre à chlorite appliqué sur des Fe-chlorites de Shea Creek donne une température approximative de 180°C indiquant des fluides plus froids vers 900 Ma.

Des enrichissements en U, V, Mg, B, Al, K, Bi, Ni, Co, Mo, As, S, W, Zn, Y et terres rares ont été mis en évidence dans les brèches. La majeure partie des éléments sauf U, B et V ont probablement leur source dans le socle et furent transportés par le fluide issu du socle. La mobilité de l'aluminium et des terres rares est en accord avec des volumes de fluide importants et suggère des complexants spécifiques comme les fluorures, les chlorures, les phosphates ou les carbonates. Les fortes concentrations en NaCl des fluides de bassin jusqu'à plus de 30 pds % éq. de NaCl suggèrent que l'uranium était complexé par les chlorures. Cependant, les fluorures ont pu avoir un rôle important puisqu'ils complexent davantage l'uranium que les fluorures à des concentrations de 10 mg/l.

Le pH du fluide minéralisateur, mélange de fluides de bassin et de socle, était probablement compris entre 4 et 5 grâce au rôle de tampon de la réaction dickite-illite. A un tel pH et à 250°C, les fluides de bassin avaient une fugacité en oxygène supérieure à 10^{-33} du fait de leur équilibre avec l'hématite.

Une étude plus approfondie des fluides, en particulier du fluide de socle, est nécessaire pour mieux contraindre le modèle de formation des gisements. Les études d'inclusions fluides en cours devraient permettre de mieux connaître la nature des différents types de fluides impliqués dans la genèse des minéralisations uranifères.

Rôle de la bréchification pour la formation des gisements d'uranium de type discordance

La formation des fractures dans les grès et des brèches immatures a permis la circulation de fluides de socle dans les grès et leur mélange avec les fluides de bassin. La dissolution massive du quartz a créé une porosité importante au sein de laquelle le fluide réducteur de socle s'est mélangé avec le fluide oxydant de bassin porteur d'uranium. La brusque diminution de la fugacité en oxygène du fluide transportant l'U provoquée par la rencontre avec les fluides réducteurs entraîna la précipitation des oxydes d'uranium dans les cavités créées par la dissolution. La dissolution massive du quartz à la discordance a donc créé l'espace nécessaire aux minéralisations uranifères massives. Le dépôt de l'uranium s'est effectué à la discordance pour plusieurs raisons. (1) L'intensité de la dissolution était la plus forte à la discordance et a donc constitué le meilleur piège. (2) Le front rédox était localisé à la discordance dans la zone de mélange de fluides réducteurs de socle ascendants et de fluides oxydants de bassin circulant latéralement le long de la discordance. (3) Les mouvements tectoniques inverses responsables de la circulation du fluide de socle provoquèrent la formation de fentes de tension et de zones d'ouvertures à la discordance favorisant ainsi le mélange de fluides attirés à la discordance par gradient de pression.

En prenant une très faible teneur en fluorures de 10^{-6} mg/l et une teneur en chlorures de 177 g/l, et à un pH de 4,45, une température de 200°C et une fugacité en oxygène de 10^{-28}, les calculs de modélisation géochimique avec EQ3NR/EQ6 suggèrent que l'uranium était transporté par des complexes hydroxydes. Dans ces conditions, le temps de dépôt de 10^4 tonnes d'U est de l'ordre du million d'années en considérant une vitesse de circulation des fluides de bassin de 10 m/an, une efficacité maximale de dépôt et une porosité connectée de 1 %. Or le temps de formation des corps de brèches est du même ordre de grandeur en considérant une vitesse de circulation supérieure de 100 m/an dans la faille et une sous-saturation en silice de 10 % juste au-dessus de la discordance. Il est donc vraisemblable que la précipitation d'uranium ait eu lieu au fur et à mesure de la dissolution du quartz sur une période de l'ordre de quelques millions d'années en considérant une efficacité de dissolution et de précipitation plus faible. Les minéralisations à Y et terres rares lourdes apparaissent moins bien contrôlées par la discordance car elles ne dépendent pas de la fO_2. La précipitation de xénotime dans la zone de Maw a probablement été provoquée par la diminution de température du mélange de fluides ascendant dans la zone plus fracturée de terminaison de failles jouant le rôle de piège secondaire par rapport à la discordance.

Par conséquent, la genèse des brèches et leur rôle dans la formation des gisements d'uranium de type discordance s'inscrit bien dans le modèle de mélange de fluides de bassin et de socle proposé par Fayek et Kyser (1997) pour les minéralisations dans les grès. L'absence ou le très faible développement de la dissolution du quartz dans les grès sus-jacents

à la minéralisation de socle de Sue C pourrait indiquer l'absence de fluide de socle et donc de mélange de fluides dans la genèse des minéralisations encaissées par les lithologies du socle. Ce serait en accord avec Fayek et Kyser (1997) qui proposent que les minéralisations de socle résulteraient d'incursions de fluides de bassin dans le socle qui, au contact de lithologies riches en graphite, précipiteraient l'uranium par diminution brusque de la fugacité en oxygène.

Par conséquent, en plus des circulations latérales de fluides diagénétiques de bassin, les échanges verticaux de fluides de part et d'autre de la discordance par le biais de failles ont une importance fondamentale dans la genèse des gisements. Cette étude montre que les circulations de fluides de socle dans les grès peuvent monter à plus de 250 mètres au-dessus de la discordance.

Différence entre Shea Creek et Sue : implications pour l'exploration

La forte silicification précoce, la chloritisation et la dravitisation observées à Shea Creek correspondent au modèle d'altération proposé par Matthews et al. (1997) pour les grès encaissant les gisements de la partie sud-Athabasca comme McArthur River. Le développement des brèches est particulièrement étendu dans les grès de Shea Creek du fait de la silicification précoce intense. La forte compétence des grès silicifiés a permis le développement d'une zone de fracturation large. La fermeture de la porosité intergranulaire par le quartz a limité la circulation des fluides dans les fractures. Ainsi, dans les zones silicifiées, les fragments ont été très lentement corrodés à partir des fractures et ont pu être en partie préservés.

A Sue et plus particulièrement le long de la structure contrôlant Sue A et B, la faible silicification et la prédominance de l'illitisation dans les grès sont plutôt en accord avec le modèle nord-Athabasca de Matthews et al. (1997). Le faible développement des brèches à Sue est dû à la faible silicification qui a permis aux fluides de corroder les grès de manière pervasive sans possibilité de préservation des fragments. Un tel processus a conduit à la formation de zones d'illite massive dans les zones à boules et autour des minéralisation dans les grès de Sue A et B. La formation des zones à boules est cependant en partie liée à des silicifications locales.

Quelle que soit la nature des minéraux d'altérations, la silicification précoce est le principal contrôle du développement des brèches. Le modèle de Matthews et al. (1997) peut donc être reconsidéré dans le cadre de cette nouvelle approche. Le type d'altération sud-Athabasca se caractérise par une forte silicification pervasive précoce et des corps de brèches très étendus dans les grès. Le type nord-Athabasca se traduit par une très faible silicification précoce et un développement de brèches très limité et davantage par une dissolution pervasive

des grès sur de grands volumes provoquant la formation d'une épaisse cape argileuse au-dessus de la minéralisation qui la préserve des remobilisations ultérieures.

Il existe une corrélation entre la teneur en quartz des lithologies du socle sous-jacentes ou à proximité des gisements et le développement de la silicification précoce dans les grès. A Shea Creek et à McArthur River, la proportion importante de faciès riches en quartz comme les gneiss felsiques et les quartzites permettraient d'expliquer les silicifications massives précoces dans les grès par reprécipitation de quartz dissous pendant l'illitisation des faciès quartzeux du socle. A Sue et à Cigar Lake, la prédominance de faciès métasédimentaires riches en graphite et pauvres en quartz permettraient de rendre compte de la faible silicification précoce dans les grès. Les brèches hydrothermales dans les grès se développeraient donc favorablement à proximité de roches de socle riches en quartz comme les quartzites, les granites ou les gneiss felsiques.

Analogues naturels

Cette étude montre que suite à la phase majeure de dépôt des minéralisations uranifères entre 1.52 et 1.25 Ga, plusieurs phases de bréchification liées à des réactivations tectoniques et/ou à la surrection du bassin ont provoqué des remobilisations de l'uranium en partie liées à l'incursion de fluides météoriques. A Shea Creek, il existe un unique forage qui contient une minéralisation massive à la discordance sans brèches sus-jacentes. C'est une minéralisation donnant un âge chimique approximatif de 350 Ma suggérant une migration latérale le long de la discordance de minéralisation primaire originellement associée à des brèches. Cependant, l'amplitude des déplacements reste de l'ordre de quelques mètres. De plus, les spectres de terres rares dans les différentes phases de brèches même les plus tardives montrent le plus souvent les mêmes enrichissements en terres rares lourdes et intermédiaires liés au phénomène minéralisateur initial. Cela montre que les terres rares n'ont presque pas été remobilisées depuis le dépôt initial des minéralisations. Par conséquent, les gisements d'uranium de type discordance ont été préservés depuis près de 1.5 Ga dans des conditions de confinement naturel. La très faible mobilité des terres rares, qui ont des comportements similaires aux radionucléides, et de l'uranium sur un tel laps de temps montre que les gisements d'uranium de type discordance constituent de très bons analogues naturels de stockage de déchets radioactifs indiquant les conditions intéressantes pour la préservation du confinement des déchets. De plus, les fluides qui ont pu circuler au niveau de la zone minéralisée lors des phases de bréchification avaient des températures inférieures à 200°C, voisines des températures maximales qui seraient atteintes dans les conditions de stockage actuelles (entre 150 et 200°C ; Cramer, 1986). Leur composition était également relativement similaire à celle attendue dans un site de stockage (Cramer, 1986).

Cette excellente préservation de la minéralisation uranifère et des terres rares est en partie due à la formation de barrières naturelles que sont les altérations entourant les gisements qui ont limité la circulation des fluides. Dans les gisements associés à des développements importants de brèches comme McArthur River ou Shea Creek, la silicification massive qui entoure les brèches et la minéralisation constitue une barrière très peu perméable. En particulier, elle limite beaucoup l'extension des altérations argileuses pervasives et rend très difficile le travail des explorateurs par la faiblesse des halos de dispersion des éléments autour du corps minéralisé. Dans les gisements où les brèches sont peu développées comme à Cigar Lake, c'est l'illitisation massive, directement liée aux pertes de volume faisant suite à la dissolution du quartz, qui constitue la barrière de perméabilité représentant un excellent analogue des barrières ouvragées argileuses.

Les faibles remobilisations spatiales de l'uranium lors des réactivations tectoniques sont probablement dues aux phénomènes d'autocicatrisation constitués par les cimentations argileuses et les effondrements gravitaires des brèches. De plus, l'amortissement souvent rapide des failles dans les grès a fortement limité les possibilités de dispersion d'éléments.

Par conséquent, malgré l'activité tectonique du bassin à certains moments de son histoire, de très bonnes conditions de confinement ont pu être maintenues grâce aux barrières naturelles constituées par les silicifications pervasives et les argilisations massives et grâce aux phénomènes d'autocicatrisation pendant les phases de réactivations tectoniques.

Perspectives

Il reste encore de nombreux problèmes à résoudre avant d'obtenir un modèle statisfaisant de genèse des gisements d'uranium de type discordance du Bassin Athabasca.

Afin de pouvoir préciser le contrôle structural des minéralisations, il serait nécessaire de connaître le régime de contraintes au cours de la phase principale de dépôt de l'uranium en relation avec un événement tectonique régional. Pour cela, il faudrait réduire l'incertitude sur l'âge de la minéralisation uranifère (entre 1.52 et 1.25 Ga) pour pouvoir la relier à une phase tectonique régionale.

On ne connaît pas encore précisément les paramètres nécessaires au développement de minéralisations à très haute teneur. Une seule phase de dépôt est-elle suffisante ? Ou est-ce que la gamme très large d'âges entre 1.52 et 1.25 Ga pour la minéralisation principale reflète un phénomène polyphasé ?

L'importance du graphite reste encore à préciser. On sait que le graphite joue probablement un rôle mécanique de concentration de la déformation du fait de ses propriétés lubrifiantes mais son rôle chimique reste très discuté. L'altération du graphite observée est-

elle une conséquence du phénomène minéralisateur ou au contraire une cause à l'origine des fluides réducteurs ?

Quelle est la nature et l'origine des fluides réducteurs ? Ont-ils une source profonde dans le socle ou dérivent-ils de fluides de bassin ? Les études d'inclusions fluides devraient permettre de préciser leur composition, leur température et leur pression afin de contraindre le modèle de circulation des fluides.

L'analyse de la composition des inclusions fluides devrait également permettre de préciser la nature des complexants qui ont transporté l'uranium et ainsi de contraindre sa solubilité, les volumes de fluide et le temps de formation des gisements. De même, la connaissance des complexants de l'aluminium permettrait de contraindre les volumes de fluide et le temps de formation des brèches à sudoite-dravite.

L'origine de la sous-saturation en silice du fluide minéralisateur reste incertaine et il serait nécessaire d'étudier en détail les différentes réactions possibles pouvant provoquer une sous-saturation du fluide de socle. En particulier, il serait très important d'étudier les cinétiques de réaction par rapport à la vitesse de circulation des fluides.

Les études d'inclusions fluides de Pagel (1975b) et de Pagel et Jaffrezic (1977) montrent que la température et la pression des fluides diagénétiques augmentent d'est en ouest du bassin de 160°C et 700 bars à Rabbit Lake, à 180°C et 1250 bars à Rumple Lake et jusqu'à 220°C et 1500 bars à Cluff Lake, donnant ainsi des gradients géothermiques moyens de 50, 38 et 39 °C/km, respectivement. Ces gradients sont anormalement élevés et il serait probablement utile de connaître l'origine de ces anomalies et de ces variations. S'agit-il d'une anomalie thermique régionale à l'est du bassin? Quelle est l'influence de cette anomalie et de ces variations sur la minéralisation ?

Les phénomènes de bréchification dans les grès associés aux gisements d'uranium de type discordance sont-ils uniques au Bassin Athabasca ? Les minéralisations de type discordance du Bassin de McArthur en Australie sont entièrement situées dans le socle. Elles sont parfois associées à d'importants phénomènes de bréchification des carbonates dans le socle. Cependant, dans la zone minéralisée de Jabiluka II, Gustafson et Curtis (1983) montrent également de très belles évidences de brèches à chlorite magnésienne du même type que celle associée à la minéralisation dans les grès de la formation Kombolgie au-dessus de la discordance. La chlorite se forme à la fois dans des veines recoupant le grès ou de manière pervasive en remplacement du quartz jusqu'à une hauteur de 312 m au-dessus de la discordance. Les analyses chimiques des grès chloritisés montrent des enrichissements en Mg, U, Zr, P, Y, Ni, Co et V, c'est-à-dire les mêmes enrichissements que ceux observés dans les brèches à sudoite du Bassin Athabasca. L'enrichissement en Zr reporté par ces auteurs indique de toute évidence des pertes de volume très probablement liées à la dissolution du quartz.

Durak (1983) décrit des phénomènes d'altérations polyphasées dans les grès Kombolgie du gisement de Jabiluka avec un épisode à illite, chlorite et dravite contemporain de la minéralisation primaire vers 1,38 Ga et 2 phases de bréchification vers 900 et 400 Ma associées à des remobilisations d'uranium, suggérant une histoire géologique comparable à celle décrite dans les grès de Shea Creek.

Par conséquent, des phénomènes d'altération et de bréchification tout-à-fait similaires semblent se développer dans les grès des deux bassins. Ceci montre qu'il serait utile d'étudier systématiquement l'origine des brèches intra-grès et leur relation avec les gisements d'uranium de type discordance afin de tenter d'établir un modèle génétique et d'exploration applicable au Canada et en Australie.

REFERENCES BIBLIOGRAPHIQUES

REFERENCES BIBLIOGRAPHIQUES

Ababou, R., 1991, Approaches to large scale unsaturated flow in heterogeneous stratified and fractured geologic media. Section 4.2: Hydraulic properties of saturated fractured media : Report NUREG/CR-5743, U.S. Nuclear Regulatory Commission, Washington D.C.

Agip Canada Ltd., 1985, Saskatchewan Energy and Mines, Assessment File 74H06-NW-0080.

Albarède, F., Michard, A., et Cuney, M., 1985, Les chronomètres uranium-thorium-plomb, *in* Roth, E., and Poty, B., eds., Méthodes de datation par les phénomènes nucléaires naturels. Applications: Paris, Masson, Série Scientifique, Collection CEA, p. 123-173.

Annesley, I.R., Madore, C., Krogh, T.E., Kwok, Y.Y., et Kamo, S.L., 1999, New U-Pb zircon and monazite geochronological results for Archean and Paleoproterozoic basement to the southeastern part of the Athabasca Basin, Saskatchewan, *in* Summary of Investigations 1999: Saskatchewan Geological Survey, Saskatchewan Energy and Mines, Miscellaneous Report 99-4.2, p. 90-99.

Antonellini, M., et Aydin, A., 1994, Effect of faulting on fluid flow in porous sandstones: petrophysical properties: American Association of Petroleum Geologists Bulletin, v. 78, p. 355-377.

Armstrong, R.L., et Ramaekers, P., 1985, Sr isotopic study of Helikian sediment and diabase dikes in the Athabasca Basin, northern Saskatchewan: Canadian Journal of Earth Sciences, v. 22, p. 399-407.

Augustithis, S.S., et Ottemann, J., 1966, On diffusion rings and sphaeroidal weathering: Chemical Geology, v. 1, p. 201-209.

Augustithis, S.S., Mposkos, E., et Vgenopoulos, A., 1980, Leaching of bauxites: "Traveaux" ICSOBA, Zagreb, v. 11, p. 334-345.

Bau, M., et Möller, P., 1991, REE systematics as source of information on minerogenesis, *in* Pagel, M., and Leroy, J., eds., Source, Transport and Deposition of Metals, Proceedings of the 25 years SGA anniversary meeting, Nancy: Balkema, Rotterdam, p. 17-20.

Baudemont, D., et Pacquet, A., 1996, The Sue D and E uranium deposits, Northern Saskatchewan: evidence for structurally controlled fluid circulation in the Athabasca Basin, *in* MinExpo'96 Symposium, Advances in Saskatchewan Geology and Mineral Exploration: p. 85-94.

Baudemont, D., Piquard, J.P., Ey, F., et Zimmerman, J., 1993, The Sue Uranium Deposits, Saskatchewan, Canada: Exploration and Mining Geology, v. 2, p. 179-202.

Bell, K., 1985, Geochronology of the Carswell area, Northern Saskatchewan, *in* Lainé, R., Alonso, D., Svab, M., eds., The Carswell structure uranium deposits, Saskatchewan: Geological Association of Canada Special Paper 29, p. 33-46.

Bérubé, D., et Jébrak, M., 1999, High precision boundary fractal analysis for shape characterization: Computers & Geosciences, v. 25, p. 1059-1071.

Binns, R.A., Mc Andrew, J. et Sun, S.S., 1980, Origin of uranium mineralization at Jabiluka, *in* Ferguson, S., and Goleby, A., eds., Uranium in the Pine Creek Geosyncline: International Atomic Energy Agency, Vienna, p. 543-562.

Bottomley, R.J., York, D., et Grieve, R.A.F., 1990, ^{40}Argon-^{39}Argon dating of impact craters, *in* Proceedings of the 20th Lunar and Planetary Science Conference: p. 421-431.

Brummer, J.J., Saracoglu, N., Wallis, R.H., et Golightly, J.P., 1981, McClean Lake Uranium Deposits, Saskatchewan: Canadian Institute of Mining, Metallurgy and Petroleum, Geology Division, Uranium Field Excursion Guidebook, p. 43-64.

Bruneton, P., 1993, Geological environment of the Cigar Lake uranium deposit: Canadian Journal of Earth Sciences, v. 30, p. 653-673.

Bruneton, P., et Caumartin, P., 1985, Le gisement d'uranium de Cigar Lake (Saskatchewan, Canada) – Contribution à la compréhension des mécanismes de formation des gisements de l'Athabasca, *in* Program and extended abstracts, Concentration mechanisms of uranium in geological environments: Nancy, France, p. 211-214.

Burley, S.D., et Kantorowicz, J.D., 1986, Thin section and S.E.M. textural criteria for the recognition of cement-dissolution porosity in sandstones: Sedimentology, v. 33, p. 587-604.

Caine, J.S., Evans, J.P., et Forster, C.B., 1996, Fault zone architecture and permeability structure: Geology, v. 24, p. 1025-1028.

Carrier, A., et Jébrak, M., 1994, Structural evolution and metallogeny of the Silidor mesothermal gold-quartz deposit, southern Abitibi greenstone belt, Quebec, *in* Annual Meeting Abstracts Geological Association of Canada - Mineralogical Association of Canada: Waterloo, no. 19, p. A-18.

Cathelineau, M., et Izquierdo, G., 1988, Temperature – composition relationships of authigenic micaceous minerals in the Los Azufres geothermal system: Contributions to Mineralogy and Petrology, v. 100, p. 418-428.

Cathelineau, M., et Nieva, D., 1985, A chlorite solid solution geothermometer. The Los Azufres (Mexico) geothermal system : Contributions to Mineralogy and Petrology, v. 91, p. 235-244.

Chiarenzelli, J., Aspler, L., Villeneuve, M., et Lewry, J., 1998, Early Proterozoic Evolution of the Saskatchewan Craton and its Allochthonous Cover, Trans-Hudson Orogen: The Journal of Geology, v. 106, p. 247-267.

Clark, A.H., 1990, The slump breccias of the Toquepala porphyry Cu-(Mo) deposit, Peru: Implications for fragment rounding in hydrothermal breccias: Economic Geology, v. 85, p. 1677-1685.

Clarke, P.J., et Fogwill, W.D., 1981, Geology of the Asamera Dawn Lake, Uranium Deposits, Northern Saskatchewan, *in* Proceedings of Canadian Institute of Mining, Metallurgy and Petroleum, Uranium Symposium.

Clauer, N., Ey, F., et Gauthier-Lafaye, F., 1985, K-Ar dating of different rock types from the Cluff Lake uranium ore deposits (Saskatchewan-Canada), *in* Lainé, R., Alonso, D., and Svab, M., eds., The Carswell structure uranium deposits, Saskatchewan: Geological Association of Canada Special Paper 29, p. 47-54.

Clendenin, C.W., et Duane, M.J., 1990, Focused fluid flow and Ozark Mississippi Valley-type deposits: Geology, v. 18, p. 116-119.

Cox, S.F., 1995, Faulting processes at high fluid pressures: an example of fault valve behavior from the Wattle Gully Fault, Victoria, Australia : Journal of Geophysical Research, v. 100, p. 12841-12859.

Cox, S.F., et Etheridge, M.A., 1989, Coupled grain-scale dilatancy and mass transfer during deformation at high fluid pressures: examples from Mount Lyell, Tasmania: Journal of Structural Geology, v. 11, p. 147-162.

Cox, S.F., Knackstedt, M.A., et Braun, J., 2000, Principles of structural control on permeability and fluid flow in hydrothermal systems: Reviews in Economic Geology, (in press).

Cramer, J.J., 1986, Sandstone-hosted uranium deposits in northern Saskatchewan as natural analogs to nuclear fuel waste disposal vaults: Chemical Geology, v. 55, p. 269-279.

Crocker, C.H., Collerson, K.D., Lewry, J.F., et Bickford, M.E., 1993, Sm-Nd, U-Pb, and Rb-Sr geochronology and lithostructural relationships in the southwestern Rae province: constraints on crustal assembly in the western Canadian shield: Precambrian Research, v. 61, p. 27-50.

Cumming, G.L., et Krstic, D., 1992, The age of unconformity-related uranium mineralization in the Athabasca Basin, northern Saskatchewan: Canadian Journal of Earth Sciences, v. 29, p. 1623-1639.

Dahlkamp, F.J., 1978, Geological appraisal of the Key Lake U-Ni deposits, northern Saskatchewan: Economic Geology, v. 73, p. 1430-1449.

Derome, D., Cuney, M., Cathelineau, M., Fabre, C., et Brisset, F., 2000a, Fluid regime in the Kombolgie sandstones in the vicinity of unconformity-type uranium deposits (Northern Territory, Australia), *in* Proceedings, GeoCanada2000, The Millennium Geoscience Summit, Calgary: GAC-MAC joint annual meeting, abstract 178 (Conference CD).

Derome, D., Cathelineau, M., Cuney, M., Fabre, C., Dubessy, J., et Lhomme, T., 2000b, Reconstitution of the composition of individual fluid inclusion using microthermometry, Raman microspectroscopy and Laser Induced Breakdown Spectroscopy. Application to the genesis of Australian and Canadian world-class unconformity-type uranium deposits, *in* Proceedings Symposium Metallogeny2000, December 2000, Nancy, France.

Doligez, B., Burrus, J., et Ungerer, P., 1988, Hydraulic fracturing during basin scale fluid migration: an integrated approach, *in* Hitchon, B., and Bachu, S., eds., Fluid flow, heat transfer and mass transport in fractured rocks: 4th Canadian/American Conference on Hydrogeology, p. 251-259.

Durak, B., 1983, Le gisement de Jabiluka, *in* Pagel, M., ed., Les gisements d'uranium liés spatialement aux discordances: Géologie et Géochimie de l'Uranium, CREGU, Mémoire 1, p. 57-93.

Dzuslynski, S., et Sass-Gustkiewicz, M., 1989, Pb-Zn ores, *in* Bosak, P., Ford, D.C., Glazek, J., and Horacek, I., eds., Paleokarst. A Systematic and Regional Review: Amsterdam and Praka, Elsevier and Academia, p. 377-396.

Egeberg, P.K., 1992, Brines in sedimentary environments: London, Academic Press.

von Einsiedel, C.A., 1981, Petrography and geochemistry of the Cluff Lake breccias, Carswell structure, Northern Saskatchewan [Bachelor thesis]: Ottawa, Carleton University.

Energy Mines and Resources, 1989, Canadian mineral deposits not being mined in 1989: National Mineral Inventory, Mineral Policy Sector, Mineral Bulletin MR 223, Sask. 47.

Etheridge, M.A., 2000, Regional to local structural controls on hydrothermal mineralisation – Practical tools for finding, delineating and mining ore deposits, *in* Proceedings, GeoCanada2000, The Millennium Geoscience Summit, Calgary: GAC-MAC joint annual meeting, abstract 1260 (Conference CD).

Ey, F., 1984, Un exemple de gisement d'uranium sous discordance: les minéralisations protérozoïques de Cluff Lake, Saskatchewan, Canada [Thèse d'Etat]: Strasbourg, Université Louis Pasteur.

Ey, F., Gauthier-Lafaye, F., Lillié, F., et Weber, F., 1985, A uranium unconformity deposit: The geological setting of the D orebody (Saskatchewan-Canada), *in* Lainé, R., Alonso, D., and Svab, M., eds., The Carswell structure uranium deposits, Saskatchewan: Geological Association of Canada Special Paper 29, p. 121-138.

Farstad, J., et Ayers, D.E., 1986, Geology of the Midwest uranium deposit, *in* Evans, E.L., ed., Uranium Deposits of Canada: Canadian Institute of Mining, Metallurgy and Petroleum Special Volume 33, p. 178-183.

Fayek, M., et Kyser, T.K., 1997, Characterization of multiple fluid-flow events and Rare-Earth-Element mobility associated with formation of unconformity-type uranium deposits in the Athabasca Basin, Saskatchewan: The Canadian Mineralogist, v. 35, p. 627-658.

Ferguson, J., Ewers, G.R., et Donnelly, T.H., 1980, Model for the development of economic uranium mineralization in the Alligators Rivers uranium field: N.T., *in* Ferguson, S. and Goleby, A., eds., Uranium in the Pine Creek Geosyncline: Vienna, International Atomic Energy Agency, p. 563-574.

Finch, W.I., 1992, Descriptive model of solution-collapse breccia pipe uranium deposits, in Bliss, J.D., ed., Developments in mineral deposit modeling: U.S. Geological Survey Bulletin 2004, p. 33-35.

Fouques, J.P., Fowler, M., Knipping, H.D., et Schimann, K., 1986, The Cigar Lake uranium deposit: discovery and general characteristics, *in* Evans, E.L., ed., Uranium Deposits of Canada: Canadian Institute of Mining Metallurgy and Petroleum, special volume 33, p.218-229.

Fournier, R.O., 1983, A method of calculating quartz solubilities in aqueous sodium chloride solutions: Geochimica et Cosmochimica Acta., v. 47, p. 579-586.

Fritz, B., 1981, Etude thermodynamique et modélisation des réactions hydrothermales et diagénétiques [Thèse de Doctorat]: Strasbourg, Université Louis Pasteur, Sciences Géologiques, mémoire 65, 197 p.

Frost, R.L., 1995, Fourier transform Raman spectroscopy of kaolinite, dickite and halloysite: Clays and Clay Minerals, v. 43, p. 191-195.

Fyfe, W.S., et Kerrich, R., 1985, Fluids and thrusting: Chemical Geology, v. 49, p. 353-362.

Gandhi, S.S., 1995, An overview of the exploration history and genesis of Proterozoic uranium deposits in the Canadian Shield, *in* First Order Uranium Exploration Target Selection in the Proterozoic of India: Exploration and Research for Atomic Minerals special issue, vol. 8, p. 1-47.

Genna, A., Jébrak, M., Marcoux, E., et Milési, J.P., 1996, Genesis of cockade breccias in the tectonic evolution of the Cirotan epithermal gold system, West Java: Canadian Journal of Earth Sciences, v. 33, p. 93-102.

Gindy, A.R., Al-Shakiry, A.J., et Sa'ad, N.A., 1985, Spheroidal weathering in marls and chalks of Gebel Gurnah near Luxor, Southern Egypt: Journal of Sedimentary Petrology, v. 55, p. 762-768.

Goddard, J.V., et Evans, J.P., 1995, Chemical changes and fluid-rock interactions in faults of crystalline thrust sheets, northwestern Wyoming, U.S.A.: Journal of Structural Geology, v. 17, p. 533-547.

Govindaraju, K., et Mevelle, G., 1987, Fully automated dissolution and separation methods for inductively coupled plasma emission spectrometry rock analysis: Journal of Analytic and Atomic Spectroscopy, v. 2, p. 615-621.

Grant, J.A., 1986, The isocon diagram, a simple solution to Gresens' equation for metasomatic alteration: Economic Geology, v. 81, p. 1976-1982.

Gresens, R.L., 1967, Composition-volume relationships of metasomatism: Chemical Geology, v. 2, p. 47-65.

Gross, M.R., Bahat, D., et Becker, A., 1997, Relations between jointing and faulting based on fracture-spacing ratios and fault-slip profiles: a new method to estimate strain in layered rocks: Geology, v. 25, p. 887-890.

Gustafson, L.B., et Curtis, L.W., 1983, Post-Kombolgie metasomatism at Jabiluka, Northern Territory, Australia, and its significance in the formation of high-grade uranium mineralization in lower Proterozoic rocks: Economic Geology, v. 78, p. 26-56.

Hajnal, Z., Annesley, I.R., White, D., Matthews, R.B., Sopuck, V., Koch, R., Leppin, M., et Ahuja, S., 1997, Sedimentary-hosted mineral deposits: a high-resolution seismic survey in the Athabasca Basin, in Gubins, A.G., ed., Proceedings of Exploration 97: Fourth Decennial International Conference on Mineral Exploration, p. 421-432.

Hall, A.J., 1986, Pyrite-pyrrhotine redox reactions in nature: Mineralogical Magazine, v. 50, p. 223-229.

Halter, G., 1988, Zonalités des altérations dans l'environnement des gisements d'uranium associés à la discordance du Protérozoïque Moyen (Saskatchewan, Canada) [Thèse de doctorat]: Strasbourg, Université Louis Pasteur, 252 p.

Halter, G., Pagel, M., Sheppard, S.M.F., Weber, F., et Clauer, N., 1988, Rétromorphose, paléoaltération, diagenèse et hydrothermalisme de l'encaissant des gisements uranifères dans la structure de Carswell (Saskatchewan-Canada), *in* Gisements Métallifères dans leur Contexte Géologique: Document du BRGM no. 158, v.1, p. 365-388.

Hanmer, S., Williams, M., et Kopf, C., 1995, Striding-Athabasca mylonite zone: implications for the Archean and Early Proterozoic tectonics of the western Canadian Shield: Canadian Journal of Earth Sciences, v. 32, p. 178-196.

Harper, C.T., 1983, The geology and uranium deposits of the central part of the Carswell Structure, Northern Saskatchewan, Canada [Thèse de doctorat]: Golden, Colorado, Colorado School of Mines.

Hecht, L., et Cuney, M., 2000a, Mechanism of uranium mobilization in the Athabasca basin and basement by hydrothermal and/or diagenetic fluids, *in* Proceedings, GeoCanada2000, The Millennium Geoscience Summit, Calgary: GAC-MAC joint annual meeting, abstract 191 (Conference CD).

Hecht, L., et Cuney, M., 2000b, Hydrothermal alteration of monazite in the Precambrian crystalline basement of the Athabasca Basin (Saskatchewan, Canada): implications for the formation of unconformity-related uranium deposits: Mineralium Deposita, v. 35, p. 791-795.

Hedenquist, J.W., Reyes, A.G., Simmons, S.F., et Taguchi, S., 1992, The thermal and geochemical structure of geothermal and epithermal systems: a framework for interpreting fluid inclusion data: European Journal of Mineralogy, v. 4, p. 989-1015.

Heine, T.H., 1986, The geology of the Rabbit Lake uranium deposit, Saskatchewan, *in* Evans, E.L., ed., Uranium Deposits of Canada: Canadian Institute of Mining, Metallurgy and Petroleum Special Volume 33, p. 134-143.

Hickman, S., Sibson, R., et Bruhn, R., 1995, Introduction to special section: mechanical involvement of fluids in faulting: Journal of Geophysical Research, v. 100, p. 12831-12840.

Hoeve, J., 1977, Uranium Metallogenetic Studies no.11: Rabbit Lake: mineralogy and geochemistry, *in* Christopher, J.E., and MacDonald, R., eds., Summary of Investigations 1977: Saskatchewan Geological Survey, Saskatchewan Energy and Mines, Miscellaneous Report, p. 103-105.

Hoeve, J., et Quirt, D., 1984, Mineralization and host rock alteration in relation to clay mineral diagenesis and evolution of the middle-Proterozoic Athabasca Basin, northern Saskatchewan, Canada: Saskatchewan Research Council Technical Report 187, 187 p.

Hoeve, J., et Quirt, D., 1985, A stationary redox front as a critical factor in the formation of high-grade, unconformity-type uranium ores in the Athabasca Basin, Saskatchewan, *in* Program and extended abstracts, Concentration mechanisms of uranium in geological environments: Nancy, France, p. 219-224.

Hoeve, J., et Sibbald, T.I.I., 1976, Rabbit Lake uranium deposit, *in* Dunn, C.E., ed., Uranium in Saskatchewan: Geological Society of Saskatchewan Special Publication no. 3, p. 331-354.

Hoeve, J., et Sibbald, T.I.I., 1978, On the genesis of Rabbit Lake and other unconformity-type uranium deposits in northern Saskatchewan, Canada: Economic Geology, v. 73, p. 1450-1473.

Hoeve, J., Sibbald, T.I.I., Ramaekers, P., et Lewry, J.F., 1980, Athabasca Basin unconformity-type uranium deposits: a special class of sandstone-type deposits?, *in* Ferguson, S., and Goleby, A., eds., Uranium in the Pine Creek Geosyncline: International Atomic Energy Agency, Vienna, p. 575-594.

Hoeve, J., Rawsthorn, K., et Quirt, D., 1981, Uranium Metallogenetic Studies: Clay Mineral Stratigraphy and Diagenesis in the Athabasca Group: Saskatchewan Research Council Technical Report no. 22, p. 76-89.

Hoffman, P.F., 1987, Continental transform tectonics: Great Slave Lake shear zone (ca. 1.9 Ga), northwest Canada: Geology, v. 15, p. 785-788.

Hoffman, P.F., 1989, Precambrian geology and tectonic history of North America, *in* Bally, A.W., and Palmer, A.R., eds., The Geology of North America - An Overview: Boulder, Colorado, Geological Society of America, The Geology of North America, v. A, p. 447-512.

Hurst, A.R., et BjØrkum, P.E., 1986, Discussion: Thin section and S.E.M. textural criteria for the recognition of cement-dissolution porosity in sandstones: Sedimentology, v. 33, p. 605-614.

Hutcheon, I., 2000, Principles of diagenesis and what drives mineral change, *in* Kyser, K., ed., Fluids and Basin Evolution: Mineralogical Association of Canada, Short Course Series, v. 28, p. 93-114.

Iida, Y., 1993, Alteration and ore-forming processes of unconformity-related uranium deposits: Resource Geology Special Issue, no. 15, p. 299-308.

Jaireth, S., 1992, The calculated solubility of platinum and gold in oxygen-saturated fluids and the genesis of platinum-palladium and gold mineralization in the unconformity-related uranium deposits : Mineralium Deposita, v. 27, p. 42-54.

Jébrak, M., 1984, Contribution à l'histoire naturelle des filons F-Ba des Hercynides françaises et marocaines [Thèse de doctorat]: Document BRGM 99.

Jébrak, M., 1992, Les textures intra-filoniennes, marqueurs des conditions hydrauliques et tectoniques: Chroniques de la Recherche Minière, v. 506, p. 25-35.

Jébrak, M., 1997, Hydrothermal breccias in vein-type ore deposits: A review of mechanisms, morphology and size distribution: Ore Geology Reviews, v. 306, p. 1-24.

Jones, B.E., 1980, The geology of the Collins Bay uranium deposits, Saskatchewan: Canadian Institute of Mining, Metallurgy and Petroleum Bulletin, v. 73, p. 84-90.

Kerrich, R., et Allison, I., 1978, Vein geometry and hydrostatics during Yellowknife mineralization: Canadian Journal of Earth Sciences, v. 15, p. 1653-1660.

Kirchner, G., et Tan, B., 1994, Key Lake: the trail of its discovery: Canadian Institute of Mining, Metallurgy and Petroleum, v. 87, p. 57-61.

Kisters, A.F.M., Kolb, J., Meyer, F.M., et Hoernes, S., 2000, Hydrologic segmentation of high-temperature shear zones: structural, geochemical and isotopic evidence from auriferous mylonites of the Renco mine, Zimbabwe: Journal of Structural Geology, v. 22, p. 811-829.

Knipe, R.J., 1993, The influence of Fault Zone Processes and Diagenesis on Fluid Flow, *in* Horbury, A.D., and Robinson, A.G., eds., Diagenesis and Basin Development: The American Association of Petroleum Geologists, Studies in Geology, v. 36, p. 135-148.

Knipping, H.D., 1974, The concepts of supergene versus hypogene emplacement of uranium at Rabbit Lake, Saskatchewan, Canada, *in* Proceedings of a symposium, Formation of Uranium Deposits, Athens, 6-10 May 1974: International Atomic Energy Agency, Vienna, p. 531-548.

Komninou, A., et Sverjensky, D.A., 1996, Geochemical modeling of the formation of an unconformity-type uranium deposit: Economic Geology, v. 91, p. 590-606.

Kotzer, T.G., et Kyser, T.K., 1995, Petrogenesis of the Proterozoic Athabasca Basin, northern Saskatchewan, Canada, and its relation to diagenesis, hydrothermal uranium mineralization and paleohydrogeology: Chemical Geology, v. 120, p. 45-89.

Kotzer, T.G., Kyser, T.K., et Irving, E., 1992, Paleomagnetism and the evolution of fluids in the Proterozoic Athabasca Basin, northern Saskatchewan, Canada: Canadian Journal of Earth Sciences, v. 29, p. 1474-1491.

Kyser, T.K., Wilson, M.R., et Ruhrmann, G., 1989, Stable isotope constraints on the role of graphite in the genesis of unconformity-type uranium deposits : Canadian Journal of Earth Sciences, v. 26, p. 490-498.

Lainé, R., 1985, The Carswell uranium deposits-An example of not so unique unconformity-related uranium mineralization, *in* Lainé, R., Alonso, D., and Svab, M., eds., The Carswell structure uranium deposits, Saskatchewan: Geological Association of Canada Special Paper 29, p. 225-230.

Langford, F.F., 1974, Origin of Australian uranium deposits: A universal process that can be applied to deposits in Saskatchewan, *in* Parslow, G.R., ed., Fuels, a geological appraisal: Geolological Society of Saskatchewan Special Publication no. 2, p. 229-244.

Langford, F.F., 1977, Superficial origin of North American pitchblende and related uranium deposits: American Association of Petroleum Geologists Bulletin, v. 61, p. 28-42.

Laznicka, P., 1988, Breccias and coarse fragmentites: Elsevier, Amsterdam, Developments in Economic Geology, 25.

Laznicka, P., 1989, Breccias and ores. Part 1: history, organization and petrography of breccias: Ore Geology Reviews, v. 4, p. 315-344.

Le Cheminant, A.N., et Heaman, L.M., 1989, Mackenzie igneous events, Canada: Middle Proterozoic hotspot magmatism associated with ocean opening: Earth Planetary Sciences Letters, v. 96, p. 38-48.

Lewry, J.F., et Sibbald, T.I.I., 1980, Thermotectonic evolution of the Churchill Province in Northern Saskatchewan: Tectonophysics, v. 68, p. 45-82.

Little, H.W., 1974, Uranium in Canada. Report of Activities, Part A: Geological Survey of Canada Paper no. 74-1, p. 137-139.

Lorilleux, G., 1997, Lithogéochimie des formations métamorphiques et plutoniques encaissant les gisements d'uranium de type discordance [Mémoire de DEA]: Nancy, Institut National Polytechnique de Lorraine, 39 p.

Lorilleux, G., Jébrak, M., Cuney, M., Baudemont, D., Bérubé, D., et Bruneton, P., 1999a, Breccias and dissolution processes in unconformity-type uranium deposits of the Athabasca Basin (Saskatchewan, Canada), *in* Proceedings, International Workshop on « Fluids and Fractures in the Lithosphere », Nancy, 26-27 March 1999, p. 90.

Lorilleux, G., Jébrak, M., Cuney, M., Baudemont, D., Bérubé, D., et Bruneton, P., 1999b Breccias associated with unconformity-type uranium deposits in the Athabasca Basin (Saskatchewan, Canada), *in* Proceedings of a conference, Sudbury, Ontario, 26-28 May 1999: GAC-MAC joint annual meeting, p. 74.

Lorilleux, G., Cuney, M., Jébrak, M., et Mondy, J., 2000, A new approach of unconformity-type uranium metallogenesis from a structural breccia study (Northern Saskatchewan, Canada), *in* Proceedings, GeoCanada2000, The Millennium Geoscience Summit, Calgary: GAC-MAC joint annual meeting, abstract 232 (Conference CD).

MacDougall, D.G., 1990, Rare Earth Element mineralization in the Athabasca Group-Maw Zone, *in* Summary of Investigations 1990: Saskatchewan Geological Survey, Saskatchewan Energy and Mines, Miscellaneous Report 90-4, p. 103-105.

Magara, K., 1986, Geological models of petroleum entrapment : London, Elsevier Applied Science Publishers, 328 p.

Mallet, J.-L., 1992, Discrete smooth interpolation : Computer – aided design, v. 24, p. 178-191.

Marrett, R., et Peacock, D.C.P., 1999, Strain and stress: Journal of Structural Geology, v. 21, p. 1057-1063.

Matthews, R., Koch, R., et Leppin, M., 1997, Advances in integrated exploration for unconformity uranium deposits in Western Canada, *in* Gubins, A.G., ed., Proceedings of Exploration 97: Fourth Decennial International Conference on Mineral Exploration, p. 993-1024.

McGill, B.D., Marlatt, J.L., Matthews, R.B., Sopuck, V.J., Homeniuk, L.A., et Hubregtse, J.J., 1993, The P2 North uranium deposit, Saskatchewan, Canada: Exploration and Mining Geology, v. 2, p. 321-331.

Montel, J.-M., Foret, S., Veschambre, M., Nicollet, C, et Provost, A., 1996, Electron microprobe dating of monazite: Chemical Geology, v. 131, p. 37-53.

Morton, R.D., 1977, The western and northern australian uranium deposits-exploration guides of exploration deterrents for Saskatchewan?, *in* Dunn, C.E., ed., Proceedings of a Symposium on Uranium in Saskatchewan: Geological Society of Saskatchewan Special Publication no. 3, p. 211-255.

Munday, R.J., 1979, Uranium mineralization in northern Saskatchewan: Canadian Mining and Metallurgical Bulletin, v. 72, p. 102-111.

Narr, W., et Suppe, J., 1991, Joint spacing in sedimentary rocks: Journal of Structural Geology, v. 13, p. 1037-1048.

Newman, J., et Mitra, G., 1993, Lateral variations in mylonite zone thickness as influenced by fluid-rock interactions, Linville Falls fault, North Carolina: Journal of Structural Geology, v.15, p. 849-863.

Nguyen Trung, C., 1985, Géochimie théorique et expérimentale des oxydes d'uranium dans des solutions aqueuses de 25 à 700°C, sous une pression de 1 à 6000 bars. Synthèse hydrothermale de certains minéraux d'uranium (VI) et (IV) [Thèse de doctorat]: Nancy, Institut National Polytechnique de Lorraine, tome I, 479 p.

O'Hara, K., et Blackburn, W.H., 1989, Volume-loss model for trace-element enrichments in mylonites: Geology, v. 17, p. 524-527.

Pacquet, A., et Weber, F., 1993, Pétrographie et minéralogie des halos d'altération autour du gisement de Cigar Lake et leurs relations avec les minéralisations: Canadian Journal of Earth Sciences, v. 30, p. 674-688.

Pagel, M., 1975a, Cadre géologique des gisements d'uranium dans la structure Carswell (Saskatchewan-Canada). Etude des phases fluides. [Thèse de doctorat]: Nancy, Université Nancy I, 156 p.

Pagel, M., 1975b, Détermination des conditions physico-chimiques de la silicification diagénétique des grès Athabasca (Canada) au moyen des inclusions fluides: Comptes Rendus de l'Académie des Sciences, v. 280, D, p. 2301-2304.

Pagel, M., 1977, Microthermometry and chemical analysis of fluid inclusions from the Rabbit Lake uranium deposit, Saskatchewan, Canada: Institution of Mining and Metallurgy Transactions, section B, v. 86, p. B157-B158.

Pagel, M., et Jaffrezic, H., 1977, Analyses chimiques des saumures des inclusions du quartz et de la dolomite du gisement d'uranium de Rabbit Lake (Canada). Aspect méthodologique et importance génétique: Comptes Rendus de l'Académie des Sciences, v. 284, série D-113.

Pagel, M., Poty, B., et Sheppard, S.M.F., 1980, Contribution to some Saskatchewan uranium deposits mainly from fluid inclusion and isotopic data, *in* Ferguson, S., and Goleby, A., eds., Uranium in the Pine Creek Geosyncline : International Atomic Energy Agency, Vienna, p. 639-654.

Pagel, M., Weatley, K., et Ey, F., 1985, The origin of the Carswell circular structure, *in* Lainé, R., Alonso, D., and Svab, M., eds., The Carswell structure uranium deposits, Saskatchewan: Geological Association of Canada Special Paper 29, p. 213-223.

Pagel, M., Pinte, G., et Rotach-Toulhoat, N., 1987, The rare earth elements in natural uranium oxides, *in* Monograph Series on Mineral Deposits: Gebrüder Borntraeger, Berlin, v. 27, p. 81-85.

Pagel, M., Halter, G., Ruhlmann, F., et Tona, F., 1988, Evolution polycyclique de la province uranifère Athabasca (Saskatchewan - Canada) et genèse des gisements liés spatialement à la discordance du Protérozoïque Moyen dans la structure de Carswell, *in* Gisements Métallifères dans leur Contexte Géologique: Document du BRGM no. 158, v.1, p. 389-413.

Passchier, C.W., et Trouw, R.A.J., 1996, Microtectonics: Springer-Verlag, Berlin, Heidelberg, 289 p.

Percival, J.B., 1990, Clay mineralogy, geochemistry and partitioning of uranium within the alteration halo of the Cigar Lake uranium deposit, Saskatchewan, Canada [Thèse de doctorat]: Ottawa, Carleton University, 343 p.

Percival, J.B., Bell, K., et Torrance, J.K., 1993, Clay mineralogy and isotope geochemistry of the alteration halo at the Cigar Lake uranium deposit: Canadian Journal of Earth Sciences, v. 30, p. 689-704.

Petit, S., and Decarreau, A., 1990, Hydrothermal (200°C) synthesis and crystal chemistry of iron-rich kaolinites: Clay Minerals, v. 25, p. 181-196.

Philippe, S., Lancelot, J.R., Clauer, N., et Pacquet, A., 1993, Formation and evolution of the Cigar Lake uranium deposit based on U-Pb and K-Ar systematics: Canadian Journal of Earth Sciences, v. 30, p. 720-730.

Phillips, W.J., 1986, Hydraulic fracturing effects in the formation of mineral deposits: Institution of Mining and Metallurgy Transactions, section B: Applied Earth Science 95, p. B17-B24.

Pittman, E.D., 1981, Effect of fault-related granulation on porosity and permeability of quartz sandstones, Simpson Group (Ordovician), Oklahoma: American Association of Petroleum Geologists Bulletin, v. 65, p. 2381-2387.

Quirt, D., 2000, Sub-Athabasca Group fanglomerate in the McArthur River-Read Lake area, Saskatchewan, *in* Proceedings, GeoCanada2000, The Millennium Geoscience Summit, Calgary: GAC-MAC joint annual meeting, abstract 251 (Conference CD).

Quirt, D., Kotzer, T., et Kyser, T.K., 1991, Tourmaline, phosphate minerals, zircon, and pitchblende in the Athabasca Group: Maw Zone and McArthur River areas, Saskatchewan, *in* Summary of Investigations 1991: Saskatchewan Geological Survey, Saskatchewan Energy and Mines, Miscellaneous Report 91-4, p. 181-191.

Raffensperger, J.P., et Garven, G., 1995a, The formation of unconformity-type uranium ore deposits; 1. Coupled groundwater flow and heat transport modeling: American Journal of Science, v. 295, p. 581-636.

Raffensperger, J.P., et Garven, G., 1995b, The formation of unconformity-type uranium ore deposits; 2. Coupled hydrochemical modeling: American Journal of Science, v. 295, p. 639-696.

Ramaekers, P., 1981, Hudsonian and Helikian basins of the Athabasca region, Northern Saskatchewan: Geological Survey of Canada Paper 81-10, p. 219-233.

Ramaekers, P., 1990, Geology of the Athabasca Group (Helikian) in Northern Saskatchewan: Saskatchewan Energy and Mines, Saskatchewan Geological Survey, report 195, 49 p.

Ramaekers, P., et Dunn, C.D., 1977, Geology and geochemistry of the eastern margin of the Athabasca Basin: Saskatchewan Geological Society Special Publication no. 3, p. 297-322.

Reeve, J.S., Cross, K.C., Smith, R.N., et Oreskes, N., 1990, Olympic Dam. Copper-Uranium-Gold-Silver deposit, *in* Hughes, E.E., ed., Geology of the mineral deposits of Australia and Papua New Guinea: The Australasian Institute of Mining and Metallurgy, Melbourne, p. 1009-1035.

Rice, J.R., 1992, Fault Stress States, Pore Pressure Distributions, and the Weakness of the San Andreas Fault, *in* Evans, B., et Wong, T.-F., eds., Fault Mechanics and Transport Properties in rocks: Academic Press, p. 475-503.

Ridley, J., 1993, The relations between mean rock stress and fluid flow in the crust: with reference to vein- and lode-style gold deposits: Ore Geology Reviews, v. 8, p. 23-37.

Rippert, J.C., Koning, E., Robbins, J., Koch, R., et Baudemont, D., 2000, The Shea Creek Uranium Project, West Athabasca Basin, Saskatchewan, Canada, *in* Proceedings, GeoCanada2000, The Millennium Geoscience Summit, Calgary: GAC-MAC joint annual meeting, abstract 570 (Conference CD).

Rives, T., Razack, M., Petit, J.-P., et Rawnsley, K.D., 1992, Joint spacing: analogue and numerical simulations: Journal of Structural Geology, v. 14, p. 925-937.

Robert, F., Brown, A.C., et Audet, A.J., 1983, Structural control of gold mineralization at the Sigma Mine, Val d'Or, Québec: Canadian Institute of Mining, Metallurgy and Petroleum Bulletin 76, p. 72-80.

Robertson, D.A., et Lattanzi, C.R., 1974, Uranium deposits of Canada: Geoscience Canada, v. 1, p. 8-19.

Robertson, D.S., Tilsley, J.E., et Hogg, G.M., 1978, The time-bound character of uranium deposits: Economic Geology, v. 73, p. 1409-1419.

Ross, G.M., et Eaton, D.W., 1997, Winagami reflection sequence: Seismic evidence for postcollisional magmatism in the Proterozoic of western Canada: Geology, v. 25, p. 199-202.

Ross, G.M., Milkereit, B., Eaton, D., White, D., Kanasewitch, E.R., et Burianyk, M.J.A., 1995, Paleoproterozoic collisional orogen beneath the western Canada sedimentary basin imaged by Lithoprobe crustal seismic-reflection data: Geology, v. 23, p. 195-199.

Rouleau, A., et Gale, J.E., 1985, Statistical characterization of the fracture system in the Stripa Granite, Sweden: International Journal of Rock Mechanics and Mining Sciences, v. 22, p. 353-367.

Ruzicka, V., 1975, Some metallogenic features of the "D" uranium deposit at Cluff Lake, Saskatchewan, *in* Report of activities, part C: Geological Survey of Canada Paper 75-1C, p. 279-283.

Ruzicka, V., 1986, Uranium deposits in the Rabbit Lake-Collins Bay area, Saskatchewan, *in* Evans, E.L., ed., Uranium Deposits of Canada: Canadian Institute of Mining Metallurgy and Petroleum Special Volume 33, p. 144-149.

Ruzicka, V.,1993, Unconformity-type uranium deposits, *in* Kirkham, R.V., Sinclair, W.D., Thorpe, R.I., et Duke, J.M., eds., Mineral Deposit Modeling: Geological Association of Canada Special paper 40, p. 125-149.

Ruzicka, V., 1996, Unconformity-associated uranium, *in* Eckstrand, O.R., Sinclair, W.D., et Thorpe, R.I., eds., Geology of Canadian Mineral Deposit Types: Geological Survey of Canada, Geology of Canada, no. 8, p. 197-210.

Salvi, S., Pokrovski, G.S., et Schott, J., 1998, Experimental investigation of aluminum-silica aqueous complexing at 300°C : Chemical Geology, v. 151, p. 51-67.

Sammis, C.G., et Biegel, R.L., 1986, A self-similar model for the kinematics of gouge deformation: Eos Transactions, v. 67, p. 1187.

Sass-Gustkiewicz, M., 1996, Internal sediments as a key to understanding the hydrothermal karst origin of the upper silesian Zn-Pb ore deposits: Society of Economic Geologists, Special Publication no. 4, p. 171-181.

Sawkins, F.J., 1969, Chemical brecciation, an unrecognized mechanism for breccia formation?: Economic Geology, v. 64, p. 613-617.

Scholz, C.H., 1990, The Mechanics of Earthquakes and Faulting: New York, Cambridge University Press.

Shahabpour, J., 1998, Liesegang blocks from sandstone beds of the Hodjedk Formation, Kerman, Iran: Geomorphology, v. 22, p. 93-106.

Sibson, R.H., 1986, Brecciation processes in fault zones: inferences from Earthquake rupturing: Pure and Applied Geophysics, v. 124, p. 161-175.

Sibson, R.H., 1994, Crustal stress, faulting and fluid flow, *in* Parnell, J., ed., Geofluids: Origin, Migration and Evolution of fluids in Sedimentary Basins : Geological Society Special Publication no. 78, p. 69-84.

Sibson, R.H., 2000, Tectonic controls on maximum sustainable overpressure: fluid redistribution from stress transitions: Journal of Geochemical Exploration, v. 69, p. 471-475.

Sibson, R.H., Robert, F., et Poulsen, K.H., 1988, High-angle reverse faults, fluid-pressure cycling, and mesothermal gold-quartz deposits: Geology, v. 16, p. 551-555.

Sillitoe, R.H., 1985, Ore-related breccias in volcanoplutonic arcs: Economic Geology, v. 80, p. 1467-1514.

Sinha, A.K., Hewitt, D.A., et Rimstidt, J.D., 1986, Fluid interaction and element mobility in the development of ultramyonites: Geology, v. 14, p. 883-886.

SMDC, 1992, Wheeler River Project. Inedited document.

Snow, D.T., 1969, Anisotropic permeability of fractured media: Water Resources Research, v. 5, p. 1273-1289.

Spoljaric, N., 1971, Origin of colors and ironstone bands in the Columbia Formation, Middletown-Odessa Area, Delaware: Southeastern Geology, Durham, North Carolina, v. 12, p. 253-266.

Strnad, J.G., 1980, Genetic models and their impact on uranium exploration in the Athabasca sandstone basin, Saskatchewan, Canada, *in* Ferguson, S., et Goleby, A., eds., Uranium in the Pine Creek Geosyncline: International Atomic Energy Agency, Vienna, p. 631-638.

Suzuki, K., et Adachi, M., 1994, Middle Precambrian detrital monazite and zircon from the Hida gneiss on Oki-Dogo Island, Japan: their origin and implications for the correlation of basement gneiss of Southwest Japan and Korea: Tectonophysics, v. 235, p. 277-292.

Tenthorey, E., Scholz, C.H., Aharonov E., et Léger, A., 1998, Precipitation sealing and diagenesis. 1. Experimental results: Journal of Geophysical Research, v. 103, p. 23951-23967.

Tester, J.W., Worley, W.G., Robinson, B.A., Grigsby, C.O., et Feerer, J.L., 1994, Correlating quartz dissolution kinetics in pure water from 25 to 625°C: Geochimica et Cosmochimica Acta, v. 58, p. 2407-2420.

Thomas, D.J., Matthews, R.B., et Sopuck, V., 1998, Athabasca Basin Unconformity-Type Uranium Deposits: A Synopsis of the Empirical Model and Review of Exploration and Production Trends, *in* Proceedings, Canadian Institute of Mining, Metallurgy and Petroleum meeting, Montréal.

Thomas, D.J., Matthews, R.B., et Sopuck, V., 2000, Athabasca Basin (Canada) unconformity-type uranium deposits : exploration model, current mine developments and exploration directions, in the Great Basin and Beyond Proceedings , Geology and Ore Deposits 2000, volume 1.

Tilsley, J.E., 1980, Continental weathering and development of paleosurface related uranium deposits: some genetic considerations, *in* Ferguson, S., and Goleby, A., eds., Uranium in the Pine Creek Geosyncline: International Atomic Energy Agency, Vienna, p. 721-732.

Tona, F., Alonso, D., et Svab, M., 1985, Geology and mineralization in the Carswell Structure - A general approach, *in* Lainé, R., Alonso, D., and Svab, M., eds., The Carswell structure uranium deposits, Saskatchewan: Geological Association of Canada Special Paper 29, p. 1-18.

Vigneresse, J.L., et Cannat, M., 1987, Mesures de paramètres physiques dans le sondage d'Echassières (vitesse sismique, porosité, densité), *in* Mémoire Géologie profonde de la France , tome 1: Géologie de la France, no. 2-3, p. 145-148.

Villeneuve, M.E., et Thériault, R.J., 1991, U-Pb ages and Sm-Nd signature of two granites from the Fort Simpson magnetic high, northwest Canada: Canadian Journal of Earth Sciences, v. 28, p. 1003-1008.

Wallis, R.H., Saracoglu, N., Brummer, J.J., et Golightly, J.P., 1983, Geology of the McLean uranium deposits, *in* Cameron, E.M., ed., Uranium exploration in Athabasca Basin, Saskatchewan, Canada: Saskatchewan Energy and Mines, Geological Survey of Canada, p. 71-110.

Wheatley, K., Murphy, J., Leppin, M., Cutts, C., et Climie, J.A., 1996, Advances in the genetic model and exploration techniques for unconformity type uranium deposits in the

Athabasca basin, *in* Proceedings, Canadian Institute of Mining, Metallurgy and Petroleum conference, May 1996.

Wilde, A.R., et Wall, V.J., 1987, Geology of the Nabarlek uranium deposit, Northern Territory, Australia : Economic Geology, v. 82, p. 1152-1168.

Wilson, M.R., et Kyser, T.K., 1987, Stable isotope geochemistry of alteration associated with the Key Lake uranium deposit : Economic Geology, v. 82, p. 1450-1557.

Wolery, T.J., et Daveler, S.A., 1992, EQ3/6, a software package for geochemical modeling of aqueous systems. UCRL-MA-110772 PT I-IV : Berkeley, University of California, Lawrence Livermore National Laboratory.

ANNEXE I :
PLANCHES PHOTOGRAPHIQUES

PLANCHES PHOTOGRAPHIQUES

Photographies d'échantillons de Shea Creek, de Sue, et de la zone de Maw

Ces planches photographiques montrent les échantillons les plus représentatifs des différents types de brèches étudiées.

Planche photographique I
(Shea Creek)

Photographie 1 : Echantillon Shea2 représentant une brèche à quartz microcristallin du stade 1 de la paragenèse à Shea Creek. Les fragments allongés et orientés indiquent une fracturation tectonique.

Photographie 2 : Echantillon Shea10 représentant une brèche de dissolution à sudoite et dravite contemporaine de la minéralisation uranifère principale (stade 2). Les textures en puzzle (ou « jigsaw ») illustrent l'origine hydraulique de la fracturation. Les grains de quartz dans la matrice sont des résidus de dissolution.

Photographie 3 : Echantillon Shea16 représentant une brèche de dissolution à sudoite (stade 2). Les rotations des fragments mises en évidence par l'orientation du litage sédimentaire sont dues à des effondrements gravitaires faisant suite aux dissolutions.

Photographie 4 : Echantillon Shea22 représentant une brèche hydraulique à calcite (stade2). Les textures en puzzle sont typiques de la brèche hydraulique. La corrosion des fragments et la quantité importante de grains de quartz détritiques dans la matrice proviennent d'une phase de dissolution antérieure (au début du stade 2).

(1)

(2)

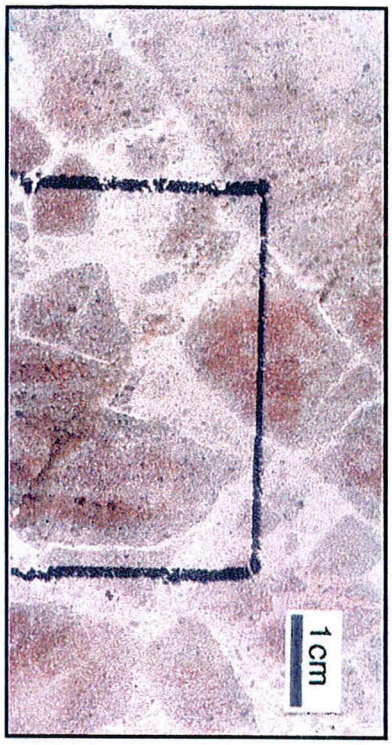

(3)

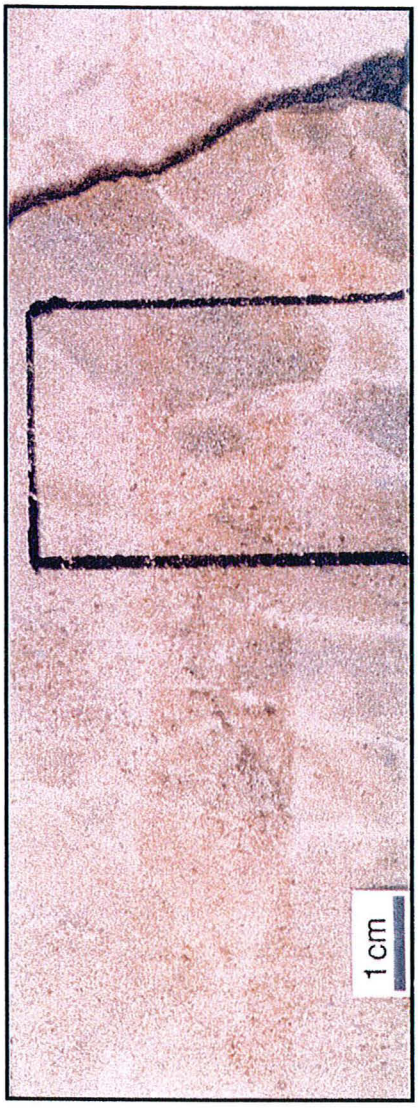

(4)

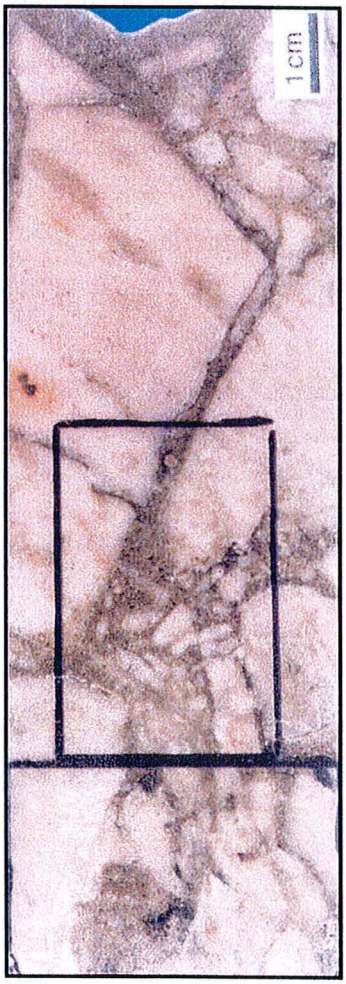

Planche photographique II
(Shea Creek)

Photographie 1 : Echantillon Shea1 représentant une brèche de dissolution-collapse à Fe-chlorite du stade 3 de la paragenèse à Shea Creek. La dissolution du quartz est exprimée par la corrosion de certains fragments et la présence de grains de quartz détritiques dans la matrice. L'effondrement gravitaire est mis en évidence par les rotations de fragments et le fait que la brèche est supportée par les fragments. Les fragments relativement angulaires et peu corrodés suggèrent que cette brèche est dans la partie supérieure d'un système d'effondrement, où les basculements de fragments prédominent sur la corrosion.

Photographie 2 : Echantillon Shea15 représentant une brèche de dissolution-collapse à Fe-chlorite du stade 3 de la paragenèse à Shea Creek. Le caractère polymicte de la brèche exprimé par le mélange de fragments silicifiés angulaires avec des fragments très corrodés est dû à des effondrements gravitaires. Les fragments supportés les uns par les autres dans le partie inférieure de la brèche sont également en accord avec un phénomène d'effondrement.

Photographie 3 : Echantillon Shea3 représentant une brèche de dissolution-collapse à Fe-chlorite du stade 3 de la paragenèse à Shea Creek. Le mélange de fragments angulaires et corrodés et les fragments supportés les uns par les autres sont typiques d'effondrements gravitaires faisant suite à la dissolution du quartz.

Photographie 4 : Echantillon Shea19 représentant une brèche de dissolution à sidérite-hématite du stade 4 de la paragenèse à Shea Creek. Le pourcentage élevé de matrice reflète un fort degré de maturité en partie lié au caractère polyphasé de la brèche qui a subi la phase de dissolution du stade 2.

(1)

(2)

(3)

(4)

Planche photographique III (MCO de Sue C)

Photographie 1 : Echantillon Sue7 représentant un grès non-altéré. La couleur pourpre est due à la préservation de l'hématite primaire.

Photographie 2 : Echantillon Sue1 de grès situé à 4 m d'une zone à boules. L'hématite primaire est lessivé et la dickite est en partie illitisée.

Photographie 3 : Echantillon Sue4 représentant une boule complètement illitisée dans une zone à boule. Malgré la perte de volume de 84 %, des niveaux de minéraux lourds sont préservés et très peu déformés.

Photographie 4 : Echantillon Sue5 représentant la matrice à illite massive d'une zone à boule.

(1)

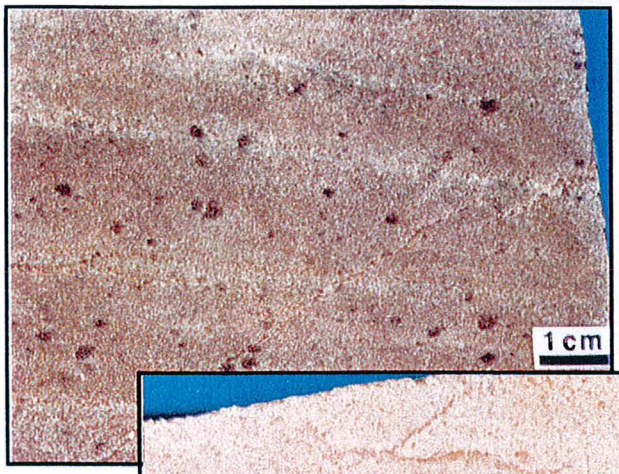

(2)

(3)

(4)

Planche photographique IV (zone de Maw)

Photographie 1 : Echantillon Maw5 représentant un grès silicifié et dravitisé (Cr-dravite).

Photographie 2 : Echantillon Maw3 représentant une brèche immature à dravite. La fracturation mal réglée est typiquement hydraulique et la corrosion du quartz reste limitée au bord des fractures.

Photographie 3 : Echantillon Maw7 représentant une brèche à dravite peu mature. Une silicification tardive a envahi la matrice. Une petite cavité de dissolution au milieu de l'échantillon contient des cristaux de quartz automorphes.

Photographie 4 : Echantillon Maw9 représentant une brèche hydraulique à quartz. La dravite cristallisée en bordure des fragments montre que le quartz est postérieur à la phase de brèche à dravite.

(1)

(2)

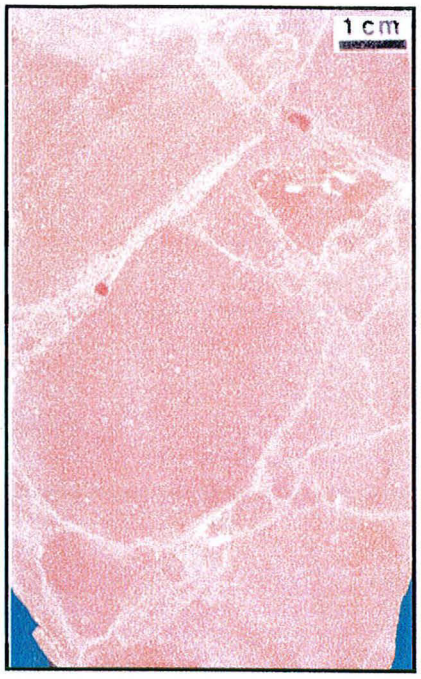

(3)

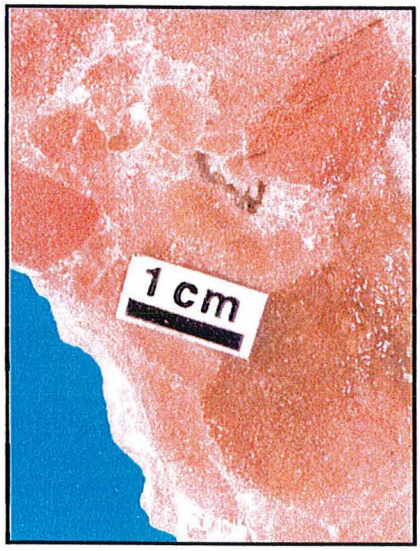

(4)

Annexe II : Modele gOcad de la Zone de Anne a Shea Creek

MODELE GOCAD DE LA ZONE DE ANNE A SHEA CREEK

Introduction

Le modèle gOcad de la zone de Anne présenté dans cette annexe a été réalisé à Nancy au LIAD par Christian Le Carlier de Veslud, David Becel, Jean-Jacques Royer et Guillaume Lorilleux. Le modèle a été construit en plusieurs étapes. Les parties lithologiques et structurales ainsi que la minéralisation uranifère ont été réalisées pendant l'été 1999 et les corps de brèches dans le courant de l'année 2000. Les données de forages (localisations, géologie, levés radiométriques) servant de base à la construction du modèle ont été transmises par le département d'exploration de CRI. Les derniers forages réalisés en 2000 ont été intégrés au modèle afin de réactualiser le contour de la minéralisation et certains contacts géologiques. L'interprétation utilisée a été réalisée en 1998 à partir des levés de carottes de forages par David Baudemont, géologue structuraliste à CRI, et Guillaume Lorilleux. La première étape a été de convertir au format gOcad les fichiers envoyés par le département d'exploration. Ensuite, les différentes coupes et cartes interprétatives réalisées dans la zone de Anne ont été digitalisées afin de les utiliser avec les données de forages comme guides pour la réalisation des surfaces d'interpolation du modèle.

La construction du modèle 3D repose sur trois types d'objets géométriques: (i) des lignes polygonales, représentant généralement les données; (ii) un modèle surfacique, basé sur des surfaces triangulées et représentant les interfaces entre les corps géologiques (failles, contacts) (Fig. AII-1), (iii) un modèle volumique, déduit automatiquement du modèle surfacique (Fig. AII-2).

La construction du modèle surfacique constitue l'un des points clé du travail. La représentation des surfaces utilise un maillage triangulaire pour lequel les points de données constituent des contraintes. L'interpolation des surfaces entre les points de données se fait par l'algorithme DSI (Mallet, 1992), complété par un large choix de contraintes permettant d'assurer la consistance géologique et géométrique des relations entre objets. On peut citer par exemple:

- les *points* ou *courbes de contrôle*, permettant de contraindre les surfaces par des données exactes (forage par exemple) ou floues (interprétation par exemple) ;
- les contraintes *sur une surface*, permettant de contraindre automatiquement une surface (un horizon par exemple) à rester en contact avec d'autres objets surfaciques (des failles par exemple).

La topologie des surfaces peut être adaptée automatiquement à la variabilité des données par des critères automatiques (calcul de courbure ou d'estimation d'erreur), permettant de ne densifier le maillage que là où nécessaire et économisant ainsi de la place. Des opérateurs arithmétiques entre surfaces (coupure, soustraction,...) facilitent la construction d'objets complexes. Ceci permet finalement de fournir un modèle 3D final lissé, conforme du point de vue géologique, notamment au niveau des failles.

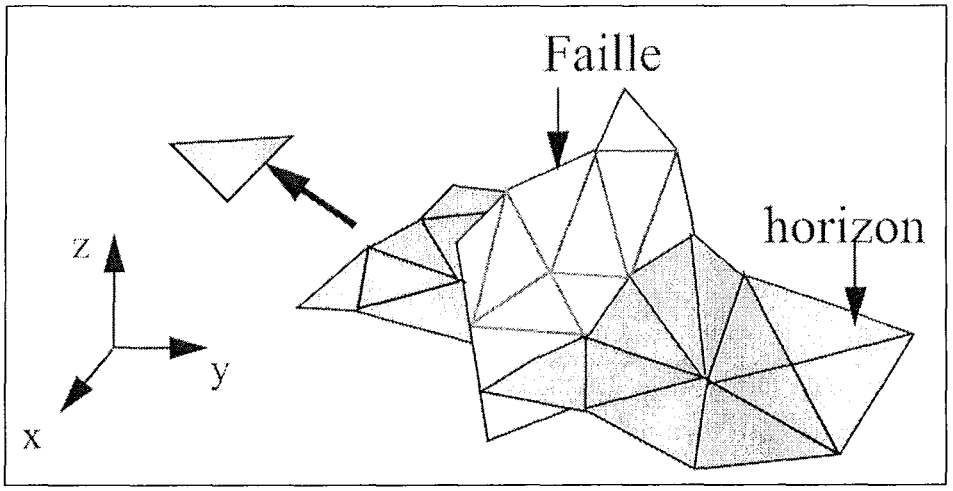

Figure AII-1 - Exemple de deux surfaces triangulées, l'une représentant un horizon, l'autre une faille.

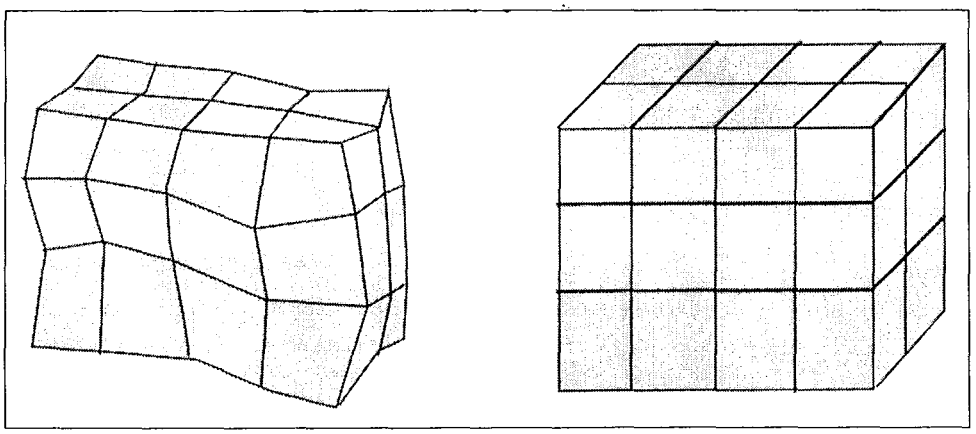

Figure AII-2 - Exemple de grille irrégulière (stratigraphic grid) ou régulière (voxet).

Pour finir, un modèle volumique 3D est utilisé pour déduire automatiquement les régions à partir du modèle surfacique. Ce modèle volumique peut se présenter sous deux formes:

- un modèle volumique de Weiler, décrivant chaque région par les morceaux de surface qui la ferment,

- un modèle volumique de grille (régulière ou non) (Fig. AII-2). Ce modèle utilise préalablement un maillage de l'espace par une grille. A partir de là, chaque région est décrite par l'union de toutes les cellules élémentaires qui la composent.

C'est le modèle de Weiler qui a été réalisé pour le modèle de la zone de Anne. Ce modèle volumique peut être utilisé pour calculer les volumes d'un corps, ou par exemple, une abondance relative. Cette partition de l'espace peut aussi être utilisée pour affecter des propriétés physiques à des roches (densité, perméabilité,...) en fonction de la lithologie, dans le but de procéder à des calculs de modélisation directe: réponse gravimétrique ou transferts de chaleur et de masse par exemple. Enfin, le modèle volumique rend également possible la réalisation de coupes dans toutes les directions et non-nécessairement rectilignes. Il suffit pour cela de tracer la ligne de coupe souhaitée sur le modèle.

Les différentes formations sédimentaires, la discordance, le graphite, les failles de type I, III et IV (voir partie II), le corps minéralisé et les corps de brèches à sudoite-dravite et Fe-chlorite ont été représentés (Fig. AII-3, AII-4, AII-5 et AII-6). Les enveloppes des corps minéralisés et de brèches ont été créées en rejoignant les contours fermés interprétés sur les coupes d'exploration par des surfaces. L'enveloppe du corps minéralisé a été dessinée en combinant le contour interprété sur les coupes d'exploration avec les intervalles des logs radiométriques correspondant à des teneurs supérieures à 3000 ppm d'uranium. Le contrôle de l'orientation des corps de brèches par les failles a servi de guide pour les surfaces d'interpolation entre les coupes.

Principaux apports du modèle

La modélisation tridimensionnelle de la zone de Anne a permis de montrer la très bonne corrélation spatiale entre le maximum de dénivellation de la discordance, lié aux failles de type I et le corps minéralisé (Fig. AII-4). Le modèle a également mis en évidence une propagation de la dénivellation à la discordance dans les couches sédimentaires sus-jacentes qui s'atténue vers le haut (Fig. II-1). Localement, des zones de dépression apparaissent. Deux interprétations sont possibles : soit cette propagation correspond aux failles inverses « aveugles » de type I qui s'atténuent dans les grès, soit il s'agit de zones d'effondrement liées à des dissolutions de grès au niveau des minéralisations sous-jacentes. Le modèle a confirmé la très bonne corrélation spatiale entre les corps de brèches et la minéralisation uranifère. Il apparaît qu'une partie importante de la minéralisation enveloppe les brèches. Dans la réalité, c'est le contraire mais l'utilisation des contours assez larges de zones minéralisées (teneur de coupure inférieures à 3000 ppm d'U) dans les coupes pour appuyer les surfaces d'interpolation ont conduit à maximiser le volume de la minéralisation. Le modèle a également permis de montrer la forme en doigts des brèches à sudoite-dravite étroitement

contrôlées par les failles de type I essentiellement (Fig. AII-5). Les brèches à Fe-chlorite ont une forme plus étalée en dôme à l'intersection de 3 types de failles, probablement due à un effondrement de type « Mississippi Valley Type deposits »faisant suite à la dissolution massive du quartz (Fig. AII-6). La fonction Getvolume de gOcad a permis de calculer facilement le volume des corps de brèches. Les brèches à sudoite-dravite dans la zone de Anne ont un volume de 166 000 m^3 tandis que les brèches à Fe-chlorite ont un volume de 30 000 m^3. Ces volumes ont été utilisés afin d'estimer le volume de fluides sous-saturés en silice qui ont circulé dans les brèches.

La modélisation tridimensionnelle a également mis en évidence un certain nombre de problèmes de correspondance entre cartes et coupes. En particulier, des choix interprétatifs ont dû être effectués concernant l'orientation et la forme des failles entre les coupes. Le dessin des corps de brèches a posé de nombreux problèmes puisque des zones importantes de brèches levées dans des forages réalisés en 1999 se sont retrouvées éloignées de toute faille pouvant les justifier. Ces difficultés ont mis en évidence les limites du modèle de 1998. Depuis, les nouveaux forages réalisés en 1999 et 2000 et surtout les premières orientations de carottes ont permis aux géologues d'exploration d'établir un nouveau modèle présenté dans la partie IV (figure 3). Ce modèle comprend une nouvelle famille de failles orientée N100-110 (type II) (voir partie IV) et qui avait été suggérée par l'orientation N100-110 de certains corps de brèches cartographiés lors de la mission de terrain de juin 1999 (Rapport interne COGEMA, Lorilleux). Ces failles corréleraient donc très bien avec les brèches isolées du modèle.

La principale difficulté rencontrée lors de la construction de ce modèle a donc été d'intégrer des données de forages récentes qui ne correspondaient pas nécessairement à l'interprétation de 1998. La reconstruction du nouveau modèle en cours, si elle a lieu, nécessitera de reprendre le travail de modélisation au point de départ puisque les changements de localisation et d'orientation des failles impliquent de reconstruire toutes les failles avec un nouveau redécoupage des failles entre elles.

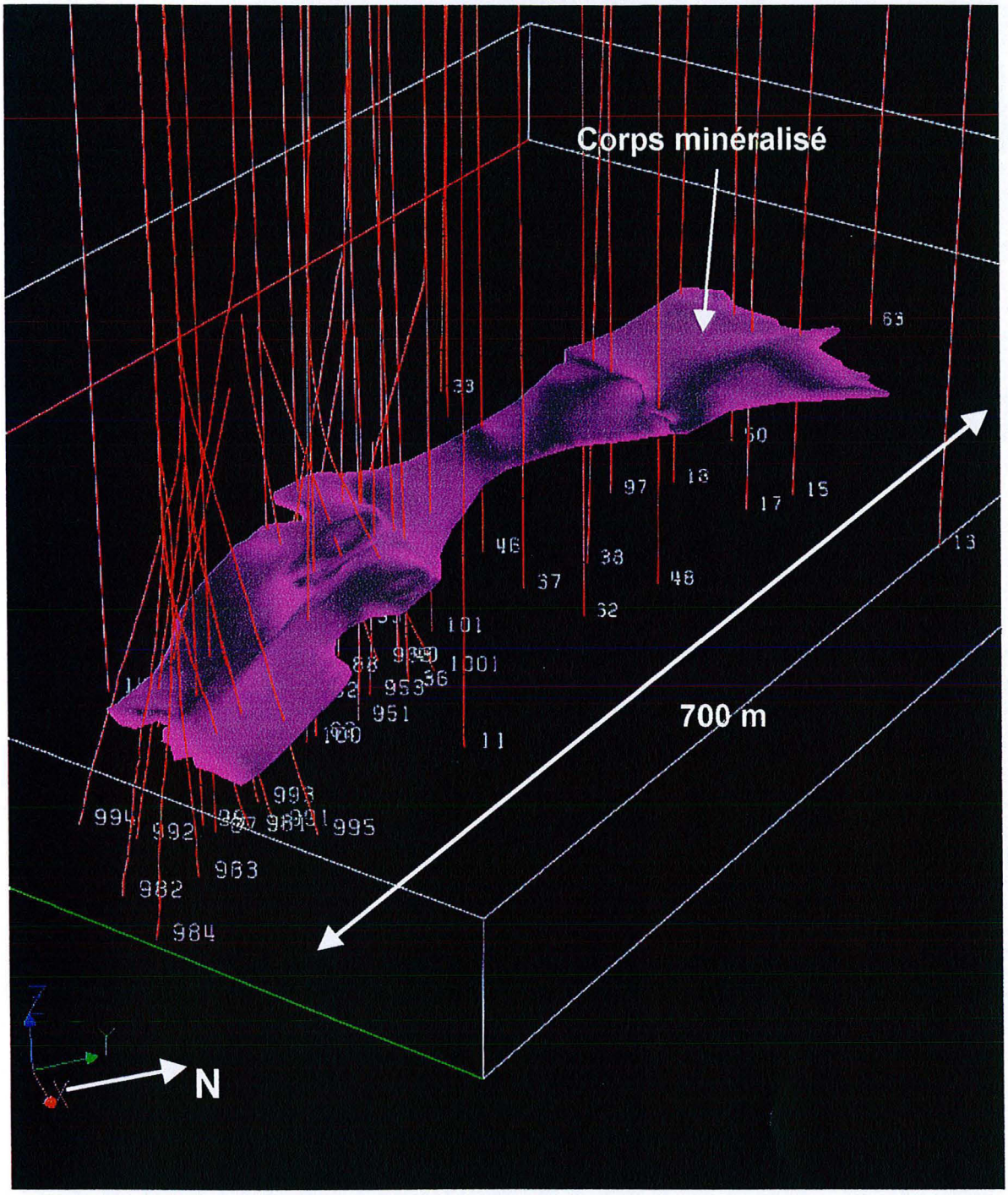

Figure AII-3 – Vue de l'est du corps minéralisé et des forages.

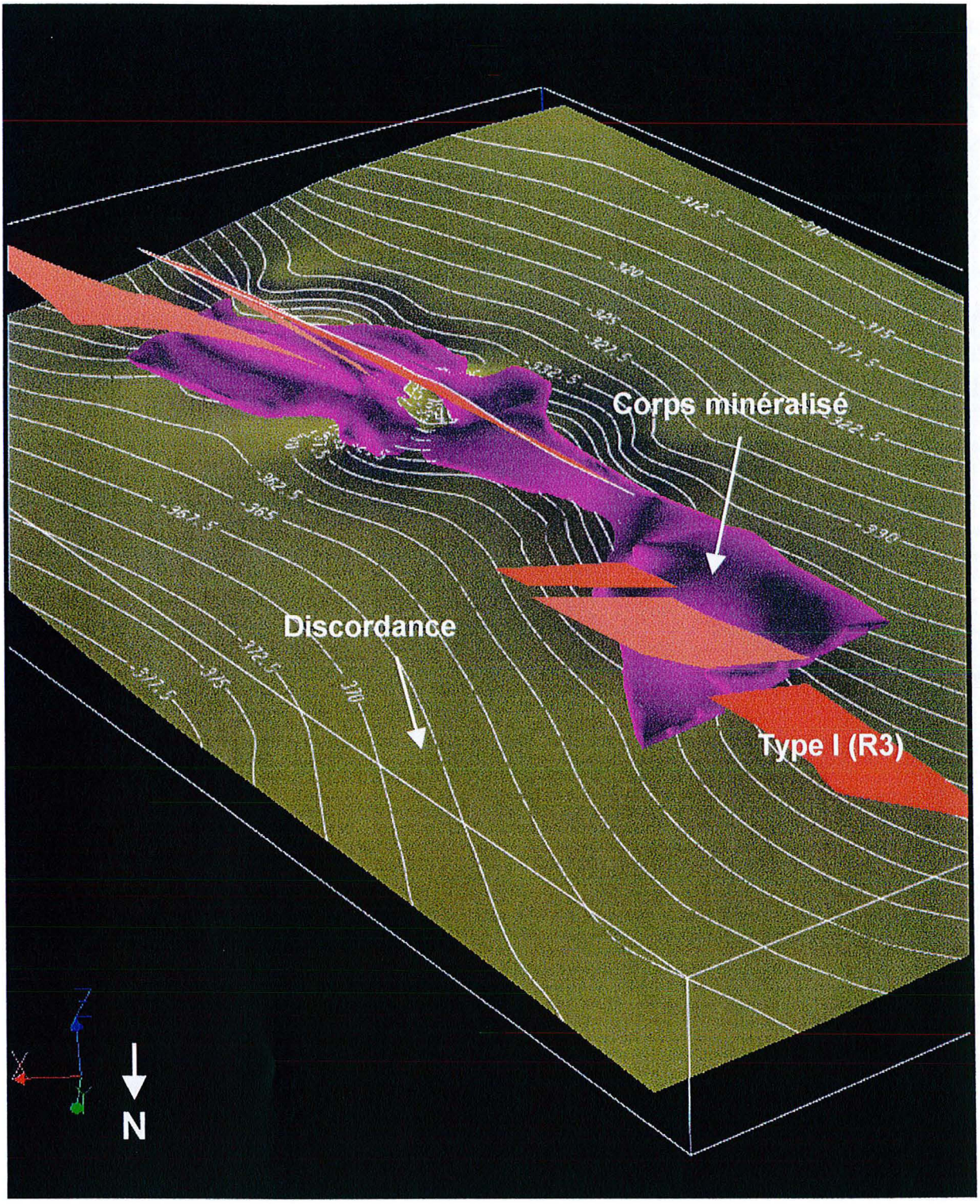

Figure AII-4 – Vue du nord du corps minéralisé, de la discordance et des failles de type I.

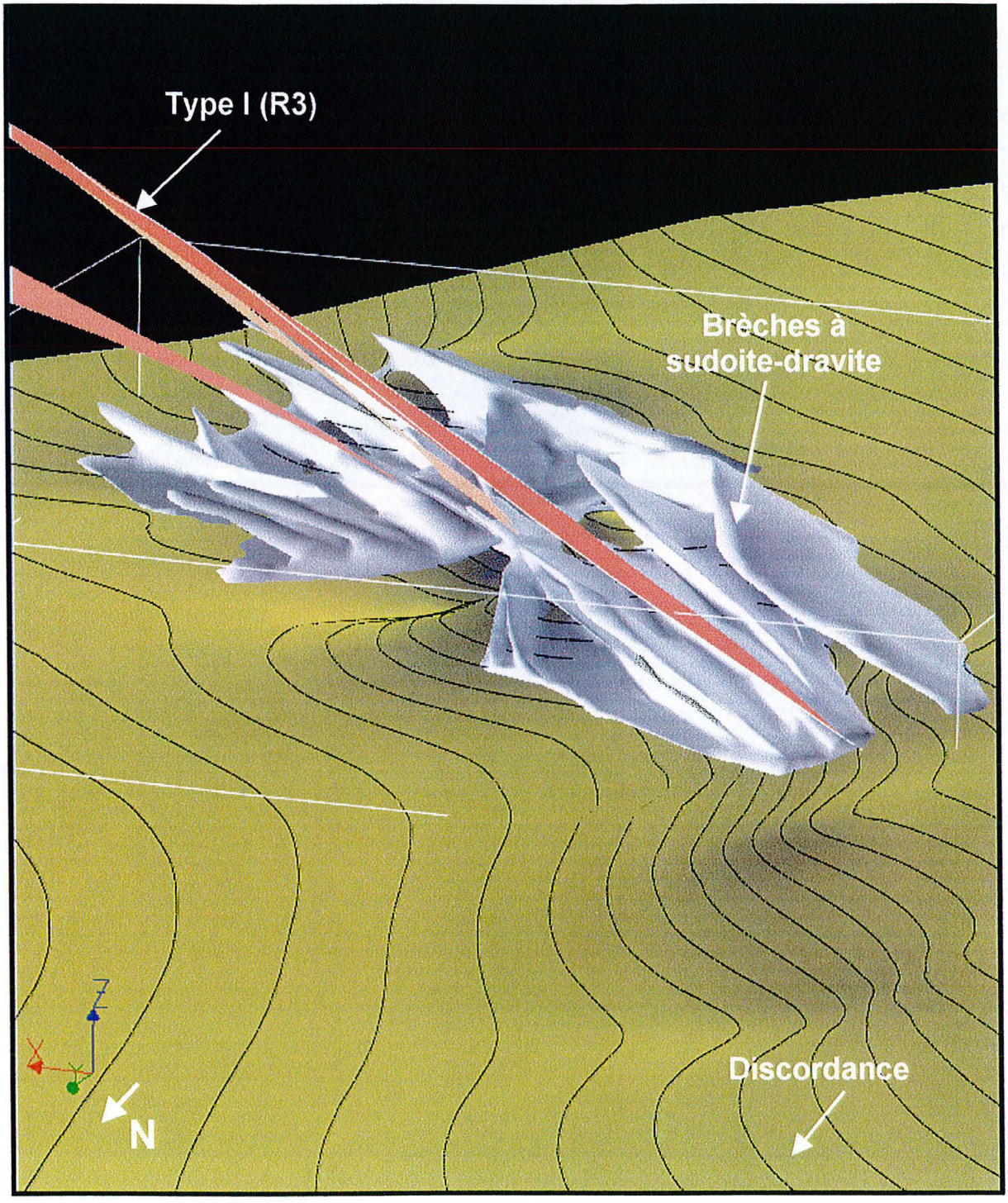

Figure AII-5 – Vue du NW du corps de brèches à sudoite-dravite avec la faille de type I.

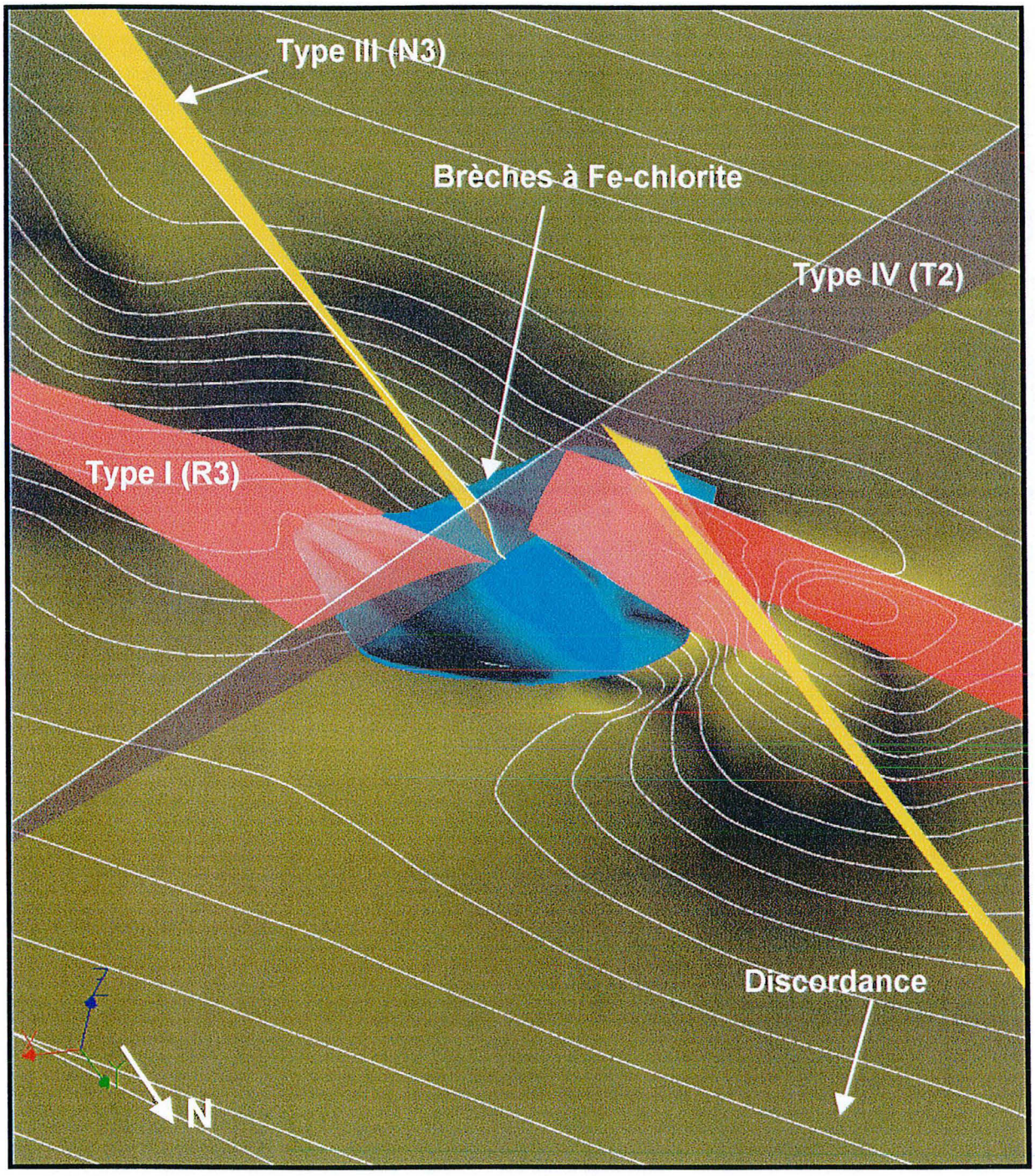

Figure AII-6 – Vue du NE du corps de brèches à Fe-chlorite à l'intersection de failles de type I, de type III et de type IV.

ANNEXE III :
METHODES DE CALCUL

METHODES DE CALCULS

I: Bilans de masse

Introduction

Les bilans de masse permettent de quantifier les gains et pertes en éléments chimiques d'une roche altérée par rapport à son équivalent non-altéré (protolite). Dans le cas d'un phénomène de bréchification hydrothermale, les variations de volume sont souvent considérables et il est nécessaire de prendre en compte la densité dans les calculs. C'est la méthode de Grant (1986), particulièrement simple d'utilisation, qui a servi pour réaliser les calculs de bilans de masse.

I:1. Mesure d'une densité globale

La méthode utilisée est celle de la pesée de l'échantillon sec puis immergé dans un picnomètre.

I:1:1. Mesure de la masse à sec

L'échantillon doit dans un premier temps être mis à l'étuve pendant 24 heures. L'élévation de température doit être progressive afin d'atténuer l'apparition de porosité par dilatation thermique (Vigneresse et Cannat, 1987). Il est préférable de ne pas dépasser la température de 100°C afin d'éviter la production de nouvelles microfractures par dilatation thermique différentielle des minéraux (Heard et Page, 1982). Une réhumidification de l'échantillon se produit dès la sortie de l'étuve. La mesure de la masse doit donc être effectuée rapidement.

I:1:2. Mesure de la masse immergée « à sec »

La masse immergée « à sec » est mesurée immédiatement après la mesure de la masse à sec. La mise de l'échantillon dans le picnomètre doit être très rapide pour éviter les pertes de bulles d'air faisant suite à la pénétration de l'eau dans l'échantillon. L'eau présente sur les parois extérieures du récipient est consciencieusement essuyée avant de mesurer la masse. La température de l'eau doit être mesurée avant et après cette mesure de masse afin d'effectuer la correction de température. En effet, si l'échantillon n'est pas poreux, sa température élevée à la

sortie de l'étuve va provoquer une dilatation de l'eau et une perte par le haut du picnomètre. Dans ce cas, le calcul de la densité devra tenir compte de la température après la mesure de la masse immergée « à sec ». Cette mesure de température doit être très rapide puisqu'elle continue à augmenter après la pesée. Si l'échantillon est poreux, l'eau va petit à petit pénétrer l'échantillon après la fermeture du picnomètre. Le niveau d'eau va donc diminuer. Dans ce cas, la température à considérer est celle de l'eau avant contact avec l'échantillon puisque c'est la masse du picnomètre plein qui importe dans le calcul de la densité.

Certains échantillons poreux ont été couverts d'une légère couche de vernis à l'aide d'un aérosol afin de vérifier que la durée de fermeture du picnomètre n'affecte pas sensiblement les résultats. Une différence moyenne de 0,01 a été obtenue sur les échantillons poreux dont la valeur de la densité globale a donc été corrigée en conséquence en l'abaissant de 0,01. Il a été vérifié sur des échantillons non poreux que la couche de vernis est suffisamment fine pour ne pas affecter la densité. Les échantillons argileux et friables ont sytématiquement été revêtus d'une couche de vernis afin d'éviter leur désaggrégation avant la fermeture du picnomètre. Il est préférable d'utiliser les plus gros échantillons possibles afin de minimiser une éventuelle légère modification de la densité du fait de l'application du vernis.

I:1:3. Calcul de la densité globale

On calcule la densité en utilisant la formule suivante :

$$D = (Ms / (Pe - Ps + Ms)) \times De$$

,où : Ms = masse de l'échantillon sec,
Pe = masse du picnomètre plein d'eau,
Ps = masse du picnomètre plein d'eau contenant l'échantillon,
De = densité de l'eau,
D = densité globale de l'échantillon.

Pe et De sont fonction de la température. Il faut donc calibrer Pe en fonction de la température expérimentalement. Cette calibration doit être précise puisque une erreur de 2 degrés sur la température induit une erreur de l'ordre de 1 centième sur la densité globale. La courbe de calibration obtenue n'est pas une droite mais une courbe dont la concavité est tournée vers le bas (Fig. AIII-1). A pression atmosphérique, la courbe atteint un maximum à 4°C. Les valeurs de De en fonction de la température ont été prises dans le Handbook of Physical Constants.

Des mesures sur les mêmes échantillons ont été réalisées plus de 10 fois et ont démontré la répétabilité des résultats avec une précision au centième. Cela a également permis de vérifier la validité de la correction de température. Sur les échantillons de brèches particulièrement hétérogènes, plusieurs mesures ont été effectuées sur des morceaux ayant des proportions de matrice différentes. Enfin, dans le cas de mesures en série, l'expérience montre qu'il très important de changer l'eau du bac servant à remplir le picnomètre entre chaque mesure afin de ne pas augmenter la densité de l'eau par la mise en solution de microparticules provenant de l'échantillon précédent.

Cette méthode a été vérifiée en l'appliquant sur des cristaux de quartz hyalin provenant de la mine de la Gardette (collection B. Poty). Ceux-ci contiennent moins de 1000 ppm d'impuretés et ont donc une densité de 2,65. Les valeurs obtenues sont en moyenne de 2,64. L'erreur de 0,01 est probablement liée à l'augmentation de température entre la pesée et la mesure de température qui dépend de la vitesse d'exécution de la manipulation. Les densités globales des échantillons de l'étude ont donc été corrigées en conséquence en leur ajoutant 0,01. Concernant les échantillons poreux, il n'y a au final aucune correction à effectuer puisque l'addition de 0,01 est compensée par une soustraction de 0,01 (voir 2-Mesure de la masse immergée « à sec »).

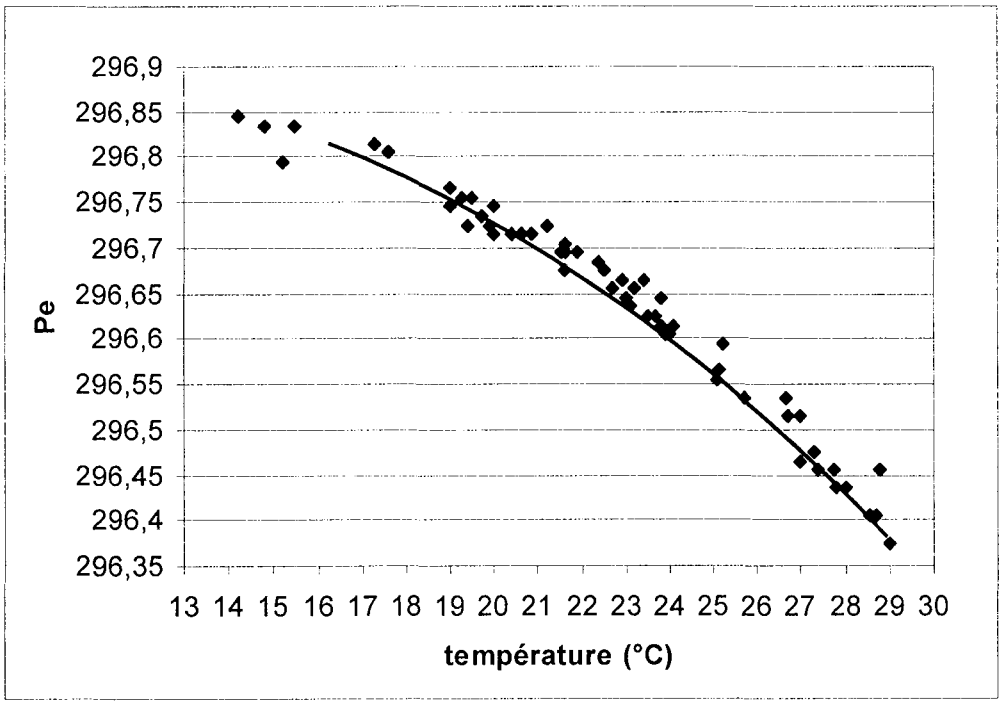

Figure AIII-1 – Courbe de calibration de la masse du picnomètre plein d'eau en fonction de la température. L'expérience montre l'augmentation de la température de l'eau entre la pesée et la mesure de température du fait du contact du picnomètre avec la main le tenant (à 37°C). Il faut en effet compter parfois plusieurs dizaines de seconde pour pouvoir ouvrir le picnomètre du fait de forces d'adhésions difficiles à dépasser. La correction de cette élévation de température conduit à décaler la courbe vers la gauche vers les valeurs de température les plus basses correspondant aux temps d'ouverture les plus faibles.

I:2. Calculs des variations de volume et des facteurs d'enrichissement et de perte : la méthode isocone

Grant (1986) a réécrit l'équation de Gresens (1967) sous la forme suivante :

$$C^A_i = (M^O / M^A) (C^O_i + \Delta C_i)$$

,où : C = concentration,
M = masse de l'échantillon,
A = indice pour altéré,
O = indice pour originel (non-altéré),
i = indice pour élément,
ΔC_i = variation de concentration de l'élément i.

Pour chaque élément, il existe une équation de cette forme pour laquelle (M^O / M^A) est une constante. En identifiant les éléments pour lesquels $\Delta C_i = 0$, on peut connaître la valeur de ce rapport en résolvant de manière simultanée un ensemble d'équations de la forme :

$$C^A_i = (M^O / M^A) C^O_i.$$

La solution peut être facilement obtenue graphiquement en traçant les valeurs de C^A_i en fonction de C^O_i (Fig. AIII-2). Les éléments immobiles génèrent alors une droite passant par l'origine de pente (M^O / M^A), qui est le rapport fondamental de masses équivalentes avant et après l'altération. Cette droite, pour laquelle $\Delta C_i = 0$, est appelée isocone, c'est-à-dire une ligne reliant des points de même concentration géochimique.
Si on considère que le Zr est immobile,

$$(M^O / M^A) = (C^A_{Zr} / C^O_{Zr}).$$

Si on considère une altération sans variation de masse,

$$(M^O / M^A) = 1.$$

Si on considère une altération à volume constant,

$$(M^O / M^A) = (d^O / d^A),$$

, où : d^O = densité de l'échantillon non-altéré,
d^A = densité de l'échantillon altéré.

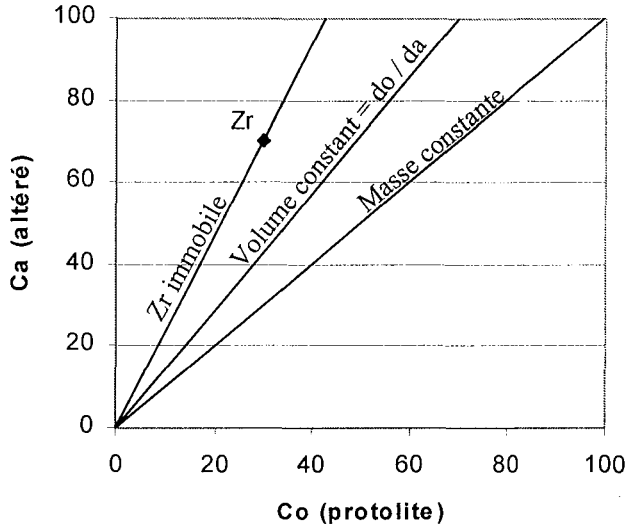

Figure AIII-2 – Diagramme isocone montrant les 3 possibilités de définir une droite isocone. Le zirconium est pris comme exemple d'élément immobile.

La formation des brèches hydrothermales s'accompagne le plus souvent de variations de masse et de volume. Le gain ou la perte de volume de l'échantillon altéré ou bréchifié par rapport au protolite est donné par la formule suivante :

$$\text{Gain/perte de volume} = 1 - (d^O / d^A)\,(M^O / M^A),$$

où : $(d^O / d^A)\,(M^O / M^A) = V^A / V^O$,
avec V^A = volume de l'échantillon altéré,
et V^O = volume du protolite.

Les gains et pertes des éléments mobiles sont donnés par le déplacement des points par rapport à la droite isocone. Le facteur d'enrichissement ou de perte d'un élément par rapport à sa concentration avant l'altération est donné par l'équation suivante :

$$(\Delta C_i / C^O_i) = (M^A / M^O)\,(C^A_i / C^O_i) - 1.$$

Dans la figure 19 de la partie IV, les facteurs d'enrichissement ou de perte sont augmentés de 1 afin de pouvoir en prendre le logarithme.

II: Rapports fluide/roche et temps de formation des brèches

Introduction

Les brèches étudiées sont caractérisées par la dissolution massive du quartz. En calculant la quantité de quartz dissous et en supposant un degré de sous-saturation en silice du fluide, on peut calculer le volume de fluide minimum nécessaire pour former un certain volume de brèche. En tenant compte de la conductivité hydraulique et de la porosité du milieu, on peut estimer un temps minimum de formation des brèches.

II:1. Rapport fluide/roche d'un échantillon de brèche

Les pourcentages de quartz d'un échantillon de brèche et de son protolite sont obtenus par calcul normatif à partir de la composition chimique de l'échantillon et des minéraux le composant. Si la bréchification ne s'est pas accompagnée de perte de volume, le pourcentage massique de quartz dissous (M_{qtz})est donné par :

$$M_{qtz} = M^{O}_{qtz} - M^{A}_{qtz},$$

où : M^{O}_{qtz} = pourcentage massique de quartz dans le protolite,
M^{A}_{qtz} = pourcentage massique de quartz dans l'échantillon bréchifié.

Si une perte de volume a eu lieu, ce qui est presque systématiquement le cas,

$$M_{qtz} = M^{O}_{qtz} - M^{A}_{qtz} (M^{A} / M^{O}).$$

Pour 1 kg de roche initiale, le nombre de moles de quartz dissous (n) est donné par :

$$n = (1000 (M_{qtz} / 100)) / 60.$$

Si on considère une solubilité (s) du quartz en mol/kg et une sous-saturation (t) du fluide en %, le rapport volumique fluide/roche cumulé (w/r) est donné par :

$$w/r = d^{O} (n / (s (t / 100))).$$

Il s'agit d'un rapport fluide/roche relatif au volume initial de roche. C'est une valeur minimale puisqu'on fait l'hypothèse que tout le fluide qui a circulé a réagi avec le quartz

de manière instantanée. Il faudrait également prendre en compte la cinétique de réaction ou le temps de diffusion des éléments dans le fluide.

II:2. Temps de formation des brèches

Afin d'estimer un temps de formation des brèches, il est nécessaire d'avoir une idée de la vitesse de circulation du fluide sous-saturé en silice, ou conductivité hydraulique. Considérant une famille de fractures parallèles avec un espacement fractural moyen (S_m) et une ouverture moyenne des fractures (A_m), la conductivité hydraulique « directionnelle » (K_m) (Snow, 1969; Ababou, 1991 ; Vuillod, 1995) est donnée par :

$$K_m = (g / 12\ \eta)\ (A_m^3 / S_m),$$

où : g = accélération gravitationnelle,

η = viscosité cinématique du fluide ($\sim 10^{-6}$).

En tenant compte de la perte de volume, le volume de fluide (Vf) nécessaire pour former un corps de brèche de volume (V) est donné par :

$$Vf = w/r\ (V\ (V^O / V^A)).$$

Considérant que le fluide traverse le corps de brèche à travers une section (S) sur une longueur (L), et en supposant une porosité (p) en %, la hauteur (H) de la colonne d'eau qui doit passer perpendiculairement à la section est donnée par :

$$H = Vf / (S\ (p / 100)).$$

Le temps minimum (T) de formation d'un corps de brèches de volume V est donc :

$$T = H / (K_m).$$

Il s'agit bien d'un temps minimum puisque w/r est également minimum.

ANNEXE IV :
LISTE DES ECHANTILLONS ET RESULTATS D'ANALYSES

LISTE DES ECHANTILLONS ET RESULTATS D'ANALYSES

Introduction

Cette annexe présente :

(1) les différents échantillons étudiés à Shea Creek, à Sue et dans la zone de Maw,

(2) les descriptions systématiques de différents types de brèches de Shea Creek,

(3) les résultats d'analyses chimiques ponctuelles à la microsonde électronique, d'analyses chimiques globales ICP-AES et –MS, de mesures de densités et d'analyses de diffraction aux rayons X, ainsi que les spectres Raman de kaolinite/dickite.

I: Etudes réalisées sur les différents échantillons de Shea Creek, de Sue et de la Maw Zone

Echantillon	Shea1	Shea2	Shea3	Shea4	Shea7	Shea8	Shea9	Shea10	Shea11
Forage	She79	Dgs11	She16	She66	She62	Dgs14	She51	She66	Dgs9
Profondeur	709	611,8	696,8	674	716	701,5	715,9	675,5	704,1
Photo	✓	✓	✓	✓	-	✓	✓	✓	✓
Analyse fractale	✓	-	✓	-	-	-	-	-	-
Lames minces	2	1	3	1	1	1	1	1	1
Lames épaisses	1	1	2	1	1	1	1	1	1
DRX	-	-	-	✓	✓	✓	-	✓	-
MEB	✓	✓	✓	✓	-	-	-	✓	-
Surface fragments au MEB	✓	-	-	-	-	-	✓	-	✓
Microsonde argiles	✓	-	✓	✓	✓	-	-	✓	-
Microsonde oxydes U	✓	-	✓	-	-	-	-	-	-
Raman	-	-	-	✓	✓	-	-	-	-
Densités	✓	✓	✓	-	✓	✓	-	✓	✓
Géochimie	✓	✓	✓	-	✓	✓	-	✓	✓

Tableau AIV-1 - Liste des travaux réalisés sur différents échantillons de Shea Creek.

Echantillon	Shea12	Shea13	Shea14	Shea15	Shea16	Shea19	Shea20	Shea21	Shea22
Forage	She16	She80	She79	She12	She16	She93	She12	Dgs11	She12
Profondeur	702,5	697,6	703,9	698,8	711,1	719,9	706	690,6	702,3
Photo	✓	✓	✓	✓	✓	✓	✓	✓	✓
Analyse fractale	-	-	-	-	✓	✓	-	-	-
Lames minces	2	2	1	2	2	1	1	1	2
Lames épaisses	1	1	1	2	1	1	1	1	1
DRX	✓	✓	✓	-	✓	✓	✓	-	-
MEB	✓	-	-	✓	✓	✓	✓	-	-
Surface fragments au MEB	-	-	✓	-	-	-	-	-	-
Microsonde argiles	✓	-	-	✓	✓	✓	-	-	-
Microsonde oxydes U	-	-	-	-	-	-	-	-	-
Raman	-	-	-	-	-	✓	-	-	-
Densités	✓	✓	-	✓	✓	✓	✓	✓	✓
Géochimie	✓	✓	-	✓	✓	✓	✓	✓	✓

Tableau AIV-2 - Liste des travaux réalisés sur différents échantillons de Shea Creek.

Echantillon	Shea23	Shea24	Shea28	Shea29	Shea31	Shea40	Shea41	Shea42	Shea43
Forage	She80	She12	She62	Dgs9	Dgs10	She66	She74	She16	She16
Profondeur	711,1	701,3	718,9	701,3	596,6	668,5	672	720,5	718,6
Photo	✓	✓	✓	✓	✓	-	-	-	-
Analyse fractale	-	-	-	-	-	-	-	-	-
Lames minces	1	3	1	1	1	1	1	1	1
Lames épaisses	1	1	1	1	1	1	1	1	1
DRX	✓	✓	-	-	-	-	-	-	-
MEB	-	✓	-	-	-	✓	-	✓	✓
Surface fragments au MEB	-	-	-	-	-	-	-	-	-
Microsonde argiles	-	-	-	-	-	-	-	-	-
Microsonde oxydes U	-	-	-	-	-	✓	-	-	✓
Raman	-	-	✓	-	-	-	-	✓	-
Densités	-	✓	✓	-	-	-	-	-	-
Géochimie	-	✓	✓	-	-	-	-	-	-

Tableau AIV-3 - Liste des travaux réalisés sur différents échantillons de Shea Creek.

Echantillon	Shea44	Shea45	Shea46	Shea47	8656-4	8615-5	8615-6
Forage	She74	She66	She87	Dgs6	She16	She15	She15
Profondeur	669,5	667,5	710,1	687,1	718,2	705,7	720
Photo	-	-	-	✓	-	-	-
Analyse fractale	-	-	-	-	-	-	-
Lames minces	1	1	1	1	1	1	1
Lames épaisses	1	1	1	0	0	0	0
DRX	-	-	-	-	-	-	-
MEB	✓	-	✓	-	✓	-	-
Surface fragments au MEB	-	-	-	-	-	-	-
Microsonde argiles	-	-	✓	-	-	-	-
Microsonde oxydes U	✓	-	✓	-	✓	-	-
Raman	-	-	-	-	-	✓	✓
Densités	-	-	-	-	-	-	-
Géochimie	-	-	-	-	-	-	-

Tableau AIV-4 - Liste des travaux réalisés sur différents échantillons de Shea Creek.

Echantillons	Sue1	Sue2	Sue3	Sue5	Sue9	Sue4	Sue6	Sue7
Photo	✓	✓	✓	✓	✓	✓	✓	✓
Lames minces	1	1	1	0	1	1	1	1
Analyse d'image	✓	✓	✓	-	✓	-	-	✓
DRX	✓	✓	✓	✓	✓	✓	✓	✓
Microsonde argiles	✓	-	✓	-	✓	-	✓	✓
Microsonde zircons	-	-	-	-	-	✓	-	-
MET	✓	-	-	✓	✓	✓	-	✓
Raman	✓	-	-	-	-	-	-	✓
Densités	✓	✓	✓	✓	✓	✓	✓	✓
Géochimie	✓	✓	✓	✓	✓	✓	✓	✓

Tableau AIV-5 - Liste des travaux réalisés sur les différents échantillons de Sue.

Echantillon	Maw1	Maw2	Maw3	Maw4	Maw5	Maw6	Maw7	Maw8	Maw9	Maw10	Maw11
Forage	Affleur.	Affleur.	Affleur.	Affleur.	Affleur.	Affleur.	84-4	84-4	84-4	ZWR3	ZQ 15
Profondeur	0	0	0	0	0	0	8	8,2	44,2	267,5	222
Photo.	✓	✓	✓	✓	✓	✓	✓	✓	✓	✓	✓
Lames minces	1	1	1	1	1	1	1	1	1	0	1
MEB	-	✓	-	-	-	-	✓	-	-	-	-
Densités	✓	✓	✓	✓	✓	✓	✓	✓	✓	-	✓
Géochimie	✓	-	✓	-	✓	-	✓	✓	✓	-	-

Tableau AIV-6 - Liste des travaux réalisés sur les différents échantillons de la Maw Zone.

II: Description et classification des brèches de Shea Creek réalisée sur le terrain

Breccia type		Quartz	Microcryst. quartz	Microcryst. quartz	Microcryst. quartz	Microcryst. quartz	Microcryst. quartz
Drill hole		Dgs10	Dgs11	She51	Dgs10	Dgs10	Dgs11
Depth		596.6	612	715.9	595	604.9	663.7
Sample			Shea2	Shea9			
Fragments	Orientation	no	locally	no	yes (steep dip)	very locally	yes
	Variety	homolithologic	homolithologic	homolithologic	homolithologic	homolithologic	homolithologic
	Shape	Sphericity = 0.6 to 0.8	Elongated where oriented	High sphericity	Elongated	Sph = 0.6 to 0.7	Sph = 0.6
	Roundness	Mostly rounded to angular	Mostly angular to sub-rounded	Sub-angular to sub-rounded	Angular	Angular	Angular
	Alteration	Thin white rim?	Few	Euhedral quartz rim	Silicified	Silicified	Silicified
	Particle Size Distribution	Normal	Log-normal? from 1 to 40 mm	Normal-from 3mm to 7 cm	Sub-normal (1mm to 3cm)	Log-normal (1mm to 2cm)	Log-normal? (1mm to 5cm)
	Rotation	60°	Not obvious	Not obvious	No	Not obvious	Not obvious
Matrix	Organization	No	No	No	No	No	No
	Nature	Druzy quartz	Aphanitic silica	Microcryst. quartz	Microcryst. quartz	Microcryst. quartz	Microcryst. quartz
	Percentage	5	10 to 50	50	10	60	40
Chronology		-	-	Microcryst. qtz post euhedral qtz	-	-	-
Texture		-	-	-	Jigsaw	-	Jigsaw
Contacts		upper: fracture lower: ?	-	-	upper and lower: plane (fracture)	-	-
Genesis		Hydraulic and beginning of corrosion	Tectonic-hydraulic	Hydraulic	Hydraulic	Hydraulic	Hydraulic

Breccia type		Microcryst. quartz	Microcryst. quartz	Microcryst. quartz	Microcryst. quartz	Chlorite	Chlorite
Drill hole		She51	Dgs11	She47	She4	She16	She80
Depth		716.8	607	718.4	715.6	710,6-711,1	711,05-711,15
Sample						Shea16	Shea23
Fragments	Orientation	No	Yes	Yes	Yes	Yes	No
	Variety	homolithologic	homolithologic	homolithologic	homolithologic	homolithologic (but variable chloritization)	homolithologic
	Shape	Sphericity = 0.7	Sph = 0.5 to 0.6	Sph = 0.6 to 0.7	Sph = 0.7	Sph = 0.6 to 0.7	Elongated
	Roundness	Sub-angular	Angular	Angular	Angular	Sub-rounded	Sub-rounded
	Alteration			Silicified	Silicified	Chlorite	Silicified and hematized
	Particle Size Distribution	Normal (few mm to 2cm)	Sub-normal (1mm to 3cm)	Log-normal probable (1mm to 2cm)	Sub-normal (1mm to 1.5cm)	Normal (1 to 4 cm)	?
	Rotation	Not obvious	No	Not obvious	Not obvious	Not obvious	Not obvious
Matrix	Organization	No	No	Zones of desilicification	Chloritized areas	No	No
	Nature	Microcryst. quartz	Microcryst. quartz	Microcryst. quartz (+local whitish clay)	Microcryst. quartz	Detrital quartz + chlorite	Detrital quartz + chlorite
	Percentage	50	25	65	70	30 - 35	40
Chronology							Chlorite post-quartz + hematite
Texture			Jigsaw	Local jigsaw	Local jigsaw		
Contacts			Upper and lower: fracture	Upper and lower: fracture			
Genesis		Hydraulic	Hydraulic	Hydraulic	Hydraulic	Dissolution after fracturing (locally collapse ?)	Dissolution

Tableau AIV-7 - Classification des brèches de Shea Creek à partir de l'analyse des textures et de la nature des ciments. Microcryst.=Microcrystalline.

Breccia type		Chlorite	Chlorite	Chlorite	Chlorite	Chlorite	Chlorite
Drill hole		Dgs9	Dgs10	She98	She94-2	She96-1	She94-6
Depth		704.3	658.8	704.2 - 704.5	715.6	703	793.5
Sample		-	-	-	-	-	-
Fragments	Orientation	No	No	Yes (locally)	No	Locally	No
	Variety	homolithologic	homolithologic	homolithologic	homolithologic	homolithologic	Heterolithic
	Shape	Sphericity = 0.6 to 07	Sph = 0.6 to 0.8	Sph = 0.4 to 0.6	Sph = 0.6 to 0.7	Sph = 0.6 to 0.7	Mainly sph = 0.7s and locally sph = 0.4
	Roundness	Angular	Sub-angular	Sub-angular	Rounded	Sub-angular (visible cusps)	Angular
	Alteration	Silicified and chloritized	Silicified and chloritized	Silicified	Silicified	Silicified and chloritized on the rim	Silicified and ± chloritized
	Particle Size Distribution	Normal (2mm to 3cm)	Log-normal ? (5mm to 5 cm)	Normal ? (2mm to 8cm)	? (5mm to 5cm)	Normal (5mm to 4cm)	? (3mm to 4cm)
	Rotation	Probable	Yes	No	Not obvious	Not obvious	Yes
Matrix	Organization	No	No	No	Layering in the lower part	No	No
	Nature	Detrital quartz + chlorite	Detrital quartz + chlorite	Detrital quartz + chlorite	Detrital quartz + chlorite	Detrital quartz + chlorite	Detrital quartz + chlorite
	Percentage	35	40	20	60	35	65
Chronology		-	-	-	Chlorite post-silicification	Chlorite post-silicification	Breccia post-euhedral quartz
Texture				Jigsaw	-	Local jigsaw	-
Contacts		-	-	-	-	Upper: fracture, lower: ?	Upper : ?, lower: fracture
Genesis		Dissolution-collapse	Dissolution	Dissolution	Dissolution	Dissolution	Dissolution-collapse

Breccia type		Chlorite	Chlorite	Chlorite	Chlorite	Chlorite	Chlorite
Drill hole		She4	She4	She62	She62	Dgs9	Dgs11
Depth		689-689.1	690.5	716	718.9	704.1	690.6
Sample		-	-	Shea7	Shea28	Shea11	Shea21
Fragments	Orientation	No	No	No	No	No	No
	Variety	homolithologic	homolithologic	-	-	Heterolithic	homolithologic
	Shape	Sph = 0.6 to 0.7	Sph = 0.6	-	-	Sph = 0.7	Elongated
	Roundness	Angular	Rounded	-	-	Rounded	Rounded
	Alteration	Silicified	Silicified	-	Silicified	Silicified and chloritized	-
	Particle Size Distribution	Sub-normal ? (1mm to 2cm)	Normal ? (5mm to 3cm)	-	-	Log-normal ? (4 cm to 3mm)	-
	Rotation	?	?	-	-	Yes	Not obvious
Matrix	Organization	Slight layering	No	No	No	No	No
	Nature	Detrital quartz + little chlorite	Detrital quartz + little chlorite	Detrital quartz + chlorite	Detrital quartz + chlorite	Detrital quartz + chlorite	Detrital quartz + silicification + chlorite
	Percentage	60	30	100	100	20	65
Chronology		-	-	-	Breccia post-silicification	-	Silicification post-chlorite
Texture		-	-	-	-	-	-
Contacts		-	-	-	Upper and lower : fractures	-	Upper : ?, lower : fracture
Genesis		Dissolution	Dissolution	Dissolution	Dissolution	Dissolution	Dissolution

Tableau AIV-8 - Classification des brèches de Shea Creek à partir de l'analyse des textures et de la nature des ciments. Microcryst.=Microcrystalline.

Breccia type		Dravite (+ illite + chlorite)	Dravite - chlorite	Dravite	Dravite	Dravite	Dravite
Drill hole		She66	She74	She4	She94-2	She66	She66
Depth		673.85-674.0	685.5	687.8-688.1	700.8	672.0-672.15	675.45-675.6
Sample		Shea4	-	-	-		Shea10
Fragments	Orientation	No	Yes	No	No	No	Weak
	Variety	Mono	Mono	Mono	Mono	homolithologic	homolithologic
	Shape	Sph = 0.5 to 0.6	Sph = 0.6	Sph = 0.5 to 0.8	Sph = 0.7	Sphericity = 0.6 to 0.8	High sphericity
	Roundness	Angular to sub-angular	Angular	Sub-angular	Sub-rounded	Angular to slightly rounded	Mostly angular to rounded
	Alteration	Silicified and hematized	Chloritized	Silicified	-	No	Hematized but not silicified
	Particle Size Distribution	Sub-normal (5mm to 5 cm)	0.5 to 3 cm	Normal ? (2mm to 10 cm)	? (2cm to 5 cm)	Normal	Normal (3 mm to 5 cm)
	Rotation	Yes	No	Probable	?	No	Very few rotations
Matrix	Organization	Less quartz grains in the bottom part	No	No	No	No	No
	Nature	Detrital quartz + dravite + illite + chlorite	Detrital quartz + clay	Detrital quartz + dravite	Detrital quartz + dravite	Dravite?	Detrital quartz + dravite + chlorite
	Percentage	60	15	60	30	10	50
Chronology		Breccia post microcryst. quartz	Post-chlorite	-	-		Post chlorite
Texture		-	Jigsaw	-	Mature jigsaw	Local jigsaw	Mature jigsaw
Contacts		Upper: fracture, lower: ?	-	-	-		Upper: fracture, lower: ?
Genesis		Dissolution-collapse	Tectonic-hydraulic breccia	Dissolution	Dissolution	Hydraulic	Hydraulic-dissolution

Breccia type		Dravite	Dravite	Calcite	Calcite	Fe-chlorite	Fe-chlorite
Drill hole		She80	She100	She12	She12	She12	She16
Depth		697.3-697.6	714.9-715.1	702.2-702.3	701.0-701.3	698.8	696.6-696.8
Sample		Shea13		Shea22	Shea24	Shea15	Shea3
Fragments	Orientation	No (yes locally)	Locally	No	No	No	No
	Variety	homolithologic	homolithologic	homolithologic	homolithologic	Heterolithic	homolithologic
	Shape	Sph. > 0.65	Sph = 0.55 to 0.7	Sph = 0.5 to 0.7	High sphericity	Sphericity = 0.7	Sph = 0.5 to 0.8
	Roundness	Sub-rounded	Sub-angular	Sub-angular	Sub-angular	Angular and rounded with large re-entrant	Angular to sub-angular
	Alteration	No	Silicified	Silicified	Silicified	Variable	More or less silicified
	Particle Size Distribution	Log-normal (3mm to 15 cm)	Log-normal ? (1mm to 6cm)	Log-normal (3mm to 8 cm)	?	Log-normal	Normal (1mm to 8 cm)
	Rotation	Probable	Not obvious	Yes	Very probable	Yes	Yes
Matrix	Organization	No	No	No	No	No	No
	Nature	Detrital quartz + dravite	Detrital quartz + dravite	Calcite	Detrital quartz + Fe-chlorite ? + calcite	Fe-chlorite +sulfides+carbonates+detrital quartz + kaolinite	Detrital quartz + siderite + Fe-chlorite + kaolinite + sulfides
	Percentage	10 - 30	20	35 - 40	40	60	20
Chronology		Post-microscryst. quartz	-	Post-silicification	Post-silicification	-	Post-silicification
Texture		-	Local jigsaw	Local jigsaw	-	-	-
Contacts		-	Upper: fracture, lower: ?	-	?	Upper: fracture lower: ?	-
Genesis		Dissolution-collapse	Hydraulic-dissolution	Hydraulic-dissolution-collapse	Dissolution	Hydraulic-dissolution	Dissolution-collapse

Tableau AIV-9 - Classification des brèches de Shea Creek à partir de l'analyse des textures et de la nature des ciments. Microcryst.=Microcrystalline.

Breccia type		Fe-chlorite	Fe-chlorite	Fe-chlorite	Fe-chlorite	Fe-chlorite	Fe-chlorite
Drill hole		She79	She16	She82	She79	She79	She79
Depth		708.6-709.2	700.4-700.7	725.4	708.4	706.6-706.9	707.8-708.2
Sample		Shea1				-	-
Fragments	Orientation	No	Yes	No	No	No	No
	Variety	homolithologic	homolithologic	homolithologic	homolithologic	homolithologic	homolithologic
	Shape	Sph = 0.7	Sph = 0.6	Sph = 0.6 to 0.8	Sph = 0.6 to 0.7	Sphericity = 0.6 to 0.8	Sph = 0.6 to 0.7
	Roundness	Corroded (cusps). rounded and angular	Angular	Sub-angular	Angular	Rounded	Angular
	Alteration	Early dissolution	Silicified and chloritized	-	Chloritized	Chloritized	Silicified
	Particle Size Distribution	Normal	Normal (1mm to 3cm)	Normal ? (2mm to 5cm)	Log-normal (1mm to 5cm)	Normal ? (3mm to 6cm)	Sub-normal (2mm to 10cm)
	Rotation	Yes (up to 90°)	No	?	Yes	Yes	Probable
Matrix	Organization	No	No	No	Heterogeneous distribution of detrital quartz	Patches without detrital quartz surrounded by siderite	Patches without detrital quartz containing siderite
	Nature	Fe-chlorite +sulfides+carbonates+detrital quartz + kaolinite	Detrital quartz + siderite + Fe-chlorite + kaolinite	Detrital quartz + Fe-chlorite + kaolinite + siderite	Fe-chlorite + kaolinite + siderite + detrital quartz	Fe-chlorite + kaolinite + siderite + detrital quartz	Fe-chlorite + kaolinite + siderite + detrital quartz
	Percentage	35	25	45	30	20	40
Chronology		Post early dissolution in some areas within fragts	-	-	-	-	-
Texture		-	Jigsaw	-	-	-	-
Contacts		-	-	-	Upper:fracture, Lower: ?	-	-
Genesis		Hydraulic-collapse	Hydraulic-dissolution	Dissolution	Dissolution	Dissolution	Dissolution-collapse

Breccia type		Fe-chlorite	Fe-chlorite	Fe-chlorite	Fe-chlorite	Fe-chlorite	Fe-chlorite
Drill hole		She12	She94-1	She94-1	She94-1	She96-1	She96-1
Depth		698.3-698.5	713.9-714.2	714.2-714.6	715.4-715.6	720.2	727.2-727.4
Sample		-	-	-	-		
Fragments	Orientation	No	No	No	No	Locally	No
	Variety	Heterolithic (variability of chloritization and silicification)	Heterolithic (sulfides. clay. sandstone)	Heterolithic (sulfides. clay. sandstone)	Heterolithic (sulfides. clay. sandstone)	homolithologic	homolithologic
	Shape	Sph = 0.6 to 0.7	Sph = 0.6 to 0.7	Sph = 0.6 to 0.7	Sph = 0.7 to 0.8	Sphericity = 0.6 to 0.7	Sph = 0.6 to 0.7
	Roundness	Angular	Angular to sub-rounded	Sub-angular to sub-rounded	Sub-angular to sub-rounded	Angular	Angular
	Alteration	Silicified or Fe-chloritized	Silicified	Silicified	Silicified	Silicified	Silicified
	Particle Size Distribution	Log-normal? (1mm to 7cm)	Log-normal? (1mm to 9cm)	Log-normal? (1mm to 9cm)	Log-normal? (1mm to 9cm)	Normal (1mm to 3cm)	Log-normal (1mm to 2cm)
	Rotation	Probable	Yes	Yes	Yes	?	Probable
Matrix	Organization	No	Local layering	Local layering	Chlorite rimming fragts	No	No
	Nature	Fe-chlorite + kaolinite (+ siderite)+ detrital quartz	Dark clay (=Fe-chlorite+ kaolinite ?) (+detrital quartz)	Dark clay (=Fe-chlorite+ kaolinite ?) (+detrital quartz)	Dark clay (=Fe-chlorite+ kaolinite ?) (+detrital quartz)	Dark clay (=Fe-chlo +kaol? + detrital quartz)	Dark clay (=Fe-chlo+ kaol? + detrital quartz)
	Percentage	55	65	60	70	40	60
Chronology		-	Post-sulfides, post-pitchblende	Post-sulfides, post-pitchblende	-	Post euhedral quartz	-
Texture		-	-	-	-	Local jigsaw	-
Contacts		-	-	-	-	Upper: fracture lower: ?	-
Genesis		Dissolution-collapse	Dissolution	Dissolution	Dissolution	Hydraulic-dissolution	Dissolution

Tableau AIV-10 - Classification des brèches de Shea Creek à partir de l'analyse des textures et de la nature des ciments. Microcryst.=Microcrystalline.

Breccia type		Fe-chlorite	Fe-chlorite	Fe-chlorite	Fe-chlorite	Fe-chlorite	Siderite
Drill hole		She96-1	She79	She12	She16	She79	She93
Depth		729-729.4	703.8-703.9	706	702.25-702.5	705.6	719.6-719.9
Sample			Shea14	Shea20	Shea12		Shea19
Fragments	Orientation	No	No	No	No	Yes in less mature part	No
	Variety	homolithologic	homolithologic	homolithologic	Heterolithic	Heterolithic	homolithologic
	Shape	Sph = 0.7	?	Sph = 0.6	Few at 0.5 but most are > 0.65	-	Sphericity = 0.7
	Roundness	Angular	Sub-angular to sub-rounded	Variable (angular to sub-rounded)	Angular	Angular with few rounded	Sub-rounded
	Alteration	Silicified	Sulfides	-	Silicified, chloritized	Silicified, chloritized	Chloritized, silicified
	Particle Size Distribution	Log-normal (1mm to 3cm)	?	Log-normal ? (<1mm to 2 cm)	Log-normal (1mm to 1cm)	Sub-normal in mature zones (1mm to 5cm) & >log-normal in immature zones	Normal ? (5mm to 3cm)
	Rotation	Probable	Not obvious	No	Yes	Yes in mature zones	Yes
Matrix	Organization	No detrital quartz in the upper part	Matrix percentage increases toward the top	No	No	Decreases toward the bottom	No
	Nature	Dark clay (=Fe-chlo+ kaol? + detrital quartz)	Detrital quartz + Fe-chlorite + kaolinite + siderite	Detrital quartz + Fe-chlorite + kaolinite	Detrital quartz + dravite + Fe-chlorite + kaolinite	Fe-chlo +sulfides +carbonates +detrital quartz +kaolinite	Detrital quartz +siderite
	Percentage	70	30 - 40	50	75	50 to 5	50
Chronology		-	-	-	Breccia ante-calcite & post-microcryst. quartz breccias	Post silicification, post chlorite, post-sulfide	Hematite post-chlorite; siderite post-chlorite?
Texture		-	-	-	-		
Contacts		-	-	Irregular and progressive	-		
Genesis		Dissolution	Dissolution	Dissolution	Hydraulic-dissolution	Hydraulic-dissolution-collapse	Dissolution and locally hydraulic

Breccia type		Siderite	Siderite	Siderite	Siderite	Siderite	Siderite
Drill hole		She45	She45	She12	She12	She96-1	She45
Depth		711.9	720.2	699.5	701.6	705.5	711.7
Sample							
Fragments	Orientation	No	No	No	No	Locally	No
	Variety	Heterolithic	homolithologic	homolithologic	homolithologic	homolithologic	homolithologic
	Shape	Sph = 0.6 to 0.7	Sph = 0.7 to 0.85	Sph = 0.6 to 0.7	Sph = 0.6 to 0.8	Sph = 0.5 to 0.7	Sph = 0.6 to 0.7
	Roundness	Angular	Angular	Angular	Sub-angular	Angular	Angular
	Alteration	Chloritized	Silicified and chloritized	Silicified	Silicified	Silicified	Silicified
	Particle Size Distribution	Sub-normal ? (5mm to 6cm)	Normal ? (5mm to 2cm)	Normal ? (2mm to 3cm)	Sub-normal? (3mm to 5cm)	Sub-normal (2mm to 3cm)	Sub-normal (1mm to 4cm)
	Rotation	?	?	?	?	Little?	Not obvious
Matrix	Organization	No	Spherulites bigger in areas without fragments	No	No	Pure siderite in the low dilation areas	No
	Nature	Detrital quartz +siderite spherulites	Detrital quartz +siderite spherulites	Detrital quartz +siderite	Detrital quartz +siderite	Detrital quartz + siderite	Detrital quartz +siderite+ hematite
	Percentage	50	60	40	55	20	40
Chronology		Siderite post-chlorite	Siderite +hematite post chlorite	-	-	-	-
Texture		-	-	-	Local jigsaw	Jigsaw	Jigsaw
Contacts		-	-	Upper: ?, lower: fracture	-	Upper and lower: fractures	-
Genesis		Dissolution	Dissolution	Dissolution	Hydraulic-dissolution	Hydraulic-dissolution	Hydraulic-dissolution

Tableau AIV-11 - Classification des brèches de Shea Creek réalisée à partir de l'analyse des textures et de la nature des ciments. Microcryst.=Microcrystalline.

III: Analyses de diffraction aux rayons X

Echantillons	Type de brèche	Micas/ illite, I/S > 90% illite	Chlorite	DI / TRI (# 4.75 Å)	M7-Serpentine	Smectite	Kaolinite/ Halloysite	Tourm.
Shea7	Sudoite	X	XXX	DT	-	-	X ?	-
Shea16	Sudoite	X ?	XXX	T	-	-	-	X
Shea4	Sudoite-illite-dravite	XX	XX	T	-	-	X ?	XX
Shea23	Sudoite	X	XXX	T	-	-	-	X
Shea10	Dravite	X	XX	DT	-	-	-	XX
Shea13	Dravite	X	-	-	X ?	-	X ?	XX
Shea24	Calcite	-	-	-	X ?	-	X ?	X
Shea12	Fe-chlorite	-	-	-	X	X		XX
Shea20	Fe-chlorite	-	-	-	X	-	X ?	X
Shea19	Sidérite-hématite	X	XXX	T	-	-	X ?	X ?
Shea8	-	XX	XXX	DT	-	-		X ?
Shea17	-	X	XXX	T	-	-	X ?	X ?
Shea14	-				-	-		X ?
Shea5	-	XX	X	DT	-	-	X ?	-

Tableau AIV-12 - Tableau de résultats d'analyses de diffraction aux rayons X de la fraction inférieure à 2µm d'échantillons de brèches de Shea Creek.

Abréviations :
XXX : très forte intensité du pic de diffraction, XX : forte intensité du pic de diffraction, X : faible intensité du pic de diffraction, X ? : présence possible mais cachée par les pics d'autres minéraux, ? : traces.
I/S > 90% illite : interstratifié illite/smectite avec plus de 90 % d'illite.
DI/TRI : DT : pic typique de la chlorite di-trioctaédrique (sudoite) ; T : pic typique de la chlorite trioctaédrique.
M7-serpentine : minéraux appartenant au sous-groupe des serpentines (serpentine sensu stricto ou 7Å minerals).
Smectite : smectite ou interstratifié illite/smectite avec plus de 40 % de smectite.
Tourm : tourmaline, essentiellement de la dravite dans ces échantillons de Shea Creek.

Echantillons	Distance « zone à boules »	Quartz	Muscovite	Kaolinite	Smectite	Hématite	Pyrite	Florencite
Sue7 (grès)	> 30	74	5,4	18,2	1	tr	-	-
Sue1 (grès)	4	54	21,8	23,7	tr	tr	-	-
Sue2 (grès)	2	47	49,5	2,2	tr	tr	-	-
Sue3 (grès)	1	45	50,2	3,1	-	0,8	0,4	?
Sue9 (grès)	0	38	62,6	2,1	-	-	-	-
Sue4 (boule)	0	0,4	94,4	2,7	tr	1,4	0,3	1
Sue5 (matrice)	0	tr	98,6	1	tr	0,1	-	?
Sue6 (boule)	0	0,6	95,6	0,6	1	1	-	0,8
Sue8 (boule)	0	-	95	3,9	0,4	0,2	-	0,4

Tableau AIV-13 - Tableau de résultats d'analyses de diffraction aux rayons X d'échantillons de grès et de zones à boules provenant de la Mine à Ciel Ouvert de Sue C. La distance des échantillons par rapport à une zone à boules est indiquée en mètres. Les pourcentages donnés pour le quartz sont très approximatifs.

IV: Analyses chimiques globales ICP-AES et –MS, densités

Echantillons Nature	Sue 7 Grès	Sue 1 Grès	Sue 2 Grès	Sue 3 Grès	Sue 9 Fragment de microconglomérat	Sue 4 Boule d'argile	Sue 5 Matrice argileuse	Sue 6 Boule d'argile	Sue 8 Boule d'argile
Distance (m)	> 30	4	2	1	0	0	0	0	0
Densité	2,44	2,48	2,42	2,44	2,42	1,37	1,32	2,25	-
SiO2 (%)	96,9	95,6	95,4	95,7	95,4	52,5	48,1	43,7	45,0
Al2O3	2,3	3,3	2,7	2,6	2,3	30,6	34,0	33,1	34,9
Fe2O3 (Fe total)	0,2	0,1	< L.D.	0,2	0,1	0,5	0,5	5,4	0,5
MnO	< L.D.	< L.D.	< L.D.	< L.D.	< L.D.	< L.D.	< L.D.	< L.D.	< L.D.
MgO	< L.D.	< L.D.	< L.D.	< L.D.	< L.D.	1,3	1,0	0,6	0,7
CaO	< L.D.	< L.D.	< L.D.	< L.D.	< L.D.	0,2	0,2	0,2	0,3
Na2O	< L.D.	< L.D.	< L.D.	< L.D.	< L.D.	< L.D.	< L.D.	< L.D.	< L.D.
K2O	< L.D.	0,40	0,68	0,63	0,56	8,89	9,57	9,32	9,31
TiO2	< L.D.	0,09	0,10	0,12	0,34	0,93	0,50	2,68	2,02
P2O5	0,05	0,05	< L.D.	< L.D.	0,06	0,24	0,46	0,3	0,73
PF	0,81	0,88	0,46	0,51	0,46	5,02	5,95	5,14	6,23
Total	*100,2*	*100,4*	*99,3*	*99,7*	*99,2*	*100,2*	*100,2*	*100,4*	*99,7*
CO2 tot	0,05	0,04	0,03	0,05	0,05	0,05	0,12	0,11	0,11
C org	< L.D.	< L.D.	< L.D.	< L.D.	< L.D.	< L.D.	0,02	0,02	0,03
S	0,01	< L.D.	< L.D.	< L.D.	< L.D.	0,021	0,056	0,031	0,078
FeO	0,03	0,04	0,1	0,09	< L.D.	< L.D.	< L.D.	< L.D.	0,07
As (ppm)	4,7	2,1	2,4	3,2	6,5	35,2	53,2	87,7	225,0
B	3	37	58	63	64	650	775	910	840
Ba	16	12	12	12	29	158	190	129	367
Be	< L.D.	< L.D.	< L.D.	< L.D.	< L.D.	3,1	5,0	4,5	7,3
Bi	< L.D.	0,22	0,11	0,23	0,45	4,21	19,76	2,31	7,87
Cd	< L.D.	< L.D.	< L.D.	< L.D.	< L.D.	0,5	< L.D.	1,1	0,5
Co	0,6	< L.D.	< L.D.	< L.D.	< L.D.	0,9	1,5	3,2	2,8
Cr	< L.D.	6	< L.D.	6	9	68	86	92	72
Cs	< L.D.	< L.D.	< L.D.	< L.D.	< L.D.	0,6	0,4	0,6	0,3
Cu	< L.D.	< L.D.	< L.D.	5	< L.D.	14	15	10	21
Ga	2,8	5,6	6,8	7,7	8,4	100,3	141,1	116,8	132,3
Ge	0,8	0,9	0,8	0,9	1,1	1,1	1,3	1,1	1,6
Hf	1,51	4,60	4,66	5,39	13,02	55,32	17,61	114,52	39,92
In	< L.D.	< L.D.	< L.D.	< L.D.	< L.D.	< L.D.	< L.D.	< L.D.	< L.D.
La	15,58	11,15	10,07	12,10	31,99	163,56	271,45	178,40	511,00
Ce	36,23	24,17	21,50	26,36	60,77	325,81	530,63	356,38	1147,00
Pr	3,35	2,33	2,10	2,65	6,61	35,30	58,33	36,69	113,02
Nd	11,7	8,4	7,2	8,8	22,6	126,0	205,6	125,8	408,1
Sm	2,04	1,42	1,31	1,59	3,75	22,20	34,23	21,54	61,89
Eu	0,30	0,24	0,24	0,25	0,55	3,57	4,70	3,49	8,26
Gd	1,2	1,2	1,1	1,2	2,9	19,4	24,7	16,2	48,2
Tb	0,19	0,16	0,14	0,18	0,42	3,43	2,71	2,41	7,18
Dy	0,79	0,88	0,82	1,04	2,32	20,08	10,29	14,01	34,20
Ho	0,14	0,17	0,16	0,20	0,40	3,50	1,35	2,79	5,71
Er	0,35	0,50	0,50	0,54	1,14	9,24	3,67	8,89	15,31
Tm	0,04	0,08	0,09	0,09	0,18	1,32	0,42	1,61	2,04
Yb	0,32	0,52	0,58	0,63	1,33	9,00	3,04	12,72	12,37
Lu	0,05	0,08	0,09	0,11	0,22	1,39	0,43	2,12	1,85
Mo	0,2	0,2	0,3	0,2	2,5	1,3	1,5	3,3	3,2
Nb	1,0	2,5	2,4	2,8	9,8	27,7	19,1	73,5	57,9
Ni	15	< L.D.	< L.D.	< L.D.	< L.D.	< L.D.	< L.D.	< L.D.	< L.D.
Pb	9,6	9,8	9,0	11,7	19,7	122,6	133,6	163,3	560,6
Rb	1	5	7	7	7	96	90	88	87
Sb	< L.D.	< L.D.	< L.D.	0,1	0,2	1,1	0,9	1,9	1,3
Sn	< L.D.	< L.D.	< L.D.	< L.D.	0,8	3,7	2,0	3,1	1,6
Sr	209	56	49	58	168	985	2610	1250	3951
Ta	0,11	0,31	0,26	0,30	1,13	3,26	1,70	9,43	6,99
Th	5,2	5,8	5,3	8,1	37,6	71,8	108,7	169,7	317,2
U	1,6	2,8	2,1	3,1	22,2	36,3	29,9	89,8	40,1
V	3	16	18	34	68	1007	1519	1217	781
W	0,2	1,2	1,3	1,5	5,2	20,7	20,8	25,1	8,8
Y	3,61	4,97	5,29	6,03	11,70	107,18	37,73	69,59	155,25
Zn	< L.D.	< L.D.	< L.D.	< L.D.	5	39	77	77	77
Zr	61,8	198,5	208,8	225,3	534,3	2121,0	725,1	5496,0	1461,0

Tableau AIV-14 - Compositions en éléments majeurs (% massique d'oxydes) et en traces (en ppm) des grès et des argiles des « zones à boules » de la Mine à Ciel Ouvert de Sue C. La distance est celle qui sépare l'échantillon d'une « zone à boules ».

Echantillons Forage- profondeur Lithologie ou type de brèche	8956-3 Erc1- 162,6 grès	8956-5 Erc1- 303,2 grès	MC98-3 Erc1-793 grès	Shea2 Dgs11-611,8 Microcryst. quartz	Shea7 She62- 716 Sudoite-dravite	Shea28 Shea62- 718,9 Sudoite-dravite	Shea11 Dgs9- 704,1 Sudoite-dravite	Shea21 Dgs11- 690,6 Sudoite-dravite	Shea16 She16-711 Sudoite-dravite	Shea10 She66- 675,5 Dravite
Densité	2,54	2,54	2,41	2,44	-	2,29	2,52	2,45	2,35	2,42
SiO2 (%)	98,7	96,7	97,0	99,0	89,4	88,6	93,6	95,5	97,4	92,5
Al2O3	0,4	0,4	0,4	0,4	5,4	4,6	1,0	1,4	1,0	3,9
Fe2O3 (Fe total)	0,2	1,9	1,9	<L.D.	0,4	0,9	0,2	0,3	0,3	0,6
MnO	<L.D.	<L.D.	<L.D.	<L.D.	<L.D.	<L.D.	<L.D.	<L.D.	<L.D.	<L.D.
MgO	<L.D.	<L.D.	<L.D.	<L.D.	1,0	1,5	0,5	0,9	0,4	1,1
CaO	<L.D.	<L.D.	<L.D.	<L.D.	<L.D.	<L.D.	<L.D.	<L.D.	<L.D.	<L.D.
Na2O	<L.D.	<L.D.	<L.D.	<L.D.	<L.D.	<L.D.	<L.D.	<L.D.	<L.D.	0,05
K2O	0,09	<L.D.	<L.D.	<L.D.	0,13	0,05	<L.D.	<L.D.	<L.D.	<L.D.
TiO2	<L.D.	<L.D.	0,22	<L.D.	1,30	0,95	1,46	0,22	0,05	0,19
P2O5	0,06	0,07	<L.D.	<L.D.	0,16	0,11	0,10	<L.D.	<L.D.	0,05
PF	0,21	0,53	0,38	0,68	2,04	2,06	3,32	0,70	0,68	1,40
Total	*99,61*	*99,65*	*99,87*	*100,09*	*99,85*	*98,77*	*100,15*	*98,97*	*99,81*	*99,87*
CO2 tot	0,06	0,39	0,04	0,8	0,17	0,07	6,63	0,05	0,07	0,1
C org	0,02	0,02	-	-	0,01	0,01	-	<L.D.	<L.D.	0,02
S	<L.D.	0,01	0,01	<L.D.	0,06	0,12	0,015	<L.D.	0,046	0,015
FeO	<L.D.	0,56	0,05	0,03	0,06	0,31	0,15	0,19	0,14	0,18
As (ppm)	1,0	0,8	<L.D.	<L.D.	4,3	17,2	1,2	<L.D.	11,1	0,7
B	14	9	28	87	295	255	64	130	285	1495
Ba	17	12	7	<L.D.	21	11	9	<L.D.	<L.D.	6
Be	<L.D.	<L.D.	<L.D.	<L.D.	1,3	1,7	<L.D.	<L.D.	<L.D.	1,3
Bi	<L.D.	<L.D.	<L.D.	0,24	0,85	0,36	0,07	<L.D.	4,33	0,08
Cd	<L.D.	<L.D.	<L.D.	<L.D.	<L.D.	0,4	<L.D.	<L.D.	0,5	<L.D.
Co	<L.D.	<L.D.	<L.D.	<L.D.	1,0	3,4	0,7	2,5	70,5	1,6
Cr	<L.D.	8	9	<L.D.	31	25	22	12	11	19
Cs	<L.D.	<L.D.	<L.D.	<L.D.	<L.D.	<L.D.	<L.D.	<L.D.	<L.D.	<L.D.
Cu	<L.D.	<L.D.	<L.D.	<L.D.	18	26	11	8	147	7
Ga	0,6	0,9	1,1	0,8	8,4	7,3	2,0	2,7	2,9	8,1
Ge	0,66	0,65	0,63	0,71	1,11	1,05	0,84	0,81	1,02	1,71
Hf	0,89	1,89	4,13	1,18	25,23	21,37	24,21	11,74	3,23	8,88
In	<L.D.	<L.D.	<L.D.	<L.D.	<L.D.	<L.D.	<L.D.	<L.D.	0,1	<L.D.
La	8,63	12,65	9,5	10,56	129,75	73,16	66,83	7,11	6,16	22,42
Ce	18,17	27,94	21,80	21,82	247,36	141,30	124,70	13,71	11,39	46,82
Pr	1,98	2,84	2,20	2,46	27,38	14,87	13,29	1,49	1,19	5,17
Nd	7,3	9,4	9,0	8,8	90,7	53,0	43,5	4,9	4,1	17,8
Sm	1,25	1,59	1,53	0,96	12,53	7,56	4,51	0,88	0,81	2,72
Eu	0,20	0,27	0,16	0,09	1,60	0,91	0,51	0,12	0,18	0,42
Gd	0,88	1,36	1,07	0,33	6,96	3,89	1,94	0,71	1,68	2,38
Tb	0,12	0,16	0,15	0,05	1,25	0,59	0,26	0,16	0,39	0,51
Dy	0,52	0,74	0,94	0,30	6,95	3,32	1,41	1,15	2,77	3,57
Ho	0,08	0,12	0,18	0,05	1,24	0,60	0,22	0,24	0,57	0,74
Er	0,26	0,34	0,39	0,15	3,30	1,70	0,75	0,61	1,34	1,68
Tm	0,03	0,05	0,07	0,03	0,42	0,23	0,12	0,11	0,19	0,24
Yb	0,26	0,33	0,56	0,19	2,75	1,58	0,85	0,84	1,06	1,47
Lu	0,04	0,05	0,08	0,03	0,40	0,27	0,16	0,15	0,16	0,22
Mo	<L.D.	0,2	0,2	<L.D.	0,3	0,8	0,2	0,4	0,8	0,5
Nb	0,6	0,6	3,1	0,3	18,1	13,0	18,7	3,5	1,0	3,3
Ni	<L.D.	<L.D.	<L.D.	<L.D.	37	93	10	17	585	20
Pb	3,0	4,0	1,5	4,1	19,3	17,7	8,0	8,0	8,7	7,7
Rb	1,5	<L.D.	1,6	<L.D.	2,3	1,2	<L.D.	<L.D.	<L.D.	<L.D.
Sb	0,7	0,1	0,7	<L.D.	0,3	0,9	0,2	0,2	1,3	0,7
Sn	<L.D.	<L.D.	0,4	<L.D.	2,0	1,6	0,6	0,7	<L.D.	1,1
Sr	84	133	48	17	335	197	157	17	17	57
Ta	0,06	0,07	0,39	0,04	2,40	1,73	2,28	0,37	0,11	0,44
Th	1,88	2,80	10,4	1,62	75,03	47,91	80,69	5,38	2,55	15,91
U	0,5	0,7	1,0	2,8	28,6	31,3	18,7	16,3	9,7	47,5
V	2	4	12	<L.D.	53	49	19	22	72	31
W	0,1	0,2	0,2	<L.D.	6,2	4,1	2,1	2,1	0,4	0,5
Y	2,17	3,13	5,58	1,43	39,19	19,96	6,54	7,16	17,50	21,83
Zn	<L.D.	<L.D.	<L.D.	<L.D.	29	27	14	15	88	6
Zr	32,5	70,8	174,6	43,0	987,0	868,0	998,0	469,0	112,0	348,3

Tableau AIV-15 - Compositions en éléments majeurs (% massique d'oxydes) et en traces (en ppm) des grès de référence de l'Ouest Athabasca et des brèches de Shea Creek.

Echantillons	Shea13	Shea22	Shea24	Shea12	Shea15	Shea1	Shea3	Shea20	Shea19	Shea8
Forage-profondeur	She80-697,6	She12-702,3	She12-701,3	She16-702,5	She12-698,8	She79-709,1	She16-696,8	She12-706	She93-719,9	Dgs14-701,5
Lithologie ou type de brèche	Dravite	Calcite	Calcite	Fe-chlorite	Fe-chlorite	Fe-chlorite	Fe-chlorite	Fe-chlorite	Sidérite-hématite	Chlor., tecto., Carswell ?
Densité	2,37	2,65	2,65	2,32	2,54	2,41	2,56	2,55	3,03	2,48
SiO2 (%)	97,1	77,7	78,2	84,3	85,4	87,7	76,5	88,5	57,9	55,6
Al2O3	0,9	0,8	0,7	4,0	2,8	1,2	1,2	3,6	1,9	21,2
Fe2O3 (Fe total)	0,1	1,0	1,5	7,1	6,1	6,3	11,9	4,5	27,5	2,4
MnO	<L.D.	0,29	0,30	<L.D.	0,18	0,15	0,48	<L.D.	0,07	<L.D.
MgO	0,2	0,3	0,3	1,0	0,8	0,7	1,3	0,7	0,4	8,5
CaO	<L.D.	10,6	10,2	0,2	0,4	0,1	0,9	0,1	<L.D.	0,2
Na2O	<L.D.	<L.D.	<L.D.	0,05	<L.D.	<L.D.	<L.D.	0,06	<L.D.	<L.D.
K2O	<L.D.	<L.D.	<L.D.	<L.D.	0,07	<L.D.	<L.D.	<L.D.	<L.D.	2,03
TiO2	0,05	0,09	0,07	0,22	0,23	0,09	0,05	0,40	0,38	2,35
P2O5	<L.D.	0,14	0,12	0,10	0,05	0,06	0,24	0,09	<L.D.	0,24
PF	0,47	8,35	8,05	3,26	3,70	3,53	7,42	2,17	11,56	7,36
Total	*98,76*	*99,25*	*99,40*	*100,16*	*99,78*	*99,78*	*99,93*	*100,07*	*99,81*	*99,93*
CO2 tot	0,17	7,99	7,55	0,44	2,61	3,05	7,72	0,19	11,92	0,09
C org	0,05	0,01	0,02	0,08	0,16	0,19	0,33	0,05	0,05	0,02
S	<L.D.	0,29	0,62	0,18	0,033	0,18	0,37	0,37	0,011	0,016
FeO	0,1	0,36	0,43	2,01	3,91	4,01	8,59	1,82	20,96	0,82
As (ppm)	4,1	90,5	76,6	35,0	24,4	96,4	603,8	46,1	1,3	4,2
B	450	280	215	1320	600	160	155	1435	150	365
Ba	<L.D.	11	10	16	7	9	26	25	8	28
Be	<L.D.	<L.D.	<L.D.	2,1	<L.D.	<L.D.	1,1	2,7	1,2	2,7
Bi	0,18	48,39	16,88	63,79	5,08	38,27	164,24	3,35	3,58	0,29
Cd	<L.D.	<L.D.	<L.D.	<L.D.	<L.D.	<L.D.	<L.D.	<L.D.	<L.D.	0,3
Co	0,6	0,9	0,3	137,8	0,4	38,6	236,4	5,5	0,4	5,5
Cr	9	18	16	47	19	13	22	23	17	52
Cs	<L.D.	<L.D.	<L.D.	<L.D.	<L.D.	<L.D.	<L.D.	<L.D.	<L.D.	0,6
Cu	25	24	19	138	8	68	377	57	8	12
Ga	2,0	2,2	1,8	8,0	4,6	2,5	4,1	6,6	3,5	34,2
Ge	0,85	0,70	0,68	1,59	1,01	0,89	0,78	1,51	0,86	1,39
Hf	2,84	3,21	2,74	8,85	6,18	3,74	3,34	7,99	11,94	35,38
In	<L.D.	<L.D.	<L.D.	0,8	<L.D.	0,3	1,9	<L.D.	<L.D.	<L.D.
La	5,18	31,97	25,69	38,23	30,81	21,95	90,95	19,34	22,81	298,20
Ce	9,98	71,33	55,78	75,01	62,73	49,98	191,50	54,98	44,80	561,78
Pr	1,05	7,78	6,15	7,82	7,24	6,20	20,05	8,15	4,93	63,68
Nd	4,2	29,0	22,7	27,0	27,0	24,7	68,3	31,0	17,2	215,1
Sm	0,64	4,50	3,21	4,70	3,95	3,65	8,18	7,06	3,14	26,89
Eu	0,10	0,76	0,58	1,04	0,66	0,63	1,30	1,45	0,48	3,22
Gd	0,66	4,04	4,10	4,86	3,91	2,52	3,89	3,71	3,31	14,13
Tb	0,14	0,97	1,06	0,92	0,94	0,41	0,55	0,68	0,68	2,20
Dy	0,87	6,59	6,95	5,68	5,96	2,27	1,97	3,43	4,49	11,41
Ho	0,19	1,23	1,24	1,05	1,11	0,40	0,27	0,55	0,85	1,94
Er	0,47	2,72	2,75	2,58	2,74	1,01	0,81	1,41	2,13	5,52
Tm	0,07	0,32	0,32	0,38	0,41	0,15	0,09	0,20	0,31	0,76
Yb	0,42	1,72	1,66	1,99	2,08	0,85	0,53	1,36	1,93	4,66
Lu	0,06	0,23	0,22	0,28	0,29	0,11	0,08	0,17	0,31	0,74
Mo	0,3	11,0	6,9	1,6	0,9	0,8	2,0	1,3	1,6	1,0
Nb	0,9	1,6	1,2	3,6	3,9	1,8	1,1	6,0	5,6	36,4
Ni	6	9	<L.D.	224	5	139	208	46	11	91
Pb	4,0	71,7	62,8	108,8	27,7	38,6	161,1	52,0	10,5	10,1
Rb	<L.D.	<L.D.	<L.D.	<L.D.	<L.D.	<L.D.	<L.D.	<L.D.	<L.D.	32,0
Sb	0,1	1,3	1,0	1,2	0,3	4,4	2,6	3,0	0,5	0,5
Sn	<L.D.	<L.D.	<L.D.	<L.D.	<L.D.	0,8	<L.D.	<L.D.	0,8	2,3
Sr	17	468	378	306	118	104	966	153	78	476
Ta	0,10	0,17	0,14	0,32	0,44	0,19	0,11	0,71	0,58	3,39
Th	2,54	4,93	4,02	8,07	11,19	6,13	3,96	15,25	14,92	105,49
U	16,5	27,0	25,6	175,0	25,4	987,0	226,0	383,0	31,0	79,9
V	41	39	26	222	58	82	45	93	48	152
W	0,2	0,9	0,7	3,6	1,7	1,2	0,8	3,4	2,0	7,4
Y	6,49	38,79	39,27	30,09	35,78	11,46	7,07	15,04	27,96	59,88
Zn	5	8	8	6	7	7	11	9	9	26
Zr	110,8	126,4	99,1	328,4	238,3	138,4	130,5	282,6	456,1	1363,0

Tableau AIV-16 - Compositions en éléments majeurs (% massique d'oxydes) et en traces (en ppm) des brèches de Shea Creek.

Echantillons Forage-profondeur Lithologie ou type de brèche	Maw1(~protolith) outcrop Dravite	Maw5 outcrop Dravite	Maw3 outcrop Dravite	Maw7 84-4 - 8 Dravite	Maw8 84-4 – 8,2 Dravite	Maw9 84-4 – 44,2 Dravite + quartz
Densité	2,62	2,62	2,62	2,59	2,58	2,61
SiO2 (%)	98,9	99,1	98,2	96,1	98,7	94,5
Al2O3	0,5	0,6	1,0	1,9	0,8	3,1
Fe2O3 (Fe total)	< L.D.	< L.D.	< L.D.	0,11	< L.D.	0,1
MnO	< L.D.	< L.D.	< L.D.	< L.D.	< L.D.	< L.D.
MgO	< L.D.	< L.D.	0,2	0,4	0,1	0,6
CaO	< L.D.	< L.D.	< L.D.	< L.D.	< L.D.	< L.D.
Na2O	< L.D.	< L.D.	< L.D.	< L.D.	< L.D.	0,05
K2O	< L.D.	< L.D.	< L.D.	< L.D.	< L.D.	< L.D.
TiO2	< L.D.	< L.D.	< L.D.	< L.D.	< L.D.	< L.D.
P2O5	< L.D.	< L.D.	< L.D.	< L.D.	< L.D.	0,05
PF	0,21	0,29	0,29	0,48	0,29	0,77
Total	*99,6*	*100,0*	*99,7*	*99,0*	*99,9*	*99,2*
CO2 tot	0.05	0.04	0.04	0.05	0.06	0.06
C org	0.02	0.01	0.01	0.01	0.01	0.02
S	< L.D.	< L.D.	< L.D.	< L.D.	< L.D.	< L.D.
FeO	< L.D.	< L.D.	< L.D.	< L.D.	< L.D.	< L.D.
As (ppm)	0,6	0,6	0,7	0,7	< L.D.	0,7
B	220	240	545	1030	250	2130
Ba	7	9	6	8	11	7
Be	< L.D.	< L.D.	< L.D.	1	< L.D.	2
Bi	< L.D.	0,49	< L.D.	0,12	< L.D.	0,06
Cd	< L.D.	< L.D.	< L.D.	< L.D.	< L.D.	< L.D.
Co	< L.D.	< L.D.	< L.D.	< L.D.	< L.D.	0,4
Cr	25	9	326	34	24	43
Cs	< L.D.	< L.D.	< L.D.	< L.D.	< L.D.	< L.D.
Cu	< L.D.	< L.D.	< L.D.	6	6	8
Ga	1,4	1,2	3,1	5,1	1,7	7,3
Ge	0,8	0,6	0,9	1,5	0,7	1,5
Hf	3,51	2,00	0,92	2,73	1,56	1,35
In	< L.D.	< L.D.	< L.D.	< L.D.	< L.D.	< L.D.
La	7,16	7,39	8,67	6,51	5,72	5,06
Ce	14,30	14,27	17,48	13,73	10,92	10,02
Pr	1,41	1,43	1,67	1,33	1,12	1,08
Nd	5,0	4,5	5,5	4,1	3,8	3,7
Sm	0,7	0,7	0,7	0,7	0,5	0,7
Eu	0,13	0,16	0,12	0,11	0,07	0,25
Gd	0,5	0,7	0,5	0,5	0,5	2,5
Tb	0,11	0,13	0,08	0,13	0,09	1,00
Dy	0,63	0,79	0,42	0,80	0,53	7,32
Ho	0,13	0,14	0,08	0,15	0,09	1,42
Er	0,32	0,36	0,22	0,37	0,27	3,19
Tm	0,05	0,06	0,04	0,06	0,04	0,39
Yb	0,35	0,41	0,25	0,38	0,27	2,33
Lu	0,06	0,06	0,04	0,07	0,05	0,30
Mo	< L.D.	0,2	< L.D.	< L.D.	< L.D.	< L.D.
Nb	0,8	0,8	0,4	0,8	0,5	0,4
Ni	< L.D.	< L.D.	< L.D.	< L.D.	< L.D.	< L.D.
Pb	1,7	2,0	1,2	1,8	1,5	1,8
Rb	< L.D.	< L.D.	< L.D.	< L.D.	< L.D.	< L.D.
Sb	< L.D.	< L.D.	< L.D.	< L.D.	< L.D.	< L.D.
Sn	< L.D.	< L.D.	< L.D.	< L.D.	< L.D.	< L.D.
Sr	21	21	28	22	14	20
Ta	0,08	0,08	0,04	0,07	0,06	0,04
Th	2,3	2,1	1,6	3,2	1,5	1,8
U	1,7	1,3	0,6	1,9	1,3	2,9
V	10	14	20	33	14	54
W	0,6	0,2	< L.D.	0,1	< L.D.	0,2
Y	3,62	4,64	2,54	4,89	3,05	48,10
Zn	< L.D.	< L.D.	< L.D.	5	< L.D.	5
Zr	135,2	77,4	34,1	113,0	57,7	53,2

Tableau AIV-17 - Compositions en éléments majeurs (% massique d'oxydes) et en traces (en ppm) de grès et de brèches de la zone de Maw.

V: Analyses chimiques ponctuelles à la microsonde électronique

Les compositions des minéraux suivants sont détaillées :

- les chlorites,
- la kaolinite riche en Fe,
- les illites
- les uraninites et pechblendes,
- la coffinite.

Echantillons forage-profondeur	SHEA10 she66-675,5	SHEA7 she62-716	SHEA7 she62-716	SHEA7 she62-716	SHEA10 she66-675,5	SHEA16 she16-711	SHEA16 she16-711	SHEA19 she93-719,9	SHEA19 she93-719,9	SHEA19 she93-719,9	SHEA19 she93-719,9	SHEA19 she93-719,9	SHEA3C she16-696,8
Numéro d'analyse	1_1	3_1	3_2	3_3	1_2	3	2	1_2	1_1	1_4	4_1	4_2	2_2
Minéral	sudoite stade1	sudoite stade1	sudoite stade1	sudoite stade1	sudoite stade1	sudoite stade1	sudoite stade1	sudoite stade5	sudoite stade5	sudoite stade5	sudoite stade5	sudoite stade5	Fe-chlorite3
Na2O	n.d.	n.d.	0,128	n.d.	n.d.	0,209	n.d.	n.d.	n.d.	n.d.	n.d.	n.d.	n.d.
MgO	11,381	11,982	11,968	11,945	12,447	12,425	14,280	6,518	8,542	9,505	8,748	9,266	2,794
Al2O3	33,361	33,588	33,819	33,703	32,507	28,337	25,445	28,824	30,223	30,594	31,423	32,563	18,623
SiO2	36,766	35,344	35,974	36,551	34,865	35,547	31,012	32,922	36,010	34,876	34,825	35,998	34,770
K2O	1,178	0,643	0,536	0,396	0,977	0,199	0,363	0,555	0,810	0,666	0,547	0,636	0,511
CaO	n.d.	0,048	0,145	0,122	n.d.	0,087	n.d.	0,149	0,204	0,157	0,146	0,208	0,329
TiO2	n.d.	n.d.	n.d.	n.d.	n.d.	n.d.	n.d.	n.d.	n.d.	n.d.	n.d.	n.d.	n.d.
MnO	n.d.	n.d.	n.d.	n.d.	n.d.	n.d.	n.d.	n.d.	n.d.	n.d.	n.d.	n.d.	n.d.
Fe2O3	1,571	1,335	1,235	1,240	2,806	5,815	5,076	16,143	12,839	11,444	9,947	9,616	31,914
FeO	1,411	1,199	1,110	1,114	2,520	5,223	4,559	14,499	11,532	10,279	8,934	8,637	28,663
Ox%(Cl)	0,094	0,055	n.d.	0,059	0,097	n.d.	n.d.	0,087	n.d.	0,085	n.d.	0,068	n.d.
VO2	n.d.	n.d.	0,184	n.d.	n.d.	0,425	0,329	n.d.	0,280	0,183	n.d.	n.d.	n.d.
Cr2O3	n.d.	n.d.	n.d.	n.d.	n.d.	n.d.	n.d.	n.d.	n.d.	n.d.	n.d.	n.d.	n.d.
NiO	n.d.	n.d.	n.d.	n.d.	n.d.	2,304	2,288	n.d.	n.d.	n.d.	n.d.	n.d.	n.d.
Total	*84,190*	*82,861*	*83,864*	*83,890*	*83,413*	*84,757*	*78,276*	*83,553*	*87,601*	*86,344*	*84,624*	*87,375*	*85,691*
Si	3,40	3,31	3,33	3,37	3,29	3,38	3,22	3,31	3,38	3,31	3,33	3,33	3,71
Al IV	0,60	0,69	0,67	0,63	0,71	0,62	0,78	0,69	0,62	0,69	0,67	0,67	0,29
Al	3,64	3,71	3,69	3,66	3,61	3,18	3,12	3,42	3,35	3,42	3,55	3,55	2,34
Al VI	3,04	3,02	3,01	3,03	2,90	2,56	2,34	2,73	2,73	2,73	2,88	2,89	2,05
Fe	0,11	0,09	0,09	0,09	0,20	0,42	0,40	1,22	0,91	0,82	0,72	0,67	2,56
Mg	1,57	1,67	1,65	1,64	1,75	1,76	2,21	0,98	1,20	1,34	1,25	1,28	0,44
Mn	-	-	-	-	-	-	-	-	-	-	-	-	-
Ca	-	0,005	0,014	0,012	-	0,009	-	0,016	0,021	0,016	0,015	0,021	0,038
Na	-	-	0,023	-	-	0,039	-	-	-	-	-	-	-
K	0,139	0,077	0,063	0,047	0,117	0,024	0,048	0,071	0,097	0,081	0,067	0,075	0,070
Ti	-	-	-	-	-	-	-	-	-	-	-	-	-
Cl	0,015	0,009	-	0,009	0,015	-	-	0,015	-	0,014	-	0,011	-
V	-	-	0,011	-	-	0,027	0,023	-	0,017	0,011	-	-	-
Cr	-	-	-	-	-	-	-	-	-	-	-	-	-
Ni	-	-	-	-	-	0,176	0,191	-	-	-	-	-	-
K+Na+2*Ca	0,139	0,087	0,115	0,071	0,117	0,081	0,048	0,103	0,138	0,112	0,097	0,116	0,145
(Fe+Mg+Mn)/3	0,559	0,589	0,578	0,576	0,649	0,726	0,869	0,733	0,701	0,720	0,655	0,649	1,001
Fe/(Fe+Mg)	0,065	0,053	0,049	0,050	0,102	0,191	0,152	0,555	0,431	0,378	0,364	0,344	0,852

Tableau AIV-18 - Compositions en % et formules structurales des chlorites et kaolinites mélangées avec des Fe-chlorites des remplissages de ciment de brèches à Shea Creek. Formules structurales calculées sur la base de 14 oxygènes. Le Fe des chlorites est supposé bivalent. (n.d. = non détecté)

Echantillons forage-profondeur	SHEA12 she16-702,5	SHEA12 she16-702,5	SHEA12 she16-702,5	SHEA3B she16-696,8	SHEA3 she16-696,8	SHEA3C she16-696,8	SHEA12 she16-702,5	SHEA12 she16-702,5	SHEA3A she16-696,8	SHEA3A she16-696,8	SHEA3A she16-696,8	SHEA3A she16-696,8	SHEA1B she79-709,1
Numéro d'analyse	3_3	2_1	2_3	6_2	1_1	1_3	3_1	3_2	3_1	3_2	1_1	1_2	3_1
Minéral	Fe-chlorite3	Fe-chlorite3	Fe-chlorite3	Fe-chlorite3	Fe-chlorite3	Fe-chlorite3	Fe-chlorite2	Fe-chlorite2	Fe-chlorite2	Fe-chlorite2	Fe-chlorite2	Fe-chlorite2	Fe-chlorite1
Na2O	0,188	n.d.	n.d.	0,149	0,266	0,189	n.d.	n.d.	n.d.	n.d.	n.d.	n.d.	n.d.
MgO	2,034	2,508	2,321	4,159	2,284	2,662	2,699	2,706	2,902	2,532	2,487	2,767	3,065
Al2O3	20,067	17,040	17,357	11,966	14,222	17,767	15,319	16,222	10,881	10,994	15,845	16,348	12,098
SiO2	32,168	29,552	28,845	27,887	24,459	27,107	28,414	27,602	22,636	22,487	28,876	29,001	23,342
K2O	2,146	0,105	0,191	n.d.	0,201	0,115	0,169	0,093	n.d.	n.d.	0,272	0,368	0,111
CaO	0,273	0,243	0,232	0,375	n.d.	0,245	0,493	0,446	0,180	0,255	0,151	0,187	0,182
TiO2	0,127	n.d.	n.d.	n.d.	n.d.	n.d.	n.d.	n.d.	n.d.	n.d.	n.d.	0,105	n.d.
MnO	n.d.	n.d.	n.d.	n.d.	n.d.	n.d.	n.d.	n.d.	n.d.	n.d.	n.d.	n.d.	n.d.
Fe2O3	22,443	27,733	25,688	26,286	21,653	20,047	31,415	31,464	27,364	25,801	35,719	36,101	34,930
FeO	20,157	24,909	23,072	23,609	19,447	18,005	28,215	28,260	24,577	23,173	32,081	32,424	31,372
Ox%(Cl)	0,180	0,224	0,159	0,178	0,390	0,436	0,164	0,106	0,330	0,335	0,165	n.d.	0,350
VO2	n.d.	n.d.	n.d.	n.d.	n.d.	n.d.	n.d.	n.d.	n.d.	n.d.	n.d.	0,197	n.d.
Cr2O3	n.d.	n.d.	n.d.	n.d.	n.d.	n.d.	n.d.	n.d.	n.d.	n.d.	n.d.	n.d.	n.d.
NiO	n.d.	n.d.	0,191	0,603	n.d.	n.d.	n.d.	n.d.	0,237	0,231	0,362	0,409	n.d.
Total	*77,340*	*74,580*	*72,368*	*68,926*	*61,269*	*66,525*	*75,473*	*75,434*	*61,743*	*60,008*	*80,238*	*81,807*	*70,519*
Si	3,70	3,62	3,62	3,76	3,64	3,61	3,55	3,45	3,53	3,58	3,46	3,40	3,30
Al IV	0,30	0,38	0,38	0,24	0,36	0,39	0,45	0,55	0,47	0,42	0,54	0,60	0,70
Al	2,72	2,46	2,57	1,90	2,49	2,79	2,25	2,39	2,00	2,06	2,24	2,26	2,01
Al VI	2,42	2,09	2,18	1,66	2,13	2,40	1,80	1,84	1,53	1,64	1,69	1,66	1,31
Fe	1,94	2,56	2,42	2,66	2,42	2,01	2,95	2,95	3,21	3,08	3,21	3,18	3,71
Mg	0,35	0,46	0,43	0,84	0,51	0,53	0,50	0,50	0,67	0,60	0,44	0,48	0,64
Mn	-	-	-	-	-	-	-	-	-	-	-	-	-
Ca	0,034	0,032	0,031	0,054	-	0,035	0,066	0,060	0,030	0,043	0,019	0,024	0,027
Na	0,042	-	-	0,039	0,077	0,049	-	-	-	-	-	-	-
K	0,315	0,016	0,031	-	0,038	0,019	0,027	0,015	-	-	0,042	0,055	0,020
Ti	0,011	-	-	-	-	-	-	-	-	-	-	0,009	-
Cl	0,035	0,047	0,034	0,041	0,098	0,098	0,035	0,022	0,087	0,090	0,033	-	0,084
V	-	-	-	-	-	-	-	-	-	-	-	0,015	-
Cr	-	-	-	-	-	-	-	-	-	-	-	-	-
Ni	-	-	0,019	0,065	-	-	-	-	0,030	0,030	0,035	0,039	-
K+Na+2*Ca	0,424	0,080	0,093	0,147	0,115	0,138	0,159	0,134	0,060	0,087	0,080	0,102	0,075
(Fe+Mg+Mn)/3	0,763	1,005	0,951	1,166	0,976	0,845	1,150	1,152	1,294	1,228	1,219	1,222	1,451
Fe/(Fe+Mg)	0,848	0,848	0,848	0,761	0,827	0,792	0,854	0,854	0,826	0,837	0,879	0,868	0,852

Tableau AIV-19 - Compositions en % et formules structurales des chlorites et kaolinites mélangées avec des Fe-chlorites des remplissages de ciment de brèches à Shea Creek. Formules structurales calculées sur la base de 14 oxygènes. Le Fe des chlorites est supposé bivalent. (n.d. = non détecté)

Echantillons forage-profondeur	SHEA1B she79-709,1	SHEA1B she79-709,1	SHEA3A she16-696,8	SHEA3A she16-696,8	SHEA3B she16-696,8	SHEA3B she16-696,8	SHEA3B she16-696,8	SHEA3D she16-696,8	SHEA3D she16-696,8	SHEA15 she12-698,8	SHEA15 she12-696,8
Numéro d'analyse	3_2	3_3	1_3	1_4	5_1	5_3	5_4	3_3	3_4	3_1	3_2
Minéral	Fe-chlorite1	Fe-chlorite1	Fe-chlorite1	Fe-chlorite1	Kaol + Fe-chlo	Kaol + Fe-chlo	Kaol + Fe-chlo	Kaol + Fe-chlo	Kaol + Fe-chlo	Kaol + Fe-chlo	Kaol + Fe-chlo
Na2O	n.d.	n.d.	n.d.	n.d.	n.d.	n.d.	0,121	0,146	n.d.	n.d.	n.d.
MgO	2,927	2,727	2,604	2,636	0,850	0,490	0,465	0,751	0,733	1,258	1,221
Al2O3	12,665	12,095	8,776	7,728	30,275	34,822	34,095	32,986	33,204	30,794	30,792
SiO2	24,829	23,599	18,774	18,321	42,560	43,934	42,647	43,849	42,409	43,236	42,475
K2O	0,117	0,165	0,095	n.d.	n.d.	n.d.	0,080	n.d.	n.d.	1,625	2,340
CaO	0,201	0,210	n.d.	0,111	0,125	n.d.	0,087	0,179	n.d.	0,184	0,143
TiO2	n.d.	n.d.	n.d.	n.d.	n.d.	n.d.	n.d.	n.d.	n.d.	n.d.	n.d.
MnO	n.d.	n.d.	n.d.	n.d.	n.d.	n.d.	n.d.	n.d.	n.d.	n.d.	n.d.
Fe2O3	37,339	33,032	27,220	26,126	10,309	6,046	6,373	8,782	7,612	9,033	7,665
FeO	33,536	29,668	24,448	23,465	9,259	5,430	5,724	7,888	6,837	8,113	6,884
Ox%(Cl)	0,294	0,320	0,067	0,093	n.d.	n.d.	n.d.	n.d.	n.d.	n.d.	n.d.
VO2	n.d.	n.d.	n.d.	n.d.	0,255	0,195	n.d.	n.d.	n.d.	n.d.	n.d.
Cr2O3	n.d.	n.d.	n.d.	n.d.	n.d.	n.d.	n.d.	n.d.	n.d.	n.d.	n.d.
NiO	n.d.	n.d.	n.d.	0,279	n.d.	n.d.	0,192	n.d.	n.d.	n.d.	n.d.
Total	*74,570*	*68,784*	*54,763*	*52,633*	*84,374*	*85,487*	*84,058*	*86,693*	*83,957*	*86,130*	*84,636*
Si	3,32	3,38	3,39	3,46	3,92	3,91	3,88	3,90	3,87	3,92	3,92
Al IV	0,68	0,62	0,61	0,54	0,08	0,09	0,12	0,10	0,13	0,08	0,08
Al	2,00	2,04	1,87	1,72	3,28	3,65	3,66	3,46	3,58	3,30	3,35
Al VI	1,31	1,42	1,26	1,17	3,20	3,56	3,54	3,36	3,45	3,22	3,28
Fe	3,75	3,55	3,70	3,70	0,71	0,41	0,44	0,59	0,52	0,62	0,53
Mg	0,58	0,58	0,70	0,74	0,12	0,06	0,06	0,10	0,10	0,17	0,17
Mn	-	-	-	-	-	-	-	-	-	-	-
Ca	0,029	0,032	-	0,022	0,012	-	0,008	0,017	-	0,018	0,014
Na	-	-	-	-	-	-	0,021	0,025	-	-	-
K	0,020	0,030	0,022	-	-	-	0,009	-	-	0,188	0,276
Ti	-	-	-	-	-	-	-	-	-	-	-
Cl	0,067	0,078	0,020	0,030	-	-	-	-	-	-	-
V	-	-	-	-	0,015	0,011	-	-	-	-	-
Cr	-	-	-	-	-	-	-	-	-	-	-
Ni	-	-	-	0,042	-	-	0,014	-	-	-	-
K+Na+2*Ca	0,077	0,095	0,022	0,045	0,025	-	0,047	0,059	0	0,224	0,304
(Fe+Mg+Mn) /3	1,444	1,379	1,466	1,482	0,277	0,157	0,167	0,229	0,208	0,263	0,234
Fe/(Fe+Mg)	0,865	0,859	0,841	0,833	0,860	0,862	0,874	0,855	0,840	0,784	0,760

Tableau AIV-20 - Compositions en % et formules structurales des chlorites et kaolinites mélangées avec des Fe-chlorites des remplissages de ciment de brèches à Shea Creek. Formules structurales calculées sur la base de 14 oxygènes. Le Fe des chlorites est supposé bivalent. (n.d. = non détecté)

Echantillons forage-profondeur	Shea46 She87-710,1	Shea46 She87-710,1	Shea46 She87-710,1	Shea46 She87-710,1	Shea46 She87-710,1	Shea46 She87-710,1	Shea46 She87-710,1
Numéro d'analyse	5C-1	5C-2	5C-3	5C-4	5C-5	5B-2	5B-3
Minéral	Illite-chlorite	Illite-chlorite	Illite-chlorite	Illite-chlorite	Illite-chlorite	Illite-chlorite	Illite-chlorite
Na2O	0,298	0,234	0,196	0,179	n.d.	n.d.	0,187
MgO	4,442	3,466	4,299	4,474	6,437	4,536	3,218
Al2O3	23,764	25,357	18,452	24,340	20,018	23,562	29,082
SiO2	40,013	40,281	45,040	41,308	42,604	39,758	40,397
K2O	5,304	4,300	6,309	5,044	5,633	3,947	3,858
CaO	0,303	0,253	0,315	0,181	0,364	0,392	0,233
TiO2	n.d.	n.d.	n.d.	n.d.	n.d.	0,180	n.d.
MnO	0,700	0,189	n.d.	n.d.	0,228	0,227	n.d.
Fe2O3	9,436	10,232	11,291	9,248	8,524	9,743	6,453
FeO	8,475	9,190	10,141	8,306	7,656	8,751	5,795
Ox%(Cl)	0,095	n.d.	0,127	n.d.	n.d.	0,072	n.d.
VO2	0,268	0,243	0,236	0,262	0,320	n.d.	n.d.
Cr2O3	n.d.	n.d.	n.d.	n.d.	n.d.	n.d.	n.d.
NiO	n.d.	n.d.	n.d.	n.d.	n.d.	n.d.	n.d.
Total	*84,622*	*84,553*	*86,264*	*85,037*	*84,126*	*82,416*	*83,427*
Si	3,05	3,04	3,37	3,10	3,24	3,07	3,02
Al IV	0,95	0,96	0,63	0,90	0,76	0,93	0,98
Al	2,13	2,25	1,63	2,15	1,80	2,15	2,56
Al VI	1,18	1,29	1,00	1,25	1,04	1,22	1,58
Fe	0,54	0,58	0,64	0,52	0,49	0,57	0,36
Mg	0,50	0,39	0,48	0,50	0,73	0,52	0,36
Mn	0,045	0,012	-	-	0,015	0,015	-
Ca	0,025	0,020	0,025	0,015	0,030	0,032	0,019
Na	0,044	0,034	0,028	0,026	-	-	0,027
K	0,516	0,414	0,603	0,482	0,547	0,389	0,368
Ti	-	-	-	-	-	0,010	-
Cl	0,012	-	0,016	-	-	0,009	-
V	0,013	0,012	0,012	0,013	0,016	-	-
Cr	-	-	-	-	-	-	-
Ni	-	-	-	-	-	-	-
K+Na+2*Ca	0,609	0,488	0,682	0,537	0,606	0,454	0,432
Fe+Mg+Mn+ Ti+AlVI	2,275	2,272	2,122	2,267	2,272	2,333	2,302
(Fe+Mg+Mn) /3	0,364	0,327	0,372	0,341	0,411	0,368	0,241
Fe/(Fe+Mg)	0,518	0,599	0,570	0,511	0,401	0,520	0,503

Tableau AIV-21 - Compositions en % et formules structurales des interstratifiés illite-chlorite au contact de la minéralisation uranifère à Shea Creek. Formules structurales calculées sur la base de 11 oxygènes. Le Fe est supposé trivalent. (n.d. = non détecté)

Echantillons	Sue1	Sue1	Sue1	Sue1	Sue1	Sue1	Sue1	Sue1	Sue1	Sue1	Sue3	Sue3	Sue3
Numéro d'analyse	4-1	4-3	4-4	3-3	2-1	2-2	2-3	1-1	1-3	1-4	4-1	4-2	3-1
Minéral	illite	illite	illite	illite	illite	illite	illite	illite	illite	illite	illite	illite	illite
Na2O	0,164	0,130	0,136	n.d.	n.d.	n.d.	n.d.	n.d.	n.d.	n.d.	n.d.	n.d.	n.d.
MgO	0,947	0,814	0,652	0,980	0,970	0,791	0,757	1,249	1,215	0,991	0,635	0,908	1,006
Al2O3	33,106	32,248	33,576	32,903	27,735	27,399	27,541	28,718	26,957	25,961	20,293	24,650	31,368
SiO2	48,441	46,452	47,591	47,126	41,077	39,577	40,748	44,349	41,755	40,344	31,865	39,263	45,398
K2O	9,259	8,551	9,505	8,775	7,633	7,818	7,746	9,002	8,141	7,374	6,039	7,297	9,098
CaO	0,109	0,077	n.d.	0,099	n.d.	n.d.	n.d.	0,100	0,097	0,085	n.d.	n.d.	n.d.
TiO2	0,325	0,152	0,184	n.d.	n.d.	n.d.	n.d.	n.d.	n.d.	n.d.	n.d.	n.d.	n.d.
MnO	n.d.	n.d.	n.d.	n.d.	n.d.	n.d.	n.d.	0,173	n.d.	n.d.	n.d.	n.d.	n.d.
Fe2O3	1,476	0,498	0,893	n.d.	n.d.	n.d.	n.d.	n.d.	n.d.	n.d.	0,303	0,441	0,767
FeO	1,326	0,447	0,802	n.d.	n.d.	n.d.	n.d.	n.d.	n.d.	n.d.	0,272	0,397	0,689
Ox%(Cl)	0,071	0,078	n.d.	0,139	0,195	0,222	0,191	0,143	0,103	0,207	0,083	n.d.	n.d.
VO2	n.d.	n.d.	n.d.	n.d.	n.d.	n.d.	n.d.	n.d.	n.d.	n.d.	n.d.	n.d.	n.d.
Cr2O3	n.d.	n.d.	n.d.	n.d.	n.d.	n.d.	n.d.	n.d.	n.d.	n.d.	n.d.	n.d.	n.d.
NiO	n.d.	n.d.	n.d.	n.d.	n.d.	n.d.	n.d.	n.d.	n.d.	n.d.	n.d.	n.d.	n.d.
Total	*93,896*	*88,999*	*92,537*	*90,023*	*77,610*	*75,806*	*76,983*	*83,733*	*78,269*	*74,962*	*59,218*	*72,560*	*87,638*
Si	3,23	3,24	3,21	3,25	3,29	3,25	3,29	3,31	3,32	3,34	3,35	3,36	3,23
Al IV	0,77	0,76	0,79	0,75	0,71	0,75	0,71	0,69	0,68	0,66	0,65	0,64	0,77
Al	2,60	2,65	2,67	2,67	2,62	2,66	2,62	2,53	2,53	2,53	2,51	2,49	2,63
Al VI	1,83	1,90	1,88	1,92	1,90	1,91	1,91	1,84	1,85	1,87	1,86	1,84	1,87
Fe	0,074	0,026	0,045	-	-	-	-	-	-	-	0,024	0,028	0,041
Mg	0,094	0,085	0,066	0,101	0,116	0,097	0,091	0,139	0,144	0,122	0,099	0,116	0,107
Mn	-	-	-	-	-	-	-	0,011	-	-	-	-	-
Ca	0,008	0,006	-	0,007	-	-	-	0,008	0,008	0,008	-	-	-
Na	0,021	0,018	0,018	-	-	-	-	-	-	-	-	-	-
K	0,79	0,76	0,82	0,77	0,78	0,82	0,80	0,86	0,83	0,78	0,81	0,80	0,83
Ti	0,016	0,008	0,009	-	-	-	-	-	-	-	-	-	-
Cl	0,008	0,009	-	0,016	0,026	0,031	0,026	0,018	0,014	0,029	0,015	-	-
V	-	-	-	-	-	-	-	-	-	-	-	-	-
Cr	-	-	-	-	-	-	-	-	-	-	-	-	-
Ni	-	-	-	-	-	-	-	-	-	-	-	-	-
K+Na+2*Ca	0,823	0,791	0,836	0,786	0,779	0,820	0,798	0,873	0,843	0,794	0,809	0,796	0,827
Fe+Mg+Mn+Ti+AlVI	2,009	2,015	2,003	2,022	2,017	2,007	2,001	1,989	1,993	1,996	1,981	1,987	2,016
(Fe+Mg+Mn)/3	0,056	0,037	0,037	0,034	0,039	0,032	0,030	0,050	0,048	0,041	0,041	0,048	0,049
Fe/(Fe+Mg)	0,441	0,236	0,409	-	-	-	-	-	-	-	0,195	0,197	0,278

Tableau AIV-22 - Compositions en % et formules structurales des illites de l'encaissant des « zones à boules » dans la Mine à Ciel Ouvert de Sue C. Formules structurales calculées sur la base de 11 oxygènes. Le Fe des illites est supposé trivalent. (n.d. = non détecté)

Echantillons	Sue3	Sue3	Sue3	Sue3	Sue3	Sue3	Sue3	Sue6	Sue6	Sue6	Sue6	Sue6	Sue6	Sue6
Numéro d'analyse	3-2	3-3	2-1	2-2	1-1	1-2	1-3	2-1	2-2	3-1	3-2	3-3	3-4	3-5
Minéral	illite	illite	illite	illite	illite	illite	illite	illite	illite	illite	illite	illite	illite	illite
Na2O	n.d.	n.d.	n.d.	n.d.	n.d.	n.d.	n.d.	n.d.	n.d.	n.d.	n.d.	n.d.	n.d.	n.d.
MgO	0,934	0,978	0,559	1,028	1,007	1,096	0,730	0,400	0,497	0,496	0,513	0,552	0,502	0,452
Al2O3	27,961	29,565	20,669	23,179	29,136	28,349	30,432	31,783	28,813	31,346	32,352	32,604	29,460	28,469
SiO2	41,869	44,637	32,665	37,010	44,709	44,048	45,128	43,875	41,423	44,280	46,090	47,167	44,069	43,790
K2O	7,928	8,575	5,883	7,553	8,670	8,062	8,953	8,579	8,889	8,994	9,897	9,433	8,437	9,122
CaO	n.d.	n.d.	n.d.	0,090	n.d.	n.d.	n.d.	0,293	n.d.	n.d.	n.d.	n.d.	n.d.	n.d.
TiO2	n.d.	n.d.	n.d.	n.d.	n.d.	n.d.	n.d.	n.d.	n.d.	n.d.	n.d.	n.d.	n.d.	n.d.
MnO	n.d.	n.d.	n.d.	n.d.	n.d.	n.d.	n.d.	n.d.	n.d.	n.d.	0,144	n.d.	n.d.	n.d.
Fe2O3	0,754	0,742	0,518	0,798	1,302	1,280	0,965	0,356	0,167	n.d.	n.d.	n.d.	n.d.	0,425
FeO	0,677	0,666	0,465	0,716	1,169	1,149	0,867	0,320	0,150	n.d.	n.d.	n.d.	n.d.	0,382
Ox%(Cl)	n.d.	n.d.	0,080	n.d.	n.d.	n.d.	n.d.	0,066	0,149	n.d.	n.d.	n.d.	0,134	0,133
VO2	n.d.	n.d.	n.d.	n.d.	n.d.	n.d.	n.d.	n.d.	n.d.	n.d.	n.d.	n.d.	n.d.	n.d.
Cr2O3	n.d.	n.d.	n.d.	n.d.	n.d.	n.d.	n.d.	n.d.	n.d.	n.d.	n.d.	n.d.	n.d.	n.d.
NiO	n.d.	n.d.	n.d.	n.d.	n.d.	0,190	n.d.	n.d.	n.d.	n.d.	n.d.	n.d.	n.d.	n.d.
Total	*79,446*	*84,496*	*60,375*	*69,657*	*84,823*	*83,026*	*86,209*	*85,352*	*79,937*	*85,115*	*88,997*	*89,756*	*82,601*	*82,391*
Si	3,28	3,29	3,36	3,33	3,29	3,31	3,27	3,20	3,25	3,24	3,24	3,27	3,31	3,32
Al IV	0,72	0,71	0,64	0,67	0,71	0,69	0,73	0,80	0,75	0,76	0,76	0,73	0,69	0,68
Al	2,58	2,57	2,50	2,46	2,53	2,51	2,60	2,73	2,66	2,70	2,68	2,66	2,61	2,55
Al VI	1,86	1,86	1,86	1,78	1,82	1,81	1,86	1,94	1,91	1,94	1,92	1,93	1,92	1,87
Fe	0,044	0,041	0,040	0,054	0,072	0,072	0,053	0,020	0,010	-	-	-	-	0,024
Mg	0,109	0,107	0,086	0,138	0,110	0,123	0,079	0,043	0,058	0,054	0,054	0,057	0,056	0,051
Mn	-	-	-	-	-	-	-	-	-	-	0,009	-	-	-
Ca	-	-	-	0,009	-	-	-	0,023	-	-	-	-	-	-
Na	-	-	-	-	-	-	-	-	-	-	-	-	-	-
K	0,79	0,81	0,77	0,87	0,81	0,77	0,83	0,80	0,89	0,84	0,89	0,83	0,81	0,88
Ti	-	-	-	-	-	-	-	-	-	-	-	-	-	-
Cl	-	-	0,014	-	-	-	-	0,008	0,020	-	-	-	0,017	0,017
V	-	-	-	-	-	-	-	-	-	-	-	-	-	-
Cr	-	-	-	-	-	-	-	-	-	-	-	-	-	-
Ni	-	-	-	-	-	0,011	-	-	-	-	-	-	-	-
K+Na+2*Ca	0,792	0,806	0,771	0,884	0,814	0,772	0,827	0,845	0,888	0,839	0,887	0,834	0,809	0,884
Fe+Mg+Mn +Ti+AlVI	2,013	2,004	1,986	1,976	2,002	2,008	1,995	1,999	1,975	1,993	1,979	1,986	1,978	1,948
(Fe+Mg+Mn)/3	0,051	0,050	0,042	0,064	0,061	0,065	0,044	0,021	0,023	0,018	0,021	0,019	0,019	0,025
Fe/(Fe+Mg)	0,290	0,277	0,319	0,282	0,395	0,371	0,400	0,310	0,146	-	-	-	-	0,322

Tableau AIV-23 - Compositions en % et formules structurales des illites de l'encaissant des « zones à boules » et d'une boule illitisée dans la Mine à Ciel Ouvert de Sue C. Formules structurales calculées sur la base de 11 oxygènes. Le Fe des illites est supposé trivalent. (n.d. = non détecté)

Echantillons forage-profondeur	8656-4 She16-718,2	8656-4 She16-718,2	8656-4 She16-718,2	8656-4 She16-718,2	8656-4 She16-718,2	8656-4 She16-718,2	8656-4 She16-718,2	8656-4 She16-718,2	8656-4 She16-718,2	8656-4 She16-718,2	8656-4 She16-718,2	8656-4 She16-718,2	8656-4 She16-718,2
Numéro d'analyse	0-G1_1_1	0-G1_1_2	0-G1_1_3	0-G1_1_4	0-G1_1_5	0-G1_1_6	0-G1_1_7	0-G1_1_8	0-G1_1_9	0-G1_1_10	0-G1_1_11	0-G1_1_12	0-G1_1_13
Minéral	uraninite	uraninite	uraninite	uraninite	uraninite	uraninite	uraninite	uraninite	uraninite	uraninite	uraninite	uraninite	uraninite
SiO2	0,453	0,268	0,207	0,224	0,366	0,421	0,313	0,271	0,357	0,287	0,265	0,212	0,253
SO3	n.d.	n.d.	n.d.	n.d.	n.d.	n.d.	n.d.	n.d.	n.d.	n.d.	n.d.	n.d.	n.d.
CaO	1,673	1,113	1,175	1,032	1,509	0,952	0,971	1,012	1,255	1,127	1,113	1,206	0,975
TiO2	n.d.	n.d.	n.d.	n.d.	n.d.	n.d.	n.d.	n.d.	n.d.	n.d.	n.d.	n.d.	n.d.
FeO	0,490	n.d.	n.d.	n.d.	n.d.	n.d.	n.d.	n.d.	n.d.	n.d.	n.d.	n.d.	n.d.
As2O3	n.d.	0,409	n.d.	n.d.	n.d.	n.d.	n.d.	n.d.	n.d.	n.d.	n.d.	n.d.	n.d.
Y2O3	0,183	n.d.	n.d.	n.d.	n.d.	n.d.	n.d.	n.d.	n.d.	n.d.	n.d.	n.d.	n.d.
Ce2O3	n.d.	n.d.	n.d.	n.d.	n.d.	n.d.	n.d.	n.d.	n.d.	n.d.	n.d.	n.d.	n.d.
Gd2O3	n.d.	n.d.	n.d.	n.d.	n.d.	n.d.	n.d.	n.d.	n.d.	n.d.	n.d.	n.d.	n.d.
Yb2O3	n.d.	n.d.	n.d.	n.d.	n.d.	n.d.	n.d.	n.d.	n.d.	n.d.	n.d.	n.d.	n.d.
PbO	12,156	14,169	13,921	14,811	12,215	13,603	13,428	14,920	12,805	14,285	14,514	14,010	14,689
ThO2	n.d.	n.d.	n.d.	n.d.	n.d.	n.d.	n.d.	n.d.	n.d.	n.d.	n.d.	n.d.	n.d.
UO2	79,562	78,742	80,112	78,015	80,716	77,904	78,493	79,108	79,569	79,138	80,710	80,426	79,180
Total	*94,516*	*94,701*	*95,414*	*94,082*	*94,806*	*92,880*	*93,204*	*95,312*	*93,987*	*94,837*	*96,601*	*95,854*	*95,096*
Age (Ga)	1,028	1,188	1,152	1,245	1,019	1,157	1,136	1,238	1,076	1,191	1,187	1,155	1,220

Echantillons forage-profondeur	8656-4 She16-718,2	8656-4 She16-718,2	8656-4 She16-718,2	8656-4 She16-718,2	8656-4 She16-718,2	8656-4 She16-718,2	8656-4 She16-718,2	8656-4 She16-718,2	8656-4 She16-718,2	8656-4 She16-718,2	8656-4 She16-718,2	8656-4 She16-718,2	8656-4 She16-718,2
Numéro d'analyse	0-G1_1_14	0-G1_2_1	0-G1_2_2	0-G1_2_3	0-G1_2_4	0-G1_2_5	0-G1_2_6	0-G1_2_7	0-G1_2_8	0-G1_2_9	0-G1_2_10	0-G1_2_11	0-G1_2_12
Minéral	uraninite	uraninite	uraninite	uraninite	uraninite	uraninite	uraninite	uraninite	uraninite	uraninite	uraninite	uraninite	uraninite
SiO2	0,153	0,262	0,418	0,217	0,242	0,180	0,414	0,306	0,286	0,463	0,206	0,180	0,288
SO3	n.d.	n.d.	n.d.	n.d.	n.d.	n.d.	n.d.	n.d.	n.d.	n.d.	n.d.	n.d.	n.d.
CaO	0,961	0,868	1,630	0,967	1,205	0,955	1,275	1,326	1,129	1,777	0,967	1,042	1,293
TiO2	n.d.	n.d.	n.d.	n.d.	n.d.	n.d.	n.d.	n.d.	n.d.	n.d.	n.d.	n.d.	n.d.
FeO	n.d.	n.d.	0,377	n.d.	n.d.	n.d.	n.d.	n.d.	0,300	0,617	n.d.	n.d.	n.d.
As2O3	n.d.	n.d.	n.d.	n.d.	n.d.	n.d.	n.d.	0,559	0,485	n.d.	n.d.	0,443	n.d.
Y2O3	n.d.	n.d.	0,150	n.d.	n.d.	n.d.	n.d.	n.d.	n.d.	0,265	n.d.	n.d.	n.d.
Ce2O3	n.d.	n.d.	n.d.	n.d.	n.d.	n.d.	n.d.	n.d.	n.d.	n.d.	n.d.	n.d.	n.d.
Gd2O3	n.d.	n.d.	n.d.	n.d.	n.d.	n.d.	n.d.	n.d.	n.d.	n.d.	n.d.	n.d.	n.d.
Yb2O3	n.d.	n.d.	n.d.	n.d.	n.d.	n.d.	n.d.	n.d.	n.d.	n.d.	n.d.	n.d.	n.d.
PbO	14,494	14,921	13,137	14,212	14,268	14,276	12,491	13,229	14,797	11,822	14,575	14,670	13,512
ThO2	n.d.	n.d.	n.d.	n.d.	n.d.	n.d.	n.d.	n.d.	n.d.	n.d.	n.d.	n.d.	n.d.
UO2	79,317	79,354	82,620	79,865	80,592	80,042	75,341	79,390	80,828	81,155	79,754	79,552	79,877
Total	*94,926*	*95,404*	*98,332*	*95,261*	*96,308*	*95,453*	*89,521*	*94,810*	*97,824*	*96,099*	*95,502*	*95,886*	*94,971*
Age (Ga)	1,204	1,235	1,065	1,176	1,171	1,179	1,105	1,110	1,206	0,984	1,204	1,214	1,125

Tableau AIV-24 - Compositions en % d'un cristal d'uraninite provenant de la minéralisation à la discordance de Shea Creek. Les âges chimiques sont calculés à l'aide de la formule de Suzuki et Adachi (1994). (n.d. = non détecté)

Echantillons forage-profondeur	8656-4 She16-718,2	8656-4 She16-718,2	8656-4 She16-718,2	8656-4 She16-718,2	8656-4 She16-718,2	8656-4 She16-718,2	8656-4 She16-718,2	8656-4 She16-718,2	8656-4 She16-718,2	8656-4 She16-718,2	8656-4 She16-718,2	8656-4 She16-718,2	8656-4 She16-718,2
Numéro d'analyse	0-G1_2_13	0-G1_2_14	0-G1_3_1	0-G1_3_2	0-G1_3_3	0-G1_3_4	0-G1_3_5	0-G1_3_6	0-G1_3_7	0-G1_3_8	0-G1_3_9	0-G1_3_10	0-G1_3_11
Minéral	uraninite	uraninite	uraninite	uraninite	uraninite	uraninite	uraninite	uraninite	uraninite	uraninite	uraninite	uraninite	uraninite
SiO2	0,179	0,214	0,326	0,244	0,223	0,211	0,213	0,236	0,222	0,239	0,175	0,267	0,447
SO3	n.d.	n.d.	n.d.	n.d.	n.d.	n.d.	n.d.	n.d.	n.d.	n.d.	n.d.	n.d.	n.d.
CaO	0,854	0,973	1,087	0,902	0,917	1,064	1,051	1,439	1,035	0,875	0,980	0,884	1,513
TiO2	n.d.	n.d.	n.d.	n.d.	n.d.	n.d.	n.d.	n.d.	n.d.	n.d.	n.d.	n.d.	n.d.
FeO	n.d.	n.d.	n.d.	n.d.	n.d.	n.d.	n.d.	n.d.	n.d.	n.d.	n.d.	n.d.	n.d.
As2O3	n.d.	n.d.	n.d.	0,441	n.d.	n.d.	n.d.	n.d.	n.d.	n.d.	0,493	n.d.	n.d.
Y2O3	n.d.	n.d.	n.d.	n.d.	n.d.	n.d.	n.d.	n.d.	n.d.	n.d.	n.d.	n.d.	n.d.
Ce2O3	n.d.	n.d.	n.d.	n.d.	n.d.	n.d.	n.d.	n.d.	n.d.	n.d.	n.d.	n.d.	n.d.
Gd2O3	n.d.	n.d.	n.d.	n.d.	n.d.	n.d.	n.d.	n.d.	n.d.	n.d.	n.d.	n.d.	n.d.
Yb2O3	n.d.	n.d.	n.d.	n.d.	n.d.	n.d.	n.d.	n.d.	n.d.	n.d.	n.d.	n.d.	n.d.
PbO	15,040	13,763	14,523	15,045	15,067	14,456	13,392	13,151	15,090	14,012	14,414	14,771	11,284
ThO2	n.d.	n.d.	n.d.	n.d.	n.d.	n.d.	n.d.	n.d.	n.d.	n.d.	n.d.	n.d.	n.d.
UO2	80,377	79,612	80,244	79,690	78,570	79,797	79,583	81,210	80,169	79,006	78,638	79,833	80,630
Total	*96,451*	*94,562*	*96,179*	*96,322*	*94,777*	*95,528*	*94,239*	*96,037*	*96,516*	*94,132*	*94,700*	*95,755*	*93,873*
Age (Ga)	1,229	1,147	1,194	1,239	1,256	1,195	1,120	1,082	1,236	1,173	1,207	1,217	0,949

Echantillons forage-profondeur	8656-4 She16-718,2	8656-4 She16-718,2	8656-4 She16-718,2	8656-4 She16-718,2	8656-4 She16-718,2	8656-4 She16-718,2	8656-4 She16-718,2	8656-4 She16-718,2	8656-4 She16-718,2	8656-4 She16-718,2	8656-4 She16-718,2	8656-4 She16-718,2	8656-4 She16-718,2
Numéro d'analyse	0-G1_3_12	0-G1_3_13	0-G1_3_14	0-G1_4_1	0-G1_4_2	0-G1_4_3	0-G1_4_4	0-G1_4_5	0-G1_4_6	0-G1_4_7	0-G1_4_8	0-G1_4_9	0-G1_4_10
Minéral	uraninite	uraninite	uraninite	uraninite	uraninite	uraninite	uraninite	uraninite	uraninite	uraninite	uraninite	uraninite	uraninite
SiO2	0,287	0,235	0,380	0,295	0,245	0,186	0,252	0,255	0,352	0,210	0,265	0,359	0,278
SO3	n.d.	n.d.	n.d.	n.d.	n.d.	n.d.	n.d.	n.d.	n.d.	0,157	n.d.	n.d.	n.d.
CaO	1,268	1,096	2,208	1,043	1,095	1,002	0,144	0,976	1,319	0,935	1,448	1,192	0,913
TiO2	n.d.	n.d.	n.d.	n.d.	n.d.	n.d.	n.d.	n.d.	n.d.	n.d.	n.d.	n.d.	n.d.
FeO	n.d.	0,295	0,298	n.d.	n.d.	n.d.	n.d.	n.d.	n.d.	n.d.	n.d.	n.d.	n.d.
As2O3	n.d.	0,507	n.d.	n.d.	n.d.	n.d.	n.d.	n.d.	0,413	0,448	n.d.	0,439	n.d.
Y2O3	n.d.	n.d.	0,293	n.d.	n.d.	n.d.	n.d.	n.d.	n.d.	n.d.	0,144	n.d.	n.d.
Ce2O3	n.d.	n.d.	n.d.	n.d.	n.d.	n.d.	0,199	n.d.	n.d.	n.d.	n.d.	n.d.	n.d.
Gd2O3	n.d.	n.d.	n.d.	n.d.	n.d.	n.d.	n.d.	n.d.	n.d.	n.d.	n.d.	n.d.	n.d.
Yb2O3	n.d.	n.d.	n.d.	n.d.	n.d.	n.d.	n.d.	n.d.	n.d.	n.d.	n.d.	n.d.	n.d.
PbO	13,750	13,897	11,223	14,773	14,194	15,275	25,691	15,010	13,495	14,433	13,243	13,886	14,152
ThO2	n.d.	n.d.	n.d.	n.d.	n.d.	n.d.	n.d.	n.d.	n.d.	n.d.	n.d.	n.d.	n.d.
UO2	77,755	80,772	81,978	80,148	80,774	79,340	7,136	80,329	79,958	79,283	82,125	79,669	79,798
Total	*93,059*	*96,802*	*96,380*	*96,259*	*96,307*	*95,802*	*33,422*	*96,569*	*95,537*	*95,467*	*97,225*	*95,545*	*95,141*
Age (Ga)	1,170	1,142	0,931	1,213	1,163	1,260	6,055	1,228	1,123	1,200	1,078	1,155	1,173

Tableau AIV-25 - Compositions en % d'un cristal d'uraninite provenant de la minéralisation à la discordance de Shea Creek. Les âges chimiques sont calculés à l'aide de la formule de Suzuki et Adachi (1994). (n.d. = non détecté)

Echantillons forage-profondeur	8656-4 She16-718,2	8656-4 She16-718,2	8656-4 She16-718,2	8656-4 She16-718,2	8656-4 She16-718,2	8656-4 She16-718,2	8656-4 She16-718,2	8656-4 She16-718,2	8656-4 She16-718,2	8656-4 She16-718,2	8656-4 She16-718,2	8656-4 She16-718,2	8656-4 She16-718,2
Numéro d'analyse	0-G1_4_11	0-G1_4_12	0-G1_4_13	0-G1_4_14	0-G1_5_1	0-G1_5_2	0-G1_5_3	0-G1_5_4	0-G1_5_5	0-G1_5_6	0-G1_5_7	0-G1_5_8	0-G1_5_9
Minéral	uraninite	uraninite	uraninite	uraninite	uraninite	uraninite	uraninite	uraninite	uraninite	uraninite	uraninite	uraninite	uraninite
SiO2	0,245	0,168	0,275	0,183	0,435	0,561	0,200	0,239	0,288	0,298	0,214	0,194	0,210
SO3	n.d.	n.d.	0,145	n.d.	n.d.	n.d.	n.d.	n.d.	n.d.	n.d.	n.d.	n.d.	n.d.
CaO	1,133	1,017	1,116	0,924	1,054	1,508	1,013	1,007	1,223	1,068	1,498	1,054	1,213
TiO2	n.d.	n.d.	n.d.	n.d.	n.d.	n.d.	n.d.	n.d.	n.d.	n.d.	n.d.	n.d.	n.d.
FeO	n.d.	n.d.	n.d.	n.d.	n.d.	0,322	n.d.	n.d.	n.d.	n.d.	0,354	n.d.	n.d.
As2O3	n.d.	n.d.	n.d.	n.d.	n.d.	n.d.	n.d.	n.d.	n.d.	0,520	n.d.	n.d.	n.d.
Y2O3	n.d.	n.d.	0,141	n.d.	n.d.	n.d.	n.d.	n.d.	n.d.	n.d.	n.d.	n.d.	n.d.
Ce2O3	n.d.	n.d.	n.d.	n.d.	n.d.	n.d.	n.d.	n.d.	n.d.	n.d.	n.d.	n.d.	n.d.
Gd2O3	n.d.	n.d.	n.d.	n.d.	n.d.	n.d.	n.d.	n.d.	n.d.	n.d.	n.d.	n.d.	n.d.
Yb2O3	n.d.	n.d.	n.d.	n.d.	n.d.	n.d.	n.d.	n.d.	n.d.	n.d.	n.d.	n.d.	n.d.
PbO	14,371	15,104	14,028	14,312	14,041	11,199	14,445	13,932	13,703	14,265	13,256	14,481	13,882
ThO2	n.d.	n.d.	n.d.	n.d.	n.d.	0,262	n.d.	n.d.	n.d.	n.d.	n.d.	n.d.	n.d.
UO2	80,742	78,477	78,175	78,390	77,543	80,471	78,181	77,938	80,525	78,473	80,055	80,078	80,227
Total	*96,490*	*94,766*	*93,879*	*93,808*	*93,072*	*94,324*	*93,839*	*93,115*	*95,738*	*94,624*	*95,377*	*95,807*	*95,533*
Age (Ga)	1,177	1,260	1,185	1,203	1,194	0,944	1,216	1,181	1,131	1,199	1,104	1,193	1,148

Echantillons forage-profondeur	8656-4 She16-718,2	8656-4 She16-718,2	8656-4 She16-718,2	8656-4 She16-718,2	8656-4 She16-718,2	8656-4 She16-718,2	8656-4 She16-718,2	8656-4 She16-718,2	8656-4 She16-718,2	8656-4 She16-718,2	8656-4 She16-718,2	8656-4 She16-718,2	8656-4 She16-718,2
Numéro d'analyse	0-G1_5_10	0-G1_5_11	0-G1_5_12	0-G1_5_13	0-G1_5_14	0-G1_6_1	0-G1_6_2	0-G1_6_3	0-G1_6_4	0-G1_6_5	0-G1_6_6	0-G1_6_7	0-G1_6_8
Minéral	uraninite	uraninite	uraninite	uraninite	uraninite	uraninite	uraninite	uraninite	uraninite	uraninite	uraninite	uraninite	uraninite
SiO2	0,208	0,216	0,210	0,298	0,324	0,438	0,285	0,366	0,260	0,449	0,236	0,339	0,252
SO3	n.d.	n.d.	n.d.	n.d.	n.d.	n.d.	n.d.	n.d.	n.d.	0,204	n.d.	n.d.	n.d.
CaO	1,040	0,891	1,004	1,014	1,270	1,071	1,220	1,368	0,931	1,242	0,873	1,115	1,231
TiO2	n.d.	n.d.	n.d.	n.d.	n.d.	0,223	n.d.	n.d.	n.d.	n.d.	n.d.	n.d.	n.d.
FeO	n.d.	n.d.	n.d.	n.d.	0,304	n.d.	0,367	n.d.	n.d.	n.d.	n.d.	n.d.	n.d.
As2O3	n.d.	n.d.	n.d.	0,405	n.d.	n.d.	n.d.	n.d.	n.d.	n.d.	n.d.	n.d.	n.d.
Y2O3	n.d.	n.d.	n.d.	n.d.	n.d.	n.d.	n.d.	n.d.	n.d.	n.d.	n.d.	n.d.	n.d.
Ce2O3	n.d.	n.d.	n.d.	n.d.	n.d.	n.d.	n.d.	n.d.	n.d.	n.d.	n.d.	n.d.	n.d.
Gd2O3	n.d.	n.d.	n.d.	n.d.	n.d.	n.d.	n.d.	n.d.	n.d.	n.d.	n.d.	n.d.	n.d.
Yb2O3	n.d.	n.d.	n.d.	n.d.	n.d.	n.d.	n.d.	n.d.	n.d.	n.d.	n.d.	n.d.	n.d.
PbO	14,322	14,596	14,879	13,906	12,944	13,775	14,290	12,237	14,865	12,196	15,127	13,824	13,720
ThO2	n.d.	n.d.	n.d.	n.d.	n.d.	n.d.	n.d.	n.d.	n.d.	n.d.	n.d.	n.d.	n.d.
UO2	78,950	78,670	79,118	81,055	79,183	78,832	80,293	79,441	77,923	79,955	78,830	70,090	78,636
Total	*94,519*	*94,373*	*95,210*	*96,678*	*94,023*	*94,339*	*96,455*	*93,412*	*93,979*	*94,046*	*95,067*	*85,368*	*93,839*
Age (Ga)	1,196	1,220	1,235	1,139	1,091	1,158	1,177	1,035	1,250	1,026	1,257	1,287	1,156

Tableau AIV-26 - Compositions en % d'un cristal d'uraninite provenant de la minéralisation à la discordance de Shea Creek. Les âges chimiques sont calculés à l'aide de la formule de Suzuki et Adachi (1994). (n.d. = non détecté)

Echantillons forage-profondeur	8656-4 She16-718,2	8656-4 She16-718,2	8656-4 She16-718,2	8656-4 She16-718,2	8656-4 She16-718,2	8656-4 She16-718,2	8656-4 She16-718,2	8656-4 She16-718,2	8656-4 She16-718,2	8656-4 She16-718,2	8656-4 She16-718,2	8656-4 She16-718,2	8656-4 She16-718,2
Numéro d'analyse	0-G1_6_9	0-G1_6_10	0-G1_6_11	0-G1_6_12	0-G1_6_13	0-G1_6_14	0-G1_7_1	0-G1_7_2	0-G1_7_3	0-G1_7_4	0-G1_7_5	0-G1_7_6	0-G1_7_7
Minéral	uraninite	uraninite	uraninite	uraninite	uraninite	uraninite	uraninite	uraninite	uraninite	uraninite	uraninite	uraninite	uraninite
SiO2	0,251	0,173	0,216	0,197	0,264	0,261	0,376	0,254	0,397	0,229	0,289	0,201	0,184
SO3	n.d.	0,125	n.d.	n.d.	n.d.	n.d.	n.d.	n.d.	n.d.	n.d.	n.d.	n.d.	n.d.
CaO	1,006	1,009	1,230	1,076	0,971	1,139	0,975	1,167	1,061	0,990	0,994	0,898	1,191
TiO2	n.d.	n.d.	n.d.	n.d.	n.d.	n.d.	n.d.	0,295	n.d.	n.d.	n.d.	n.d.	n.d.
FeO	n.d.	n.d.	n.d.	n.d.	n.d.	n.d.	n.d.	n.d.	n.d.	n.d.	n.d.	n.d.	n.d.
As2O3	n.d.	0,344	0,468	n.d.	n.d.	n.d.	n.d.	n.d.	0,458	n.d.	n.d.	n.d.	n.d.
Y2O3	n.d.	n.d.	n.d.	n.d.	n.d.	0,149	n.d.	n.d.	n.d.	n.d.	n.d.	n.d.	n.d.
Ce2O3	n.d.	n.d.	n.d.	n.d.	n.d.	n.d.	n.d.	n.d.	n.d.	n.d.	n.d.	n.d.	n.d.
Gd2O3	n.d.	n.d.	n.d.	n.d.	n.d.	n.d.	n.d.	n.d.	n.d.	n.d.	n.d.	n.d.	n.d.
Yb2O3	n.d.	n.d.	n.d.	n.d.	n.d.	n.d.	n.d.	n.d.	n.d.	n.d.	n.d.	n.d.	n.d.
PbO	14,855	14,195	14,754	14,614	14,171	15,393	13,096	14,761	12,602	15,006	13,586	15,377	14,635
ThO2	n.d.	n.d.	n.d.	n.d.	n.d.	n.d.	n.d.	n.d.	n.d.	n.d.	n.d.	n.d.	n.d.
UO2	78,095	79,183	79,352	77,469	77,288	77,123	77,612	79,095	79,000	77,760	78,188	76,816	79,589
Total	*94,207*	*95,029*	*96,020*	*93,356*	*92,693*	*94,064*	*92,059*	*95,572*	*93,519*	*93,984*	*93,057*	*93,292*	*95,598*
Age (Ga)	1,247	1,184	1,222	1,238	1,208	1,300	1,122	1,226	1,068	1,263	1,152	1,304	1,211

Echantillons forage-profondeur	8656-4 She16-718,2	8656-4 She16-718,2	8656-4 She16-718,2	8656-4 She16-718,2	8656-4 She16-718,2	8656-4 She16-718,2	8656-4 She16-718,2	8656-4 She16-718,2	8656-4 She16-718,2	8656-4 She16-718,2	8656-4 She16-718,2	8656-4 She16-718,2	8656-4 She16-718,2
Numéro d'analyse	0-G1_7_8	0-G1_7_9	0-G1_7_10	0-G1_7_11	0-G1_7_12	0-G1_7_13	0-G1_7_14	0-G1_8_1	0-G1_8_2	0-G1_8_3	0-G1_8_4	0-G1_8_5	0-G1_8_6
Minéral	uraninite	uraninite	uraninite	uraninite	uraninite	uraninite	uraninite	uraninite	uraninite	uraninite	uraninite	uraninite	uraninite
SiO2	0,228	0,230	0,227	0,216	0,376	0,299	0,190	0,348	0,411	0,286	0,216	0,233	0,252
SO3	n.d.	n.d.	n.d.	n.d.	n.d.	n.d.	n.d.	n.d.	n.d.	n.d.	n.d.	n.d.	n.d.
CaO	1,082	0,976	0,973	1,069	1,030	0,891	0,925	0,985	1,123	1,238	1,218	1,044	1,441
TiO2	n.d.	n.d.	n.d.	n.d.	n.d.	n.d.	n.d.	n.d.	n.d.	0,282	n.d.	n.d.	n.d.
FeO	n.d.	n.d.	0,287	n.d.	n.d.	n.d.	n.d.	n.d.	n.d.	n.d.	n.d.	n.d.	0,436
As2O3	0,508	n.d.	0,489	0,443	n.d.	n.d.	n.d.	n.d.	n.d.	n.d.	n.d.	0,474	n.d.
Y2O3	n.d.	n.d.	n.d.	n.d.	n.d.	n.d.	n.d.	0,163	n.d.	0,167	n.d.	n.d.	n.d.
Ce2O3	n.d.	n.d.	n.d.	n.d.	n.d.	n.d.	n.d.	n.d.	n.d.	n.d.	n.d.	n.d.	n.d.
Gd2O3	n.d.	n.d.	n.d.	n.d.	n.d.	n.d.	n.d.	n.d.	n.d.	n.d.	n.d.	n.d.	n.d.
Yb2O3	n.d.	n.d.	n.d.	n.d.	n.d.	n.d.	n.d.	n.d.	n.d.	n.d.	n.d.	n.d.	n.d.
PbO	14,446	15,420	14,740	14,654	12,608	14,345	14,957	14,255	13,742	12,967	14,069	13,999	13,812
ThO2	n.d.	n.d.	n.d.	n.d.	n.d.	n.d.	n.d.	n.d.	n.d.	n.d.	n.d.	n.d.	n.d.
UO2	77,270	78,291	77,827	77,361	79,573	78,111	79,064	80,096	79,023	79,478	77,667	78,066	79,640
Total	*93,534*	*94,917*	*94,542*	*93,744*	*93,586*	*93,647*	*95,136*	*95,847*	*94,299*	*94,418*	*93,169*	*93,815*	*95,580*
Age (Ga)	1,228	1,285	1,242	1,243	1,061	1,209	1,241	1,177	1,153	1,089	1,195	1,184	1,150

Tableau AIV-27 - Compositions en % d'un cristal d'uraninite provenant de la minéralisation à la discordance de Shea Creek. Les âges chimiques sont calculés à l'aide de la formule de Suzuki et Adachi (1994). (n.d. = non détecté)

Echantillons forage-profondeur	8656-4 She16-718,2	8656-4 She16-718,2	8656-4 She16-718,2	8656-4 She16-718,2	8656-4 She16-718,2	8656-4 She16-718,2	8656-4 She16-718,2	8656-4 She16-718,2	8656-4 She16-718,2	8656-4 She16-718,2	8656-4 She16-718,2	8656-4 She16-718,2	8656-4 She16-718,2
Numéro d'analyse	0-G1_8_7	0-G1_8_8	0-G1_8_9	0-G1_8_10	0-G1_8_11	0-G1_8_12	0-G1_8_13	0-G1_8_14	0-G1_9_1	0-G1_9_2	0-G1_9_3	0-G1_9_4	0-G1_9_5
Minéral	uraninite	uraninite	uraninite	uraninite	uraninite	uraninite	uraninite	uraninite	uraninite	uraninite	uraninite	uraninite	uraninite
SiO2	0,198	0,308	0,264	0,231	0,534	0,228	0,221	0,183	0,296	0,533	0,421	0,264	0,298
SO3	n.d.	n.d.	n.d.	n.d.	n.d.	n.d.	n.d.	n.d.	n.d.	n.d.	n.d.	n.d.	n.d.
CaO	0,975	1,045	0,970	1,168	1,052	1,105	1,186	1,186	0,830	1,449	1,526	0,818	1,043
TiO2	n.d.	n.d.	n.d.	n.d.	n.d.	n.d.	n.d.	n.d.	n.d.	n.d.	n.d.	0,202	n.d.
FeO	n.d.	0,274	n.d.	n.d.	0,356	n.d.	n.d.	n.d.	n.d.	0,346	n.d.	n.d.	n.d.
As2O3	n.d.	n.d.	n.d.	n.d.	n.d.	n.d.	n.d.	n.d.	n.d.	0,476	n.d.	n.d.	0,439
Y2O3	n.d.	n.d.	n.d.	n.d.	n.d.	0,186	n.d.	n.d.	n.d.	n.d.	0,161	n.d.	n.d.
Ce2O3	n.d.	n.d.	n.d.	n.d.	n.d.	n.d.	n.d.	n.d.	n.d.	n.d.	n.d.	n.d.	n.d.
Gd2O3	n.d.	n.d.	n.d.	n.d.	n.d.	n.d.	n.d.	n.d.	n.d.	n.d.	n.d.	n.d.	n.d.
Yb2O3	n.d.	n.d.	n.d.	n.d.	n.d.	n.d.	n.d.	n.d.	n.d.	n.d.	n.d.	n.d.	n.d.
PbO	14,126	13,164	14,071	13,769	14,778	14,829	14,567	14,574	14,857	12,970	11,174	14,675	14,195
ThO2	n.d.	n.d.	n.d.	n.d.	n.d.	n.d.	n.d.	n.d.	n.d.	n.d.	n.d.	n.d.	n.d.
UO2	77,707	78,337	78,212	79,193	44,534	80,267	77,515	78,290	77,368	75,595	79,981	77,237	78,828
Total	*93,005*	*93,129*	*93,517*	*94,361*	*61,254*	*96,614*	*93,489*	*94,233*	*93,351*	*91,368*	*93,263*	*93,196*	*94,803*
Age (Ga)	1,199	1,118	1,188	1,153	1,979	1,216	1,234	1,224	1,257	1,139	0,948	1,246	1,189

Echantillons forage-profondeur	8656-4 She16-718,2	8656-4 She16-718,2	8656-4 She16-718,2	8656-4 She16-718,2	8656-4 She16-718,2	8656-4 She16-718,2	8656-4 She16-718,2	8656-4 She16-718,2	8656-4 She16-718,2	8656-4 She16-718,2	8656-4 She16-718,2	8656-4 She16-718,2	8656-4 She16-718,2
Numéro d'analyse	0-G1_9_6	0-G1_9_7	0-G1_9_8	0-G1_9_9	0-G1_9_10	0-G1_9_11	0-G1_9_12	0-G1_9_13	0-G1_9_14	0-G1_10_1	0-G1_10_2	0-G1_10_3	0-G1_10_4
Minéral	uraninite	uraninite	uraninite	uraninite	uraninite	uraninite	uraninite	uraninite	uraninite	uraninite	uraninite	uraninite	uraninite
SiO2	0,270	0,301	0,271	0,257	0,407	0,232	0,335	0,235	0,311	0,311	0,368	0,356	0,201
SO3	n.d.	n.d.	n.d.	n.d.	n.d.	n.d.	0,177	n.d.	n.d.	n.d.	n.d.	n.d.	n.d.
CaO	1,187	1,359	1,116	1,010	1,435	1,080	1,034	1,307	1,289	0,847	1,243	1,332	0,859
TiO2	n.d.	n.d.	n.d.	n.d.	n.d.	n.d.	n.d.	n.d.	n.d.	n.d.	n.d.	n.d.	0,225
FeO	n.d.	0,326	n.d.	n.d.	0,646	n.d.	n.d.	n.d.	n.d.	n.d.	n.d.	n.d.	n.d.
As2O3	0,517	0,458	0,459	n.d.	n.d.	n.d.	n.d.	0,401	n.d.	n.d.	0,476	n.d.	n.d.
Y2O3	n.d.	n.d.	n.d.	0,158	0,218	n.d.	n.d.	n.d.	0,159	0,147	n.d.	n.d.	n.d.
Ce2O3	n.d.	n.d.	n.d.	n.d.	n.d.	n.d.	n.d.	n.d.	n.d.	n.d.	n.d.	n.d.	n.d.
Gd2O3	n.d.	n.d.	n.d.	n.d.	n.d.	n.d.	n.d.	n.d.	n.d.	n.d.	n.d.	n.d.	n.d.
Yb2O3	n.d.	n.d.	n.d.	n.d.	n.d.	n.d.	n.d.	n.d.	n.d.	n.d.	n.d.	n.d.	n.d.
PbO	13,936	13,045	13,748	13,882	12,064	15,086	13,029	14,329	13,325	14,561	13,403	13,617	14,603
ThO2	n.d.	n.d.	n.d.	n.d.	n.d.	n.d.	n.d.	n.d.	n.d.	n.d.	n.d.	n.d.	n.d.
UO2	78,845	79,454	78,868	77,230	80,654	76,488	76,954	79,648	78,289	77,638	79,357	78,266	79,622
Total	*94,755*	*94,943*	*94,462*	*92,536*	*95,425*	*92,887*	*91,529*	*95,921*	*93,373*	*93,503*	*94,846*	*93,571*	*95,509*
Age (Ga)	1,169	1,096	1,155	1,187	1,008	1,287	1,126	1,188	1,131	1,232	1,123	1,153	1,208

Tableau AIV-28 - Compositions en % d'un cristal d'uraninite provenant de la minéralisation à la discordance de Shea Creek. Les âges chimiques sont calculés à l'aide de la formule de Suzuki et Adachi (1994). (n.d. = non détecté)

Echantillons forage-profondeur	8656-4 She16-718,2	8656-4 She16-718,2	8656-4 She16-718,2	8656-4 She16-718,2	8656-4 She16-718,2	8656-4 She16-718,2	8656-4 She16-718,2	8656-4 She16-718,2	8656-4 She16-718,2	8656-4 She16-718,2	8656-4 She16-718,2	8656-4 She16-718,2	8656-4 She16-718,2
Numéro d'analyse	0-G1_10_5	0-G1_10_6	0-G1_10_7	0-G1_10_8	0-G1_10_9	0-G1_10_10	0-G1_10_11	0-G1_10_12	0-G1_10_13	0-G1_10_14	P1-_1	P1-_2	P1-_3
Minéral	uraninite	uraninite	uraninite	uraninite	uraninite	uraninite	uraninite	uraninite	uraninite	uraninite	uraninite	uraninite	uraninite
SiO2	0,207	0,329	0,243	0,309	0,337	0,360	0,226	0,291	0,195	0,294	0,221	0,284	0,228
SO3	n.d.	0,397	n.d.	n.d.	n.d.	n.d.	n.d.	n.d.	n.d.	n.d.	n.d.	n.d.	n.d.
CaO	0,927	1,123	0,866	1,333	1,555	1,185	0,982	1,312	1,005	0,805	1,058	1,105	0,995
TiO2	n.d.	n.d.	n.d.	n.d.	n.d.	n.d.	n.d.	n.d.	n.d.	n.d.	0,188	0,236	n.d.
FeO	n.d.	n.d.	n.d.	n.d.	n.d.	n.d.	n.d.	n.d.	n.d.	n.d.	n.d.	n.d.	n.d.
As2O3	n.d.	0,404	n.d.	0,439	n.d.	n.d.	0,418	n.d.	n.d.	n.d.	n.d.	n.d.	n.d.
Y2O3	n.d.	0,148	n.d.	n.d.	n.d.	0,223	n.d.	0,205	n.d.	n.d.	n.d.	0,126	n.d.
Ce2O3	n.d.	n.d.	n.d.	n.d.	n.d.	n.d.	n.d.	n.d.	n.d.	n.d.	n.d.	n.d.	n.d.
Gd2O3	n.d.	n.d.	n.d.	n.d.	n.d.	n.d.	n.d.	n.d.	n.d.	n.d.	n.d.	n.d.	n.d.
Yb2O3	n.d.	n.d.	n.d.	n.d.	n.d.	n.d.	n.d.	n.d.	n.d.	n.d.	n.d.	n.d.	n.d.
PbO	13,550	13,661	15,074	13,331	12,901	13,066	14,508	13,299	15,217	14,283	13,444	12,069	13,830
ThO2	n.d.	n.d.	n.d.	n.d.	n.d.	n.d.	n.d.	n.d.	n.d.	n.d.	n.d.	n.d.	n.d.
UO2	78,604	78,418	78,574	78,728	78,939	78,430	78,941	78,673	78,645	77,777	79,946	78,584	78,053
Total	*93,287*	*94,479*	*94,757*	*94,140*	*93,731*	*93,264*	*95,075*	*93,780*	*95,061*	*93,158*	*94,857*	*92,404*	*93,105*
Age (Ga)	1,144	1,155	1,256	1,126	1,091	1,110	1,210	1,124	1,266	1,209	1,119	1,032	1,172

Echantillons forage-profondeur	8656-4 She16-718,2	8656-4 She16-718,2	8656-4 She16-718,2	8656-4 She16-718,2	8656-4 She16-718,2	8656-4 She16-718,2	8656-4 She16-718,2	8656-4 She16-718,2	8656-4 She16-718,2	8656-4 She16-718,2	8656-4 She16-718,2	8656-4 She16-718,2	8656-4 She16-718,2
Numéro d'analyse	P1-_4	P1-_5	P2-1	P2-2	P2-3	P2-4	P2-5	P2-6	2/P3-_1	2/P3-_2	2/P3-_3	2/P3-_4	2/P3-5
Minéral	uraninite	uraninite	uraninite	uraninite	UO2-coffinite	UO2-coffinite	uraninite	UO2-coffinite	uraninite	uraninite	uraninite	uraninite	UO2-coffinite
SiO2	0,235	0,162	1,177	0,876	6,651	5,384	0,169	6,069	0,146	0,283	0,148	1,058	4,591
SO3	n.d.	n.d.	n.d.	n.d.	n.d.	0,930	n.d.	0,608	n.d.	n.d.	n.d.	n.d.	n.d.
CaO	1,299	0,859	0,989	0,961	1,031	1,236	0,908	0,886	1,228	1,283	1,234	1,786	1,799
TiO2	0,483	0,202	n.d.	n.d.	0,279	0,443	n.d.	0,606	n.d.	0,320	0,186	n.d.	0,380
FeO	n.d.	n.d.	n.d.	n.d.	0,327	n.d.	n.d.	0,295	n.d.	0,277	n.d.	0,306	0,824
As2O3	n.d.	n.d.	n.d.	n.d.	n.d.	n.d.	n.d.	n.d.	n.d.	n.d.	n.d.	n.d.	n.d.
Y2O3	0,157	n.d.	0,112	n.d.	1,127	0,212	n.d.	0,913	0,089	0,161	0,117	0,215	n.d.
Ce2O3	n.d.	n.d.	n.d.	n.d.	n.d.	n.d.	n.d.	n.d.	n.d.	n.d.	n.d.	n.d.	n.d.
Gd2O3	n.d.	n.d.	n.d.	n.d.	0,272	n.d.	n.d.	0,350	n.d.	n.d.	n.d.	n.d.	n.d.
Yb2O3	n.d.	n.d.	n.d.	n.d.	n.d.	n.d.	n.d.	n.d.	n.d.	n.d.	n.d.	n.d.	n.d.
PbO	12,288	13,639	12,278	13,401	6,036	9,338	14,176	6,719	12,604	11,555	12,412	11,410	0,631
ThO2	n.d.	n.d.	n.d.	n.d.	n.d.	n.d.	n.d.	n.d.	n.d.	n.d.	n.d.	n.d.	n.d.
UO2	79,255	78,555	77,141	77,334	74,434	72,141	77,956	70,230	77,301	79,307	79,904	79,864	81,869
Total	*93,716*	*93,417*	*91,697*	*92,572*	*90,156*	*89,683*	*93,209*	*86,674*	*91,369*	*93,185*	*94,000*	*94,639*	*90,093*
Age (Ga)	1,041	1,151	1,066	1,149	0,573	0,885	1,199	0,669	1,089	0,985	1,043	0,967	0,057

Tableau AIV-29 - Compositions en % d'uraninites et de coffinites provenant de la minéralisation à la discordance de Shea Creek. Les âges chimiques sont calculés à l'aide de la formule de Suzuki et Adachi (1994). (n.d. = non détecté)

Echantillons forage-profondeur	8656-4 She16-718,2	8656-4 She16-718,2	8656-4 She16-718,2	8656-4 She16-718,2	8656-4 She16-718,2	8656-4 She16-718,2	8656-4 She16-718,2	8656-4 She16-718,2	8656-4 She16-718,2	8656-4 She16-718,2	8656-4 She16-718,2	8656-4 She16-718,2	8656-4 She16-718,2
Numéro d'analyse	2/P3-6	2/P3-7	2/P3-8	2/P3-9	3/P4-_1	3/P4-_2	3/P4-_3	3/P4-_4	3/P4-_5	3/P4-_6	3/P4-_7	3/P4-_8	3/P4-_9
Minéral	UO2-coffinite	coffinite	uraninite	uraninite	uraninite	uraninite	uraninite	uraninite	uraninite	uraninite	uraninite	uraninite	uraninite
SiO2	7,126	10,748	0,362	0,439	0,138	0,078	0,188	0,088	0,549	0,124	0,163	0,156	0,166
SO3	n.d.	n.d.	n.d.	n.d.	n.d.	n.d.	n.d.	n.d.	n.d.	n.d.	n.d.	n.d.	0,292
CaO	1,661	0,808	1,708	0,949	1,199	0,962	1,213	1,027	1,166	1,479	1,106	0,925	1,126
TiO2	0,707	0,706	0,459	n.d.	n.d.	n.d.	n.d.	n.d.	n.d.	n.d.	n.d.	n.d.	n.d.
FeO	0,844	0,417	n.d.	n.d.	n.d.	n.d.	n.d.	n.d.	0,296	n.d.	n.d.	n.d.	n.d.
As2O3	n.d.	0,649	n.d.	n.d.	n.d.	n.d.	n.d.	n.d.	0,494	n.d.	n.d.	n.d.	n.d.
Y2O3	n.d.	0,308	0,210	n.d.	0,093	n.d.	0,137	n.d.	n.d.	0,150	n.d.	n.d.	n.d.
Ce2O3	n.d.	n.d.	n.d.	n.d.	n.d.	n.d.	n.d.	n.d.	n.d.	n.d.	n.d.	n.d.	n.d.
Gd2O3	n.d.	n.d.	n.d.	n.d.	n.d.	n.d.	n.d.	n.d.	n.d.	n.d.	n.d.	n.d.	n.d.
Yb2O3	n.d.	n.d.	n.d.	n.d.	n.d.	n.d.	n.d.	n.d.	n.d.	n.d.	n.d.	n.d.	n.d.
PbO	1,074	0,554	12,535	12,358	12,921	14,470	12,901	14,291	13,464	12,483	14,180	13,969	13,946
ThO2	n.d.	n.d.	n.d.	n.d.	n.d.	n.d.	n.d.	n.d.	n.d.	n.d.	n.d.	n.d.	n.d.
UO2	79,308	74,156	78,581	80,250	80,099	76,912	79,271	77,067	77,276	77,677	78,133	77,183	77,610
Total	*90,720*	*88,346*	*93,855*	*93,995*	*94,450*	*92,422*	*93,710*	*92,474*	*93,244*	*91,913*	*93,583*	*92,233*	*93,140*
Age (Ga)	0,100	0,056	1,068	1,035	1,079	1,235	1,087	1,220	1,155	1,075	1,197	1,194	1,187

Echantillons forage-profondeur	8656-4 She16-718,2	8656-4 She16-718,2	8656-4 She16-718,2	8656-4 She16-718,2	8656-4 She16-718,2	8656-4 She16-718,2	8656-4 She16-718,2	8656-4 She16-718,2	8656-4 She16-718,2	8656-4 She16-718,2	8656-4 She16-718,2	8656-4 She16-718,2	8656-4 She16-718,2
Numéro d'analyse	3/P4-_10	4/P5-_1	4/P5-_2	4/P5-_3	4/P5-_4	4/P5-_5	4/P5-_6	4/P5-_7	4/P5-_8	4/P5-_9	4/P5-_10	5/P6-_1	5/P6-_2
Minéral	uraninite	uraninite	uraninite	uraninite	UO2-coffinite	UO2-coffinite	UO2-coffinite	UO2-coffinite	uraninite	uraninite	UO2-coffinite	uraninite	uraninite
SiO2	0,451	0,160	0,194	0,075	6,465	7,422	7,224	12,230	1,433	0,167	4,031	0,127	1,126
SO3	n.d.	n.d.	n.d.	n.d.	n.d.	n.d.	n.d.	n.d.	n.d.	n.d.	0,332	n.d.	n.d.
CaO	1,197	0,905	1,146	0,818	1,724	1,360	1,147	0,831	1,503	0,893	2,228	1,084	1,339
TiO2	0,289	n.d.	n.d.	n.d.	0,211	0,605	0,204	n.d.	0,601	0,261	0,214	n.d.	0,286
FeO	0,409	n.d.	0,294	n.d.	0,510	0,674	0,576	0,492	0,445	n.d.	0,819	n.d.	0,471
As2O3	0,504	n.d.	n.d.	n.d.	n.d.	n.d.	n.d.	0,514	n.d.	n.d.	0,455	n.d.	n.d.
Y2O3	n.d.	n.d.	n.d.	n.d.	n.d.	0,241	0,097	0,462	n.d.	n.d.	n.d.	n.d.	n.d.
Ce2O3	n.d.	n.d.	n.d.	n.d.	n.d.	n.d.	n.d.	n.d.	n.d.	n.d.	n.d.	n.d.	n.d.
Gd2O3	n.d.	n.d.	n.d.	n.d.	n.d.	n.d.	n.d.	n.d.	n.d.	n.d.	n.d.	n.d.	n.d.
Yb2O3	n.d.	n.d.	n.d.	n.d.	n.d.	n.d.	n.d.	n.d.	n.d.	n.d.	n.d.	n.d.	n.d.
PbO	11,628	14,216	14,000	14,738	0,558	0,608	2,185	0,513	10,354	14,148	1,613	14,259	10,655
ThO2	n.d.	n.d.	n.d.	n.d.	n.d.	n.d.	n.d.	n.d.	n.d.	n.d.	n.d.	n.d.	n.d.
UO2	78,551	78,139	79,705	78,071	79,536	79,235	77,994	72,278	80,873	78,207	74,705	77,279	80,029
Total	*93,029*	*93,420*	*95,338*	*93,702*	*89,004*	*90,144*	*89,427*	*87,320*	*95,207*	*93,677*	*84,397*	*92,749*	*93,906*
Age (Ga)	0,999	1,199	1,163	1,239	0,052	0,057	0,205	0,053	0,876	1,194	0,159	1,214	0,908

Tableau AIV-30 - Compositions en % d'uraninites et de coffinites provenant de la minéralisation à la discordance de Shea Creek. Les âges chimiques sont calculés à l'aide de la formule de Suzuki et Adachi (1994). (n.d. = non détecté)

Echantillons forage-profondeur	8656-4 She16-718,2	8656-4 She16-718,2	8656-4 She16-718,2	8656-4 She16-718,2	8656-4 She16-718,2	8656-4 She16-718,2	8656-4 She16-718,2	8656-4 She16-718,2	8656-4 She16-718,2	8656-4 She16-718,2	8656-4 She16-718,2	8656-4 She16-718,2	Shea46 She87-710,1
Numéro d'analyse	5/P6-_3	5/P6-_4	5/P6-_5	5/P6-_6	5/P6-_7	5/P6-_8	5/P6-_9	5/P6-10	5-11	5-12	5-13	5-14	3-1
Minéral	UO2-coff.	pechblende	UO2-coff.	UO2-coff.	coffinite	UO2-coff.	coffinite	coffinite	uraninite	uraninite	pechblende	UO2-coff.	UO2-coff.
SiO2	4,580	0,766	5,868	6,860	9,155	6,442	9,868	9,619	0,969	0,332	2,600	5,490	4,299
SO3	n.d.	n.d.	n.d.	n.d.	n.d.	n.d.	n.d.	n.d.	n.d.	n.d.	n.d.	0,426	n.d.
CaO	1,626	1,096	1,842	1,147	1,310	1,610	0,928	1,366	1,289	1,258	1,546	1,718	9,524
TiO2	0,428	n.d.	0,185	n.d.	n.d.	0,242	n.d.	n.d.	n.d.	0,228	0,595	0,652	11,624
FeO	0,716	n.d.	0,601	0,725	0,736	0,722	0,446	0,506	n.d.	n.d.	0,654	0,815	0,462
As2O3	n.d.	n.d.	n.d.	n.d.	0,676	0,624	n.d.	n.d.	n.d.	n.d.	n.d.	n.d.	n.d.
Y2O3	n.d.	n.d.	0,090	0,194	0,448	n.d.	0,459	0,710	0,157	0,110	n.d.	n.d.	0,204
Ce2O3	n.d.	n.d.	n.d.	n.d.	n.d.	n.d.	n.d.	n.d.	n.d.	n.d.	n.d.	n.d.	n.d.
Gd2O3	n.d.	n.d.	n.d.	n.d.	n.d.	n.d.	n.d.	0,211	n.d.	n.d.	n.d.	n.d.	n.d.
Yb2O3	n.d.	n.d.	n.d.	n.d.	n.d.	n.d.	n.d.	n.d.	n.d.	n.d.	n.d.	n.d.	n.d.
PbO	4,347	12,166	0,949	0,736	0,981	0,959	0,480	0,771	11,993	13,362	7,547	3,889	0,861
ThO2	n.d.	n.d.	n.d.	n.d.	n.d.	n.d.	n.d.	n.d.	n.d.	n.d.	n.d.	n.d.	n.d.
UO2	79,528	78,193	80,871	79,240	77,470	80,399	74,276	74,836	79,311	78,496	79,238	78,240	52,183
Total	*91,223*	*92,221*	*90,404*	*88,902*	*90,777*	*90,998*	*86,457*	*88,019*	*93,720*	*93,785*	*92,180*	*91,229*	*79,155*
Age (Ga)	0,393	1,044	0,087	0,069	0,094	0,088	0,048	0,076	1,018	1,131	0,666	0,359	0,122

Echantillons forage-profondeur	Shea46 She87-710,1	Shea46 She87-710,1	Shea46 She87-710,1	Shea46 She87-710,1	Shea46 She87-710,1	Shea46 She87-710,1	Shea46 She87-710,1	Shea46 She87-710,1	Shea46 She87-710,1	Shea46 She87-710,1	Shea46 She87-710,1	Shea46 She87-710,1	Shea46 She87-710,1
Numéro d'analyse	3-2	3-4	4/P1-_1	4/P1-_2	4/P1-_3	4/P1-_4	4/P1-_5	4/P1-_6	4-7	4-8	4-9	4-10	4-11
Minéral	UO2-coff.	pechblende	pechblende	pechblende	pechblende	pechblende	pechblende	pechblende	pechblende	pechblende	pechblende	UO2-coff.	UO2-coff.
SiO2	5,418	0,763	0,864	0,635	0,869	0,815	1,676	2,516	2,451	2,983	2,788	4,168	3,709
SO3	n.d.	n.d.	n.d.	n.d.	n.d.	n.d.	n.d.	n.d.	n.d.	n.d.	n.d.	n.d.	n.d.
CaO	3,238	4,637	1,996	2,218	2,052	2,410	2,827	5,158	4,656	5,026	4,944	5,512	7,059
TiO2	23,524	0,234	n.d.	n.d.	n.d.	n.d.	0,354	1,017	1,768	n.d.	n.d.	n.d.	n.d.
FeO	1,268	n.d.	0,314	n.d.	n.d.	0,488	0,836	1,131	1,201	1,116	1,194	0,606	0,610
As2O3	n.d.	n.d.	n.d.	n.d.	n.d.	n.d.	n.d.	n.d.	n.d.	n.d.	n.d.	n.d.	n.d.
Y2O3	0,186	0,518	0,295	0,275	0,284	0,316	0,410	1,023	0,941	1,167	1,535	9,846	6,007
Ce2O3	n.d.	0,243	n.d.	n.d.	n.d.	n.d.	n.d.	0,410	0,271	0,413	0,373	0,294	0,243
Gd2O3	n.d.	n.d.	n.d.	n.d.	n.d.	n.d.	n.d.	0,347	0,267	n.d.	0,479	1,060	0,717
Yb2O3	n.d.	n.d.	n.d.	n.d.	n.d.	n.d.	n.d.	n.d.	n.d.	n.d.	n.d.	n.d.	n.d.
PbO	0,447	1,707	4,065	3,899	4,248	3,314	1,508	1,612	1,960	1,559	1,728	1,042	1,270
ThO2	n.d.	n.d.	n.d.	n.d.	n.d.	n.d.	n.d.	n.d.	n.d.	n.d.	n.d.	n.d.	n.d.
UO2	48,476	80,940	83,385	84,506	82,664	82,861	82,809	73,640	75,293	76,006	74,328	58,692	60,616
Total	*82,556*	*89,042*	*90,919*	*91,533*	*90,117*	*90,206*	*90,420*	*86,854*	*88,807*	*88,270*	*87,368*	*81,220*	*80,230*
Age (Ga)	0,069	0,155	0,352	0,334	0,371	0,291	0,134	0,161	0,191	0,151	0,171	0,131	0,154

Tableau AIV-31 - Compositions en % d'uraninites, de pechblendes et de coffinites provenant de la minéralisation à la discordance de Shea Creek. Les âges chimiques sont calculés à l'aide de la formule de Suzuki et Adachi (1994). (n.d. = non détecté ; coff. = coffinite)

Echantillons forage-profondeur	Shea46 She87-710,1	Shea46 She87-710,1	Shea46 She87-710,1	Shea46 She87-710,1	Shea46 She87-710,1	Shea46 She87-710,1	Shea46 She87-710,1	Shea46 She87-710,1	Shea46 She87-710,1	Shea46 She87-710,1	Shea46 She87-710,1	Shea46 She87-710,1	Shea46 She87-710,1
Numéro d'analyse	4-12	4-13	5-1	5-2	5-3	5-4	7-1	7-2	7-3	7-4	7-5	7-6	7-7
Minéral	UO2-coffinite	UO2-coffinite	pechblende	pechblende	UO2-coffinite	UO2-coffinite	UO2-coffinite	UO2-coffinite	UO2-coffinite	UO2-coffinite	pechblende	pechblende	pechblende
SiO2	5,720	6,421	3,200	2,205	6,879	5,227	5,138	4,701	5,651	4,718	0,988	1,229	1,173
SO3	n.d.	n.d.	n.d.	n.d.	n.d.	n.d.	n.d.	n.d.	n.d.	n.d.	n.d.	n.d.	n.d.
CaO	5,460	5,281	6,085	8,922	4,953	5,789	5,166	5,526	6,529	5,339	3,494	2,067	3,146
TiO2	n.d.	n.d.	0,700	n.d.	0,460	0,442	n.d.	0,519	6,128	4,469	0,629	1,450	2,048
FeO	n.d.	n.d.	0,443	0,334	n.d.	0,406	0,464	0,550	n.d.	0,531	n.d.	0,638	0,689
As2O3	n.d.	n.d.	n.d.	n.d.	n.d.	n.d.	n.d.	n.d.	n.d.	n.d.	n.d.	n.d.	n.d.
Y2O3	13,603	14,092	4,309	0,319	17,455	14,324	0,875	0,701	0,575	0,615	0,508	0,453	0,505
Ce2O3	0,172	0,181	0,407	0,269	0,193	0,351	0,297	0,348	0,427	0,380	0,188	0,206	0,277
Gd2O3	1,298	1,406	0,551	0,232	1,707	1,407	0,345	0,355	0,290	0,249	n.d.	n.d.	n.d.
Yb2O3	0,416	0,384	n.d.	n.d.	n.d.	n.d.	n.d.	n.d.	n.d.	n.d.	n.d.	n.d.	n.d.
PbO	0,756	0,617	1,384	2,769	0,299	0,783	0,976	1,243	1,925	1,885	1,670	1,094	1,089
ThO2	n.d.	n.d.	n.d.	n.d.	n.d.	n.d.	n.d.	n.d.	0,523	0,308	n.d.	n.d.	n.d.
UO2	47,871	45,699	64,575	66,908	34,340	48,160	69,802	69,760	63,880	70,707	81,643	81,684	78,427
Total	*75,296*	*74,081*	*81,655*	*81,958*	*66,286*	*76,889*	*83,062*	*83,704*	*85,928*	*89,201*	*89,121*	*88,820*	*87,352*
Age (Ga)	0,117	0,100	0,158	0,301	0,065	0,120	0,104	0,132	0,220	0,195	0,151	0,099	0,103

Echantillons forage-profondeur	Shea46 She87-710,1	Shea46 She87-710,1	Shea46 She87-710,1	Shea46 She87-710,1	Shea46 She87-710,1	Shea46 She87-710,1	Shea46 She87-710,1	Shea46 She87-710,1	Shea46 She87-710,1	Shea46 She87-710,1	Shea46 She87-710,1	Shea46 She87-710,1	Shea46 She87-710,1
Numéro d'analyse	7-8	7-9	7-10	7-11	7-12	7-13	7-14	7-15	10-1	10-2	10-3	10-4	10-5
Minéral	pechblende	pechblende	pechblende	pechblende	pechblende	pechblende	pechblende	UO2-coff.	pechblende	pechblende	pechblende	pechblende	UO2-coff.
SiO2	1,085	0,494	0,683	0,664	1,542	2,805	2,860	3,771	0,695	1,712	2,712	2,031	3,515
SO3	n.d.	n.d.	n.d.	n.d.	n.d.	n.d.	n.d.	n.d.	n.d.	n.d.	n.d.	n.d.	n.d.
CaO	3,268	1,802	1,819	1,738	3,570	3,624	4,447	5,355	2,058	4,669	6,038	6,828	6,002
TiO2	1,938	1,444	0,466	0,429	n.d.	n.d.	n.d.	3,955	n.d.	2,447	3,793	0,289	4,323
FeO	0,666	0,465	n.d.	n.d.	1,000	0,820	0,453	0,493	n.d.	0,640	0,712	0,471	0,636
As2O3	n.d.	n.d.	n.d.	n.d.	n.d.	n.d.	n.d.	n.d.	n.d.	n.d.	n.d.	n.d.	n.d.
Y2O3	0,474	0,117	0,240	0,266	0,515	0,914	1,034	0,600	0,243	0,627	0,625	1,512	0,604
Ce2O3	0,205	n.d.	n.d.	n.d.	0,172	0,411	0,347	0,293	n.d.	0,303	n.d.	0,212	0,377
Gd2O3	0,214	n.d.	n.d.	n.d.	n.d.	0,330	0,395	n.d.	n.d.	n.d.	n.d.	0,394	n.d.
Yb2O3	n.d.	n.d.	n.d.	n.d.	n.d.	n.d.	n.d.	n.d.	n.d.	n.d.	n.d.	n.d.	n.d.
PbO	1,205	2,854	3,749	3,575	1,120	1,337	1,150	1,867	3,891	1,330	1,869	1,196	1,978
ThO2	n.d.	n.d.	n.d.	n.d.	n.d.	n.d.	n.d.	0,342	n.d.	n.d.	n.d.	n.d.	n.d.
UO2	79,494	86,054	84,626	85,152	80,040	78,972	77,287	69,767	83,814	76,144	72,051	72,653	70,893
Total	*88,549*	*93,230*	*91,584*	*91,825*	*87,960*	*89,211*	*87,973*	*86,443*	*90,700*	*87,870*	*87,799*	*85,587*	*88,328*
Age (Ga)	0,112	0,242	0,321	0,305	0,104	0,125	0,110	0,196	0,336	0,129	0,191	0,122	0,205

Tableau AIV-32 - Compositions en % d'uraninites, de pechblendes et de coffinites provenant de la minéralisation à la discordance de Shea Creek. Les âges chimiques sont calculés à l'aide de la formule de Suzuki et Adachi (1994). (n.d. = non détecté ; coff. = coffinite)

Echantillons forage-profondeur	Shea46 She87-710,1	Shea46 She87-710,1	Shea46 She87-710,1	Shea46 She87-710,1	Shea46 She87-710,1	Shea46 She87-710,1	Shea46 She87-710,1	Shea46 She87-710,1	Shea46 She87-710,1	Shea46 She87-710,1	Shea46 She87-710,1	Shea46 She87-710,1	Shea46 She87-710,1
Numéro d'analyse	10-6	10-7	10-8	10-9	9-P2bis_1	9-P2bis_2	9-P2bis_3	9-P2bis_4	9-P2bis_5	9-P2bis_6	9-P2bis_7	9-P2bis_8	9-P2bis_9
Minéral	pechblende	pechblende	pechblende	pechblende	coffinite	UO2-coffinite	pechblende	UO2-coffinite	UO2-coffinite	UO2-coffinite	pechblende	UO2-coffinite	pechblende
SiO2	0,538	1,461	0,793	0,610	7,567	3,821	1,699	3,675	4,472	4,221	3,754	6,010	3,284
SO3	n.d.	n.d.	n.d.	n.d.	n.d.	n.d.	n.d.	n.d.	n.d.	n.d.	n.d.	n.d.	n.d.
CaO	1,966	2,795	1,992	1,989	9,814	4,506	3,646	7,291	6,180	6,945	7,437	6,488	6,220
TiO2	n.d.	0,979	n.d.	n.d.	0,564	4,060	1,307	2,021	1,560	1,561	2,065	0,980	n.d.
FeO	0,328	0,945	0,366	0,328	0,250	0,328	0,698	0,928	0,636	0,968	0,681	0,466	0,681
As2O3	n.d.	n.d.	n.d.	n.d.	n.d.	n.d.	n.d.	n.d.	n.d.	n.d.	n.d.	n.d.	n.d.
Y2O3	0,210	0,766	0,264	0,189	15,890	2,749	0,495	1,633	6,822	2,580	1,458	11,041	7,667
Ce2O3	n.d.	0,317	n.d.	n.d.	0,195	0,171	n.d.	0,382	0,322	0,421	0,335	0,231	0,171
Gd2O3	n.d.	0,220	n.d.	n.d.	1,676	0,452	n.d.	n.d.	1,013	n.d.	n.d.	1,129	1,102
Yb2O3	n.d.	n.d.	n.d.	n.d.	n.d.	n.d.	n.d.	n.d.	n.d.	n.d.	n.d.	n.d.	n.d.
PbO	3,591	1,062	4,257	3,879	0,336	1,184	1,400	1,585	1,392	1,535	1,832	0,819	1,144
ThO2	n.d.	n.d.	n.d.	n.d.	n.d.	n.d.	n.d.	n.d.	n.d.	n.d.	n.d.	n.d.	n.d.
UO2	84,295	77,549	84,215	83,366	27,216	63,492	82,598	61,826	62,755	62,992	64,177	50,876	73,688
Total	*90,928*	*86,094*	*91,887*	*90,360*	*63,509*	*80,763*	*91,844*	*79,340*	*85,151*	*81,224*	*81,739*	*78,040*	*93,957*
Age (Ga)	0,309	0,101	0,365	0,337	0,092	0,138	0,125	0,188	0,163	0,179	0,209	0,119	0,115

Echantillons forage-profondeur	Shea46 She87-710,1	Shea46 She87-710,1	Shea46 She87-710,1	Shea46 She87-710,1	Shea46 She87-710,1	Shea46 She87-710,1	Shea46 She87-710,1	Shea46 She87-710,1	Shea46 She87-710,1	Shea46 She87-710,1	Shea46 She87-710,1	Shea46 She87-710,1	Shea46 She87-710,1
Numéro d'analyse	9-P2bis_10	9-P2bis_11	10-P10_1	10-P10_2	10-P10_3	10-P10_4	10-P10_5	10-P10_6	10-P10_7	10-P10_8	10-P10_9	10-P10_10	4-P11_1
Minéral	pechblende	UO2-coff.	pechblende	pechblende	pechblende	pechblende	pechblende	pechblende	pechblende	pechblende	pechblende	pechblende	pechblende
SiO2	2,481	6,116	0,932	0,874	0,835	0,993	1,052	1,058	0,823	0,967	1,018	1,261	1,164
SO3	n.d.	n.d.	n.d.	n.d.	n.d.	n.d.	n.d.	n.d.	n.d.	n.d.	n.d.	n.d.	n.d.
CaO	7,893	6,709	2,059	2,193	2,077	1,868	2,086	1,883	2,540	2,063	2,312	1,930	1,910
TiO2	n.d.	n.d.	n.d.	0,281	0,674	n.d.	0,225	n.d.	0,209	n.d.	n.d.	n.d.	n.d.
FeO	0,740	n.d.	n.d.	0,321	0,420	0,404	n.d.	0,364	n.d.	n.d.	0,330	n.d.	n.d.
As2O3	n.d.	n.d.	n.d.	n.d.	n.d.	n.d.	n.d.	n.d.	n.d.	n.d.	n.d.	n.d.	n.d.
Y2O3	1,119	16,321	0,301	0,199	n.d.	0,196	0,261	0,157	0,251	0,179	0,259	0,207	0,205
Ce2O3	0,224	0,232	n.d.	n.d.	n.d.	n.d.	n.d.	n.d.	n.d.	n.d.	n.d.	n.d.	n.d.
Gd2O3	n.d.	1,693	n.d.	n.d.	n.d.	n.d.	n.d.	n.d.	n.d.	n.d.	n.d.	n.d.	n.d.
Yb2O3	n.d.	0,624	n.d.	n.d.	n.d.	n.d.	n.d.	n.d.	n.d.	n.d.	n.d.	n.d.	n.d.
PbO	1,285	n.d.	4,701	4,044	3,662	4,017	4,355	4,561	4,638	5,052	4,343	4,493	4,451
ThO2	n.d.	n.d.	n.d.	n.d.	n.d.	n.d.	n.d.	n.d.	n.d.	n.d.	n.d.	n.d.	n.d.
UO2	72,852	29,116	86,023	86,227	87,877	87,030	84,878	85,733	86,086	86,035	86,263	86,647	85,217
Total	*86,593*	*60,810*	*94,016*	*94,139*	*95,545*	*94,508*	*92,857*	*93,756*	*94,547*	*94,295*	*94,526*	*94,538*	*92,948*
Age (Ga)	0,130	-	0,393	0,339	0,303	0,334	0,370	0,383	0,388	0,421	0,364	0,374	0,377

Tableau AIV-33 - Compositions en % d'uraninites, de pechblendes et de coffinites provenant de la minéralisation à la discordance de Shea Creek. Les âges chimiques sont calculés à l'aide de la formule de Suzuki et Adachi (1994). (n.d. = non détecté ; coff. = coffinite)

Echantillons forage-profondeur	Shea46 She87-710,1	Shea46 She87-710,1	Shea46 She87-710,1	Shea46 She87-710,1	Shea46 She87-710,1	Shea46 She87-710,1	Shea46 She87-710,1	Shea46 She87-710,1	Shea46 She87-710,1	Shea46 She87-710,1	Shea46 She87-710,1	Shea46 She87-710,1	Shea46 She87-710,1
Numéro d'analyse	4-P11_2	4-P11_3	4-P11_4	4-P11_5	4-P11_6	4-P11_7	4-P11_8	4-P11_9	4-P11_10	4-P11_11	4-P11_12	4-P11_13	4-P11_14
Minéral	pechblende	pechblende	pechblende	pechblende	pechblende	pechblende	pechblende	pechblende	pechblende	pechblende	pechblende	pechblende	pechblende
SiO2	1,429	1,251	1,138	1,011	1,248	1,341	1,183	1,486	2,060	2,252	1,983	2,029	3,406
SO3	n.d.	n.d.	n.d.	n.d.	n.d.	n.d.	n.d.	n.d.	n.d.	n.d.	n.d.	n.d.	n.d.
CaO	1,988	1,889	2,120	2,311	2,084	2,568	3,377	2,671	1,777	1,577	2,769	2,959	2,118
TiO2	n.d.	n.d.	n.d.	n.d.	n.d.	0,954	0,599	0,361	1,872	1,812	1,711	1,267	1,428
FeO	n.d.	0,431	0,325	n.d.	0,446	0,781	0,900	1,300	1,154	1,113	0,993	0,933	0,888
As2O3	n.d.	n.d.	n.d.	n.d.	n.d.	n.d.	n.d.	n.d.	n.d.	n.d.	n.d.	n.d.	n.d.
Y2O3	0,344	0,320	0,312	0,226	0,359	0,429	0,411	0,414	0,352	0,379	0,493	0,417	0,453
Ce2O3	n.d.	n.d.	n.d.	n.d.	n.d.	0,254	n.d.	0,163	0,233	n.d.	0,257	0,191	0,204
Gd2O3	n.d.	n.d.	n.d.	n.d.	n.d.	n.d.	n.d.	n.d.	n.d.	0,396	n.d.	n.d.	n.d.
Yb2O3	n.d.	n.d.	n.d.	n.d.	n.d.	n.d.	n.d.	n.d.	n.d.	n.d.	n.d.	n.d.	n.d.
PbO	4,503	4,536	4,300	4,041	4,616	1,334	1,513	1,429	1,131	0,757	1,305	1,315	1,010
ThO2	n.d.	n.d.	n.d.	n.d.	n.d.	n.d.	n.d.	n.d.	n.d.	n.d.	n.d.	n.d.	n.d.
UO2	85,231	85,087	86,072	87,285	85,612	84,463	83,881	83,813	84,167	83,108	82,419	81,337	81,828
Total	*93,495*	*93,513*	*94,267*	*94,874*	*94,364*	*92,124*	*91,865*	*91,635*	*92,745*	*91,394*	*91,929*	*90,449*	*91,334*
Age (Ga)	0,381	0,384	0,361	0,335	0,388	0,117	0,133	0,126	0,100	0,068	0,117	0,120	0,092

Echantillons forage-profondeur	Shea46 She87-710,1	Shea46 She87-710,1	Shea46 She87-710,1	Shea46 She87-710,1	Shea46 She87-710,1	Shea46 She87-710,1	Shea3 She16-696,8 (Fe-chlo)	Shea3 She16-696,8 (Fe-chlo)	Shea3 She16-696,8 (Fe-chlo)	Shea3 She16-696,8 (Fe-chlo)	Shea1 She79-709 (Fe-chlo)	Shea1 She79-709 (Fe-chlo)	Shea1 She79-709 (Fe-chlo)
Numéro d'analyse	4-P11_15	4-P11_16	4-P11_17	4-P11_18	4-P11_19	4-P11_20	3C/3-1	3C/3-2	3D/2-1	3D/2-2	1B/2-1	1B/2-2	1B/2-3
Minéral	pechblende	pechblende	pechblende	pechblende	pechblende	pechblende	coffinite	coffinite	UO2-coff.	UO2-coff.	pechblende	pechblende	pechblende
SiO2	2,080	1,267	1,916	2,113	1,721	1,289	10,917	9,336	4,669	5,039	3,738	3,673	2,132
SO3	n.d.	n.d.	n.d.	n.d.	n.d.	n.d.	2,899	2,720	n.d.	0,243	n.d.	0,268	0,150
CaO	1,941	4,045	2,869	2,515	2,611	3,549	2,141	2,828	1,490	1,353	2,057	2,029	3,559
TiO2	1,322	n.d.	0,240	0,507	0,370	n.d.	0,291	0,390	n.d.	n.d.	0,224	0,329	0,592
FeO	0,889	n.d.	1,086	1,163	1,141	1,051	-	-	-	-	-	-	-
As2O3	n.d.	n.d.	n.d.	n.d.	n.d.	n.d.	1,237	0,745	0,431	0,653	n.d.	n.d.	0,569
Y2O3	0,418	0,615	0,588	0,492	0,419	0,591	1,072	1,020	n.d.	n.d.	n.d.	n.d.	n.d.
Ce2O3	0,258	0,228	0,240	0,168	0,194	n.d.	0,310	0,262	n.d.	n.d.	n.d.	n.d.	n.d.
Gd2O3	n.d.	n.d.	n.d.	n.d.	n.d.	n.d.	0,428	0,418	n.d.	n.d.	n.d.	n.d.	n.d.
Yb2O3	n.d.	n.d.	n.d.	n.d.	n.d.	n.d.	n.d.	n.d.	n.d.	n.d.	n.d.	n.d.	n.d.
PbO	1,122	1,768	1,218	1,172	1,111	1,475	0,630	0,657	0,251	1,163	0,307	0,239	0,616
ThO2	n.d.	n.d.	n.d.	n.d.	n.d.	n.d.	0,206	0,229	n.d.	n.d.	n.d.	n.d.	0,152
UO2	83,987	81,967	80,881	83,568	82,753	81,769	61,403	58,467	81,711	76,845	81,825	82,098	74,104
Total	*92,016*	*89,889*	*89,036*	*91,698*	*90,319*	*89,724*	*81,534*	*77,070*	*88,552*	*85,296*	*88,151*	*88,636*	*81,875*
Age (Ga)	0,099	0,159	0,111	0,104	0,099	0,133	0,076	0,083	0,023	0,112	0,028	0,022	0,062

Tableau AIV-34 - Compositions en % d'uraninites, de pechblendes et de coffinites provenant de la minéralisation à la discordance de Shea Creek et de celle associée aux brèches à Fe-chlorite. Les âges chimiques sont calculés à l'aide de la formule de Suzuki et Adachi (1994). (n.d. = non détecté ; coff. = coffinite)

Echantillons	Shea1	Shea1	Shea1	Shea1	Shea1	Shea1	Shea1	Shea1	Shea3	Shea3

forage-profondeur	She79-709 (Fe-chlo)	She79-709 (Fe-chlo)	She79-709 (Fe-chlo)	She79-709 (Fe-chlo)	She79-709 (Fe-chlo)	She79-709 (Fe-chlo)	She79-709 (Fe-chlo)	She79-709 (Fe-chlo)	She16-696,8 (Fe-chlo)	She16-696,8 (Fe-chlo)
Numéro d'analyse	1B/2-4	1B/2-5	1B/2-6	1B/2-7	1B/2-8	1B/2-9	1B/2-10	1B/2-11	3D/2-3	3D/2-4
Minéral	pechblende	UO2-coffinite	UO2-coffinite	pechblende	pechblende	pechblende	pechblende	pechblende	pechblende	pechblende
SiO2	1,327	6,781	7,876	1,845	1,408	4,232	3,032	3,935	4,378	4,132
SO3	0,246	0,350	1,208	0,218	0,368	1,398	0,572	0,837	0,397	n.d.
CaO	3,566	5,220	5,462	2,723	2,726	2,920	9,255	5,738	1,923	1,610
TiO2	0,826	n.d.	n.d.	0,890	1,266	3,648	2,762	2,268	n.d.	n.d.
FeO	-	2,308	2,735	3,223	3,424	3,440	2,720	4,292	2,636	2,488
As2O3	0,624	0,485	0,430	n.d.	n.d.	0,708	0,724	0,762	n.d.	n.d.
Y2O3	n.d.	0,757	0,648	n.d.	n.d.	n.d.	n.d.	n.d.	n.d.	n.d.
Ce2O3	n.d.	0,204	0,413	n.d.	n.d.	0,305	0,559	0,379	n.d.	n.d.
Gd2O3	n.d.	n.d.	0,331	n.d.	n.d.	n.d.	n.d.	n.d.	n.d.	n.d.
Yb2O3	n.d.	n.d.	n.d.	n.d.	n.d.	n.d.	n.d.	n.d.	n.d.	n.d.
PbO	0,447	n.d.	n.d.	0,442	0,508	0,623	1,634	1,890	0,462	0,274
ThO2	0,175	n.d.	n.d.	n.d.	n.d.	n.d.	n.d.	0,113	n.d.	n.d.
UO2	72,771	70,277	60,504	78,957	77,309	64,102	55,160	54,480	81,392	80,029
Total	*79,982*	*86,380*	*79,606*	*88,298*	*87,009*	*81,375*	*76,418*	*74,694*	*91,188*	*88,533*
Age (Ga)	0,046	-	-	0,042	0,049	0,072	0,217	0,253	0,042	0,026

Echantillons	Shea3	Shea1	Shea43	Shea43	Shea43	Shea43	Shea43	Shea44	Shea44	Shea40
forage-profondeur	She16-696,8 (Fe-chlo)	She79-709 (Fe-chlo)	She16-718,6 (Fe-chlo)	She16-718,6 (Fe-chlo)	She16-718,6 (Fe-chlo)	She16-718,6 (Fe-chlo)	She16-718,6 (Fe-chlo)	She74-669,5 (hématite)	She74-669,5 (hématite)	She66-668,5 (hématite)
Numéro d'analyse	3D/2-5	1B/2-12	43A/3-1	43A/3-2	43A/3-3	43A/3-4	43A/3-5	44A/2-1	44A/2-2	40A/2-1
Minéral	pechblende	pechblende	pechblende	pechblende	pechblende	coffinite	coffinite	uraninite	uraninite	pechblende
SiO2	3,920	2,822	0,855	0,330	0,362	8,120	9,435	0,097	0,208	1,519
SO3	n.d.	1,216	5,210	3,801	n.d.	n.d.	n.d.	n.d.	n.d.	n.d.
CaO	1,784	0,687	n.d.	n.d.	n.d.	1,115	1,102	1,911	1,843	0,357
TiO2	n.d.	n.d.	n.d.	n.d.	n.d.	n.d.	n.d.	n.d.	n.d.	n.d.
FeO	2,462	8,637	-	43,200	n.d.	1,086	0,372	1,706	1,498	16,121
As2O3	n.d.	1,670	79,995	86,970	91,551	13,791	n.d.	n.d.	n.d.	n.d.
Y2O3	n.d.	n.d.	n.d.	n.d.	n.d.	0,513	0,359	n.d.	n.d.	n.d.
Ce2O3	n.d.	n.d.	n.d.	n.d.	n.d.	n.d.	n.d.	n.d.	n.d.	n.d.
Gd2O3	n.d.	n.d.	n.d.	n.d.	n.d.	n.d.	n.d.	n.d.	n.d.	n.d.
Yb2O3	n.d.	n.d.	n.d.	n.d.	n.d.	n.d.	n.d.	n.d.	n.d.	n.d.
PbO	0,506	n.d.	n.d.	n.d.	n.d.	0,593	0,470	4,242	4,591	2,834
ThO2	n.d.	n.d.	n.d.	n.d.	n.d.	n.d.	n.d.	n.d.	n.d.	n.d.
UO2	82,582	68,345	n.d.	n.d.	n.d.	67,552	71,071	92,853	90,857	76,025
Total	*91,253*	*83,378*	*86,061*	*134,301*	*91,912*	*92,769*	*82,808*	*100,808*	*98,997*	*96,856*
Age (Ga)	0,046	-	0,076	0,083	0,023	0,065	0,049	0,331	0,365	0,272

Tableau AIV-35 - Compositions en % d'uraninites, de pechblendes et de coffinites provenant de la minéralisation associée aux brèches à Fe-chlorite et à hématite à Shea Creek. Les âges chimiques sont calculés à l'aide de la formule de Suzuki et Adachi (1994). (n.d. = non détecté)

V: Spectres Raman de kaolinite/dickite

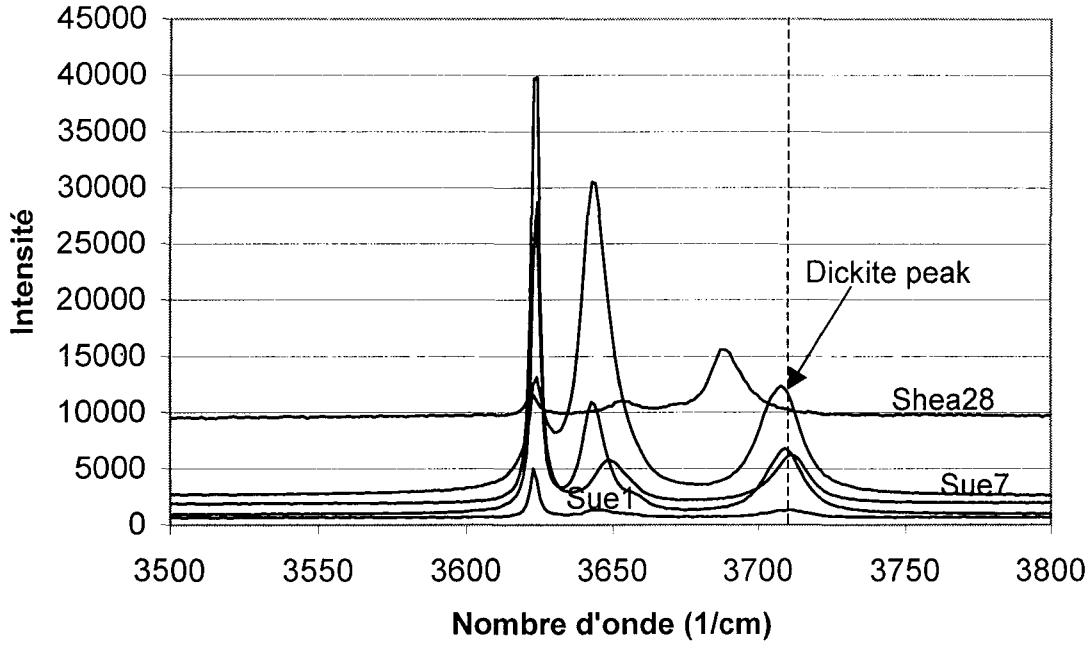

Figure AIV-1 - Spectres Raman de dickites des grès de la Mine à Ciel Ouvert de Sue C et d'un minéral probablement interstratifié kaolinite/dickite dans une brèche à Shea Creek (échantillon Shea28). Le pic vers 3710 cm^{-1} est caractéristique de la dickite (Frost, 1995).

INSTITUT NATIONAL
POLYTECHNIQUE
DE LORRAINE

AUTORISATION DE SOUTENANCE DE THESE DU DOCTORAT DE L'INSTITUT NATIONAL POLYTECHNIQUE DE LORRAINE

o0o

VU LES RAPPORTS ETABLIS PAR :
Monsieur PAGEL Maurice, Professeur, Université Paris Sud XI, Orsay

Monsieur KYSER Kurt, Professeur, Queen's University, Ontario - Canada

Le Président de l'Institut National Polytechnique de Lorraine, autorise :

Monsieur LORILLEUX Guillaume

à soutenir devant un jury de l'INSTITUT NATIONAL POLYTECHNIQUE DE LORRAINE, une thèse intitulée :

"Les brèches associées aux gisements d'uranium de type discordance du bassin Athabasca (Saskatchewan, Canada)".

NANCY BRABOIS
2, AVENUE DE LA
FORET-DE-HAYE
BOITE POSTALE 3
F - 5 4 5 0 1
VANDŒUVRE CEDEX

en vue de l'obtention du titre de :

DOCTEUR DE L'INSTITUT NATIONAL POLYTECHNIQUE DE LORRAINE

Spécialité : « **Géosciences** »

Fait à Vandoeuvre, le 02 février 2001
Le Président de l'I.N.P.L.,
J. HARDY

INSTITUT NATIONAL POLYTECHNIQUE DE LORRAINE - NANCY -

TEL. 33/03.83.59.59.59
FAX. 33/03.83.59.59.55

Résumé : Les gisements d'uranium de type discordance du Bassin Athabasca (Canada) sont fréquemment associés à des corps de brèches qui forment l'encaissant et enveloppent la minéralisation dans des grès quartzeux. Afin de comprendre les mécanismes de formation de ces brèches et leur rôle dans la genèse de ces gisements d'uranium, les brèches associées aux minéralisations en U du prospect de Shea Creek et de la Mine à Ciel Ouvert de Sue C, et à la minéralisation en Y, terres rares et U de la zone de Maw ont été étudiées.

La cartographie structurale et la modélisation 3D mettent en évidence le contrôle de la géométrie des brèches par des failles généralement inverses et graphiteuses dans le socle. L'étude des paragenèses minérales et les calculs d'âges chimiques U-Pb à Shea Creek mettent en évidence 3 phases de bréchification à sudoite-dravite, à Fe-chlorite et à hématite-sidérite. Elles sont respectivement contemporaines de 3 épisodes de réactivations tectoniques et/ou de surrection du bassin entre 1,52 et 1,25 Ga pendant la principale phase de dépôt des minéralisations à haute teneur et vers 900 et 350 Ma au cours de remobilisations des minéralisations uranifères. Les brèches contemporaines de la genèse de la minéralisation primaire se sont formées en 3 stades caractérisées par l'analyse fractale des formes de fragments exprimant leur degré de maturité.

Le premier stade de formation des brèches a été initiée par une réactivation des failles inverses à graphite qui a provoqué une fracturation tectonique localisée dans le cœur des failles et une fracturation hydraulique, plus étendue, dans les zones de silicification massive précoce des grès.

Le deuxième stade correspond à la dissolution du quartz due à la circulation verticale d'un fluide de socle sous-saturé par rapport au quartz dans les grès fracturés. Les rapports fluide/roche minimaux calculés sont très élevés de l'ordre de 3 000 dans la zone de Maw et de 38 000 dans les zones à boules de Sue. Cette variation reflète la diminution de l'intensité de la dissolution avec la distance à la discordance. Le volume minimal de fluide de socle ayant circulé dans les brèches est de l'ordre du kilomètre cube. Les calculs de bilans de masse montrent que les fluides ont apporté les éléments U, V, Mg, B, Al, K, Bi, Ni, Co, Mo, As, S, W, Zn, Y et terres rares, conformément aux néoformations d'illite, de sudoite magnésienne et de dravite et au caractère polymétallique des minéralisations dans les grès.

Le troisième stade s'exprime par des phénomènes d'effondrements gravitaires faisant suite à la formation de cavités de dissolution du quartz. Dans les zones à boules développées dans le cœur des failles, c'est la contraction tectonique qui a progressivement refermé les espaces vides créés par la dissolution. Les pertes de volumes peuvent atteindre 90 % dans les zones de dissolution les plus intenses, proches de la discordance. Dans les zones de faille à très fort pendage, les effondrements se sont propagés jusqu'à plus de 250 m au-dessus de la discordance comme dans la zone de Maw, de la même manière que dans un karst.

La précipitation d'uranium provoquée par le mélange du fluide réducteur de socle sous-saturé par rapport au quartz (> 250°C) avec des fluides diagénétiques oxydants de bassin (< 240°C) a eu lieu pendant un temps de l'ordre de plusieurs millions d'années, en liaison avec la dissolution progressive du quartz libérant l'espace nécessaire au piégeage des minéralisations massives.

BRECCIAS ASSOCIATED WITH UNCONFORMITY-TYPE URANIUM DEPOSITS IN THE ATHABASCA BASIN (SASKATCHEWAN, CANADA)

Abstract : Unconformity-type uranium deposits in the Athabasca Basin (Canada) are commonly hosted and surrounded by breccia bodies in quartzose sandstones. In order to understand the mechanisms of breccia formation and their significance for the genesis of uranium deposits, the breccias associated with U mineralizations of the Shea Creek prospect and Sue C open pit, and with the Y-REE-U mineralization of the Maw Zone were studied.

Structural mapping and 3D modeling evidence the control of breccia geometries by reverse faults that are graphite-rich in the basement. The study of mineral paragenesis and calculations of U-Pb chemical ages at Shea Creek reveal 3 breccia phases with sudoite-dravite, Fe-chlorite and hematite-siderite cements. These breccias developed over more than 1 Ga respectively during 3 stages of tectonic reactivations and/or basin uplift mainly between 1.52 and 1.25 Ga during the main event of primary uranium deposition and at about 900 and 350 Ma during phases of uranium remobilization. The breccias coeval with the genesis of the primary mineralization developed in 3 stages characterized by fractal analysis of fragment shapes expressing their degree of maturity.

The first stage of breccia formation has been triggered by a reactivation of graphite-rich reverse faults inducing localized tectonic fracturing in the core of faults and widespread hydraulic fracturing in early silicified zones.

The second stage corresponds to quartz dissolution due to the vertical circulation of a basement fluid undersaturated relative to silica in fractured sandstones. Calculated minimum fluid/rock ratios are very high with values of 3,000 at the Maw Zone and 38,000 in the Sue « zones à boules » reflecting the decrease of dissolution intensity with the increase of distance to the unconformity. The minimum volume of basement fluids that have circulated through the breccias is about 1 km^3. Mass balance calculations show an input of U, V, Mg, B, Al, K, Bi, Ni, Co, Mo, As, S, W, Zn, Y and REE, in accordance with the new formation of illite, Mg-rich sudoite and dravite and with the polymetallic sandstone-hosted mineralization.

The third stage is expressed by gravity-driven collapse phenomenons resulting from the cavities created by quartz dissolution. In « zones à boules » developed in the core of faults, it is the tectonic contraction that progressively closed the open spaces formed by quartz dissolution. Volume loss values reach 90 % in zones of intense dissolution close to the unconformity. In steeply dipping fault zones, collapse propagated up to more than 250 m above the unconformity as observed at the Maw Zone, like in a karst.

Uranium deposition induced by mixing of the reducing basement fluid undersaturated relative to quartz (> 250°C) with diagenetic oxidizing basin fluids (< 240°C) occurred during about several million years, simultaneously with quartz dissolution providing the space needed to form the massive mineralizations.

Mots-clefs : brèche, uranium, discordance, grès, zone de faille, dissolution, bilans de masse, analyse fractale.

Keywords : breccia, uranium, unconformity, sandstone, fault zone, dissolution, mass balance, fractal analysis.

UMR G2R 7566 - Géologie et Gestion des Ressources Minérales et Énergétiques
Université Henri Poincaré Nancy 1, Faculté des Sciences, BP 239, 54506 Vandoeuvre-lès-Nancy Cedex